STATE OF THE CLIMATE IN 2010

J. Blunden, D. S. Arndt, and M. O. Baringer, Eds.

Associate Eds. H. J. Diamond, A. J. Dolman, R. L. Fogt, B. D. Hall, M. Jeffries, J. M. Levy,
J. M. Renwick, J. Richter-Menge, P. W. Thorne, L. A. Vincent, and K. M. Willett

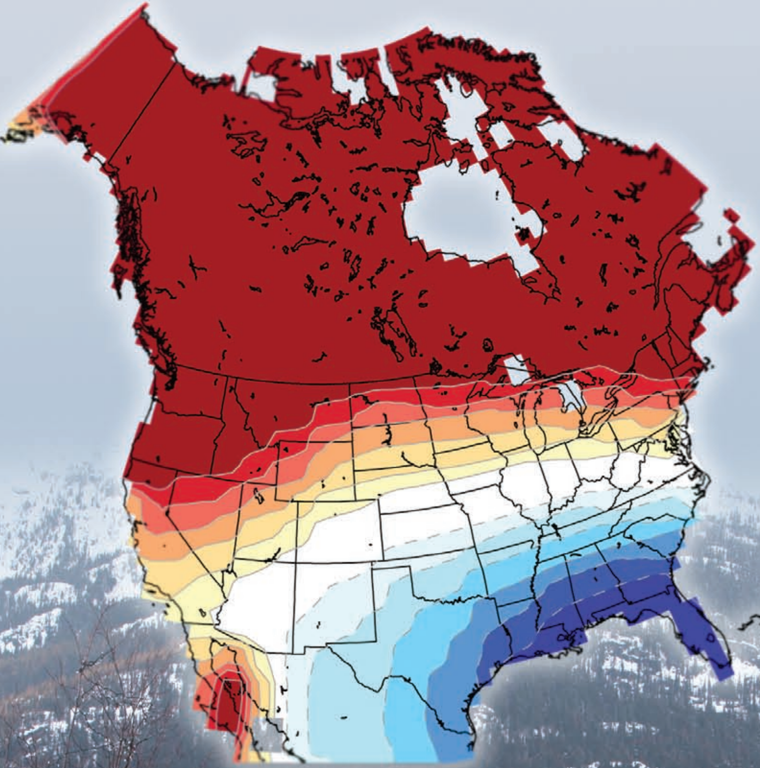

Special Supplement to the
Bulletin of the American Meteorological Society
Vol. 92, No. 6, June 2011

STATE OF THE CLIMATE IN 2010

HOW TO CITE THIS DOCUMENT

Citing the complete report:

Blunden, J., D. S. Arndt, and M. O. Baringer, Eds., 2011: State of the Climate in 2010. *Bull. Amer. Meteor. Soc.*, **92** (6), S1–S266.

Citing a chapter (example):

Fogt, R. L., Ed., 2011: Antarctica [in "State of the Climate in 2010"]. *Bull. Amer. Meteor. Soc.*, **92** (6), S161–S171.

Citing a section (example):

Wovrosh, A. J., S. Barreira, and R. L. Fogt, 2011: [Antarctica] Circulation [in "State of the Climate in 2010"]. *Bull. Amer. Meteor. Soc.*, **92** (6), S161–S163.

EDITOR & AUTHOR AFFILIATIONS (ALPHABETICAL BY NAME)

Achberger, Christine, Earth Sciences Centre, University of Gothenburg, Gothenburg, Sweden

Ackerman, Steven A., CIMSS University of Wisconsin - Madison, Madison, Wisconsin

Ahlstrøm, A., Geological Survey of Denmark and Greenland (GEUS), Copenhagen, Denmark

Alfaro, Eric J., Center for Geophysical Research and School of Physics, University of Costa Rica, San Jose, Costa Rica

Allan, Robert J., Met Office Hadley Centre, Exeter, Devon, United Kingdom

Alves, Lincoln, CPTEC/Instituto Nacional de Pesquisas Espaciais (INPE), São Paulo, Brazil

Amador, Jorge A., Center for Geophysical Research and School of Physics, University of Costa Rica, San Jose, Costa Rica

Amelie, Vincent, Seychelles Meteorological Services, Seychelles

Andrianjafinirina, Solonomenjanahary, Direction Générale de la Météorologie Madagascar

Antonov, John, NOAA/NESDIS National Oceanographic Data Center, Silver Spring, Maryland, and UCAR Joint Office for Science Support, Boulder, Colorado

Arndt, Derek S., NOAA/NESDIS National Climatic Data Center, Asheville, North Carolina

Ashik, Igor, Arctic and Antarctic Research Institute, St. Petersburg, Russia

Atheru, Zachary, IGAD Climate Prediction and Applications Centre, Nairobi, Kenya

Attaher, Samar M., Agricultural Research Center, MALR, Cairo, Egypt

Baez, Julian, DMH-DINAC/CTA-UCA, Asunción, Paraguay

Banzon, Viva, NOAA/NESDIS National Climatic Data Center, Asheville, North Carolina

Baringer, Molly O., NOAA/OAR Atlantic Oceanographic and Meteorological Laboratory, Miami, Florida

Barreira, Sandra, Argentine Naval Hydrographic Service, Buenos Aires, Argentina

Barriopedro, David, Centro de Geofísica da Universidade de Lisboa, Lisbon, Portugal

Barthia, Pawan K., NASA Goddard Space Fight Center, Greenbelt, Maryland

Beal, Lisa M., Division of Meteorology and Physical Oceanography, Rosenstiel School of Marine and Atmospheric Science, Miami, Florida

Becker, Andreas, Global Precipitation Climatology Centre, Deutscher Wetterdienst, Offenbach am Main, Germany

Behrenfeld, Michael J., Oregon State University, Corvallis, Oregon

Bell, Gerald D., NOAA/NWS Climate Prediction Center, Camp Springs, Maryland

Belward, Alan S., Global Environment Monitoring Unit, IES, EC Joint Research Centre, Ispra, Italy

Benedetti, Angela, European Centre for Medium-Range Weather Forecasts, Reading, United Kingdom

Berrisford, Paul, NCAS-Climate, European Centre for Medium-Range Weather Forecasts, Reading, United Kingdom

Berry, David I., National Oceanography Centre, Southampton, United Kingdom

Beszczynska-Moeller, Agnieszka, Alfred Wegener Institute, Bremerhaven, Germany

Bhatt, Uma S., Geophysical Institute, University of Alaska Fairbanks, Fairbanks, Alaska

Bidegain, Mario, Unidad de Ciencias de la Atmósfera, Facultad de Ciencias, Universidad de la República, Uruguay

Bindoff, Nathaniel L., Centre for Australian Weather and Climate Research, CSIRO Marine and Atmospheric Research; and Institute for Marine and Antarctic Studies, University of Tasmania; and Antarctic Climate and Ecosystems Cooperative Research Centre, Hobart, Tasmania, Australia

Bissolli, Peter, Deutscher Wetterdienst (German Meteorological Service, DWD), Offenbach, Germany, and WMO RA VI Regional Climate Centre on Climate Monitoring, Offenbach, Germany

Blake, Eric S., NOAA/NWS National Hurricane Center, Miami, Florida

Blunden, Jessica, STG Inc., NOAA/NESDIS National Climatic Data Center, Asheville, North Carolina

Booneeady, Prithiviraj, Mauritius Meteorological Services, Vacoas, Mauritius

Bosilovich, Michael G., Global Modeling and Assimilation Office, NASA Goddard Space Flight Center, Greenbelt, Maryland

Boudet, Dagne R., Institute of Meteorology of Cuba, Habana, Cuba

Box, Jason E., Byrd Polar Research Center, The Ohio State University, Columbus, Ohio

Boyer, Timothy P., NOAA/NESDIS National Oceanographic Data Center, Silver Spring, Maryland

Bromwich, David H., Byrd Polar Research Center, The Ohio State University, Columbus, Ohio

Brown, Ross, Climate Research Division, Environment Canada, Montréal, Canada

Bryden, Harry L., National Oceanography Centre, Southampton, United Kingdom

Bulygina, Olga N., Russian Institute for Hydrometeorological Information, Obninsk, Russia

Burrows, John, University of Bremen, Bremen, Germany

Butler, J., NOAA/OAR Earth System Research Laboratory, Boulder, Colorado

Cais, Philippe, Laboratoire des Sciences du Climat et de l'Environment (LSCE), CEA-CNR-UVSQ, Gif-sur-Yvette, France

Calderon, Blanca, Center for Geophysical Research, University of Costa Rica, San Jose, Costa Rica

Callaghan, T. V., Royal Swedish Academy of Sciences, Abisko Naturvetenskapliga Station, Abisko, Sweden

Camargo, Suzana J., Lamont-Doherty Earth Observatory, The Earth Institute at Columbia University, Palisades, New York

Cappelen, John, Danish Meteorological Institute, Copenhagen, Denmark

Carmack, Eddy, Institute of Ocean Sciences, Fisheries and Oceans Canada, Sidney, Canada

Chambers, Don P., University of South Florida, St. Petersburg, Florida

Chelliah, Muthuvel, NOAA/NWS Climate Prediction Center, Camp Springs, Maryland

Chidichimo, Maria P., Max-Planck-Institut für Meteorologie, Hamburg, Germany

Christiansen, H., University Centre in Svalbard, Longyearbyen, Norway

Christy, John, University of Alabama, Huntsville, Alabama

Coelho, Caio A. S., CPTEC/INPE, Center for Weather Forecasts and Climate Studies, Cachoeira Paulista, Brazil

Colwell, Steve, British Antarctic Survey, Cambridge, United Kingdom

Comiso, Josefino C., NASA Goddard Space Flight Center, Greenbelt, Maryland

Compo, Gilbert P., CIRES Climate Diagnostics Center, University of Colorado, and NOAA/Earth System Research Laboratory, Boulder, Colorado

Crouch, Jake, NOAA/NESDIS National Climatic Data Center, Asheville, North Carolina

Cunningham, Stuart A., National Oceanography Centre, Southampton, United Kingdom

Cutié, Virgen C., Institute of Meteorology of Cuba, Habana, Cuba

Dai, Aiguo, Earth Observation Laboratory, NCAR, Boulder, Colorado

Davydova-Belitskaya, Valentina, Department of Environmental Sciences, CUCBA, University of Guadalajara, Mexico

de Jeu, Richard, Faculty of Earth and Life Sciences, Department of Hydrology and Geo-Environmental Sciences, VU University, Amsterdam, the Netherlands

Decker, David, Byrd Polar Research Center, The Ohio State University, Columbus, Ohio

Dee, Dick, European Centre for Medium-Range Weather Forecasts, Reading, United Kingdom

Demircan, M., Turkish State Meteorological Service, Kalaba, Ankara, Turkey

Derksen, Chris, Climate Research Division, Environment Canada, Downsview, Canada

Diamond, Howard J., NOAA/NESDIS National Climatic Data Center, Silver Spring, Maryland

Dlugokencky, Ed J., NOAA/OAR Earth System Research Laboratory, Boulder, Colorado

Dohan, Kathleen, Earth and Space Research, Seattle, Washington

Dolman, A. Johannes, Department of Earth Sciences, Faculty of Earth and Life Science, VU University Amsterdam, the Netherlands

Dorigo, Wouter, Institute for Photogrammetry and Remote Sensing, Vienna University of Technology, Vienna, Austria

Drozdov, Dmitry S., Earth Cryosphere Institute, Tumen, Russia

Durack, Paul J., Centre for Australian Weather and Climate Research, CSIRO Marine and Atmospheric Research; and Institute for Marine and Antarctic Studies, University of Tasmania; and Wealth from Oceans National Research Flagship, CSIRO, Hobart, Tasmania, Australia

Dutton, Geoffrey S., Cooperative Institute for Research in Environmental Sciences, University of Colorado, Boulder, Colorado

Easterling, David, NOAA/NESDIS National Climatic Data Center, Asheville, North Carolina

Ebita, Ayataka, Japan Meteorological Agency (JMA), Tokyo, Japan

Eischeid, Jon, NOAA/OAR Earth System Research Laboratory, Boulder, Colorado

Elkins, James W., NOAA/OAR Earth System Research Laboratory, Boulder, Colorado

Epstein, Howard E., Department of Environmental Sciences, University of Virginia, Charlottesville, Virginia

Euscátegui, Christian, Instituto de Hidrología de Meteorología y Estudios Ambientales de Colombia (IDEAM), Colombia

Faijka-Williams, Eleanor, National Oceanography Centre, Southampton, United Kingdom

Famiglietti, James S., UC Center for Hydrologic Modeling Earth System Science, Civil and Environmental Engineering, University of California, Irvine, California

Faniriantsoa, Rija, Direction Générale de la Météorologie Madagascar

Feely, Richard A., NOAA/OAR Pacific Marine Environmental Laboratory, Seattle, Washington

Fekete, Balázs M., CUNY Environmental CrossRoads Initiative, NOAA-CREST Center, The City College of New York City, University of New York, New York, New York

Fenimore, Chris, NOAA/NESDIS National Climatic Data Center, Asheville, North Carolina

Fettweis, Xavier, Department of Geography, University of Liège, Liège, Belgium, and Institute for Marine and Atmospheric Research, Utrecht University, Utrecht, the Netherlands

Fields, Eric, University of California at Santa Barbara, Santa Barbara, California

Fioletov, Vitali E., Environment Canada, Toronto, Canada

Fogarty, Chris T., Environment Canada, Dartmouth, Canada

Fogt, Ryan L., Department of Geography, Ohio University, Athens, Ohio

Forbes, B. C., Arctic Centre, University of Lapland, Rovaniemi, Finland

Foster, Michael J., CIMSS University of Wisconsin Madison, Madison, Wisconsin

Frajka-Williams, E., Ocean Observing and Climate Research Group, National Oceanography Centre, Southampton, United Kingdom

Free, Melissa, NOAA/OAR Air Resources Laboratory, Silver Spring, Maryland

Frolov, Ivan, Arctic and Antarctic Research Institute, St. Petersburg, Russia

Ganesan, A. L., Center for Global Change Science, Massachusetts Institute of Technology, Cambridge, Massachusetts

Ganter, Catherine, Bureau of Meteorology, Melbourne, Australia

Gibney, Ethan J., IMSG, Inc., NOAA/NESDIS National Climatic Data Center, Asheville, North Carolina

Gill, Stephen, NOAA/NOS Center for Operational Oceanographic Products and Services, Silver Spring, Maryland

Gill, M., Environment Canada, Whitehorse, Canada

Gitau, Wilson, Department of Meteorology, University of Nairobi, Kenya

Gleason, Karin L., NOAA/NESDIS National Climatic Data Center, Asheville, North Carolina

Gobron, Nadine, Global Environment Monitoring Unit, IES, EC Joint Research Centre, Ispra, Italy

Goldenberg, Stanley B., NOAA/OAR Atlantic Oceanographic and Meteorological Laboratory, Miami, Florida

Goni, Gustavo J., NOAA/OAR Atlantic Oceanographic and Meteorological Laboratory, Miami, Florida

González, Idelmis G., Institute of Meteorology of Cuba, Habana, Cuba

Good, Simon A., UK Met Office Hadley Centre, Exeter, United Kingdom

Gottschalck, Jonathan, NOAA/NWS Climate Prediction Center, Camp Springs, Maryland

Gould, William A., USDA Forest Service, International Institute of Tropical Forestry, San Juan, Puerto Rico

Gouveia, Celia M., Centro de Geofísica da Universidade de Lisboa, Lisbon Portugal

Griffiths, Georgina M., NIWA, Auckland, New Zealand

Guard, Chip, Weather Forecast Office, Guam

Guevara, Vladimir V., Institute of Meteorology of Cuba, Habana, Cuba

Haas, C., Earth Observation System Laboratory, University of Alberta, Edmonton, Canada

Hall, Bradley D., NOAA/OAR Earth System Research Laboratory, Boulder, Colorado

Halpert, Michael S., NOAA/NWS Climate Prediction Center, Camp Springs, Maryland

Heidinger, Andrew K., NOAA/NESDIS University of Wisconsin Madison, Madison, Wisconsin

Heil, A., ICG-2, Forschungszentrum Jülich, Jülich, Germany

Heim, Richard R., Jr., NOAA/NESDIS National Climatic Data Center, Asheville, North Carolina

Hennon, Paula A., STG, Inc., NOAA/NESDIS National Climatic Data Center, Asheville, North Carolina

Henry, Greg H. R., Geography Department, University of British Columbia, Vancouver, Canada

Hidalgo, Hugo G., Center for Geophysical Research and School of Physics, University of Costa Rica, San Jose, Costa Rica

Hilburn, Kyle, Remote Sensing Systems, Santa Rosa, California

Hirschi, Joël J-M., National Oceanography Centre, Southampton, United Kingdom

Ho, Shu-peng (Ben), NCAR COSMIC, Boulder, Colorado

Hobgood, Jay S., The Ohio State University, Columbus, Ohio

Hoerling, Martin, NOAA/OAR Earth System Research Laboratory, Boulder, Colorado

Holgate, Simon, National Oceanography Centre, Liverpool, United Kingdom

Hook, Simon J., Jet Propulsion Laboratory, Pasadena, California

Hugony, Sebastien, Météo-France, French Polynesia

Hurst, D., Cooperative Institute for Research in Environmental Sciences, University of Colorado Boulder/NOAA, Boulder, Colorado

Ishihara, Hiroshi, Japan Meteorological Agency, Tokyo, Japan

Itoh, M., Japan Agency for Marine-Earth Science and Technology, Tokyo, Japan

Jaimes, Ena, Servicio Nacional de Meteorología e Hidrología de Perú (SENAMHI), Perú

Jeffries, Martin, Geophysical Institute, University of Alaska Fairbanks, Fairbanks, Alaska

Jia, Gensu J., RCE-TEA, Chinese Academy of Sciences, Institute for Atmospheric Physics, Beijing, China

Jin, Xiangze, Woods Hole Oceanographic Institution, Woods Hole, Massachusetts

Johns, William E., Division of Meteorology and Physical Oceanography, Rosenstiel School of Marine and Atmospheric Science, Miami, Florida

Johnson, Bryan, NOAA/OAR Earth System Research Laboratory, and University of Colorado, Boulder, Colorado

Johnson, Gregory C., NOAA/OAR Pacific Marine Environmental Laboratory, Seattle, Washington

Jones, Philip D., Climatic Research Unit, University of East Anglia, Norwich, United Kingdom

Jumaux, Guillaume, Météo-France, Réunion

Kabidi, Khadija, Direction de la Météorologie Nationale, Rabat, Morocco

Kaiser, Johannes W., European Centre for Medium-Range Weather Forecasts, Reading, United Kingdom

Kanzow, Torsten O., IFM-GEOMAR, Kiel, Germany

Kaplan, Alexey, Lamont-Doherty Earth Observatory of Columbia University, Palisades, New York

Kearns, Edward J., NOAA/NESDIS National Climatic Data Center, Asheville, North Carolina

Keller, Linda M., Department of Atmospheric and Oceanic Sciences, University of Wisconsin-Madison, Madison, Wisconsin

Kennedy, John J., Met Office, Exeter, Devon, United Kingdom

Khatiwala, Samar, Lamont-Doherty Earth Observatory, Columbia University, Palisades, New York

Kholodov, Alexander, Geophysical Institute, University of Alaska Fairbanks, Fairbanks, Alaska

Khoshkam, Mahbobeh, Islamic Republic of Iranian Meteorological Organization (IRIMO), Tehran, Iran

Kikuchi, T., Japan Agency for Marine-Earth Science and Technology, Tokyo, Japan

Kimberlain, Todd B., NOAA/NWS National Hurricane Center, Miami, Florida

Knaff, John A., NOAA/NESDIS Center for Satellite Applications and Research, Fort Collins, Colorado

Kobayashi, Shinya, Japan Meteorological Agency (JMA), Tokyo, Japan

Kokelj, Steve V., Water Resources Division, Indian and Northern Affairs Canada, Yellowknife, Canada

Korshunova, Natalia N, All-Russian Research Institue of Hydrometeorological Information – World Data Center, Obninsk, Russia

Kratz, David P., NASA Langley Research Center, Hampton, Virginia

Krishfield, Richard, Woods Hole Oceanographic Institution, Woods Hole, Massachusetts

Kruger, Andries, South African Weather Service, Pretoria, South Africa

Kruk, Michael C., STG, Inc., NOAA/NESDIS National Climatic Data Center, Asheville, North Carolina

Kumar, Arun, NOAA/NWS Climate Prediction Center, Camp Springs, Maryland

Lammers, Richard B., University of New Hampshire, Durham, New Hampshire

Lander, Mark A., University of Guam, Mangilao, Guam

Landsea, Chris W., NOAA/NWS National Hurricane Center, Miami, Florida

Lantuit, Hugues, International Permafrost Association Secretariat, Alfred Wegener Institute for Polar and Marine Research, Potsdam, Germany

Lantz, Trevor C., University of Victoria, British Columbia, Canada

Lapinel, Braulio P., Institute of Meteorology of Cuba, Habana, Cuba

Lareef, Zubair, International Research Institute for Climate and Society, Palisades, New York

Lazzara, Matthew A., Space Science and Engineering Center, University of Wisconsin-Madison, Madison, Wisconsin

León, Antonia L., Institute of Meteorology of Cuba, Habana, Cuba

León, Gloria, Instituto de Hidrología de Meteorología y Estudios Ambientales de Colombia (IDEAM), Colombia

Leuliette, Eric, NOAA/NESDIS Laboratory for Satellite Altimetry, Silver Spring, Maryland

Levitus, Sydney, NOAA/NESDIS National Oceanographic Data Center, Silver Spring, Maryland

Levy, Joel M., NOAA/OAR Climate Program Office, Silver Spring, Maryland

L'Heureux, Michelle, NOAA/NWS Climate Prediction Center, Camp Springs, Maryland

Lin, I-I, Department of Atmospheric Sciences, National Taiwan University, Taipei, Taiwan

Liu, Hongxing, Department of Geography, University of Cincinnati, Cincinnati, Ohio

Liu, Yanju, Beijing Climate Center, China Meteorological Administration, Beijing, China

Liu, Yi, School of Civil and Environmental Engineering, University of New South Wales, Sydney, Australia

Loeb, Norman G., NASA Langley Research Center, Hampton, Virginia

Long, Craig S., NOAA/NWS National Centers for Environmental Prediction, Camp Springs, Maryland

Lorrey, Andrew M., National Institute of Water and Atmospheric Research, Ltd., Auckland, New Zealand

Lumpkin, Rick, NOAA/OAR Atlantic Oceanographic and Meteorological Laboratory, Miami, Florida

Luo, Jing-Jia, Research Institute for Global Change, JAMSTEC, Yokohama, Japan

Lyman, John M., NOAA/OAR Pacific Marine Environmental Laboratory, Seattle, Washington; and Joint Institute for Marine and Atmospheric Research, University of Hawaii, Honolulu, Hawaii

Macdonald, Alison M., Woods Hole Oceanographic Institution, Woods Hole, Massachusetts

Maddux, Brent C., AOS/CIMSS University of Wisconsin Madison, Madison, Wisconsin

Maier, Frank, Laboratory for Climatology and Remote Sensing (LCRS), Department of Geography, University of Marburg, Germany

Malkova, Galina, Earth Cryosphere Institute, Tumen, Russia

Marchenko, Sergey, Geophysical Institute, University of Alaska Fairbanks, Fairbanks, Alaska

Marengo, Jose A., CCST/INPE, São Paulo, Brazil

Maritorena, Stephane, University of California at Santa Barbara, Santa Barbara, California

Marotzke, Jochem, Max-Planck-Institut für Meteorologie, Hamburg, Germany

Martínez Güingla, Rodney, Centro Internacional para la Investigación del Fenómeno El Niño (CIIFEN), Guayaquil, Ecuador

Maslanik, Jochem, Aerospace Engineering Sciences, University of Colorado, Boulder, Colorado

Masson, Robert A., Australian Antarctic Division and Antarctic Climate and Ecosystems Cooperative Research Center (ACE CRC), University of Tasmania, Sandy Bay, Australia

McBride, Charlotte, South African Weather Service, Pretoria, South Africa

McGree, Simon, National Climate Centre, Australian Bureau of Meteorology, Melbourne, Australia

McLaughlin, Fiona, Institute of Ocean Sciences, Fisheries and Oceans Canada, Sidney, Canada

McPeters, Rich, NASA Goddard Space Flight Center, Greenbelt, Maryland

McVicar, Tim R., CSIRO Land and Water, Canberra, Australia

Mears, Carl A., Remote Sensing Systems, Santa Rosa, California

Medany, Mahmoud A., Agricultural Research Center, MALR, Cairo, Egypt

Meier, Walt, National Snow and Ice Data Center, University of Colorado, Boulder, Colorado

Meinen, Christopher S., NOAA/OAR Atlantic Oceanographic and Meteorological Laboratory, Miami, Florida

Merrifield, Mark A., University of Hawaii at Manoa, Honolulu, Hawaii

Miller, Laury, NOAA/NESDIS Laboratory for Satellite Altimetry, Silver Spring, Maryland

Mitchum, Gary T., College of Marine Science, University of South Florida, St. Petersburg, Florida

Montzka, Steve, NOAA/OAR Earth System Research Laboratory, Boulder, Colorado

Morcrette, Jean-Jacques, European Centre for Medium-Range Weather Forecasts, Reading, United Kingdom

Mote, Thomas, Department of Geography, University of Georgia, Athens, Georgia

Mühle, Jens, Scripps Institution of Oceanography, University of California San Diego, La Jolla, California

Mullan, A. Brett, National Institute of Water and Atmospheric Research, Ltd., Wellington, New Zealand

Murray, Don, NOAA/OAR Earth System Research Laboratory, Boulder, Colorado

Nash, Eric R., Science Systems and Applications, Inc., NASA Goddard Space Flight Center, Greenbelt, Maryland

Nerem, Steven R., University of Colorado, Boulder, Colorado

Newman, Paul A., Laboratory for Atmospheres, NASA Goddard Space Flight Center, Greenbelt, Maryland

Nishino, S., Japan Agency for Marine-Earth Science and Technology, Tokyo, Japan

Njau, Leonard, African Centre of Meteorological Applications for Development (ACMAD), Niamey, Niger

Noetzli, J., University of Zürich, Zürich, Switzerland

Oberbauer, S. F., Department of Biological Sciences, Florida International University, Miami, Florida

Oberman, Naum, MIREKO, Syktivkar, Russia

Obregón, Andre, Deutscher Wetterdienst (German Meteorological Service, DWD), Offenbach, Germany, and WMO RA VI Regional Climate Centre on Climate Monitoring, Offenbach, Germany

Ogallo, Laban, IGAD Climate Prediction and Applications Centre (ICPAC), Nairobi, Kenya

Oludhe, Christopher, Department of Meteorology, University of Nairobi, Kenya

O'Malley, Robert T., Oregon State University, Corvallis, Oregon

Overland, James, NOAA/OAR Pacific Marine Environmental Laboratory, Seattle, Washington

Park, Geun-Ha, NOAA/OAR Atlantic Oceanographic and Meteorological Laboratory, Miami, Florida

Parker, David E., Met Office, Exeter, Devon, United Kingdom

Pasch, Richard J., NOAA/NWS National Hurricane Center, Miami, Florida

Pegion, Phil, NOAA/OAR Earth System Research Laboratory, Boulder, Colorado

Peltier, Alexandre, Météo-France, Noumea, New Caledonia

Pelto, Mauri S., Nichols College, Dudley, Massachusetts

Penalba, Olga C., Departamento de Ciencias de la Atmósfera y los Océanos, Universidad de Buenos Aires, Argentina

Pérez, Ramón S., Institute of Meteorology of Cuba, Habana, Cuba

Perlwitz, Judith, NOAA/OAR Earth System Research Laboratory, Boulder, Colorado

Perovich, Donald, ERDC-Cold Regions Research and Engineering Laboratory, Hanover, New Hampshire

Peterson, Thomas C., NOAA/NESDIS National Climatic Data Center, Asheville, North Carolina

Pezza, Alexandre B., University of Melbourne, Melbourne, Australia

Phillips, David, Environment Canada, Toronto, Canada

Pinzon, Jorge E., NASA Goddard Space Flight Center, Greenbelt, Maryland

Pitts, Michael C., NASA Langley Research Center, Hampton, Virginia

Proshutinsky, A., Woods Hole Oceanographic Institution, Woods Hole, Massachusetts

Quegan, S., Centre for Terrestrial Carbon Dynamics, University of Sheffield, Sheffield, United Kingdom

Quintana, Juan, Dirección Meteorológica de Chile, Santiago, Chile

Quintero, Alexander, Servicio de Meteorología de la Aviación (SEMETAVIA), Venezuela

Rabe, B., Alfred Wegener Institute, Bremerhaven, Germany

Rahimzadeh, Fatemeh, Atmospheric Science and Meteorological Research Center (ASMERC), Tehran, Iran

Rajeevan, Madhavan, National Atmospheric Research Laboratory, Gadanki, India

Rayner, Darren, National Oceanography Centre, Southampton, United Kingdom

Rayner, Nick A., Met Office Hadley Centre, Exeter, United Kingdom

Raynolds, Martha K., Institute of Arctic Biology, University of Alaska Fairbanks, Fairbanks, Alaska

Razuvaev, Vyacheslav N., All-Russian Research Institute of Hydrometeorological Information, Obninsk, Russia

Reagan, James R., NOAA/NESDIS National Oceanographic Data Center, Silver Spring, Maryland

Reid, Phillip, Australian Bureau of Meteorology and CAWRC, Hobart, Australia

Renwick, James A., National Institute of Water and Atmospheric Research, Ltd., Wellington, New Zealand

Revadekar, Jayashree, Indian Institute of Tropical Meteorology, Pune, India

Reynolds, Richard W., Cooperative Institute for Climate and Satellites – NC, North Carlina State University, and NOAA/NESDIS National Climatic Data Center, Asheville, North Carolina

Richter-Menge, Jacqueline, ERDC-Cold Regions Research and Engineering Laboratory, Hanover, New Hampshire

Rignot, Eric, University of California-Irvine, NASA Jet Propulsion Laboratory, Irvine, California

Robinson, David A., Rutgers University, Piscataway, New Jersey

Rodell, Matthew, Hydrospheric and Biospheric Sciences Laboratory, NASA Goddard Space Flight Center, Greenbelt, Maryland

Rogers, Mark, Met Office, Exeter, Devon, United Kingdom

Romanovsky, Vladimir, Geophysical Institute, University of Alaska Fairbanks, Fairbanks, Alaska

Romero-Cruz, Fernando, National Meteorological Service of Mexico, CONAGUA, Mexico City, Mexico

Ronchail, Josyane, Université of Paris-Diderot, France

Rosenlof, Karen, NOAA/OAR Earth System Research Laboratory, Boulder, Colorado

Rossi, Shawn, National Weather Service, San Juan, Puerto Rico

Rutledge, Glenn, NOAA/NESDIS National Climatic Data Center, Asheville, North Carolina

Saatchi, Sassan, Jet Propulsion Laboratory, Pasadena, California

Sabine, Christopher L., NOAA/OAR Pacific Marine Environmental Laboratory, Seattle, Washington

Saha, Suranjana, NOAA/NWS Environmental Modeling Center, Camp Springs, Maryland

Sánchez-Lugo, Ahira, NOAA/NESDIS National Climatic Data Center, Asheville, North Carolina

Santee, Michelle L., NASA Jet Propulsion Laboratory, Pasadena, California

Sato, Hitoshi, European Centre for Medium-Range Weather Forecasts, Reading, United Kingdom, and Japan Meteorological Agency (JMA), Tokyo, Japan

Sawaengphokhai, P., Science Systems Applications, Inc., Hampton, Virginia

Sayouri, Amal, Direction de la Météorologie Nationale, Rabat, Morocco

Scambos, Ted A., National Snow and Ice Data Center, University of Colorado, Boulder, Colorado

Schauer, U., Alfred Wegener Institute, Bremerhaven, Germany

Schemm, Jae, NOAA/NWS Climate Prediction Center, Camp Springs, Maryland

Schmid, Claudia, NOAA/OAR Atlantic Oceanographic and Meteorological Laboratory, Miami, Florida

Schneider, Philipp, Jet Propulsion Laboratory, Pasadena, California

Schueller, Dominique, Météo-France, Réunion

Sensoy, Serhat, Turkish State Meteorological Service, Kalaba, Ankara, Turkey

Sharp, Martin, Department of Earth and Atmospheric Sciences, University of Alberta, Edmonton, Canada

Shaver, Gus R., Ecosystem Center, Marine Biological Laboratory, Woods Hole, Massachusetts

Shiklomanov, Alexander I., University of New Hampshire, Durham, New Hampshire

Shiklomanov, N., George Washington University, Washington D.C.

Shimada, Koji, Tokyo University of Marine Science and Technology, Tokyo, Japan

Siegel, David A., University of California at Santa Barbara, Santa Barbara, California

Simmons, Adrian, European Centre for Medium-Range Weather Forecasts, Reading, United Kingdom

Skansi, Maria, Servicio Meteorológico Nacional, Buenos Aires, Argentina

Smith, Adam, NOAA/NESDIS National Climatic Data Center, Asheville, North Carolina

Smith, Cathy, CIRES Climate Diagnostics Center, University of Colorado, and NOAA/Earth System Research Laboratory, Boulder, Colorado

Smith, S., Geological Survey of Canada, Ottawa, Canada

Smith, Thomas M., NOAA/NESDIS Center for Satellite Applications and Research, Silver Spring, Maryland; and Cooperative Institute for Climate and Satellites, University of Maryland, College Park, Maryland

Sokolov, Vladimir, Arctic and Antarctic Research Institute, St. Petersburg, Russia

Spence, Jacqueline M., Meteorological Service of Jamaica, Kingston, Jamaica

Srivastava, Arvind Kumar, India Meteorological Department, Pune, India

Stackhouse, Paul W., Jr., NASA Langley Research Center, Hampton, Virginia

Stammerjohn, Sharon, University of California Santa Cruz, Santa Cruz, California

Steele, Mike, University of Washington, Seattle, Washington

Steinbrecht, Wolfgang, DWD (German Weather Service), Hohenpeissenberg, Germany

Stephenson, Tannecia S., University of the West Indies, Mona, Jamaica

Stolarski, Richard S., Johns Hopkins University, Baltimore, Maryland

Tahani, Lloyd, Ministry of Environment, Climate Change, Disaster Management and Meteorology, Honiara, Solomon Islands

Takahashi, Taro, Lamont-Doherty Earth Observatory, Columbia University, Palisades, New York

Taylor, Michael A., University of the West Indies, Mona, Jamaica

Thépaut, Jean-Noël, European Centre for Medium-Range Weather Forecasts, Reading, United Kingdom

Thiaw, Wassila M., NOAA/NWS Climate Prediction Center, Camp Springs, Maryland

Thorne, Peter W., Cooperative Institute for Climate and Satellites, NCSU/NOAA NCDC, Asheville, North Carolina

Timmermans, M.-L., Yale University, New Haven, Connecticut

Tobin, Skie, Bureau of Meteorology, Melbourne, Australia

Toole, John, Woods Hole Oceanographic Institution, Woods Hole, Massachusetts

Trewin, Blair C., National Climate Centre, Australian Bureau of Meteorology, Melbourne, Australia

Trigo, Ricardo M., Centro de Geofísica da Universidade de Lisboa, Lisbon, Portugal

Tucker, Compton J., NASA Goddard Space Flight Center, Greenbelt, Maryland

Tweedie, Craig E., Department of Biology, University of Texas at El Paso, El Paso, Texas

van As, D., Geological Survey of Denmark and Greenland (GEUS), Copenhagen, Denmark

van de Wal, R. S. W., Institute for Marine and Atmospheric Research, Utrecht University, Utrecht, the Netherlands

van der A, Ronald J., KNMI (Royal Netherlands Meteorological Institute), De Bilt, the Netherlands

van der Werf, G. R., Department of Earth Sciences, Faculty of Earth and Life Sciences, VU University Amsterdam, the Netherlands

Vautard, Robert, Laboratoire des Sciences du Climat et de l'Environment (LSCE), CEA-CNR-UVSQ, Gif-sur-Yvette, France

Vieira, G., University of Lisbon, Lisbon, Portugal

Vincent, Lucie A., Environment Canada, Toronto, Canada

Vinther, B., Niels Bohr Institute, Copenhagen, Denmark

Vose, Russell, NOAA/NESDIS National Climatic Data Center, Asheville, North Carolina

Wagner, Wolfgang, Institute for Photogrammetry and Remote Sensing, Vienna University of Technology, Vienna, Austria

Wahr, John, Department of Physics, University of Colorado, Boulder, Colorado

Walker, David A., Institute of Arctic Biology, University of Alaska Fairbanks, Fairbanks, Alaska

Walsh, John, International Arctic Research Center, University of Alaska Fairbanks, Fairbanks, Alaska

Wang, Chunzai, NOAA/OAR Atlantic Oceanographic and Meteorological Laboratory, Miami, Florida

Wang, Junhong, Earth Observation Laboratory, NCAR, Boulder, Colorado

Wang, Lei, Department of Geography and Anthropology, Louisiana State University, Baton Rouge, Louisianna

Wang, Muyin, Joint Institute for the Study of the Atmosphere and Ocean, University of Washington, Seattle, Washington

Wang, Sheng-Hung, Byrd Polar Research Center, The Ohio State University, Columbus, Ohio

Wanninkhof, Rik, NOAA/OAR Atlantic Oceanographic and Meteorological Laboratory, Miami, Florida

Weaver, Scott, NOAA/NWS Climate Prediction Center, Camp Springs, Maryland

Webber, Patrick J., Department of Plant Biology, Michigan State University, East Lansing, Michigan

Weber, Mark, University of Bremen, Bremen, Germany

Weller, Robert A., Woods Hole Oceanographic Institution, Woods Hole, Massachusetts

Weyman, James, NOAA/NWS Central Pacific Hurricane Center, Honolulu, Hawaii (retired)

Whitewood, Robert, Environment Canada, Toronto, Canada

Wijffels, Susan E., Centre for Australian Weather and Climate Research, CSIRO Marine and Atmospheric Research, and Wealth from Oceans National Research Flagship, CSIRO, Hobart, Tasmania, Australia

Wilber, Anne C., Science Systems Applications, Inc., Hampton, Virginia

Willett, Katharine M., Met Office Hadley Centre, Exeter, Devon, United Kingdom,

Williams, W., Institute of Ocean Sciences, Fisheries and Oceans Canada, Sidney, British Columbia, Canada

Willis, Joshua K., Jet Propulsion Laboratory, California Institute of Technology, Pasadena, California

Wolken, Gabriel, Alaska Division of Geological & Geophysical Surveys, Fairbanks, Alaska

Wong, Takmeng, NASA Langley Research Center, Hampton, Virginia

Woodgate, Rebecca, University of Washington, Seattle, Washington

Woodworth, Philip, National Oceanography Centre, Liverpool, United Kingdom

Wovrosh, Alex J., Department of Geography, Ohio University, Athens, Ohio

Xue, Yan, NOAA/NWS Climate Prediction Center, Camp Springs, Maryland

Yamamoto-Kawai, M., Tokyo University of Marine Science and Technology, Tokyo, Japan

Yin, Xungang, STG, Inc., NOAA/NESDIS National Climatic Data Center, Asheville, North Carolina

Yu, Lisan, Woods Hole Oceanographic Institution, Woods Hole, Massachusetts

Zhang, Liangying, Earth Observation Laboratory, NCAR, Boulder, Colorado

Zhang, Peiqun, National Climate Centre, CMA, Beijing, China

Zhao, L., Cold and Arid Regions Environmental and Engineering Research Institute, Lanzhou, China

Zhou, Xinjia, NCAR COSMIC, Boulder, Colorado

Zimmermann, S., Institute of Ocean Sciences, Fisheries and Oceans Canada, Sidney, Canada

TABLE OF CONTENTS

ABSTRACT—J. BLUNDEN, D. S. ARNDT, AND M. O. BARINGER

Several large-scale climate patterns influenced climate conditions and weather patterns across the globe during 2010. The transition from a warm El Niño phase at the beginning of the year to a cool La Niña phase by July contributed to many notable events, ranging from record wetness across much of Australia to historically low Eastern Pacific basin and near-record high North Atlantic basin hurricane activity. The remaining five main hurricane basins experienced below- to well-below-normal tropical cyclone activity. The negative phase of the Arctic Oscillation was a major driver of Northern Hemisphere temperature patterns during 2009/10 winter and again in late 2010. It contributed to record snowfall and unusually low temperatures over much of northern Eurasia and parts of the United States, while bringing above-normal temperatures to the high northern latitudes. The February Arctic Oscillation Index value was the most negative since records began in 1950.

The 2010 average global land and ocean surface temperature was among the two warmest years on record. The Arctic continued to warm at about twice the rate of lower latitudes. The eastern and tropical Pacific Ocean cooled about 1°C from 2009 to 2010, reflecting the transition from the 2009/10 El Niño to the 2010/11 La Niña. Ocean heat fluxes contributed to warm sea surface temperature anomalies in the North Atlantic and the tropical Indian and western Pacific Oceans. Global integrals of upper ocean heat content for the past several years have reached values consistently higher than for all prior times in the record, demonstrating the dominant role of the ocean in the Earth's energy budget. Deep and abyssal waters of Antarctic origin have also trended warmer on average since the early 1990s. Lower tropospheric temperatures typically lag ENSO surface fluctuations by two to four months, thus the 2010 temperature was dominated by the warm phase El Niño conditions that occurred during the latter half of 2009 and early 2010 and was second warmest on record. The stratosphere continued to be anomalously cool.

Annual global precipitation over land areas was about five percent above normal. Precipitation over the ocean was drier than normal after a wet year in 2009. Overall, saltier (higher evaporation) regions of the ocean surface continue to be anomalously salty, and fresher (higher precipitation) regions continue to be anomalously fresh. This salinity pattern, which has held since at least 2004, suggests an increase in the hydrological cycle.

Sea ice conditions in the Arctic were significantly different than those in the Antarctic during the year. The annual minimum ice extent in the Arctic—reached in September—was the third lowest on record since 1979. In the Antarctic, zonally averaged sea ice extent reached an all-time record maximum from mid-June through late August and again from mid-November through early December. Corresponding record positive Southern Hemisphere Annular Mode Indices influenced the Antarctic sea ice extents.

Greenland glaciers lost more mass than any other year in the decade-long record. The Greenland Ice Sheet lost a record amount of mass, as the melt rate was the highest since at least 1958, and the area and duration of the melting was greater than any year since at least 1978. High summer air temperatures and a longer melt season also caused a continued increase in the rate of ice mass loss from small glaciers and ice caps in the Canadian Arctic. Coastal sites in Alaska show continuous permafrost warming and sites in Alaska, Canada, and Russia indicate more significant warming in relatively cold permafrost than in warm permafrost in the same geographical area. With regional differences, permafrost temperatures are now up to 2°C warmer than they were 20 to 30 years ago. Preliminary data indicate there is a high probability that 2010 will be the 20th consecutive year that alpine glaciers have lost mass.

Atmospheric greenhouse gas concentrations continued to rise and ozone depleting substances continued to decrease. Carbon dioxide increased by 2.60 ppm in 2010, a rate above both the 2009 and the 1980–2010 average rates. The global ocean carbon dioxide uptake for the 2009 transition period from La Niña to El Niño conditions, the most recent period for which analyzed data are available, is estimated to be similar to the long-term average. The 2010 Antarctic ozone hole was among the lowest 20% compared with other years since 1990, a result of warmer-than-average temperatures in the Antarctic stratosphere during austral winter between mid-July and early September.

1. INTRODUCTION—D. S. Arndt, J. Blunden, and M. O. Baringer

The primary goal of the annual *State of the Climate* collection of articles is to document the weather and climate events of the most recent calendar year and put them into accurate historical perspective, with a particular focus on unusual or anomalous events. This is the 21st annual edition of this effort, including its origin as NOAA's *Climate Assessment*, and the 16th consecutive year of its association with the *Bulletin of the American Meteorological Society*. The *State of the Climate* series continues to grow in scope and authorship. This edition presents contributions from the largest body of authors to date and brings several new sections to the readership.

The year 2010 was notable for its globally-averaged warmth and for the far-reaching impacts related to significant behavior of several modes of climate variability. These modes have unique influences and impacts throughout the climate system. Indeed, each chapter in this document contains special mention of ENSO, or the various hemispheric indices such as the Arctic Oscillation or Southern Annular Mode. Sidebar 1.1, which was coordinated by the Chapter 2 (Global Climate) editors, is intended as an introductory overview of selected known modes of variability. More practically, it serves as a data-laden reference for readers of later chapters. The online supplement includes additional data that allow the reader to investigate further.

Different regions have different sensitivities and thus varying definitions of ENSO. This, combined with the global authorship of the *State of the Climate in 2010*, led to various descriptors of the peak strengths of the early-2010 El Niño episode and the late-2010 La Niña. This was standardized, where possible, using NOAA's description of "strong" for El Niño and "moderate-to-strong" for La Niña. In more regional discussions, these descriptors have not been changed.

To build a broader description of the climate system, this report aims each year to increase the number of represented Essential Climate Variables (ECVs), as defined and maintained by the climate observing community through the Global Climate Observing System (GCOS 2003; Fig. 1.1). To that end, new editors representing expertise in two broad disciplines (terrestrial processes and atmospheric composition) were added to the panel serving Chapter 2.

The following ECVs included in this edition are considered "fully monitored", such that they are observed and analyzed across much of the world, with a sufficiently long-term dataset that has peer-reviewed documentation:

- Atmospheric Surface: air temperature, precipitation, air pressure, water vapor*.
- Atmospheric Upper Air: earth radiation budget, temperature, water vapor, cloud properties.
- Atmospheric Composition: carbon dioxide, methane, ozone, nitrous oxide, chlorofluorocarbons, hydrochlorofluorocarbons, hydrofluorocarbons, sulphur hexafluorides, perflurocarbons*, aerosols.
- Ocean Surface: temperature, salinity, sea level, sea ice, current, ocean color.
- Ocean Subsurface: temperature, salinity*.
- Terrestrial: snow and ice cover.

ECVs in this edition that are considered "partially monitored", meeting some but not all of the above requirements, include:

- Atmospheric Surface: wind speed and direction.
- Atmospheric Composition: long-lived greenhouse gases not listed as fully monitored above.
- Ocean Surface: carbon dioxide.
- Ocean Subsurface: current, carbon.
- Terrestrial: soil moisture, permafrost, glaciers and ice sheets, river discharge, groundwater*, lake levels, fraction of absorbed photosynthetically-active radiation, biomass, fire disturbance.

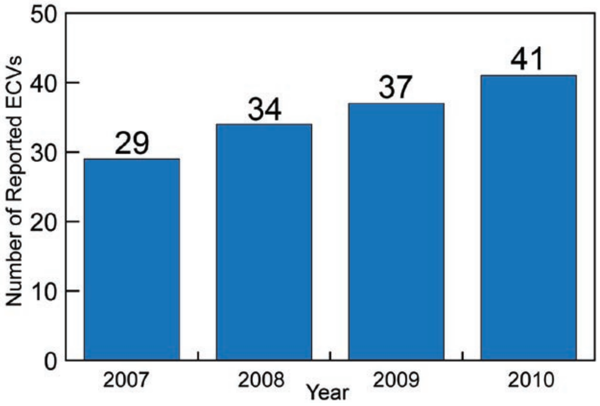

Fig. 1.1. Number of fully or partially monitored Essential Climate Variables (ECVs) reported in the annual *State of the Climate* editions since 2007. Atmospheric surface water vapor, atmospheric perfluorocarbons, oceanic subsurface salinity, and terrestrial groundwater have been introduced in this current edition.

ECVs that are expected to be added in the future include:

- Atmospheric Surface: surface radiation budget.
- Atmospheric Upper Air: wind speed and direction.
- Ocean Surface: sea state.
- Ocean Subsurface: nutrients, ocean tracers, phytoplankton.
- Terrestrial: surface ground temperature, subsurface temperature and moisture, water use, albedo, land cover, leaf area index.

**These ECVs were introduced to the report in this edition.*

A brief overview of the findings in this report is presented in the Abstract and shown in Fig. 1.2. The remainder of the report is organized starting with global-scale climate variables (Chapter 2) to increasingly divided geographic regions described in Chapters 3 through 7. Chapter 3 highlights the global ocean and Chapter 4 includes tropical climate phenomena such as El Niño/La Niña and tropical cyclones. The Arctic and Antarctic respond differently through time and hence are reported in separate chapters (5 and 6). Chapter 7 provides a regional perspective authored largely by local government climate specialists. Sidebars included in each chapter are intended to provide background information on a significant climate event from 2010, a developing technology, or an emerging dataset germane to the chapter's content.

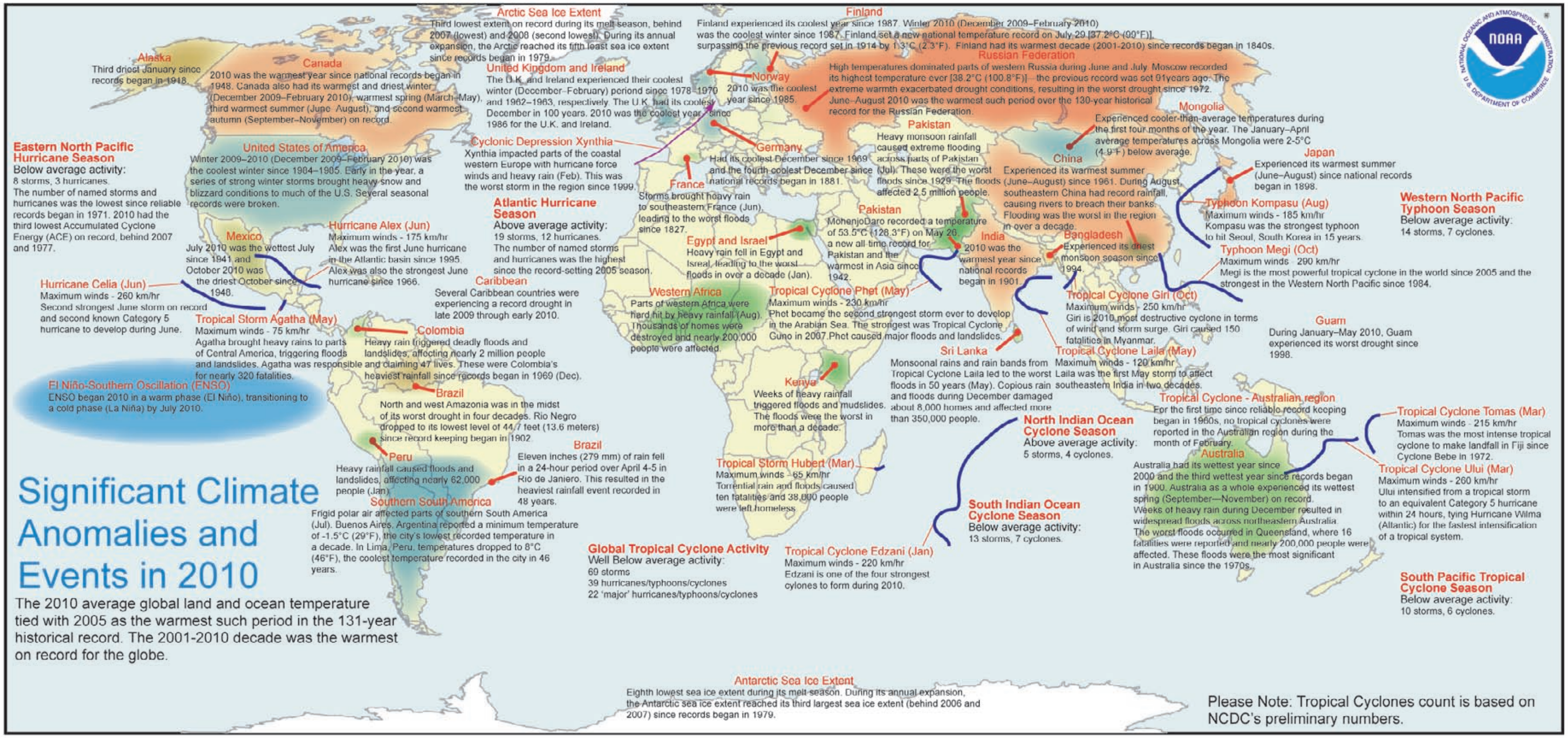

Significant Climate Anomalies and Events in 2010

The 2010 average global land and ocean temperature tied with 2005 as the warmest such period in the 131-year historical record. The 2001-2010 decade was the warmest on record for the globe.

Alaska
Third driest January since records began in 1918.

Canada
2010 was the warmest year since national records began in 1948. Canada also had its warmest and driest winter (December 2009–February 2010), warmest spring (March–May), third warmest summer (June–August), and second warmest autumn (September–November) on record.

Arctic Sea Ice Extent
Third lowest extent on record during its melt season, behind 2007 (lowest) and 2008 (second lowest). During its annual expansion, the Arctic reached its fifth least sea ice extent since records began in 1979.

United Kingdom and Ireland
The U.K. and Ireland experienced their coolest winter (December–February) periond since 1978–1979 and 1962–1963, respectively. The U.K. had its coolest December in 100 years. 2010 was the coolest year since 1986 for the U.K. and Ireland.

Finland
Finland experienced its coolest year since 1987. Winter 2010 (December 2009–February 2010) was the coolest winter since 1987. Finland set a new national temperature record on July 29 [37.2°C (99°F)], surpassing the previous record set in 1914 by 1.3°C (2.3°F). Finland had its warmest decade (2001-2010) since records began in 1840s.

Norway
2010 was the coolest year since 1985.

Russian Federation
High temperatures dominated parts of western Russia during June and July. Moscow recorded its highest temperature ever [38.2°C (100.8°F)]—the previous record was set 91years ago. The extreme warmth exacerbated drought conditions, resulting in the worst drought since 1972. June–August 2010 was the warmest such period over the 130-year historical record for the Russian Federation.

Mongolia
Experienced cooler-than-average temperatures during the first four months of the year. The January–April average temperatures across Mongolia were 2-5°C (4-9°F) below average.

Japan
Experienced its warmest summer (June–August) since national records began in 1898.

Eastern North Pacific Hurricane Season
Below average activity:
8 storms, 3 hurricanes.
The number of named storms and hurricanes was the lowest since reliable records began in 1971. 2010 had the third lowest Accumulated Cyclone Energy (ACE) on record, behind 2007 and 1977.

United States of America
Winter 2009–2010 (December 2009–February 2010) was the coolest winter since 1984–1985. Early in the year, a series of strong winter storms brought heavy snow and blizzard conditions to much of the U.S. Several seasonal records were broken.

Cyclonic Depression Xynthia
Xynthia impacted parts of the coastal western Europe with hurricane force winds and heavy rain (Feb). This was the worst storm in the region since 1999.

Germany
Had its coolest December since 1969 and the fourth coolest December since national records began in 1881.

France
Storms brought heavy rain to southeastern France (Jun), leading to the worst floods since 1827.

Pakistan
Heavy monsoon rainfall caused extreme flooding across parts of Pakistan (Jul). These were the worst floods since 1929. The floods affected 2.5 million people.

China
Experienced its warmest summer (June–August) since 1961. During August, southeastern China had record rainfall, causing rivers to breach their banks. Flooding was the worst in the region in over a decade.

Typhoon Kompasu (Aug)
Maximum winds - 185 km/hr
Kompasu was the strongest typhoon to hit Seoul, South Korea in 15 years.

Western North Pacific Typhoon Season
Below average activity:
14 storms, 7 cyclones.

Mexico
July 2010 was the wettest July since 1941 and October 2010 was the driest October since 1948.

Hurricane Alex (Jun)
Maximum winds - 175 km/hr
Alex was the first June hurricane in the Atlantic basin since 1995. Alex was also the strongest June hurricane since 1966.

Atlantic Hurricane Season
Above average activity:
19 storms, 12 hurricanes.
The number of named storms and hurricanes was the highest since the record-setting 2005 season.

Egypt and Israel
Heavy rain fell in Egypt and Isreal, leading to the worst floods in over a decade (Jan).

Pakistan
MohenjoDaro recorded a temperature of 53.5°C (128.3°F) on May 26, a new all-time record for Pakistan and the warmest in Asia since 1942.

India
2010 was the warmest year since national records began in 1901.

Bangladesh
Experienced its driest monsoon season since 1994.

Typhoon Megi (Oct)
Maximum winds - 290 km/hr
Megi is the most powerful tropical cyclone in the world since 2005 and the strongest in the Western North Pacific since 1984.

Hurricane Celia (Jun)
Maximum winds - 260 km/hr
Second strongest June storm on record and second known Category 5 hurricane to develop during June.

Caribbean
Several Caribbean countries were experiencing a record drought in late 2009 through early 2010.

Western Africa
Parts of western Africa were hard hit by heavy rainfall (Aug). Thousands of homes were destroyed and nearly 200,000 people were affected.

Tropical Cyclone Phet (May)
Maximum winds - 230 km/hr
Phet became the second strongest storm ever to develop in the Arabian Sea. The strongest was Tropical Cyclone Guno in 2007.Phet caused major floods and landslides.

Tropical Cyclone Giri (Oct)
Maximum winds - 250 km/hr
Giri is 2010 most destructive cyclone in terms of wind and storm surge. Giri caused 150 fatalities in Myanmar.

Tropical Storm Agatha (May)
Maximum winds - 75 km/hr
Agatha brought heavy rains to parts of Central America, triggering floods and landslides. Agatha was responsible for nearly 320 fatalities.

Colombia
Heavy rain triggered deadly floods and landslides, affecting nearly 2 million people and claiming 47 lives. These were Colombia's heaviest rainfall since records began in 1969 (Dec).

Guam
During January–May 2010, Guam experienced its worst drought since 1998.

Sri Lanka
Monsoonal rains and rain bands from Tropical Cyclone Laila led to the worst floods in 50 years (May). Copious rain and floods during December damaged about 8,000 homes and affected more than 350,000 people.

Tropical Cyclone Laila (May)
Maximum winds - 120 km/hr
Laila was the first May storm to affect southeastern India in two decades.

El Niño-Southern Oscillation (ENSO)
ENSO began 2010 in a warm phase (El Niño), transitioning to a cold phase (La Niña) by July 2010.

Brazil
North and west Amazonia was in the midst of its worst drought in four decades. Rio Negro dropped to its lowest level of 44.7 feet (13.6 meters) since record keeping began in 1902.

Kenya
Weeks of heavy rainfall triggered floods and mudslides. The floods were the worst in more than a decade.

Tropical Cyclone - Australian region
For the first time since reliable record keeping began in 1960s, no tropical cyclones were reported in the Australian region during the month of February.

Tropical Cyclone Tomas (Mar)
Maximum winds - 215 km/hr
Tomas was the most intense tropical cyclone to make landfall in Fiji since Cyclone Bebe in 1972.

North Indian Ocean Cyclone Season
Above average activity:
5 storms, 4 cyclones.

Brazil
Eleven inches (279 mm) of rain fell in a 24-hour period over April 4-5 in Rio de Janiero. This resulted in the heaviest rainfall event recorded in 48 years.

Peru
Heavy rainfall caused floods and landslides, affecting nearly 62,000 people (Jan).

Southern South America
Frigid polar air affected parts of southern South America (Jul). Buenos Aires, Argentina reported a minimum temperature of -1.5°C (29°F), the city's lowest recorded temperature in a decade. In Lima, Peru, temperatures dropped to 8°C (46°F), the coolest temperature recorded in the city in 46 years.

Tropical Storm Hubert (Mar)
Maximum winds - 65 km/hr
Torrential rain and floods caused ten fatalities and 38,000 people were left homeless.

Australia
Australia had its wettest year since 2000 and the third wettest year since records began in 1900. Australia as a whole experienced its wettest spring (September—November) on record.
Weeks of heavy rain during December resulted in widespread floods across northeastern Australia. The worst floods occurred in Queensland, where 16 fatalities were reported and nearly 200,000 people were affected. These floods were the most significant in Australia since the 1970s.

Tropical Cyclone Ului (Mar)
Maximum winds - 260 km/hr
Ului intensified from a tropical storm to an equivalent Category 5 hurricane within 24 hours, tying Hurricane Wilma (Atlantic) for the fastest intensification of a tropical system.

South Indian Ocean Cyclone Season
Below average activity:
13 storms, 7 cyclones.

Global Tropical Cyclone Activity
Well Below average activity:
69 storms
39 hurricanes/typhoons/cyclones
22 'major' hurricanes/typhoons/cyclones

Tropical Cyclone Edzani (Jan)
Maximum winds - 220 km/hr
Edzani is one of the four strongest cylones to form during 2010.

South Pacific Tropical Cyclone Season
Below average activity:
10 storms, 6 cyclones.

Antarctic Sea Ice Extent
Eighth lowest sea ice extent during its melt season. During its annual expansion, the Antarctic sea ice extent reached its third largest sea ice extent (behind 2006 and 2007) since records began in 1979.

Please Note: Tropical Cyclones count is based on NCDC's preliminary numbers.

Fig. 1.2. Geographical distribution of notable climate anomalies and events occurring around the planet in 2010.

SIDEBAR 1.1: PATTERNS AND INDICES OF CLIMATE VARIABILITY—

A. KAPLAN

Climate variability is not uniform in space; it can be described as a combination of some "preferred" spatial patterns. The most prominent of these are known as modes of climate variability, which affect weather and climate on many spatial and temporal scales. The best known and truly periodic climate variability mode is the seasonal cycle. Others are quasi-periodic or of wide spectrum temporal variability. Climate modes themselves and their influence on regional climates are often identified through spatial teleconnections, i.e., relationships between climate variations in places far removed from each other.

For example, Walker (1924) named the Southern Oscillation (SO) and associated its negative phase with Indian monsoon failure. Later, Bjerknes (1969) connected negative SO phases with El Niño occurrences episodes of amplified seasonal ocean surface warming in the eastern equatorial Pacific and coastal Peru (Fig. 1.3a). Subsequently, the El Niño—Southern Oscillation (ENSO) was observed to be a powerful, demonstrably coupled tropical ocean-atmosphere variability with a global set of climate impacts. In recent years, ENSO events were separated into canonical (Eastern Pacific) and Central Pacific ENSO events (a.k.a. "Modoki", Fig. 1.3b; see Ashok et al. 2007).

Walker (1924) also noticed a smaller-scale (compared to the SO) seesawing surface pressure between the Azores and Iceland (Fig. 1.3c) and named it the North Atlantic Oscillation (NAO; Stephenson et al. 2003). A positive phase of the NAO strengthens the Atlantic storm track and moves it northward, resulting in warm and wet European winters, and cold and dry winters in Greenland and northeastern Canada. In the negative phase the storm track is weaker and more eastward in direction, resulting in wetter winters in southern Europe and the Mediterranean and a colder northern Europe (Hurrell et al. 2003).

Traditionally, indices of climate variability were defined as linear combinations of seasonally-averaged anomalies from meteorological stations chosen in the proximity of maxima and minima of the target pattern. Since gridded fields of climate variables are now available, appropriate regional averages often replace station data. The strongest teleconnections in a climate field are also identified by pairs of grid points with the strongest anti-correlation (Wallace and Gutzler 1981). Table 1.1 defines the most prominent modes of largescale climate variability and the various indices used to define them; changes in these indices are associated with large-scale changes in climate fields. With some exceptions, indices included in Table 1.1 generally have been (1) used by a variety of authors and (2) defined relatively simply from raw or statistically analyzed observations of a single surface climate variable, so that observational datasets longer than a century exist.

Climate variability modes sometimes force other modes of climate variability. For example, a principal component analysis of the North Pacific sea surface temperature (SST) anomaly field (20°N–70°N), relative to the global mean, gives a pattern and index of the Pacific Decadal Oscillation (PDO; Mantua et al. 1997; Zhang et al. 1997), illustrated in Fig. 1.3d. It is different from ENSO but thought to be connected to it through atmospheric bridges and/or internal oceanic wave propagation (Newman et al. 2003; Newman 2007; Schneider and Cornuelle 2005). Despite being defined with Northern Hemisphere data only and being similar to the simple mean sea level pressure-based North Pacific Index (NPI; Trenberth and Hurrell 1994), the PDO index captures well variability in both hemispheres and is similar to the Interdecadal Pacific Oscillation (IPO; Folland et al. 1999; Power et al. 1999).

Principal component analysis of the entire Northern Hemisphere extratropical sea level pressure field identifies a leading mode known as the Northern Annular Mode (NAM) or Arctic Oscillation (AO), which turns out to be very similar to the NAO (Thompson and Wallace 1998, 2000). The Pacific North American pattern (PNA; Fig. 1.3e) also appears as one of the leading variability patterns in the Northern Hemisphere. A Southern Hemisphere analogue of the NAM is the Southern Annular Mode (SAM, Fig. 1.3f), also referred to as the Antarctic Oscillation (AAO), calculated using mean sea level pressure, 850 hPa, or 750 hPa geopotential height in the extratropical Southern Hemisphere (Gong and Wang 1999; Thompson and Wallace 2000).

Atlantic Ocean meridional circulation is affected by the Atlantic Meridional Oscillation (AMO; Fig. 1.3g), which is indexed by the average Atlantic Ocean SST from which the long-term trend is removed (Enfield et al. 2001; Trenberth and Shea 2006). Regional modes of tropical climate variability were identified in Atlantic and Indian Oceans: Atlantic Niño mode and tropical Atlantic meridional mode, Indian Ocean Basin Mode, and Indian Ocean Dipole mode (Fig. 1.3h-k). These modes dominate SST variability in these regions (Deser et al. 2010). The "Cold Ocean-Warm Land" (COWL, Fig. 1.3l) variability is not thought to represent a "true" climate variability mode (Wallace et al. 1995) but has proved very useful for interpreting variations in the hemispheric-scale surface temperature means (Thompson et al. 2008).

The multiplicity of indices defining the same climate phenomenon arises because no index can achieve a perfect separation of a target phenomenon from all other effects in the real climate system [e.g., see Compo and Sardeshmukh (2010) discussion for the ENSO case]. As a result, each index is affected by many climate phenomena whose relative contributions change with time periods and data used. Limited length and quality of observational record compounds this problem. Thus the choice of indices is always application specific.

Table 1.1: Established indices of climate variability with global or regional influence.

Climate Phenomenon	Index name	Index Definition	Primary References	Characterization / Comments
El Niño – Southern Oscillation (ENSO) - canonical, Eastern Pacific ENSO	NINO3	SST anomaly averaged over (5°S–5°N, 150°W–90°W)	Cane et al. (1986); Rasmusson and Wallace (1983)	Traditional SST-based ENSO index
	NINO3.4	SST anomaly averaged over (5°S–5°N, 170°W–120°W)	Trenberth (1997)	Used by NOAA to define El Niño/La Niña events. Detrended form is close to the 1st PC of linearly detrended global field of monthly SST anomalies (Deser et al. 2010)
	Cold Tongue Index (CTI)	SSTA (6°N–6°S, 180°–90°W) minus global mean SSTA	Deser and Wallace (1990)	Matches “cold tongue” area, subtracts effect of the global average change
	Troup SOI	Standardized for each calendar month MSLP difference: Tahiti minus Darwin, x10	Troup (1965)	Used by Australian Bureau of Meteorology
	SOI	Standardized difference of standardized MSLP anomalies: Tahiti minus Darwin	Trenberth (1984)	Maximizes signal to noise ratio of linear combinations of Darwin/Tahiti records
	Darwin SOI	Standardized Darwin MSLP anomaly	Trenberth and Hoar (1996)	Introduced to avoid use of the Tahiti record, considered suspicious before 1935.
	Equatorial SOI (EQSOI)	Standard difference of standard MSLP anomalies over equatorial (5°S–5°N) Pacific Ocean; east (130°W–80°W) minus west (90°E–140°E)	Bell and Halpert (1998)	
Central Pacific El Niño (Modoki)	El Niño Modoki Index (EMI)	SSTA: [165°E–140°W, 10°S–10°N] minus ½[110°W–70°W, 15°S–5°N] minus ½[125°E–145°E, 10°S-20°N]	Ashok et al. (2007)	A recently identified ENSO variant: Modoki or Central Pacific El Niño (non-canonical)

cont. SIDEBAR 1.1: PATTERNS AND INDICES OF CLIMATE VARIABILITY—A. KAPLAN

Climate Phenomenon	Index name	Index Definition	Primary References	Characterization / Comments
Pacific Decadal and Interdecadal Variability	Pacific Decadal Oscillation (PDO)	1st PC of the N. Pacific SST anomaly field (20°N–70°N) with subtracted global mean	Mantua et al. (1997); Zhang et al. (1997)	
	Intedecadal Pacific Oscillation (IPO)	The 3rd EOF3 of the 13-year low-pass filtered global SST, projected onto annual data	Folland et al. (1999); Power et al. (1999)	
	North Pacific Index (NPI)	SLP (30°N–65°N, 160°E–140°W)	Trenberth and Hurrell (1994)	
North Atlantic Oscillation	Lisbon/Ponta Delgada-Stykkisholmur/ Reykjavik North Atlantic Oscillation (NAO) Index	Lisbon/Ponta Delgada minus Stykkisholmur/ Reykjavik standardized MSLP anomalies	Hurrell (1995)	A primary NH teleconnection both in MSLP and Z500 anomalies (Wallace and Gutzler 1981); one of rotated EOFs of NH Z500 (Barnston and Livezey 1987) . MSLP anomalies can be monthly, seasonal or annual averages. Each choice carries to the temporal resolution of the NAO index produced that way.
	Gibraltar - Reykjavik NAO Index	Gibraltar minus Reykjavik standardized MSLP anomalies	Jones et al. (1997)	
	PC-based NAO Index	Leading PC of MSLP anomalies over the Atlantic sector (20°N–80°N, 90ºW–40ºE)	Hurrell (1995)	
Annular modes: Arctic Oscillation (AO), a.k.a. Northern Annular Mode (NAM) Index and Antarctic Oscillation (AAO), a.k.a. Southern Annular Mode (SAM) Index	PC-based AO index	1st PC of the monthly mean MSLP anomalies poleward of 20°N	Thompson and Wallace (1998, 2000)	Closely related to the NAO
	PC-based AAO index	1st PC of 850hPa or 700hPa height anomalies south of 20ºS	Thompson and Wallace (2000)	
	Grid-based AAO index: 40°S–65°S difference	Difference between normalized zonal mean MSLP at 40°S and 65°S, using gridded SLP analysis	Gong and Wang (1999)	
	Grid-based AAO index: 40°S–70°S difference	Same as above but uses latitudes 40°S and 70°S	Nan and Li (2003)	
	Station-based AAO index: 40°S–65°S	Difference in normalized zonal mean MSLP at 40°S and 65°S, using station data	Marshall (2003)	

Climate Phenomenon	Index name	Index Definition	Primary References	Characterization / Comments
Pacific/North America (PNA) atmospheric teleconnection	PNA pattern index	¼[Z(20°N, 160°W) - Z(45°N, 165°W) + Z(55°N, 115°W) - Z(30°N, 85°W)], Z is the location's standardized 500 hPa geopotential height anomaly	Wallace and Gutzler (1981)	A primary NH teleconnection both in MSLP and Z500 anomalies
Atlantic Ocean Themohaline circulation	Atlantic Multidecadal Oscillation (AMO) index	10-yr running mean of de-trended Atlantic mean SST anomalies (0°–70°N)	Enfield et al. (2001)	Called "virtually identical" to the smoothed first rotated N. Atlantic EOF mode
	Revised AMO index	As above, but subtracts global mean anomaly instead of de-trending	Trenberth and Shea (2006)	
Tropical Atlantic Ocean non-ENSO variability	Atlantic Niño Index, ATL3	SSTA (3°S–3°N, 20°W–0°)	Zebiak (1993)	Identified as the two leading PCs of detrended tropical Atlantic monthly SSTA (20°S–20°N): 38% and 25% variance respectively for HadISST1, 1900–2008 (Deser et al. 2010)
	Atlantic Niño Index, PC-based	1st PC of the detrended tropical Atlantic monthly SSTA (20°S–20°N)	Deser et al. (2010)	
	Tropical Atlantic Meridional Mode (AMM)	2nd PC of the detrended tropical Atlantic monthly SSTA (20°S–20°N)		
Tropical Indian Ocean non-ENSO variability	Indian Ocean Basin Mode (IOBM) Index	The 1st PC of the IO detrended SST anomalies (40°E–110°E, 20°S–20°N)	Deser et al. (2010)	Identified as the two leading PCs of detrended tropical Indian Ocean monthly SSTA (20°S–20°N): 39% and 12% of the variance, respectively, for HadISST1, 1900–2008 (Deser et al. 2010)
	Indian Ocean Dipole mode (IODM), PC-based index	The 2nd PC of the IO detrended SST anomalies (40°E–110° E, 20°S–20°N)		
	Indian Ocean Dipole Mode Index (DMI)	SST anomalies: 50°E–70°E, 10°S–10°N)-(90°E–110°E, 10°S–0°)	Saji et al. (1999)	
Cold Ocean – Warm Land (COWL) Variability	COWL Index	Linear best fit to the field of deviations of NH temperature anomalies from their spatial mean; the COWL pattern itself is proportional to the covariance pattern of the NH spatial mean with these deviations.	Wallace et al. (1995); Thompson et al. (2008)	Useful for removing some effects of natural climate variability from spatially averaged temperature records.

cont. SIDEBAR 1.1: PATTERNS AND INDICES OF CLIMATE VARIABILITY—A. KAPLAN

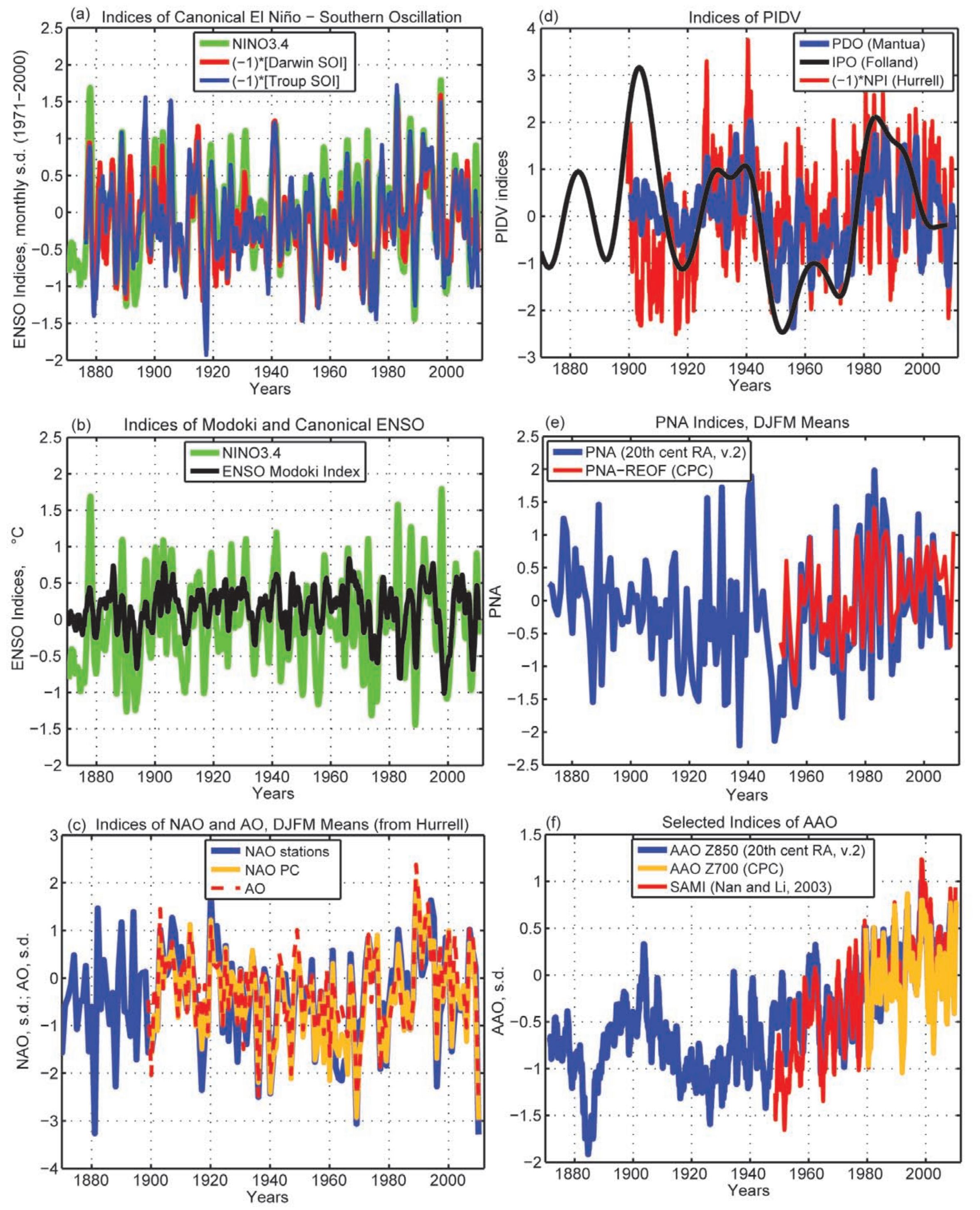

Fig. 1.3. Selected indices of climate variability, as specified in Table 2.3, for the period 1880–2010, grouped into categories: (a) Canonical El Nino-Southern Oscillation (ENSO); (b) the Modoki variant of ENSO; (c) Northern Hemisphere oscillations (NAO, AO, NAM) for the boreal cold season; (d) indices of Pacific Interdecadal Variability; (e) Pacific-North American indices for the boreal cold season; (f) Southern

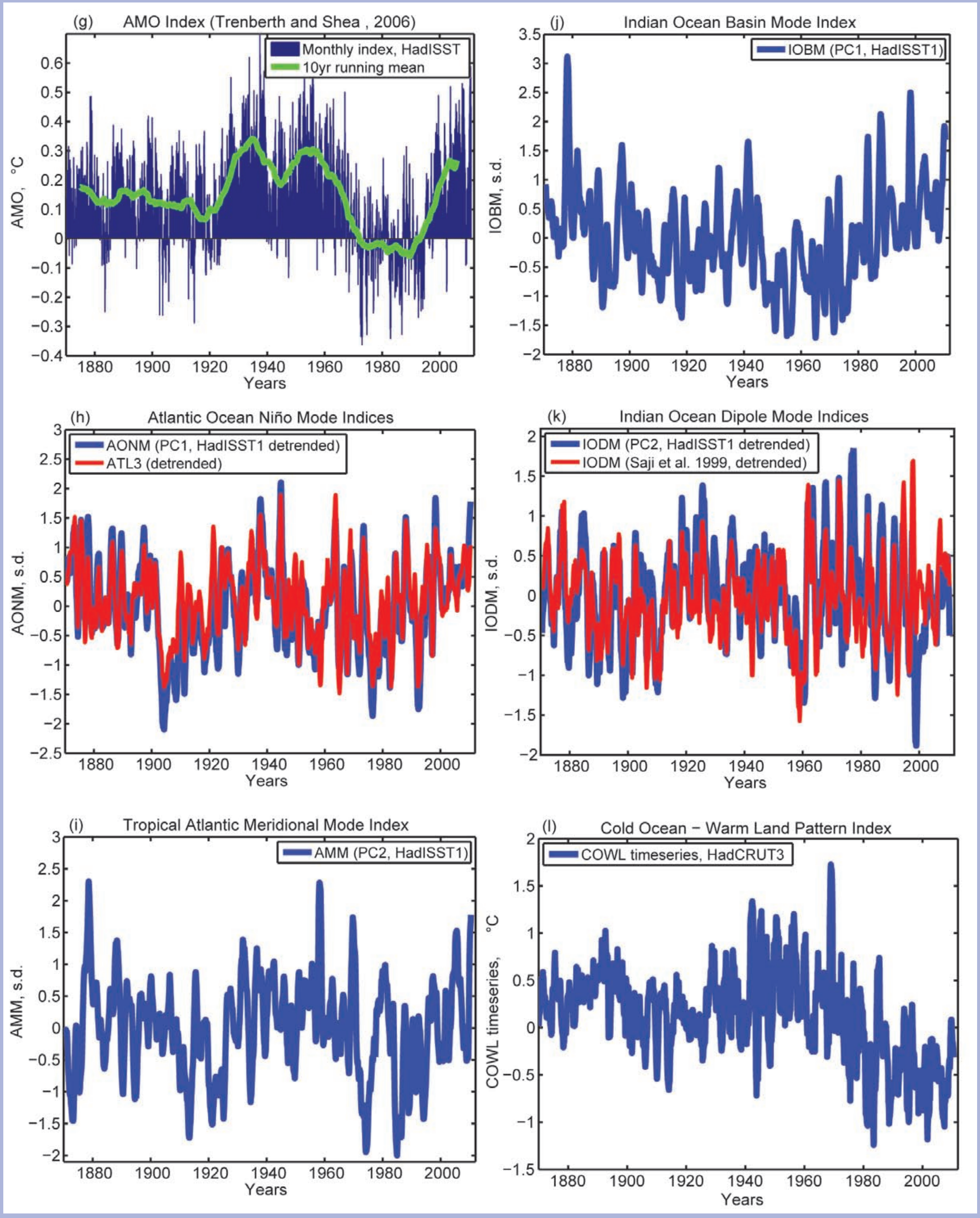

Hemisphere oscillations (SAM, AAO) for the austral cold season; (g) Atlantic Meridional Oscillation index; (h) Atlantic Niño Mode indices; (i) Tropical Atlantic Meridional Mode Index; (j) Indian Ocean Basin Mode Index; (k) Indian Ocean Dipole indices; and (l) Cold Ocean—Warm Land pattern. Unless otherwise noted in their panel, 13-month running means of monthly data are shown.

2. GLOBAL CLIMATE—K. M. Willett, A. J. Dolman, B. D. Hall, and P. W. Thorne, Eds.

a. Introduction—P. W. Thorne

The year 2010 was among the two warmest years globally since the start of the surface instrumental record in the late 19th century, although the range makes it impossible to call the ranking definitively. It was also the second warmest year in tropospheric records since the mid-20th century. Glaciers very likely experienced the 20th consecutive year of negative mass balance. The hydrological cycle experienced many extremes and global land precipitation was anomalously high. Greenhouse gases continued to increase and ozone depleting substances continued to decrease. The stratosphere continued to be anomalously cold. This chapter describes these and other indicators of ongoing changes in the Earth's climate system including atmospheric composition and terrestrial and cryospheric variables.

Climate is not just about decadal-scale externally forced variability, thus substantial attention is given to the major modes of natural variability (see Sidebar 1.1 for a general overview). Globally, 2010 was dominated by two modes of natural climate variability–the El Niño-Southern Oscillation (ENSO) and the Arctic Oscillation (AO). ENSO transitioned from a strong El Niño in early 2010 to a moderate-to-strong La Niña by the end of the year. Global temperatures typically lag ENSO by a few months, thus the warm El Niño phase had the larger impact upon 2010 temperatures. The AO reached its most negative value on record over the winter of 2009/10 and was negative again in the early winter of 2010/11. This led to extreme cold winter conditions and snow cover through much of the Northern Hemisphere midlatitudes and above-normal winter temperatures in the high northern latitudes.

A number of new variables are included in this year's report. There is a renewed focus on composition changes and changes in terrestrial variables, providing a greater reach into these areas than ever before. As discussed below, global lake temperatures have increased since 1985 and show similar spatiotemporal evolution to available land surface records. Global groundwater fluctuations show a combination of climate effects and direct human influences. Biomass inventories show general decreases in the tropics and increases in midlatitudes, reflecting deforestation and afforestation, respectively. However, these are uncertain and may have country-specific errors. The reader will find many further new insights into ongoing changes in the Earth and its climate.

Several issues of general interest are highlighted in sidebars within the chapter to illustrate both the complexities of global climate monitoring and the opportunities that new technologies and approaches afford the community. Building upon the introduction of ERA reanalyses last year, several alternative reanalysis products are included for temperature, humidity, wind speed, and global aerosols. Reanalysis products are also used to estimate global river discharge patterns. To aid interpretation, Sidebar 2.1 provides a high-level exposition of reanalyses outlining recent developments along with potential caveats. This is the first time that many of these products have been shown together with more traditional climate datasets, enabling simple broad-brush comparisons. Satellite data from GRACE satellites are shown to be hugely important for characterizing changes in ice sheet mass balance, groundwater, and deep ocean mass. Land surface winds are immensely challenging to analyze for long-term behavior but indicate likely weakening ('stilling') over time. Stratospheric water vapor is very important for radiative balance, with effects potentially felt at the surface, but it is extremely challenging to monitor and several mysteries remain regarding both mechanisms and trends.

Publicly available datasets used in this chapter are detailed in Table 2.1. Anomalies for 2010 for all those variables that could be calculated are given in Plate 2.1 and all available time series compiled into Plate 2.2, allowing ease of comparison.

Plate 2.1. Global annual anomaly maps for those variables for which it is possible to create a meaningful 2010 anomaly estimate. Reference base periods differ among variables, but spatial patterns should largely dominate over choices of base period. Dataset sources/names are as follows: lower stratospheric temperature (ERA-Interim); lower tropospheric temperature (ERA-Interim); surface temperature (NOAA/NCDC); cloudiness (PATMOS-x); total column water vapor (AMSR-E over ocean, ground-based GPS over land); surface specific humidity (ERA-Interim); precipitation (RSS over ocean, GHCN (gridded) over land); groundwater 2010–2009 differences (the sum of groundwater, soil water, surface water, snow, and ice, as an equivalent height of water in cm) (GRACE); river discharge absolute values (authors); mean sea level pressure (HadSLP2r); surface wind speed (AMSR-E over ocean, authors in situ over land); ozone (SBUVs/OMI/TOMS/GOME1/SCIAMACHY/GOME2, base period data from the multi-sensor reanalysis, MSR); FAPAR [SeaWiFS (NASA) and MERIS (ESA) sensors]; biomass burning (GFAS). See relevant section text and figures for more details.

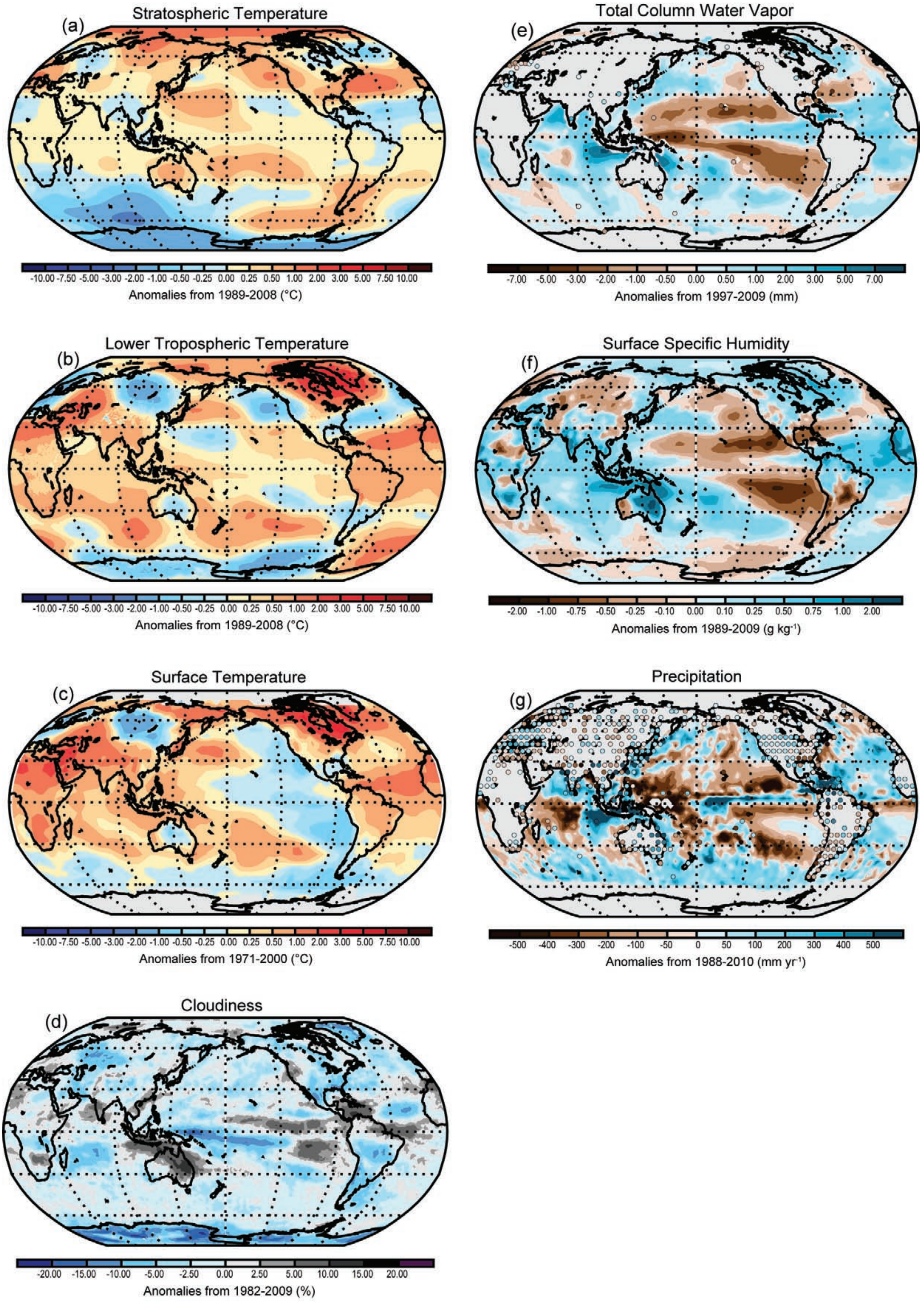
Stratospheric Temperature
(a)
-10.00 -7.50 -5.00 -3.00 -2.00 -1.00 -0.50 -0.25 0.00 0.25 0.50 1.00 2.00 3.00 5.00 7.50 10.00
Anomalies from 1989-2008 (°C)
Total Column Water Vapor
(e)
-7.00 -5.00 -3.00 -2.00 -1.00 -0.50 0.00 0.50 1.00 2.00 3.00 5.00 7.00
Anomalies from 1997-2009 (mm)
Lower Tropospheric Temperature
(b)
-10.00 -7.50 -5.00 -3.00 -2.00 -1.00 -0.50 -0.25 0.00 0.25 0.50 1.00 2.00 3.00 5.00 7.50 10.00
Anomalies from 1989-2008 (°C)
Surface Specific Humidity
(f)
-2.00 -1.00 -0.75 -0.50 -0.25 -0.10 0.00 0.10 0.25 0.50 0.75 1.00 2.00
Anomalies from 1989-2009 (g kg^{-1})
Surface Temperature
(c)
-10.00 -7.50 -5.00 -3.00 -2.00 -1.00 -0.50 -0.25 0.00 0.25 0.50 1.00 2.00 3.00 5.00 7.50 10.00
Anomalies from 1971-2000 (°C)
Precipitation
(g)
-500 -400 -300 -200 -100 -50 0 50 100 200 300 400 500
Anomalies from 1988-2010 (mm yr^{-1})
Cloudiness
(d)
-20.00 -15.00 -10.00 -5.00 -2.50 0.00 2.50 5.00 10.00 15.00 20.00
Anomalies from 1982-2009 (%)

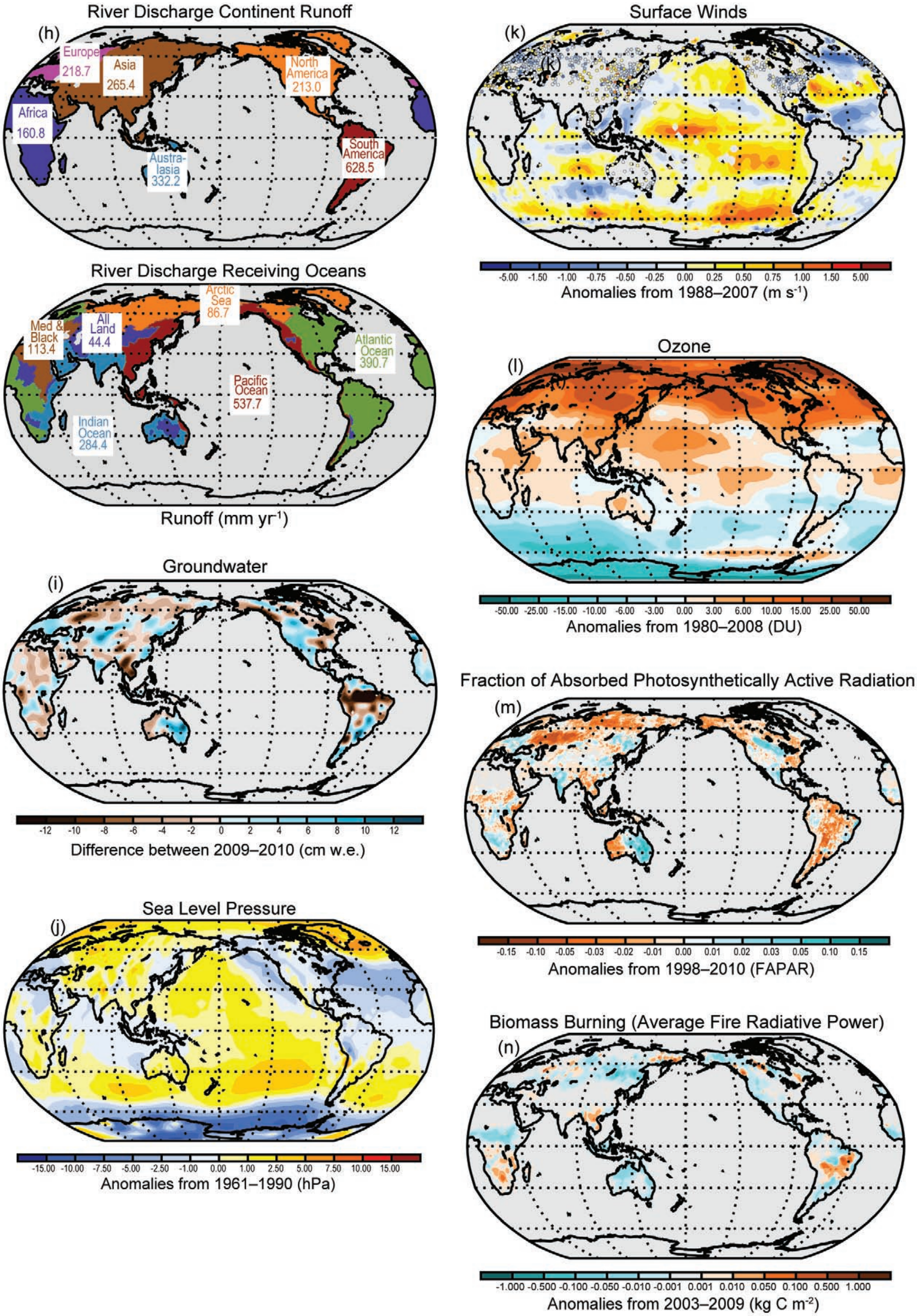

River Discharge Continent Runoff

River Discharge Receiving Oceans

Groundwater

Sea Level Pressure

Surface Winds

Ozone

Fraction of Absorbed Photosynthetically Active Radiation

Biomass Burning (Average Fire Radiative Power)

Table 2.1. Sources of those datasets used in this chapter that are publicly available.

Source	Datasets	Section
http://nomads.ncdc.noaa.gov/	NCEP CFSR	Sidebar 2.1, b1, c1, d2
http://gmao.gsfc.nasa.gov/merra/	MERRA	Sidebar 2.1, b1, b2, b3, c1, d2
http://www.esrl.noaa.gov/psd/data/20thC_Rean/	20CR	Sidebar 2.1, b2, b3, c1, d2
http://www.ecmwf.int/research/era	ERA-Interim	Sidebar 2.1, b1, b2, b3, c1, d2, Sidebar 2.3
http://www.ecmwf.int/research/era	ERA-40	Sidebar 2.1, b1, b2, b3, c1, d2, Sidebar 2.3
http://jra.kishou.go.jp/	JRA-25	Sidebar 2.1, b1, b2, c1, d2
Observations – Atmospheric Dynamics		
http://www.metoffice.gov.uk/hadobs	HadCRUT3; HadSLP2r; HadAT2; HadCRUH	b1, b2, b3, c1, d1
http://www.ncdc.noaa.gov/cmb-faq/anomalies.html	NOAA/NCDC	b1
http://data.giss.nasa.gov/gistemp/	NASA GISS	b1, b4
http://www.ncdc.noaa.gov/oa/climate/ratpac	RATPAC	b2, b3
http://www.univie.ac.at/theoret-met/research	Raobcore 1.4, RICH	b2, b3
http://vortex.nsstc.uah.edu/public/msu/	UAH v5.4	b2, b3
http://www.remss.com	RSS v3.3, SSM/I, AMSR-E, TMI	b2, b3, c2, c3, d2
http://www.star.nesdis.noaa.gov/smcd/emb/mscat/mscat-main.htm	STAR 2.0	b2, b3
http://www.noc.soton.ac.uk/noc_flux/noc2.php, http://dss.ucar.edu/datasets/ds260.3/	NOCS 2.0	c1
by mail to adai@ucar.edu	Dai	c1
http://cosmic-io.cosmic.ucar.edu/cdaac/index.html	COSMIC	c2
http://www.eol.ucar.edu/deployment/field-deployments/field-projects/gpspw	GPS	c2
http://precip.gsfc.nasa.gov	GPCP	c3
http://www.ncdc.noaa.gov/oa/climate/ghcn-monthly/indes.php	GHCN	c3
http://www.esrl.noaa.gov/psd/data/gridded/data.gpcc.html	GPCC	c3
http://www.esrl.noaa.gov/psd	CMAP	c3
http://www.ncdc.noaa.gov/cdr/operationalcdrs.html	PATMOS-X	c5
http://www.ncdc.noaa.gov/HObS/	HIRS	c5
http://ladsweb.nascom.nasa.gov	MODIS	c5
http://eosweb.larc.nasa.gov/PRODOCS/misr/level3/overview.html	MISR	c5, f2
http://www.atmos.washington.edu/~ignatius/CloudMap	SOBS	c5
http://isccp.giss.nasa.gov	ISCCP D2	c5
http://www.ncdc.noaa.gov/oa/climate.isd.index.php?name=isdlite	ISD-LITE	Sidebar 2.3
http://ceres.larc.nasa.gov/sitemap_ceres.php	CERES	e

Terrestrial		
http://largelakes.jpl.nasa.gov/2010-result	Lake Temperature Data	b4
http://climate.rutgers.edu/snowcover	Snow Cover	c4
http://grdc.bafg.de http://www.gtn-h.net	River Discharge	c6
http://nsidc.org/data/g02190.html	Permafrost Data	c7
http://gracetellus.jpl.nasa.gov/relatedSites/ http://www.csr.utexas.edu/grace/science_links.html	GRACE	c 8 Sidebar 2.2
http://www.ipf.tuwien.ac.at/insitu http://gcmd.nasa.gov/records/GCMD_GES_DISC_LPRM_AMSRE_SOILM2_V001.html	Soil Moisture	c9
http://tethys.eaprs.cse.dmu.ac.uk/RiverLake/shared/main http://www.legos.obs-mip.fr/soa/hydrologie/hydroweb/ http://www.pecad.fas.usda.gov/cropexplorer/global_reservoir/index.cfm	Altimetric Lake Level products	c10
http://gcmd.nasa.gov/records/GCMD_GLWD.html	The Global Lake and Wetland Database	c10
http://www.geo.unizh.ch/wgms/	Glaciers	g1
http://fapar.jrc.ec.europa.eu/	FAPAR	g2
http://www.globalfiredata.org/	Biomass Burning	g3
http://gmes-atmosphere.eu/fire	GFAS/GFED	g3
Atmospheric Composition		
http://www.esrl.noaa.gov/gmd/dv/iadv/	CO_2, CH_4, CO	f1
http://www.cmdl.noaa.gov/odgi/	ODGI	f1
http://www.esrl.noaa.gov/gmd/hats/combined/N2O.html	N_2O	f1
http://www.esrl.noaa.gov/gmd/hats/combined/SF6.html	SF_6	f1
http://www.esrl.noaa.gov/gmd/hats/combined/CFC11.html	CFC-11	f1
http://www.esrl.noaa.gov/gmd/hats/combined/CFC12.html	CFC-12	f1
http://www.esrl.noaa.gov/gmd/aggi/	AGGI	f1
http://agage.eas.gatech.edu/	PFCs	f1
http://www.gmes-atmosphere.eu/data/	Aerosols	f2
http://acdb-ext.gsfc.nasa.gov/Data_services/merged/	SBUV/TOMS/OMI MOD V8 merged ozone dataset	f3
http://www.iup.uni-bremen.de/gome/wfdoas	GOME/SCIAMACHY/GOMES2 total ozone datasets, GSG merged data	f3
ftp://ftp.tor.ec.gc.ca/Projects-Campaigns/ZonalMeans/	WOUDC groundbased ozone	f3
http://mirador.gsfc.nasa.gov/cgi-bin/mirador/presentNavigation.pl?tree=projectandproject=OMI	OMI total ozone (OMTO3)	f3
http://www.temis.nl/protocols/O3global.html	Multi sensor reanalysis (MSR) of total ozone	f3
http://www.cpc.ncep.noaa.gov/products/precip/CWlink/daily_ao_index/ao.shtml	Arctic Oscillation (AO)	f3
ftp://ftp.cmdl.noaa.gov/ozwv/water_vapor/Boulder_New/	Boulder water vapor balloon	Sidebar 2.4
http://disc.sci.gsfc.nasa.gov/Aura/data-holdings/MLS/index.shtm	MLS data	Sidebar 2.4
http://haloe.gats-inc.com/home/index.php	HALOE data	Sidebar 2.4

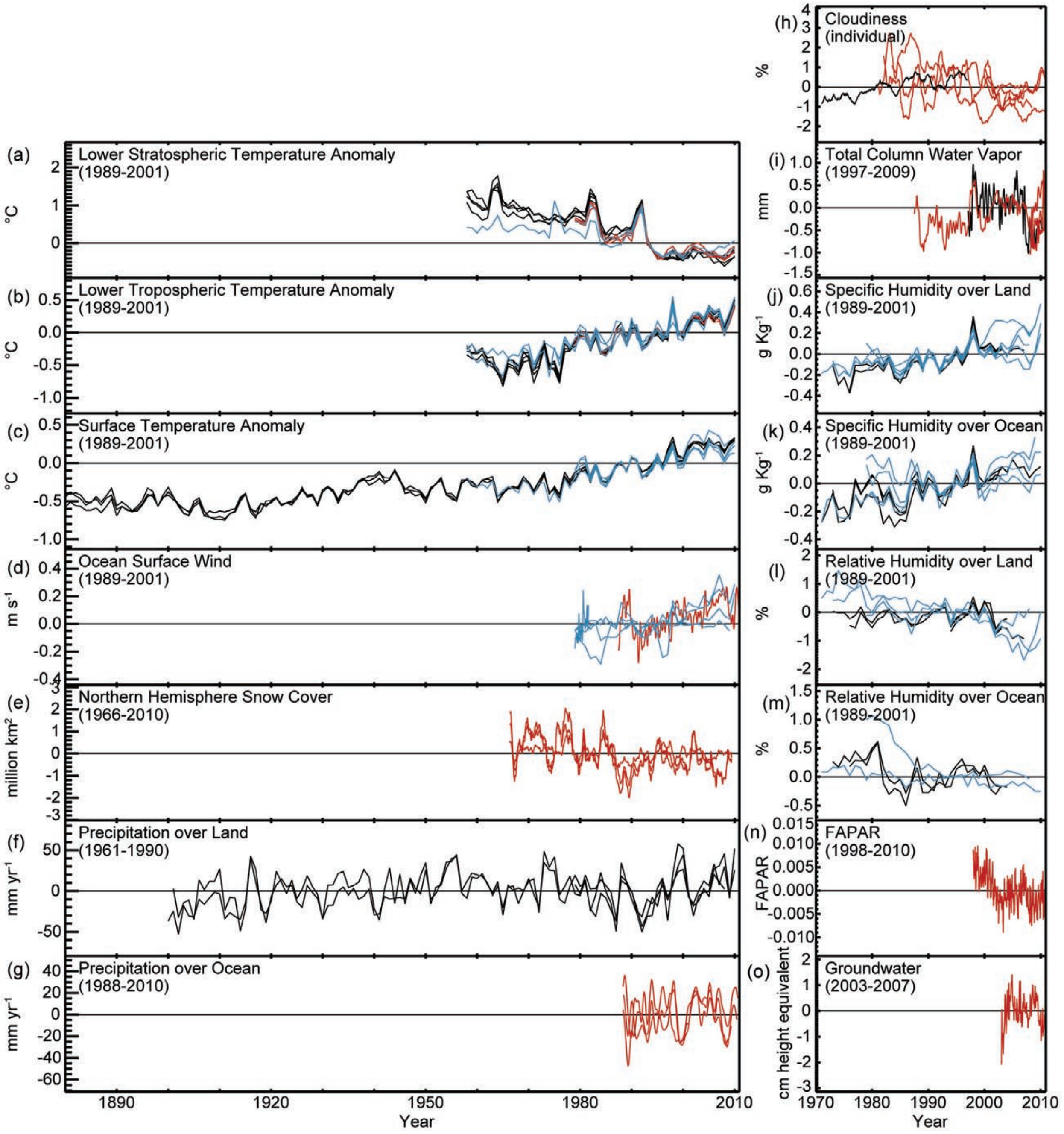

Plate 2.2. Global average anomaly time series for those variables for which it is possible to create a meaningful estimate. Reference base periods differ among variables, even within panels. For comparison, all time series for each variable have been adjusted to have a mean of zero over a common period which is labeled. Dataset types are as follows: lower stratospheric temperature (a; 4 radiosondes - black, 3 satellites - red, 3 reanalyses - blue); lower tropospheric temperature (b; 4 radiosondes - black, 2 satellites - red, 5 reanalyses - blue); surface temperature (c; 3 in situ – black, 5 reanalyses - blue); surface wind speed over ocean (d; 1 satellite - red, 6 reanalyses - blue); Northern Hemisphere snow cover (e; 3 satellite regions - red); precipitation over land (f; 3 in situ - black); precipitation over ocean (g; 3 satellites - red); cloudiness (h; 1 in situ – black, 5 satellites - red); total column water vapor (i; 3 satellites - red, 1 GPS - black); surface specific humidity over land (j; 2 in situ - black, 6 reanalyses - blue); surface specific humidity over ocean (k; 3 in situ - black, 3 reanalyses - blue); surface relative humidity over land (l; 2 in situ - black, 5 reanalyses - blue); surface relative humidity over ocean (m; 2 in situ - black, 2 reanalyses - blue);. Fraction of Absorbed Photosynthetically Active Radiation (FAPAR) (n; 1 satellite – red); groundwater (o; 1 satellite – red). See relevant section text and figures for more details including data sources.

Table 2.2. Reanalyses products included in the Global Chapter.

Reanalyses Product and Reference	Data Assimilated	Variables shown in the Global Chapter
NCEP CFSR, Saha et al. 2010	Atmospheric data: wind, temperature, humidity from radiosonde / dropsonde /pilot balloons/ profilers / aircraft; Surface pressure, temperature, humidity, wind, from ship/buoy reports; Surface land pressure from SYNOP/METAR; Retrieved ozone from satellites; Retrieved winds and radiances from geostationary satellites, Ocean surface wind from scatterometers; Radiances from temperature and humidity sounders: AIRS, HIRS, MSU, SSU, AMSU-A/B, MHS; Radiances from passive microwave imagers over ocean: SSM/I, AMSR-E; GPSRO bending angles from CHAMP, COSMIC (from 2001); Multi-sensor retrieved snow cover from NOAA/NESDIS (from 2003) Precipitation data: Pentad data set of CPC Merged Analysis of Precipitation and the CPC unified global daily gauge analysis. Ocean data: Temperature profiles from mobile platforms: expendable bathy thermographs and Argo drifting floats; and fixed platforms: TAO, TRITON, PIRATA, RAM; Salinity profiles synthesized from temperature profiles and climatological temperature correlations and observed by Argo drifting floats. SST: Two daily SST analysis products were developed using optimum interpolation (OI).	2m temperature; 2m specific humidity; 10m ocean windspeed
MERRA, Rienecker et al. 2011	Atmospheric data: Winds, temperature and humidity profiles from radiosondes, dropsondes, pilot balloons and profilers; NEXRAD radar winds (1998–present); Surface pressure from land SYNOP reports; surface pressure, winds, temperature and humidity from ships and buoys; synthetic surface pressure observations (PAOBS); Temperature- and humidity-sensitive infrared radiances from HIRS and SSU (1979–2006); Temperature-sensitive microwave radiances from MSU (1979–2007) and AMSU-A (1998–present); Wind and temperature reports from aircraft; Cloud-track winds from geostationary satellites and from MODIS (2002-present); Moisture-sensitive radiances from SSM/I (1987–2009) and AMSU-B (1998–present), precipitation, and surface wind-speed over the ocean from SSM/I; Marine surface winds from ERS-1 (1991–1996), ERS-2 (1996–2001) and QuikScat (1999–2009); Temperature and moisture sensitive radiances from GOES sounders; TRMM rain rate; Temperature- and humidity-sensitive IR radiances from AIRS	2m temperature; MSU 2LT equivalent lower tropospheric temperature; MSU 4 equivalent lower stratospheric temperature; 2m specific humidity; 10m ocean windspeed
JRA-25, Onogi et al. 2007	Atmospheric data: Surface pressure, Radiosondes, Wind profiler, Aircraft wind, PAOBS, Tropical cyclone wind retrieval, AMV (including reprocessed wind), Infrared radiances from HIRS/SSU, Microwave radiances from MSU/AMSU/MHS, Precipitable water retrieval from microwave imagers, Scatterometer wind Surface data: Surface temperature, humidity and wind; Snow depth (including digitized data over China), Snow cover retrieval from microwave imagers	2m temperature; MSU 2LT equivalent lower tropospheric temperature; 2m specific humidity; 2m relative humidity; 10m ocean windspeed
ERA-Interim, Dee et al. 2011	Atmospheric data: Upper-air wind, temperature and humidity from radiosondes; dropsondes; pilot balloons and profilers; aircraft; Surface pressure, temperature and humidity from land SYNOP reports; surface pressure, temperature, humidity and wind from SHIP reports; surface pressure, temperature and wind from buoys; surface pressure from METAR; snow depth from SYNOP reports; Retrieved ozone from satellites; Retrieved winds from geostationary satellites; Radiances from temperature and humidity sounders: HIRS, SSU, MSU, AMSU-A/B, MHS; Radiances from passive microwave imagers over ocean: SSM/I, SSMI/S, AMSR-E; Ocean surface wind from scatterometers on ERS-1, ERS-2, QuikSCAT (from 1992); Radiances from geostationary infrared imagers on GOES, Meteosat and MTSAT (from 2001); GPSRO bending angles from CHAMP, COSMIC, GRAS (from 2001); Radiances from high-spectral resolution sounder: AIRS (from 2003); Retrieved winds from polar orbiting satellites: MODIS (from 2007) Surface data: Multisensor retrieved snow cover from NOAA/NESDIS (from 2003)	2m temperature; MSU 2LT equivalent lower tropospheric temperature; MSU 4 equivalent lower stratospheric temperature; 2m specific humidity; 2m relative humidity; 10m ocean windspeed; 10m land windspeed
ERA-40, Uppala et al. 2005	Atmospheric data: Upper-air wind, temperature and humidity from radiosondes, dropsondes, pilot balloons, TWERLE balloons (1975–1976) and US profilers (from 1996); Surface pressure, temperature and humidity from land SYNOP reports; surface pressure, temperature, humidity and wind from SHIP reports; snow depth from SYNOP reports and specialised datasets; Temperature- and humidity-sensitive infrared radiances from VTPR (1973–1978) and HIRS/SSU (from 1979); Flight-level wind and temperature from aircraft (from 1973); Temperature-sensitive microwave radiances from MSU and AMSU-A (from 1979); Retrieved winds from geostationary satellites (from 1979); Surface pressure, temperature and wind from buoys (from 1979); Total ozone from TOMS and ozone profiles from SBUV (from 1979); Total column water vapour and surface wind-speed over ocean from SSM/I (from 1987) Surface data: Synthetic surface-pressure obs from satellite imagery (from 1973); Oceanic wave height and surface wind from ERS 1&2 (from 1992)	2m temperature; MSU 2LT equivalent lower tropospheric temperature; MSU 4 equivalent lower stratospheric temperature; 2m specific humidity (not ocean); 2m relative humidity (not ocean); 10m ocean windspeed
20CR, Compo et al. 2011	Surface and Sea Level Pressure only	MSU 2LT equivalent lower tropospheric temperature; 2m specific humidity; 2m relative humidity; 10m ocean windspeed

SIDEBAR 2.1: THE USE OF REANALYSIS DATA FOR MONITORING THE STATE OF THE CLIMATE—D. DEE, P. BERRISFORD, M. G. BOSILOVICH, M. CHELLIAH, G. COMPO, A. EBITA, P. D. JONES, S. KOBAYASHI, A. KUMAR, G. RUTLEDGE, S. SAHA, H. SATO, A. SIMMONS, C. SMITH, AND R. VOSE

Estimates of atmospheric temperature, humidity, and wind from several reanalyses have been included among the many datasets used in this issue of *BAMS State of the Climate in 2010* (Table 2.2). A global atmospheric reanalysis is a coherent, multivariate reconstruction to determine the state of the atmosphere using observations and a consistent technique to combine them objectively (Fig. 2.1). The reconstructions are created with model-based data assimilation methods similar to those employed for numerical weather prediction. Reanalyses rely on a forecast model to propagate information in space and time, and to impose physically meaningful constraints on the estimates produced. In this way it is possible, for example, to extract useful information about rainfall from satellite observations of temperature and humidity, or to infer large-scale features of the global circulation in the early 20th century from only surface pressure observations available at the time (e.g., Compo et al. 2011).

Several centers now routinely extend their latest reanalyses close to real time and provide product updates to users at a short delay. Timely, comprehensive estimates of global climate variables, consistently produced with an unchanged data assimilation system, can be useful for climate monitoring. It is clearly necessary, however, to evaluate uncertainties before drawing conclusions from assessments of year-to-year changes in climate based on reanalysis data. The accuracy of estimated trends and variability for any given variable depends on the strength of the observational constraint. This constraint varies throughout the reanalysis period as the input observations change in quality, quantity, and platform type. The contribution of observations also depends on the biases, errors, and uncertainties in the forecast models. Intercomparison of different reanalyses can be useful when considering trends over longer periods. Where possible, estimates from reanalysis data should also be compared with independent estimates based on observations alone. This is especially important for variables (such as precipitation) that are only indirectly constrained by the assimilated observations and hence depend crucially on the quality of the assimilating forecast model (Fig. 2.2).

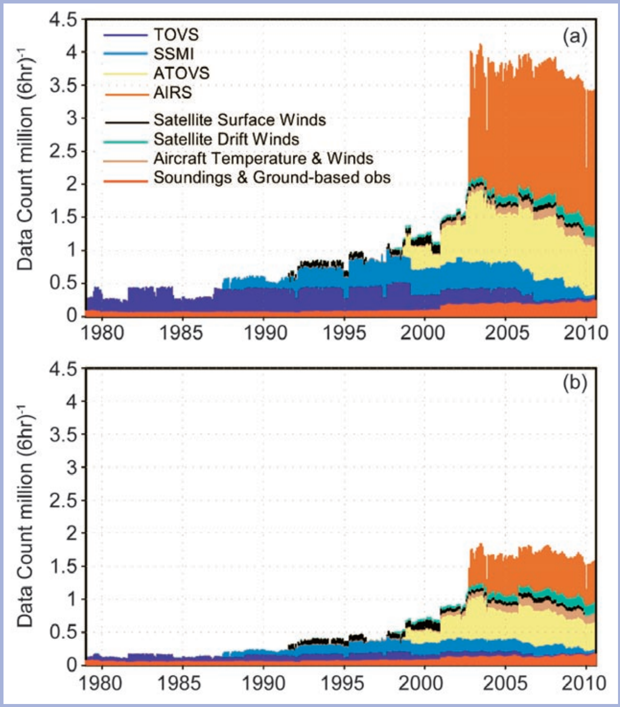

Fig. 2.1. Time series of (a) the number (millions) and types of observations considered for assimilation during a six-hour window and (b) those observations actually assimilated. (Source: Rienecker et al. 2011)

Since first produced in the 1980s, reanalysis data have been widely used for research in the atmospheric sciences. Reanalysis is a rapidly evolving field; successive generations of products have improved in quality and diversity, reflecting major advances in modeling and data assimilation in recent decades. New reanalysis products additionally benefit from improvements in the observations and other required input datasets, such as specifications of sea surface temperature and sea ice concentration. These are the result of ongoing efforts in data reprocessing and recalibration by satellite agencies and other data providers, as well as recovery and digitization of early instrumental data that have not previously been used. The value and appeal of reanalyses arise from the accumulation of these benefits and their encapsulation in a comprehensive dataset conveniently provided on global grids. As reanalyses proliferate, metadata about the assimilated observations and forecast model become essential components for any assessment. A forum for sharing such information among producers and users of reanalysis data has recently been established at http://www.reanalyses.org.

Evaluation of the quality of reanalysis products is often provided by users, based on many different measures. Applications vary greatly, ranging from predictability and process studies to the validation of ecological models of biodiversity. Producers of reanalysis datasets closely monitor the quality of fit to observations used, the ability of the assimilating model to predict those observations, and the adjustments made to

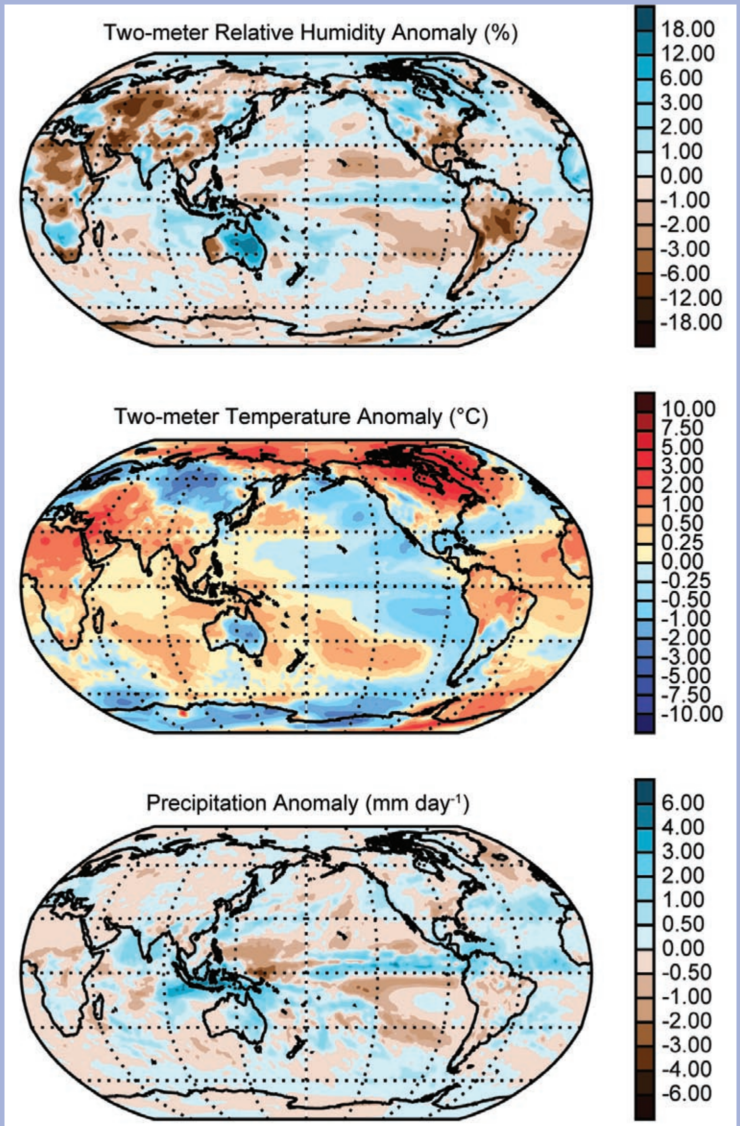
Two-meter Relative Humidity Anomaly (%)

Two-meter Temperature Anomaly (°C)

Precipitation Anomaly (mm day^{-1})

Fig. 2.2. ERA-Interim 2010 anomaly maps for 2 m relative humidity, 2 m temperature, and precipitation (accumulated in the 12 hr–24 hr range from twice-daily forecasts initiated at 00 UTC and 12 UTC), all relative to 1989–2008 base period averages. Note effects of the Russian dry heat wave and extreme rainfall in Australia. There is higher confidence in temperature and humidity where these are well constrained by observations and independently verified (Simmons et al. 2010). Uncertainties are largest in polar areas and central Africa. There is less confidence in precipitation, which is only indirectly constrained by observations—anomalies are likely excessive over tropical oceans but reasonable over most land points (Dee et al. 2011).

the predictions by the data assimilation procedure. These so-called analysis increments represent the net impact of the observations on the reanalyzed atmospheric fields. Systematic increments may be due to residual biases in observations, in the forecast model, or both. They can introduce artificial sources and sinks of heat, energy, and water in the reanalysis, and hence affect the global budgets for these quantities. Changes in the mean increments (e.g., associated with changes in the observing system) can affect trend estimates for basic climate variables derived from reanalysis data.

Reanalyses are used in the analysis of several variables in this chapter. Like more traditional observational datasets, individual reanalysis datasets have strengths and weaknesses. Although there have been a limited number of peer-reviewed comparisons [e.g., Simmons et al. (2010) for surface temperature and humidity; Dessler and Davis (2010) for free tropospheric humidity], in general, the performance of individual reanalysis products for specific parameters has not been rigorously quantified. The construction of reanalysis is a complex endeavor, and it is not unexpected that there will be a degree of spread among the reanalyses. Contemporary reanalysis products show considerably smaller spread than earlier generations, reflecting substantial advances in analysis methods, especially in the area of satellite data assimilation and in the ability to deal with biases in observations. These advances are expected to continue with coming generations of new reanalysis products.

REANALYSES.ORG
INTERCOMPARISON AND OBSERVATIONS

b. Temperatures

1) Surface temperatures—A. Sánchez-Lugo, J. J. Kennedy, and P. Berrisford

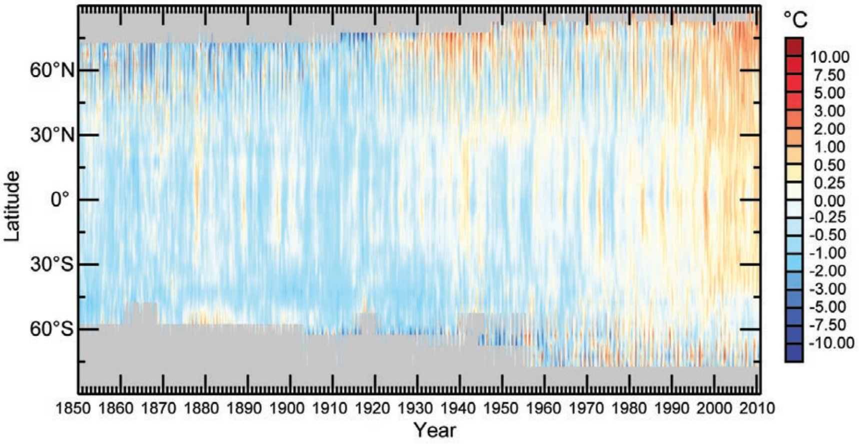

Fig. 2.4. HadCRUT3 monthly mean anomalies of surface temperature by latitude based on the 1961–90 base period. Gray areas indicate regions where data are unavailable.

Global mean surface temperature in 2010 ranked as either the warmest or second warmest year in the instrumental record. The rank depends on which of the three methodologically independent analyses presented in this section are considered (NASA/GISS, Hansen et al. 2010; HadCRUT3, Brohan et al. 2006; and NOAA/NCDC, Smith et al. 2008). The year was 0.50°C above the 1961–90 average annual value in HadCRUT3 (second warmest after 1998), 0.52°C in the NOAA/NCDC analysis (tied warmest with 2005), and 0.56°C in the NASA/GISS analysis (tied warmest with 2005). The analyses use air temperatures over land and sea surface temperatures observed from ships and buoys. While they differ in their methods, which can lead to differences in the annual ranks, all three analyses are in close agreement (Fig. 2.3) that the global average surface temperature increased at a rate of 0.7°C per century since 1900 and approximately 0.16°C per decade since 1970.

Global average temperature can also be estimated from reanalyses (see Sidebar 2.1). These all indicate 2005 as the warmest year on record. Two of the reanalyses (ERA-Interim and JRA) give 2010 as the second warmest year (Fig. 2.3).

The year 2010 was characterized by two large-scale modes of variability that affected weather conditions across the globe—the El Niño-Southern Oscillation (ENSO) and the Arctic Oscillation (AO). The strong El Niño in the tropical Pacific Ocean during the first half of 2010 contributed to the exceptional warmth observed globally, resulting in one of the top two warmest January–June periods on record. El Niño persisted through April, but sea surface temperatures then declined rapidly across the tropical Pacific Ocean, giving way to La Niña conditions. By July La Niña was well established and by the end of the year it had intensified to a moderate-to-strong La Niña. Despite the rapid development and strength of the La Niña, global average sea surface temperatures remained relatively high throughout the year. Above-average sea surface temperatures were present during the year across the Atlantic and Indian Oceans, with the most prominent warmth across the tropical Atlantic (Plate 2.1c).

A strong negative phase AO influenced temperature patterns across the Northern Hemisphere during most of 2010, contributing to unusually low temperatures over much of northern Eurasia and parts of the United States. Abnormal warmth affected much of Africa and southern Asia, with notable warm anomalies also across Canada and northern South America. Overall,

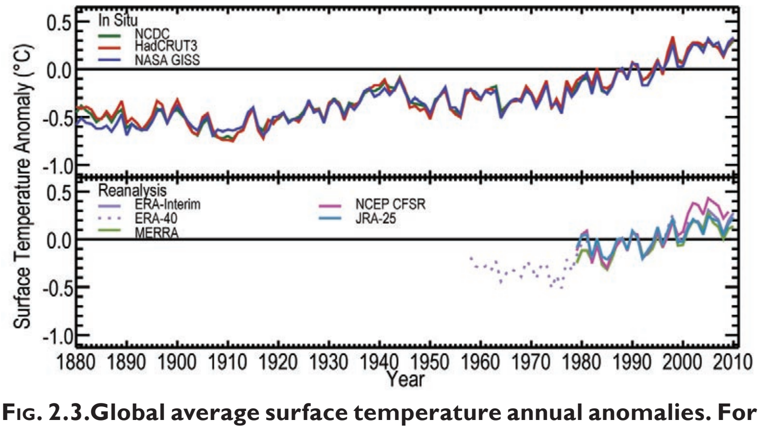

Fig. 2.3.Global average surface temperature annual anomalies. For the in situ datasets 2 m surface temperature is used over land and sea surface temperature over the oceans. For the reanalyses, a 2 m temperature is used over the whole globe. In situ datasets and the ERA-40 reanalysis use the 1961–90 base period whereas all other reanalysis datasets use the 1989–2008 base period. However, to aid comparison, all time series have been adjusted such that they give a mean of zero over the common period 1989–2001.

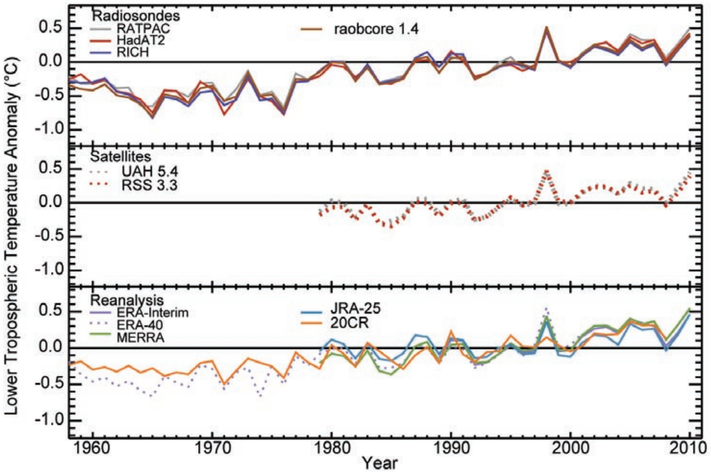

Fig. 2.5. Global average lower tropospheric temperature annual anomalies for the MSU 2LT (or equivalent) layer. Radiosonde [HadAT2 (Thorne et al. 2005–465 day, 384 night stations), RATPAC (Free et al. 2005–85 stations), RAOBCORE 1.4 (Haimberger 2007–1184 stations) and RICH (Haimberger et al. 2008–1184 stations)] and Satellite [UAHv5.4 (Christy and Norris 2009) and RSSv3.3 (Mears and Wentz 2009)] datasets use the 1981–2010 base period. ERA-40 uses the 1961–90 base period whereas all other reanalysis datasets use the 1989–2008 base period. However, to aid comparison, all time series have been adjusted such that they give a mean of zero over the common period 1989–2001.

the Northern Hemisphere land temperature was well above average throughout the year (Fig. 2.4).

2) Lower tropospheric temperatures—J. Christy

Based on several sources of processed observations, the global lower tropospheric layer (TLT, surface to ~8 km) was approximately +0.4°C warmer than the 1981–2010 period average (Fig. 2.5, shown using a different base period). The year began in a strong warm-phase ENSO (El Niño) with individual monthly anomalies for January–April in some datasets being the warmest observed. When the tropical Pacific Ocean experiences large ENSO temperature anomalies, global TLT responds with similar temperature changes which, for the global average, lag the surface fluctuations by two to four months (Christy and McNider 1994). The 2010 warm phase switched rapidly to a cool phase (La Niña) as the year progressed. Given the lagged response, global TLT anomalies remained above average and cooled slowly while those of the tropical Pacific Ocean fell below average in the second half of the year (Fig. 2.6).

For the previous 32 (satellite) and 53 (radiosonde) years of records, 2010 ranked as warmest in RATPAC and second warmest year to 1998 in most of the datasets, though the difference is sufficiently small as to not be considered significant (Fig. 2.5). Global average anomalies were constructed using three systems: balloon-based radiosondes; satellite-based microwave sensors; and reanalyses (see Sidebar 2.1 for general information about reanalysis).

In the zonal mean, the evolution from a clear La Niña signal of cool tropics in the first half of 2008 to warm El Niño conditions through most of 2010 is marked (Fig. 2.6). Other longer-lived cool tropical events occurred around 1985, 1989, and 2000. Warmth similar to 2010 is seen in warm El Niños of 1982/83 and 1997/98. The cooling seen in 1992 is related to the volcanic eruption of Mount Pinatubo. Since the very warm 1998 El Niño, there appears to be a prevalence of warmer temperatures in the northern latitudes, tropics, and southern midlatitudes relative to prior years. In high southern latitudes, there appears to be no long-term trend.

The estimated linear trend for the entire time series (Fig. 2.5) beginning in 1958 (radiosonde era) and also beginning in 1979 (satellite era) is +0.15 ± 0.02°C per decade where the "±0.02" represents the range of the values calculated from the various data products listed. There is no indication of acceleration of the

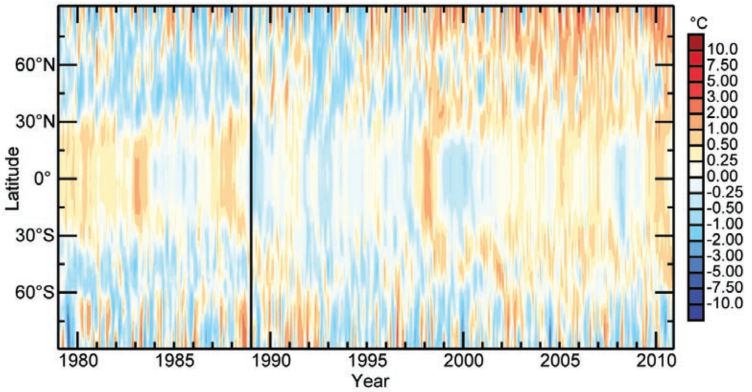

Fig. 2.6. Combined ERA-40 (1979–88) and ERA-interim (1989–2010) monthly mean anomalies of lower tropospheric temperature by latitude. ERA-40 uses the 1961–90 base period whereas ERA-interim uses the 1989–2008 base period. Both datasets have been adjusted to have a mean of zero over the common period 1989–98 so that they can be shown together with the changeover indicated by the vertical black line.

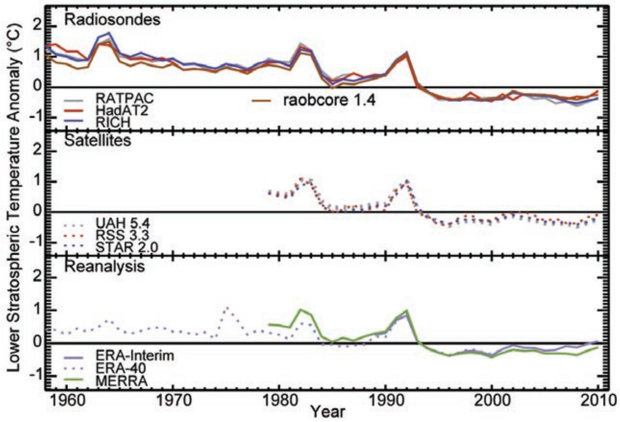

Fig. 2.7. Global average lower stratospheric temperature annual anomalies for the MSU 4 (or equivalent) layer. Radiosonde [HadAT2 (Thorne et al. 2005–465 day, 384 night stations), RATPAC (Free et al. 2005–85 stations), RAOBCORE 1.4 (Haimberger 2007–1184 stations) and RICH (Haimberger et al. 2008–1184 stations)] and Satellite [UAHv5.4 (Christy and Norris 2009), RSSv3.3 (Mears and Wentz 2009) and STAR 2.0 (Zou et al. 2009)] datasets use the 1981–2010 base period. ERA-40 uses the 1961–90 base period and all other reanalysis datasets use the 1989–2008 base period. All time series have been adjusted such that they give a mean of zero over the common period 1989–2001 to aid comparison.

trend, though the relatively large excursions from the trend line make possible other interpretations than a single straight line (Seidel and Lanzante 2004).

The teleconnection patterns related to El Niño are somewhat muted in the 2010 annual average as the opposing effects of La Niña appeared late in the period. The El Niño impact is seen in the geographical distribution of anomalies in Plate 2.1b with widespread warmer-than-average tropical values and cooler-than-average anomalies in the northeast and southeast Pacific. Significant warm anomalies are seen from Hudson Bay to Greenland, the tropical North Atlantic eastward to Russia, and in much of the midlatitude Southern Hemisphere. Regions of cooler-than-average anomalies occurred in the southeastern U.S. northeastward to Europe, northern Asia, Australia, southern South America, and western Antarctica.

3) Lower stratospheric temperatures—M. Free

Efforts are underway to produce improved climate data records from the Stratospheric Sounding Unit (SSU) data and ultimately to merge them with the ongoing Advanced Microwave Sounding Unit (AMSU) data (Randel et al. 2009a). However, this work does not yet enable reliable assessment of recent changes in temperature in the upper stratosphere and therefore the scope of this section is limited to the lower stratosphere.

The average temperature of the global lower stratosphere in 2010, for the layer measured by the MSU satellite data, was warmer than the mean of the previous 10 years in most datasets (Plate 2.1a; Figs. 2.7 and 2.8) but more than 1°C cooler than the early 1960s. It was ~0.1°C–0.2°C warmer than 2009 and ranked roughly 14th coolest since 1979—the exact ranking depends on the dataset. The global mean trends for 1958–2010 in radiosonde datasets (weighted to approximate the MSU retrieval) range from -0.29°C to -0.36°C per decade, and the trends for radiosonde and MSU datasets for 1979–2010 are -0.31°C to -0.54°C per decade. The MSU data show smaller cooling trends than the radiosonde datasets. Most reanalyses show generally similar evolution of the global mean stratospheric temperature to that shown by the other datasets. In the tropics, cooling trends for 1979–2010 are strongest in boreal winter months and minimal in March–April, while trends in Arctic temperatures have a roughly opposite seasonality. Trends in the Antarctic stratosphere show the strongest cooling from November to February (Free 2011), and November and December 2010 were unusually cool in that region.

Figures 2.7 and 2.8 show an overall cooling trend through the mid-1990s, interrupted by volcanic warming, with little change in temperature since 1995. Interannual variability in global mean temperatures in the lower stratosphere is dominated by warming resulting from the major volcanic eruptions of Mount Agung (1963), El Chichón (1982) and MountPinatubo (1991). This effect is largest in the tropics and tends to be accompanied by a strengthening of the Arctic polar vortex and cooling near the North Pole. In the tropical stratosphere, the Quasi-

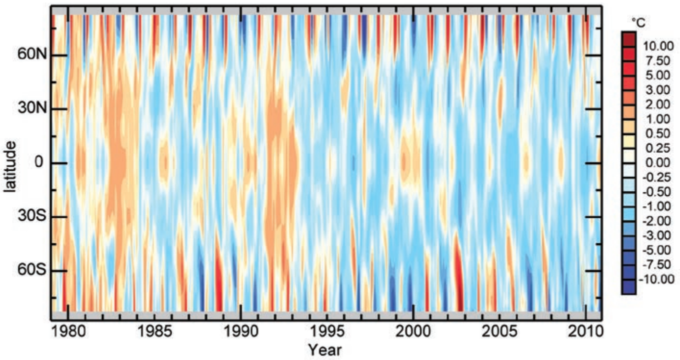

Fig. 2.8. RSS monthly mean anomalies of lower stratospheric temperature by latitude. A 1989–98 base period is used. Gray areas indicate regions where data are unavailable.

Biennial Oscillation (QBO) is the strongest source of interannual temperature variation (Baldwin et al. 2001; Fig. 2.8). This oscillation in temperature and zonal wind direction propagates from the upper to the lower stratosphere with a time period of about 24–30 months for a complete cycle. The QBO response in the deep tropics is out of phase with its counterparts at higher latitudes (Fig. 2.8), and so the QBO effect on stratospheric temperature is much smaller in the global mean than in the tropics. Similarly, although El Niño tends to cool the lower stratosphere in the tropics and warm it in the Arctic (Free and Seidel 2009; Randel et al. 2009b), especially in boreal winter, its effects are not obvious when layer-mean stratospheric temperatures are averaged globally. The lower stratosphere also tends to be warmer when the 11-year solar cycle is at its maximum and cooler at its minimum. The observed global time series of lower stratospheric temperature reflects the combination of these natural sources of interannual variability with long-term anthropogenic cooling effects from ozone depletion and greenhouse gases.

In 2010, the QBO began in an easterly phase and then shifted to the westerly phase in the second half of the year, and this plus the shift to La Niña conditions caused the tropical stratosphere to warm in the fall (Fig. 2.8). Although the Arctic stratosphere warmed in February, this warming was not as unusually large as that of 2009. The Antarctic polar vortex was larger than average during 2010 and was relatively undisturbed after two warming events in July and August. The behavior of the Antarctic ozone hole is discussed in section 6g.

4) Lake temperature—P. Schneider and S. J. Hook

The temperatures of lakes and other inland water bodies are excellent indicators of climate change (Austin and Colman 2008; Livingstone 2003; Williamson et al. 2009). Previously, in situ temperature data have been used to measure the impact of climate change on lakes (Coats 2010; Quayle et al. 2002; Verburg et al. 2003). While these data are usually quite accurate, their availability is restricted to a few sites and continuous, reliable, long-term in situ observations are rare. Satellite thermal infrared (TIR) data have also been used to measure lake surface temperature (Crosman and Horel 2009; Hook et al. 2003; Hook et al. 2007; Reinart and Reinhold 2008; Schneider et al. 2009), though these studies were still limited geographically.

To provide a more global scope, Schneider and Hook (2010) utilized 25 years of TIR satellite data at 104 inland water bodies worldwide in order to determine possible trends in the seasonal nighttime surface water temperatures and to investigate if any spatial patterns in the trends would emerge. The study used seasonally averaged (July–September and January–March) nighttime data from the series of Advanced Very High Resolution Radiometers (AVHRR) and the series of Along-Track Scanning Radiometers (ATSR) obtained between 1985 and 2009. Satellite-based trends were found to closely match those derived from buoy data obtained from the National Data Buoy Center (NDBC), as validated over the American Great Lakes (Fig. 2.9). Using a merged dataset consisting of data from two sensors improves the agreement considerably.

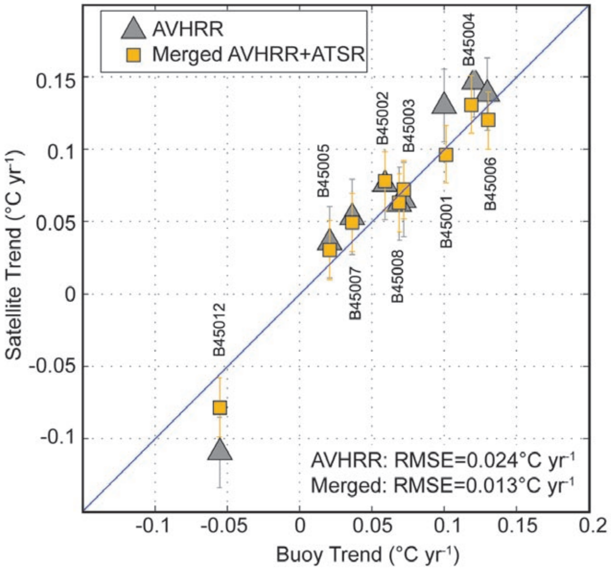

Fig. 2.9. Comparison of 1985–2009 Jul–Sep nighttime lake surface temperature trends derived from satellite data with those obtained from hourly measurements at nine buoys in the Great Lakes.

Several consistent spatial patterns emerge from the mapped trends of the seasonal nighttime lake surface temperature (Fig. 2.10a). The area of the strongest and most consistent lake surface temperature increase is Northern Europe, where Lake Vänern, Lake Vättern, Lake Ladoga, and Lake Onega have warmed at an average rate of around 0.08°C yr^{-1}. The magnitude of the trends decreases slightly towards southeastern Europe and the Middle East. A more rapid decline in trend magnitude is visible towards central Asia. Lakes in North America have been warming at rates around 0.05°C yr^{-1}–0.06°C yr^{-1} on average. At lower latitudes, most inland water bodies showed much slower warming of 0.025°C yr^{-1} on average. A comparison with data from the GISTEMP (NASA GISS in section 2b1)

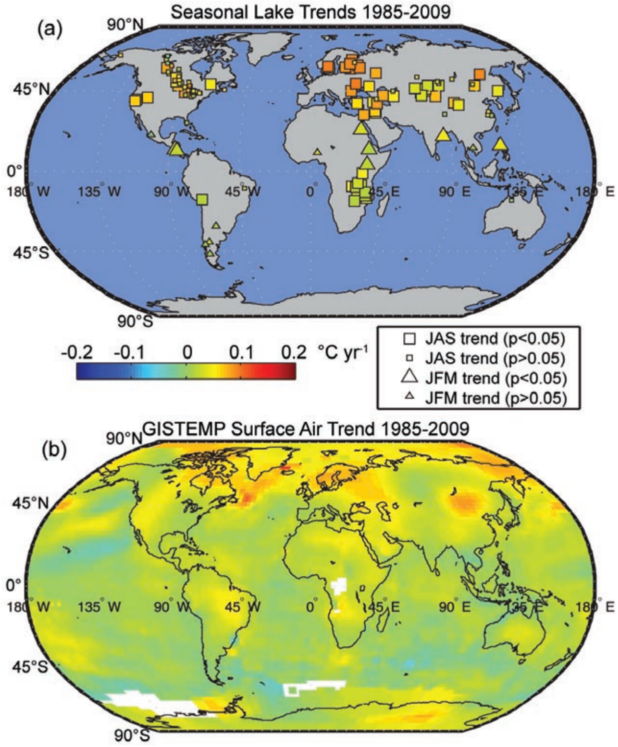

Fig. 2.10. Global (a) satellite-derived seasonal [Jul–Sep (JAS) and Jan–Mar (JFM)] nighttime lake surface temperature trends between 1985 and 2009, and (b) corresponding 1985 through 2009 JAS trends in surface air temperature obtained from GISTEMP (Hansen et al. 2006). JFM trends are not shown due to low number of JFM stations.

surface air temperature analysis (Hansen et al. 2006; Fig. 2.10b) shows qualitative agreement.

The average of all time series (Fig. 2.11) highlights features such as the cooling effect caused by the 1992 Mount Pinatubo eruption and the warm anomaly caused by the strong 1998 El Niño event. The mean trend over all sites is 0.045 ± 0.011°C yr^{-1} ($p < 0.001$) and is dominated by the large number of water bodies in the midlatitudes of the Northern Hemisphere. When Northern and Southern Hemisphere are weighted equally, the global trend is 0.037 ± 0.011°C yr^{-1}. The spaceborne TIR lake temperatures provide additional independent evidence on temperature change over land and for assessing the impacts of climate change throughout the world.

c. Hydrological cycle

1) Surface humidity—K. Willett, A. Dai, and D. Berry

Surface humidity has been monitored at some sites since the 19th century (e.g., Butler and García-Suárez 2011). Only during recent decades has the coverage become near-global, by weather stations over the land and ship and buoy observations over the oceans. Historically, both specific humidity (*q*) and relative humidity (RH) have been derived from paired wet bulb and dry bulb thermometers. However, it is becoming increasingly common to use capacitance sensors to directly derive RH or dewpoint temperature.

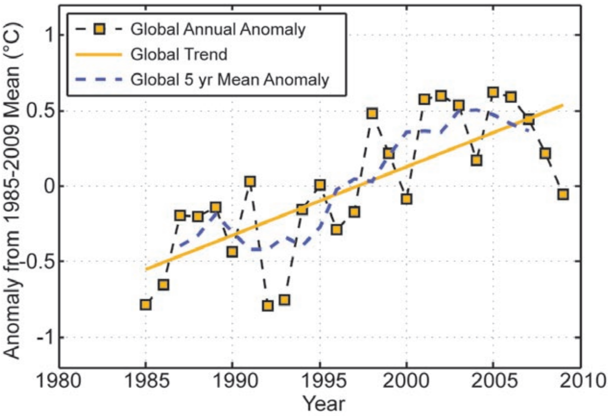

Fig. 2.11. Global average nighttime lake surface temperature anomalies averaged over all study sites.

There are three recent global-scale analyses of surface humidity: Dai (*q* and RH over land and ocean; Dai 2006); HadCRUH (*q* and RH over land and ocean; Willett et al. 2008); and the NOCS 2.0 (*q* only) ocean dataset (Berry 2009; Berry and Kent 2009). Only the NOCS 2.0 is updated to include 2010, but plans are underway to update HadCRUH over land on an annual basis, and to homogenize and update the Dai analysis. While all datasets use ship data over the ocean, HadCRUH and Dai include data from buoys, which are excluded from NOCS 2.0 owing to quality issues. All NOCS 2.0 data are then filtered by confidence in data quality and thus spatial coverage is far less than that of Dai and HadCRUH, especially over the Southern Hemisphere. NOCS 2.0 has also been bias adjusted for changes in ship height and instrument type over time and includes uncertainty estimates. Over land, Dai and HadCRUH contain many of the same station input data but methodologies are different. HadCRUH has been adjusted to remove gross inhomogeneities over land.

Recently, the ECMWF reanalysis product ERA-Interim and its predecessor ERA-40 were compared with land surface humidity from HadCRUH (Simmons et al. 2010) where good overall agreement was found. For this reason, ERA-Interim is considered suitable to monitor land surface humidity and so is used here to provide data for 2010. Other fourth generation reanalyses products are also shown where humidity fields are available for comparison.

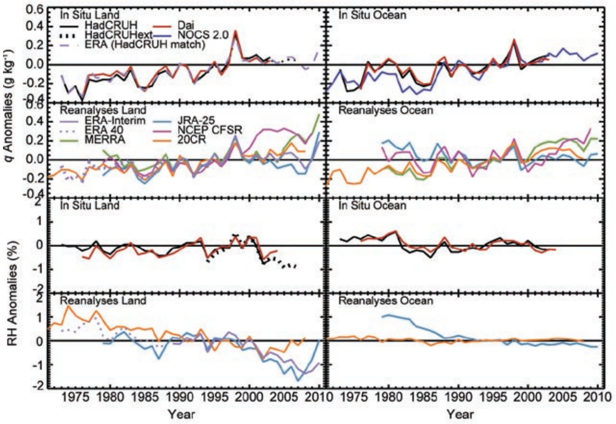

Fig. 2.12. Global average surface humidity annual anomalies. For the in situ datasets 2 m surface humidity is used over land and ~10 m over the oceans. For the reanalysis datasets, 2 m humidity is used over the whole globe. The specific humidity *(q)* and relative humidity (RH) are shown for land and ocean separately. HadCRUH, HadCRUHext, and ERA (HadCRUH match) use the 1974–2003 base period. Dai uses the 1976–2003 base period. NOCS 2.0 uses the 1971–2010 base period. The combined ERA-40 (1973–88) and ERA-Interim (1989–2010) use the 1989–2009 base period. All other reanalysis datasets use the 1989–2008 base period. All datasets are adjusted to have a mean of zero over the common period 1989–2001 to allow direct comparison. Differences in data ingestion and sea ice cover between reanalysis datasets, and in spatial coverage between reanalysis and in situ data, should be taken into account. For example, slight differences are shown between ERA spatially matched to the sampling of HadCRUH (see 'In situ Land' panel) compared to the full spatial coverage time series (see 'Reanalyses Land' panel).

Global surface moisture content, as shown by *q*, has been gradually increasing since the early 1970s, consistent with increasing global temperatures (Fig. 2.12). Trends are similar for both the land and oceans but with apparent peaks during strong El Niño events (1982/83, 1997/98). Since 1998 *q* over land has flattened somewhat but 2010 shows an increase from 2009. Although there is some spread across the datasets, there is good general agreement—less so for the reanalysis-generated ocean *q*.

Globally, specific humidity for 2010 (Plate 2.1f) strongly resembles a La Niña pattern, and is broadly consistent with that of precipitation (Plate 2.1g) and total column water vapor (Plate 2.1e). There are dry anomalies over the eastern tropical Pacific and moist anomalies over the western tropical Pacific.

ERA-Interim and HadCRUH-ext show a slight decline in global land RH from 1998 to present (Simmons et al. 2010), also shown in MERRA, consistent with a steady *q* and coincident rising temperature over this period. However, 2010 appears to be a more humid year on average. Prior to 1982, Dai and HadCRUH show positive RH anomalies over oceans. While Willett et al. (2008) speculate non-climatic causes, more recent investigation by Berry (2009) appears to implicate the North Atlantic Oscillation (NAO). RH in the reanalyses oceans is inconclusive.

2) Total column water vapor—C. Mears, J. Wang, S. Ho, L. Zhang, and X. Zhou

The map of total column water vapor (TCWV) anomalies for 2010 (Plate 2.1e) includes data both from the Advanced Microwave Scanning Radiometer EOS (AMSR-E; over the oceans; Wentz 1997; Wentz et al. 2007) and from a subset of the ground-based GPS stations with continuous data from 1997 through 2010 (J. Wang et al. 2007). This subset was chosen so that a meaningful anomaly estimate could be calculated—many more stations would be available if this

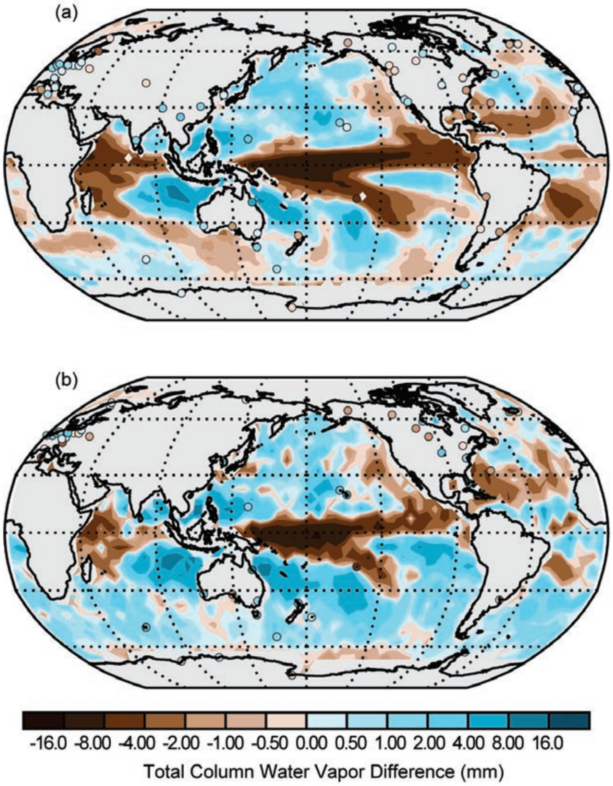

Fig. 2.13. Change in total column water vapor anomalies from Jan–Jun 2010 to Jul–Dec 2010. (a) Measurements from AMSR-E and ground-based GPS stations. (b) Measurements from COSMIC, calculated using climatological data from SSM/I and AMSR-E over ocean and using climatological data from ground-based GPS over land.

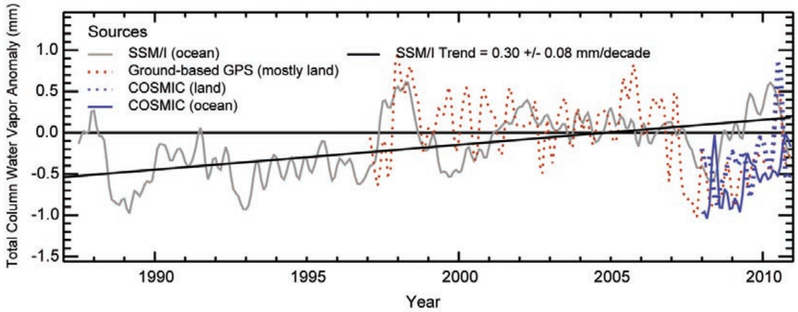

Fig. 2.14. Anomaly time series of total column water vapor both from SSM/I, ground-based GPS, and COSMIC (1997–2009 base period). The COSMIC ocean anomalies are calculated relative to an SSM/I climatology for 1997–2009. The COSMIC land anomalies are calculated only at the locations of GPS ground stations, and are relative to a 1997–2009 ground-based GPS climatology. The time series have been smoothed to remove variability on time scales shorter than six months.

requirement were relaxed since the size of the network is increasing rapidly with time. There is general agreement between the AMSR-E and ground-based GPS measurements at locations where overlaps occur with differences typically less than 0.5 mm. In the Pacific Ocean there is a large "C"-shaped dry anomaly, while in the oceans surrounding northern Australia, there is a very strong wet anomaly. Both features are associated with the onset of a moderate-to-strong La Niña event during the latter half of 2010. The onset of La Niña is depicted more clearly by plotting the TCWV difference between the July–December and January–June averages for 2010 (Fig. 2.13). The changes in TCWV from early to late 2010 measured by three different measurement systems [AMSR-E (ocean), GPS (land) and the Constellation Observing System for Meteorology, Ionosphere and Climate (COSMIC; land and ocean; Anthes et al. 2008; Ho et al. 2010] show the dramatic drying of the tropical Pacific as the climate system shifted to moderate-to-strong La Niña conditions by fall 2010.

The combined Special Sensor Microwave Imager (SSM/I) AMSR-E TCWV, from the world's ice-free oceans, shows dramatic maxima in 1987/88, 1997/98, and 2009/10, associated with El Niño events (Fig. 2.14). Minima are apparent in Northern Hemisphere winters during the La Niña events of 1988/89, 1992/93 (also influenced by the eruption of Mount Pinatubo), 1999/2000, 2007/08, and late 2010. GPS data, only available since 1997, show similar features (Fig. 2.14). An exact match between SSM/I and AMSR-E and GPS is not expected since the two measurement systems sample different regions of the globe. The COSMIC data are in good agreement with the GPS data, but are biased slightly low relative to the SSM/I and AMSR-E data. A Hovmöller plot derived from SSM/I and AMSR-E (Fig. 2.15) shows that the changes associated with El Niño/La Niña are largest in the tropics.

3) Precipitation—P. Hennon, M. Kruk, K. Hilburn, X. Yin, and A. Becker

Annual land precipitation anomalies (Fig. 2.16) were calculated from the Global Historical Climatology Network Monthly Version 2 (GHCN; Peterson and Vose 1997), the Global Precipitation Climatology (GPCC; Schneider et al. 2008), and the Global Precipitation Climatology Project Version 2.1 (GPCP; Adler et al. 2003) datasets, and were determined with respect to the 1961–90 mean using stations reporting a minimum of 25 years of data during the base period. The global anomaly for 2010 and percent change over time are shown using GHCN in Plate 2.1g and Fig. 2.17, respectively.

The year 2010 exhibited a large positive mean precipitation anomaly in GHCN and GPCC (no 2010 data is yet available for GPCP). The GHCN indicates the globally averaged annual precipitation over land was 1112.1 mm, or 50.4 mm above normal. According to GPCC, the anomaly was 938.5 mm or 21.5 mm above normal. While both positive, the difference in magnitude between

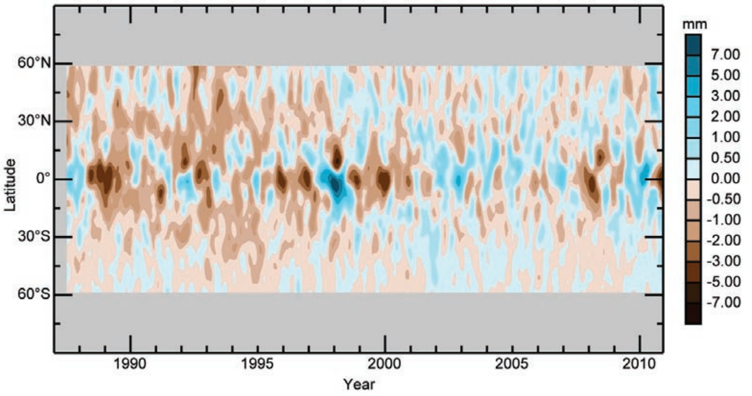

Fig. 2.15. SSM/I and AMSR-E measurements of monthly mean total column water vapor anomalies by latitude. The anomalies are relative to a base period of 1997–2009 smoothed in the time direction to remove variability on time scales shorter than four months. Gray areas indicate regions where data are unavailable.

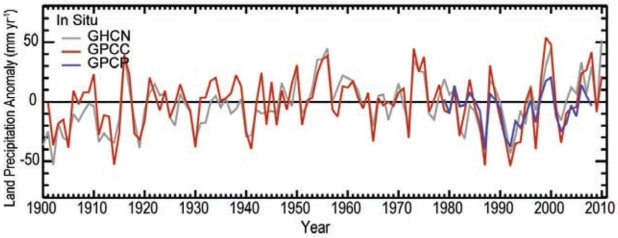

Fig. 2.16. Global average precipitation annual anomalies over land from in situ data. All data are shown relative to a 1961–90 base period.

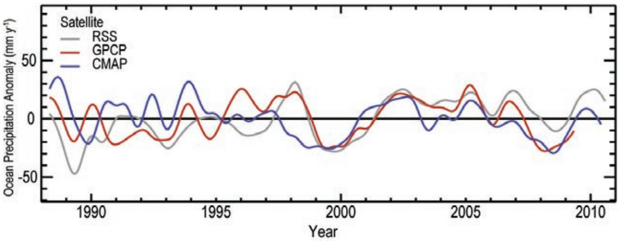

Fig. 2.18. Global average precipitation annual smoothed anomalies over ocean from satellites. All datasets are shown relative to a 1988–2010 base period.

the GHCN and the GPCC time series is presumably tied to the number of available stations for use in the analysis, with GPCC incorporating at least an order of magnitude more stations than GHCN (NOAA, 7 January 2011: http://www.ncdc.noaa.gov/ghcnm/v2.php; Rudolf and Becker 2011).

Global ocean coverage is provided by satellite-based observations. Microwave sensors measure the total liquid in the column. The microwave era now spans 23 complete years, enabling the monitoring of climate variations. The global ocean precipitation climatology is produced using Remote Sensing Systems (RSS) intercalibrated passive microwave rain retrievals from a total of eight microwave imagers (Hilburn and Wentz 2008a). For 2010, data are available from the TRMM Microwave Imager (TMI) and the Advanced Microwave Scanning Radiometer-EOS (AMSR-E). Data from F13 Special Sensor Microwave Imager (SSM/I) stopped in November 2009; and while F15 is still producing data, contamination from a RADCAL beacon (Hilburn and Wentz 2008b) precludes their usage for climate monitoring.

Figure 2.18 shows global ocean time series for RSS as well as Version 2.1 GPCP (Adler et al. 2003) and V1101 CPC Merged Analysis of Precipitation (CMAP) data (Xie and Arkin 1997). Analysis of these satellite datasets shows a return to drier anomalies in 2010 after a wet year in 2009. The contrast between the global land and ocean precipitation is notable.

Precipitation anomalies in 2010, over both land and ocean reflected the transition from El Niño to La Niña during the boreal summer 2010. Over land there are drier conditions across the Southern Hemisphere and wetter-than-average conditions across the Northern Hemisphere midlatitudes (Fig. 2.17). Over the ocean, the time-latitude section (Fig. 2.19) shows a wet anomaly just north of the Equator, replaced by a dry anomaly midyear. The subtropical Southern Hemisphere was covered by an expansive but weak dry anomaly. Both the northern and southern midlatitudes had moist anomalies. The anomaly map for 2010 (Plate 2.1g) shows a complex mix of El Niño- and La Niña-related anomalies over the western tropical Pacific and wet anomalies over the southern Indian Ocean. Wet anomalies surrounded the Indian subcontinent and the Atlantic Ocean.

The seasonal analyses of global precipitation anomalies over land (Fig. 2.20) show patterns consistent with El Niño in December–February (a) and the transition to the developing La Niña in late-season [March–May, (b)], with classic La Niña patterns by June–August (c) continuing through September–November (d). During March–May the Northern Hemisphere exhibited wetter-than-average conditions. In

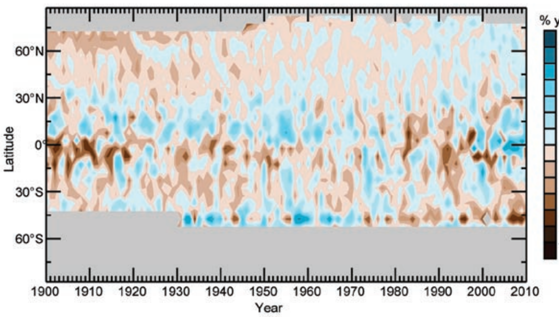

Fig. 2.17. GHCN measurements of annual mean precipitation anomalies over land by latitude. The anomalies are relative to a base period of 1961–90. Gray areas indicate regions where data are unavailable.

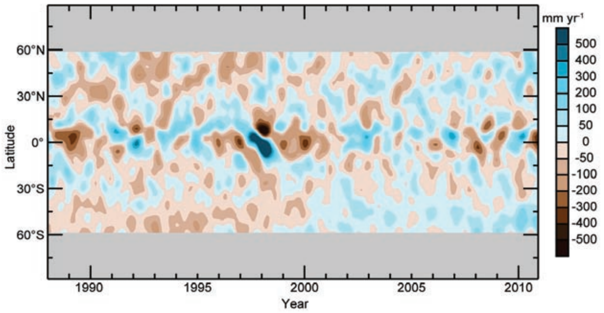

Fig. 2.19. RSS measurements of monthly mean precipitation anomalies over ocean by latitude. The anomalies are relative to a base period of 1988–2010. Gray areas indicate regions where data are unavailable.

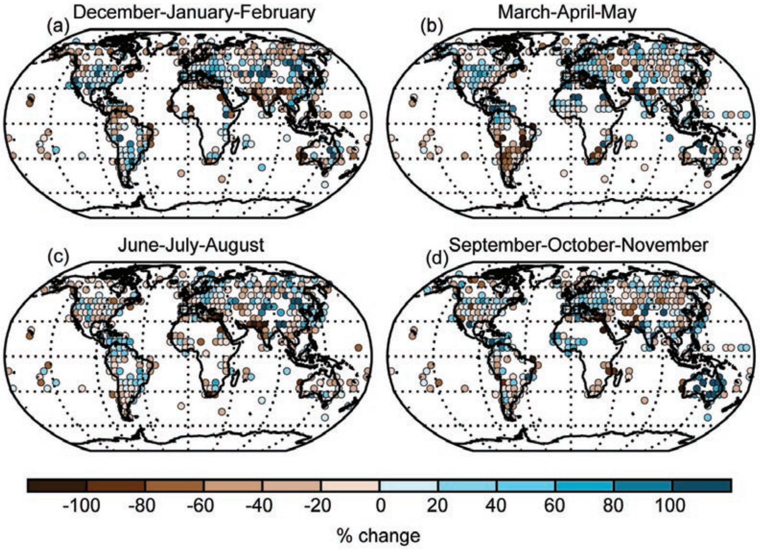

Fig. 2.20. Seasonal global precipitation anomalies determined using the GHCN-monthly dataset for (a) Dec 2009–Feb 2010, (b) Mar–May 2010, (c) Jun–Aug 2010 and (d) Sep–Nov 2010. Seasonal anomalies are shown relative to a 1961–90 base period, where, for inclusion, at least 66% of years without missing data during the base period are required.

the Southern Hemisphere, dry conditions prevailed along the western continental margins consistent with a developing La Niña. In September–November, the Southern Hemisphere precipitation anomalies exhibited classic La Niña signals with predominantly dry conditions in South America and South Africa and wet conditions in central and eastern Australia.

4) NORTHERN HEMISPHERE CONTINENTAL SNOW COVER EXTENT—D. A. Robinson

Annual snow cover extent (SCE) over Northern Hemisphere land averaged 24.6 million km^2 in 2010. This is 0.4 million km^2 less than the 41-year average and ranks 2010 as having the 13th least extensive cover on record (Table 2.3). This evaluation considers snow over the continents, including the Greenland ice sheet. The SCE in 2010 ranged from 48.4 million km^2 in February to 2.4 million km^2 in August. Monthly SCE is calculated at the Rutgers Global Snow Lab from daily SCE maps produced by meteorologists at the National Ice Center (a U.S. joint NOAA, Navy, and Coast Guard facility), who rely primarily on visible satellite imagery to construct the maps.

The year began with SCE in the highest quartile over Eurasia and North America. February had the third greatest SCE over North America and the Northern Hemisphere. Eurasia remained in the top quartile in March while snow melted exceedingly quickly over North America, resulting in a decline to the lowest quartile. April SCE was the lowest on record across North America, with both North America and Eurasia ranking lowest in May and June. The 2010/11 snow season began with SCE a little above average in October and November, rising to the fourth highest value across Northern Hemisphere lands in December.

The expansive fall and winter SCE of the past two years has generally countered the low extents of spring and summer. Thus the 12-month running Northern Hemisphere SCE mean has recently been just below the long-term average (Fig. 2.21). Recent means are higher than throughout immediate preceding years.

The expansive winter cover appears to be associated with a strongly negative Arctic Oscillation during early and late 2010. This delivered enough cold air to midlatitude regions to result in significant snowfall and an expansion of SCE. This is apparent over the contiguous United States, where SCE ranked in the highest quartile during January and February 2010, before falling to the lowest quartile in April and May. New seasonal snow at year's end resulted in a top quartile ranking for November and December SCE. Alaskan snow melt was on the early side, with May and June SCE in the lower quartile. A slow start to the 2010/11 Alaskan snow season was followed by above-average SCE in November.

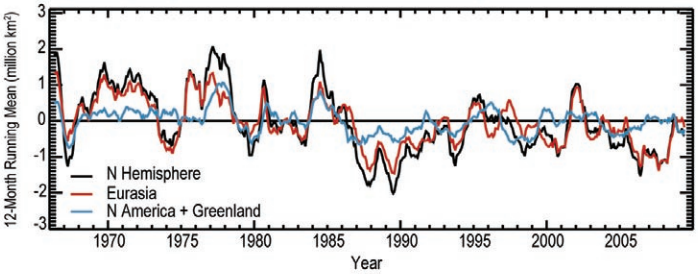

Fig. 2.21. Twelve-month running anomalies of monthly snow cover extent over Northern Hemisphere land (including Greenland) as a whole and Eurasia and North America separately between Nov 1966 and Dec 2010. Anomalies are calculated from NOAA snow maps. Mean hemispheric snow extent is 25.0 million km^2 for the full period of record. Monthly means for the period of record are used for nine missing months between 1968 and 1971 in order to create a continuous series of running means. Missing months fall between June and October; no winter months are missing.

Table 2.3. Monthly and annual climatological information on Northern Hemisphere and continental snow extent between November 1966 and December 2010. Included are the numbers of years with data used in the calculations, means, standard deviations, 2010 values, and rankings. Areas are in millions of square kilometers. 1968, 1969, and 1971 have 1, 5, and 3 missing months respectively, thus are not included in the annual (Ann) calculations. North America (N. Am.) includes Greenland. Ranks are from most extensive (1) to least (ranges from 41 to 45 depending on the month).

	Yrs	Mean	Std. Dev.	2010	2010 N.Hem. rank	Eurasia rank	N. Am. rank
Jan	44	46.7	1.5	48.3	6	11	6
Feb	44	45.6	1.8	48.4	3	10	3
Mar	44	40.3	1.8	40.6	18	10	37
Apr	44	30.5	1.7	28.3	41	21	44
May	44	19.5	1.8	15.2	44	44	44
Jun	43	10.1	2.1	6.0	43	43	43
Jul	41	4.2	1.2	2.6	40	40	40
Aug	42	3.1	0.7	2.4	36	38	32
Sep	42	5.3	0.9	5.3	19	20	20
Oct	43	17.9	2.5	18.8	15	13	17
Nov	45	33.6	2.0	34.0	20	25	13
Dec	45	43.3	1.8	45.7	4	6	7
Ann	41	25.0	0.9	24.6	29	21	33

Maps depicting daily, weekly (new), and monthly conditions, daily (new) and monthly anomalies, and monthly climatologies for the entire period of record may be viewed at the Rutgers Global Snow Lab website (see Table 2.1). Monthly SCE for the Northern Hemisphere, Eurasia, North America, the contiguous United States, Alaska, and Canada are also posted, along with information on how to ftp weekly areas and the weekly and monthly gridded products.

5) Global cloudiness—M. Foster, S. A. Ackerman, A. K. Heidinger, and B. Maddux

Global cloudiness in 2010 was characterized by a shift in the El Niño-Southern Oscillation, a negative phase of the Arctic Oscillation, and some continental cloudiness anomalies. During the early part of the year, sea surface temperature and wind field anomalies associated with El Niño drove enhancement of large-scale convection in the central Pacific and suppression of convective activity in the western Pacific near Indonesia, as shown by PATMOS-X cloudiness in Fig. 2.22a. During the boreal spring (Fig. 2.22b) a transition from El Niño to ENSO-neutral occurred, resulting in positive cloudiness anomalies around Indonesia and negative anomalies around the central equatorial Pacific by midyear (Fig. 2.22c). La Niña conditions emerged in July and persisted through the rest of the year. As a consequence of both phases of ENSO occurring in 2010, the annual global cloudiness anomaly map does not show a strong ENSO signature over much of the Pacific (Plate 2.1d), though the ~20% negative anomaly off the coast of Papua New Guinea is statistically significant at the 5% level, as is the dipole off the coast of Peru and Chile.

The Arctic Oscillation was negative for most of 2010. This may partially explain the 2010 cloud anomalies seen in the Northern Hemisphere winter, e.g., lower cloud amount over Eurasia, the North Atlantic, and northeast Pacific, and increased cloud amounts over eastern North America.

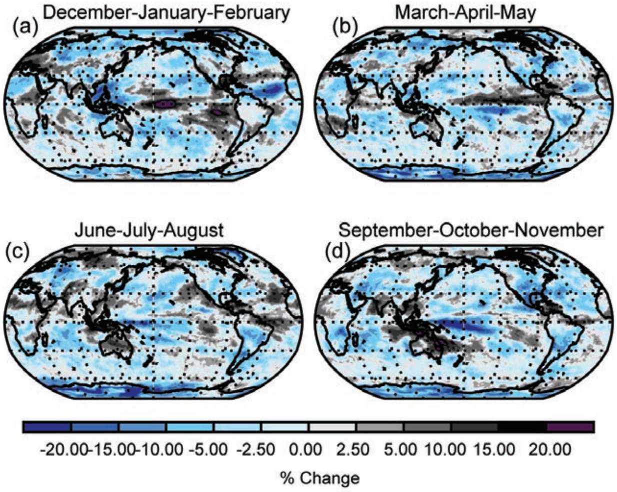

Fig. 2.22. Seasonal global cloudiness anomalies determined using the PATMOS-X dataset for (a) Dec 2009–Feb 2010, (b) Mar–May 2010, (c) Jun–Aug 2010, and (d) Sep–Nov 2010. Seasonal anomalies are calculated by subtracting the mean cloud fraction over the 1982–2010 base period from that of 2010.

Some annual cloudiness anomalies that are significant at the 5% level coincided with some continental extreme weather conditions. For example, positive annual cloudiness anomalies occurred over eastern Australia, which experienced one of its wettest years on record (see section 7h1). Significant negative annual anomalies occurred over Russia and northwestern Brazil, where severe drought conditions persisted for much of the year (see sections 7g1 and 7d2, respectively).

Figure 2.23 shows global mean monthly cloud anomalies from six cloud records. The HIRS cloud retrieval record works on the premise that synthesis of discrete carbon dioxide absorption bands in the IR spectrum can be used to detect the presence of cloud. In addition, an updated version of the PATMOS-x record (Version 5) is used, which includes a new Bayesian cloud masking algorithm and a diurnal correction to account for satellite drift. The monthly mean values from which the anomalies are derived are necessarily different for each record as the periods and lengths of the records vary, making a direct comparison challenging. The cloud record anomalies are smaller than the seasonal and diurnal variability within each data record. Relative differences between the records can in part be attributed to variations in how cloud-masking algorithms define cloud versus clear-sky thresholds. Artifacts within each record may also arise from factors such as satellite drift and sensor calibration. Relative to the entire PATMOS-x time series, 2010 was less cloudy than average. The mean cloudiness for the year was 64.6%, which is 1.2% lower than the 29-year average, making 2010 the seventh least cloudy year of the record. All twelve months were less cloudy than their climatological monthly means over the entire record.

6) River discharge—B. M. Fekete and A. Macdonald

The lack of a global, real-time reporting, discharge-monitoring network still hinders the accurate assessment of river flow. Although the monitoring infrastructure is largely in place (Hannah et al. 2011), continued difficulty in attracting funding and fostering international cooperation are major obstacles even though traditional in situ networks are much cheaper than satellite platforms. Remote sensing capabilities to estimate riverine water fluxes have been discussed by a number of authors (Alsdorf and Lettenmaier 2003; Alsdorf et al. 2007; Andreadis et al. 2007; Brakenridge et al. 2005). Recently, Syed et al. (2010) proposed calculation of fresh water fluxes from the continents, based on satellite-measured precipitation and evaporation over the ocean in conjunction with sea level measurement. The authors identified a weak overall increase in discharge to the oceans during the 1994–2006 period composed of a rapid increase between 1994 and 2000, followed by

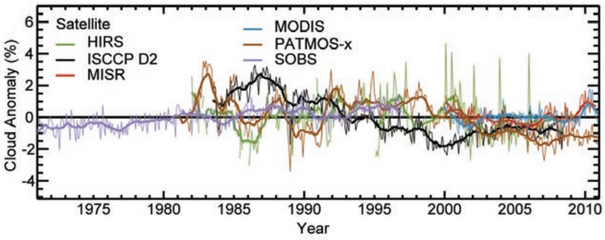

Fig. 2.23. Global average cloudiness monthly anomalies, defined as the current month minus the mean over the entire dataset for the corresponding month. The datasets include (a) surface weather observations (SOBS; Hahn and Warren 2007) spanning 1971–96; (b) Moderate Resolution Imaging Spectroradiometer (MODIS; Ackerman et al. 2008); (c) Multiangle Imaging Spectroradiometer (MISR; Di Girolamo et al. 2010) instruments, which are located on NASA's Terra satellite and span 2000–present (a MODIS instrument is also located on NASA's Aqua satellite and is included in the climatology); (d) International Satellite Cloud Climatology Project (ISCCP) data derived from the imaging radiometers on the operational weather satellites of several nations for the period 1983–2008; (e) High Resolution Infrared Sounder (HIRS; Wylie et al. 2005); and (f) PATMOS-x AVHRR (Heidinger and Pavolonis 2009), which are instruments located on the NOAA polar orbiting satellite series. Thick solid lines represent the time series of average cloudiness with a 12-month boxcar filter applied.

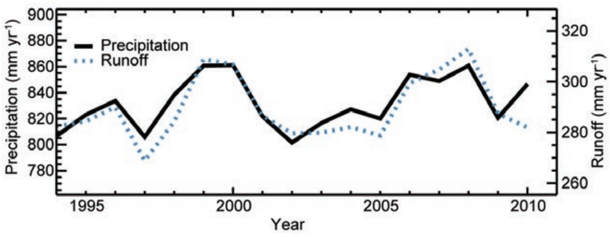

Fig. 2.24. Annual continental precipitation from GPCC full product extended with the monitoring product for 2010 and the corresponding water balance model-simulated continental runoff using NCEP air temperature forcing.

a slow decline during the next six years. The Syed et al. (2010) study is consistent with the water balance calculations presented here, that are forced by NCEP reanalysis (Kalnay et al. 1996; Kistler et al. 2001) air temperatures combined with monthly precipitation estimates from the Global Precipitation Climate Center (GPCC; Fig. 2.24). The error bars reported by Syed et al. (2010) are of similar magnitude to uncertainties in typical water balance calculations (Vörösmarty et al. 1998); however, the former approach lacks spatial specificity within the continental land mass. Traditional hydrological model simulations appear to offer the best approximation of water resources when in situ observations are missing.

In 2010, GPCC revised its full product from V004 (covering 1901–2007) to V005 for the 20th century. They introduced a new monitoring product, V3, which addressed the bias between the full and monitoring products that were reported here last year. The improved consistency between the full and monitoring products allowed a continuous river discharge simulation from the historical past to the present. The historical simulation (1901–2002) combines the GPCC full product with gridded monthly air temperature (T_A) from the Climate Research Unit of University of East Anglia (CRU; New et al. 2000). Contemporary simulations (1948–present) use NCEP reanalysis daily air temperature as forcing and precipitation for downscaling monthly GPCC precipitation products to daily temporal frequency, while maintaining the monthly totals from GPCC.

Global runoff in 2010 decreased slightly compared to 2009 (Fig. 2.25; Plate 2.1h—absolute values) but it remained higher than the long-term 20th century average. In 2010, Asia experienced greater runoff compared to both the 20th century and the last decade (Fig. 2.25a). This can also be seen in the higher than long-term average runoff to the Indian and Pacific Oceans (Fig. 2.25b). In contrast, South America remained drier and the Atlantic Ocean received less runoff than the long-term average. These continental and ocean basin trends have significant spatial variations within continents, as shown in Fig. 2.26. Re-

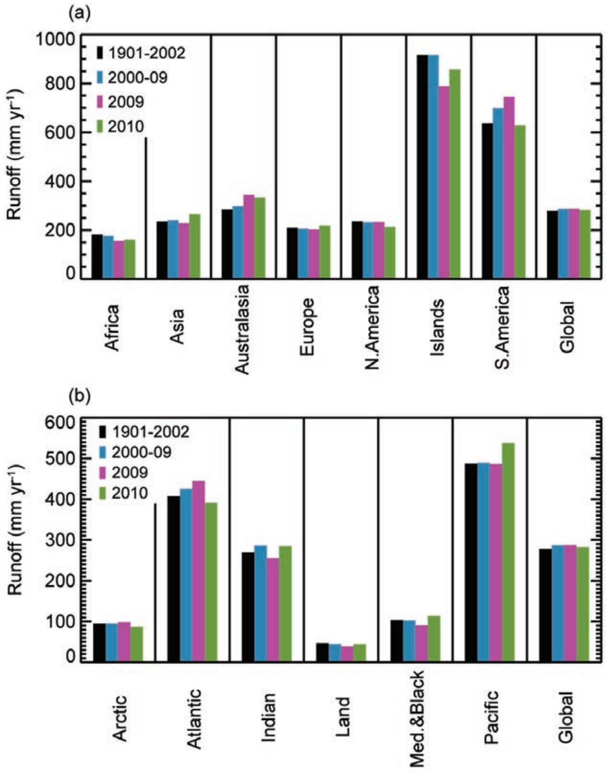

Fig. 2.25. River runoff by (a) continent and (b) receiving oceans, comparing average runoff over the 1901–2002 and 2000–09 periods to 2009 and 2010. "Islands" refers to the Pacific Islands, "Med.+Black" refers to the Mediterranean and Black Sea drainage regions and "Land" represents the mean of all internal (endorheic) basins found on every continent.

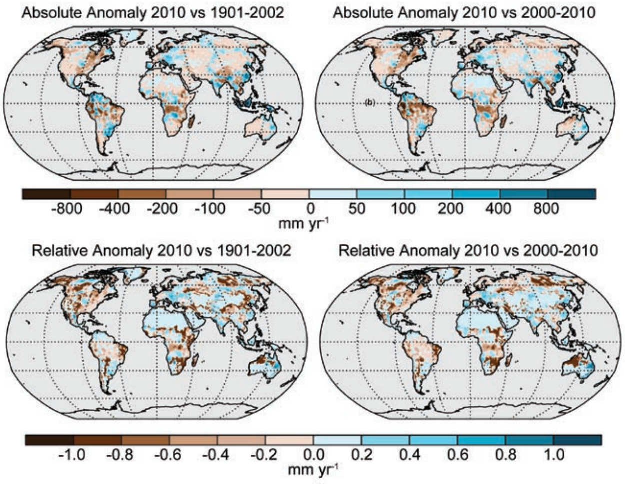

Fig. 2.26. Absolute and relative anomalies for river discharge in 2010 with respect to the long-term average over the 20th century and for the last decade.

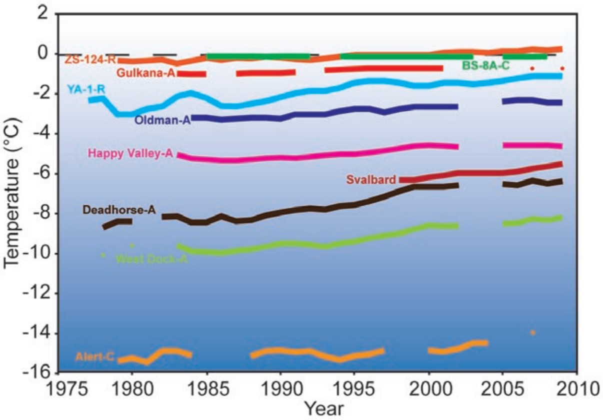

Fig. 2.27. Time series of mean annual ground temperatures at depths between 10 m and 20 m for boreholes throughout the circumpolar northern permafrost regions. Data sources: North American (Smith et al. 2010), Russian (Romanovsky et al. 2010b), and Nordic sites (Christiansen et al. 2010). 'C' denotes a Canadian site; 'A' denotes an Alaskan site; and 'R' denotes a Russian site. The Svalbard site is Janssonhaugen, which is also called PACE-10 (Isaksen et al. 2007). Measurement depth for Russian boreholes and 85-8A is 10 m; Gulkana, Oldman and Alert are 15 m; and all other boreholes are 20 m. Coordinates for borehole locations are: ZS-124: 67.4°N, 63.4°E; 85-8A: 61.6°N, 121.1°W; Gulkana: 62.2°N, 145.5°W; YA-1: 67.5°N, 64°E; Oldman: 66.4°N, 150.6°W; Happy Valley: 69.1°N, 148.8°W; Svalbard: 78.2°N, 16.5°E; Deadhorse: 70.2°N, 148.5°W; West Dock: 70.4°N, 148.5°W; Alert: 82.5°N, 62.4°W. [Source: Romanovsky et al. (2010b)]

gions with higher-than-average runoff were southern Spain, Central Europe, Pakistan, India, and China, while Brazil, the eastern United States, and Alaska were drier than average.

7) PERMAFROST THERMAL STATE—H. Lantuit, H. Christiansen, J. Noetzli, V. Romanovsky, N. Shiklomanov, S. Smith, G. Vieira, and L. Zhao

During the International Polar Year (IPY) in 2008 and 2009 there was substantial enhancement of the permafrost monitoring network in the polar regions (e.g., Christiansen et al. 2010; Romanovsky et al. 2010a; Smith et al. 2010; Vieira et al. 2010), and also in the high altitude regions of Europe, Scandinavia, and Asia (PERMOS 2010; Schoeneich et al. 2010; Isaksen et al. 2011; Zhao et al. 2010). Current permafrost thermal state data are now publicly available (see Table 2.1). Enhancement of the network has been aimed at areas with little recent information and to cover the range of climate, vegetation, geomorphologic, and geologic conditions in the global permafrost regions. Data from Russia and North America (see Table 2.1) indicate that permafrost temperatures within the discontinuous zone fall within a narrow range, generally 0°C to -2.5°C. In the continuous zone (e.g., high Arctic), permafrost can be as cold as -15°C (Fig. 2.27; Romanovsky et al. 2010a; Smith et al. 2010). New information on permafrost in Antarctica showed temperatures slightly below 0°C in the South Shetlands near sea level, decreasing southwards and eastwards in the Antarctic Peninsula region. In other regions of the Antarctic continent, temperatures are much lower, varying from -8°C at low-altitude coastal sites to below -17°C at the McMurdo Dry Valleys and higher elevation sites. Active layer depths range from over 1.6 m, especially at bedrock sites in the maritime Antarctic, to less than 0.1 m in some sites in continental Antarctica (Vieira et al. 2010). Here, temperatures are often taken from shallow boreholes and may not be representative of the mean annual ground temperature (MAGT). In Central Asia, much of the permafrost is currently close to 0°C (Zhao et al. 2010). In the European Alps and Scandinavian mountains, permafrost distribution is discontinuous and MAGT measured in boreholes are typically between 0°C and -3°C, with sites at very high elevation as well as in polar mountain regions being considerably colder (e.g., Haeberli et al. 2010; Fig. 2.28). Spatial variability of surface thermal conditions is high here and results from steep topography, heterogeneous surface characteristics, and snow cover.

Data records, some 30 years in length, are available for some sites in polar and mountain regions of

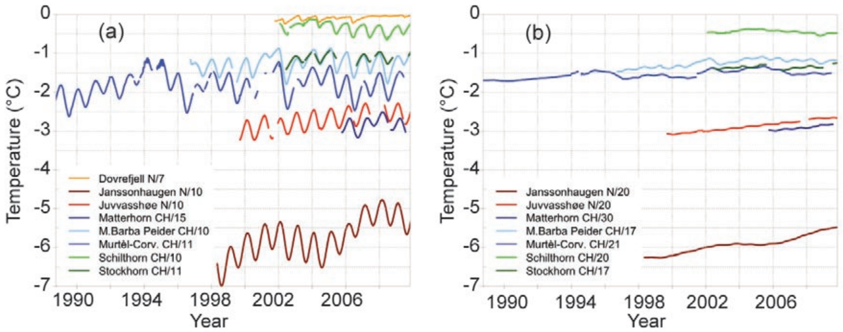

Fig. 2.28. Observed subsurface temperatures at (a) 10 m and (b) 20 m depth for selected boreholes in mountain permafrost: the sites of the PACE transect, the Matterhorn and M.d. Barba Peider sites in Switzerland, and Dovrefjell in Norway. Data for Swiss sites are provided by PERMOS, and for Norwegian sites by the Norwegian Meteorological Institute. [Modified from Haeberli et al. (2010, figure 4).]

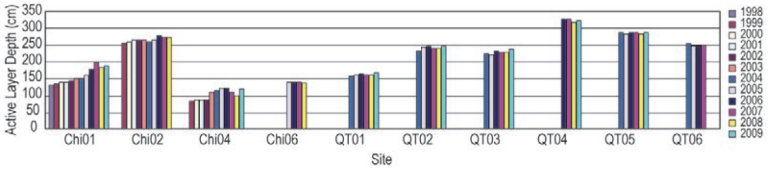

Fig. 2.29. Temporal trends in active layer depths along the Qinghai-Tibet Railway. [Modified from source: Zhao et al. (2010).]

the Northern Hemisphere for both permafrost temperatures and active layer depths. The latter respond to seasonal fluctuations in climate while changes of the deeper ground temperatures indicate long-term trends since shorter-term variations attenuate with depth. The deeper the temperatures are measured, the further back in time the surface temperature conditions they represent.

Permafrost generally warmed across the Northern Hemisphere during the past 20 to 25 years of the 20th century, and into the first few years of the 21st century (e.g., Romanovsky et al. 2007; Harris et al. 2003; Isaksen et al. 2007). Analyses of more recent data indicate that warming has generally continued. Permafrost temperatures are now up to 2°C warmer than they were 20 to 30 years ago although there are regional differences (Fig. 2.27). The overall range in permafrost temperature has decreased and is now about 1°C less than it was about 30 years ago in the polar Northern Hemisphere (Romanovsky et al. 2010b). Smaller warming rates are observed at temperatures close to 0°C compared to colder permafrost. This is especially true for ice-rich permafrost where latent heat effects dominate the ground thermal regime at temperatures close to 0°C (e.g., Romanovsky et al. 2010a; Smith et al. 2010), as well as for mountain regions in Europe where large permafrost areas are close to melting (PERMOS 2010; Haeberli et al. 2010; Isaksen et al. 2011). In European mountain permafrost, some 10-year records show a general warming trend (Isaksen et al. 2007; Haeberli et al. 2011) and permafrost temperature anomalies associated with extreme warm years (2003, 2009) have also been observed (Fig. 2.28; PERMOS 2010; Phillips et al. 2009; Zenklusen Mutter et al. 2010; Harris et al. 2003). However, trends are more pronounced in Scandinavia than in Central Europe, where only small changes or even cooling trends (Zenklusen Mutter et al. 2010) can be observed because of the strong influence of the snow cover and temperature ranges subject to latent heat effects. In the higher altitudes of Asia, ground temperatures have increased up to 0.5°C decade^{-1} since the early 1990s, accompanied by a general increase in active layer thickness (e.g., Zhao et al. 2010; Fig. 2.29). Although the observed trends in permafrost temperatures are consistent with changes in air temperatures, other factors such as snow cover, soil properties (including ice and moisture content), and vegetation are important factors determining the magnitude of the changes in the ground thermal regime (e.g., Haeberli et al. 2010; Romanovsky et al. 2010b).

8) Groundwater and terrestrial water storage—

M. Rodell, D. P. Chambers, and J. S. Famiglietti

Most people think of groundwater as a resource, but it is also a useful indicator of climate variability and human impacts on the environment. Groundwater storage varies slowly relative to other non-frozen components of the water cycle, encapsulating long period variations and trends in surface meteorology. On seasonal to interannual timescales, groundwater is as dynamic as soil moisture (Rodell and Famiglietti 2001; Alley et al. 2002), and it has been shown that groundwater storage changes have contributed to sea-level variations (Milly et al. 2003; Wada et al. 2010).

Groundwater monitoring well measurements are too sporadic and poorly assembled outside of the United States and a few other nations to permit direct global assessment of groundwater variability. However, observational estimates of terrestrial water storage (TWS) variations from the GRACE satellites (see Sidebar 2.2) largely represent groundwater storage variations on an interannual basis, save for high latitude/altitude (dominated by snow and ice) and wet tropical (surface water) regions (Rodell and Famiglietti 2001).

Plate 2.1i maps changes in mean annual TWS from 2009 to 2010, based on GRACE, reflecting hydroclimatic conditions in 2010. Severe droughts impacted Russia and the Amazon, and drier-than-normal weather also affected the Indochinese peninsula, parts of central and southern Africa, and western Australia. Groundwater depletion continued in northern India (Rodell et al. 2009; Tiwari et al. 2009), while heavy rains in California helped to replenish aquifers that have been depleted by drought and withdrawals for irrigation, though they are still below normal levels (Famiglietti et al. 2011). Droughts in northern Argentina and western China similarly abated. Wet weather raised aquifer levels broadly across Western Europe. Rains in eastern Australia caused flooding to the north and helped to mitigate a decade-long drought in the south. Significant reductions in TWS seen in the coast of Alaska and the

SIDEBAR 2.2: CONTRIBUTIONS OF GRACE TO CLIMATE MONITORING—M. RODELL, J. S. FAMIGLIETTI, D. P. CHAMBERS, AND J. WAHR

The NASA/German Gravity Recovery and Climate Experiment (GRACE) was launched in March 2002. Rather than looking downward, GRACE continuously monitors the locations of and precise distance between twin satellites that orbit in tandem about 200 km apart. Variations in mass near Earth's surface cause heterogeneities in its gravity field, which in turn affect the orbits of satellites. Thus, scientists can use GRACE data to map Earth's gravity field with enough accuracy to discern month-to-month changes caused by ocean circulation and redistribution of water stored on and in the land (Tapley et al. 2004; Wahr et al. 2004). Sources of uncertainty include the inherent limitations of the measurement technique and instruments, issues associated with spatial resolution and mathematical representation of the gravity field, and inaccuracy in removing other gravitational influences, such as atmospheric circulation, post-glacial rebound, and solid earth movements, which are either independently modeled and removed or are assumed to be negligible on a monthly to sub-decadal timescales.

Despite its coarse spatial (> 150 000 km^2 at midlatitudes) and temporal (~monthly) resolutions, GRACE has enabled significant advances in oceanic, hydrologic, and cryospheric science, and has great potential for climate monitoring because it is the only global observing system able to measure ocean bottom pressures, total terrestrial water storage, and ice mass changes.

The best known GRACE results are estimates of Greenland and Antarctic ice sheet loss rates (Fig. 2.30). Previously, scientists had estimated ice mass losses using ground and satellite-based altimetry and surface mass balance estimates based on snowfall accumulation and glacier discharge. While such measurements are still very useful for their spatial detail, they are imperfectly correlated with large-scale ice mass changes, due to snow and ice compaction and incomplete spatial coverage. GRACE enables scientists to generate monthly time series of Greenland and Antarctic ice mass, which have confirmed the shrinking of the polar ice sheets, one of the most obvious and indisputable manifestations of climate change (e.g., Velicogna and Wahr 2006a, 2006b). Further, GRACE has located and quantified hot spots of ice loss in southeastern Greenland and western Antarctica (e.g., Luthcke et al. 2006). For 2002 to present, the mean annual rate of ice mass loss has been estimated between 200 Gt yr^{-1} and 300 Gt yr^{-1} in Greenland and between 70 Gt yr^{-1} and 210 Gt yr^{-1} in Antarctica, and some scientists are suggesting that the rates are accelerating (Velicogna 2009). Similarly, GRACE has been used to monitor mass changes in alpine glaciers. Tamisiea et al. (2005) first characterized glacier melt along the southern coast of Alaska, more recently estimated to be occurring at a rate of 84 ± 5 Gt yr^{-1} (Luthcke et al. 2008). Chen et al. (2007) estimated that Patagonian glaciers are melting at a rate of 28 ± 11 Gt yr^{-1}, and Matsuo and Heki (2010) estimated that the high mountains of central Asia lose ice at a rate of 47 ± 12 Gt yr^{-1}.

Tapley et al. (2004) and Wahr et al. (2004) presented the first GRACE-based estimates of changes in column-integrated terrestrial water storage (TWS; the sum of groundwater, soil moisture, surface waters, snow, ice, and water stored in vegetation) at continental scales. Since then, dozens of studies have shown that GRACE-based estimates of regional- to continental-scale TWS variations agree with independent information and some innovative uses of GRACE data have been developed. Rodell et al. (2004) and Swenson and Wahr (2006) demonstrated that by combining GRACE-derived terrestrial water storage changes with observations of precipitation and runoff in a river basin scale water budget, it was possible to produce new estimates of evapotranspiration and atmospheric moisture convergence, essential climate variables that are difficult to estimate accurately. Similarly, GRACE has been used to constrain estimates of global river discharge and the contribution of changes in TWS to sea-level rise (Seo et al. 2009; Syed et al. 2009, 2010). Crowley et al. (2006) observed a negative correlation between interannual TWS anomalies in the Amazon and the Congo River basin. Yeh et al. (2006) and Rodell et al. (2007) estimated regionally-

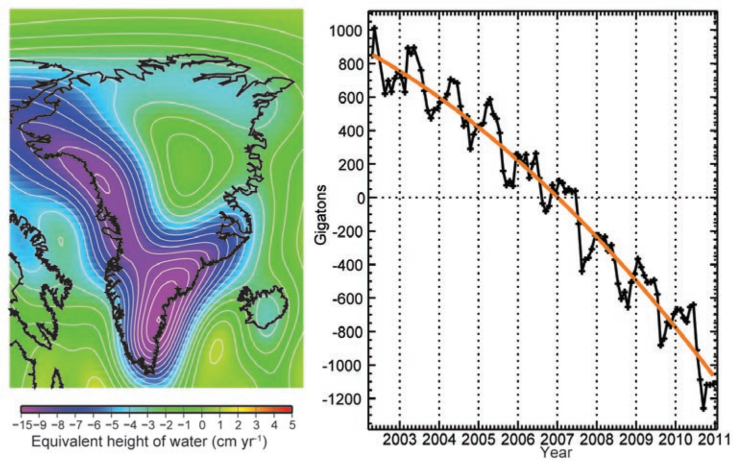

FIG. 2.30. (Left) Rate of ice sheet mass change (cm yr^{-1}, equivalent height of water) in Greenland from GRACE, April 2002–November 2010. (Right) Time series of Greenland total ice sheet mass (Gigatons) relative to the period mean.

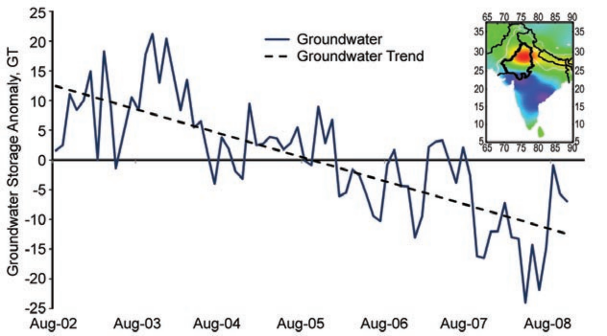

Fig. 2.31. Time series of groundwater storage in northwest India from August 2002 to October 2008 relative to the period mean. The inset panel shows areas of depletion in warm colors and areas of increase in cool colors, with the study region (the Indian states of Rajastan, Punjab, and Haryana) outlined in black. Based on data from Rodell et al. (2009).

averaged groundwater storage variations based on GRACE and auxiliary observations. Rodell et al. (2009) and Tiwari et al. (2009) applied that method to quantify massive groundwater depletion in northern India caused by over reliance on aquifers for irrigation (Fig. 2.31), and Famiglietti et al. (2011) found a similar situation in California's Central Valley. Zaitchik et al. (2008) and Lo et al. (2010) described approaches to use GRACE to constrain hydrological models, enabling integration of GRACE data with other observations and achieving much higher spatial and temporal resolutions than GRACE alone. Such approaches are now supporting applications including drought and water resources monitoring (Houborg and Rodell 2010; Bolten et al. 2010).

Oceanography has likewise benefitted from the independent nature of GRACE observations. One application is measurement of the mass component of sea-level rise, which complements radar altimetry and in situ measurements. GRACE also measures ocean bottom pressures (OBP), which help to refine understanding and modeling of ocean circulation and the ocean's fresh water budget, among other things (Fig. 2.32). Morison et al. (2007) used GRACE to describe important decadal-scale shifts in circulation and an ongoing trend of freshening of part of the Arctic Ocean, important indicators of climate variability. The research of Song and Zlotnicki (2008) and Chambers and Willis (2008) on GRACE-derived ocean bottom pressures in the subpolar gyre led to the discovery of an ENSO teleconnection and a long-term change in OBP in the North Pacific subpolar gyre that was not predicted by an ocean model. Further, Chambers and Willis (2009) were able to identify an interannual redistribution of mass between oceans, which was not predicted by an ocean model and was the first direct evidence of sustained mass transport from one ocean basin to another on periods longer than a year. Boening et al. (2011) observed a record increase in OBP over part of the southeastern Pacific in late 2009 and early 2010, primarily caused by wind stress curl associated with a strong and persistent anticyclone and likely related to the concurrent central Pacific El Niño.

GRACE has far surpassed its five-year design lifetime, but it will likely succumb to the aging of batteries and instrument systems sometime in the next few years. NASA has begun initial development of a follow-on to GRACE with very similar design, which could launch as soon as 2016 and would provide continuity in the data record while improving resolution slightly. Higher resolution time variable gravity missions are also on the drawing board (NRC 2007).

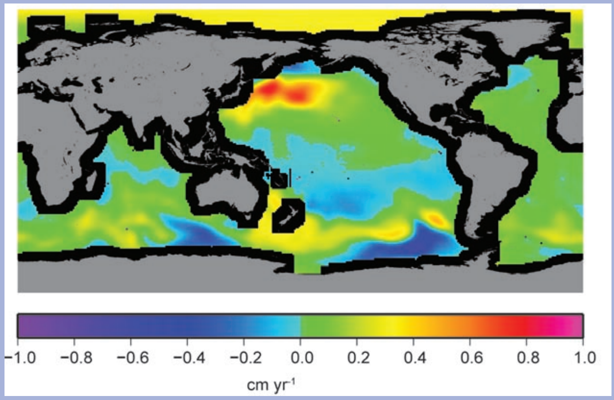

Fig. 2.32. Mean rate of change of ocean bottom pressure (cm yr^{-1} in equivalent sea level) from January 2003 to August 2010, computed from GRACE data projected onto empirical orthogonal functions (EOF) modes from a model (Chambers and Willis 2008). The large trends in the North Pacific, South Pacific, and Arctic are related to changing circulation and wind stress, and have been described by Chambers and Willis (2008), Boening et al. (2011), and Morison et al. (2007), respectively.

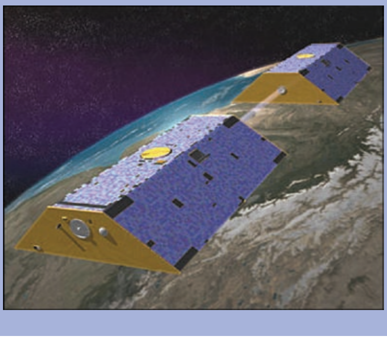

Image courtesy of NASA

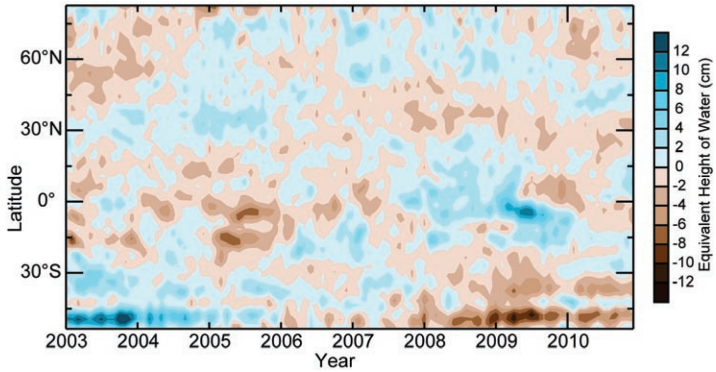

Fig. 2.33. GRACE measurements of terrestrial water storage anomalies in cm equivalent height of water by latitude. The anomalies are relative to a base period of 2003–07. Gray areas indicate regions where data are unavailable.

Patagonian Andes represent ongoing glacier melt, not groundwater depletion.

Figures 2.33 and 2.34 plot time series of zonal mean and global GRACE derived non-seasonal TWS anomalies (deviation from the mean of each month of the year) excluding Greenland and Antarctica. The two figures show that terrestrial water storage in 2010 was the lowest since 2003, though it recovered in the second half of the year. The drought in the Amazon was largely responsible, but an excess of water in 2009 seems to have buffered that drought to some extent (Fig. 2.33). The drying trend in the 25°S–55°S zone is a combination of Patagonian glacier melt and drought in parts of Australia.

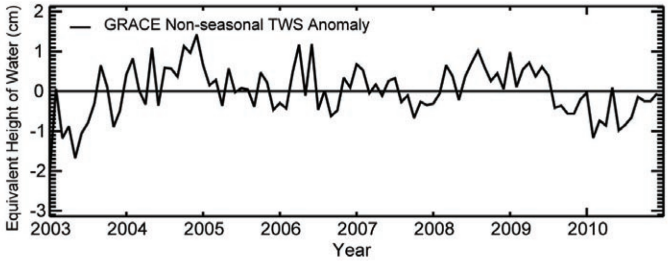

Fig. 2.34. Global average terrestrial water storage anomalies in cm equivalent height of water calculated using a 2003–07 base period.

9) Soil moisture—R. de Jeu, W. Dorigo, W. Wagner, and Y. Liu

In 2010, significant progress was made in consolidating globally available soil moisture datasets from a large number of ground-based stations and satellite platforms. Such harmonized datasets are essential for studying climate-related variability. Regarding the in situ component, the International Soil Moisture Network (ISMN; Dorigo et al. 2011) was established as the successor of the renowned Global Soil Moisture Data Bank (Robock et al. 2000), which has been extensively used for climate studies. The ISMN offers a centralized system where historic and current in situ soil moisture measurements from around the world are collected, harmonized, and made available to users (see Table 2.1).

Satellite-based soil moisture estimates have significantly improved in recent years to the point where now several continental-to-global scale soil moisture products are available (e.g., Wagner et al. 2003; Njoku et al. 2003; Owe et al. 2008). These products represent moisture conditions in the top few centimeters and depend on observation wavelength and soil wetness (Schmugge 1985; Kuria et al. 2007). Due to different observation wavelengths and retrieval methods, the quality of these products varies. Scipal et al. (2008) and Dorigo et al. (2010), using a statistical method called triple collocation, quantified satellite-based soil moisture errors in the order of 0.01 $m^3 m^{-3}$–0.04 $m^3 m^{-3}$ for the regions with a (semi) transparent vegetation cover, and > 0.04 $m^3 m^{-3}$ for the more densely vegetated regions. Several studies have revealed that satellite-based products are highly correlated with in situ measurements (R between 0.6 and 0.8) with root mean square errors (RMSE) ranging between 0.03 $m^3 m^{-3}$ for semi arid regions (e.g., Africa and Australia) to 0.1 $m^3 m^{-3}$ in France (Gruhier et al. 2010; Draper et al. 2009; Rüdiger et al. 2009).

Satellite-based soil moisture products can provide reliable estimates over sparse to moderately vegetated regions. Current satellites are not yet able to monitor soil moisture variations over densely vegetated regions (e.g., tropical rainforests) because the signals received by satellites are severely disturbed by vegetation. Over regions with snow cover and frozen soils, satellite-based microwave instruments cannot provide reliable estimates either.

The historical microwave satellites have been used to compile a consistent 20-year record of global soil moisture (Liu et al. 2009, 2011; Su et al. 2010). Satellite-based soil moisture products from both passive and active instruments were collected and harmonized in one system, covering a period since January 1991, with a spatial resolution of 0.25° and a daily time step.

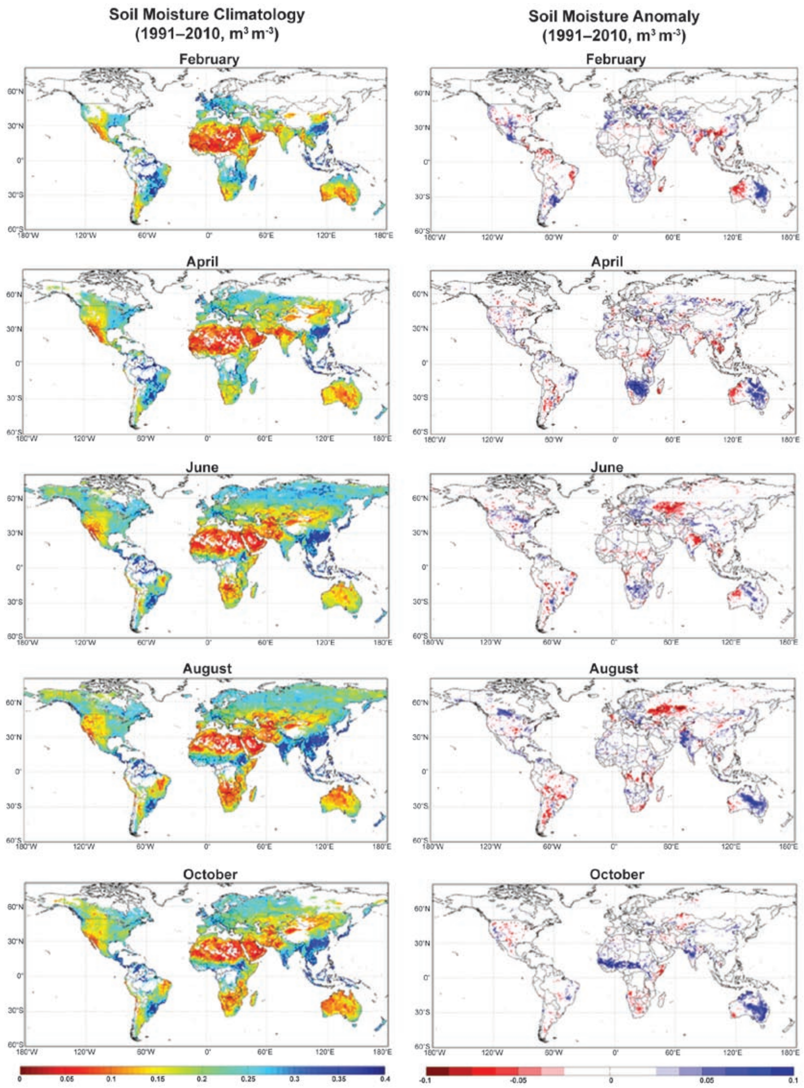

Fig. 2.35. Monthly soil moisture climatology (1991–2010) (left) and 2010 soil moisture anomaly (right) as derived from both passive and active microwave satellite sensors.

The monthly dynamics in global soil moisture are strongly driven by monsoonal circulations. During the winter phase of the monsoon, there is a low-level flow of dry, cool air from the cold continent to the warmer ocean, and precipitation over land is generally reduced. During the summer phase, there is a strong flow of atmospheric moisture from the cooler ocean to the warmer land, where the upward motion of the heated air produces the heavy rains of the monsoon season (Hastenrath 1985). These patterns are clearly visible in the soil moisture climatology (Fig. 2.35, left column). Over the Indian Peninsula, low soil moisture values between 0 m^3 m^{-3} and 0.2 m^3 m^{-3} are observed during February–April and high values between 0.2 m^3 m^{-3} and 0.4 m^3 m^{-3} are observed during August–October. Over northern Australia, dry conditions are seen during June–August while wet conditions are seen during February–April. In Africa, the equatorial region near the Intertropical Convergence Zone is the wettest portion of the continent. Annually, the rain belt across the continent marches northward into Sub-Saharan Africa by August, then moves back southward into south-central Africa by March, resulting in wet soil moisture patterns in Sub-Saharan Africa in August and in south-central Africa in February–April.

A series of climatic events had a strong impact on the global distribution of precipitation and temperature in 2010, and these are reflected in the soil moisture anomalies (Fig. 2.35, right column). In February, both a wet (west) and dry (east) anomaly was detected over continental Australia. In April, south-central Africa was extremely wet due to excessive rainfall. In June, the first signs of the long, dry anomaly were detected over Russia and Kazakhstan. The anomaly lasted until the end of the summer. The hottest summer in Russia on record dried out a large area and led to several hundred wildfires in response (see Sidebar 7.8 for further details about this heat wave). In August, a wet anomaly was reflected over Pakistan, caused by extreme wet conditions and the additional flooding events (see section 7g3). The strong 2010 soil moisture anomalies from July onwards appear related to the oceanic phenomenon La Niña.

10) Lake levels—*C. Birkett and J-F. Cretaux*

Lake level as a climatic index was highlighted for the first time last year (Birkett 2010). Because lake volumes respond to changes in precipitation integrated over their catchment basins, they are indirect indicators of climatic change. The response can be seen in open lakes and reservoirs but is particularly marked for closed lakes, i.e., those having no significant surface or subsurface outflow. Closed lakes can act as low-pass filters to variations in aridity, with a characteristic time constant of between 1 and 1000 years, depending largely on lake geomorphology (Birkett 2010). Deep lakes with steep shore topography are good proxies for high amplitude-low frequency changes, while shallow water basins are better indicators for rapid low-amplitude changes (Hostetler 1995).

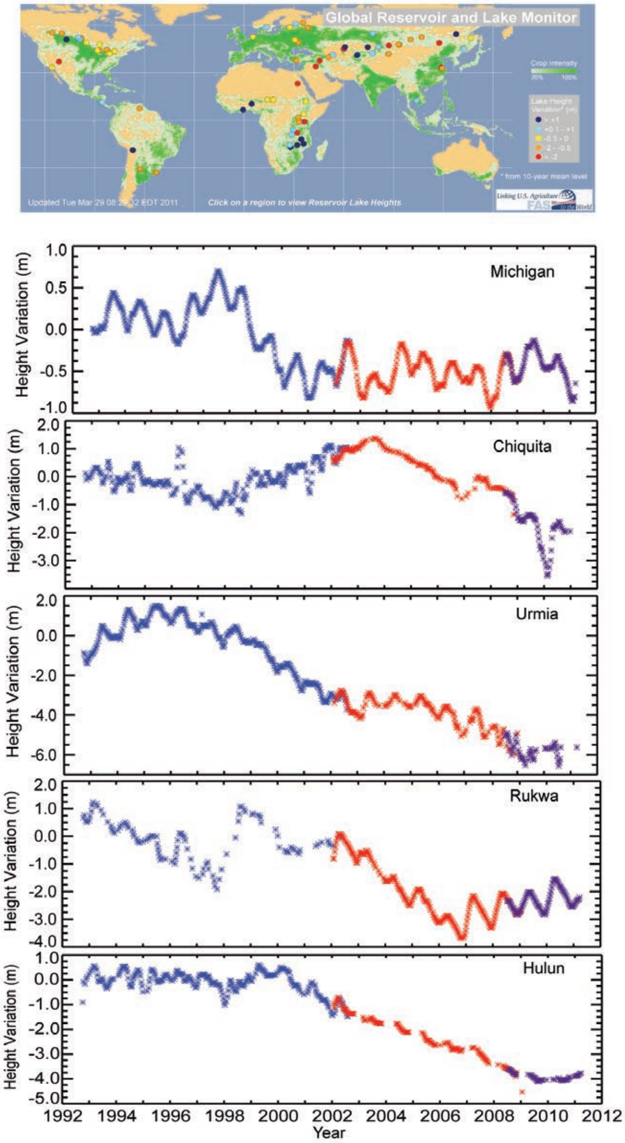

Fig. 2.36. (Top) Map showing the near real time lake level status of ~70 lakes with respect to a short-term mean (1992–2002). Red depicts low water drought and navy depicts high water. (Bottom) Examples of lake level time series for the United States (Michigan), Argentina (Chiquita), Iran (Urmia), Tanzania (Rukwa), and China (Hulun). (Courtesy of the USDA/FAS CropExplorer, http://www.pecad.fas.usda.gov/cropexplorer/global_reservoir/index.cfm.)

Lake variations can act as climate proxies with correlations to several modes of variability, e.g., ENSO, Indian Ocean, Pacific Decadal, or North Atlantic Oscillations (see Sidebar 1.1 for information about modes of variability). However, to date, studies have only been regional or individual in scope. Global analyses require the systematic monitoring of all global lake volumes. Satellite imagery could assist with the monitoring of changing lake surface area but currently no such products exist. Satellite-based radar altimetry does offer ~20-year lake level datasets which can stand alone or be combined with ground-based measurements (see Table 2.1). Satellite products have varying temporal/spatial resolutions and several centimeters accuracy at best (Fig. 2.36). Ground-based products can be found via local, state, or national agency web sites. Various lakes databases are also currently available that can assist with the identification of lake location and type (e.g., Lehner and Döll 2004; Fig. 2.37).

The NASA/USDA web site offers an indicative guide in terms of drought or high water (Fig. 2.36) but it is essential to build a global database that not only provides lake volume parameters (level, area) but includes or links to related, climatically sensitive measurements such as surface water temperature (section 2b4), air temperature (Smith et al. 2005; Liu et al. 2010), water salinity, ice cover duration and thickness (Karetnikov and Naumenko 2008; Mishra et al. 2011), and basin-scale water storage anomalies (e.g., Becker at al. 2010). The type of lake included should be challenged to encompass existing, emerging, and ephemeral high latitude lakes, including supraglacial (Box and Ski 2007; Bagshaw et al. 2010), and subglacial (Fricker et al. 2007; Smith et al. 2009) in the light of recent research.

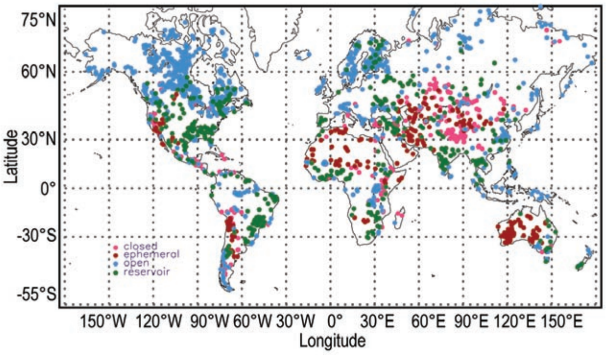

Fig. 2.37. Global location of large (≥ 100 km²) lakes; closed (pink), ephemeral (red), open (blue), and reservoirs (green). Based on Birkett and Mason (1995).

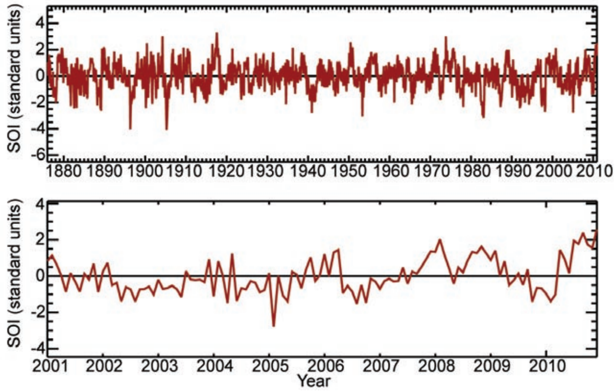

Fig. 2.38. The Australian Bureau of Meteorology Southern Oscillation Index time series for (top) 1876 to 2010 and (bottom) from 2001 to 2010 relative to the 1879–2010 average. Data for HadSLP2r (Allan and Ansell 2006) are shown.

d. Atmospheric Circulation

1) Mean sea level pressure—R. Allan

In 2010, El Niño conditions gave way to La Niña, with a major event having developed by the latter part of the year. Indications are that it could be one of the strongest La Niña events in the historical instrumental record, with major precipitation and temperature impacts across the Indo-Pacific region and at higher latitudes in both hemispheres. Record positive Southern Oscillation Index (SOI) measurements were reached for March (since records began in 1876) and April (since 1971) according to the Australian Bureau of Meteorology (http://www.bom.gov.au/climate/enso/).

El Niño and La Niña can be quantified by the SOI—the normalized mean sea level pressure (MSLP) difference between Tahiti and Darwin (Allan et al. 1996). Other indices, using sea surface temperatures, are also commonly utilized (see Sidebar 1.1). El Niños (negative SOI) and La Niñas (positive SOI) vary in magnitude, duration, and evolution, with no two events or episodes exactly the same. The SOI since 1900 is dominated by interannual to multidecadal vacillations, but longer-term trends are not evident (Fig. 2.38, top). The SOI trace since 2000 highlights the shift from the La Niña of 2007/08 through the El Niño of 2009/10 to the moderate-to-strong La Niña of 2010/11 (Fig. 2.38, bottom). Major El Niño and La Niña events can be near-global in their influence on world weather patterns, owing to ocean-atmosphere interactions across the Indo-Pacific region with teleconnections to higher latitudes in both hemispheres.

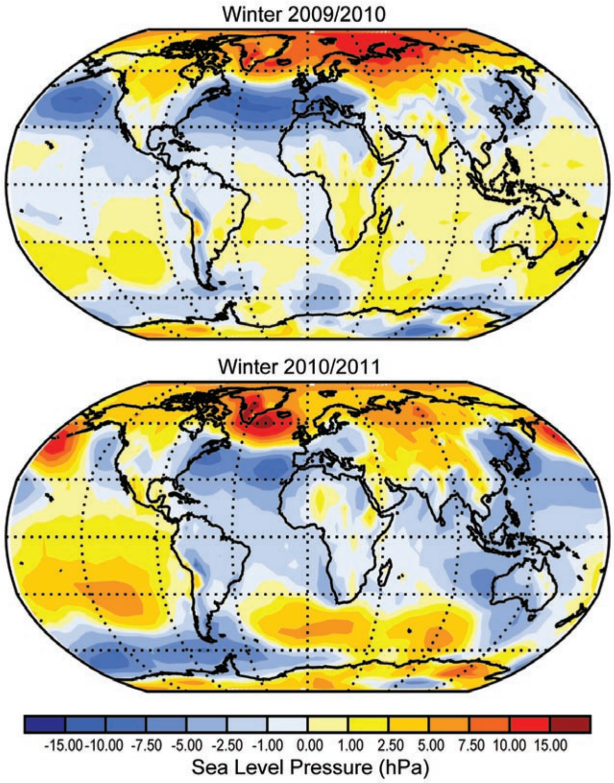

Fig. 2.39. Winter sea level pressure anomalies (1961–90 base period) averaged over Dec–Feb for (top) 2009/10 and (bottom) 2010/11. The data shown are from HadSLP2r.

The Northern Hemisphere winters of 2009/10 and 2010/11 were dominated by long periods of extremely negative North Atlantic Oscillation (NAO)/Arctic Oscillation (AO) conditions (Fig. 2.39, top and bottom). There were positive pressure anomalies over higher latitudes and negative anomalies over the midlatitudes and an associated reduction in westerlies. This is further evident in Fig. 2.40 (top and bottom), where periods of negative observed and modeled daily and five-day northern NAO/AO values for December 2009–February 2010 and December 2010–January 2011, respectively, highlight the major snow and cold temperature events across parts of Europe in the last two boreal winters.

In the Southern Hemisphere, the latter half of 2010 experienced one of the strongest periods of positive values of the Antarctic Oscillation (AAO)/Southern Annual Mode (SAM; the Antarctic counterpart to the AO) observed in the historical record (see Sidebar 1.1 and section 6b for further details). The combination of both a strong and positive AAO/SAM and SOI (reflecting the moderate-to-strong La Niña) has been suggested as leading to the above-average levels of Antarctic sea-ice observed in the last four months of 2010 (NSIDC, 5 January 2011: http://nsidc.org/arcticseaicenews/).

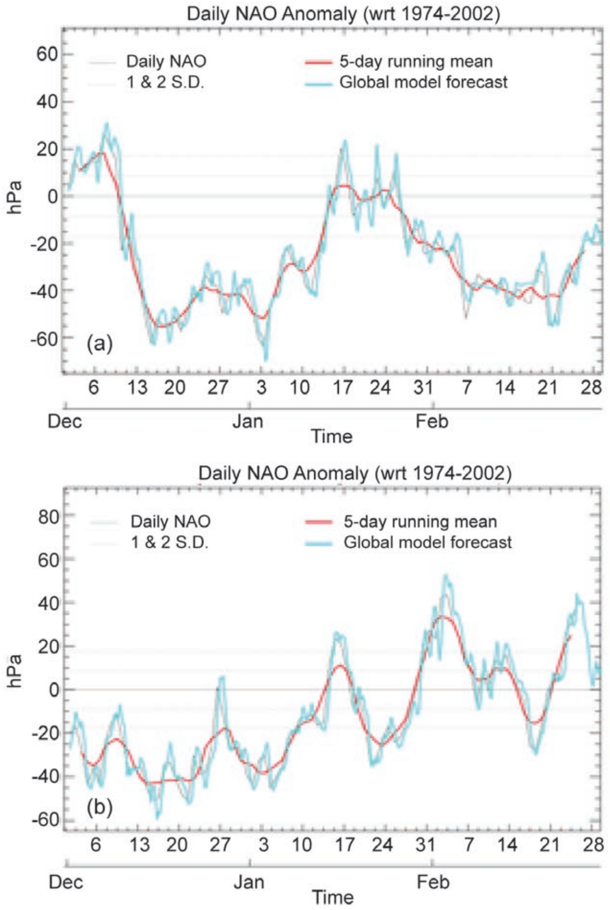

Fig. 2.40. The North Atlantic Oscillation Index is shown for winter (top) 2009/10 and (bottom) 2010/11 using station data (red) and the Met Office Global Model forecast (blue). (Courtesy of the UK Met Office Hadley Centre.)

2) Ocean surface wind speed—C. Mears

Surface wind speed over the world's oceans began to be monitored continuously with the launch of the first Special Sensor Microwave Imager (SSM/I) satellite in late 1987. The SSM/I instrument is a microwave radiometer that makes measurements of upwelling microwave radiation to infer the surface roughness of the world's oceans, and thus the surface wind speed (Wentz 1997). Since the first SSM/I instrument, a number of additional microwave imaging sensors, including the Advanced Microwave Scanning Radiometer-EOS (AMSR-E) and Windsat have been launched and intercalibrated to the accuracy necessary for climate studies (Wentz et al. 2007). Globally-averaged winds from satellite-borne radiometers and six reanalysis datasets are plotted in Fig. 2.41. Some reanalysis-generated winds (see Sidebar 2.1) show much less variability than the satellite data (NCEP CFSR, ERA-40), while others show more variability and greater long-term changes. A further complication is that surface wind speed over the oceans is dominated by short-term variability and regional character (Fig. 2.42), making it difficult to discern long-term trend behavior.

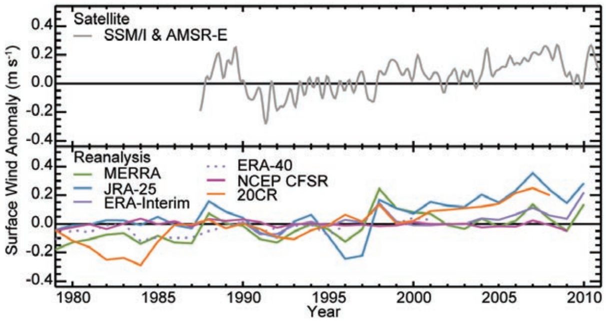

Fig. 2.41. Global average surface windspeed anomalies over ocean shown for the SSM/I and AMSR-E combined monthly smoothed observations (1988–2007 base period) and six reanalyses annual products (1989–2008 base period for all except ERA-40 which uses 1961–90). All time series are adjusted to have a mean of zero over the common period 1989–2001 to aid comparison. The extent to which inhomogeneities in the observations assimilated by the reanalyses, arising from changes in measurement systems, impact the accuracy of the analyzed surface winds is not yet known.

Winds in the tropics, especially the central tropical Pacific, were above normal in 2010, as the tropical Pacific transitioned to La Niña. Negative wind anomalies in the Atlantic around 55°N coincided with the strong negative phase of the North Atlantic Oscillation (Hurrell et al. 2003) during most of 2010. Positive wind anomalies in the South Pacific and Indian Oceans near 55°S are correlated with the intensification of the Southern Annular Mode (Hall and Visbeck 2002) during 2010 (Plate 2.1k).

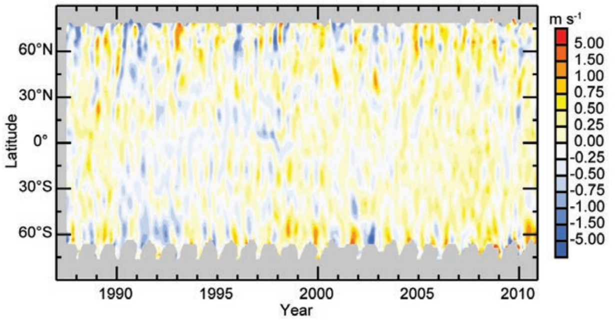

Fig. 2.42. SSM/I and AMSR-E combined smoothed monthly average surface ocean wind speed anomalies (1988–2007 base period) by latitude for the period June 1987 to December 2010. Gray areas indicate regions where data are unavailable.

SIDEBAR 2.3: SURFACE WINDS OVER LAND—T. C. PETERSON, R. VAUTARD, T. R. McVICAR, J-N THÉPAUT, AND P. BERRISFORD

Wind speed and direction have been observed at many thousands of stations around the world. These data are regularly transmitted on an hourly or synoptic basis. Figure 2.43 shows the annual mean wind speed at 11 853 stations with at least five years of data since 1979 from the Integrated Surface Database (ISD-Lite; Lott et al. 2008) hosted at NOAA's National Climatic Data Center (NCDC). While such analysis offers guidance on where to install wind-energy generators, wind data have a variety of problems that limit their usefulness in climate change analysis.

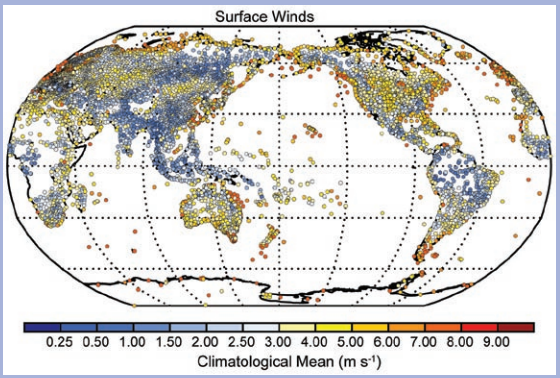

Fig. 2.43. Observed mean wind speed at 11 853 stations with at least five years of observations in Lott et al. (2008) between 1979 and 2010.

These problems include limited periods of record and missing data, due to either operations at a station or data transmission. They also include breaks in time series due to station moves, exposure changes due to modification in nearby obstacles, as well as instrument, observation protocol, or units changes. For instance, new instruments are often more sensitive to very light breezes and therefore have fewer observations of zero wind speed.

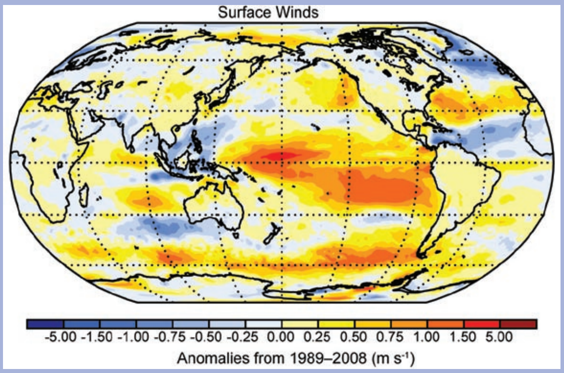

Fig. 2.44. 2010 wind speed anomalies from ERA-Interim reanalysis. Note that the base period used here (1989–2008) differs slightly from that used in Plate 2.1k (1988–2007).

Therefore, to accurately assess wind speed anomalies and particularly trends, careful attention must be paid to the homogeneity of station time series. This was done by Vautard et al. (2010) and McVicar et al. (2008). Their homogeneous wind data, with updates to McVicar et al. (2008) provided by data in Lott et al. (2008), allows an assessment of station wind anomalies for 2010 (Plate 2.1k), but with less than 10% of the stations shown in Fig. 2.43. These data were stitched onto the time series using a First Difference approach to avoid creating discontinuities at the transition (Peterson et al. 1998; Free et al. 2004). For complete global coverage of 2010 wind anomalies, one can use reanalysis (Fig. 2.44).

Observed wind speed over much of the global land areas, as shown in Fig. 2.45, tends to be decreasing (e.g., Roderick et al. 2007). Yet mean reanalysis wind speed does not show this decrease (Fig. 2.46). The difference is hypothesized to be at least partly due to increases in surface roughness associated growth of vegetation over much of the region with adequate long-term observations (Vautard et al. 2010; McVicar and Roderick 2010). These land-surface changes are currently not fully represented in present-day reanalysis systems and it is unclear how roughness changes near observing sites can be translated to higher elevation sites that are important for wind energy.

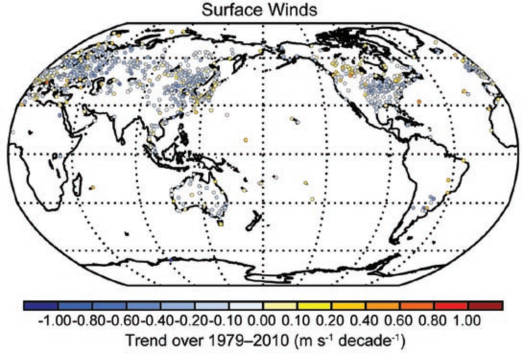

Fig. 2.45. Observed trends in wind speeds at locations with long and fairly homogeneous data records.

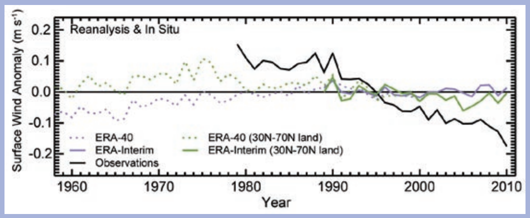

Fig. 2.46. Global average wind speed anomalies over land from reanalysis and observations. The green curves display the wind speed anomalies over land restricted to 30°N–70°N from reanalyses (corresponding to the area covered by the bulk of surface observations). The base period for the anomalies is the 1989–2001 period of overlap from all three datasets.

e. *Earth radiation budget at top-of-atmosphere*—D. P. Kratz, P. W. Stackhouse, Jr., T. Wong, P. Sawaengphokhai, A. C. Wilber, and N. G. Loeb

The net radiation at the top of the atmosphere provides an estimate of the balance between the incoming shortwave flux from the sun with the outgoing reflected shortwave and emitted longwave fluxes from the Earth-atmosphere. Analyses of the Clouds and Earth's Radiant Energy System (CERES; Wielicki et al. 1998) instrument data taken aboard the Terra spacecraft revealed that between 2009 and 2010 the global-annual mean outgoing longwave radiation (OLR) increased by ~0.40 W m^{-2} and the reflected shortwave radiation (RSW) increased by ~0.60 W m^{-2} (Table 2.4). Data from the Solar Radiation and Climate Experiment (SORCE; Kopp et al. 2005) indicated that the annual average total solar irradiance (TSI) also increased by ~0.10 W m^{-2} from 2009 to 2010. Thus, the changes in the combined global-annual averaged OLR and absorbed shortwave (TSI minus RSW) fluxes resulted in a reduction of ~0.90 W m^{-2} in total net radiation into Earth's climate system for 2010 as compared with 2009. The data between July 2010 and December 2010, however, may include modest instrument drift artifacts (below ±0.1%), since the final instrument calibration coefficients for those months are not yet available. Relative to the multiyear dataset average for 2001–09, the 2010 global-annual mean anomaly (Table 2.4) is +0.00 W m^{-2}/+0.50 W m^{-2}/-0.55 W m^{-2} for OLR/RSW/total net radiation, respectively. These results are comparable to the corresponding 2-sigma interannual variability for this period.

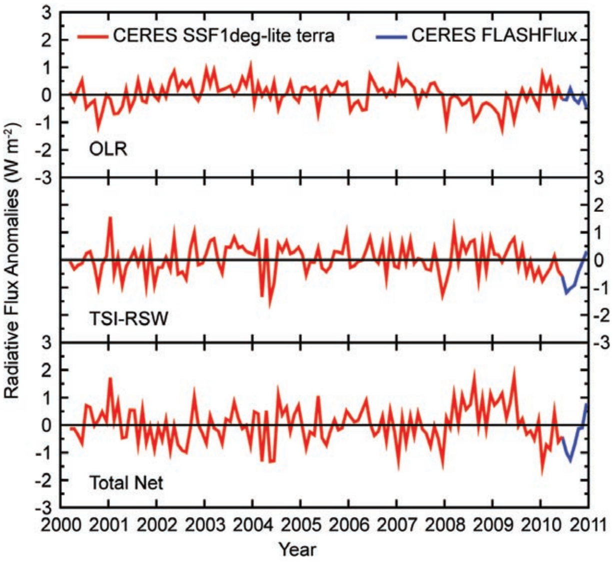

Fig. 2.47. Global average monthly mean deseasonalized anomalies of top-of-atmosphere earth radiation budget for outgoing longwave radiation (upper panel), absorbed shortwave (TSI minus RSW) (middle panel), and total net (TSI minus RSW minus OLR) (lower panel) from Mar 2000 to Dec 2010. Anomalies are computed relative to the calendar month climatology derived for the Mar 2000 to Dec 2010 period. The time series shows the CERES SSF 1Deg Lite Ed2.5 data (Mar 2000 to Jun 2010) by a red line, and the CERES FLASHFlux data (Jul 2010 to Dec 2010) by a blue line. Mean differences between datasets were removed using available data from the overlap period from Mar 2007 through Feb 2010 and the absolute value of the CERES SSF 1Deg Lite results before deseasonalization (see Table 2.1 for source information).

Global-monthly mean deseasonalized anomalies since March 2000 have been produced by merging Earth Radiation Budget (ERB) datasets from two sources: (1) the CERES SSF (Single Scanner Footprint) 1x1 Degree Lite [SSF 1Deg Lite Ed2.5 Top-of-Atmosphere (TOA) only version] using the Edition 3 instrument calibration, and (2) the CERES Fast Longwave and Shortwave Radiative Fluxes (FLASHFlux) product (Stackhouse et al. 2006; L'Ecuyer et al. 2008). The results are presented in Fig. 2.47, where the FLASHFlux data have been normalized to the SSF 1Deg Lite data using TOA fluxes from both datasets for the three-year period from March 2007 though February 2010. The 2-sigma monthly uncertainty from this overlap period was ±0.55 W m^{-2}/±0.50 W m^{-2}/±0.70 W m^{-2} for the OLR/RSW/total net radiation, respectively. The OLR showed a general, albeit somewhat irregular,

Table 2.4. Global-annual mean Top-of-Atmosphere radiative flux changes between 2009 and 2010, the 2010 global-annual mean radiative flux anomalies relative to their corresponding 2001-10 mean climatological values, and the 2-sigma interannual variabilities of 2001–10 global-annual mean fluxes (units in W m^{-2}) for the outgoing longwave radiation (OLR), total solar irradiance (TSI), reflected shortwave (RSW) and total net fluxes. All flux values have been rounded to the nearest 0.05 W m^{-2}.

	One year change (2010 minus 2009)	2010 anomaly (relative to climatology)	Interannual variability (2001 to 2010)
OLR	0.40	0.00	±0.55
TSI	0.10	-0.05	±0.20
RSW	0.60	0.50	±0.50
Net	-0.90	-0.55	±0.70

downward oscillation from late 2009 throughout 2010. Changes in the absorbed shortwave (TSI minus RSW) showed a significant decrease in the first several months, followed by a reversal of that decrease in the latter half of 2010. Although dominated by the RSW, the relative month-to-month level of the absorbed shortwave was raised by the recovery of the TSI after a prolonged minimum stretching back to late 2007. The combined OLR and absorbed shortwave resulted in a minimum in the total net TOA flux at midyear, with a recovery to levels at the end of 2010 comparable to the beginning of the year. A smoothed version of the averaged TOA OLR showed a general agreement in fluctuations with a similarly smoothed multivariate ENSO index, where the index peaked positively at the beginning of 2010 before falling. Thus, the change in the ENSO intensity appears to influence strongly the global averaged monthly TOA variability during this time period. Finally, the dynamic nature of the OLR and RSW between 2009 and 2010 produced one-year changes that were comparable to the 2-sigma interannual variability. Further fluctuations are anticipated as the ENSO cycle evolves. Thus, long-term trend analyses are discouraged due to the natural fluctuation in ERB relating to ENSO activity in the short record, the large uncertainty from the data merging process, and instrument drift potential in the FLASHFlux data. A long-term homogeneous data source with in-depth instrument stability analysis is required to reduce uncertainties in future reassessment activity.

f. Atmosphere composition

1) Atmospheric chemical composition

(i) Carbon dioxide, methane, and carbon monoxide—

E. J. Dlugokencky

(A) Carbon dioxide

The contribution of carbon dioxide (CO_2) towards Earth's total terrestrial greenhouse effect is 20%, with non-CO_2 greenhouse gases (GHG; 5%), water vapor (50%), and clouds (25%) comprising the remainder (Lacis et al. 2010). During the past few decades, most of the increase in the atmospheric burden of CO_2 (Fig. 2.48a) has been due to fossil fuel combustion. This is known from multiple lines of observational evidence (Tans 2009). Measurements of atmospheric CO_2 at Mauna Loa, Hawaii, and the South Pole show that the north to south difference is increasing, consistent with increasing CO_2 emissions from fossil fuel combustion, predominantly in the Northern Hemisphere. Strong evidence also comes from measurements of tracers such as ^{14}C in CO_2, which is decreasing as a result of adding CO_2 from fossil fuel combustion (depleted of ^{14}C), ^{13}C in CO_2, which shows that the added CO_2 is of organic origin, and measurements of a decrease in the ratio of O_2:N_2, which is also consistent with O_2 consumption by fossil fuel combustion. The current rate of increase in atmospheric CO_2 is exceptional when compared to changes on geological time scales, as assessed from measurements of air trapped in ice cores.

Despite the long-term trend in atmospheric CO_2 being driven by fossil fuel emissions, interannual variability in the rate of increase of atmospheric CO_2 is driven by small changes in the net fluxes between the atmosphere and terrestrial biosphere and the atmosphere and oceans. During 2010, globally averaged atmospheric CO_2 at Earth's surface increased by 2.60 ± 0.07 ppm (see Conway et al. 1994 for a description of sampling network and methods); uncertainty 1

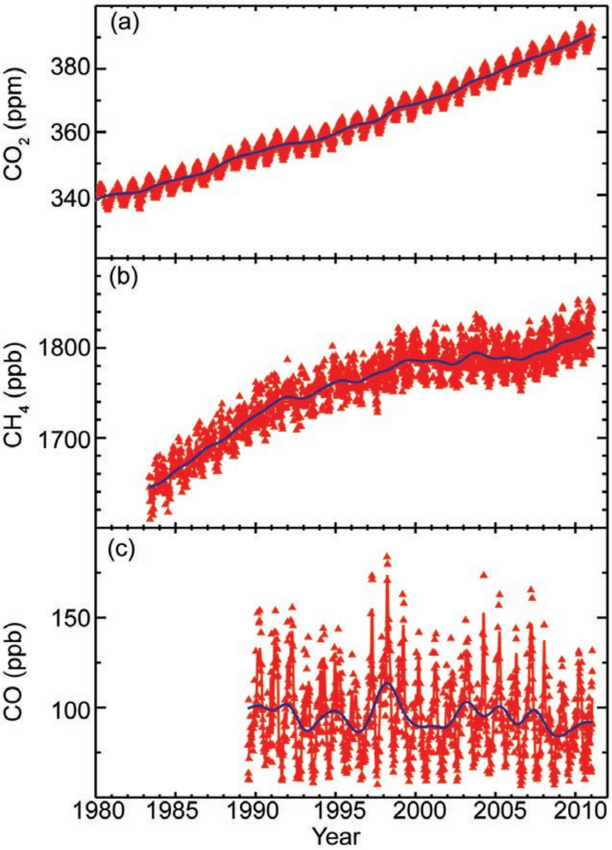

Fig. 2.48. Mixing ratios (dry air mole fraction) of (a) CO_2, (b) CH_4, and (c) CO from measurements of discrete air samples collected approximately weekly at NOAA's Mauna Loa observatory. Symbols are the average of two samples collected in series. Red lines are smooth curves fitted to the data. Blue lines are deseasonalized trend curves.

standard deviation. This is greater than the average rate of increase from 1980 through 2010 of 1.69 ± 0.58 ppm yr^{-1}. It is also larger than the increase in 2009 of 1.62 ± 0.07 ppm.

(B) Methane

After a decade of near-zero growth, atmospheric methane (CH_4) increased globally in 2007 and 2008 by ~7.5 ppb yr^{-1} (Rigby et al. 2008; Dlugokencky et al. 2009). Bousquet et al. (2010) used two different inversion models to estimate changes in emissions and sinks during 2006 to 2008 and found that global CH_4 emissions exceeded the 1999–2006 average by 19 Tg CH_4 (16 Tg–21 Tg) in 2007 and 13 Tg CH_4 (6 Tg–20 Tg) in 2008. Changes in tropical wetland emissions were the dominant driver in 2007, with a minor contribution from Arctic wetlands. Although the inversion models gave inconsistent results for 2008, the global vegetation model used by Bousquet et al. (2010) implied a tropical source for the excess methane. Bousquet et al. (2010) found that changes in hydroxyl (OH) radical concentrations, the primary oxidant for CH_4, were less than 1%, and had only a small impact on observed CH_4 changes. During both 2009 and 2010 (Fig. 2.48b), globally averaged atmospheric CH_4 provisionally increased by ~5 ± 2 ppb yr^{-1}; the causes of this continued increase are not yet known, but it is likely related to increasing emissions from rapidly developing economies in Asia.

(C) Carbon monoxide

Carbon monoxide (CO) is a key species in atmospheric chemistry, particularly in cycling of reactive species like the hydroxyl (OH) and hydroperoxyl (HO_2) radicals. The four major sources of CO to the atmosphere are: biomass burning, mostly from forest clearing and savannah burning in the tropics; combustion of fossil fuels; atmospheric oxidation of natural volatile organic compounds; and atmospheric oxidation of CH_4. There has been no significant long-term CO trend since NOAA/ESRL measurements began in 1990 (Novelli et al. 2003), but CO anomalies occurred during 1997 to 1998, and again in 2002 to 2003 (Fig. 2.48c). These anomalies are likely the result of interannual variability in the rates of tropical and boreal biomass burning (section 2g3). Since the lifetime of CO is only a few months, the CO enhancements quickly disappeared. The preliminary globally averaged CO mole fraction in 2010 is ~83 ppb, slightly larger than in 2009.

(ii) Nitrous oxide and sulfur hexafluoride—J. W. Elkins and G. S. Dutton

Atmospheric nitrous oxide (N_2O) and sulfur hexafluoride (SF_6) have significant man-made sources and are two of six gases selected for emission reduction under the Kyoto Protocol of the United Nations Framework Convention on Climate Change. Atmospheric N_2O currently has the third strongest climate forcing of the long-lived trace gases after carbon dioxide (CO_2) and methane (CH_4), recently surpassing chlorofluorocarbon (CFC)-12, and is considered a major greenhouse gas (Forster et al. 2007; Hofmann et al. 2006).

Current emissions of nitrous oxide are expected to contribute more to future ozone depletion than current emissions of halogenated ozone-depleting substances (ODS) (Ravishankara et al. 2009). Nitrous oxide is produced naturally by both the oxidation of ammonium and the denitrification of nitrate. Significant emissions of nitrous oxide occur during the application of nitrogen fertilizers on agricultural crops (Davidson 2009). This, along with other anthropogenic sources, contribute to an almost 30% imbalance in the budget of atmospheric N_2O, where the global growth rate has averaged 0.75 ± 0.01 ppb yr^{-1}

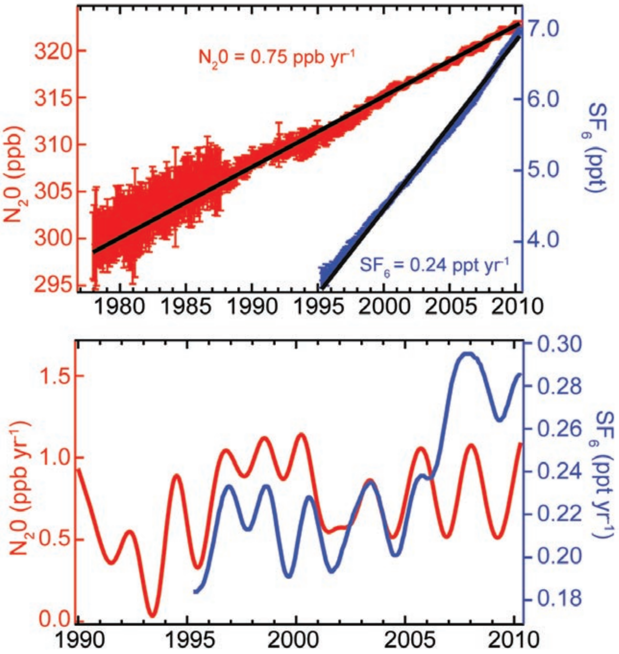

Fig. 2.49. (Top) Global monthly mean mixing ratios of N_2O (red) and SF_6 (blue) with estimates for the linear growth rate from NOAA/ESRL in situ and flask observations, and (bottom) instantaneous growth rates of N_2O and SF_6 derived using a Fast Fourier Transform smoothing algorithm (Thoning et al. 1989) with a two year filter.

since 1977 (Fig 2.49). However, the observed growth rate of N_2O exhibits interannual variability, some of which may be the result of limited global sampling and changes in atmospheric transport (Fig. 2.49, bottom). The mean global atmospheric N_2O mixing ratio for 2010 was 323.16 ± 0.21 ppb. On average, global N_2O concentrations between the two major global networks, NOAA and the Advanced Global Atmospheric Gases Experiment (AGAGE), agree to within 0.2 ppb (Huang et al. 2008).

Sulfur hexafluoride (SF_6) is an important greenhouse gas because it has one of the strongest global warming potentials of all trace gases—23 900 times greater than carbon dioxide (CO_2) with a 100-year time horizon and a very long atmospheric lifetime of 3200 years (Solomon et al. 2007). Sulfur hexafluoride is primarily used as a dielectric insulator for transmission of electricity and emissions are entirely anthropogenic. Its global average concentration for 2010 was 7.02 ± 0.05 ppt (Fig. 2.49, top). The average linear growth rate has been 0.24 ± 0.01 ppt yr^{-1} since 1995. The global atmospheric growth rate increased after 2006 from a mean of 0.22 ± 0.01 ppt yr^{-1} to 0.28 ± 0.02 ppt yr^{-1} (Fig. 2.49, bottom). The increase in emissions could be the result of new electrical capacity in Southeast Asia (Rigby et al. 2010). The decline in the growth rate noted in last year's report appears to have been short-lived. Data from the two networks generally agree very well for atmospheric SF_6, with a mean bias (NOAA minus AGAGE) of around +0.02 ppt with a standard deviation of 0.05 ppt determined from coincident measurements (Rigby et al. 2010). Currently, the global radiative forcing due to SF_6 is small; however, its rapid growth rate (4% per year), high global warming potential, and long atmospheric lifetime mean that SF_6 could contribute significantly to climate forcing by the end of the century.

(iii) Changes in atmospheric abundances of ozone-depleting gases and their replacements—S. A. Montzka and G. Dutton

Long-lived halocarbons affect the radiative balance of the atmosphere because they efficiently absorb terrestrial IR radiation (section 2f1*v*). Long-lived halocarbons containing bromine (Br) and chlorine (Cl) also influence the radiative atmospheric balance indirectly through their destruction of stratospheric ozone. Because of concern over stratospheric ozone depletion, production of many halocarbons has been restricted in recent years through amendments and adjustments to the 1987 Montreal Protocol on Substances that Deplete the Ozone Layer. As a result, mixing ratios of most of the potent ozone-depleting gases have been declining at Earth's surface; this decline continued in 2010 (Fig. 2.50).

The NOAA/ESRL data show that mixing ratios of some halogenated gases continue to increase globally

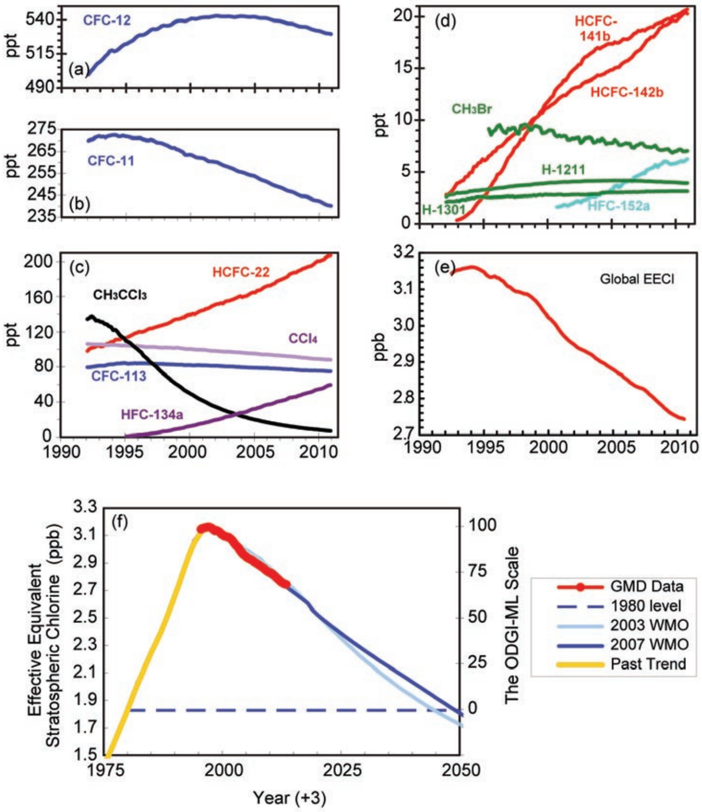

Fig. 2.50. (a, b, c, d) Atmospheric abundances (global mean tropospheric mixing ratios, dry air mole fraction) of the most abundant CFCs, HCFCs, HFCs, chlorinated solvents, and brominated gases, (e) changes in atmospheric Equivalent Effective Chlorine (EECl; ppb), and (f) recent changes in Equivalent Effective Stratospheric Chlorine (EESC; ppb) observed by the NOAA/ESRL global network relative to the secular changes observed in the past, including the level observed in 1980 when the ozone hole was first observed, and a projected future through 2050 (Daniel et al. 2010). EECl is derived as the sum of [Cl + (Br •60)] from observed mixing ratios of ozone-depleting substances appearing in the other four panels. EESC is derived from EECl here by adding three years to the time axis to represent the lag associated with mixing air from the troposphere to the middle stratosphere, where the ozone layer resides. The Ozone Depleting Gas Index for midlatitudes (ODGI-ML) is derived (right-hand axis) from rescaling EESC. [Source: Montzka et al. (1996, 1999)]

(Fig. 2.50c,d). The most rapid increases are observed for hydrochlorofluorocarbons (HCFCs) and hydrofluorocarbons (HFCs), which are common replacements for chlorofluorocarbons (CFCs), halons, and other ozone-depleting gases. Increases in HCFCs have recently accelerated owing to enhanced use in developing countries (Montzka et al. 2009). Both HCFCs and HFCs are efficient absorbers of infrared radiation (Table 2.5). While HCFCs contain chlorine and deplete ozone with a reduced efficiency compared to CFCs, HFCs do not participate in ozone-destroying reactions.

Future levels of ozone-depleting halogens in the stratosphere (and, therefore, the threat to stratospheric ozone) can be estimated from weighted sums of Cl and Br in long-lived halocarbons, accounting for the enhanced efficiency for Br to destroy ozone [a factor of 60 is used here (Montzka et al. 2011)]. These sums are derived from surface-based measurements and are expressed as Equivalent Effective Chlorine (EECl; Fig. 2.50e) or Equivalent Chlorine (ECl), depending on if weightings are chosen to be relevant for the midlatitude (EECl) or polar stratosphere (ECl). EECl, for example, provides an estimate of the near-future ozone-depleting power of trace gases, i.e., once air at Earth's surface becomes mixed into the midlatitude stratosphere. An additional metric, Equivalent Effective Stratospheric Chlorine (EESC), provides an estimate of the ozone-depleting power of trace gases in the stratosphere and is often derived from EECl or ECl with the addition of a time lag owing to transport.

The EECl content of the lower atmosphere has declined fairly steadily through 2010 at a mean rate of 27 ppt yr^{-1} since the peak in 1994 (Fig. 2.50e). Despite these substantial changes, full recovery of stratospheric ozone is not expected until the middle to latter part of the 21st century owing to the long lifetimes of many of these chemicals (Table 2.5). A similar conclusion can also be drawn from measurements of trace gases obtained by the AGAGE group. Both NOAA and AGAGE measurements show similar trends in EECl in recent years (Montzka et al. 2011). Progress towards EECl reductions can now be readily assessed with the NOAA Ozone-Depleting Gas Index (ODGI; see Table 2.1; Hofmann and Montzka 2009). This index is derived from EECl (Fig. 2.50f). It is scaled so that a value of 100 represents the EECl (or EESC) abundance at its peak, and zero represents the 1980 level (a reference point during which ozone depletion was thought to have been small). In 2010, the ODGI-Midlatitudes was 67.1. Less progress is evident for the index when the tropospheric data are weighted to be relevant for considering Antarctic changes; the ODGI-Antarctica was 82.6 in 2010.

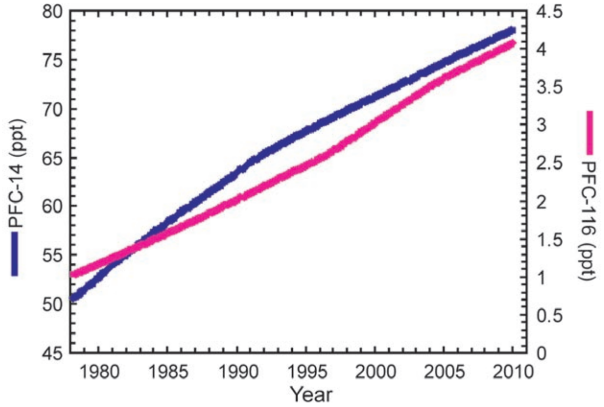

Fig. 2.51. Global average surface concentrations of PFC-14 and PFC-116 (ppt) from the AGAGE network (Mühle et al. 2010).

(iv) Perfluorocarbons—J. Mühle and A. L. Ganesan

Perfluorocarbons (PFCs) are extremely long-lived, potent greenhouse gases. PFC-14 (CF_4) and PFC-116 (C_2F_6) have conservative lower limits for atmospheric lifetimes of 50 000 and 10 000 years, respectively, and global warming potentials (100-year time horizon) of 7390 and 12 200, respectively (Ravishankara et al. 1993; Morris et al. 1995; Forster et al. 2007; Montzka et al. 2011). Anthropogenic PFC-14 and PFC-116 were historically emitted as by-products of aluminum production and are now also emitted from the electronics industry. However, the onset and extent of PFC emissions from the electronics industry is poorly known due to limited reporting (Khalil et al. 2003; Worton et al. 2007; EDGAR 2009; Mühle et al. 2010).

A small natural source of PFC-14 from degassing of Earth's crust has been identified (Harnisch and Eisenhauer 1998; Harnisch et al. 2000), which, because of its extraordinarily long atmospheric lifetime, accounts for its significant pre-industrial abundance (Harnisch et al. 1996a, 1996b) of 34.7 ± 0.2 ppt (Mühle et al. 2010), or ~44% of its 2010 abundance.

Global average surface concentrations of PFC-14 and PFC-116, respectively (Fig. 2.51), were 50.8 ± 0.8 ppt and 1.0 ± 0.1 ppt in 1978, 77.7 ± 0.1 ppt and 4.01 ± 0.01 ppt in 2009, and 78.3 ± 0.1 ppt and 4.09 ± 0.02 ppt in 2010 (Mühle et al. 2010). PFC-14 rose at ~1.1 ppt yr^{-1} from the late 1970s to the early 1990s and by ~0.7 ppt yr^{-1} since that time. PFC-116 rose at ~0.09 ppt yr^{-1} from the late-1970s to the mid-1990s followed by an increase to ~0.12 ppt yr^{-1} until the mid-2000s and a subsequent decline to ~0.09 ppt yr^{-1} afterwards (Mühle et al. 2010).

Table 2.5. Mixing ratios, radiative efficiencies and lifetimes of chemicals considered in the AGGI (CO_2 mixing ratios in ppm, N_2O and CH_4 in ppb, all others in ppt).

Industrial Designation or Common Name	Chemical Formula	AGGI	ODGI	Radiative Efficiency (W m^{-2} ppb^{-1})[a]	Mean suface mixing ratio mid-2010 [change from prior year][b]	Lifetime (years)
Carbon Dioxide	CO_2	Y	N	1.41×10^{-5}	388.5[2.2]	
Methane	CH_4	Y	N	3.7×10^{-4}	1799.2[5.0][c]	~9
Nitrous oxide	N_2O	Y	N	3.03×10^{-3}	323.2[0.9]	114[d]
Chlorofluorocarbons						
CFC-11	CCl_3F	Y	Y	0.25	241.0[-2.2]	45
CFC-12	CCl_2F_2	Y	Y	0.32	530.5[-2.5]	100
CFC-113	CCl_2FCClF_2	Y	Y	0.30	75.4[-0.5]	85
Hydrochlorofluorocarbons						
HCFC-22	$CHClF_2$	Y	Y	0.20	204.0[7.3]	11.9
HCFC-141b	CH_3CCl_2F	Y	Y	0.14	20.4[0.6]	9.2
HCFC-142b	CH_3CClF_2	Y	Y	0.20	20.1[0.7]	17.2
Hydrofluorocarbons						
HFC-134a	CH_2FCF_3	Y	N	0.16	57.2[5.0]	13.4
HFC-152a	CH_3CHF_2	Y	N	0.09	6.0[0.2]	1.5
HFC-143a	CH_3CF_3	Y	N	0.13	10.1[1.1][c]	47.1
HFC-125	CHF_2CF_3	Y	N	0.23	8.3[1.0][c]	28.2
HFC-23	CHF_3	Y	N	0.19	23.3[0.7][c]	222
Chlorocarbons						
Methyl Chloroform	CH_3CCl_3	Y	Y	0.06	7.6[-1.5]	5.0
Carbon Tetrachloride	CCl_4	Y	Y	0.13	88.5[-1.0]	26
Methyl Chloride	CH_3Cl	N	Y	0.01	536[-3]	1.0
Bromocarbons						
Methyl Bromide	CH_3Br	N	Y	0.01	7.1[0.0]	0.8
Halon 1211	$CBrClF_2$	Y	Y	0.30	3.9[-0.06]	16.0
Halon 1301	$CBrF_3$	Y	Y	0.32	3.1[0.02]	65
Halon 2402	$CBrF_2CBrF$	Y	Y	0.33	0.46[-0.01]	20
Fully fluorinated species						
Sulfur Hexafluoride	SF_6	Y	N	0.52	7.02[0.28]	3,200
PFC-14	CF_4	N	N	0.10	78.3[0.6]	> 50 000
PFC-116	C_2F_6	N	N	0.26	4.09[0.08]	> 10 000

[a] Radiative efficiencies and lifetimes are taken from Daniel et al. (2007), Montzka et al. (2011), and Prinn et al. (2005).

[b] Mixing ratios are global surface means determined from the NOAA global cooperative sampling network (Hofmann et al. 2006), except for PFC-14 and PFC-116, and HFC-23 in 2009 which were measured by the AGAGE group (Mühle et al. 2010; Miller et al. 2010). Changes indicated in brackets are simply the difference between the 2010 and 2009 annual global surface mean mixing ratios. Units are ppm for CO_2, ppb for CH_4 and N_2O, and ppt for all others.

[c] Preliminary estimate for 2010.

[d] Perturbation lifetime

(v) The combined influence of long-lived trace gases on the radiative balance of the atmosphere —B. D. Hall, J. Butler, and S. A. Montzka

Long-lived trace gases have direct and indirect influences on the energy balance of the atmosphere. The direct radiative forcing (RF) of a trace gas is proportional to its change in atmospheric abundance since the start of the Industrial Revolution around 1750 and how efficiently it absorbs available infrared radiation (its radiative efficiency; Table 2.5). The NOAA Annual Greenhouse Gas Index (AGGI) was developed based upon the direct RF from long-lived trace gases (Hofmann et al. 2006). It represents the RF due to these trace gases in a given year relative to 1990, the Kyoto Protocol baseline year. Indirect effects (e.g., arising from stratospheric ozone depletion or water vapor feedbacks) are not considered in this index. The index is derived from global, surface measurements of carbon dioxide (CO_2), methane (CH_4), nitrous oxide (N_2O), chlorofluorocarbons CFC-12 and CFC-11 (the major long-lived greenhouse gases), and 15 minor greenhouse gases (e.g., HCFCs, HFCs; see Table 2.5). The AGGI offers a relatively straightforward way to assess the increase in direct RF due to long-lived trace gases since 1990.

By mid-2010, the increases in the abundances of these gases over their preindustrial values amounted to a direct RF to the atmosphere totaling approximately 2.80 W m^{-2} (Fig. 2.52). This compares with 2.17 W m^{-2} in 1990. With the AGGI defined as 1.0 in 1990, the preliminary value of the AGGI in 2010 was 1.29. Thus, the accumulation of long-lived trace gases in the atmosphere since 1990 has resulted in a 29% increase in RF due to long-lived gases. The direct RF increased by about 0.043 W m^{-2} each year in the 1980s and by about 0.031 W m^{-2} in the 1990s and 2000s. Currently, carbon dioxide accounts for about 64% of the RF due to long-lived trace gases (Fig. 2.52).

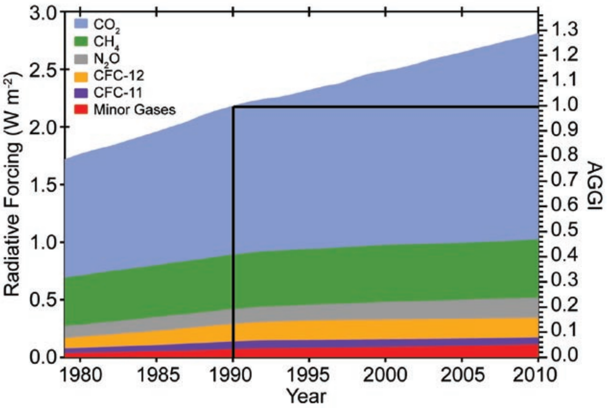

Fig. 2.52. Direct radiative forcing (W m^{-2}) due to long-lived trace gases relative to 1750 (left axis) and the total radiative forcing from long-lived trace gases, relative to 1990, defined as the Annual Greenhouse Gas Index (AGGI; right axis). The value of the AGGI was 1.29 in 2010, an increase of 29% since 1990.

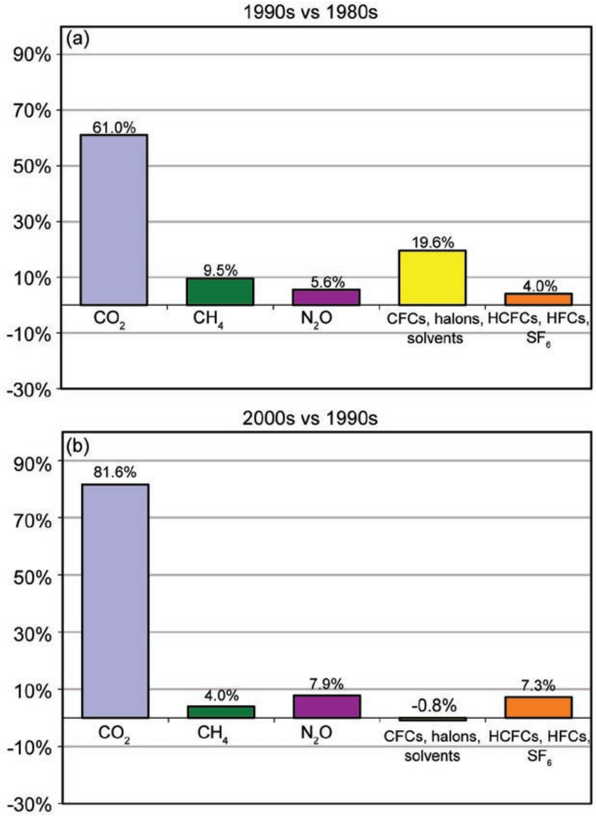

Fig. 2.53. Average relative contributions to changes in direct radiative forcing due to various trace gases through three decades. For example, comparing decadal averages, changes in CO_2 are responsible for 61% of the change in radiative forcing between the 1980s and 1990s.

While an increase in the abundance in CO_2 is responsible for the majority of the increase in RF, the relative contributions of CO_2 and other trace gases to increases in RF have changed over time. Nitrous oxide has recently overtaken CFC-12 as the third most important long-lived trace gas contributing to RF (Forster et al. 2007). Chlorofluorocarbons (CFCs) and other ozone-depleting substances played a larger role in the relative changes in the 1980s and 1990s (Fig. 2.53). Through the dual benefits of the Montreal Protocol on Substances that Deplete the Ozone Layer (Velders et al. 2007), the relative contribution of CFCs, halons, carbon tetrachloride (CCl_4), and methyl chloroform (CH_3CCl_3) to changes in RF has decreased in the last decade, partially offseting increases due to other gases.

2) Aerosols—A. Benedetti, J. W. Kaiser, and J.-J. Morcrette

The importance of atmospheric aerosols with respect to climate has long been recognized and highlighted in scientific studies (Haywood and Boucher 2000; Kaufman et al. 2002; Yu et al. 2006). Aerosols are often cited as one of the most uncertain factors influencing climate (Solomon et al. 2007), due to both their direct radiative effects and their indirect radiative effects linked to cloud feedbacks. Absorbing aerosols such as black carbon can have a net warming effect, while reflecting aerosols have a cooling impact that can partially offset the warming induced by greenhouse gases.

Aerosol abundance and distributions are influenced by many factors including land cover, surface winds, volcanic activity, biomass burning, and other human activities, and remain a major source of uncertainty in modeling. Progress in aerosol physical parameterizations has improved models, while advances in observing techniques from satellite, aircraft, and ground-based sensors have made it possible to better describe and understand aerosol properties. However, to obtain a more integrated view of the aerosol distribution, and to be able to understand aerosol climatic impacts, it is necessary to integrate the information from models and observations into a common framework. Reanalyses can provide this framework and offer some insight into changes in key climate variables.

ECMWF's operational numerical weather prediction model has recently been extended to include prognostic aerosols and related sources, sinks, and physical processes, underpinned by 4DVAR assimilation of observations of Aerosol Optical Depth (AOD) at 550 nm from the MODIS sensor (Benedetti et al. 2009; Morcrette et al. 2009). Results from an initial aerosol reanalysis were obtained as part of the GEMS (Global and regional Earth-system Monitoring using Satellite and in situ data) project (Hollingsworth et al. 2008) and presented in last year's *State of the Climate* report (Kaiser et al. 2010a). The follow-on project, Monitoring Atmospheric Composition and Climate (MACC) is currently providing an improved aerosol reanalysis for use in climate evaluation and assessment (Simmons 2010). The MACC reanalysis system uses upgraded inventories of biomass burning emissions (GFED V3; van der Werf et al. 2010), an updated aerosol model with improved organic matter modeling and revised dust source, and a global adaptive bias correction for MODIS aerosol data in the assimilation. These major changes have resulted in a new set of reanalysis data, and highlighted the need for continuous development and research in this area in order to establish high-quality long-term climatologies for aerosols. In parallel to the reanalysis, MACC also runs a Near Real Time Analysis/Forecast (NRTA/F) suite. The model versions used in the NRTA/F and in the reanalysis system are based on the same meteorological cycle with identical dynamical cores and physical processes. However, differences exist in the treatment of the bias correction of the MODIS data and in the definition of the observation error. Moreover the resolution of the initial-guess forecast is higher than in the reanalysis fields. Despite these differences, the spatial patterns of the AOD distribution and their variations with respect to the multiyear average can be attributed to changes in atmospheric state rather than to model changes. The MACC reanalysis will eventually cover the period 2003–11, and will then provide a consistent dataset for a possible trend analysis. Here we compare the global aerosol distribution for 2010 produced by the MACC NRTA/F system with the MACC reanalysis data for years 2003–06.

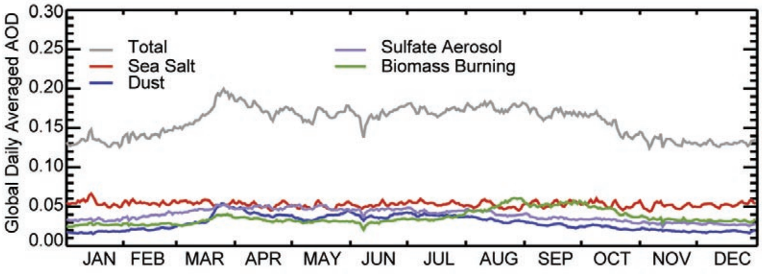

Fig. 2.54. Daily means of globally-averaged forecast aerosol optical depth (AOD) at 550 nm for 2010.

Figure 2.54 shows the daily mean AOD at 550 nm for 2010 derived from the NRTA/F run for the different species. Dust aerosols show a fairly regular annual cycle with a maximum in the boreal summer. In 2010, the boreal spring peak is also quite pronounced. The annual cycle of sulfate shows consistent boreal spring/summer maxima. Biomass burning aerosols (organic matter and black carbon) peak around September–October, consistently with the seasonality of wildfires in South America and southwestern Africa. Note also the high values of biomass burning AOD starting in August, related to the Russian/Siberian fires. Sea salt AOD does not show a seasonal dependence.

Maps of average AOD for the years 2003–06 (reanalysis) and 2010 (NRTA/F) are shown along with the absolute difference between the two (Fig. 2.55).

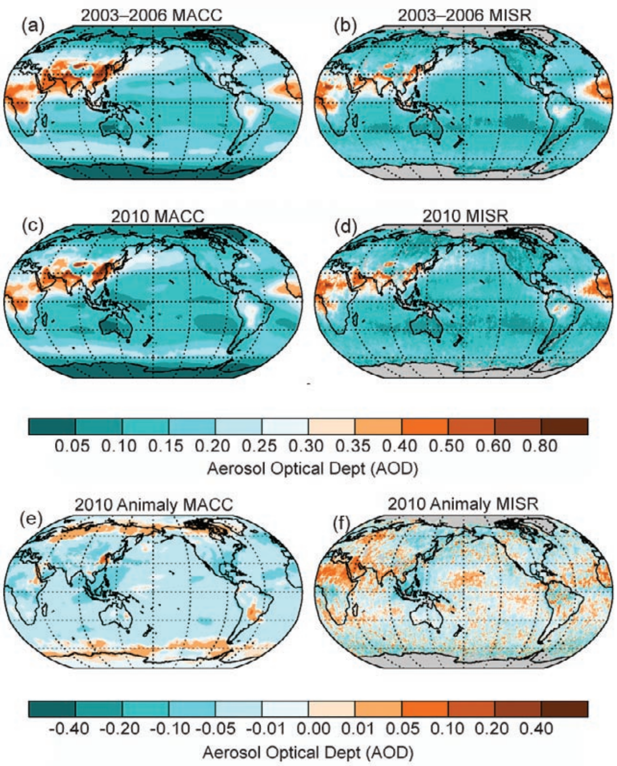

Fig. 2.55. Total aerosol optical depth (AOD) at 550 nm for (top) 2003–06, (middle) 2010, and (bottom) absolute difference between 2010 and the multiyear average. Left panels are derived from MACC data and right panels are from MISR data. (Courtesy of Goddard Earth Sciences Data and Information Services Center, through the GIOVANNI interface; see Table 2.1.)

A general decrease in total AOD is evident, although some areas show an increase in AOD: the high latitudes in the Northern Hemisphere, where the increase can be attributed to the Alaskan fires in spring/early summer and the Russian/Siberian fires in summer; South America, due to the particularly lively biomass burning fall season; and eastern China, most likely due to high values of sulfate aerosols. A decrease in AOD is seen over Indonesia, consistent with a lower-than-average burning season, as also indicated from satellite observations of fire radiative power (section 2g3). This is also confirmed by independent AOD observations from the Multi-angle Imaging Spectro-Radiometer (MISR; Kahn et al. 2010), shown in Fig. 2.55. Discrepancies between MISR and the MACC datasets are evident over the Sahara Desert where no data are assimilated and the MACC systems have too little dust. All other regions show good agreement with the reanalysis and NRTA/F systems.

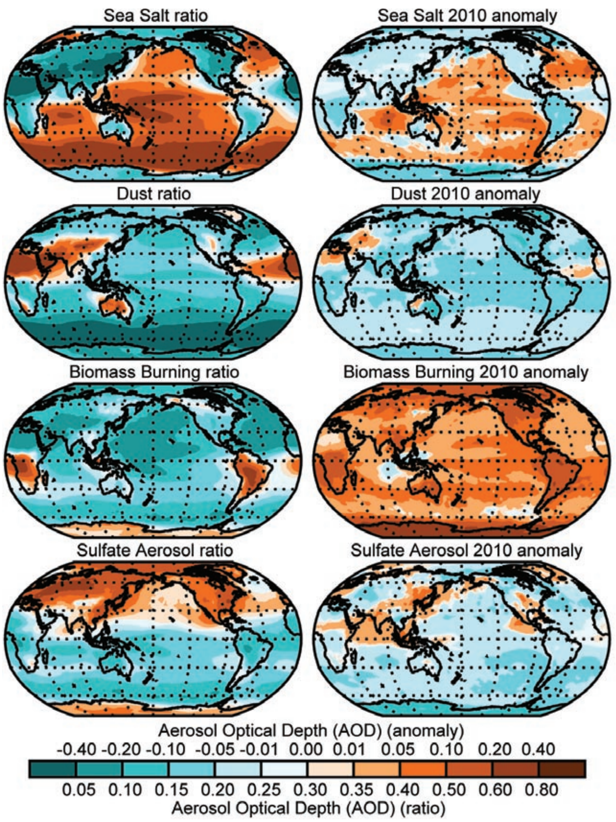

Fig. 2.56. 2010 fractional contributions of sea salt, dust, biomass burning, and sulfate aerosols, respectively from top to bottom, defined as the ratio between the aerosol optical depth (AOD) due to a given species and the total AOD (left). Right panels show the differences between the single-species fractional contributions for 2010 and for the 2003–06 base period.

Figure 2.56 shows fractional contributions to the total AOD at 550 nm from the different modeled aerosol species. Sea salt aerosols are the largest contributors in the Southern Ocean and along the storm tracks. The Sahara, with its outflow over the Atlantic, and the Middle East are the areas with the largest contribution from dust to the total AOD. Biomass burning aerosols are dominant over the Amazon, southern Africa, over boreal forests, and over the Southern Hemisphere high latitudes (although total AOD is low at southern latitudes). The maxima in fractional contribution of sulfate aerosols reflect the anthropogenic emission inventory used in the model, with sources in North America, Europe, India, and China. Note the large contribution from sulfate over the Arctic. Differences in single-species fractional contributions between 2010 and the multiyear average (right panels of Fig. 2.56) highlight an increase in sea salt contribution over the tropical oceans. Increased sea salt fractional contribution is also evident around the storm tracks in both hemispheres. The fractional contribution of desert dust for 2010 is lower than the multiyear average everywhere except in the Middle

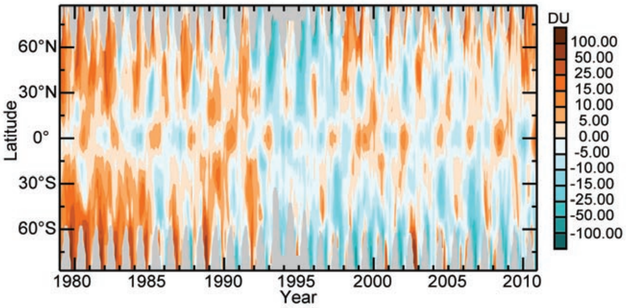

Fig. 2.57. Time variation (1979–2010) of total ozone anomalies. Anomalies are based on the SBUV/TOMS/OMI MOD V8 merged data record (1978–96; Frith et al. 2004) and GOME1/SCIAMACHY/GOME2 (GSG) merged total ozone (mainly GOME2 data in 2010; Weber et al. 2007). Anomalies were calculated from area weighted monthly mean zonal mean data in 5° latitude steps after removing the seasonal mean from the base period 1980–2008, which was derived from the MSR analysis (Van der A et al. 2010). Possible corrections from the overlap period (1996–2009) with MOD V8 were not applied to the GSG data set. Grey areas indicate regions where data are unavailable.

East region. Biomass burning aerosol fractional contribution to total AOD is substantially larger in 2010 nearly everywhere, while sulfate shows regional increases in already-polluted areas.

3) STRATOSPHERIC OZONE—M. Weber, W. Steinbrecht, R. J. van der A, P. K. Barthia, V. E. Fioletov, R. McPeters, and R. S. Stolarski

The 2010 annual mean ozone anomaly was positive for most of the Northern Hemisphere, with values of up to 40 DU above the 1980–2008 mean (Plate 2.1l). Similar high positive anomalies were observed in the late 1990s, but more frequently in the 1980s (Fig. 2.57). Above Central Europe, the annual mean was the highest of the last 25 years (Steinbrecht et al. 2011). This is also true for the midlatitude zonal mean (30°N–60°N; Fig. 2.58). The Arctic stratosphere in spring was characterized by very high ozone anomalies exceeding 100 DU in the Eurasian sector in February. The positive anomaly in the Northern Hemisphere persisted throughout the year.

In the tropics, annual mean ozone was close to the long-term mean. During the first half of 2010, ozone anomalies were quite negative (below -15 DU) and changed to positive in the second half (above +15 DU). This is largely attributed to the switch from the easterly phase of the quasi-biennial oscillation (QBO) to the westerly phase (Fig. 2.57; Baldwin et al. 2001). In the Southern Hemisphere, annual ozone was close to the long-term mean at midlatitudes and negative in the polar region. The depleted polar ozone reflected a deeper than average ozone hole during Antarctic spring (see section 6g). From Fig. 2.57, it is evident that the QBO modulates extratropical and polar ozone as well.

Long-term trends in total ozone (Fig. 2.58) are confined to the extratropics. The midlatitude losses between 1980 and the early 1990s were followed by stable values in the Southern Hemisphere and in-

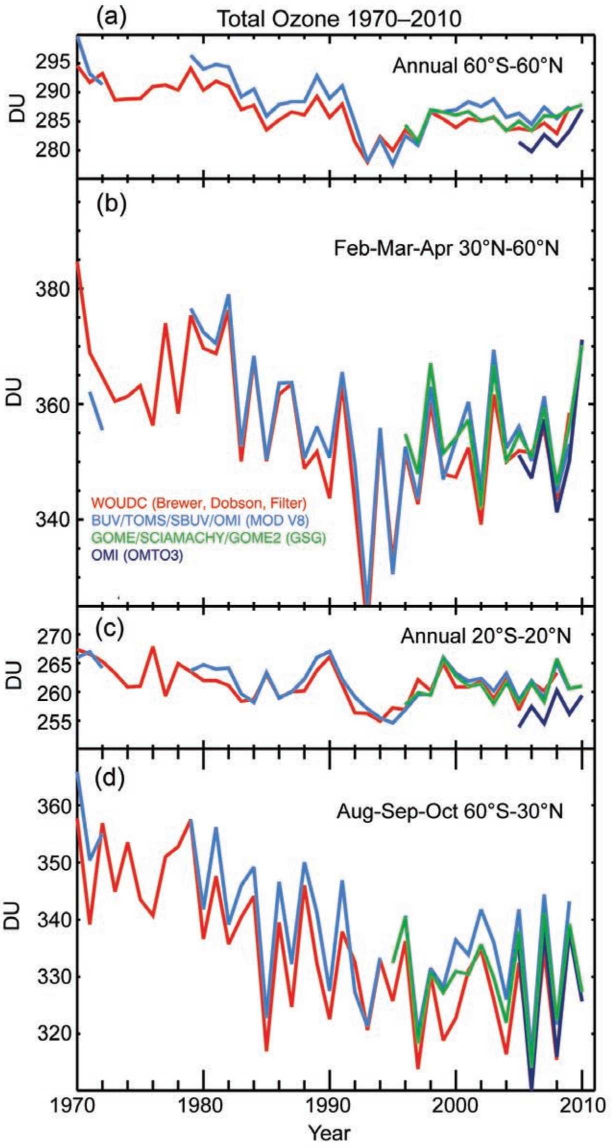

Fig. 2.58. Annual mean total ozone time series of ground-based measurements combining Brewer, Dobson, and filter spectrometer data (red; Fioletov et al. 2002), merged BUV/SBUV/TOMS/OMI MOD V8 (blue; Frith et al. 2004), GOME1/SCIAMACHY/GOME2 GSG (green; Weber et al. 2007), and OMI OMTO3 (OMI-TOMS; Kroon et al. 2008; McPeters et al. 2008) satellite data in the (a) 60°S–60°N, (b) 30°N–60°N, (c) 20°S–20°N, and (d) 30°S–60°S zonal bands.

creases in the Northern Hemisphere. The substantial minimum in the Northern Hemisphere in the early 1990s arose from additional ozone loss associated with the Mount Pinatubo volcanic eruption and a series of unusually cold Arctic winters with reduced ozone transport and enhanced polar ozone loss (e.g., Dhomse et al. 2006). Total ozone is expected to recover because stratospheric halogens leveled off in the late 1990s and are now declining (see Fig. 2.50 and section 2f1*iii*). However, other factors like the 11-year solar cycle and, in particular, changes in stratospheric circulation patterns [i.e., Brewer-Dobson circulation, teleconnection patterns such as the North Atlantic Oscillation (NAO), and annular modes of internal variability such as the Arctic Oscillation (AO)] contribute to variations on interannual to decadal time scales (Appenzeller et al. 2001; Steinbrecht et al. 2001; Weber et al. 2003; Orsolini et al. 2004; Yang et al. 2005; Dhomse et al. 2006; Stolarski and Frith 2006; Vyushin et al. 2007; Harris et al. 2008).

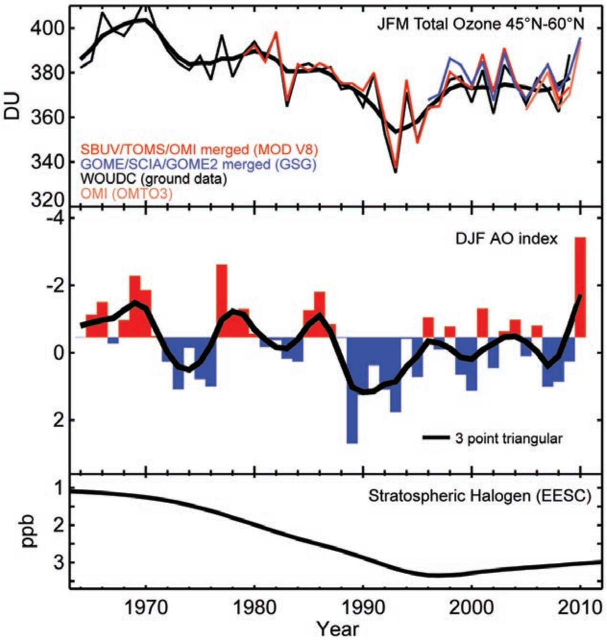

Fig. 2.59. Top: Jan–Mar (JFM) total ozone area weighted between 45°N and 60°N as measured from ground (Fioletov et al. 2002) and satellites, SBUV/TOMS/OMI MOD V8 data in red, GOME/SCIAMACHY/GOME2 GSG merged data in blue, and OMI OMTO3/OMI-TOMS (Kroon et al. 2008; McPeters et al. 2008) in light brown. The thick black line is the three point triangular smooth of the ground data. Middle panel: Dec–Feb (DJF) Arctic Oscillation (AO) index (blue values correspond to positive AO values). Thick black line is the three point triangular smooth of the AO index. Bottom panel: Equivalent effective stratospheric chlorine (EESC; Newman et al. 2007) drawn with a reversed y-axis.

The very high 2010 total ozone anomaly poleward of about 30°N coincided with an unusually pronounced negative phase of the AO, starting in December 2009 and lasting throughout most of 2010 (Steinbrecht et al. 2011). Winters with large negative AO indices are characterized by the enhancement and deflection of planetary waves towards the polar region. This is associated with an enhanced Brewer-Dobson circulation that transports more ozone into the extratropics, weakens the polar vortex, and reduces polar ozone loss (Hartmann et al. 2000; Randel et al. 2002; Weber et al. 2003). The easterly QBO phase during the first half of 2010 further strengthened the deflection of planetary waves (Baldwin et al. 2001). Winter/spring ozone anomalies in the Northern Hemisphere usually weaken due to photochemical decay, but persist until the end of the following fall (Fioletov and Shepherd 2003); in 2010 this resulted in very high 2010 annual mean ozone in the Northern Hemisphere (Steinbrecht et al. 2011).

Figure 2.59 highlights the long-term evolution of the winter AO, stratospheric halogen load (Equivalent Effective Stratospheric Chlorine, EESC), and northern midlatitude ozone in January–March (JFM) over the last 40 years. Apart from the year-to-year variability, the AO state changed from negative to a positive state in the late 1980s and since then has trended back to negative values. Decadal changes in stratospheric circulation as expressed by the AO appear to go hand in hand with chemical changes (EESC). As the AO is a leading mode of Northern Hemispheric climate variability and couples the stratosphere and troposphere (Thompson and Wallace 2000; Hartmann et al. 2000), stratospheric ozone changes may have contributed on long time scales to changes in the global circulation and climate (Steinbrecht et al. 2011). When attributing different factors to long-term changes in ozone, it is, however, difficult to separate dynamical and chemical contributions (Kiesewetter et al. 2010).

g. Land surface properties

1) Alpine glaciers and ice sheets—M. S. Pelto

The World Glacier Monitoring Service (WGMS) record of mass balance and terminus behavior (WGMS 2008; WGMS 2009) provides a global index for alpine glacier behavior. Mass balance was negative in 2009 for the 19th consecutive year. Preliminary data for 2010 from Austria, Greenland, Italy, Norway, New Zealand, and the United States indicate it is highly likely that 2010 will be the 20th consecutive year of negative annual balances.

Alpine glaciers have been studied as sensitive indicators of climate for more than a century, most commonly focusing on changes in terminus position and mass balance (Oerlemans 1994). The worldwide retreat of mountain glaciers is one of the clearest signals of ongoing climate change (Haeberli et al. 2000). The retreat is a reflection of strongly negative mass balances over the last 30 years (WGMS 2008). Glacier mass balance is the difference between accumulation and ablation. A glacier with a sustained negative balance is out of equilibrium and will retreat. The recent rapid retreat has led to some glaciers disappearing (Pelto 2010).

The cumulative mass balance loss of the last 30 years is 12.3 m w.e., the equivalent of cutting a 14 m thick slice off the top of the average glacier (Fig. 2.60). The trend is remarkably consistent from region to region (WGMS 2009). WGMS mass balance results based on 30 reference glaciers with 30 years of record are not appreciably different from the results for all reporting glaciers. The decadal mean annual mass balance was -198 mm in the 1980s, -382 mm in the 1990s, and -654 mm for 2000–09. The declining mass balance trend during a period of retreat indicates alpine glaciers are not approaching equilibrium and retreat will continue to be the dominant terminus response.

In 2010 winter accumulation on Austrian and Italian glaciers was about average, and summer temperature was above the mean in 2010. The result was mass losses on glaciers in the Alps: Sonnblickkees, Austria, -790 mm; Ciardoney, Italy, -830 mm; and Fontana Bianca, Italy, -130 mm. The Swiss Glacier Monitoring Network reported that in 2010 the termini of 86 glaciers were in retreat, six were stationary, and three advanced.

In Norway, terminus fluctuation data from 30 glaciers for 2010 indicate 27 retreating, one stable, and two advancing. The average terminus change was -17 m, compared to -183 m in 2009. Mass balance surveys found deficits on all Norwegian glaciers. Winter 2009/10 was cold but with little snow on the glaciers, 50%–80% of the long-term normal. Summer was warmer than normal in the south and a bit colder than normal in the north. (L. Andreasson 2011, personal communication).

In the North Cascades, Washington (M. Pelto 2011, personal communication), a transition from El Niño to La Niña conditions led to equilibrium mass balances. El Niño winter conditions led to reduced winter snowfall. La Niña conditions developed by summer causing low summer melting, which offset the low accumulation. The result was positive annual balance on four glaciers, negative balance on five glaciers, and an equilibrium balance on one glacier. All 33 glaciers observed retreated in 2010. In southeast Alaska, snowlines were 50 m above average on Lemon Creek and Taku Glacier of the Juneau Icefield indicative of moderate negative balances.

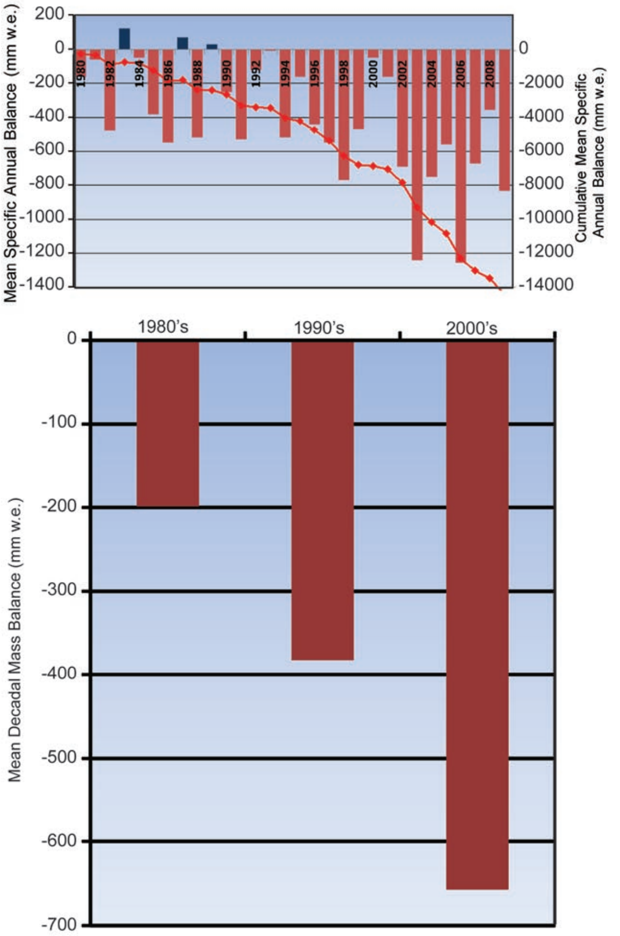

Fig. 2.60. The (top) annual mean and cumulative annual mean balance and (bottom) decadal mean cumulative specific mass balance (mm w.e.) reported for the 30 reference glaciers to the WGMS.

In New Zealand, El Niño led to normal to below-normal temperatures through summer and into fall 2010, leading to snowlines in a near steady state (J. Hendrikx 2011, personal communication). On 50 glaciers surveyed, the average snowline was at the equilibrium snowline elevation, after two strongly negative years in 2008 and 2009.

For information on 2010 ice melt on the Greenland ice sheet and in Antarctica please refer to sections 5f and 6e, respectively.

SIDEBAR 2.4: STRATOSPHERIC WATER VAPOR—K. H. ROSENLOF AND D. F. HURST

Stratospheric water vapor modulates Earth's climate, directly through long-wave radiative processes, and indirectly through its influence on stratospheric ozone abundance (Shindell 2001). An increase (decrease) radiatively warms (cools) the troposphere and cools (warms) the stratosphere. Solomon et al. (2010) modeled the radiative forcing of an observed rapid 10% (~0.5 ppmv) post-2000 decrease and found that it slowed the rate of increase in global surface temperature over 2000–09 by about 25% compared to that which would have occurred from well-mixed greenhouse gases. This makes it imperative that stratospheric water vapor be closely monitored.

The main sources of stratospheric water vapor are entry through the tropical tropopause (Brewer 1949) and in situ oxidation of methane (CH_4) and hydrogen (H_2), yielding two water molecules for each CH_4 molecule oxidized (LeTexier et al. 1988). The stratosphere is extremely dry (< 10 ppmv) because water vapor is condensed out as air moves through the extremely cold tropical tropopause region. Other sources include convective overshooting of ice particles and transport across the tropopause into the extratropical lower stratosphere. Both are difficult to globally quantify but are likely minor contributors. The main loss process, polar dehydration during Antarctic winter, annually removes ~2% of the water vapor burden (Douglass and Stanford 1982).

Near-global measurements by satellites began in late 1978 with seven months of Limb Infrared Monitor of the Stratosphere (LIMS) measurements (Gille and Russell 1984) that provided the first insights into the global budget (Jones et al. 1986). Longer-term datasets from satellite-borne instruments have been available since 1984, with the longest records from the Stratospheric Aerosol and Gas Experiment (SAGE II) (1984–2005) and the Halogen Occultation Experiment (HALOE) (1991–2005). The Aura Microwave Limb Souder (MLS), active since 2004, provides a critical extension to HALOE.

Entry into the tropical lower stratosphere varies with the seasonal cycle of temperatures near the tropical tropopause, with minima and maxima during the Northern Hemisphere (NH) winter and summer, respectively (Reed and Vleck 1969). As air enters the stratosphere it is imprinted with a seasonally-dependent water vapor mixing ratio (Fig. 2.61). The seasonality is large, typically 50%–60% of the annual mean. Air masses retain these imprints as they are advected to higher altitudes in the tropics by the Brewer-Dobson circulation (BDC), a phenomenon dubbed "the tropical tape recorder" by Mote et al. (1996). Seasonal signals are gradually eroded through mixing as air moves upward and poleward. Mixing ratios increase with altitude as greater fractions of CH_4 and H_2 are oxidized.

The global distribution and variance are controlled by the seasonal cycle of tropical entry conditions coupled with seasonally-dependent transport by the BDC, with stronger extratropical downwelling during winter. The NH winter downwelling is stronger than in the Southern Hemisphere (SH), and is accompanied by the strongest tropical upwelling with the coldest tropical tropopause. Hence, in January the tropics are extremely dry, especially over the Western Pacific, while the Arctic is significantly moistened by strong downwelling with minimal polar dehydration (Fig. 2.62a). At the lowest stratospheric levels, longitudinal structure reflects the impacts of tropospheric dynamics, while distributions are zonally uniform in the mid- and upper stratosphere. In July (Fig. 2.62b), lower stratospheric mixing ratios over Antarctica are extremely low within the vortex, substantially higher within a zonal band surrounding the vortex, and highest over the Indian subcontinent as the lower stratosphere is moistened by convective uplift within the monsoon. The net result is that the annual mean SH is drier than the NH (Rosenlof et al. 1997).

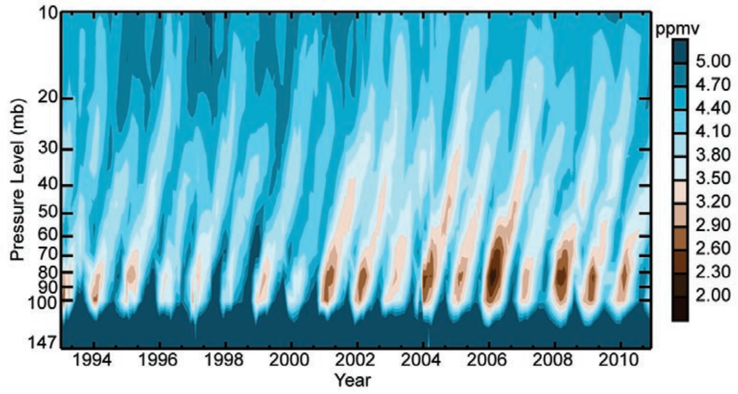

FIG. 2.61. Vertical profiles of tropical (10°N–10°S) stratospheric water vapor mixing ratios from HALOE (1991–2005) and Aura MLS (2004–present). HALOE version 20 mixing ratios were adjusted to better agree with the MLS version 3.3 based on coincident profiles during 2004–05. Adjustments are altitude dependent with a maximum shift of ~0.5 ppmv.

The determination of multidecadal trends from satellite-based datasets is challenging and uncertain because there are significant discrepancies between coincident measurements by the different sensors (Vömel et al. 2007; Kley et al. 2000; Randel et al. 2004; Lambert et al. 2007). These discrepancies,

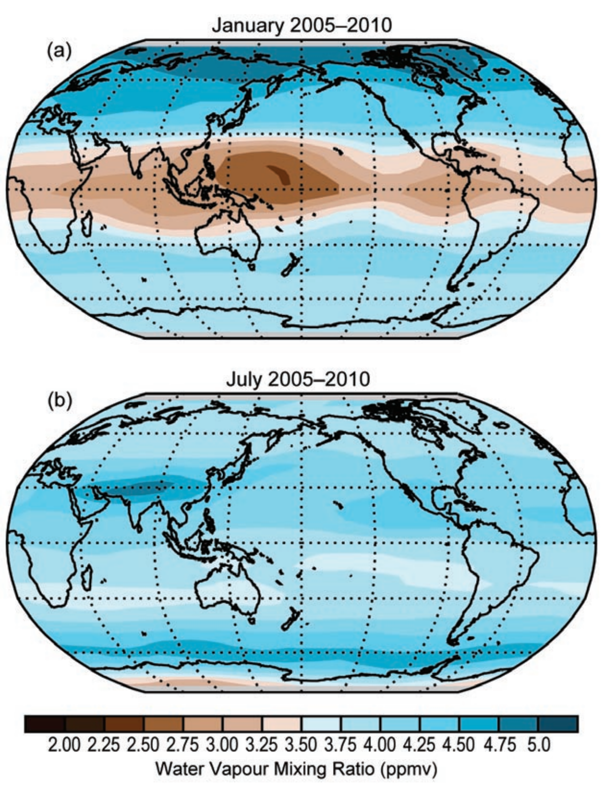

Fig. 2.62. Six-year (2005–10) average global distributions of water vapor at 82 hPa, near the point of stratospheric entry in the tropics, as measured by Aura MLS during (a) January and (b) July, the months of seasonal extremes in water vapor entry mixing ratios.

ranging from 10% to 50% or even greater in some cases, preclude simple compositing to produce longer-term records.

The longest continuous record is in the NH midlatitudes over Boulder, Colorado, (40°N) from balloon-borne frost point hygrometers (FPHs; Fig. 2.63). These data portray net increases over Boulder of 14 ± 2% (0.6 ± 0.1 ppmv) during 1980–2000 (Scherer et al. 2008) and 27 ± 6% (1.0 ± 0.2 ppmv) during 1980–2010 (Hurst et al. 2011). These and other in situ and satellite data in the NH imply a 50% increase in entry-level stratospheric water vapor during 1950–2000 (Rosenlof et al. 2001) while tropopause temperatures decreased (Zhou et al. 2001).

Prominent in both HALOE and NOAA FPH data over Boulder (Fig. 2.63), and in tropical HALOE data (Fig. 2.61), is a ~10% (~0.5 ppmv) decrease after 2000. Randel et al. (2006) attributed this to anomalously cold tropical tropopause temperatures and increased tropical upwelling. Although attribution of this large and rapid decrease supports the idea that tropical tropopause temperatures control stratospheric water vapor entry (Randel et al. 2004; Fueglistaler and Haynes 2005; Rosenlof and Reid 2008), trends in tropical cold point temperatures cannot explain the long-term increase in the NH midlatitudes. With only ~30% of the observed increase attributable to CH_4 growth (Rohs et al. 2006), the predominant cause(s) remains unidentified. Hurst et al. (2011) noted that water vapor growth over Boulder during 2006–10 strengthened with altitude in the absence of sufficient CH_4 growth, requiring a dominant mechanism other than an increase in water vapor in the tropical lower stratosphere. Identifying the underlying cause(s) of the observed long-term net increase remains elusive despite substantial ongoing efforts.

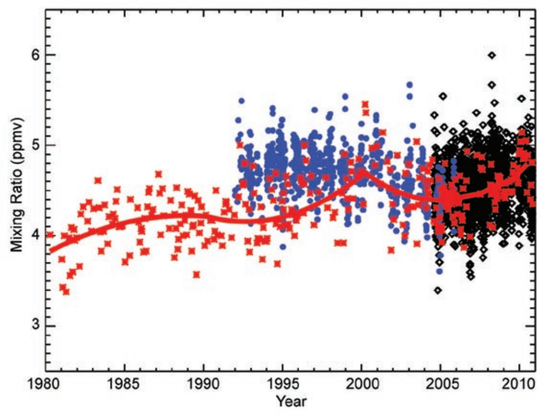

Fig. 2.63. Stratospheric water vapor mixing ratios at 46 hPa over Boulder, Colorado. The NOAA FPH data (red markers) and smooth curves (red) in four discrete trend periods depict a net increase of 27 ± 6% since FPH measurements began in 1980 (Hurst et al. 2011). Data from Aura MLS (black markers) and adjusted data from HALOE (blue markers) are also included. Note the post-2000 decrease in both the FPH and HALOE data, and the post-2006 increase in both the FPH and MLS data.

Photo Courtesy of Allen Jordan (NOAA/ESRL Global Monitoring Div.)

Balloon launch at Marshall Field Site, Boulder, Colorado

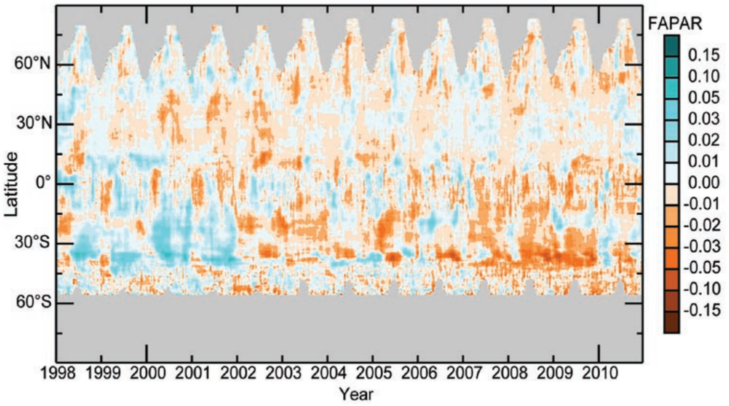

Fig. 2.64. Fraction of Absorbed Photosynthetically Active Radiation (FAPAR) anomalies from the 1998–2010 base period by latitude provided by SeaWiFS (NASA) and MERIS (ESA) sensors. Gray areas indicate regions where data are unavailable.

2) Fraction of Absorbed Photosynthetically Active Radiation (FAPAR)—N. Gobron and A. S. Belward

Analysis of a 13-year record of global earth observations has showed considerable variations in vegetation dynamics on regional and continental scales. The state of vegetation has been monitored using estimates of the Fraction of Absorbed Photosynthetically Active Radiation (FAPAR) from 1998 to 2010 (Gobron et al. 2010). These data highlight geographical regions with anomalous vegetation in 2010 with respect to previous years.

In Plate 2.1m, positive anomalies indicate favorable vegetation growing conditions in 2010, while negative values, in brown, imply vegetation stress. The strongest positive anomalies are found in central and eastern Australia, followed by minor positive anomalies over the middle of the United States, India, central Europe, and southern Africa. Strong negative anomalies occurred in Russia and South America.

The situation in Australia contrasts notably with previous years' values and provides quantitative confirmation of the break in the persistent droughts that have affected this region over the last decade. Vegetation activity in 2010 has now returned to levels seen in 2000–01.

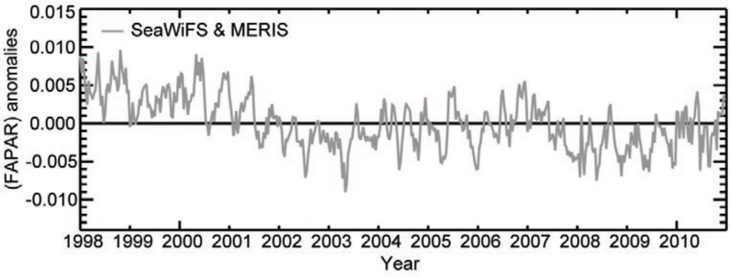

Fig. 2.65. Globally averaged Fraction of Absorbed Photosynthetically Active Radiation (FAPAR) anomalies from the 1998–2010 base period.

The most striking negative anomaly occurred in central Russia, where high temperatures and low rainfall have translated into extreme FAPAR negative anomalies. Cropland, grassland, and forests were all affected. In some cases, catastrophic fires occurred, but fire apart, the region as a whole exhibits significantly depressed levels of photosynthetic activity and plant growth. Amazonia was also affected by strong droughts in September 2010 and the effects of this are seen in Plate 2.1m. However, in comparison with previous years and in terms of the annual average, these anomalies are not as strong as in Russia.

Figure 2.64 shows zonally-averaged FAPAR anomalies since 1998. The Southern Hemisphere contrasts markedly with the Northern because of persistent negative anomalies through all seasons from around 2002 up to 2009. This feature ended in 2010, with positive anomalies in the Southern Hemisphere at the beginning and end of the year.

Despite dramatic regional impacts, neither the renewed plant growth vigor in Australia nor the widespread vegetation stress in central Russia were large enough to cause major changes in the global average. When globally averaged (Fig. 2.65), 2010 appears to be part of a gradual return to positive values, though not to the levels seen between 1998 and 2001.

3) Biomass burning—J. W. Kaiser, A. Heil, and G. R. van der Werf

Biomass burning occurs in all vegetated terrestrial ecosystems. Humans ignite most fires in the tropics and subtropics, while lightning fires are more common in remote boreal regions. Fires contribute to the buildup of carbon dioxide (CO_2) through deforestation and tropical peatland fires, and from areas that see an increase in the fire frequency. They also emit other greenhouse gases and are a major source of aerosols, carbon monoxide (CO), and oxides of nitrogen (NOx), impacting local and regional air quality. Overall, fires impact 8 out of 13 identified radiative forcing agents (Bowman et al. 2009) and indirectly impact the fluxes of water and energy by modifying vegetation.

Satellite observations of burned area (Giglio et al. 2010) in combination with biogeochemical modeling indicate that carbon emissions from fires were 2.0 Pg

C yr^{-1}, averaged over 1997–2009 (van der Werf et al. 2010; Global Fire Emissions Database, GFED). About a quarter (0.5 Pg C yr^{-1}) is emitted from fires used in the deforestation process or in degraded peatlands and is a net source of CO_2. The remainder is balanced by CO_2 uptake of regrowing vegetation. Deforestation and peat fires in particular show large variability from year to year, partly related to changes in annual deforestation rates and drought conditions in deforestation zones.

In addition to providing updates to GFED, the European Union (EU) Monitoring Atmospheric Composition and Climate (MACC) project assimilates satellite-observed fire radiative power (FRP) to estimate biomass burning trace gases and aerosol emissions (Kaiser et al. 2010b; Global Fire Assimilation System, GFAS). The products are available starting in 2003 and are extended in real time. Initial field research (e.g., Wooster et al. 2005) indicated that FRP is universally proportional to biomass consumed. However, a biome dependency has been found and implemented following Heil et al. (2010). The presented GFAS data are based on Moderate Resolution Imaging Spectroradiometer (MODIS) FRP only to ensure consistency of the time series. GFED and GFAS agree within about 25%, as illustrated in Fig. 2.66.

The annual biomass combustion calculated by GFAS for the reference period 2003–09 is shown in Fig. 2.67 and the anomaly for 2010 is shown in Plate 2.1n. The global- and continental-scale budgets are summarized in Table 2.6, alongside GFED emissions, which span a longer timeframe (1997–2009) but cannot be calculated in real time.

Table 2.6. Annual continental-scale biomass burning budgets in terms of burnt carbon (Tg C yr^{-1})

Dataset		GFED3.1		GFAS1.0				
Time Period		1997–2009		2003–2009		2010	2010 w.r.t. 2003–2009	
Quantity		mean	range	mean	range	value	absolute anomaly	relative anomaly
Global		2000	1514–2760	2062	177–2305	1876	-185	-9%
N America	30°N–57°N, 190°E–330°E	62	9–140	98	70–137	106	8	8%
C America	30°N–57°N, 190°E–330°E	43	23–112	67	56–91	53	-14	-21%
SH America	0°–60°S, 190°E–330°E	269	90–570	348	176–456	418	70	20%
Europe and Mediterranean	30°N–75°N, 330°E–60°E	19	8–31	33	30–41	61	28	85%
NH Africa	0°–30°N, 330°E–60°E	478	358–584	425	378–459	332	-94	-22%
SH Africa	0°–35°S, 330°E–60°E	552	478–676	511	485–589	571	60	12%
N Asia	30°N–75°N, 60°E–190°E	148	30–366	214	111–466	105	-110	-51%
SE Asia	10°N–30°N, 60°E–190°E	103	38–170	132	111–161	157	25	19%
Tropical Asia	10°N–10°S, 60°E–190°E	192	21–1065	103	36–217	22	-81	-79%
Australia	10°S–50°S, 60°E–190°E	134	78–185	130	87–175	53	-77	-59%

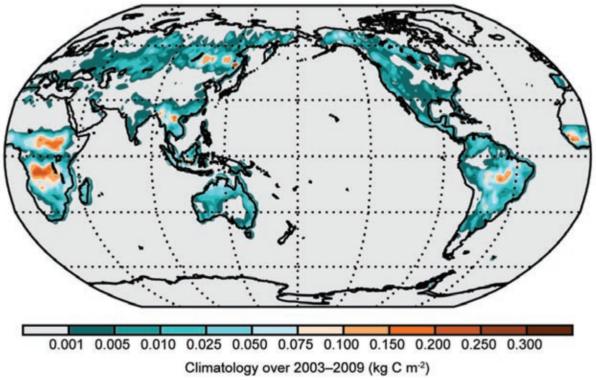

Fig. 2.67. Climatological global biomass burning over the 2003–09 base period as burnt carbon area density (kg C m^{-2}).

In 2010, global emissions were 9% below the 2003–09 mean, well within the historic range. The distribution of fire activity, however, was anomalous with more fire activity in Southern Hemisphere (SH) America and Europe, notably European Russia, and less fire activity in Australia, Northern Hemisphere (NH) Africa, Central America, and northern and tropical Asia.

The combustion rate in SH America was 20% above the 2003–09 average, and more than double that of 2009 (Table 2.6; Fig. 2.66). SH America experienced drought conditions during the fire season in the southern Amazon where most fire activity is concentrated in the arc of deforestation. The increase is remarkable because the Brazilian space agency has reported a downward trend in deforestation since 2004 for the Brazilian Amazon (Regalado 2010; http://www.obt.inpe.br/prodes/). Fire data support this trend, except for 2007 and 2010. The Amazon fires in 2010 have been linked to a warm sea surface temperature anomaly of the tropical North Atlantic via the geographical pattern of the accompanying drought, similar to the situation in 2005 (Lewis et al. 2011; Marengo et al. 2008). Both 2007 and 2010 also feature strong transitions from El Niño to La Niña. Finally, part of the increase in 2010 stemmed from fires that were out of control in Bolivia and Peru, while understory fires, maintenance fires, and deforestation fires in areas not covered by the assessment of the Brazilian space agency could have also contributed to the strong fire season.

Western Russia experienced anomalously dry and hot conditions during May to August 2010. They triggered widespread fire activity in an area east of Moscow, where drained organic soils provided ample fuel for prolonged burning of peaty soils. High rates of smoke emissions and atmospheric subsidence led to a severe impact on air quality in July and August 2010. This area is included in Europe in Table 2.6 and explains the large positive anomaly; fire activity in Europe excluding Russia was below average.

The low combustion rate in NH Africa with its peak in boreal winter appears to continue a negative trend that is beginning to emerge from the GFED dataset (Fig. 2.66). The negative anomaly in 2010 could also be related to a relatively late fire season, transferring part of the emissions to 2011.

The strongest relationships between the El Niño-Southern Oscillation and fire are usually found in Indonesia and Australia, where El Niño-induced drought in general leads to higher fire activity (vice versa for La Niña), although low rainfall rates in Australia's more arid regions may actually lower fire activity because of reduced fuel availability (van der Werf et al. 2008). In 2010, the transition to La Niña conditions occurred before the fire season started in Indonesia and northern Australia, and anomalous wet conditions strongly inhibited fire rates in both regions (Table 2.6).

The positive aerosol anomaly over SH America and a negative one over Indonesia reported in section 2f2 (Fig. 2.56) is likely to be explained by the fire anomalies reported here.

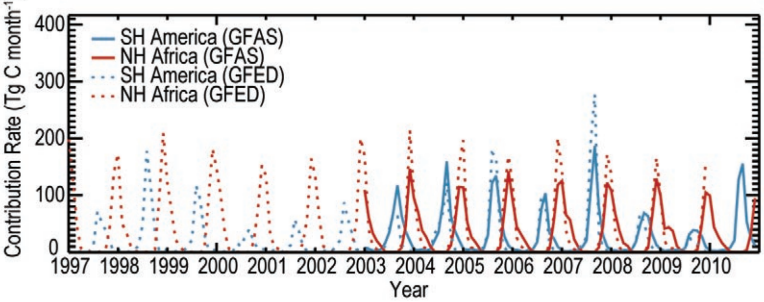

Fig. 2.66. Monthly carbon combustion rate (kg C mo^{-1}) in Northern Hemisphere Africa (red) and Southern Hemisphere America (blue) by GFED (dashed line) and GFAS (solid line).

4) Forest biomass and biomass change—

P. Cais, S. Quegan, and S. Saatchi

Biomass stored in forests is a major global carbon stock whose dynamics affect climate both through emissions when forest is cleared or degraded and by taking up carbon dioxide (CO_2) when forest is growing. Key sources of information on global biomass and its change in each country are the periodic Global Forest Resource Assessment (FRA) reports of the Food and Agriculture

Organization (FAO 2006, 2010), which are typically based on inventory data. The uncertainties in the country data are not reported and are likely to be highly variable, particularly for countries without a well-developed forest monitoring infrastructure (as is the case in many tropical forest countries). Individual plot data are not distributed, but the data underlying the individual country estimates in the FRA can be accessed through FAO. Revisit of inventories allows measurement of biomass changes over periods of several years.

The key findings of FAO (2010) are: (1) that the global forest area extent is 40 M km^2, storing a total biomass of 290 Pg C; (2) that the rate of tropical deforestation since 2000, 0.13 M km^2 yr^{-1}, seems to have decreased compared to the 1990s rate of 0.16 M km^2 yr^{-1}; Brazil and Indonesia, which had the highest forest loss rates in 1990s, have reduced deforestation in the 2000s; and (3) that large-scale forest plantation partly counterbalances tropical forest loss. Biomass stocks are decreasing in tropical countries because of deforestation, but increasing in temperate countries due to forest growth, and increased forest stand density in Europe and in the United States. China also has a major reforestation program. Forest in European Russia seems to be gaining carbon, but this is counterbalanced in Asian Russia by increased fire disturbance losses (Shvidenko et al. 2010).

Carbon dioxide emissions from land use change (LUC; mainly tropical deforestation) were revised to 2009 by Friedlingstein et al. (2010) using data on forest cover reported by FAO (2010) incorporated in a LUC emission model (Houghton 2003). The average LUC emissions estimate for the period 2000–09 is 1.1 ± 0.7 Pg C yr^{-1}, which is lower than the previous estimate of 1.5 ± 0.7 Pg C yr^{-1} with the same LUC emission model when driven by data from FAO (2006), mainly because of replacement of the originally anticipated rates of deforestation in tropical Asia by actual values. The downward revision of LUC emissions to 2009 by Friedlingstein et al. (2010) is also consistent with satellite observations over the Brazilian Amazon indicating a slowdown of deforestation in that region (Regalado 2010). There are two major sources of uncertainty in these estimates: the area of forest lost and the average biomass of this forest. Differences in the assumed value of the average biomass gave rise to differences of 1 Pg C yr^{-1} in the range of estimates of emissions from tropical deforestation (Houghton 2005). Satellite estimates of deforestation also tend to be significantly lower than inventory-based estimates (Achard et al. 2004; DeFries et al. 2002). A recent benchmark map developed from ground and satellite observations provides spatially refined and methodologically comparable carbon stock estimates for forests across 75 developing countries in tropical regions (Fig. 2.68). The map improves upon previous assessments based on often old and incomplete national forest inventory data and earlier spatial products. With systematic quantification of the errors, the map improves and constrains the pantropical estimate of total tropical forest biomass carbon (247 Gt C at 10% tree cover), and similarly national-scale carbon stocks (Saatchi et al. 2011). With the uncertainties quantified spatially along with biomass values, estimates of emission from tropical forests can improve significantly.

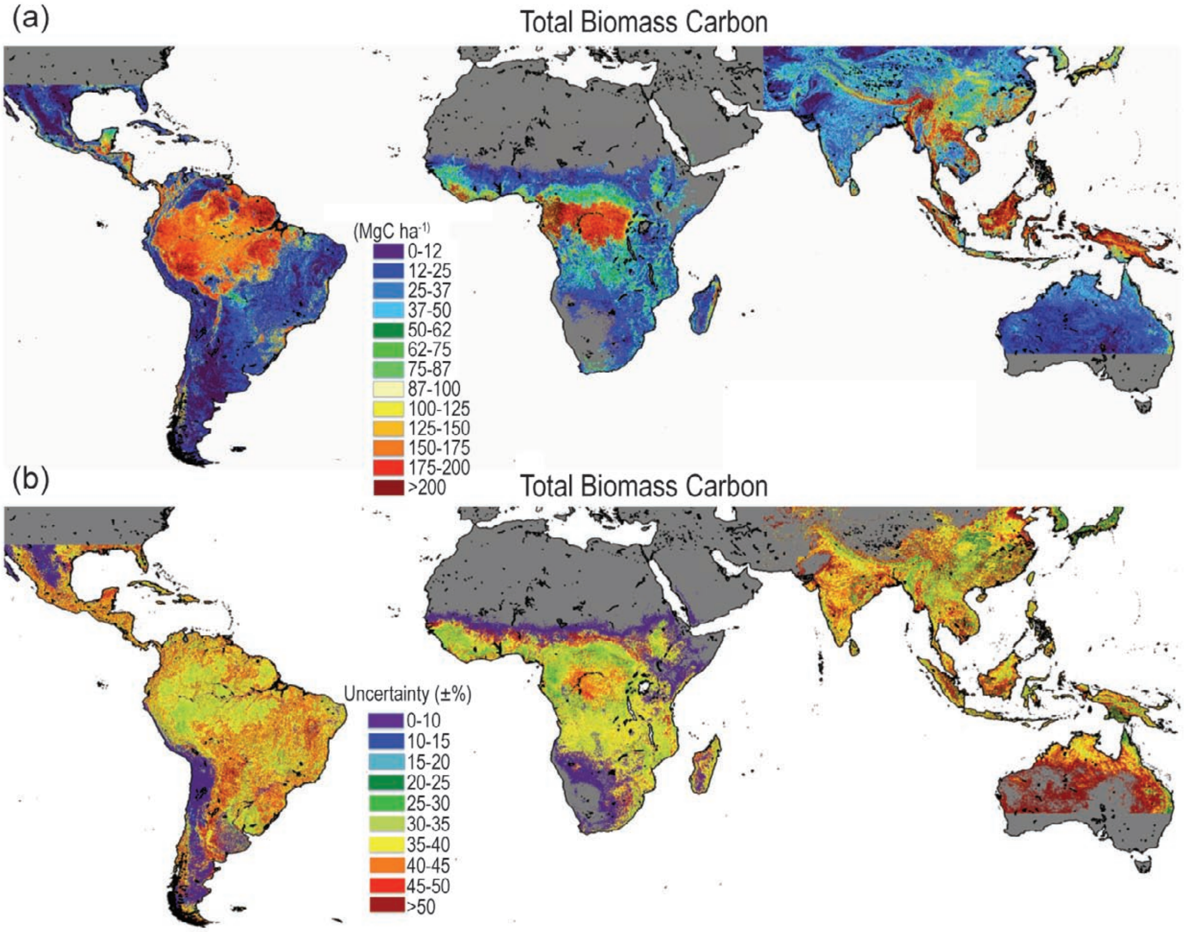

FIG. 2.68. Benchmark map of magnitude and uncertainty of forest carbon stock in tropical regions. (a) Forest carbon stock defined as 50% of AGB+BGB is mapped at 1-km pixel resolution and colored based on 12 Mg C ha^{-1}–25 Mg C ha^{-1} range to show the spatial patterns. (b) The uncertainty of the benchmark map is estimated using error propagation through spatial modeling approach. The uncertainty is given in terms ±% and it includes all errors associated with prediction from spatial modeling, sampling errors associated with variability of forest AGB at 1-km grids, estimation of Lorey's height from ICESAT GLAS Lidar used to sample the forest structure over all tropical forests, estimation of AGB from Lorey's height using inventory data from 493 plots distributed over three continents, and errors associated with BGB estimation from allometry relating AGB and BGB (Saatchi et al. 2011).

3. GLOBAL OCEANS—J. M. Levy, Ed.

a. Overview—E. J. Kearns and J. M. Levy

Calendar year 2010 exhibited anomalies in ocean temperature, salinity, sea level, heat content, currents, carbon, and phytoplankton that were highly influenced by the transition from El Niño to La Niña conditions in the Pacific Ocean, maintenance of a negative phase of the North Atlantic Oscillation, and transition to a negative phase of the Pacific Decadal Oscillation. Consequentially, the state of the ocean climate in 2010 was characterized by relatively anomalous patterns compared with climatologies and with the previous calendar year. The following highlights are fully described in the chapter that follows:

- The global sea surface temperature variations observed in 2010 were characterized by the transition from El Niño to La Niña during the summer 2010, the development of a negative Pacific Decadal Oscillation pattern in the North Pacific during the fall/winter of 2010, and the development of a tripole sea surface temperature (SST) anomaly pattern in the North Atlantic.
- Global integrals of upper ocean heat content for the past several years have reached values consistently higher than for all prior times in the historical record, consistent with the dominant role of the ocean in the Earth's net energy uptake. Deep and abyssal waters of Antarctic origin have also trended warmer on average since the early 1990s.
- The global ocean latent and sensible heat fluxes in 2010 reflected a primary role of near-surface wind anomalies in causing heat flux anomalies; the latter, in turn, served as a forcing mechanism for many of the SST anomalies in the North Atlantic and the tropical Indian and western Pacific Oceans. The globally-averaged heat flux from the ocean was close to that in 2009, remaining below the peak value seen about a decade ago.
- The sea surface became saltier in 2010 relative to 2009 in the western equatorial Pacific, and fresher in the central equatorial Pacific, mostly owing to an eastward shift in convection and precipitation associated with El Niño. Overall, saltier (higher evaporation) regions of the ocean surface continue to be anomalously salty, and fresher (higher precipitation) regions anomalously fresh in 2010. This pattern, which has held over the last several decades, suggests an increase in the hydrological cycle, consistent with climate model predictions for a warming atmosphere. Changes between 2009 and 2010 in subsurface salinity of 0.02–0.04 (Practical Salinity Scale) have occurred in the upper 1000 m of all three major ocean basins.
- Westward La Niña-associated surface current anomalies in the equatorial Pacific were the strongest seen in the last decade. The Kuroshio shifted northward compared with the previous four years, and an anomalously high North Brazil Current shed rings into the Northern Hemisphere.
- The meridional overturning circulation shows no statistically significant trend between April 2004 and April 2009, and there are no unusual anomalous features of note. A significant surface component of this circulation, the Florida Current, has continued the slight decrease observed over the past four years, and now falls within its lowest 25% of all annual mean values from the 29-year record.
- The effects of negative Pacific Decadal Oscillation and North Atlantic Oscillation states are evident in regional sea level changes in the North Pacific and North Atlantic during 2010, as well as in extreme coastal sea level amplitudes with above-normal levels off the west coast of North America and below-normal levels in Northern Europe.
- The global net carbon uptake flux for the 2009 transition period from La Niña to El Niño conditions is estimated to be 1.40 Pg C yr^{-1}, very similar to the 27-year mean. A recent synthesis suggests that, between 1800 and 2008, up to 8.2 Pg C accumulated in the marginal seas, i.e., approximately 6% of the global ocean storage of 148 Pg C.
- Estimates of chlorophyll trends were derived from the SeaWiFS sensor, whose 13-year mission ended in December 2010. A statistically-significant, decadal decrease in chlorophyll concentration at midlatitudes reflects the trend in positive SST anomalies. The cool Southern Ocean shows an increase in concentrations that may be tied to a decrease in mean SST in that region. Historical in situ studies confirm the signs of the trends but suggest a larger rate of change than that derived from SeaWiFS.

b. Sea surface temperatures—Y. Xue, R. W. Reynolds, V. Banzon, T. M. Smith, and N. A. Rayner

The global sea surface temperature (SST) variations in 2010 were characterized by: (1) the transition from El Niño to La Niña during the boreal summer 2010; (2) the development of a negative Pacific Decadal Oscillation (PDO) pattern (Mantua et al. 1997) in the North Pacific during the fall and winter 2010; and (3) the development of a tripole SST anomaly (SSTA) pattern in the North Atlantic. To quantify uncertainties in SSTA, three SST products were used: (1) the Optimal Interpolation SST version 2 (OISST; Reynolds et al. 2002); (2) the Extended Reconstructed SST version 3b (ERSST; Smith et al. 2008); and (3) the UK Met Office Hadley Centre sea ice and SST dataset (HadISST1; Rayner et al. 2003). The OISST is a satellite-based analysis that uses in situ data for bias adjustments of the satellite data for the period since November 1981, when satellite AVHRR became available. The ERSST and HadISST1 analyses are historical analyses beginning in the 19th century, and both analyses use statistics from the more recent period that includes satellite data. The ERSST includes in situ data only, while the HadISST1 includes both in situ measurements and AVHRR retrievals from 1982 onwards.

In this section, SSTA is defined as departure from the 1981–2010 climatology, which was recently constructed to meet the World Meteorological Organization's standard for climatology to reflect the most recent 30-year period (http://www.wmo.int/pages/prog/wcp/wcdmp/documents/WCDMPNo61.pdf). The 1981–2000 climatology, which was utilized in past *State of the Climate* reports, is about 0.2°C higher than the 1971–2000 climatology (Xue et al. 2003) over much of the tropical oceans and North Atlantic (see details in http://www.cpc.ncep.noaa.gov/products/people/yxue/sstclim/Note_SST_Climatology_1981-2010.doc).

The yearly mean SSTA in 2010 was characterized by negative SSTA in the tropical central and tropical eastern Pacific (Fig. 3.1a), reflecting the dominant influence of La Niña (see section 4b). Outside of the tropical Pacific, the 2010 SSTA was characterized by a negative PDO pattern in the North Pacific, a tripole pattern in the North Atlantic, and general warmth in the Indian Ocean, the central-west South Pacific, and the South Atlantic (Fig. 3.1a). The 2010 minus 2009 SST differences show a cooling of about 1°C in the central and eastern tropical Pacific related to the transition from El Niño to La Niña, a moderate cooling in the midlatitude eastern North Pacific, a strengthening of the tripole SSTA in the North Atlantic and a moderate warming near the Maritime Continents, in the midlatitude southern Indian Ocean and central-west South Pacific (Fig. 3.1b).

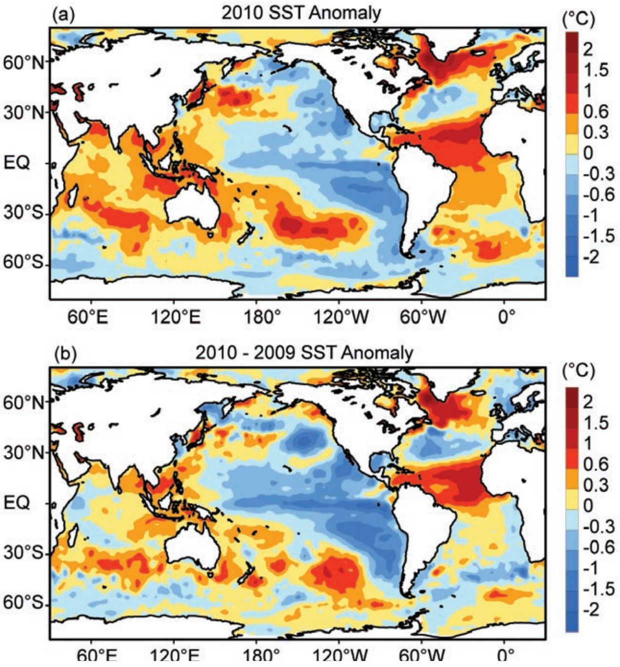

Fig. 3.1. (a) Yearly mean OISST anomaly in 2010, (b) 2010 minus 2009 OISST anomaly.

The evolution of seasonal mean SSTA in 2010 is shown in Fig. 3.2. Positive SSTA dominated in the central tropical Pacific during the winter 2009/10 (December–February) with an amplitude of more than +1.5°C (Fig. 3.2a). By the spring (March–May) 2010, SST had returned to near-normal conditions in the eastern tropical Pacific while SST remained weakly above normal west of 150°W (Fig. 3.2b). Negative SSTA developed and covered the equatorial Pacific east of 170°E during the summer (June–August), indicative of development of La Niña conditions (Fig. 3.2c). At the same time, a negative PDO pattern developed, characterized by positive SSTA (more than +1.0°C) in the midlatitude western and central North Pacific and negative SSTA (less than -1.0°C) extending from the central tropical Pacific to the west coast of North America and Gulf of Alaska (Fig. 3.2c). The negative SSTA near the Gulf of Alaska and along the North America west coast were associated with enhanced upwelling and anomalous anticyclonic winds in the northeast Pacific. During the fall (September–November), negative SSTA strengthened in the central and eastern tropical Pacific, while negative SSTA near the Gulf of Alaska weakened associated with suppressed upwelling.

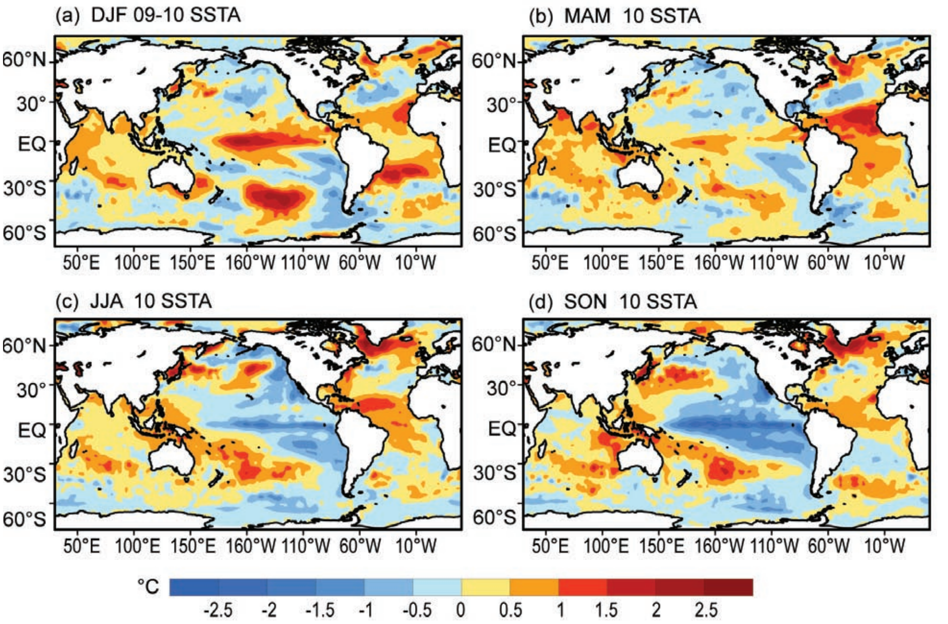

Fig. 3.2. Seasonal mean SSTAs (°C) for (a) December 2009–February 2010, (b) March–May 2010, (c) June–August 2010 and (d) September–November 2010. SSTs are the monthly fields temporally averaged from the weekly 1° OISST.

Positive (negative) SSTA usually appear in ocean basins away from the Pacific approximately three to six months after El Niño (La Niña) peaks in the tropical Pacific (Klein et al. 1999; Enfield and Mayer 1997); due to the remote impacts of the El Niño, positive SSTA strengthened in the tropical Indian Ocean and tropical North Atlantic during the spring 2010 (Fig. 3.2b). In fact, the SST in the tropical North Atlantic reached a historical high during the spring and summer 2010 that has been attributed to combined forcing from the El Niño, the persistent negative phase of the North Atlantic Oscillation (NAO; Fig. 3.3a) and the long-term trend (Hu et al. 2011). Positive SSTA in the tropical Indian Ocean weakened gradually from values higher than +0.5°C during the spring to less than 0°C during the fall 2010 in the western and central tropical Indian Ocean (Figs. 3.2b–d). The cooling is probably associated with the remote impacts of La Niña.

The tripole SSTA in the North Atlantic, characterized by positive (negative) SSTA in the subtropics and high latitudes (midlatitudes), developed during the winter of 2009/10 and spring 2010 (Figs. 3.2a,b), and strengthened during the summer and fall, due to substantial warming in the subpolar region (Figs. 3.2c,d). Figure 3.3 shows the evolution of the zonal average SSTA in the North Atlantic along with the NOAA Climate Prediction Center's NAO index from January 2009 to December 2010. There is a southward propagation of negative (positive) SSTA from high latitudes to midlatitudes (midlatitudes to subtropics) during the latter half of 2009. Those anomalies evolved into a tripole SSTA in which positive (negative) SSTA in the subtropics (midlatitudes) strengthened, and positive SSTA developed in high latitudes (Fig. 3.3b). The warming of the subtropical North Atlantic SST in the early spring can be attributed to the combined forcings from the El Niño and a persistent negative NAO that often warms the

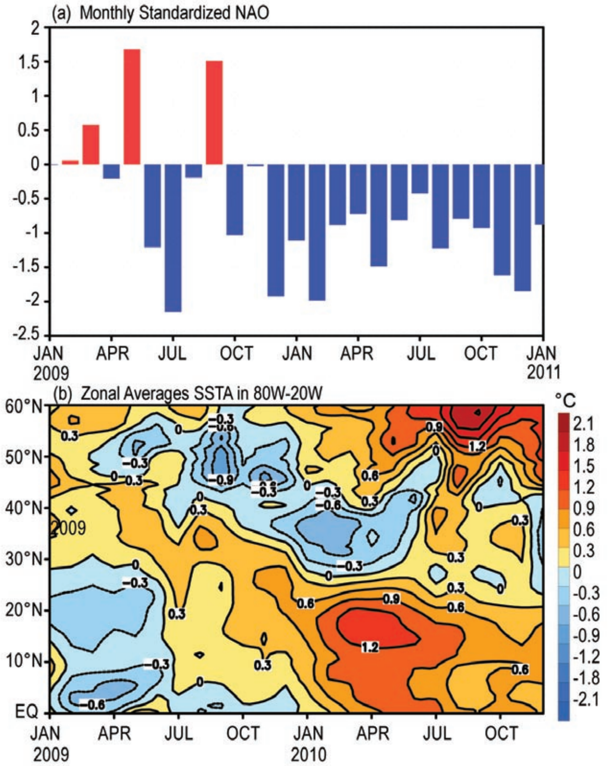

Fig. 3.3. (a) Monthly standardized NAO index from http://www.cpc.ncep.noaa.gov. (b) Time-Latitude section of SST anomalies averaged between 80°W and 20°W. SSTs are the monthly fields temporally averaged from the weekly 1° OISST.

SST in the subtropics and high latitudes, and cools the SST in midlatitudes by modifying evaporative heat loss from the ocean (Deser and Blackmon 1993). Positive SSTA in the subtropics decayed rapidly from +1.2°C in April to -0.6°C in September when El Niño dissipated rapidly during the spring and transitioned into La Niña during the summer. The tripole SSTA persisted from January 2010 through December 2010, and this persistence is largely attributed to the consistently negative NAO during the period from October 2009 to December 2010 (Fig. 3.3a).

The historical perspective of the 2010 SSTA is shown separately for the (a) global ocean, (b) tropical Indian Ocean, (c) tropical Pacific, (d) North Pacific, (e) tropical Atlantic, and (f) North Atlantic using OISST and ERSST in Fig. 3.4. The SSTA time series of OISST and ERSST are very similar during 1982–2010, and the similarity suggests that the SSTA signals discussed below are robust and insensitive to SST analysis techniques. The mean SSTA in the global ocean has a dominant warming trend over which are superimposed interannual variations that are largely associated with El Niño and La Niña events (Fig. 3.4a). For example, the peaks and valleys in the global ocean SSTA often correspond with those in the tropical Pacific SSTA (Fig. 3.4c). However, the correspondence is not present in 2010. The tropical Pacific SSTA cooled by 0.3°C from 2009 to 2010 under the influence of La Niña, while the global ocean SSTA remained largely the same due to a substantial warming in the tropical Atlantic (Fig. 3.4e) and a small warming in the tropical Indian Ocean (Fig. 3.4b). The tropical Indian Ocean SSTA increased by 0.17°C from 2009 to 2010, reaching a historical high in 2010, slightly higher than the value in 1998 (Fig. 3.4b). The tropical Indian Ocean SSTA is dominated by an upward trend with an increase of 0.9°C over the period 1950–2010. The interannual variations in the tropical Indian Ocean SSTA correspond well with those in the tropical Pacific SSTA due to remote influences of ENSO (Klein et al. 1999). In the tropical Atlantic, SSTA increased by 0.33°C from 2009 to 2010 and reached a historical high that is about 0.2°C higher than the previous high in 1998 (Fig. 3.4e). In contrast, there is little upward trend in the North Atlantic and North Pacific SSTA. The North Pacific SSTA trended downward from 1950 to 1987, and then rebounded from -0.5°C in 1987 to +0.31°C in 1990, and has been persistently positive since then (Fig. 3.4d). The North Atlantic SSTA has decreased from 1951 to early 1970s, and then increased and reached a historical high in 2006. It has been trending downward since 2006 (Fig. 3.4f).

There are some uncertainties in the analysis of SSTA; the 2010 SST based on OISST is about 0.4°C higher than that based on HadISST1 in the southeastern tropical Indian Ocean, Bay of Bengal, and Arabian Sea (Fig. 3.5a). The SST differences in the southeastern tropical Indian Ocean also led to uncertainties in the Indian Ocean Dipole Mode Index (DMI), defined as the SSTA differences in the western tropical Indian Ocean and southeastern tropical Indian Ocean (Saji et al. 1999). DMI was about -0.9°C during September–October in OISST but was about -0.2°C in HadISST1 (not shown). The reasons for the large SST uncertainties are suspected to be related to satellite bias adjustments, and will be investigated in the future. In addition, the OISST is generally cooler than the HadISST1 in the North Pacific and high latitude Southern Ocean (Fig. 3.5a). Differences near the western boundary currents and equatorial Pacific upwelling regions might be due to differences in resolution. The OISST and ERSST also have large differences near western boundary currents, equatorial Pacific upwelling regions, and high latitude Southern Ocean, but the two SST products agree well in the

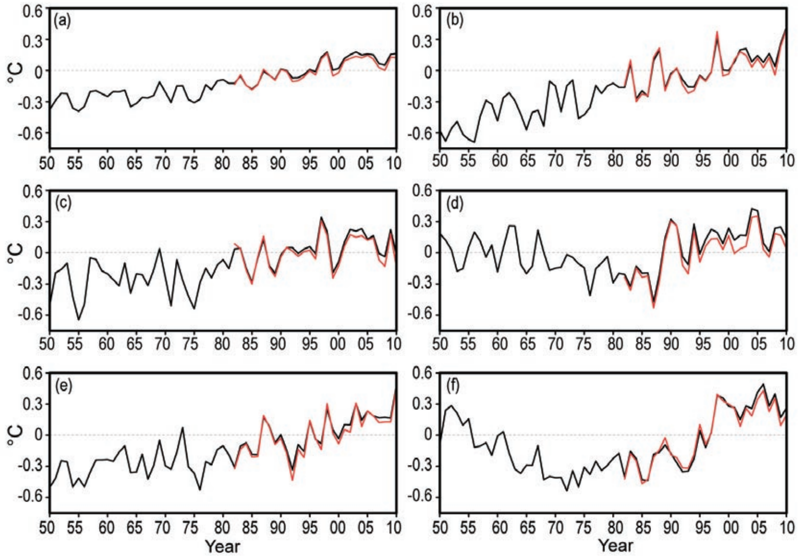

Fig. 3.4. Yearly mean SST anomalies (°C) from ERSST in 1950–2010 (black) and OISST in 1982–2010 (red) averaged in the (a) global ocean, (b) tropical Indian Ocean, (c) tropical Pacific, (d) North Pacific, (e) tropical Atlantic, (f) North Atlantic.

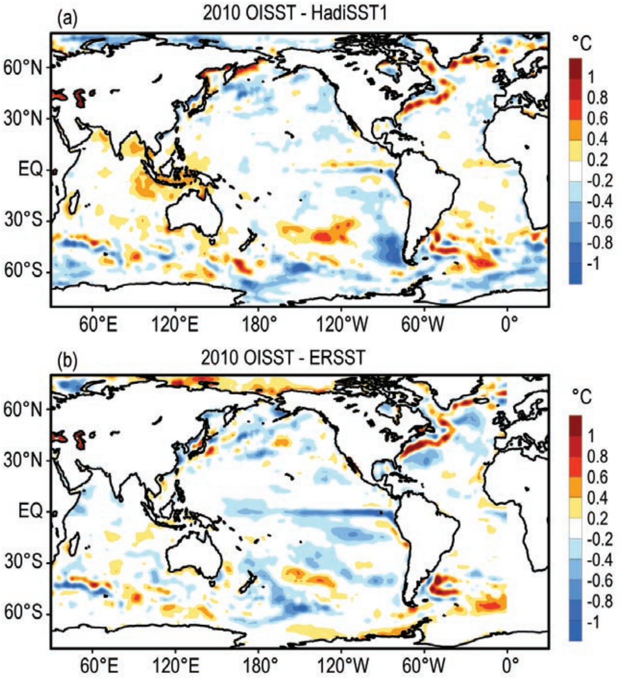

Fig. 3.5. (a) Yearly mean OISST minus HadISST1 in 2010, (b) yearly mean OISST minus ERSST in 2010.

southeastern tropical Indian Ocean and near the Maritime Continents (Fig. 3.5b).

c. Ocean heat content—G. C. Johnson, J. M. Lyman, J. K. Willis, S. Levitus, T. Boyer, J. Antonov, and S. A. Good

Storage and transport of heat in the ocean are central to aspects of climate such as El Niño (Zebiak 1989), the North Atlantic Oscillation (Curry and McCartney 2001), hurricanes (Mainelli et al. 2008), sea-level rise (Domingues et al. 2008), the global energy budget (Trenberth 2009), and constraining global warming scenarios (Knutti and Tomassini 2008).

First an estimate of upper (0 m–700 m) ocean heat content anomaly (OHCA) for the period 1 January–31 December 2010 (Fig. 3.6a) is discussed, computed from a combination of in situ ocean temperature data (Johnson et al. 2009; World Ocean Database 2009, http://www.nodc.noaa.gov/OC5/indprod.html; and Argo, Roemmich et al. 2009) and satellite altimetry data following Willis et al. (2004), but displayed relative to a 1993–2010 baseline, hereafter the combined estimate. Then changes in the combined estimate between 2010 and 2009 (Fig. 3.6b) are described, as well as maps of the linear trend of the combined estimate from 1993 to 2010 and its statistical significance (Fig. 3.7). Three different time series of global integrals of in situ-only estimates of upper OHCA are presented (Fig. 3.8). Finally, the contribution of warming deep and bottom water of Antarctic origin since the 1990s to ocean heat content is assessed. Since OHCA changes are related to depth-integrated ocean temperature changes, increases in OHCA are sometimes referred to below as warming and OHCA decreases as cooling.

In recent years, many of the globally distributed in situ subsurface ocean temperature data are from Argo. Data from Argo floats with possible uncorrected systematic pressure biases (http://www.argo.ucsd.edu/Acpres_drift_apex.html) have been removed from the combined estimate. In addition, annual estimates of expendable-bathythermograph (XBT) fall rate corrections have been applied for deep and shallow probe data using Table 2 of Wijffels et al. (2008), but with no XBT data used after 2005. Details of all the fields analyzed here may change after more Argo real-time data are subject to delayed-mode scientific quality control, as more data are reported, and as XBT corrections improve.

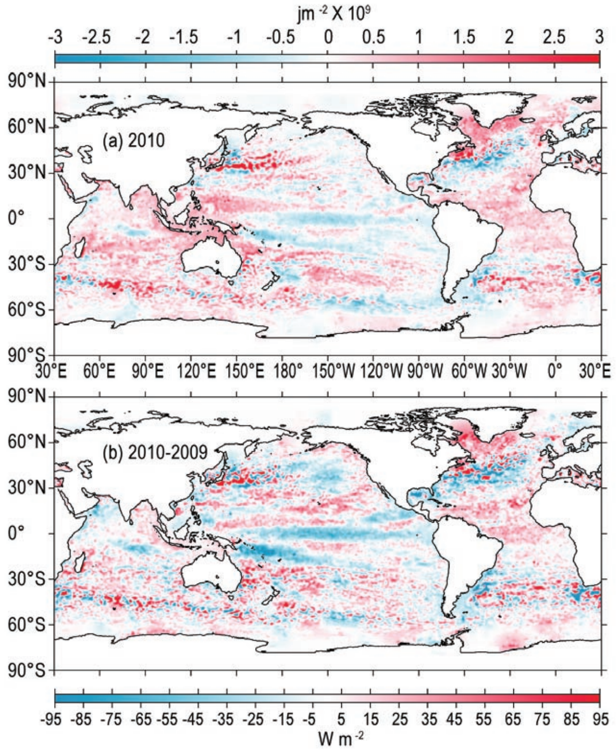

Fig. 3.6. (a) Combined satellite altimeter and in situ ocean temperature data estimate of upper (0 m–700 m) ocean heat content anomaly OHCA (10^9 J m^{-2}) for 2010 analyzed following Willis et al. (2004), but relative to a 1993–2010 baseline. (b) The difference of 2010 and 2009 combined estimates of OHCA expressed as a local surface heat flux equivalent (W m^{-2}). For panel comparisons, note that 95 W m^{-2} applied over one year results in a 3 × 10^9 J m^{-2} change of OHCA.

The combined estimate of OHCA in 2010 (Fig. 3.6a) shows eddy and meander variability down to the 100-km mapping scales, as does, to a greater extent, the difference of the 2010 and 2009 combined estimates (Fig. 3.6b). Strong small-scale spatial variability in OHCA fields is associated with the western boundary currents in every gyre, as well as the Antarctic Circumpolar Current (Fig. 3.6b). The difference in the combined estimates between 2010 and 2009 (Fig. 3.6b) illustrates the large year-to-year variability in regional ocean heat storage, with changes reaching or exceeding the equivalent of a 95 W m^{-2} magnitude surface flux applied over one year ($\sim 3 \times 10^9$ J m^{-2}). Ocean advection likely plays a dominant role in many of these changes.

Upper OHCA and salinity variability, deep OHCA and salinity variability, and mass signals all contribute to local sea level anomalies (Llovel et al. 2009). Despite these confounding factors, there are many large-scale visual similarities between the combined estimate (Fig. 3.6a) and sea level (Fig. 3.26a) fields in 2010. This similarity reflects the large contribution of upper ocean heat content variations to sea level variations.

Large-scale patterns are evident in the combined estimate of OHCA for 2010 (Fig. 3.6a) and its difference from 2009 (Fig. 3.6b). With an El Niño giving way to La Niña early in 2010, the pattern of annual mean OHCA on the Equator in the Pacific mostly reflects La Niña conditions, with a band of anomalously low values around the Equator except in the far west. In addition, a band of the lowest values in the southwest tropical Pacific since 1998 (another post-El Niño year) is found in 2010. The annual averaging period presented here is too long for detailed study of the ocean advection of heat associated with ENSO dynamics (but see Fig. 3.25 and section 4b).

The North Pacific shows a narrow band of high OHCA in the midlatitudes in 2010, perhaps associated with a Kuroshio Extension position northward of the long-term mean (see Fig. 3.21), but little else in the way of strong patterns (Fig. 3.6a). The band of high OHCA in the South Pacific that extends from the eastern Coral Sea in the west to about 50°S in the central and eastern regions (Fig. 3.6a) appears to have migrated south from tropical latitudes since 2006 (see previous *State of the Climate* reports).

Except for a small patch off Somalia and another centered near 10°S, in 2010 the Indian Ocean is mostly higher in OHCA than the baseline period (Fig. 3.6a), with that patch at 10°S and the Arabian Sea cooling between 2009 and 2010 (Fig. 3.6b). The low patch of OHCA at 10°S is associated with anomalously eastward currents to its north and anomalously westward surface currents to its south (Fig. 3.19). A zonal band of high OHCA around the Tropic of Capricorn (southern tropic) is evident in 2010. A high OHCA patch in the region west of Indonesia and extending across the Timor Sea to northern Australia also stands out in 2010.

In the subpolar North Atlantic, the Labrador and Irminger Seas are high in OHCA in 2010 (Fig. 3.6a), and have warmed quite a bit since 2009 (Fig. 3.6b). This change is consonant with strong wintertime convection in this region during early 2008 (Våge et al. 2009) being followed by warming during subsequent years with weaker winter convection. The continued high OHCA values in the eastern subpolar North Atlantic (Fig. 3.6a) suggest that subtropical influences are strong there (e.g., Johnson and Gruber 2007), consistent with anomalously salty surface conditions in that region in 2010 (Fig. 3.12a). In 2010, a band of low OHCA is evident in the region of the Gulf Stream extension, resulting from a large local cooling from 2009 to 2010. This band is consistent with a southward shift of that current (Fig. 3.19), which might be anticipated given the low North Atlantic Oscillation index in the winter of 2010 (Fig. 3.3) and pronounced local anomalies in wind stress curl (Fig. 3.27). This shift is sooner than expected given the two-year lag estimated by Taylor and Stephens (1998), but the index was quite low in winter 2009/10, and stayed low throughout 2010, which might modify the phasing. The tropical Atlantic warmed considerably from 2009 to 2010, with OHCA values higher than the mean in 2010.

A few distinct (Fig. 3.7a) and statistically significant (Fig. 3.7b) regional patterns stand out in the 1993–2010 local linear trends of OHCA. In the Indian Ocean, the warming trend is widespread, and significant. In the Atlantic Ocean, the Labrador, Irminger, and Greenland-Iceland-Norwegian Seas have all trended warmer over the interval, reflecting a robust regional warming trend over the longer time period (Fig. 3.7a) that is reinforced by the warming from 2009 to 2010 (Fig. 3.6b). These changes are probably due to an overall decrease in the North Atlantic Oscillation index from 1993 to 2010. In addition, the eastern portions of the Atlantic trend warmer across both hemispheres. As in the 2010 OHCA map, areas with warming trends appear more widespread than areas of cooling, with the latter being limited in the Atlantic to the Gulf Stream extension.

The statistically significant (Fig. 3.7b) 1993–2010 regional trends in the Pacific Ocean (Fig. 3.7a) are of warming in the western tropical Pacific and extratropical cooling in the east, consistent (via the geostrophic relation) with general strengthening of the interior subtropical-tropical circulation in the past two decades (McPhaden and Zhang 2004). The low 2010 OHCA values in the southwestern tropical Pacific (Fig. 3.6a) tend to oppose the warming trend there, but do not negate its statistical significance over the length of the record (Fig. 3.7b). The statistically significant warming in the central North Pacific and cooling south of Alaska and off the west coast of North America are also consistent with an overall downward trend in the Pacific Decadal Oscillation index from 1993 to 2010, and there is similar-looking pattern in the South Pacific.

The overall 1993–2010 trends in Southern Ocean OHCA are towards warming, consistent with previous analyses (e.g., Boning et al. 2008), but with some local cooling trends evident in the eastern Pacific and western Atlantic sectors (Fig. 3.7a).

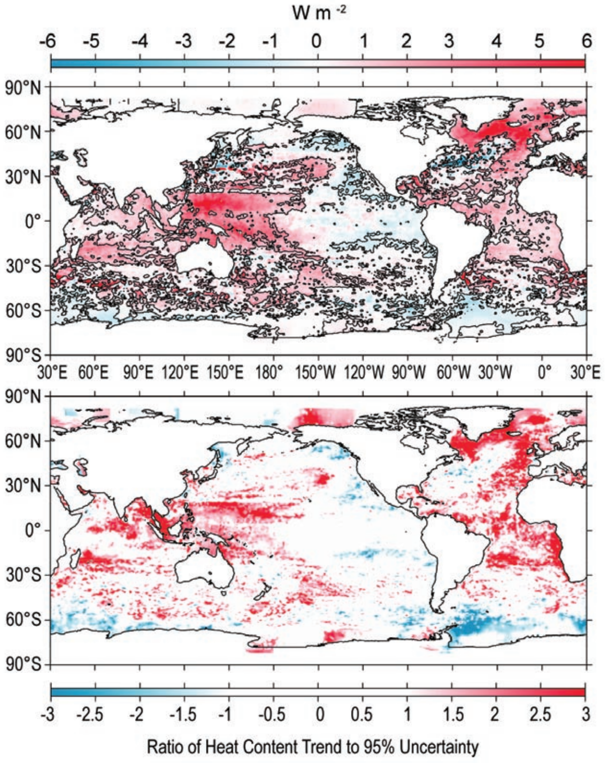

Fig. 3.7. (a) Linear trend from 1993 to 2010 of the combined satellite altimeter and in situ ocean temperature data estimate of upper (0 m–700 m) ocean heat content anomaly OHCA (W m^{-2}) analyzed following Willis et al. (2004). Areas with statistically significant trends are outlined in black. (b) Signed ratio of the linear trend to its 95% uncertainty estimate, with increasing color intensity showing regions with increasingly statistically significant trends.

Three different upper ocean estimates (0 m–700 m) of globally integrated in situ OHCA (Fig. 3.8) reveal a large increase in global integrals of that quantity since 1993. The interannual details of the time series differ for a variety of reasons including differences in climatology, treatment of the seasonal cycle, mapping methods, instrument bias corrections, quality control, and other factors (Lyman et al. 2010). Some of these factors are not taken into account in some of the displayed uncertainties, hence while the error bars shown do not always overlap among the three estimates, they are not necessarily statistically different from each other. Errors are too large to obtain reliable trends over a few years. However, the

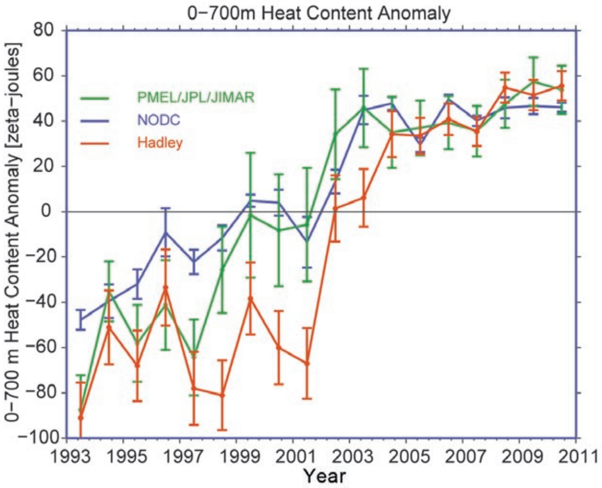

Fig. 3.8. Time series of annual average global integrals of in situ estimates of upper (0 m–700 m) OHCA (10^{21} J, or ZJ) for 1993–2010 with standard errors of the mean. The NODC estimate (http://www.nodc.noaa.gov/OC5/indprod.html) follows Levitus et al. (2009) with uncertainties derived solely from the variance of quarterly estimates of OHCA. The PMEL/JPL/JIMAR estimate is a weighted integral (Lyman and Johnson, 2008) using Argo and WOD 2009 (Johnson et al. 2009) data relative to a 2004–10 climatology with the Wijffels et al. (2008) Table 2 XBT bias adjustments applied and no XBT data after 2005 with error estimate methodology following Lyman et al. (2010). The Hadley estimate applies XBT bias adjustments from Table 1 of Wijffels et al. (2008) to the EN3 dataset (Ingleby and Huddleston 2007; http://www.metoffice.gov.uk/hadobs) also relative to a 2004–10 climatology and is computed from estimates of monthly OHCA following Palmer et al. (2007) and Palmer and Brohan (2010) with error estimate methodology similar to Rayner et al. (2006) but adding uncertainty in the XBT bias correction. For comparison, all estimates have been individually offset (vertically on the plot), first to their individual 2004–10 means (the best sampled time period), and then to their collective 1993–2010 mean (the record length).

three curves all agree on a significant decadal warming of the upper ocean since 1993, accounting for a large portion of the global energy imbalance over this time period (Trenberth 2009).

In addition to the upper (0 m–700 m) ocean warming discussed here, a number of regional studies have shown that deep and bottom waters of Antarctic origin have been warming since the early 1990s, strongest near their source, but with abyssal warming spreading north into the eastern Indian, western Atlantic, and central Pacific Oceans as summarized by Purkey and Johnson (2010). Their global synthesis of these warming changes centered on 1992–2005 estimates a trend in deep OHCA of 48 ± 32 TW (10^{12} W). The upper ocean estimates reported here have linear trends over that time period that range from 224 TW to 326 TW, therefore deep changes add a measurable fraction to the total OHCA.

d. Global ocean heat fluxes—L. Yu, X. Jin, and R. A. Weller

Latent heat (evaporation) and sensible heat fluxes (hereafter their sum is referred to as LHF+SHF) are the primary mechanism by which the oceans release much of the absorbed solar energy back to the atmosphere. These heat transfers from the ocean to the atmosphere are a cooling mechanism for the oceans but a source of heating for the atmosphere. The cooling and heating change the temperature gradients and energize the circulations in the ocean and atmosphere, which in turn affect air-sea temperature and humidity contrasts and modify the magnitudes of the ocean heat fluxes. Because of the key role air-sea heat exchange plays in the coupled atmosphere-ocean interactions and in the global energy balance, changes in global heat flux fields on short- and long-term timescales have important implications for global weather and climate patterns (e.g., Emanuel 1986; Cayan 1992).

Estimates of LHF and SHF over the global oceans are being routinely produced by the Objectively Analyzed air-sea Fluxes (OAFlux) project (http://oaflux.whoi.edu) at the Woods Hole Oceanographic Institution (Yu and Weller 2007). The computation of the OAFlux products uses the state-of-the-art bulk flux algorithm version 3.0 developed from the Coupled Ocean-Atmosphere Response Experiment (COARE; Fairall et al. 2003), with the surface meteorological variables determined from an optimal blending of satellite retrievals of surface-wind and temperatures and surface-meteorology from reanalysis/forecast models. The accuracy of the OAFlux LHF and SHF estimates was evaluated using 126 buoys available over the global oceans (Yu et al. 2008); the averaged root mean square differences between OAFlux and buoy over the buoy locations are 9.6 W m^{-2} for LHF and 2.6 W m^{-2} for SHF.

The annual-mean LHF+SHF in 2010 (Fig. 3.9a) shows that the ocean heat loss is most intense in the vicinity of the warm western boundary currents (WBCs), such as the Kuroshio off Japan, the Gulf Stream off the United States, the Agulhas Current off the African coast, the Falkland/Brazilian Current off South America, and the East Australian Current. Magnitude of the annual mean LHF+SHF in these regions exceeds 200 W m^{-2}, produced largely during the fall-to-winter seasons by strong winds and cold and dry air masses coming from the lands. Away from the WBCs, larger ocean heat loss occurs mostly over the broad subtropical oceans, with a maximum at about 20°S in the southern Indian Ocean. The air-sea heat exchange in these regions is sustained by strong trade winds in the fall/winter. The spatial

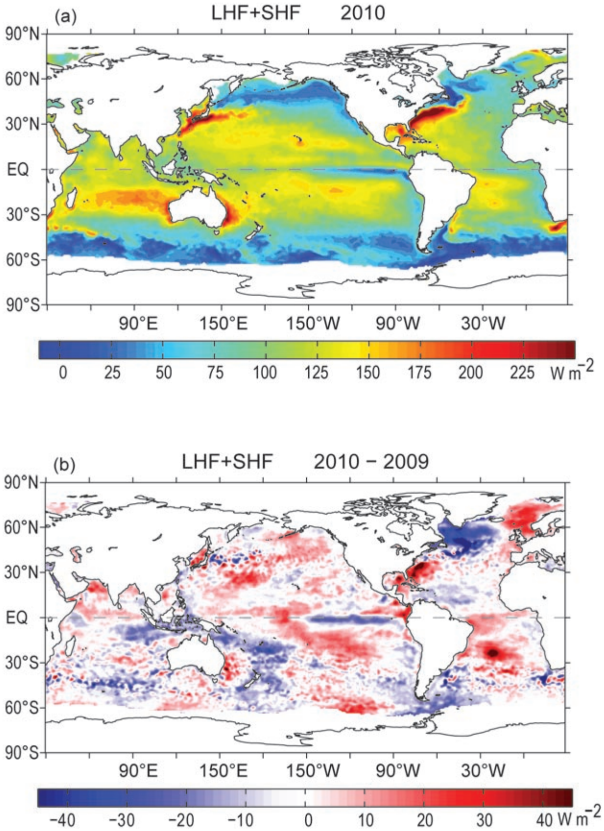

Fig. 3.9. (a) Annual mean latent plus sensible heat fluxes in 2010. The sign is defined as upward (downward) positive (negative). (b) Differences between the 2010 and 2009 annual mean latent plus sensible heat fluxes. Positive (negative) values denote an enhancement (a reduction) of ocean heat fluxes in 2010 compared to 2009.

distribution of the global LHF+SHF mean field suggests a close relationship of LHF+SHF to SST and winds (Cayan 1992).

The 2010-minus-2009 difference plot of LHF+SHF (Fig. 3.9b) shows large-scale variability over the global oceans, in which two organized patterns of change are most striking. One of such large-scale changes is the tripole structure in the North Atlantic, featuring reduced latent and sensible heat loss (negative anomalies) in the subpolar region, enhanced ocean heat loss (positive anomalies) in the middle latitudes centered off Cape Hatteras, and reduced ocean heat loss (negative anomalies) in the subtropics between the Equator and 25°N. The tripole pattern is associated with the atmospheric conditions of a persistent negative phase of NAO, which has lasted since October 2009 (Fig. 3.3a). A negative NAO state has a weak subtropical high and a weak Icelandic low. The reduced pressure gradient causes a southward displacement and weakening of the westerlies across the midlatitudes and meanwhile slackens the trade winds in the tropical oceans (Hurrell 1995; Visbeck et al. 2001). The change in wind is evident in the 2010-minus-2009 difference plot of wind speed, which is shown in Fig. 3.10 with the mean 2010 ocean-surface wind vectors at a 10 m height superimposed. Positive (negative) wind speed anomalies denote strengthening (weakening or reversing) of prevailing winds in 2010 compared with 2009. The global daily wind analysis is developed by the OAFlux project (Yu and Jin 2010) from synergizing passive radiometer wind speed retrievals and radar scatterometer vector wind retrievals. The wind analysis for the post-QuikSCAT (after November 2009) period uses satellite retrievals from the Special Sensor Microwave Imager (SSM/I), the Advanced Microwave Scanning Radiometer for EOS (AMSR-E), and the Advanced Scatterometer (ASCAT) aboard the EUMETSAT METOP satellite.

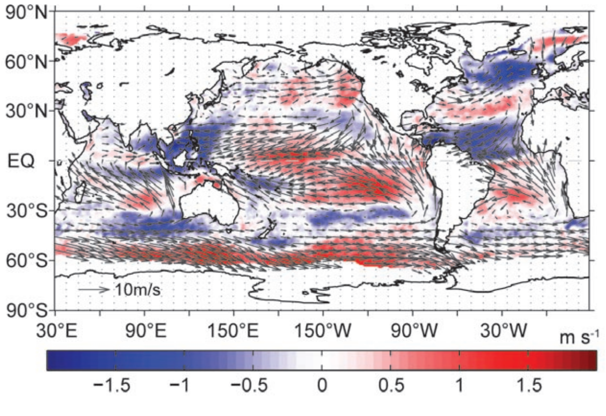

Fig. 3.10. Differences between the 2010 and 2009 wind speed at 10 m (colored background), with the 2010 mean wind vector superimposed (black arrows). Positive (negative) values denote the strengthening (weakening) of the prevailing winds compared to 2009.

The tripole pattern in the North Atlantic LHF+SHF correlates well with the NAO-induced change in the surface wind field. Positive (negative) LHF+SHF anomalies occurred in the regions of stronger (weaker) wind speeds, as wind speed facilitates the heat exchange by evaporation and conduction. Interestingly, wind direction is a more important factor. The intensified heat flux anomaly off Cape Hatteras resulted from the interaction between the warm boundary current and the cold and dry air advected by the strengthened westerlies from inland. Similarly, the large heat flux anomalies in the Norwegian Sea (north of 60°N) were due primarily to the intrusion of the cold Arctic air associated with the strengthening of the prevailing northerly winds. It is known that the basin-scale SST variability on NAO time scales is driven primarily by the atmospheric forcing via the effects of LHF+SHF, mixing, and the wind-driven Ekman currents (Cayan 1992; Deser and Blackmon 1993). It is not a surprise to see that the Atlantic sea surface had a significant warming (cooling) (Fig.3.1b) in regions of reduced (enhanced) LHF+SHF and weakened (strengthened) winds.

The other large-scale organized pattern of change in LHF+SHF is associated with the transition from El Niño to La Niña in the tropical Pacific and the coinciding development of a negative PDO in the North Pacific. Compared to 2009, the sea surface in 2010 was colder in the central and eastern equatorial basin and warmer in the western basin (Fig. 3.1b). It is interesting to observe that the correlation between SST and LHF+SHF in the tropical Pacific is not as linear as that in the North Atlantic, because LHF+SHF has reduced not only over the cooler sea surface in the east but also over the warmer sea surface in the west. That LHF+SHF decreased over the colder tongue can be explained by thermodynamic considerations. The SST in the region is controlled by ocean dynamics through wind-driven upwelling of cold water from the thermocline (Wyrtki 1981). The cold tongue became colder as the trade winds became stronger during La Niña (Fig. 3.10), which reduced the evaporation and led to a positive correlation between SST and LHF+SHF. This suggests that LHF+SHF responded to the SST anomalies in the cold tongue and acted as damping to suppress the growth of these ENSO anomalies.

On the other hand, the decrease of LHF+SHF over the warmer warm pool in the western Pacific and southeastern Indian Oceans is governed not by SST, but by atmospheric dynamics as manifested by changes in wind speed (Zhang and McPhaden 1995). Deep convection in the Indo-Pacific warm pool intensifies during La Niña (Plate 2.1g), leading to enhanced low-level convergence. By mass continuity, the center of convergence is the area of low wind speed. In 2010 both the easterlies in the central Pacific and the westerlies in the central Indian Ocean strengthened near the equatorial latitudes, while the wind speed was considerably weaker in the center of the convection over the warm pool (Fig. 3.10). It is this low wind speed that appears to have limited LHF+SHF over the warm pool. The weak LHF+SHF in turn released less heat to the atmosphere, and the weaker wind induced less mixing. Both effects caused the sea surface warming that is observed in the Indo-Pacific warm pool region (Fig.3.1b). Overall, the change in 2010 LHF+SHF in the tropical Pacific reflects more the wind speed anomalies than the SST anomalies.

The annual mean time series of the globally averaged LHF+SHF from 1958 to 2010 (Fig. 3.11) indicates that the 2010 LHF+SHF was slightly up from the 2009 mean. Nevertheless, the downward trend that started around 2000 still prevails. The 53-year time series from 1958 to 2010 displays an oscillatory nature, with a low of 99 W m^{-2} in 1977 and a high of 109 W m^{-2} in 1999. The decadal cycle is driven primarily by LHF, with minor contribution from SHF.

e. *Sea surface salinity*—G. C. Johnson and J. M. Lyman

Ocean storage and transport of freshwater are intrinsic to aspects of global climate, including the water cycle (e.g., Schanze et al. 2010), El Niño (e.g., Maes et al. 2006), and anthropogenic climate change (e.g., Held and Soden 2006). Only since 2004 has the advent of Argo allowed an annual assessment of global upper ocean salinity and its complement, freshwater. (The Argo array of profiling floats measures temperature and salinity year round in the upper 2 km of the ice-free global ocean, nominally at 10 day intervals and 3°× 3° spacing; Roemmich et al. 2009).

The near-global Argo data are used to determine an annual average sea surface salinity (SSS) anomaly for 2010 relative to a climatology and to describe how annual SSS anomalies have changed in 2010 relative to 2009, as well as to assess 2004–10 SSS trends and their statistical significance. The data, downloaded from an Argo Global Data Assembly Center in January 2011, are a mix of real-time (preliminary) and delayed mode (scientific quality controlled). The estimates of SSS presented could change after all the data have been subjected to careful scientific quality control and as other data sources are integrated into the estimates. [Remote sensing of SSS began in late 2009 with one satellite (http://www.esa.int/esaLP/LPsmos.html), with a second satellite anticipated to be launched in 2011 (http://aquarius.gsfc.nasa.gov/).]

The shallowest Argo salinity values flagged as good (excluding any with pressure > 25 dbar) are used in this analysis. They are generally at 9-dbar pressure, with some as shallow as 4 dbar. These values are subject to a statistical check to discard extreme outliers. Extreme outliers are defined as points within a 3° radius of a data point with temperature or salinity values three times the interquartile range above the third or below the first quartiles. After this check, the remaining data are cast as differences from a climatological mean surface salinity field from the World Ocean Atlas based on historical data reported through 2001 to contrast the Argo period with the earlier record (WOA 2001; Boyer et al. 2002). The resulting anomalies are objectively mapped (Bretherton et al. 1976) for each year using a covariance function combining a 6° (latitude and longitude) length-scale Gaussian with a 9° length-scale exponential and a noise-to-signal variance ratio of 2.2.

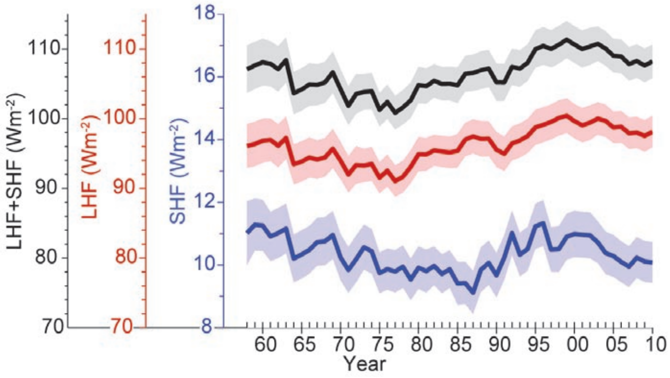

Fig. 3.11. Year-to-year variations of global averaged annual mean latent plus sensible heat flux (black curve), latent heat flux (red curve), and sensible heat flux (blue curve). The shaded areas indicate the error bars of the flux estimates at the 95% confidence level.

Climatological SSS patterns are correlated with surface freshwater flux: the sum of evaporation, precipitation, and river runoff (e.g., Béranger et al. 1999) where advection processes are not dominant. In each ocean basin in both the Northern and Southern Hemispheres, subtropical salinity maxima centered between roughly 20° and 25° in latitude are signatures of the predominance of evaporation over precipitation. Conversely, in most regions where climatological surface salinities are relatively fresh, such as the high latitudes and the Inter Tropical Convergence Zones (ITCZs), precipitation generally dominates over evaporation.

The 2010 SSS anomalies from WOA 2001 (Fig. 3.12a) reveal some large-scale patterns that also hold in 2004 through 2009. The regions around the subtropical salinity maxima are mostly salty with respect to WOA 2001. Most of the high-latitude climatologically fresh regions appear fresher than WOA 2001, including most of the Antarctic circumpolar current near 50°S and the subpolar gyre of the North Pacific. These patterns are consistent with an increase in the hydrological cycle (that is, more evaporation in drier locations and more precipitation in rainy areas), as seen in simulations of global warming. These simulations suggest this signal might be discernible over the last two decades of the 20th century (Held and Soden 2006), consistent with the multiyear nature of these anomalies. While anomalous ocean advection could influence the SSS pattern over decadal time scales, changes observed at the local extrema are presumably relatively insensitive to such effects. The analysis presented here for SSS anomalies is supported by others: difference of maps of 2003–07 Argo data and historical 1960–89 ocean data prepared in the same fashion show a similar pattern (Hosoda et al. 2009), as do estimates of linear trends from 1950 to 2008 (Durack and Wijffels 2010; see Sidebar 3.1 for further discussion, including interior ocean trends).

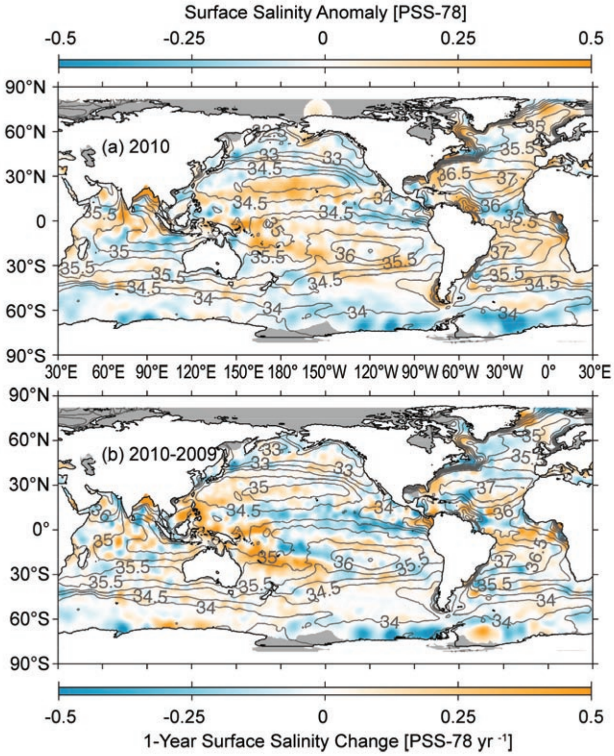

Fig. 3.12. (a) Map of the 2010 annual surface salinity anomaly estimated from Argo data [colors in 1978 Practical Salinity Scale (PSS-78)] with respect to a climatological salinity field from WOA 2001 (gray contours at 0.5 PSS-78 intervals). (b) The difference of 2010 and 2009 surface salinity maps estimated from Argo data [colors in PSS-78 yr^{-1} to allow direct comparison with (a)]. Gray areas are too data-poor to map. While salinity is often reported in practical salinity units (PSU), it is actually a dimensionless quantity reported on the PSS-78.

In contrast to the other high latitude areas, the subpolar North Atlantic and Nordic seas in 2010 are mostly anomalously salty (except east of Greenland) with respect to WOA 2001 (Fig. 3.12a), as they have been since at least 2004 (see previous *State of the Climate* reports). On the basin scale the North Atlantic loses some freshwater to the atmosphere whereas the North Pacific gains some (Schanze et al. 2010), thus the changes here may again be consistent with an increased hydrological cycle. In addition, the salty anomaly in this region is consistent with a stronger influence of subtropical gyre waters in the northeastern North Atlantic in recent years coupled with a reduced extent of the subpolar gyre (Häkkinen et al. 2011).

Sea surface salinity changes from 2009 to 2010 (Fig. 3.12b) strongly reflect 2010 anomalies in precipitation (Plate 2.1g), as well as year-to-year changes in evaporation, with the latter being closely related to latent plus sensible heat flux anomalies (Fig. 3.9b). Advection by anomalous ocean currents (Fig. 3.19) also plays a strong role in year-to-year variability of sea surface salinity. For instance, the western equatorial Pacific became considerably saltier from 2009 to 2010 while the central-eastern equatorial Pacific became fresher (Fig. 3.12b). This shift is likely partially owing to advection of salty water from the east by the anomalously westward surface currents on the Equator during that time, but an eastward shift in convection and precipitation in the equatorial Pacific during the strong El Niño in boreal winter 2009/10 also plays a large role. This pattern appears only partly compensated by the onset of La Niña later in 2010. The portion of the southwestern tropical region that became saltier in 2010 relative to 2009 may also have changed partly owing to anomalous westward surface currents. The eastern Pacific and Atlantic ITCZs also became fresher during this time period, at least partly owing to anomalously strong precipitation in these regions during 2010. Anomalous vertical advection may also play a role in these changes, but is not analyzed here. There are strong correspondences between the surface salinity changes from 2009 to 2010 and subsurface changes over the same period (Figs. 3.14–3.16), with some of the surface changes apparently penetrating deep into the water column, suggesting influences of shifting ocean currents and fronts.

Trends from 2004 through 2010 are estimated by local linear fits to annual average SSS maps (Fig. 3.13a). The ratio of these trends to their 95% significance are also assessed (Fig. 3.13b). The starting year is 2004 because Argo coverage became near global then. The most striking trend patterns are in the Pacific. Saltier surface values in the western and central tropical Pacific extend into the eastern Pacific subtropics in both hemispheres. A strong freshening also occurs in the western subtropics of each hemisphere in the Pacific and the far western tropical Pacific, extending into the Indian Ocean northwest of Australia. Large-scale freshening is also evident in the tropical Southeast Pacific. These recent trends differ from the 50-year trends discussed in the salinity sidebar of this chapter. These differences are not surprising given the very different time periods over which the trends are computed.

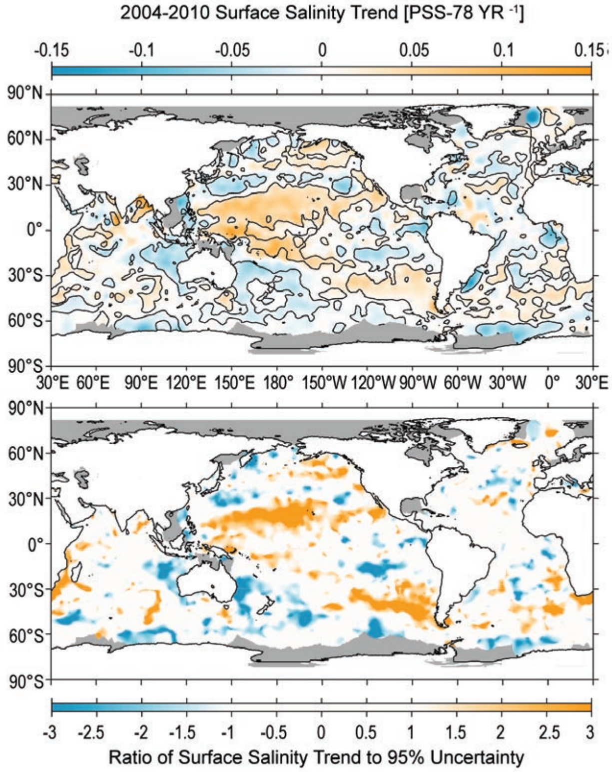

Fig. 3.13. (a) Map of local linear trends estimated from annual surface salinity anomalies for the years 2004 through 2010 estimated from Argo data (colors in PSS-78 yr^{-1}). (b) Signed ratio of the linear trend to its 95% uncertainty estimate, with increasing color intensity showing regions with increasingly statistically significant trends. Gray areas are too data-poor to map.

f. Subsurface salinity—S. Levitus, J. Antonov, T. Boyer, J. Reagan, and C. Schmid

Levitus (1989a, 1989b, 1989c), Antonov et al. (2002), Boyer et al. (2005), and Durack and Wijffels (2010) documented basin-scale changes of salinity for all or part of the world ocean on interpentadal or interdecadal time scales. Salinity changes reflect changes in the Earth's hydrological cycle and also contribute to change in sea level and ocean currents (Levitus 1990; Greatbatch et al. 1991; Sidebar 3.1).

The World Ocean Database 2009 (Boyer et al. 2009) updated through December 2010 has been used as the source of subsurface salinity data used in the analyses of 2009 and 2010 and climatological salinity conditions presented here. For 2009–10 it is primarily data from Argo profiling floats (approximately 109 000 profiles) that extend as deep as 2000 m and provide near-global coverage for the region within 60° of the Equator. Data from the TAO/TRITON, PIRATA, and RAMA arrays of tropical moored buoys provide important data in the upper 500 m of the water column. Approximately 13 000 ship-based conductivity/temperature/depth casts and 52 635 glider casts (these were highly localized in space) were also used. Final quality control has not been performed on some of the most recent observations used here, but it is not believed that additional quality control will substantially affect the results presented here. All data are available at http://www.nodc.noaa.gov.

The analysis procedure is as follows. First, monthly global analyses of salinity anomalies at standard depth levels from the sea surface to 2000 m depth are computed for years 2009 and 2010. For initial fields in the objective analyses the monthly salinity climatologies from the World Ocean Atlas 2009 (WOA09; Antonov et al. 2010) are used. Then observed data averaged on a 1° square grid at each standard depth are subtracted from the appropriate 1° climatological monthly mean. The next step is to objectively analyze (Antonov et al. 2010) these anomaly fields to generate a monthly anomaly field with an anomaly value defined at each grid point. The monthly anomaly fields are time averaged at each depth and gridpoint to define an annual mean anomaly field for each standard depth level. This is done for 2009 and 2010.

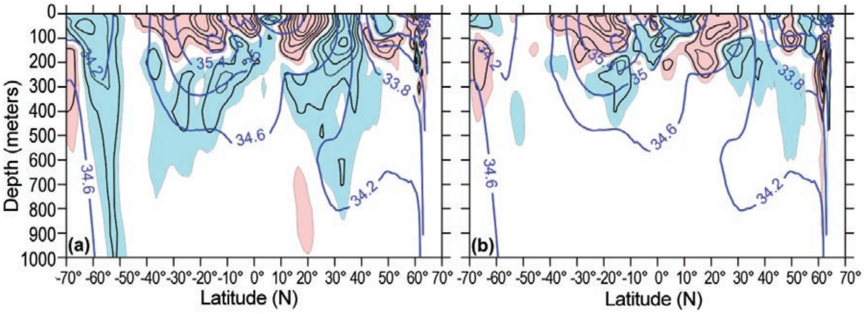

Fig 3.14. (a) Zonal mean 2010 salinity anomaly vs. latitude and depth for the Pacific Ocean. (b) Salinity anomaly 2010 minus 2009 vs. latitude and depth for the Pacific Ocean. For both plots blue shading is for areas of negative (fresh) anomaly < -0.01. Red shading is for areas of positive (salty) anomaly > 0.01. Contour interval shown for anomalies is 0.02. In the background (thick blue contours) is the zonally averaged climatological mean salinity. Contour intervals for the background are 0.4. All values are on the Practical Salinity Scale. WOA09 was used as the reference climatology for anomalies and for background means.

Subsurface changes in salinity for the three major basins of the world ocean are documented in two ways. The first is to zonally average the WOA09 climatology and the 2010 annual mean field for each basin and plot these difference fields as a function of depth and latitude for the upper 1000 m of each basin as in Figs. 3.14a, 3.15a, and 3.16a. Examining these figures allows documentation of the difference in salinity conditions between 2010 and the "long-term" mean as best as can be determined with the historical data available used to construct WOA09. We only document variability in the upper 1000 m where signals are the largest and the figures can clearly document the changes that have occurred. This does not imply that changes deeper than 1000 m have not occurred, especially for the Atlantic. The second way is to document changes between these two years by zonally averaging the 2009 annual mean field by basins and plotting the 2010 minus the 2009 fields. It should be noted that it is only the advent of the Argo profiling float observing system that allows such a computation.

Figure 3.14a shows the 2010 minus climatology changes in salinity for the Pacific Ocean. There is a strong region of freshening (negative values) located in the 50°S–70°S region extending to 1000 m depth. In the 0°–45°S region there is a region of strong salinification (positive values) in the upper 200 m. This overlies a region of freshening that extends to about 700 m depth. In the 10°N–28°N region salinity has increased in the upper 125 m indicating an increase in the salinity of subtropical mode water (SMW; Yasuda and Hanawa 1997), an increase in the amount of SMW formed or both. In the 30°N–40°N region freshening occurred with the freshening extending as far south as 10°N at subsurface depths.

Figure 3.14b shows the 2010 minus 2009 changes in salinity for the Pacific Ocean. Most changes in subsurface salinity occur in the upper 400 m of this basin. At the sea surface, the 15°N–32°N region has become more saline with the positive anomaly extending south to about 10°N with increasing depth. This suggests changes in the properties of, or the amount of, SMW formed. A similar feature appears in the South Pacific centered around 20°S but with the more saline near-surface waters extending both further south and north. The subsurface high saline tongue extends northward to about 10°S. A surface freshening has occurred centered near 12°N that extends southward with increasing depth. This surface freshening may represent changes in rainfall in the Intertropical Convergence Zone (ITCZ). A relative maximum in freshening occurs centered at about 2°N at 125 m depth. This may not be directly related to changes in the ITCZ but could be linked to changes in upwelling or downwelling near the Equator which could be further linked to changes in the equatorial and tropical wind fields. Another region of subsurface freshening is centered near 12°S at 225 m depth. This might be related to changes in the tropical wind field.

Figure 3.15a shows the 2010 minus climatology changes in salinity for the Indian Ocean. Similar to the Pacific a region of freshening located in the 50°S–70°S region that extends to 1000 m depth. Immediately to the north of this feature a region (30°S–45°S) of salinification has occurred. Another region of salinification has occurred extending northward and downward from 30°S. Freshening has occurred in the 10°S–20°S region and salinification has occurred in the 10°S–12°N region.

Figure 3.15b shows the 2010 minus 2009 changes in salinity for the Indian Ocean. As in the Pacific, most changes in subsurface salinity occur in the upper 400 m of this basin. A notable exception occurs at 50°S. At 16°N and a depth of 50 m a relatively strong freshening occurred that extends to about 400 m depth. A possible explanation for this strong freshening at the

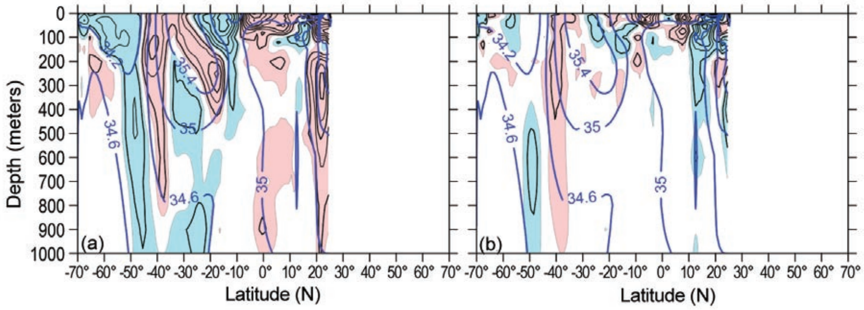

Fig 3.15. (a) Zonal mean 2010 salinity anomaly vs. latitude and depth for the Indian Ocean. (b) Salinity anomaly 2010 minus 2009 vs. latitude and depth for the Indian Ocean. For both plots blue shading is for areas of negative (fresh) anomaly < -0.01. Red shading is for areas of positive (salty) anomaly > 0.01. Contour interval shown for anomalies is 0.02. In the background (thick blue contours) is the zonally averaged climatological mean salinity. Contour intervals for the background are 0.4. All values are on the Practical Salinity Scale. WOA09 was used as the reference climatology for anomalies and for background means.

surface and deeper depths could be the ENSO impact on the Asian summer monsoon. In 2009 a strong El Niño occurred, whereas in 2010 conditions changed to a moderate-to-strong La Niña. It has been shown by Lim and Kim (2007) that during warm ENSO events (e.g., 2009), the Walker circulation in the tropical Pacific is displaced eastward resulting in higher sea level pressure in the western tropical Pacific and consequently results in subsidence over the western tropical Pacific and Indian Ocean. This pattern in turn, inhibits the ability for the monsoon to strengthen and thus less rainfall than normal falls (e.g., less freshening). Cold ENSO (e.g., 2010) events produce the reverse, with more lift in the Indian Ocean and western tropical Pacific resulting in stronger monsoons and more rainfall (e.g., more freshening). It should be noted that based on the work done by Kumar et al. (1999), this simple inverse relationship between ENSO and the Asian summer monsoon has weakened over the past two of decades. At 8°N a relatively strong increase in salinity has occurred extending to about 125 m with a similar increase in the 2°S–12°S region within the top 50 m of the water column. Another region of freshening is centered at 15°S and 100 m depth.

Figure 3.16a shows the 2010 minus climatology changes in salinity for the Atlantic Ocean. Similar to the Pacific and Indian oceans, a region of freshening occurs at high latitudes of the southern hemisphere extending to relatively deep depths (900 m). Immediately to the north is a region of salinification that is greater in magnitude than the corresponding region in the Indian Ocean. Unlike the North Pacific, the North Atlantic is characterized by an increase in salinity extending to several hundred meters depth. One exception is a very shallow region of freshening in the 0°–10°N region.

Figure 3.16b shows the 2010 minus 2009 changes in salinity for the Atlantic Ocean. Unlike the other two basins, changes in salinity have occurred to depths of 1000 m even on this one year time scale. This may be due in part to deep convection and the shifting position of large-scale fronts that have large vertical extension. Levitus (1989c) documented statistically significant large-scale changes at 1750 m depth for this basin on time scales of 20 years. Yashayaev and Loder (2009) discuss the variability of production of convectively formed Labrador Sea water. In the 60°N–70°N region, salinification has occurred that is strongest at the sea surface but extends vertically to 500 m depth. In the 50°N–60°N region,

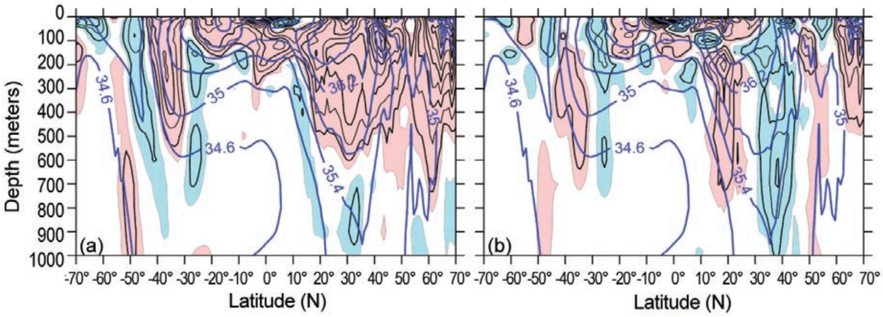

Fig 3.16. (a) Zonal mean 2010 salinity anomaly vs. latitude and depth for the Atlantic Ocean. (b) Salinity anomaly 2010 minus 2009 vs. latitude and depth for the Atlantic Ocean. For both plots blue shading is for areas of negative (fresh) anomaly < -0.01. Red shading is for areas of positive (salty) anomaly > 0.01. Contour interval shown for anomalies is 0.02. In the background (thick blue contours) is the zonally averaged climatological mean salinity. Contour intervals for the background are 0.4. All values are on the Practical Salinity Scale. WOA09 was used as the reference climatology for anomalies and for background means.

SIDEBAR 3.1: OCEAN SALINITY: A WATER CYCLE DIAGNOSTIC?—

P. J. DURACK, S. E. WIJFFELS, AND N. L. BINDOFF

Present-day civilizations thrive in a wide range of temperatures at different latitudes across the Earth, but cannot cope without available freshwater. Changes to global water distribution are anticipated in the 21st century as anthropogenic climate change signatures become more apparent from natural variability of the climate system; future projections of surface moisture fluxes suggest that regions dominated by evaporation (over rainfall over the course of a year), will become drier, while regions dominated by rainfall (over evaporation) will become wetter (Allen and Ingram 2002; Held and Soden 2006; Meehl et al. 2007; Wentz et al. 2007; Seager et al. 2010). In water-stressed areas the human population and surrounding ecosystems are particularly vulnerable to decreasing or more variable rainfall due to climate change. Therefore, understanding probable future changes to the global water cycle are vital, as the projections of future climate show considerable changes to the water cycle are likely to significantly impact much of the world's population.

The global oceans cover 71% of the global surface, experience 75%–90% of global surface water fluxes, and contain 97% of the global freshwater volume (Schmitt 1995). As the ocean and land surface warms, so will the lower troposphere, and the amount of water vapor it can carry increases; this simple effect is anticipated to drive a stronger water cycle, with arid regions becoming drier and wet regions wetter (Held and Soden 2006). As the oceans are the engine room of the global water cycle, ocean salinity changes can be used to provide an estimate of broad-scale global water cycle changes and their regional patterns. Here, we review some of the major progress in understanding observed global water cycle changes in the ocean since the publication of the IPCC Fourth Assessment Report (AR4; Bindoff et al. 2007).

Global surface salinity is strongly correlated with the spatial patterns of E-P [evaporation (E) minus precipitation (P)] in the climatological mean. This relationship—where regions of low salinity correspond with regions of low (or negative) E-P and regions of high salinity with high E-P—provide some confidence in using salinity as a marker of global water cycle changes. Over long-timescales, the ocean integrates and smoothes high frequency and spatially patchy E-P fluxes at the ocean surface and provides a smoothed salinity anomaly field that facilitates detection of large-scale changes.

Patterns of long-term changes to surface salinity are now available, based on both trend fits directly to ocean data (e.g., Freeland et al. 1997; Curry et al. 2003; Boyer et al. 2005; Gordon and Giulivi 2008; Durack and Wijffels 2010) and comparisons of Argo era (2003–present) modern- to historical-ocean climatologies (e.g., Johnson and Lyman 2007; Hosoda et al. 2009; Roemmich and Gilson 2009; von Schuckmann et al. 2009; Helm et al. 2010). The patterns of multidecadal salinity change from these analyses show remarkable similarities between the mean E-P field and mean salinity field (Fig. 3.17). Rainfall-dominated regions such as the western Pacific warm pool, for example, have undergone a long-term freshening, and arid regions in the subtropical, evaporation-dominated 'desert latitudes' have generally increased in salinity (e.g., Fig. 3.17b).

Observed surface salinity changes suggest that changes in the global water cycle have occurred. The mean surface salinity climatology and the pattern of multidecadal (50-year) linear surface salinity changes (Durack and Wijffels 2010) have a spatial correlation of 0.7 (Fig. 3.18). Using this spatial relationship the amount of salinity pattern amplification can be obtained, with these data implying an amplification of the mean ocean surface salinity pattern of 8.0% has occurred between 1950 and 2000 (Fig. 3.18). In order to enhance the signal-to-noise for pattern

Continues on next page

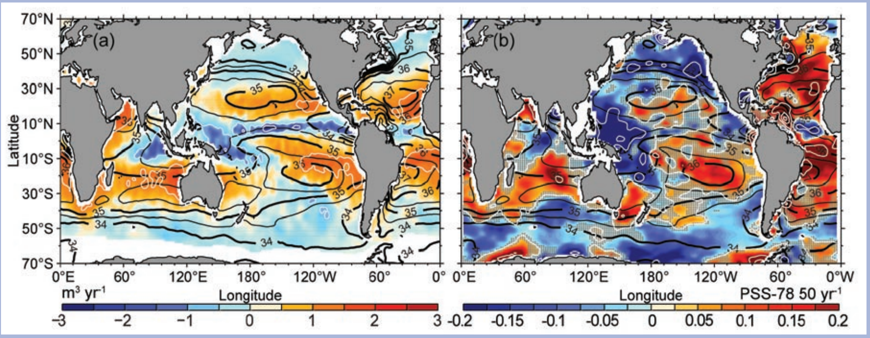

Fig. 3.17. (a) Ocean-atmosphere freshwater flux (E-P; m^3 yr^{-1}) averaged over 1980–93 (Josey et al. 1998). Contours every 1 m^3 yr^{-1} in white. (b) The 50-year linear surface salinity trend (PSS-78 50 yr^{-1}). Contours every 0.25 (PSS-78) are plotted in white. On both panels, the 1975 surface mean salinity is contoured black [contour interval 0.5 (PSS-78) for thin lines, 1 for thick lines]. Due to limited observational E-P coverage a direct 1950–2000 climatology is not currently available, however the field produced by Josey et al. 1998 closely matches climatological means developed from many varied products over differing time periods (e.g. da Silva et al. 1994; Schanze et al. 2010) and provide a very similar spatial E-P pattern of correspondence with surface climatological mean salinity. Reproduced from Durack and Wijffels (2010).

cont. SIDEBAR 3.1: OCEAN SALINITY: A WATER CYCLE DIAGNOSTIC?—
P. J. DURACK, S. E. WIJFFELS, AND N. L. BINDOFF

amplification a spatial smoothing technique is applied to the global data; this develops basin-bound zonal means for both climatological mean salinity anomalies (compared with the global surface climatological mean salinity) and their associated 50-year salinity trends, and are termed basin-zonally-averaged means and anomalies, respectively. This robust global tendency towards an enhanced surface salinity pattern provides broad-scale agreement with the regional studies of Cravatte et al. (2009) and Curry et al. (2003), and numerous global analyses of surface salinity change (e.g., Boyer et al. 2005; Hosoda et al. 2009; Roemmich and Gilson 2009). These ocean surface salinity changes demonstrate that wet regions get fresher and dry regions saltier, following the expected response of an amplified water cycle.

Patterns of long-term subsurface salinity changes on pressure surfaces also largely follow an enhancement of the existing mean pattern. The interbasin contrast between the Atlantic (salty) and Pacific (fresh) intensifies over the observed record (e.g., Boyer et al. 2005; Johnson and Lyman 2007; Gordon and Giulivi 2008; Hosoda et al. 2009; Roemmich and Gilson 2009; von Schuckmann et al. 2009; Durack and Wijffels 2010). These deep-reaching salinity changes suggest that past water cycle changes have propagated into the ocean interior, with a clear enhancement to the high-salinity subtropical waters, and freshening of the high-latitude waters. A particularly strong and coherent freshening expressed in the Antarctic intermediate water subduction pathway centered around 50°S has also been detected (Johnson and Orsi 1997; Wong et al. 1999; Bindoff and McDougall 2000; Antonov et al. 2002; Curry et al. 2003;

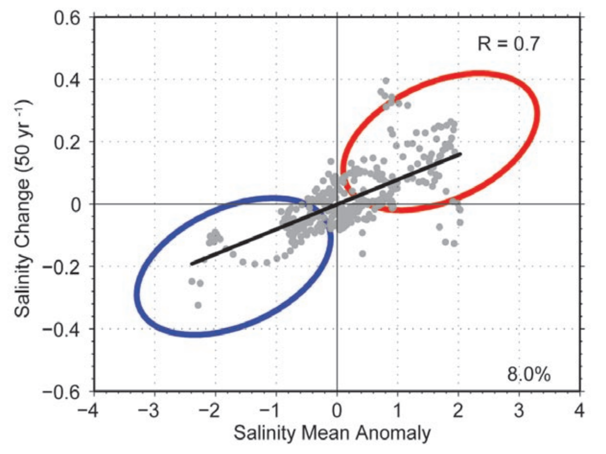

FIG. 3.18. Observed surface salinity changes versus mean salinity anomalies—fresh gets fresher and salty waters saltier. The x-axis is the basin zonally-averaged anomaly from the mean surface salinity (34.8 PSS-78), and the y-axis is the associated basin zonally-averaged multidecadal linear salinity change trend (PSS-78 50 yr^{-1}). The blue and red ellipses are representative of regions where fresh (compared to the global surface mean salinity) are getting fresher and salty getting saltier, respectively. Using the full global surface salinity analysis (Durack and Wijffels 2010), and basin-zonal mean averaging to enhance the signal-to-noise, yields a mean salinity climatology pattern amplification of 8%.

freshening has occurred in the upper 100 m. A region of salinification occurs centered at 48°N. Freshening occurs in the 30°N–45°N belt extending to 1000 m depth. Salinification occurs in the upper 50 m of the 10°N–30°N belt. At 12°N, freshening occurs centered about a depth of 100 m. A belt of salinification occurs centered at 20°N between 150 m and 800 m depth. In the 0°–10°S, belt there is a region of relatively large salinification limited to approximately the upper 50 m. In the 10°S–20°S region, there is salinification suggesting an increase in SMW production or an increase in its salinity. In the region 25°S–30°S, freshening has occurred. Centered at 40°S, salinification has occurred in the 125 m–700 m layer.

g. Surface currents—R. Lumpkin, K. Dohan, and G. Goni

Near-surface currents are measured in situ by drogued satellite-tracked drifting buoys and by current meters on moored Autonomous Temperature Line Acquisition System (ATLAS) buoys.[1] During 2010, the drifter array ranged in size from a minimum of 887 drogued buoys to a maximum of 1184, with a median size of 1129 drogued buoys (undrogued drifters continue to measure SST, but are subject to significant wind slippage; Niiler et al. 1987). The moored array included 37 buoys with current meters, all between 12°S and 21°N. These tropical moorings compose the TAO/TRITON (Pacific; 16 buoys with current meters), PIRATA (Atlantic; 6 buoys) and RAMA (Indian; 15 buoys) arrays.

---

[1] Drifter data is distributed by NOAA/AOML at http://www.aoml.noaa.gov/phod/dac/gdp.html. Moored data is distributed by NOAA/PMEL at http://www.pmel.noaa.gov/tao. OSCAR gridded currents are available at http://www.oscar.noaa.gov/ and http://podaac.jpl.nasa.gov/. AVISO gridded altimetry is produced by SSALTO/DUACS and distributed with support from CNES, at http://www.aviso.oceanobs.com/. Analyses of altimetry-derived surface currents are available at http://www.aoml.noaa.gov/phod/altimetry/cvar.

Boyer et al. 2005; Roemmich and Gilson 2009; Hosoda et al. 2009; Durack and Wijffels 2010; Helm et al. 2010). Studies have also reported long-term and coherent salinity changes on subsurface density horizons (e.g., Wong et al. 1999; Curry et al. 2003; Helm et al. 2010). In this framework Durack and Wijffels (2010), show that many changes are dominated by subduction into the deep ocean driven by a broad-scale warming, and thus are less useful in reflecting changes in the water cycle.

In summary, several recent studies employing different analysis techniques find a clear multidecadal ocean surface salinity change. Broad-scale changes can be characterized as an amplification of the climatological salinity pattern, a tendency also found in the subsurface. The consensus view of coherent salinity change arises, even though many different analysis techniques and ocean salinity observing platforms have been used—reflecting the robustness of the signal. To first order, this suggests that broad zonal changes to E-P have changed ocean surface salinity, and changes are propagating into the subsurface ocean following the mean circulation pathways. An enhancement to mean salinity patterns and basin contrasts are the result.

How rates of salinity changes translate into rates of water cycle change remains to be determined. The ocean mixing through circulation and subduction of salinity anomalies reduces the E-P surface flux changes expressed in surface ocean salinity. Global coupled ocean-atmosphere climate models are the best tools currently available to investigate salinity and E-P change relationships, as the current observed record is too temporally and spatially sparse.

Many previous studies have used regional and global estimates of ocean salinity changes to infer water cycle changes. Hosoda et al. (2009) presented estimates of water cycle enhancement, derived from ocean salinity change trends by comparing the Argo period (2003–07) against the World Ocean Database (~1960–89). They reported an inferred global E-P enhancement of 3.7 ± 4.6% over their 30-year comparison, which considered surface salinity layer changes to 100 m depth. This enhancement is supported by the results of Trenberth et al. (2007) and Yu (2007), obtained from correlations with SST 1970–2005 (4%) and evaporation estimates 1978–2005 (~10%) respectively.

This ocean footprint of a strengthening water cycle captured in surface (and subsurface) salinity changes suggests that the remaining 29% of the global terrestrial surface has also likely experienced changes over the 1950–2000 period. Continued monitoring of future ocean property changes are necessary to effectively monitor and diagnose the effect of anthropogenic change and the rate of its evolution on our global climate system.

For homogeneous coverage and analyses such as the one presented here, ocean currents are estimated using two methodologies, both using the Archiving, Validation and Interpretation of Satellite Oceanographic data (AVISO) multimission altimeter near-real time gridded product. The first is a synthesis of AVISO with in situ drifter measurements and reanalysis winds (Niiler et al. 2003), which adjusts the altimeter-derived geostrophic velocity anomalies to match the observed in situ eddy kinetic energy. The second is the purely satellite-based OSCAR (Ocean Surface Current Analyses–Real time) product, which uses AVISO altimetry, winds, SST, and the Rio05 mean dynamic topography (Rio and Hernandez 2004) to create a 0.33°-resolution surface current maps averaged over the 0 m–30 m layer of the ocean (Bonjean and Lagerloef 2002). In both cases, anomalies are calculated with respect to the time period 1992–2007.

Global zonal current anomalies, and changes in anomalies from 2009, are shown in Figs. 3.19 and 3.20 and discussed below for individual ocean basins. In the analysis, an "eastward anomaly" is an increase in an eastward current, or a decrease in a westward current, and indicated as a positive zonal current anomaly. Similarly, negative anomalies are westward (decrease in an eastward current, or increase in a westward one).

1) Pacific Ocean

In the equatorial Pacific, 2010 began with equatorial eastward anomalies of ~50 cm s^{-1} in the center and western side of the basin, associated with the El Niño event of 2009 (Fig. 3.20). By the end of January, eastward anomalies persisted west of the dateline, but strong (30 cm s^{-1}–50 cm s^{-1}) westward anomalies had developed in the longitude band 130°W–160°W. The region of eastward anomalies propagated east across the Pacific during February through early March, while westward anomalies grew in their wake. By

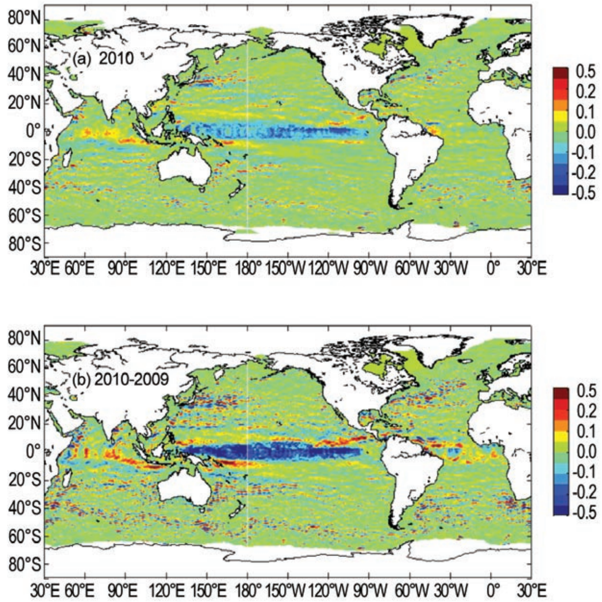

Fig. 3.19. Global zonal geostrophic anomalies for 2010 (top) and 2010 minus 2009 (bottom), cm s^{-1}, derived from a synthesis of drifters, altimetry, and winds.

April, westward anomalies were found across the entire equatorial Pacific. These anomalies reached their maximum amplitudes in mid-to-late May, with values of 60 cm s^{-1}–70 cm s^{-1} in the longitude band 110°W–140°W. This La Niña pattern persisted through boreal summer, although its amplitude diminished through this time period. The anomalous westward advection of salty water likely contributed to salty surface anomalies in the western equatorial Pacific (Fig. 3.12b). By October, the westward anomaly pattern was sufficiently weak that mesoscale patterns associated with tropical instability waves began dominating the surface current anomaly field in the region.

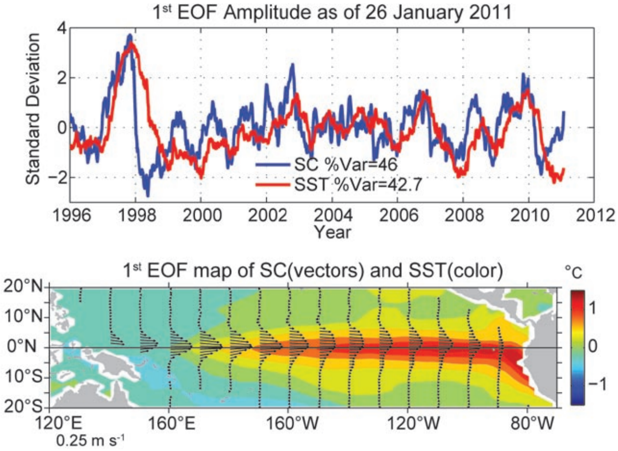

Fig. 3.20. Principal empirical orthogonal functions (EOF) of surface current (SC) and of SST anomaly variations in the tropical Pacific from the OSCAR model. Top: Amplitude time series of the EOFs normalized by their respective standard deviations. Bottom: Spatial structures of the EOFs.

Surface current anomalies in the equatorial Pacific typically lead SST anomalies by several months, with a magnitude that scales with the SST anomaly magnitude. Recovery to normal current conditions is also typically seen before SST returns to normal. Thus, current anomalies in this region are a valuable predictor of the evolution of SST anomalies and their related climate impacts. This leading nature can be seen clearly in the first principal empirical orthogonal function (EOF) of surface current anomaly and separately of SST anomaly in the tropical Pacific basin (Fig. 3.20). In mid-2010, the values of the normalized surface current and SST EOFs exceeded those of the 2000 and 2008 La Niñas, and hence by this metric, this year's La Nina was the strongest such event in the last decade.

In 2010, the Kuroshio Current exhibited a more stable path than in the last several years, with a narrower and stronger annual mean signature and a reduced area of enhanced eddy kinetic energy. Compared to 2006–09, the Kuroshio shifted approximately 1° in latitude to the north (Fig. 3.21). This shift may be related to the Kuroshio extension jet entering the strong phase of a decadal-scale fluctuation associated with the strength of the Kuroshio recirculation gyre and stability of the jet (Qiu and Chen 2005). Qiu and Chen (2005) hypothesized that this fluctuation is driven by the Pacific Decadal Oscillation (PDO), which in its negative (positive) phase generates negative (positive) sea height anomalies in the northeast Pacific which propagate to the western boundary and weaken (strengthen) the Kuroshio jet. Possibly consistent with this hypothesis, the PDO index generally dropped from 2004 to 2008 but rapidly increased through the latter part of 2009 and early 2010 (Yu and Weller 2010). However, it subsequently dropped precipitously in July 2010 (see the "Monthly Ocean Briefing" presentation by NOAA's Climate Prediction Center at http://www.cpc.ncep.noaa.gov/products/GODAS), suggesting that the northward shift may not persist through 2011.

2) Indian Ocean

Westward equatorial anomalies began developing in the western Indian Ocean in January, and by mid-February exceeded 50 cm s^{-1} at 50°E–65°E, with weaker westward anomalies from 80°E to the West African coast. This short-lived anomaly pattern was gone by the end of March. In July, weaker eastward anomalies began developing in the center and eastern side of the

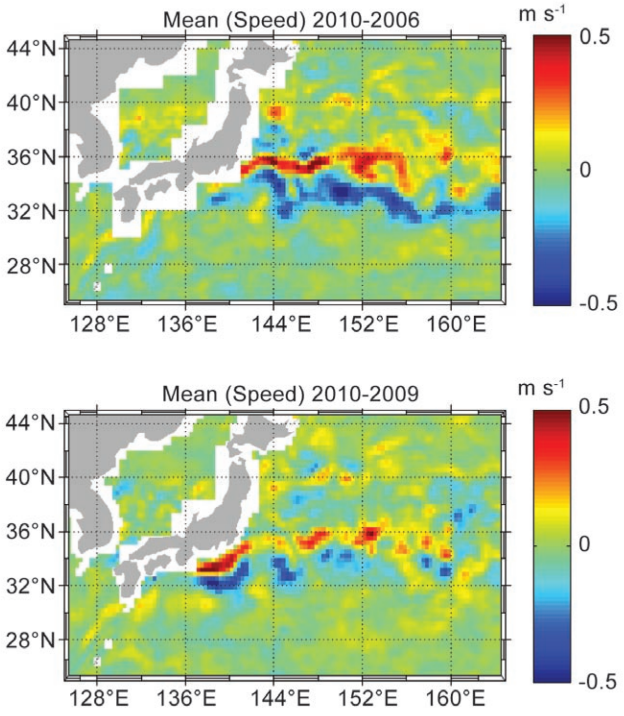

Fig. 3.21. Mean speed of the Kuroshio Current, 2010 minus 2006 (top) and 2010 minus 2009 (bottom) from OSCAR. Differences between 2010 and 2007–2008 (not shown) are similar.

basin, and were present across the basin in August–September. Eastward anomalies persisted through the remainder of the year in the center of the basin, albeit with less organization than seen in late boreal summer.

3) Atlantic Ocean

In the tropical Atlantic, near-equatorial surface currents were anomalously westward in February–April, with peak values of 20 cm s^{-1}–40 cm s^{-1} east of 30°W in mid-March, associated with anomalously cold SSTs of -0.5°C to -0.7°C at 12°W–18°W (the western half of the Atlantic cold tongue). Through boreal summer, equatorial current anomalies were less organized, although westward anomalies tended to dominate in the eastern half of the basin. In September, eastward anomalies began to develop across the basin, reaching ~25 cm s^{-1} by mid-October. These eastward anomalies persisted through November and weakened through December.

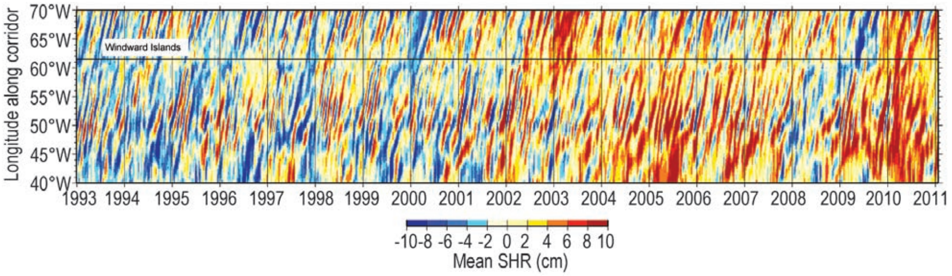

Fig. 3.22. Sea height residual (annual signal removed) from AVISO altimetry in the ring shedding corridor region of the North Brazil Current (NBC), 0°–15°N. Propagating high (red) signals indicate anticyclonic NBC rings. The longitude of the Windward Islands, which separates the Atlantic from the Caribbean, is indicated by a horizontal line.

The North Brazil Current (NBC) plays an important role the Atlantic Meridional Overturning Circulation by periodically shedding rings which transfer water of Southern Hemisphere origin to the Northern Hemisphere. In 2010, the NBC demonstrated extremely anomalous conditions, with very high values of annually-averaged sea height in the ring corridor region, superimposed on the higher-frequency sea height peaks of anticyclonic rings shed from the current (Fig. 3.22). Anomalies of this magnitude have not been seen previously in the altimeter time period (1993–present).

Against the east coast of South America, the southward-flowing warm, salty Brazil Current meets the northward flowing cold, fresh Malvinas Current to create the Confluence Front. The location of this front exhibits strong fluctuations at time scales from intraseasonal and seasonal to interannual and decadal (Goni and Wainer 20001; Lumpkin and Garzoli 2010). The front shifted south approximately 1° in latitude between late 1992 and 1998, while its annual-averaged position did not change significantly from 1998 to 2009. In 2010 the annual mean location of the Confluence at the South American continental shelf break was 37.5°S, further north than has been seen since 1997. The 1992–98 trend in the Confluence location may be part of a multidecadal oscillation related to surface temperature anomalies advected from the Indian Ocean into the Atlantic via the Agulhas-Benguela pathway (Lumpkin and Garzoli 2010).

h. Meridional overturning circulation observations in the subtropical North Atlantic—M. O. Baringer, T. O. Kanzow, C. S. Meinen, S. A. Cunningham, D. Rayner, W. E. Johns, H. L. Bryden, E. Faika-Williams, J. J-M. Hirschi, M. P. Chidichimo, L. M. Beal, and J. Marotzke

The meridional redistribution of mass and heat associated with the large-scale vertical circulation within an ocean basin such as the Atlantic is typically called the meridional overturning circulation (MOC).

The most common definition of the strength of the MOC is the maximum of the vertically integrated basin-wide stream function, which changes as a function of latitude and time and is influenced by many physical systems embedded within it. Substantial progress has been made on developing a coordinated observing system to begin to measure the MOC, through plans outlined at the international conference OceanObs'09 in September 2009 (e.g., Cunningham et al. 2010; Rintoul et al. 2010) and subsequent planning workshops focused on expanding existing observations to include the subpolar North and South Atlantic (e.g., Garzoli et al. 2010). A small portion of the recommended observing system has been in place since April 2004 spanning the subtropical gyre in the North Atlantic near 26.5°N. The system is composed of UK-NERC RAPID MOC moorings, US-NSF Meridional Overturning Circulation Heat-Transport Array (MOCHA), and the US-NOAA Western Boundary Time Series program (see also Chidichimo et al. 2010; Rayner et al. 2011). For the rest of the global ocean, changes in the complex, global MOC can also be inferred only from observations of individual components of the MOC (for example, a specific current or ocean layer; e.g., Dong et al. 2009), which are not discussed here.

The estimates of the MOC from the 26.5°N array include data from April 2004 to April 2009 (see also Kanzow et al. 2010). Over this time period the MOC has averaged 18.5 Sv with a high of 34.0 Sv, a low of 3.2 Sv, and a standard deviation of 4.7 Sv [using the twice daily values filtered with a 10-day cutoff as described in Cunningham et al. (2007); note Sv is a Sverdrup, equal to 10^6 m^3 s^{-1}, a unit commonly used for ocean volume transports]. These data suggest no statistically significant trend in the strength of the MOC for this extremely temporally limited dataset (-0.8 ± 1.6 Sv $decade^{-1}$, with 95% confidence limits). After five years of data, however, a clear seasonal signal is beginning to emerge (Fig. 3.23), with a low MOC in April and a high MOC in October with peak to trough range of 6.9 Sv. The MOC can be divided into three components: the northward western boundary Florida Current, the wind-driven Ekman transport, and the southward "interior" transport (upper ocean geostrophic flow between the Bahamas and Africa). The seasonal cycle of the MOC appears to be largely attributable to seasonal variability in the interior rather than Ekman or Florida Current fluctuations; Kanzow et al. (2010) show that the interior seasonal cycle is likely due to seasonal upwelling through a direct wind-driven response off Africa. Of note is that all the MOC transport values estimated from five repeated CTD (Conductivity, Temperature, Depth) sections by Bryden et al. (2005) can be found within the seasonal range of the MOC time series (values ranged from 22.9 Sv in 1957 to 14.8 Sv in 2004). In fact, Kanzow et al. (2010) demonstrated that removing the seasonal cycle estimates from Bryden et al. would effectively eliminate a statistically significant trend in the transport.

These results do not disprove the presence of a long-term trend in the strength of the MOC [e.g., Longworth et al. (2011) and Wunsch and Heimbach (2006) both found significant long-term decreases in the MOC], but they do suggest that a careful error analysis must be performed that includes the impact of the underlying higher-frequency variability of the MOC on trend estimates (see also Baehr 2010; Baehr et al. 2008; Brennan et al. 2008). Other recent studies of the MOC trend are contradictory, with some reporting a decrease in the MOC [e.g., Wunsch and Heimbach (2006), using data assimilating models; Longworth et al. (2011), using end-point hydro-

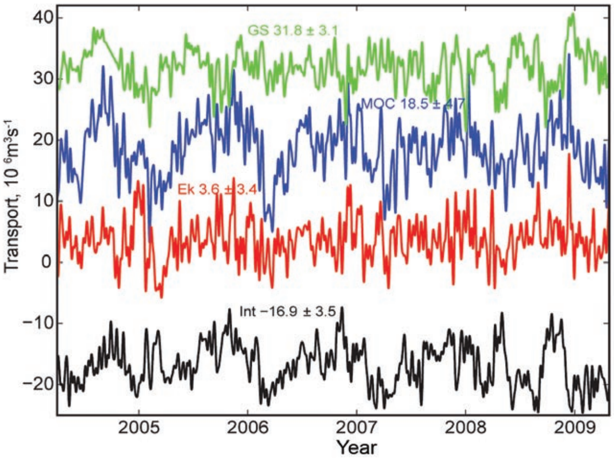

Fig. 3.23. Daily estimates of the strength of the meridional overturning circulation (MOC: blue line) and its components, the Florida Current (GS: green), wind-driven Ekman transport (Ek: red) and the geostrophic interior (Int: black), as measured by the UK National Environmental Research Council (NERC) Rapid Climate Change Program, the National Science Foundation Meridional Overturning and Heat Transport Array, and the long-term NOAA funded Western Boundary Time Series Program. The interior volume transport estimate (accurate to 1 Sv, Cunningham et al. 2007) is based on the upper ocean transport from April 2004 to April 2009 (see also Kanzow et al. 2010), with a ten-day low pass filter applied to the daily transport values. Smooth curves are the annual climatology of each component estimates from the full five years of data.

graphic observations following the 26°N mooring design principles] while others suggest no change or even an increase [e.g., Lumpkin et al. (2008), using hydrographic sections]. Some estimates showing an increase (C. Wang et al. 2010) and no trend (e.g., Schott et al. 2009) did not include basin-wide estimates of the MOC. Clearly, while disagreement remains over the details of findings from any particular observing systems (e.g., Kanzow et al. 2009), agreement exists that longer time series at multiple locations, particularly of the deep transport components, are needed (e.g., Zhang et al. 2010; Zhang 2008). New efforts are focusing on the use of state estimation models and "fingerprints" of other readily observed variables linked to changes in the MOC (e.g., Msadek et al. 2010; Lorbacher et al. 2010; Baehr 2010). Trends in the MOC can also be determined through proxies of the MOC strength, such as paleo observations (e.g., Y. Luo et al. 2010), tracers (e.g., Nelson et al. 2010; LeBel et al. 2008) and water mass characteristic (e.g. Kouketsu et al. 2009; Zhang 2008). For example, temperature and salinity observations in the Labrador Sea showed an abrupt return of deep convection between 2007 and 2008 (Våge 2009). Using water mass properties, Yashayaev and Loder (2009) showed that the enhanced deep convection in the Labrador Sea in the winter of 2008 was the deepest since 1994 and included the largest heat loss from the ocean to the atmosphere since the mid-1990s, exceeding the long term mean by 50%. Such anomalous local events may be a precursor to changes in the MOC strength (e.g., Lohmann et al. 2009).

One of the main contributions to the MOC estimate near 26.5°N is the Florida Current transport, the longest transport time series of an ocean circulation feature directly linked to the MOC. Near this latitude in the Atlantic, the bulk of the warm upper limb of the Atlantic MOC is thought to be carried to the north in the Florida Current through the Straits of Florida and the majority of the cold lower limb is believed to be carried to the south in the Deep Western Boundary Current (DWBC) just east of the Bahamas (e.g., Meinen et al. 2010; Baringer and Larsen 2001). Since 1982, Florida Current transport has been monitored using a submarine cable across the Straits of Florida in combination with regular hydrographic sections. In 2010, the mean transport through the Florida Straits continued the decrease over the past four years to 30.7 ± 1.5 Sv (95% confidence limits), lower than the 2009 31.3 ± 1.2 Sv, 2008 31.7 ± 2.2 Sv , and 2007 32.1 ± 1.0 Sv mean transports (error bars represent standard error of daily values using degrees of freedom calculated for each year, representing a typical decorrelation time scale of around 20 days). The annual mean of 2010 falls within the lowest quartile of mean annual values (32 ± 0.14 Sv). Note that while recently the annual means appear to have decreased (trend of -0.88 ± 0.85 Sv decade^{-1} from April 2004 to April 2009, 95% significance), there is only a very small significant long-term trend to the Florida Current transport (Fig 3.24; trend for full time series is -0.14 ± 0.06 Sv per decade).

The daily fluctuations of the Florida Current transport throughout the year are fairly similar to 2009 and generally fall within 90% confidence levels (Fig. 3.24). There were, however, a few unusual low transport events during the year (Fig. 3.24; the most significant or occurring over three-day or more

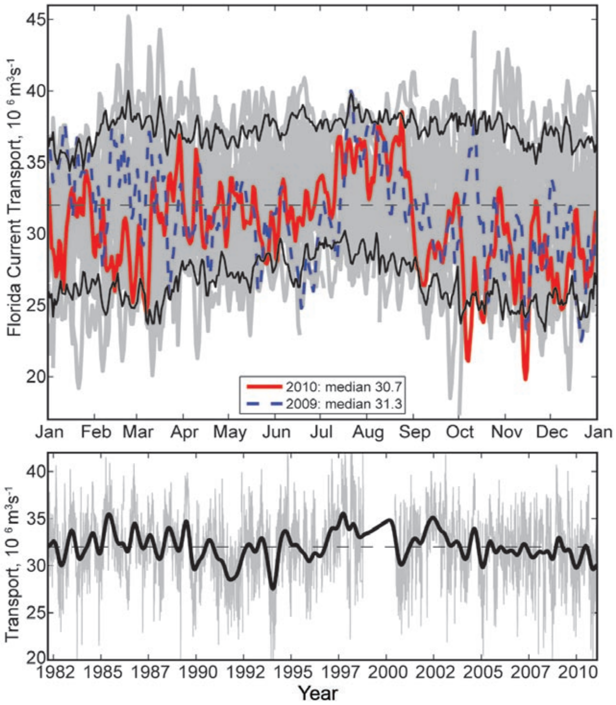

Fig. 3.24. (top) Daily estimates of the transport of the Florida Current during 2010 (red solid line) compared to 2009 (dashed blue line). The daily values of the Florida Current transport for other years since 1982 are shown in light gray and the 90% confidence interval of daily transport values computed from all years is shown in black (solid line); the long-term annual mean is dashed black. The mean transport in 2010 of 30.7 ± 1.5 Sv decreased for the fourth year in a row, below the long-term mean for the daily values of the Florida Current transport (32.2 Sv). (bottom) Daily estimates of the Florida Current transport for the full time series record (light gray), a smoothed version of transport (heavy black line; using a 30-day running mean six times) and the mean transport for the full record (dashed black).

events during 25–27 May, 5–9 October, 15–17 October, 15-17 November, and 8–10 December with values as low as 19.8 Sv). In comparison, only the transport on 24 August was higher than the 90% confidence range, with a daily average transport of 38.5 Sv. Due to the fact that these events were relatively short-lived, it is likely they are local responses to atmospheric forcing and coastally trapped wave processes and are not particularly indicative of a climatically important shift (e.g., Mooers et al. 2005). These transient fluctuations can have important environmental consequences. As examples, in the summer of 2009, the East Coast of the United States experienced a high sea-level event that was unusual due to its unexpected timing, large geographic scope, and coastal flooding that was not associated with any storms (Sweet et al. 2009). Sweet et al. (2009) showed that this anomalous event was related to the anomalously low Florida Current transport: a reduced Florida Current transport corresponds to a lower sea surface height gradient across the front and hence higher sea level onshore. In 2010, the low transport events could reasonably be inferred to have influenced sea level along the eastern U.S.; as of this report no relationship has been documented. For longer time scales, the same mechanical effect due to a reduction in ocean currents causes sea-level changes associated with geostrophy; Yin et al. (2010) showed that the dynamical response to MOC reductions associated with carbon dioxide (CO_2) emission scenarios would lead to approximately 20 cm rise in regional sea-level along the East Coast of the U.S. due to this sort of circulation change alone. Yin et al (2010) suggest that this region may be in greater jeopardy from regional effects of ocean circulation changes on top of the global mean sea-level rise predicted by climate models.

i. Sea level variations—M. Merrifield, G. Mitchum, E. Leuliette, D. Chambers, S. Nerem, P. Woodworth, S. Holgate, L. Miller, and S. Gill

Sea surface height (SSH) variations exhibited weak-to-moderate amplitudes during 2010, with the most evident patterns associated with a transition from a weak La Niña during most of 2009 to a weak El Niño (in terms of sea level) that peaked in late 2009 to early 2010 (Fig. 3.25a), returning to La Niña conditions during the remainder of 2010. In the annual mean SSH for 2010 (Fig. 3.26a), this sequence of events led to a dominant La Niña pattern in the tropical Pacific, consisting of low SSH anomalies (relative to a 1993–2010 baseline) in the central equatorial region and high SSH anomalies in the western tropical Pacific, particularly north of the Equator. SSH anomalies in other regions of the ocean that stand out in 2010 (relative to the 1993–2010 mean) include negative anomalies in the Southern Ocean to the west of South America, negative anomalies in the North Atlantic, and positive anomalies in the northwest Pacific with negative anomalies farther east (Fig. 3.26a).

The SSH tendency during 2010 is measured by the difference between the 2010 and 2009 annual means (Fig. 3.26b). The tendency in the tropical Pacific reflects the transition from El Niño to La Niña conditions, with falling SSH in the central equatorial Pacific and in the South Pacific Convergence Zone region. Other SSH tendencies of note during 2010 include negative changes in the North Pacific in the region of the Aleutian Low, with positive coastal sea level anomalies along Alaska and Canada. A similar pattern arises with falling SSH in the North Atlantic, with positive sea level anomalies along the

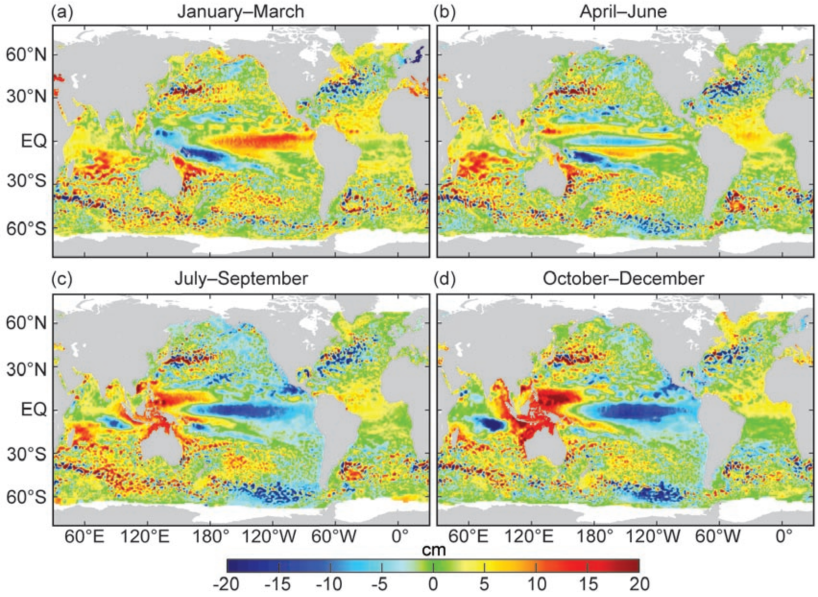

Fig. 3.25. Seasonal SSH anomalies (cm) for 2010 relative to the 1993–2010 baseline average are obtained using the multimission gridded sea surface height altimeter product produced by Ssalto/Duacs and distributed by AVISO, with support from CNES (http://www.aviso.oceanobs.com).

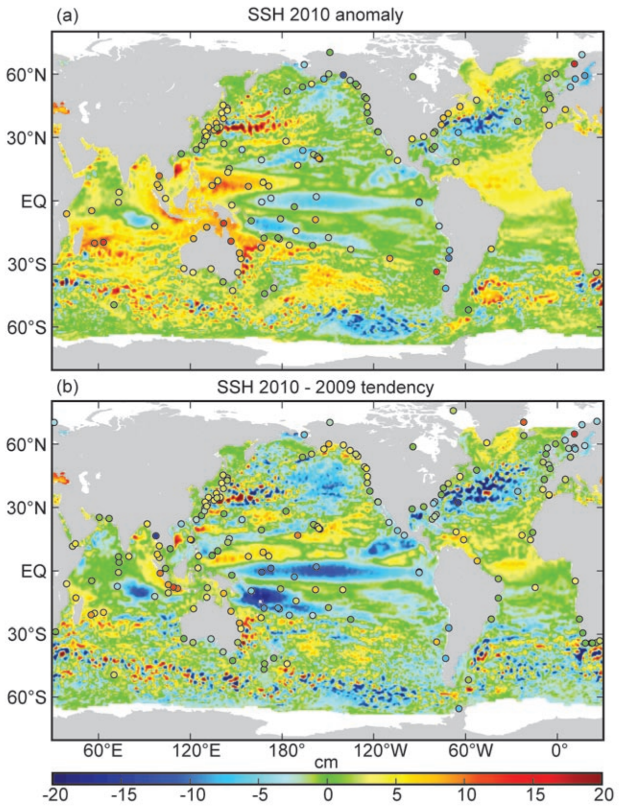

Fig. 3.26. (a) The 2010 SSH anomaly (Ssalto/Duacs product with anomaly, cm) from the 1993 to 2010 baseline is compared to the 2010 anomaly computed for tide gauge data (dots) obtained from the University of Hawaii Sea Level Center (http://uhslc.soest.hawaii.edu/). (b) The difference between 2010 and 2009 annual means (cm).

coast of the Northeast U.S. and Canada. The North Pacific pattern is associated with a deeper Aleutian Low, increasing cyclonic wind stress curl (Fig. 3.27), and lower SSH in the region of the anomalously low surface pressure. The same wind pattern accounts for greater Ekman convergence along the west coast of North America and a positive sea level tendency. These conditions are consistent with a switch toward a colder phase of the Pacific Decadal Oscillation (PDO). A similar change occurs in the North Atlantic, where the tendency from 2009 to 2010 was associated with a reduction of the midlatitude westerlies (Fig. 3.27), with an associated wind stress curl anomaly that favors lower SSH in the mid-latitude North Atlantic. The same wind change leads to Ekman convergence and higher sea levels along the east coast of North America. These conditions are consistent with a switch toward a more negative North Atlantic Oscillaion (NAO) state.

The importance of the negative PDO and NAO states during 2010 is also reflected in extreme sea level patterns. Extremes are measured here as the average of the top 2% largest daily averaged sea levels from tide gauge data. Extremes generally are larger at high latitudes (Fig. 3.28a), as is to be expected given that the extreme sea levels primarily indicate the influence of storm forcing associated with subtropical cyclones. To determine where the amplitude of extremes were below normal, normal, and above normal, we fit a generalized extreme value (GEV) distribution to the annual averages of the top 2% largest daily sea levels, using all available years at each station. The 2010 values (Fig. 3.28a) are assigned a probability based on the GEV distribution (Fig. 3.28b). The most notable region of above-average extremes (i.e., less likely occurrence and therefore low probability) is along the west coast of North America from the Aleutians all the way to San Diego (Fig. 3.28b). We attribute the above-average extremes to a combination of increased storminess during the cold PDO state, and high sea levels along the coast associated with El Niño and PDO downwelling-favorable winds. Extremes were consistently below normal in Northern Europe, which we associate with the negative NAO phase during 2010, which is characterized by a milder winter in Northern Europe.

The global rate of sea level change computed over the years 1993–2010 (Beckley et al. 2010; Leuliette and Scharroo 2010; Nerem et al. 2010) is 3.1 ± 0.4 mm yr^{-1} (one sigma). Note that the global budget of recent sea level change can be monitored by comparing total sea level measured by satellite altimeters to the sum of changes due to ocean density changes and ocean mass inputs and redistributions. For the period January 2005 to September 2010, when ocean temperature and salinity observations from the Argo float array and ocean mass variations from the Gravity Recovery

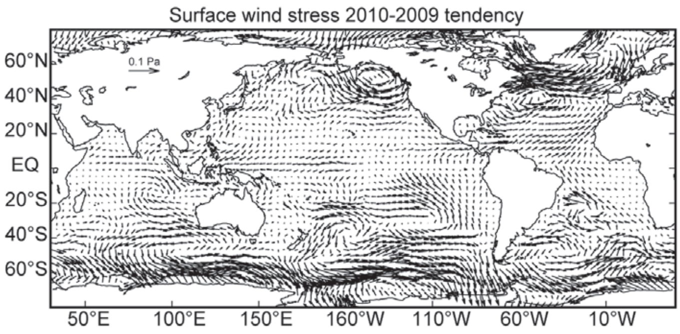

Fig. 3.27. Difference in annual mean wind stress, 2010 minus 2009. NCEP Reanalysis data provided by the NOAA/OAR/ESRL SD, http://www.esrl.noaa.gov/psd.

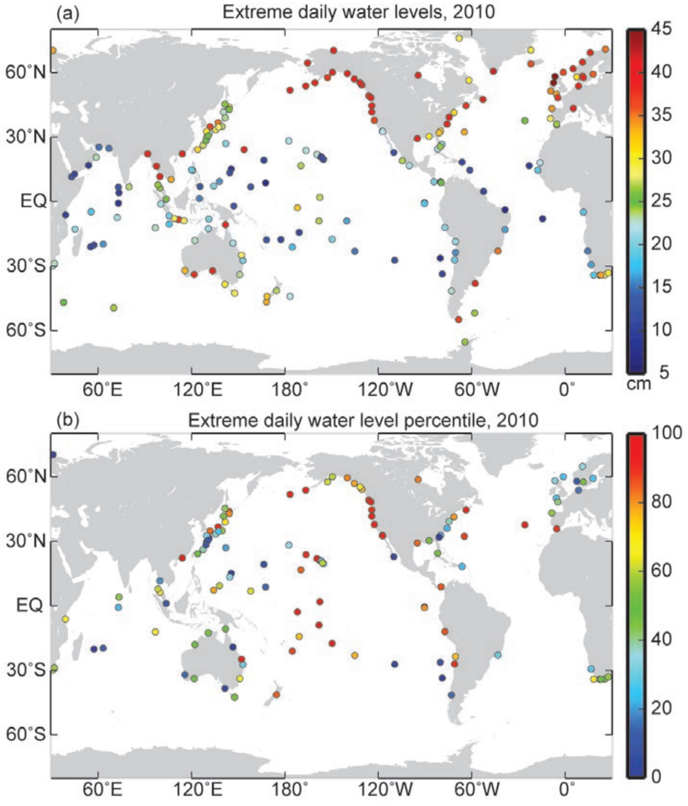

Fig. 3.28. (a) 2010 extreme sea levels measured as the average of 2% largest daily values relative the 2010 annual mean at each station. (b) Generalized extreme Value (GEV) percentiles for the 2010 extreme sea levels.

and Climate Experiment (GRACE) are available, an update to the sea level budget analyses of Leuliette and Miller (2009) and Chambers et al. (2010) shows that the recent sea level budget can be closed to within the range of uncertainties, although contribution of deep ocean heat content requires attention (see section 3c). This will be addressed in future assessments, but for now this contribution appears to be well within the error bar. Over this brief time period and in areas more than 200 km from the nearest coast where comparisons can be made with Argo and GRACE, the mean rate of total sea level rise is 1.5 ± 0.9 mm yr^{-1} (note that the uncertainties from here to the end of this section are 95% confidence levels). This rate cannot be compared with the global average over the entire altimeter time period cited above since at least 10 years of data are required to determine a reliable rate (Nerem et al. 1999). This rate is, however, in agreement (Fig. 3.29) with the sum (1.6 ± 0.6 mm yr^{-1}) of the rates of the upper (depths < 700 m) ocean steric (0.5 ± 0.5 mm yr^{-1}) and ocean mass components (1.1 ± 0.6 mm yr^{-1}).

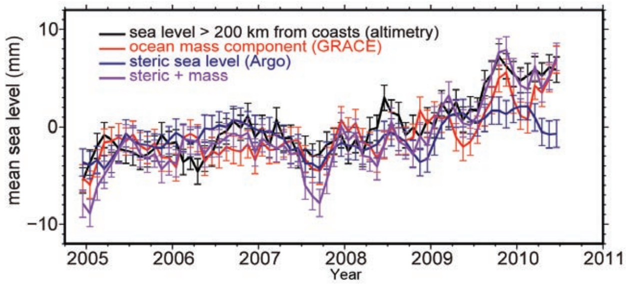

Fig. 3.29. Monthly estimates from Jason-1 and Jason-2 of global mean sea level for areas greater than 200 km from the coast (black), which are in general agreement with the sum (purple) of the ocean mass component from GRACE (red) and the steric component of the upper 700 m from Argo (blue). Seasonal signals were removed and the time series smoothed with a three-month running mean.

GRACE also allows for the monitoring of ocean mass exchange between the basins and the associated sea level change. For January 2005 to September 2010, the Indian basin shows the continued mass loss observed by Chambers and Willis (2009), equivalent to −1.3 ± 0.5 mm yr^{-1} of sea level change, while the Pacific and Atlantic have gained mass (+2.1 ± 0.5 mm yr^{-1}, +0.6 ± 0.5 mm yr^{-1}, respectively). Note that these numbers include both the mean ocean mass trend and the internal redistribution of mass. On balance, the Atlantic and Indian Oceans have been losing mass to the Pacific over this time period, but the relative contributions of fresh water inputs in each basin versus the basin-to-basin exchanges of mass are not addressed in this calculation.

In the future, total sea level changes will be understood through assessment of altimetry and tide gauges in terms of ocean density and mass changes in terms of both buoyancy and mass inputs as well as redistributions of each quantity. As of yet, the Argo and GRACE series are too short to be definitive, but in future years such analyses will be of central importance in this annual review.

j. The global ocean carbon cycle—C. L. Sabine, R. A. Feely, R. Wanninkhof, T. Takahashi, S. Khatiwala, and G.-H. Park

1. Air-sea carbon dioxide fluxes

Global surface ocean CO_2 levels are extremely variable in space and time, especially on seasonal time scales. To document the changing patterns of air-sea CO_2 exchange, an extensive observational program is required. The latest published global flux map, based on a compilation of approximately three million measurements collected between 1970 and 2007 (hereafter referred to as LDEO), provides information on the monthly patterns of air-sea CO_2 fluxes during a "normal" non-El Niño year taken to be 2000 (Takahashi et al. 2009). The number of annual surface CO_2 observations has been growing exponentially since the 1960s such that today well over one million observations are reported to data centers each year. An update to the LDEO climatology was released in 2010 which not only includes new recent data up to 2008, but also a large number of the data from the 1957 to 1962 International Geophysical Year cruises in the Atlantic, Pacific, and Indian Oceans (Takahashi 1961; Waterman et al. 2006a, 2006b, 2006c, 2006d) thus extending the dataset by another decade (Takahashi et al. 2010).

The LDEO climatology is significant because it is directly based on in situ partial pressure of CO_2 (pCO_2) observations, but it does not provide information on how air-sea CO_2 fluxes vary from one year to the next. Annually varying global air-sea CO_2 flux estimates are based on empirical approaches relating in situ measurements with satellite observations of wind and sea surface temperature (Sabine et al. 2008, 2009, 2010). The latest empirical approach for quantifying the air-sea CO_2 exchange utilizing in situ, climatological, and satellite data from 1982 to 2007 is described in Park et al. (2010). Figure 3.30 extends these estimates through 2009. Lags in availability of quality-controlled data streams including atmospheric CO_2, satellite data, and assimilation products preclude real-time analysis such that consistent, climate-quality seasonal air-sea CO_2 flux maps are only available through 2009. The global mean air-sea CO_2 flux for the period from 1982 to 2009 using the Park et al. approach gives an average contemporary net uptake of 1.47 Pg (10^{15}g) C yr^{-1}. Following the Gruber et al. (2009) estimate that the pre-industrial steady state ocean was a source of 0.45 Pg C yr^{-1}, the estimated average net flux equates to an ocean anthropogenic CO_2 uptake of 1.92 Pg C yr^{-1}, at the lower end of the range of estimates (1.8 Pg C yr^{-1}–2.4 Pg C yr^{-1}) recently summarized by Gruber et al. (2009).

The global net CO_2 uptake flux for the 2009 transition period from La Niña to El Niño conditions (see Halpert et al. 2010) is estimated to be 1.40 Pg C yr^{-1}. During 2009, greater CO_2 uptake is found in the high northern and southern Atlantic Ocean and higher CO_2 outgassing is observed in the high northern and southern Pacific, and also the eastern Pacific Ocean compared with long-term averages (Fig. 3.31a). However, in the equatorial Pacific during the La Niña that occurred during the first half of 2009 (Fig 3.31b), the increased outgassing is offset by a decreased efflux during the El Niño that started in May–June 2009 and persisted for the remainder of the year (Fig. 3.31c). Therefore, on an annual basis, much of the equatorial Pacific shows no net anomaly (Fig. 3.30). A unique feature of the El Niño in 2009 is that the largest negative CO_2-flux anomalies occur in the central equatorial Pacific rather than in the eastern equatorial Pacific (blue colors in Fig. 3.31c). This is a direct result of greater sea surface temperature anomalies in the central equatorial Pacific than the eastern equatorial Pacific (Lee and McPhaden 2010). This change in El Niño patterns commenced in the 1990s and is referred to as El Niño Modoki. (Ashok et al. 2007).

Negative CO_2 flux anomalies found in the high-latitude Atlantic Ocean are caused primarily by increased wind speed but reinforced by SST anomalies in the region. For the high latitude Pacific Ocean, the CO_2 flux anomalies are predominantly caused by SST anomalies and partially compensated or reinforced by wind speed changes (Fig. 3.31a). Net CO_2 uptake in subtropics (42°N–42°S except the eastern equatorial Pacific) shows the second lowest value over the last 28 years (Fig. 3.30). The regional net air-sea CO_2

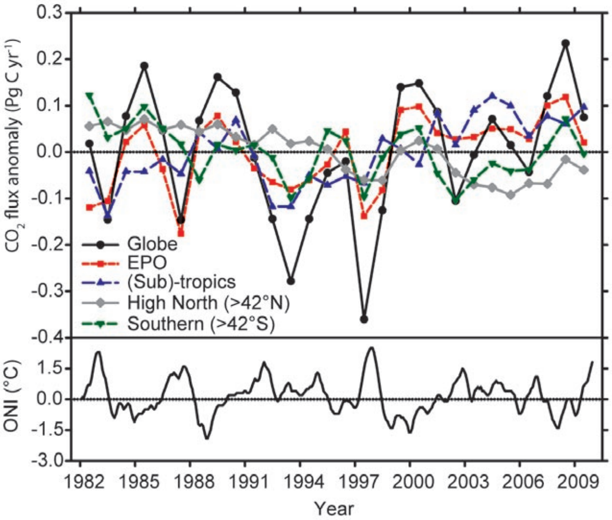

Fig. 3.30. Annual air-sea CO_2 flux anomalies 1982–2009 for the globe (black line), the equatorial Pacific Ocean (EPO; 10°N–10°S, 80°W–135°E; red dashed line), (Sub)-tropics (42°N–42°S except the EPO; blue dashed line), and high-latitude oceans (> 42°N or > 42°S; gray and green lines). The lower panel shows the Oceanic Niño Index (ONI) based on SST change in the Niño-3.4 region (Trenberth 1997). For comparison with ONI, the annual CO_2 flux anomalies are plotted in the middle of each corresponding year.

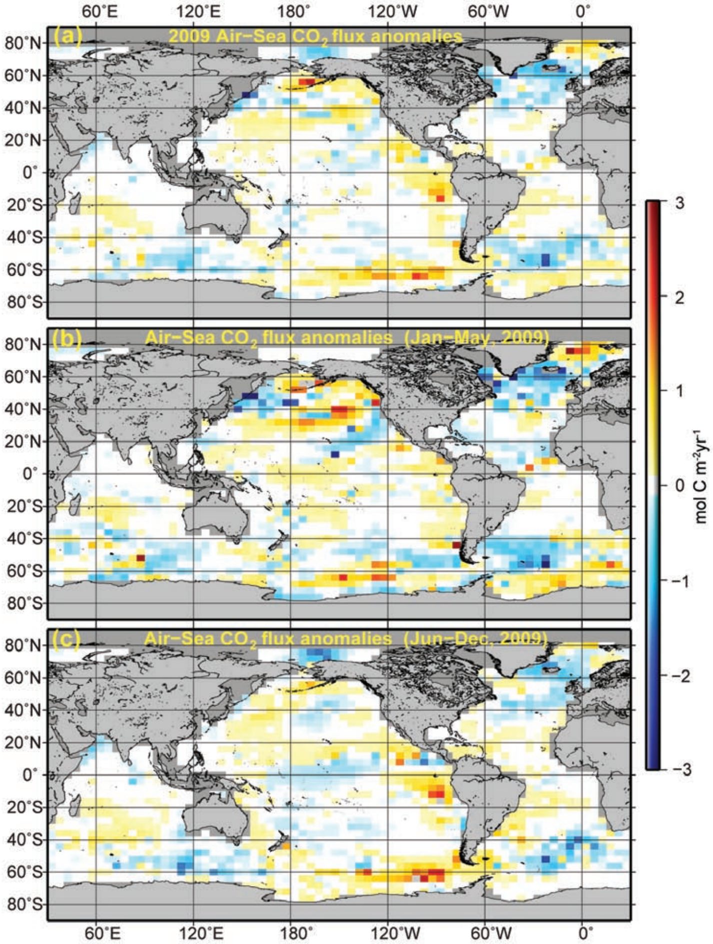

Fig. 3.31. Global distributions of air-sea CO$_2$ flux anomalies for the full year of 2009 (a) January to May, (b) and June to December, and (c) compared to the 28-year mean values for the corresponding months as calculated from the Park et al. (2010) approach. Positive values indicate less uptake or more release of CO$_2$ by the ocean^{1,}. The results for air-sea CO$_2$ flux anomalies are for the calendar year 2009 due to lags in data availability.

fluxes in 2009 in the equatorial Pacific, the Southern Ocean, and the high northern ocean are very close to 28-year mean values. The global air-sea CO$_2$ fluxes are closely related to the El Niño-Southern Oscillation. Higher oceanic CO$_2$ uptake (negative anomalies) occurs during the El Niño periods. The increase of global oceanic CO$_2$ uptake is not only caused by decreased CO$_2$ efflux in the equatorial Pacific but is also reinforced by CO$_2$ fluxes in the Southern Ocean and the subtropics. The monthly flux maps and anomalies from 1982 to 2009 can be created at the interactive website: http://cwcgom.aoml.noaa.gov/erddap/griddap/aomlcarbonfluxes.graph.

Implicit in the above estimates is an assumption that, at least on basin scales, the surface water pCO$_2$ is increasing at the same rate as the atmospheric CO$_2$ (i.e., ΔpCO$_2$ is not changing with time) and that the surface water pCO$_2$ is only affected by SST anomalies. The LDEO surface water pCO$_2$ database, with observations collected over the past three decades, reveals the mean decadal rate of increase in surface water pCO$_2$ in areas where sufficient number of intra- and interannual measurements are available. In Fig. 3.32, the 1981–2007 mean rates of change in sea-air pCO$_2$ difference (ΔpCO$_2$) are expressed as deviations of observed surface pCO$_2$ change relative to the mean rate of change in atmospheric pCO$_2$ of 1.68 µatm yr^{-1} (Le Quéré et al. 2010). The red circles in the North Atlantic and the red box areas in the western equatorial Pacific (Feely et al. 2006) and Southern Ocean (Takahashi et al. 2009) indicate the ocean areas where surface pCO$_2$ is increasing faster than the atmospheric pCO$_2$ and hence the ocean CO$_2$ sink is weakening. The blue circles indicate the ocean areas where surface pCO$_2$ is increasing slower than the atmospheric pCO$_2$ and hence the ocean CO$_2$ sink is intensifying. Note that the annual CO$_2$ flux anomalies for 2009 (from the 28-year mean; Fig. 3.31) can differ from the long-term trend of ΔpCO$_2$ shown in Fig. 3.32 as there is significant regional interannual variability superimposed on long-term trends. The most likely processes responsible for these observations are changes in the lateral and vertical circulation of the ocean and/or changes in marine ecosystems. Regardless of the mechanism, these data show that different ocean regions have varying responses to rising atmospheric CO$_2$.

2. Subsurface Carbon Inventory

In the 1990s, carbon samples were collected and analyzed from approximately 95 research cruises run as part of the international World Ocean Circulation Experiment (WOCE) and the Joint Global Ocean Flux Study (JGOFS). Based on these data, Sabine et al. (2004) estimated that the total inventory of anthropogenic CO$_2$ in the ocean (C$_{ant}$) in 1994 was 118 ± 19 Pg C, accounting for 48% of the CO$_2$ released from fossil fuel burning between 1800 and 1994. Since then, two approaches that heavily rely on chlorofluorocarbon data have published global inventory estimates for the reference year 1994: 94 Pg C–121 Pg C based on

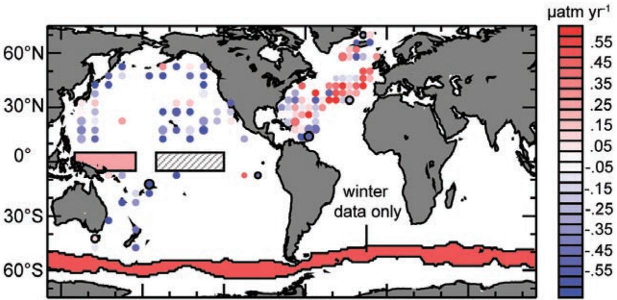

Fig. 3.32. The 1981–2007 observed rates of increase in sea-air pCO_2 difference. Red circles and areas indicate that the sea surface pCO_2 is increasing at a rate faster than the atmospheric increase rate of 1.68 µatm yr^{-1}, and hence the ocean uptake is weakening; and the blue areas show that the ocean uptake is becoming more intense. Large, medium, and small circles signify the estimated errors of < 0.25, 0.25 to 0.50, and > 0.50 µatm yr^{-1}, respectively. A single trend is shown for the Southern Ocean representing the circumpolar averaged for temperature between 0.8°C and 6.5°C using winter observations only. The gray hatched box in the central equatorial Pacific identifies the El Niño-3.4 region where observations exist but the variability is too large to clearly identify a trend (Le Quéré et al. 2010).

the TTD method (Waugh et al. 2006) and 114 ± 22 Pg C using a Green function approach (Khatiwala et al. 2009).

None of the global estimates published thus far have directly evaluated the contributions of marginal seas (defined as a semi-closed sea adjacent to a continent that is connected to the ocean), although recent work shows that several marginal seas store more C_{ant} per unit area than the global ocean and that marginal seas contribute significant C_{ant} to their adjacent major ocean basins. A key process in determining the C_{ant} uptake efficiency of these marginal seas is overturning circulation; however, the intensity of this process appears to have weakened in recent years (Lee et al. 2011). A recent synthesis of C_{ant} storage estimates for the major marginal seas suggests that as of 2008 up to 8.2 Pg C may be stored in these regions, i.e., approximately 6% of the global ocean C_{ant} storage (Lee et al. 2011). Figure 3.33 shows a compilation of these recent marginal sea estimates together with the 2008 open ocean C_{ant} distributions estimated using the approach of Khatiwala et al. (2009). This compilation gives a total ocean C_{ant} inventory estimate of 148 ± 27 Pg C for 2008. All three of the published global C_{ant} estimates assume steady state ocean circulation and use tracer information, which tends to underestimate natural variability and changes in ocean biogeochemistry. Thus, perturbations in oceanic dissolved inorganic carbon (DIC) concentrations due to anthropogenically-forced changes in large-scale circulation, ventilation, or biological activity are only partially included in these estimates.

Despite numerous technological advances over the last several decades, ship-based hydrography remains the only method for obtaining high-quality, high spatial, and vertical resolution measurements of a suite of physical, chemical, and biological parameters over the full water column. Ship-based hydrography is essential for documenting ocean changes throughout the water column, especially for the deep ocean below 2 km (52% of global ocean volume not sampled by profiling floats). Over the last decade there has been a collaborative international effort to reoccupy a subset of WOCE/JGOFS ocean survey lines to quantify changes in heat content, carbon, and anthropogenic tracers throughout the water column. A compendium of planned cruises can be found at http://www.go-ship.org/CruisePlans.html.

In late 2009 and early 2010, a zonal line (designated

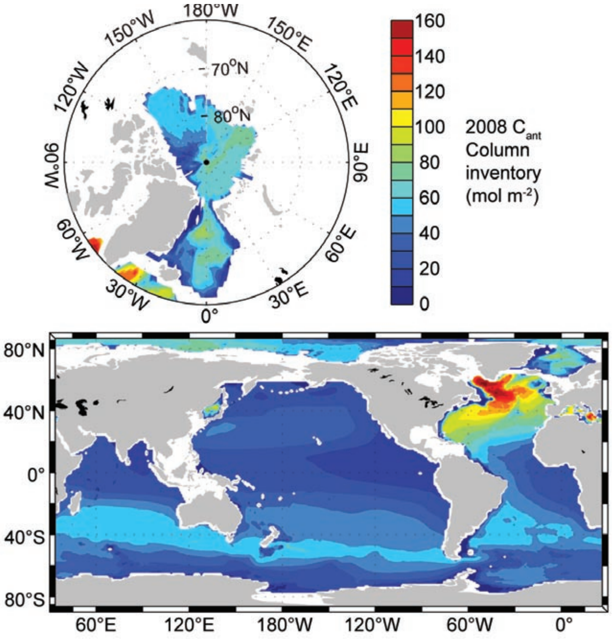

Fig. 3.33. Compilation of 2008 column inventories (mol m^{-2}) of anthropogenic CO_2 (C_{ant}): the global Ocean excluding the marginal seas (Khatiwala et al. 2009), 140 ± 25 Pg C; Arctic Ocean (Tanhua et al. 2009) 2.6 Pg C–3.4 Pg C; the Nordic seas (Olsen et al. 2010) 1.0 Pg C–1.5 Pg C; the Mediterranean Sea (Schneider et al. 2010) 1.5 Pg C–2.4 Pg C; the East Sea (Sea of Japan; Park et al. 2006) 0.40 ± 0.06 Pg C. All the marginal sea estimates were computed for 1994 and then scaled to 2008 assuming transient steady state storage of anthropogenic carbon (C_{ant}).

as P06), nominally along 32°S across the South Pacific, was completed. The top panel of Fig. 3.34 shows a section of DIC recently collected along P06. The previous occupation of that line was in 2003. The DIC from the 2003 cruise is shown in the middle panel. The bottom panel shows the difference between the two sections. To first order the DIC distributions look similar for both years, but the difference plot (Fig. 3.34, bottom) shows that DIC generally increased in the upper 500 m of the water column, presumably resulting primarily from the uptake of anthropogenic CO_2 from the atmosphere. Larger and deeper changes are observed in the eastern and western edges of the basin in association with the boundary currents in these areas. The magnitude of the changes is quite patchy with variations ranging from about -30 µmol kg^{-1} to +50 µmol kg^{-1}.

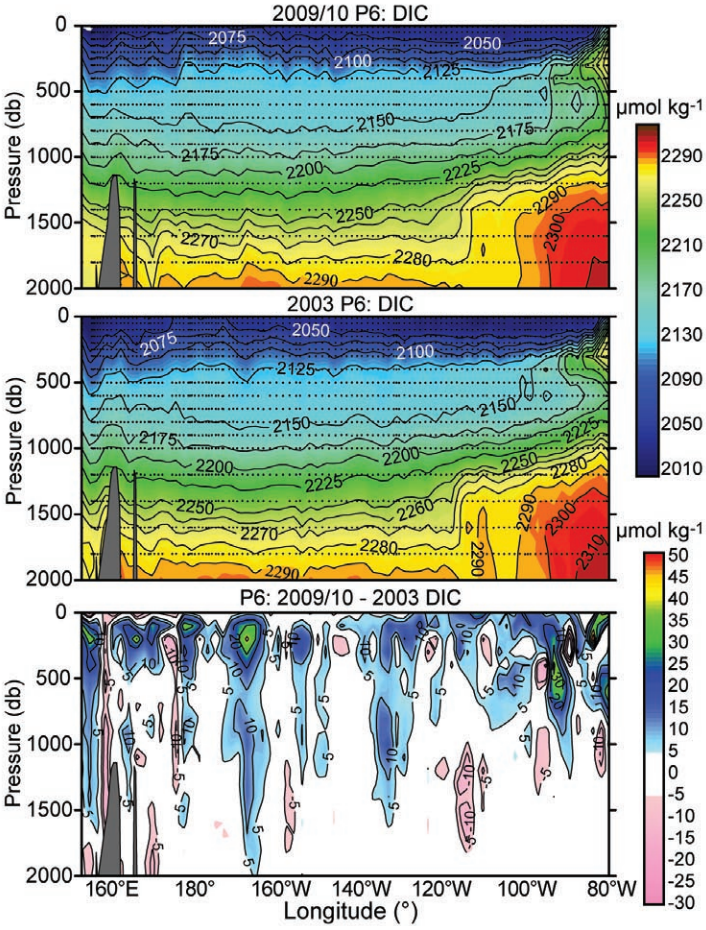

Fig. 3.34. Sections of dissolved inorganic carbon (µmol kg^{-1}) nominally along 32°S in 2009/10 conducted as part of the U.S. CLIVAR/CO_2 Repeat Hydrography Program (top) and 2003 BEAGLE cruise conducted by the Japan Agency for Marine-Earth Science and Technology (middle). Black dots show sample locations. The bottom section shows the DIC change (µmol kg^{-1}) between the two cruises (2009/10 minus 2003).

The observed changes along P06 reflect both natural carbon variations as well as the secular anthropogenic carbon increases. Techniques are being developed to isolate the anthropogenic component of the DIC change. For example, results of a previous reoccupation of the meridional section A16, through the center of the Atlantic Ocean from Iceland to 56°S, show a clear pattern of change in CO_2 inventory between 1989 and 2005. That pattern of change, however, cannot be completely attributed to invasion of anthropogenic CO_2 (Wanninkhof et al. 2010). Concomitant large changes in dissolved oxygen suggest that processes acting on the natural carbon cycle also contribute to ΔDIC. To isolate the anthropogenic CO_2 component (ΔC_{ant}) from ΔDIC, an extended multilinear regression approach was applied along isopycnal surfaces. The change in C_{ant} inventory computed using this approach is shown in Fig. 3.35. The pattern of inventory change is qualitatively similar to the C_{ant} changes in the Atlantic since the start of the industrial era (Lee et al. 2003) with significant changes in storage in the subtropical and subpolar gyres and much smaller changes in the tropical Atlantic. An important difference between the decadal C_{ant} change compared with the total inventory, however, is that the largest accumulation of carbon over the last decade is in the South Atlantic (15°S–56°S, 0.76 mol m^{-2} yr^{-1}) as opposed to the North Atlantic (15°N–62°N, 0.57 mol m^{-2} yr^{-1}). This is opposite of the long-term trend (Fig. 3.32). This difference is attributed to reduced uptake in high northern latitudes and reduced transport of anthropogenic CO_2 northward in the Southern Hemisphere (Quay et al. 2007).

The estimated C_{ant} patterns are generally consistent with changes observed in other anthropogenic tracers (e.g., chlorofluorocarbons and pCO_2) along A16. These other tracers suggest that there is also a very small anthropogenic signal penetrating into the bottom waters (> 3500 m) from the south, but this signal seems to be too small to detect with the extended multilinear regression (eMLR) approach given the current uncertainties of the calculations. Observations and the subsequent approaches to understand the processes driving the observed changes in tracer distributions

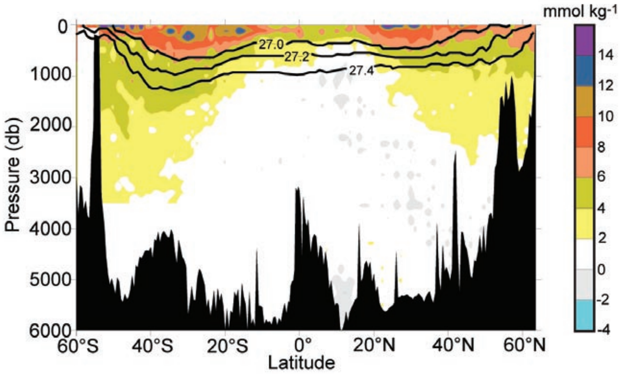

Fig. 3.35. The decadal change in anthropogenic carbon along the A16 transect. For the North Atlantic the change is between 1993 and 2003, and for the South Atlantic it is from 1989 to 2005. The estimated is based on the extended multilinear regression (eMLR) method with separate multilinear regressions (MLRs) determined for each of 23 distinct density ranges. The eMLR-based change in anthropogenic carbon is computed utilizing S, T, AOU, NO$_3^-$, and SiO$_2$ from 2003–05 as input parameters. The solid lines indicate potential density horizons, sigma-0 = 27.0, 27.2, and 27.4 kg m^{-3} (from Wanninkhof et al. 2010).

have the potential to provide a powerful constraint on the global estimates of ocean uptake and storage.

3. Global ocean phytoplankton—D. A. Siegel, M. J. Behrenfeld, S. Maritorena, R. T. O'Malley, and E. Fields

Photosynthesis by phytoplankton in the upper sunlit euphotic layer of the global ocean is the dominant source of organic matter that fuels marine ecosystems. Phytoplankton contribute roughly half of the global (land and ocean) net primary production (NPP; gross photosynthesis minus plant respiration), and phytoplankton carbon fixation is the primary conduit through which atmospheric CO$_2$ concentrations interact with the ocean's organic carbon pools. Phytoplankton productivity depends on the availability of sunlight, macronutrients (e.g., nitrogen and phosphorous), and micronutrients (e.g., iron), and thus is sensitive to climate-driven changes in the delivery of these resources to the euphotic zone.

Since 1997, a near-continuous record of global satellite ocean color observations has been available from the Sea viewing Wide-Field of view Sensor (SeaWiFS; McClain 2009). SeaWiFS observations have enabled investigators to address the relationships among ocean environmental conditions and phytoplankton productivity. The ecosystem property most often derived from ocean color data is surface chlorophyll concentration (Chl). Chl provides a measure of phytoplankton pigments and its variability reflects the combined influences of changes in phytoplankton biomass and its physiological responses to light and nutrient levels (e.g., Falkowski 1984; Behrenfeld et al. 2005). Figure 3.36a shows the SeaWiFS mission mean (October 1997 to November 2010) fields of Chl. Values of Chl span three orders of magnitude globally (0.03 mg m^{-3} to greater than 30 mg m^{-3}) and its spatial patterns mimic large-scale, climatological patterns in Ekman pumping and seasonal convective mixing (Sverdrup 1955; Yoder et al. 1993). Higher values of Chl are found in regions of seasonal deep mixing (e.g., North Atlantic and in the Southern Ocean) and sustained vertical upwelling (e.g., equatorial Atlantic and Pacific Oceans, off California and Peru coasts), while low values are found in the low-nutrient, permanently stratified central ocean gyres.

The SeaWiFS mission is the most consistent satellite ocean color data record ever collected (e.g., McClain 2009; NRC 2011). The entire SeaWiFS dataset has recently been reprocessed and its performance has been rigorously validated against at-sea observations (http://oceancolor.gsfc.nasa.gov/WIKI/OCReproc20100SW.html and links therein). Figure 3.36b shows the natural log (ln)-transformed Chl anomalies for the year 2010. These are calculated as the difference between monthly data for 2010 and the long-term monthly climatology and are averaged over the year 2010. Log transformations are commonly used to interpret data that vary over many orders of magnitude, and differences in ln (Chl) can be interpreted as the difference in Chl normalized by its mean value, or simply a percentage change (Campbell 1995; Boyce et al. 2010). Annual means are calculated as the composite of monthly anomalies of ln(Chl) from December 2009 through the end of November 2010 as the SeaWiFS mission ended on 14 December 2010 (http://oceancolor.gsfc.nasa.gov/forum/oceancolor/topic_show.pl?tid=3897).

Satellite chlorophyll values in 2010 show differences from the long-term mean greater than 40% in many areas (Fig. 3.36b). High Chl anomalies during 2010 occur east of Greenland, in the western equatorial Pacific, and throughout the Southern Ocean south of 55°S. Conspicuously low values of Chl during 2010 were found in the western Indian Ocean, north of Iceland, and in the eastern Atlantic off North Africa. Sea surface temperature variations for the year 2010 (Fig. 3.36c) can be characterized by: (1) a transition from El Niño to La Niña conditions during the summer 2010; (2) the development of a negative Pacific Decadal Oscillation pattern in the North Pacific during the fall/winter of 2010; and (3)

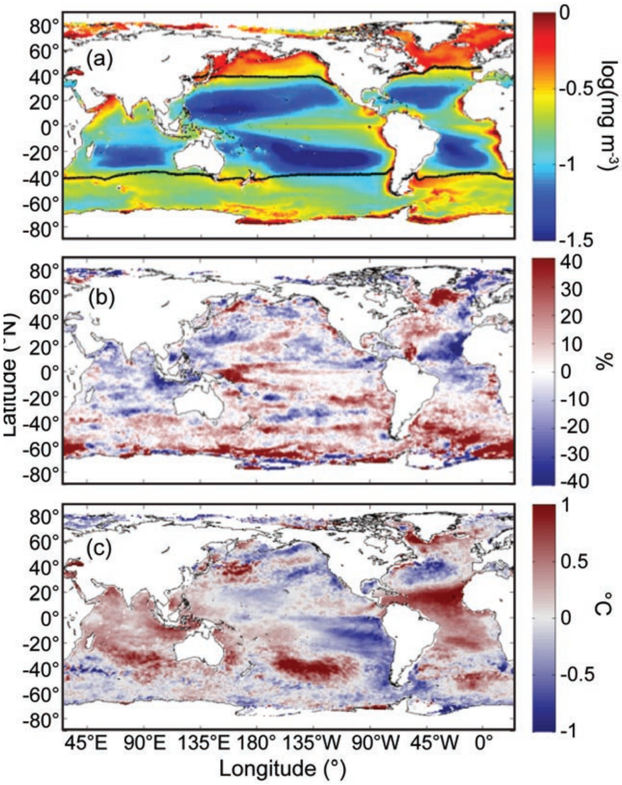

Fig. 3.36. (a) Mean Chl distribution calculated over the entire SeaWiFS record (1 November 1997 to 30 November 2010) in units of log(mg Chl m^{-3}). Also shown is the location of the mean 15°C SST isotherm (black line). Spatial distribution of anomalies for 2010 for (b) the log$_e$(Chl) (units are % difference from monthly mean) and (c) SST anomaly (units are °C). Chl anomalies are calculated using monthly OC4v6 products while SST values are from the MODIS Aqua SST4 product. Anomalies are calculated as differences in the year 2010 from monthly mean distribution for the entire SeaWiFS mission period. SST monthly means are calculated using optimally merged MODIS Aqua/Terra SST4 and AVHRR Pathfinder night-time SST products. All analyses are performed on 1° bins. The year 2010 is defined here as 1 Dec 2009 to 30 Nov 2010 as SeaWiFS ceased operating on 14 Dec 2010.

the development of a tripole SST anomaly pattern in the North Atlantic (as explained in section 3b). As seen by Behrenfeld et al. (2006), increased values of Chl generally correspond to reduced SST (and vice versa), supporting the importance of physical processes regulating global chlorophyll concentrations where changes in SST are a proxy for light, nutrient availability, and other forcing factors. In particular, a horseshoe-shaped positive Chl anomaly is observed centered on the western equatorial Pacific Ocean, indicative of an El Niño to La Niña transition (Fig. 3.36b).

The processing of SeaWiFS data makes extensive use of external standards (lunar views and intense ground efforts) to set sensor gains and offsets, and advanced algorithms to correct satellite signals for the atmospheric path radiance and establish the relationships between ocean reflectance spectra and ocean properties (McClain 2009; Ahmad et al. 2010; NRC 2011). This enables one to assess changes in Chl over its 14 years of operation. Figure 3.37 shows standardized monthly anomalies for ln(Chl) and SST aggregated over (a) the cool region of the Northern Hemisphere (NH) oceans (mean SST < 15°C), (b) the warm ocean (mean SST > 15°C), and (c) the cool region of the Southern Hemisphere (SH) oceans. (Figure 3.36a shows the location of the mean 15°C isotherm.) The sign of the SST standardized anomalies in Fig. 3.37 is flipped to accentuate the correspondence between ln(Chl) and negative SST (-SST). Broad correspondence is observed between ln(Chl) and -SST for the three regions although the only statistically significant (95% confidence interval) correlations are found for the warm ocean region where the mean SST is greater than 15°C ($R^2 = 0.19$; $p = 0.00$). An interesting feature is that the ln(Chl) and –SST anomalies appear to be coherent at low frequencies [i.e., decreases in SST correspond to increases in ln(Chl)], while on higher frequencies (many months to a few years) the cool SH region shows an inverse correlation [i.e., increases in SST correspond to increases in ln(Chl)].

A statistically significant decreasing time trend for ln(Chl) over the length of the SeaWiFS mission is found for the warm ocean region (trend = -0.19% yr^{-1}; p = 0.01; Fig. 3.37b), which corresponds to a significant increasing trend in SST (trend = 0.014°C yr^{-1}; p = 0.00). The opposing signs of these trends are consistent with ideas of a warming ocean reducing nutrient supply to the upper layers, thereby reducing phytoplankton pigment biomass (e.g., Behrenfeld et al. 2006). Significant trends are also found for the cool SH oceans (Fig. 3.37c), but are in the opposite direction compared with the warm ocean. The cool SH oceans show increasing anomalies in ln(Chl) over time (0.82% yr^{-1}; p = 0.00) and a cooling trend in the SST (-0.024°C yr^{-1}; p = 0.00). Significant time trends in ln(Chl) and SST anomalies are not found for the cool NH ocean (Fig. 3.37a).

The regional time trends presented here from the SeaWiFS mission are inconsistent with a recent analysis of centennial-scale Secchi disk and chlorophyll determinations made by Boyce et al. (2010). Boyce and his coauthors show global chlorophyll levels decreasing over the past century at a rate nearly equal to 1% per year (as well as decreasing trends for six of eight regions in their analysis). For the warm ocean, the present trends from SeaWiFS (Fig. 3.37b) are roughly one-fifth of the centennial trends found by Boyce et al. (2010); while for the cool SH ocean, a trend of increasing chlorophyll concentrations is observed (Fig. 3.37c). Obviously, these two ocean Chl trend estimates are not evaluating the same period of time and work is needed to connect these two datasets to make a consistent long-term estimate of change in phytoplankton chlorophyll levels.

The time trends of ln(Chl) and SST are shown on local scales in Fig. 3.38. The correlation coefficient between local anomalies in ln(Chl) and SST is shown in Fig. 3.38a where significantly (95% confidence interval) positive correlations are in red and negative correlations in blue. Sites with insignificant correlation are plotted in gray. The dominant pattern here is the large degree of significant inverse correlation between local-scale ln(Chl) and SST anomalies throughout the warm ocean. Positive local-scale correlations are also found in the cool NH and SH Atlantic Ocean and for the Bering Sea.

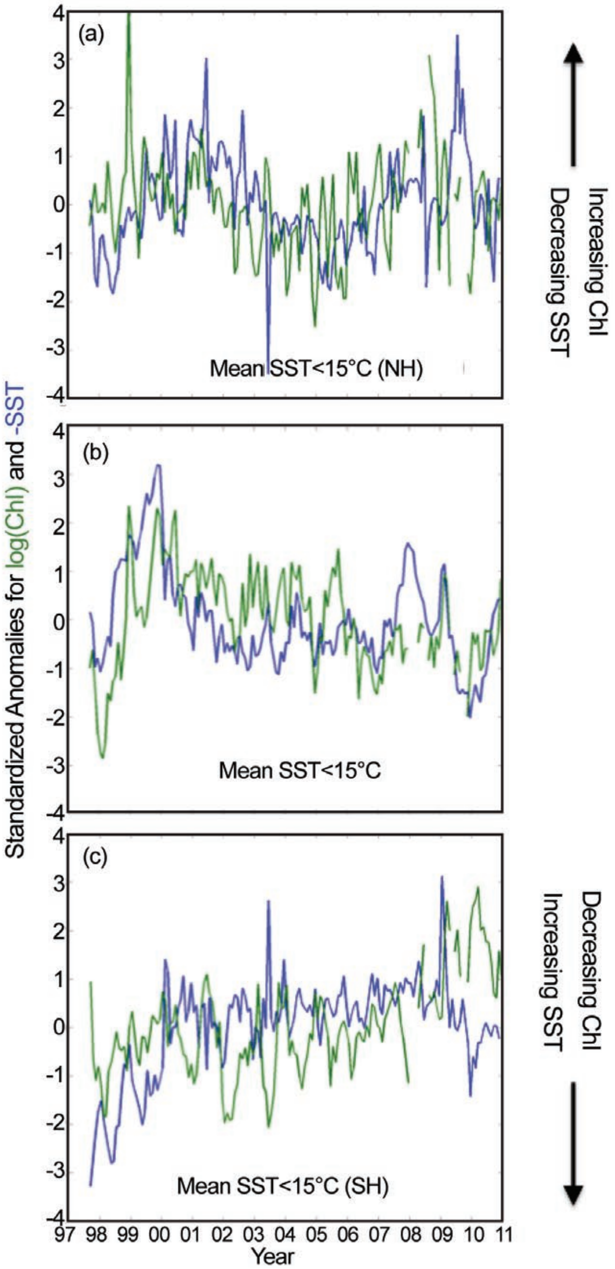

Fig. 3.37. Time series of standardized ln(Chl) (green) and negative SST (blue) monthly anomalies for (a) ocean regions of the Northern Hemisphere where the mean SST < 15°C, b) the warm ocean where mean SST values are greater than 15°C, and (c) regions of the Southern Hemisphere where the mean SST < 15°C. Anomalies are plotted in standardized form (unit variance and zero mean). SST time series are created from optimally merging MODIS Aqua/Terra SST4 and AVHRR Pathfinder products on 1° bins and monthly anomalies are summed over the three regions.

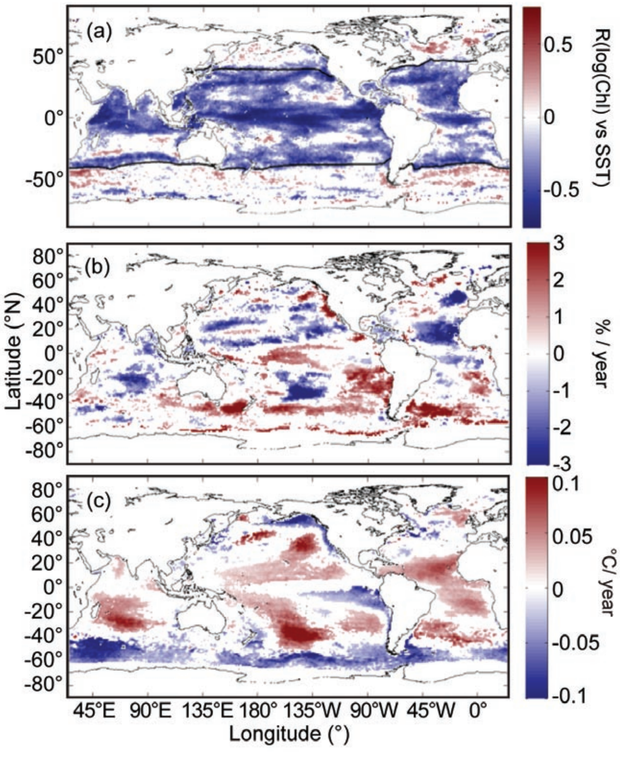

Fig. 3.38. (a) Spatial distribution of the local-scale correlation coefficient (R) between ln(Chl) and SST, (b) local-scale time trends in ln(Chl) anomalies (in % yr^{-1}), and (c) local-scale time trends in SST anomalies (in °C yr^{-1}). Only significant (95% confidence interval) correlations and trends are plotted. Calculations are made over the entire SeaWiFS record (Oct 1997–Dec 2010) and on a local-scale 1° bin in latitude and longitude. Also shown in (a) is the 15°C SST isotherm (black line).

Spatial patterns in local-scale time trends can also be examined. Local-scale trends in ln(Chl) and SST anomalies are shown in Figs. 3.38b and 3.38c, respectively. Here, regions of significantly decreasing Chl values are found throughout the warm oceans and in particular in the tropical Atlantic Ocean (Fig. 3.38b). Values of increasing Chl are found in the southern Atlantic and Pacific Oceans, the tropical Pacific, and for the eastern boundary currents of the Pacific Ocean. Local-scale SST anomaly trends show interesting patterns with significantly increasing SST within the major subtropical gyres and decreasing SST within the Southern Ocean, in the eastern Pacific, and the Gulf of Alaska (Fig. 3.38c). Clearly, the aggregated trends shown in Fig. 3.37 have many local-scale nuances and demonstrate the importance of global observations for assessing long-time changes in the oceans.

This section has focused on addressing changes seen from the SeaWiFS climate data record. The loss of this satellite, and hence the data record, creates a huge hole in observing capability and leaves open the question of how to bridge existing satellite datasets to make consistent long-term records of ocean biological properties (Siegel and Franz 2010; NRC 2011). Both NASA's MODIS Aqua and ESA's MERIS sensors are global missions and are operating well; fortunately, similar patterns in Chl are seen with MODIS Aqua observations. However SeaWiFS data were an important part of the calibrations for MODIS Aqua (see http://oceancolor.gsfc.nasa.gov/REPROCESSING/R2009/modisa_calibration) and MERIS is now being reprocessed and going through a vicarious calibration with ground data. At this point, the continuation of the climate data record initiated by SeaWiFS is not fully guaranteed as current sensors are aging and issues exist with its identified successors (e.g., NRC 2011).

4. THE TROPICS—H. J. Diamond, Ed.

a. Overview—H. J. Diamond

The year was characterized by a strong El Niño at the beginning of the year, followed by a transition to La Niña conditions in the middle part of the year, and then finally to a moderate-to-strong La Niña by the end of the year. By November, the equatorial cold tongue had intensified significantly, and the Oceanic Niño Index (ONI) dropped to -1.4°C, as the area of sea surface temperature (SST) anomalies colder than -1.0°C expanded westward to cover the entire central and east-central equatorial Pacific.

Overall, global tropical cyclone (TC) activity during 2010 was well-below average, with the lowest number of named storms globally (70) in the last 33 years. Only one basin, the North Atlantic, experienced above-normal activity. This was also the most active season, and the only hyperactive season, on record in the North Atlantic to have no hurricane landfalls in the United States. On the other hand, eastern Canada experienced one of its most active TC seasons on record, as documented in Sidebar 4.1.

This chapter consists of seven sections: (1) El Niño-Southern Oscillation (ENSO) and the Tropical Pacific; (2) Tropical Intraseasonal Activity; (3) seasonal TC activity in the seven TC basins: the North Atlantic, Eastern North Pacific, Western North Pacific, North Indian and South Indian Oceans, Southwest Pacific, and Australia; (4) Tropical Cyclone Heat Potential, which aids in summarizing the section for TCs from an ocean heat perspective; (5) Intertropical Convergence Zone (ITCZ) behavior in the Pacific and Atlantic basins; and (6) the Indian Ocean Dipole (IOD). A new section detailing the Atlantic Multidecadal Oscillation (AMO) has been added to complement some of the other work related to ENSO, the IOD, and the Madden-Julian Oscillation (MJO).

b. ENSO and the Tropical Pacific—G. D. Bell, M. Halpert, and M. L'Heureux

1) Oceanic Conditions

El Niño and La Niña represent opposite phases of the El Niño-Southern Oscillation (ENSO), a coupled ocean-atmosphere phenomenon centered in the equatorial Pacific Ocean. NOAA's Climate Prediction Center (CPC) classifies El Niño and La Niña episodes using the Niño-3.4 index, which reflects area-averaged sea surface temperature (SST) anomalies in the east-central equatorial Pacific between 5°N–5°S and 170°W–120°W.

For historical purposes, the CPC classifies an El Niño (La Niña) episode when the three-month running mean value of the Niño-3.4 index (called the Oceanic Niño Index, ONI) is greater (less) than or equal to +0.5°C (-0.5°C) for five consecutive overlapping months. A time series of the Niño-3.4 index indicates that both El Niño and La Niña occurred during 2010 (Fig. 4.1), with El Niño during January–April and La Niña from July through the end of the year.

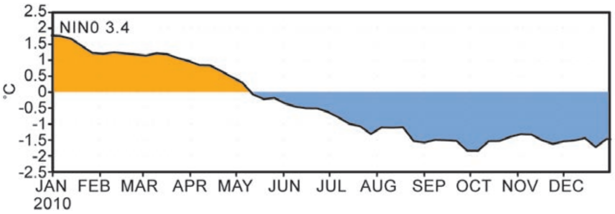

Fig. 4.1. Time series of weekly sea surface temperature anomalies (°C) in the Niño-3.4 region (5°N–5°S, 170°–120°W). Anomalies are departures from the 1971–2000 weekly adjusted OISST climatology of Smith and Reynolds (1998).

A strong El Niño[1] was present during December 2009–February 2010 (DJF), as indicated by an ONI of +1.7°C. During this period, exceptionally warm SSTs (≥ 29°C) extended across the east-central equatorial Pacific, and the warmest SSTs in the entire Pacific basin were located east of the International Date Line (hereafter date line) instead of in their normal position north of Papua New Guinea (Fig. 4.2a). Equatorial SST anomalies during this period exceeded +1°C across most of the Pacific Ocean east of the date line (Fig. 4.2b). During March–May (MAM), El Niño became a weak event as the region of warmest SSTs retracted to well west of the date line (Fig. 4.2c) and the SST anomalies decreased across the eastern half of the equatorial Pacific (Fig. 4.2d).

During June–August (JJA), the equatorial Pacific continued to cool east of the date line, and an anomalously strong cold tongue became established (Figs. 4.2e,f). The resulting SST anomalies reflected the development of a weak La Niña[2], as the ONI dropped to -0.6°C. During September–November (SON), La Niña was a moderate-strength event as the ONI dropped to -1.4°C and the equatorial cold tongue intensified and expanded westward (Fig. 4.2g). The area of SST anomalies colder than -1.0°C also expanded

---

[1] The CPC unofficially uses an ONI ≥ +1.5°C to classify a strong El Niño. They classify a moderate strength El Niño by an ONI of +1.0°C to +1.4°C, and a weak El Niño by an ONI of +0.5°C to +0.9°C.

[2] CPC unofficially classifies a weak La Niña by an ONI of -0.5°C to -0.9°C, and a moderate strength La Niña by an ONI of -1.0°C to -1.4°C. A strong La Niña is unofficially classified by an ONI ≤ -1.5°C.

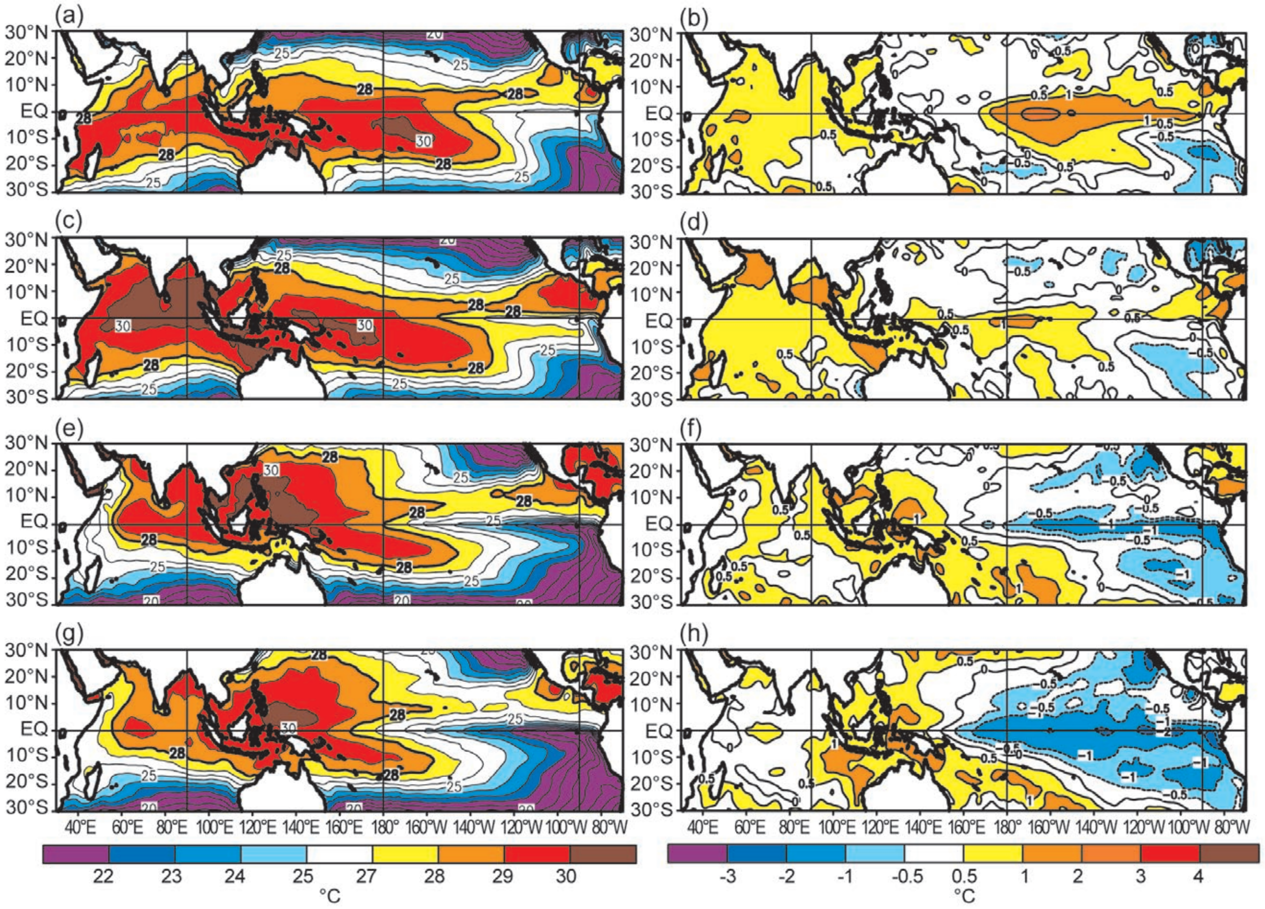

Fig. 4.2. Seasonal SST (left) and anomaly (right) for (a, b) DJF 2009/10, (c, d) MAM 2010, (e, f) JJA 2010 and (g, h) SON 2010. Contour interval for total (anomalous) SST is 1°C (0.5°C). Anomalies are departures from the 1971–2000 seasonal adjusted OISST climatology of Smith and Reynolds (1998).

westward to cover the entire central and east-central equatorial Pacific (Fig. 4.2h).

The subsurface thermal structure is a critical feature of ENSO. As seen during DJF, El Niño featured a deep layer of anomalously warm ocean temperatures east of the date line (Fig. 4.3a), in association with a deeper-than-average thermocline in the central and eastern equatorial Pacific. During MAM, the total volume of anomalously warm water decreased substantially across the eastern half of the equatorial Pacific and the anomalously warm water became confined to the near surface (Fig. 4.3b). This evolution reflected a shoaling of the oceanic thermocline and signified the imminent demise of El Niño.

During JJA and SON, the subsurface thermal structure reflected a markedly increased east-west slope of the oceanic thermocline, which is consistent with La Niña's formation and intensification (Figs. 4.3c,d). This structure reflected a shallower-than-normal thermocline and a deep layer of negative subsurface temperature anomalies in the east-central and eastern Pacific. It also reflected a deeper-than-normal thermocline and positive subsurface temperature anomalies in the western Pacific. By SON, the thermocline in the eastern Pacific had reached the surface and was approximately 120 m shallower than observed earlier in the year in association with El Niño.

2) Atmospheric Circulation: Tropics

El Niño and La Niña both impacted the atmospheric circulation and patterns of tropical convection during 2010, in a manner consistent with past episodes (Chelliah and Bell 2004). As seen during DJF, a key atmospheric component of El Niño is a reduced strength of the normal tropical easterly trade winds (i.e., westerly anomalies) east of the date line (Fig. 4.4a). This wind pattern contributed to a reduction in upwelling and to an anomalous eastward transport of warm water from the western Pacific, both of which strengthened El Niño.

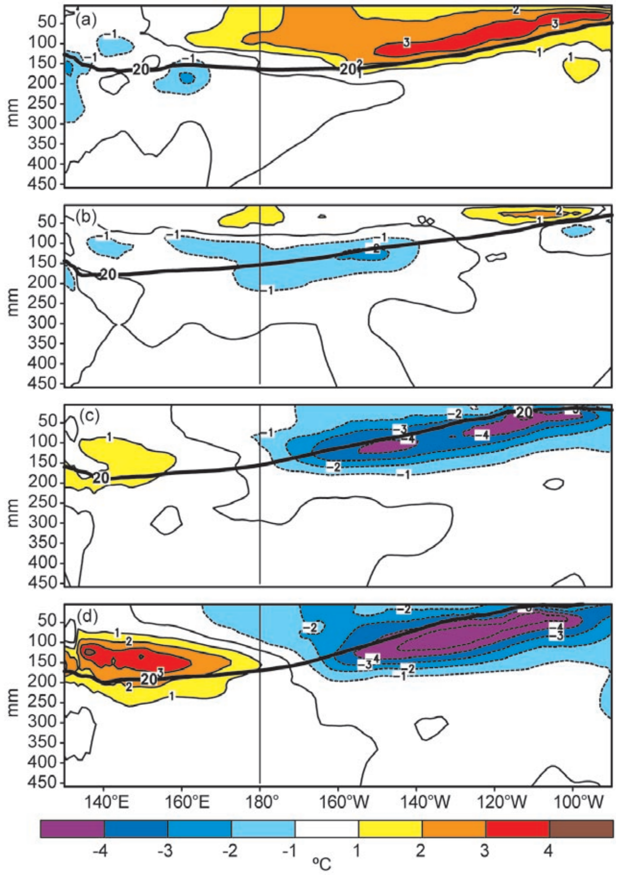

Fig. 4.3. Equatorial depth-longitude section of ocean temperature anomalies (°C) averaged between 5°N and 5°S during (a) DJF 2009/10, (b) MAM 2010, (c) JJA 2010, and (d) SON 2010. The 20°C isotherm (thick solid line) approximates the center of the oceanic thermocline. The data are derived from an analysis system that assimilates oceanic observations into an oceanic global circulation model (Behringer et al. 1998). Anomalies are departures from the 1971–2000 period monthly means.

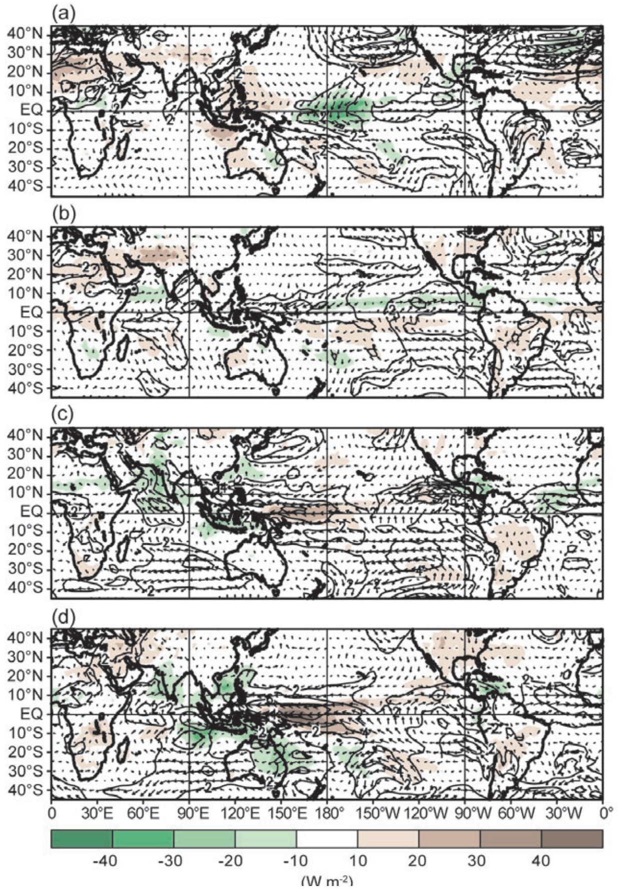

Fig. 4.4. Anomalous 850-hPa wind vector and speed (contours, m s^{-1}) and anomalous outgoing longwave radiation (shaded, W m^{-2}) during (a) DJF 2009/10, (b) MAM 2010, (c) JJA 2010, and (d) SON 2010. Anomalies are departures from the 1979–95 period monthly means.

During this period, convection was enhanced (green shading) over the central and east-central equatorial Pacific, and suppressed (brown shading) over the western Pacific and Indonesia. At 200 hPa, these conditions resulted in anticyclonic circulation anomalies in the subtropics of both hemispheres flanking the region of enhanced convection, and cyclonic circulation anomalies in both hemispheres flanking the region of suppressed convection (Fig. 4.5a). Collectively, the above conditions reflect a weakening of the equatorial Walker circulation, along with an anomalously weak (strong) Hadley circulation over the western (central) Pacific.

El Niño's weakening during MAM was associated with two main changes in the low-level winds (Fig. 4.4b). First, the trade winds became enhanced west of the date line, which acted to transport exceptionally warm water toward the western Pacific. Second, an anomalously strong cross-equatorial flow became established over the east-central equatorial Pacific, which resulted in increased upwelling and cooler sea surface and subsurface temperatures in that region.

La Niña's development and intensification during JJA and SON was associated with a further strengthening of the anomalous easterly trade winds across the western tropical Pacific and with an expansion in the area of anomalous cross-equatorial flow to cover the entire eastern half of the equatorial Pacific (Figs. 4.4c,d). Consistent with this evolution, equatorial convection became suppressed across a large area west of the date line, and enhanced over Indonesia and the eastern Indian Ocean. These conditions are typical of La Niña and reflected an enhanced equatorial Walker circulation and a suppressed Hadley circulation over the central Pacific.

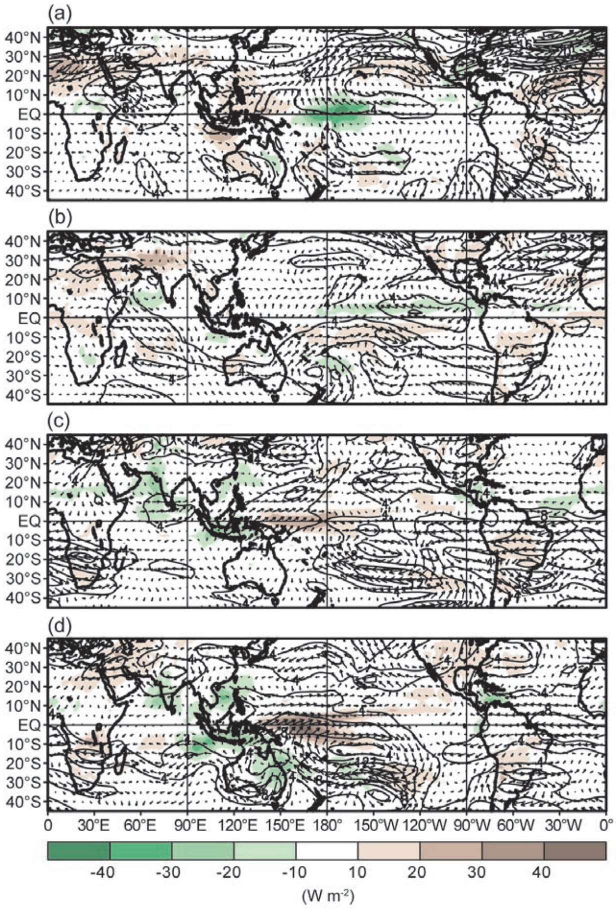

FIG. 4.5. Anomalous 200-hPa wind vector and speed (contours, m s^{-1}) and anomalous outgoing longwave radiation (shaded, W m^{-2}) during (a) DJF 2009/10, (b) MAM 2010, (c) JJA 2010, and (d) SON 2010. Anomalies are departures from the 1979–95 period monthly means.

As a result, La Niña impacts on the upper-level circulation were seen across the tropical and subtropical Pacific in both seasons (Figs. 4.5c,d). These impacts included the development and strengthening of cyclonic circulation anomalies in the subtropics of both hemispheres, in association with the region of suppressed convection. In both seasons, the resulting downstream easterly wind anomalies extended across the eastern North Pacific and Caribbean Sea, which acted to: (1) reduce the vertical wind shear and enhance the Atlantic hurricane season (section 4d2) and (2) increase the vertical wind shear and suppress hurricane activity in both the Central and Eastern North Pacific hurricane basins (section 4d3).

3) ATMOSPHERIC CIRCULATION: EXTRATROPICS

As seen during DJF, El Niño was associated with an eastward extension of deep tropical convection and deep tropospheric heating to well east of the date line, resulting in an eastward extension of the subtropical ridges in both hemispheres. The wintertime East Asian jet stream, which is intrinsically linked to the poleward flank of the subtropical ridge, also extended eastward to span the entire Pacific basin. Likewise, the associated jet exit region (and therefore the main cyclogenesis region) shifted eastward to the area immediately upstream of the southwestern U.S. (Fig. 4.6, shading).

These observations highlight key jet-like features of the El Niño-related anomalous anticyclonic circulation over the east-central Pacific. These features include: (1) an anomalous westerly jet core along its northern flank (near 30°N between the date line and the western U.S.), which coincides with the observed East Asian jet axis; (2) anomalous southwesterly winds and speed acceleration (solid contours) along its western flank near the date line, which represent the anomalous jet entrance region; and (3) anomalous northwesterly winds and speed deceleration (dashed contours) along its eastern flank over the eastern Pacific, which capture the anomalous jet exit region.

Consistent with the above conditions, the Pacific storm track was shifted well south and east of normal during DJF, resulting in increased storminess and above-average precipitation across the southern U.S. Also, the 500-hPa Hudson Bay trough was weaker than average and the trough over the southeastern U.S. was stronger than average (see Fig. 8.2). As a result, a more zonally-uniform distribution of both temperature and winds, which is characteristic of El Niño, prevailed across the Pacific basin and much of North America.

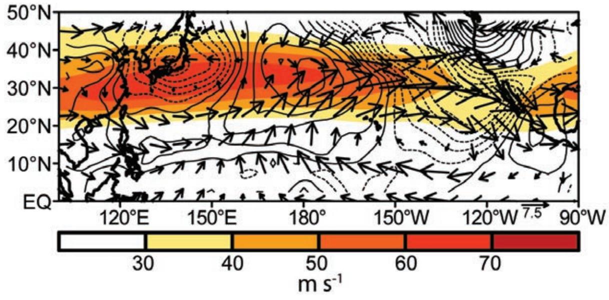

FIG.4.6. DJF 2009/10: Total 200-hPa wind speed (m s^{-1}, shaded), anomalous wind vector, and anomalous horizontal wind speed tendency (d/dt) (contours, interval is 1 x 10^{-4} m s^{-2}). Solid (dashed) contours show anomalous speed acceleration (deceleration), where

$$dV_a/dt = (-V\bullet\nabla Z) - (-V_c\bullet\nabla Z_c)$$

where V is the observed total vector wind, Z is the observed total geopotential height, and the subscript "c" denotes the climatological mean values. Anomalies are departures from the 1971–2000 period monthly means. Vector scale is shown at bottom right.

Later in the year, La Niña affected the extratropical circulation over the South Pacific basin. For example, the cyclonic anomalies over the central subtropical South Pacific during SON reflected a strengthening of the normal mid-Pacific trough, and a westward retraction of the subtropical ridge axis to the extreme western Pacific (Fig. 4.5d). These conditions were associated with easterly 200-hPa wind anomalies across the central Pacific near 30°S, which coincided with the exit region of the South Pacific jet core and therefore reflected a weakening and westward retraction of that jet to west of the date line.

4) ENSO Temperature and Precipitation Impacts

During DJF 2009/10, the precipitation patterns typically associated with El Niño (Ropelewski and Halpert 1987) were observed over parts of the world. These included above-average precipitation over the central equatorial Pacific, the southern U.S., southeastern South America, and equatorial eastern Africa (see Fig. 8.1). They also included below-average precipitation over Indonesia, parts of the Amazon Basin, and southeastern Africa.

Typical El Niño-related temperature impacts during DJF included warmer-than-average conditions over southeastern Asia, Canada, and southeastern Brazil, and cooler-than-average conditions across the southern United States. In the U.S., the temperature and precipitation patterns were also modulated by a strong negative phase of the Arctic Oscillation (AO) and North Atlantic Oscillation (NAO), which favored exceptionally cool conditions across much of the country and contributed to a series of heavy snowfall events along the east coast (see section 7b2 and Sidebar 7.1 for more details).

La Niña impacted global precipitation patterns during JJA and SON in a manner consistent with past cold episodes (Ropelewski and Halpert 1989). These impacts included suppressed convection across the central equatorial Pacific, coupled with above-average rainfall across much of the Maritime Continent (Indonesia, Philippines, Malaysia, and Borneo). La Niña impacts during SON also included below-average precipitation in southeastern South America, and above-average rainfall across eastern Australia (see Fig. 8.7).

c. Tropical Intraseasonal Activity—J. Gottschalck, G. D. Bell, and S. Weaver

The Madden-Julian Oscillation (MJO) (Madden and Julian 1971, 1972, 1994) is a leading climate mode of tropical convective variability that occurs on intraseasonal timescales. The convective anomalies associated with the MJO often have the same spatial scale as ENSO, but differ in that they exhibit a distinct eastward propagation. If the MJO remains active, convective anomalies at a given location repeat approximately every 30–60 days on average. The MJO can strongly affect the tropical and extratropical atmospheric circulation patterns, and may produce short-lived ENSO-like convective anomalies across the tropics (Mo and Kousky 1993; Kousky and Kayano 1994; Kayano and Kousky 1999) .The MJO is often quite variable in a given year, with periods of moderate-to-strong activity sometimes followed by little or no activity. Overall, the MJO tends to be most active during neutral and weak ENSO periods, and is often absent during strong El Niño events (Hendon et al. 1999; Zhang and Gottschalck 2002; Zhang 2005).

The MJO is seen by continuous eastward propagation of 200-hPa velocity potential anomalies around

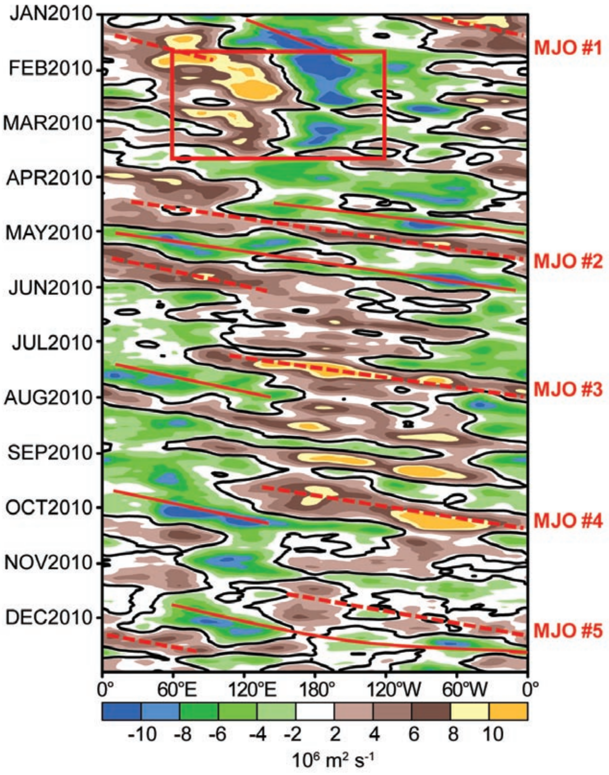

Fig. 4.7. Time-longitude section for 2010 of anomalous 200-hPa velocity potential (x 10^6 m^2 s^{-1}) averaged between 5°N and 5°S. For each day, the period mean is removed prior to plotting. Green (brown) shading highlights likely areas of anomalous divergence and rising motion (convergence and sinking motion). Red lines and labels highlight the main Madden Julian Oscillation episodes. Anomalies are departures from the 1971–2000 base period daily means.

the globe. A time-longitude section of this parameter shows five MJO episodes during 2010 (Fig. 4.7). These include: (1) a strong episode that continued from late 2009 into early February 2010 (MJO #1); (2) a moderate-strength episode with higher frequency during April and May (MJO #2); (3) a moderate-strength but short-lived episode during July and also during September–October (MJO #3 and #4); and (4) a generally weak and short-lived episode during mid-November to mid-December (MJO #5).

The first MJO (MJO #1) featured strong convective anomalies that propagated eastward and became in phase with those associated with El Niño. The observations suggest that this evolution likely aided the development of more persistent and stationary El Niño-related convective anomalies during late January through early March, as highlighted in the red box in Fig. 4.7 by suppressed convection over Indonesia and enhanced convection near the date line. Prior to this, the El Niño-related enhanced convection was more sporadic over the central equatorial Pacific.

Also associated with MJO #1 were strong low-level westerly wind anomalies (not shown) within and to the rear of the main area of enhanced convection. The resulting westerly wind burst triggered a downwelling oceanic Kelvin wave (Fig. 4.8, dashed line). This wave formed over the western equatorial Pacific in late January and reached the South American coast in late March and early April. Oceanic warming associated with this wave likely contributed to the apparent intensification of El Niño. This was the only appreciable downwelling oceanic Kelvin wave of the year.

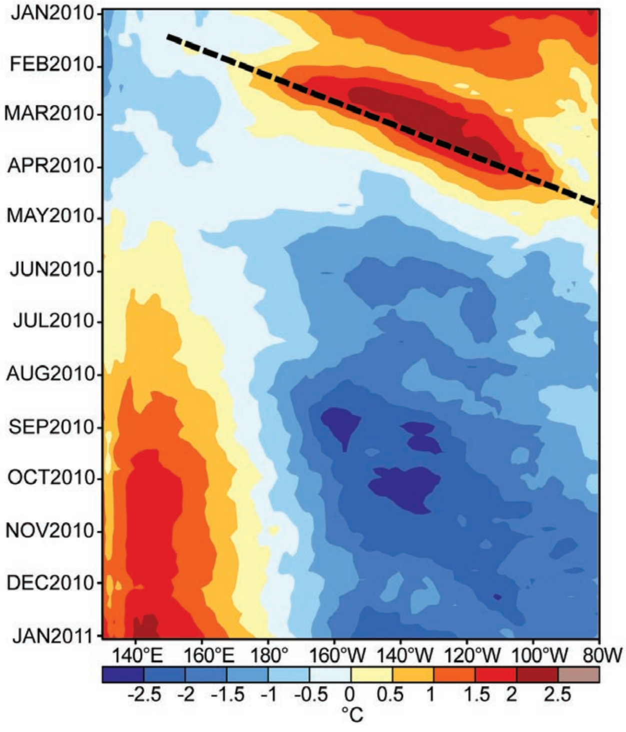

Fig 4.8. Time-longitude section for 2010 of the anomalous upper ocean (0 m–300 m) heat content averaged between 5°N and 5°S. Blue (yellow/red) shading indicates below (above) average heat content. The downwelling phases (dashed lines) of equatorial oceanic Kelvin waves are indicated. Anomalies are departures from the 1982–2004 base period pentad means.

The moderate-strength MJO activity during April and May (MJO #2) had a shorter periodicity (approximately 30 days) than that observed earlier in the year. Short-lived, moderate-strength MJO activity was also observed during July (MJO #3). Following this event, the intraseasonal variability during August and much of September primarily reflected higher frequency atmospheric Kelvin wave activity (Wheeler and Kiladis 1999; Wheeler and Weickmann 2001).

The two remaining MJO events (MJO #4 and #5) were characterized by enhanced convection that was primarily limited to Indonesia and to the western Pacific across the South Pacific Convergence Zone (SPCZ). This off-equatorial displacement of the convective anomalies was primarily a result of La Niña, which contributed to above-average sea surface temperatures in the SPCZ region and to much-below-normal sea surface temperatures across the equatorial Pacific Ocean.

d. Tropical Cyclones

1) Overview—H. J. Diamond and B. C. Trewin

The global tallying of total tropical cyclone (TC) numbers is challenging and involves more than simply adding up basin totals because some storms cross basin boundaries, some basins overlap, and multiple agencies are involved in tracking and forecasting TCs. Compiling the activity over all seven TC basins, the 2010 season (2009/10 in the Southern Hemisphere) saw a well-below-normal (1981–2009 base) number of named storms [NS; wind speeds ≥ 34 kts (17.5 m s^{-1})] and a below-average number of hurricanes/typhoons/cyclones [HTC; ≥ 64 kts (32.9 m s^{-1})] and major HTCs [≥ 96 kts (49.4 m s^{-1})]. Globally, 70 named storms[3] developed during the 2010 season (global average is 86.5), with 42 becoming HTCs (global average is 45.4). Of these, 22 (compared to 26 in 2006, 18 in 2007, 20 in 2008, and 16 in 2009) attained major/intense status

---

[3] It should be noted that in the Western North Pacific there were an additional five unnamed tropical depressions recorded by the Japan Meteorological Agency that were not included in this total.

(global average is 21.9). Therefore, while overall NS count was well-below average, the number of major/intense storms was near the global average[4].

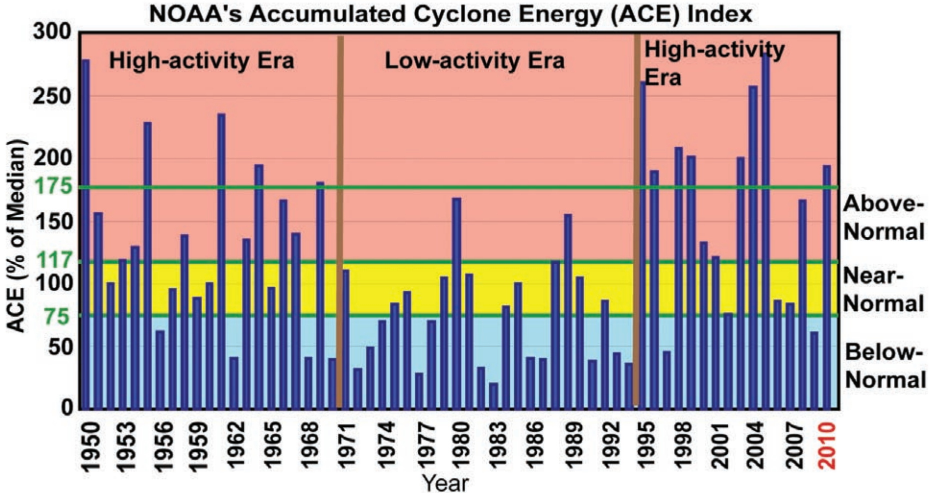

Fig. 4.9. NOAA's Accumulated Cyclone Energy (ACE) Index in the Atlantic Basin expressed as percent of the 1950–2000 median value (87.5×10^4 kt^2). The ACE is a wind energy index that measures the combined strength and duration of the named storms. ACE is calculated by summing the squares of the six-hourly maximum sustained wind speed (measured in knots) for all periods while the named storm has at least tropical storm strength. Pink, yellow, and blue shadings correspond to NOAA's classifications for above-, near- and below-normal seasons, respectively. The 175% threshold for a hyperactive season is indicated. Vertical brown lines separate high-activity and low-activity eras.

Globally, the 2009/10 season featured the fewest number of NSs since the 2006/07 season (84). However, while the total number of NSs was less than the 2006/07 season, it is interesting to note that the total number of HTCs (42) was nearly the same as in 2006/07 (43). Historically, NS records are incomplete in all basins, especially prior to the beginning of reasonably comprehensive satellite coverage around 1970. Based on the International Best Tracks Archive for Climate Stewardship (IBTrACS) dataset (Knapp et al. 2010), the 2009/10 global NS total was the third lowest since 1970 and only slightly above the record low of 63 NSs observed during the 1976/77 season. Focusing only on the January–December calendar year, 2010 featured the lowest number of NSs (67) since 1970. The previous record-low NS activity in any calendar year was 68, observed in both 1976 and 1977.

The 2009/10 seasonal total of 70 TCs thus nearly equals the most inactive season globally since 1976/77 when there were 63 storms globally. No year in recent times has approached the 2010 seasonal low; the last sub-75 storm season was 1987/88 (73), and the last sub-80 storm season was 1994/95 (78). It was a particularly exceptional record-low season in the North Pacific. The northwest Pacific had its most inactive year since satellite records began, while the northeast Pacific equaled its record low. The 22 named storms across the two basins were less than half the usual number in what are normally the world's most active tropical cyclone regions. Activity in the North and South Indian Ocean was also substantially below normal, while the southwest Pacific was close to normal. Conversely, the Atlantic basin produced 19 NSs, well exceeding the long-term average of 11. In the southwest Pacific, NS activity during 2010 was near normal. However, the latter part of the hurricane season in this region was extremely active, producing three Category 4 TCs and one Category 5 TC. These storms resulted in a total of 14 fatalities and produced a minimum estimated damage of $163 million (U.S. dollars). Scaling these numbers for a region as sparsely populated and undeveloped as the southwest Pacific, these are actually very large totals.

2) Atlantic Basin—G. D. Bell, E. S. Blake, T. B. Kimberlain, C. W. Landsea, J. Schemm, R. J. Pasch, and S. B. Goldenberg

(i) 2010 Seasonal Activity

The official Atlantic hurricane season lasts from June through November, with August–October (ASO) typically being the peak months of the season. The 2010 Atlantic hurricane season produced 19 NSs, of which 12 became hurricanes and 5 became major hurricanes. All but two NSs formed during ASO. The 1950–2000 seasonal averages are 11 named storms[5],

---

[4] Global averages are calculated from the International Best Tracks Archive for Climate Stewardship dataset at http://www.ncdc.noaa.gov/oa/ibtracs/.

[5] Landsea et al. (2010) indicate that because of improved monitoring and analysis of weak, short-lived tropical cyclones in the last decade, the climatological averages since 1950 may be biased low by about two tropical storms per year, giving a more realistic climatology value of about 13 named storms per year.

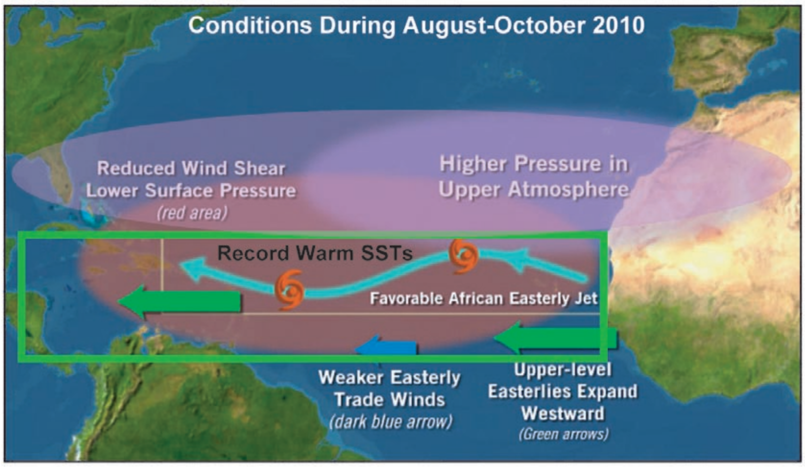

Fig. 4.10. Schematic depiction of atmospheric and oceanic conditions over the Atlantic basin during August–October 2010. Green box denotes the Main Development Region (MDR).

six hurricanes, and two major hurricanes. The IBTrACS 1980–2009 seasonal averages are 12.2 NSs, 6.6 hurricanes, and 2.7 major hurricanes.

The 2010 seasonal Accumulated Cyclone Energy (ACE) value (Bell et al. 2000) was 166.3 x 10^4 kt^2, which corresponds to 190% of the 1950–2000 median value (Fig. 4.9). This places 2010 as the 10th most active season since 1950. This year also marks the ninth hyperactive season (ACE ≥ 175% of the median) since the high activity era for Atlantic hurricanes began in 1995 (Goldenberg et al. 2001). By comparison, no hyperactive seasons occurred during the preceding 24-year period (1971–94), which is a low activity era in the Atlantic Basin.

As is typical of very active seasons, conditions for tropical cyclone formation and intensification during 2010 were exceptionally conducive within the Main Development Region (MDR), which encompasses the Caribbean Sea and tropical Atlantic Ocean between 9.5°N and 21.5°N (Fig. 4.10). Most (14 of 19) named storms formed in the MDR, accounting for 10 of 12 hurricanes, all five major hurricanes, and 93% of the seasonal ACE value.

(ii) Storm Tracks and Landfalls

The Atlantic storm tracks during 2010 were generally divided into two clusters. One cluster comprised eight storms that formed over the eastern tropical Atlantic. Five of these eventually became hurricanes (four became major hurricanes) and three remained tropical storms. The majority of these storms (six of eight) tracked northwestward and then recurved out to sea. Two (Earl and Igor) struck Nova Scotia and Newfoundland, respectively (see Sidebar 4.1 for more detailed information on the 2010 Atlantic hurricane season impacts on Canada). This landfall ratio (25%) is close to the historical probability (29%) for a North America landfall by storms forming over the eastern Atlantic (Kossin et al. 2010).

The second cluster of storm tracks consisted of 11 systems that formed over or near the Caribbean Sea. This region typically sees significantly increased hurricane activity during hyperactive seasons. Many of

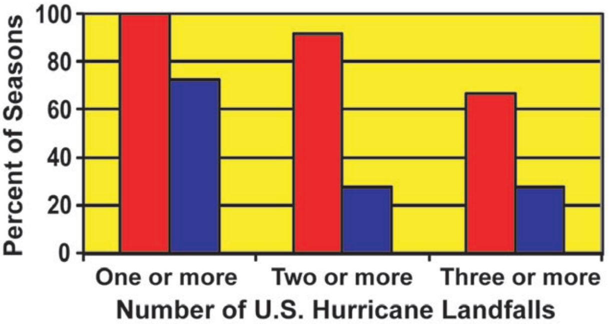

Fig. 4.11. Seasonal frequency of Atlantic basin hurricanes making landfall in the United States (during 1950–2009) for hyperactive seasons (red bars) and for above-normal seasons that are not hyperactive (blue bars). Landfalls are based on the HURDAT data produced by the National Hurricane Center and compiled by Blake et al. (2007). Only one U.S. hurricane landfall per storm is counted.

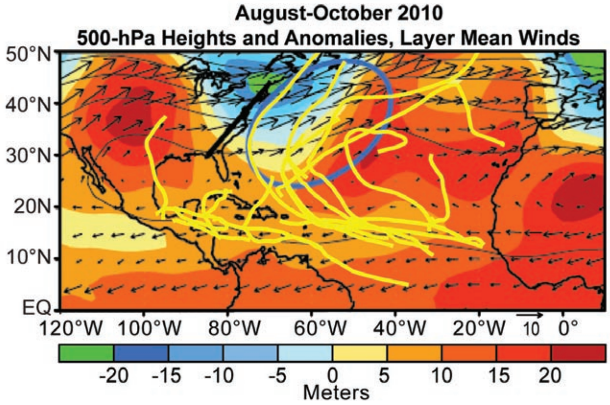

Fig. 4.12. Map of August–October 2010 500-hPa heights (contours, m) and anomalies (shading), and layer mean vector wind (m s^{-1}) between 600 hPa and 300 hPa. Vector scale is located at bottom right. Thick solid line indicates weakness in upper-level ridge and blue circle indicates extensive southwesterly flow over the western Atlantic. August–October 2010 Atlantic named storm tracks are shown in yellow.

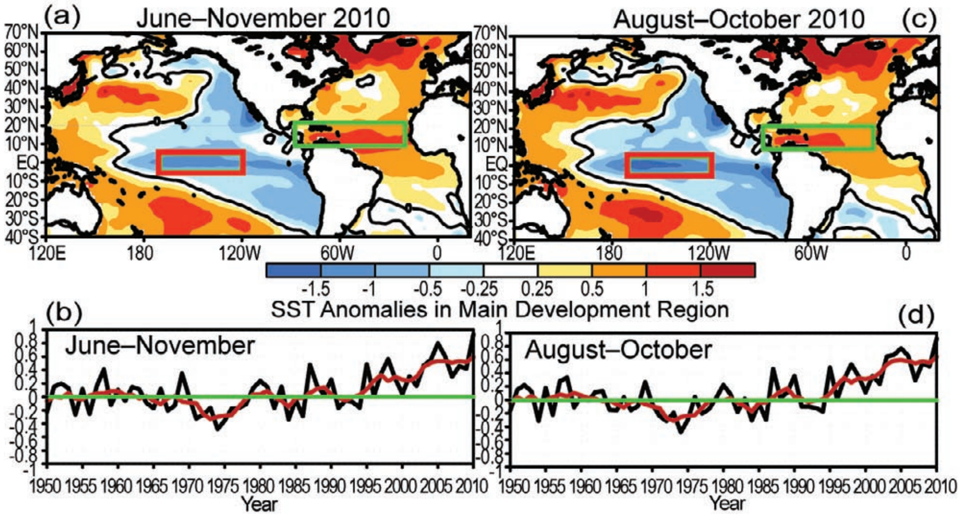

Fig. 4.13. (Top) Sea surface temperature (SST) anomalies (°C) during (a) June–November 2010 and (c) August–October 2010. (Bottom) Time series of consecutive area-averaged SST anomalies in the Main Development Region (MDR) during (b) June–November, and (d) August–October. Red line shows the corresponding five-year running mean. Green boxes in (a) and (c) denote the MDR. Anomalies are departures from the ERSST-V3b (Smith et al. 2008) 1971–2000 period monthly means.

these storms during 2010 formed near land over the western Caribbean/Mexico/Central America region. Five systems in this second cluster made landfall as tropical storms, three made landfall as Category 1–2 hurricanes, and one made landfall as a major hurricane (Category 3–5). It is atypical for above-normal seasons to have no NSs in the northern Gulf of Mexico. However, no NSs tracked over this region during 2010, meaning minimal adverse affects on the oil well capping and associated cleanup efforts associated with the Deepwater Horizon accident.

The U.S. also did not experience any landfalling hurricanes during 2010. This was the most active season—and the only hyperactive season—on record with no U.S. hurricane landfalls. For the 12 hyperactive seasons that occurred during 1950–2009, each produced at least one U.S. landfalling hurricane and 90% produced at least two U.S. landfalling hurricanes (Fig. 4.11, red bars). This rate of multiple hurricane landfalls is more than triple that (25%) associated with other above-normal seasons that were not hyperactive (blue bars).

The lack of U.S. hurricane landfalls during 2010 can be attributed to several factors. First, there was a pronounced weakness over the eastern U.S. in the extensive subtropical ridge that otherwise extended from Africa to the southwestern U.S. (Fig. 4.12). This weakness reflected mean troughing near the U.S. East Coast, and was associated with midlevel southwesterly flow that steered all approaching hurricanes away from the United States. Second, no hurricanes formed or tracked over the central and northern Gulf of Mexico, which can be attributed in part to the enhanced subtropical ridge over the Caribbean Sea. This ridge prevented storms over this region from propagating northward into the central Gulf. Third, some storms formed and remained over the extreme eastern tropical Atlantic throughout their life.

(iii) Atlantic sea surface temperatures

Mean sea surface temperatures (SSTs) in the MDR

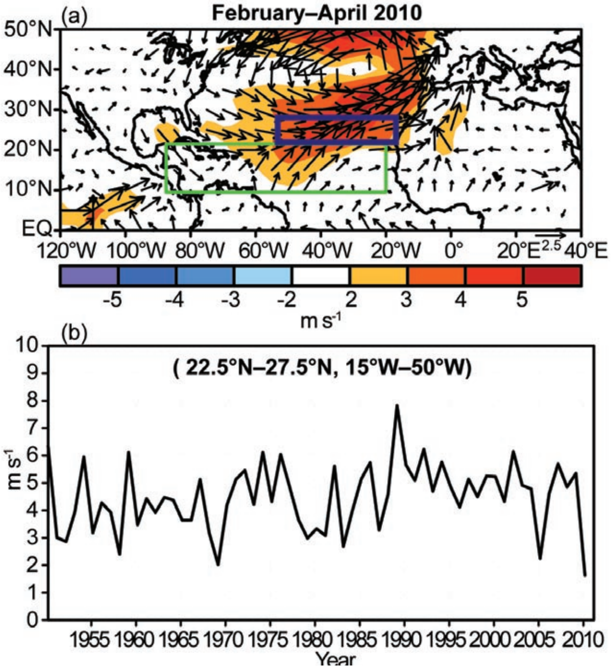

Fig. 4.14. (a) Map of February–April 2010 1000-hPa anomalous wind speed (shaded, m s^{-1}) and vector winds, and (b) time series of consecutive area-averaged total wind speed (m s^{-1}) at 1000 hPa in the area bounded by 22.5°N–27.5°N, 15°W–50°W (blue box in panel a). Green box in (a) denotes the Main Development Region.

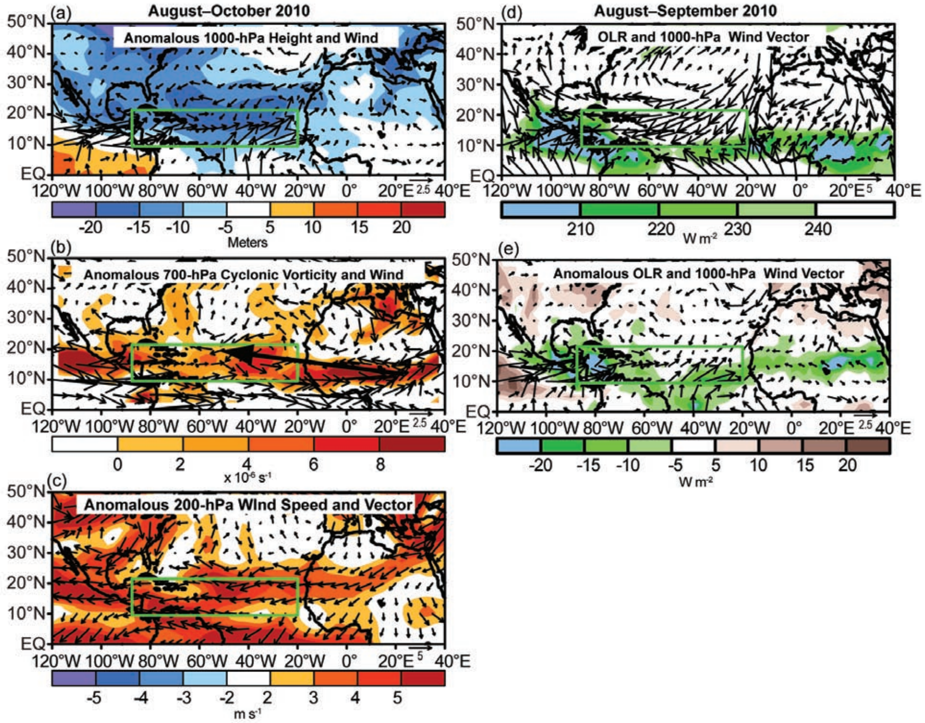

Fig. 4.15. Atmospheric circulation (left) August–October 2010 and (right) August–September 2010: (a) August–October anomalous 1000-hPa height (shading) and vector wind (m s^{-1}), (b) August–October anomalous 700-hPa cyclonic relative vorticity (shading, x 10^{-6} s^{-1}) and vector wind, with thick solid line indicating the axis of the African easterly jet, and (c) August–October anomalous 200-hPa wind speed (shading) and vector wind. Panels (d, e) show August–September conditions: (d) total Outgoing Longwave Radiation (OLR, W m^{-2}) and 1000-hPa vector wind; and (e) August–September anomalous OLR (W m^{-2}) and 1000-hPa anomalous vector wind. Green boxes denote the Main Development Region. Vector scale is at bottom right of each panel. Circulation (OLR) anomalies are with respect to the 1971–2000 period monthly means.

during June–November were 0.93°C above average (Fig. 4.13a). This departure exceeds the previous high (dating back to 1854) of +0.80°C set in 2005 (Fig. 4.13b). The SSTs in the MDR during August–October 2010 were 0.91°C above average (Fig. 4.13c), which also exceeds the previous high August–October departure of +0.77°C set in 2005 (Fig. 4.13d). These record SSTs first appeared during February–April 2010, in association with a pronounced weakening of the anti-cyclonic gyre over the central North Atlantic (Fig. 4.14a) and with unusually weak trade winds north of the MDR (Fig. 4.14b). These conditions were associated with an all-time negative phase of the North Atlantic Oscillation (NAO) during December–April, as measured by the 500 hPa-based NAO index produced by the Climate Prediction Center (CPC; data available at ftp://ftp.cpc.ncep.noaa.gov/wd52dg/data/indices/tele_index.nh). During December–February, this pattern was coupled with a record negative phase of the hemispheric-scale Arctic Oscillation (data available at http://www.cpc.ncep.noaa.gov/products/precip/CWlink/daily_ao_index/monthly.ao.index.b50.current.ascii.table).

The unusually warm SSTs persisted in the MDR through September, as the area of exceptionally weak trade winds subsequently shifted into the deep tropics (Fig. 4.15a). Weaker-than-normal trade winds and anomalously warm SSTs have generally prevailed in the MDR since 1995, in association with the warm phase of the Atlantic Multidecadal Oscillation (AMO; Enfield and Mestas-Nuñez 1999) and active Atlantic phase of the tropical multidecadal signal (Bell and Chelliah 2006; Bell et al. 2009). These conditions have been superimposed upon a weaker long-term warming trend, which some studies suggest is partly linked to anthropogenic greenhouse warming (Santer et al. 2006).

(iv) Atmospheric circulation

Conditions within the MDR reflected an interrelated set of atmospheric anomalies (Fig. 4.10) that are typical of recent active hurricane seasons (Landsea et al. 1998; Bell et al. 1999, 2000, 2004, 2006, 2009; Goldenberg et al. 2001; Bell and Chelliah 2006; Kossin and Vimont 2007). These conditions, combined with La Niña and record warm Atlantic SSTs, set the stage for the 2010 Atlantic hurricane season.

In the lower atmosphere, August–October conditions within the MDR included weaker trade winds, a deep layer of anomalous cross-equatorial flow, and below-average heights/sea-level pressure (Fig. 4.15a,

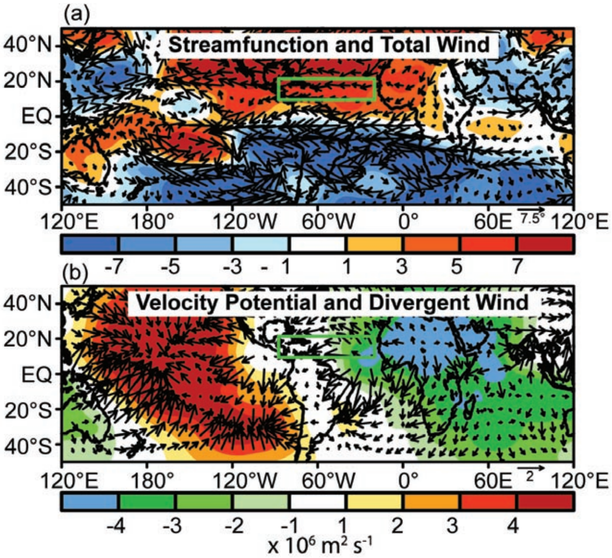

Fig. 4.16. Map of August–October 2010 200-hPa anomalies of (a) streamfunction (shading, x 10^6 m^2 s^{-1}) and vector wind (m s^{-1}) and (b) velocity potential (shading, x 10^6 m^2 s^{-1}) and divergent vector wind (m s^{-1}). Vector scale is at bottom right of each panel. Departures are with respect to the 1971–2000 period. In (a) anomalous ridges are indicated by positive values (red) in the Northern Hemisphere (NH) and negative values (blue) in the Southern Hemisphere (SH). Anomalous troughs are indicated by negative values in the NH and positive values in the SH. Green boxes denote the Main Development Region.

blue shading). Across the Atlantic basin and Sub-Saharan Africa, the low-level westerly anomalies extended above 700 hPa, the approximate level of the African Easterly Jet (AEJ; Fig. 4.15b), and were associated with an anomalous 5° latitude northward shift of the AEJ core (black arrow).

As a result, the bulk of the African easterly wave energy (Reed et al. 1977) was often centered well within the MDR. The AEJ also featured increased cyclonic shear along its equatorward flank within the MDR (Fig. 4.15b, red shading), which dynamically favors stronger easterly waves and an increased cyclonic rotation within which thunderstorms can organize.

An opposite pattern of wind anomalies was evident at 200 hPa, where anomalous easterly flow extended from subtropical central Africa to the eastern North Pacific (Fig. 4.15c). This pattern reflected a stronger and more westward extension of the tropical easterly jet, which occurred in association with an enhanced upper-level ridge that spanned the entire subtropical North Atlantic (Fig. 4.16a).

These conditions were accompanied by a northward shift of the Atlantic Intertropical Convergence Zone (ITCZ), which extended into the southern MDR during August and September (Fig. 4.15d), and resulted in enhanced convection across the region (Fig. 4.15e, green shading). They were also associated with an amplified West African Monsoon system during August–October, as indicated by enhanced convection across the African Sahel and Sudan regions and by a large area of negative velocity potential anomalies over northern Africa (Fig. 4.16b).

Within the MDR, the low-level westerly and upper-easterly anomalies resulted in weak vertical wind shear (less than 8 m s^{-1}) across the entire MDR (Fig. 4.17a). The most anomalously weak shear spanned the central tropical Atlantic and Caribbean Sea (Fig. 4.17b, orange shading), where the total shear was less than 4 m s^{-1}. These conditions were part of a larger-scale pattern that included increased shear across the eastern equatorial Atlantic and over the eastern tropical North Pacific (Fig. 4.17b, blue shading). This pattern is typical of other very active Atlantic hurricane seasons (Bell and Chelliah 2006). At the same time, historically low hurricane activity prevailed across the central and eastern Pacific hurricane basins (see section 4d3).

For the Atlantic basin, the above conditions meant that tropical storms developed primarily within the MDR from amplifying easterly waves moving westward from Africa. These systems quickly entered

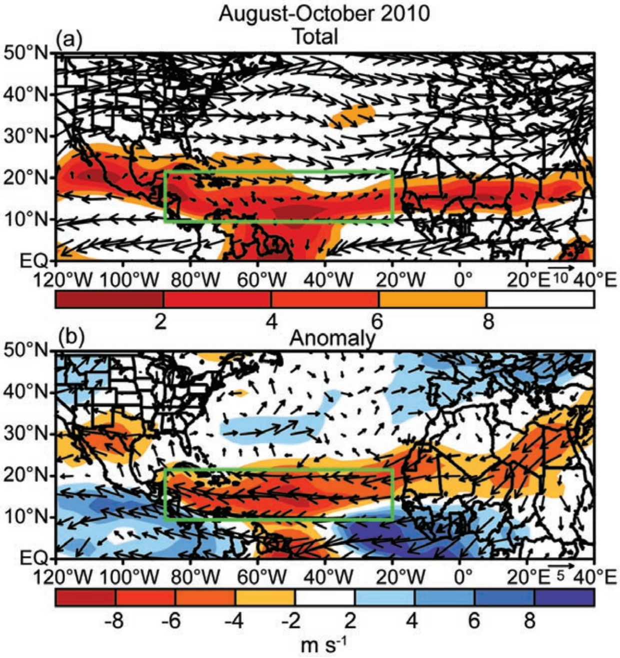

Fig. 4.17. Maps of August–October 2010 (a) total and (b) anomalous vertical wind shear magnitude and vector (m s^{-1}). Vector scale is at bottom right of each panel. Departures are with respect to the 1971–2000 period monthly means.

an extensive area of below-average pressure, deep tropical moisture, increased low-level convergence associated with the ITCZ, and increased cyclonic shear south of the AEJ core. Many of these systems then strengthened while propagating westward within the extended region of very weak vertical wind shear and often over record-warm SSTs. These overall anomaly patterns have favored increased storm formation and intensification since 1995.

(v) Links to Global Climate Patterns

The regional atmospheric conditions during 2010 showed strong links to a combination of three climate factors. The first is the active Atlantic phase of the tropical multidecadal signal, which reflects an interrelated set of conditions that have been conducive to increased Atlantic hurricane activity since 1995 (Bell and Chelliah 2006). The second is La Niña, which contributed to the extensive area of weak vertical wind shear and upper-level easterlies across the MDR. The third is record-warm SSTs in the MDR, as discussed above.

(vi) The Tropical Multidecadal Signal and La Niña

Since 1995, more than two-thirds (11 of 16) of Atlantic hurricane seasons have been above normal and only two have been below normal (Fig. 4.9). This elevated level of activity contrasts sharply with the preceding low-activity era of 1971–94, during which one-half of the seasons were below normal and only three were above normal.

The transition to the current era of high activity was associated with a phase change in the tropical multidecadal signal, which reflects the leading modes of tropical convective rainfall variability and Atlantic SSTs occurring on multidecadal time scales (Bell and Chelliah 2006; Bell et al. 2007). This signal directly links low-frequency atmospheric variability across the central and eastern MDR to an east-west oscillation in anomalous convection between western Africa (Landsea and Gray 1992; Goldenberg and Shapiro 1996) and the Amazon Basin (Fig. 4.16).

All key features of this signal were again present during 2010, suggesting no weakening of the very conducive conditions that have prevailed throughout this Atlantic high-activity era. One key feature of the tropical multidecadal signal seen since 1995 has been an enhanced West African monsoon system (Fig. 4.16b), which is associated with several of the interrelated atmospheric anomalies described previously (Landsea et al. 1998; Bell et al. 1999, 2000, 2004, 2006, 2009; Goldenberg et al. 2001; Bell and Chelliah 2006; Kossin and Vimont 2007). These include the enhanced low-level southwesterly flow into the West African monsoon region (Fig. 4.15a) and the enhanced upper-level divergent flow out of that region (Fig. 4.16b). They also include the stronger upper-level ridges over the eastern MDR and across the subtropical South Atlantic (Fig. 4.16a), along with the stronger and westward extended tropical easterly jet.

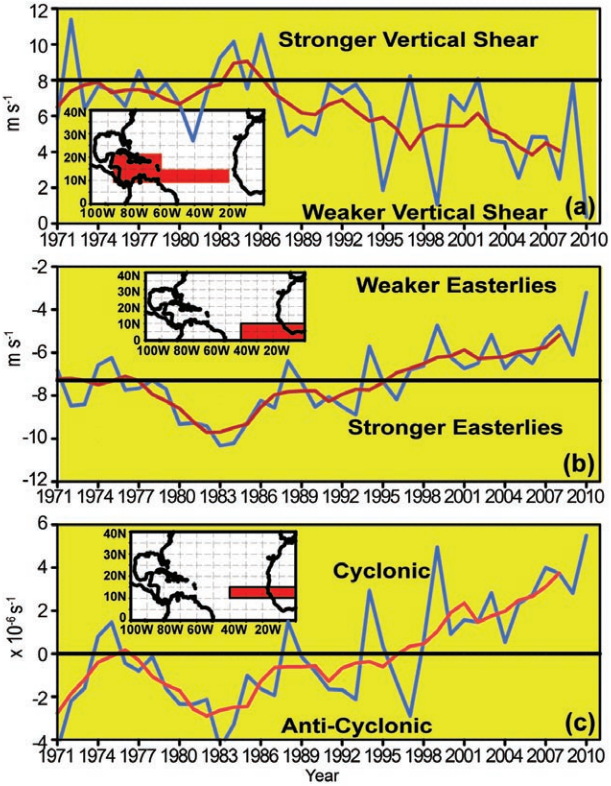

Fig. 4.18. Time series showing consecutive August–October values of area-averaged (a) 200 hPa – 850 hPa vertical shear of the zonal wind (m s^{-1}), (b) 700-hPa zonal wind (m s^{-1}), and (c) 700-Pa relative vorticity (x 10^{-6} s^{-1}). Blue curve shows unsmoothed values and red curve shows a five-point running mean of the time series. Averaging regions are shown in the insets.

Accompanying these conditions, the vertical wind shear (Fig. 4.18a) and 700-hPa zonal winds (Fig. 4.18b) remained much weaker in critical parts of the MDR compared to the preceding low-activity era, and the 700-hPa relative vorticity remained cyclonic across the southern MDR rather than anticyclonic (Fig. 4.18c).

Another major climate factor known to affect Atlantic hurricane seasons is ENSO, which produces a combination of vertical shear and atmospheric stability variations (Gray 1984; Tang and Neelin 2004). According to the CPC, La Niña developed during July 2010 (Fig. 4.1), and was a moderate-strength event during August–October.

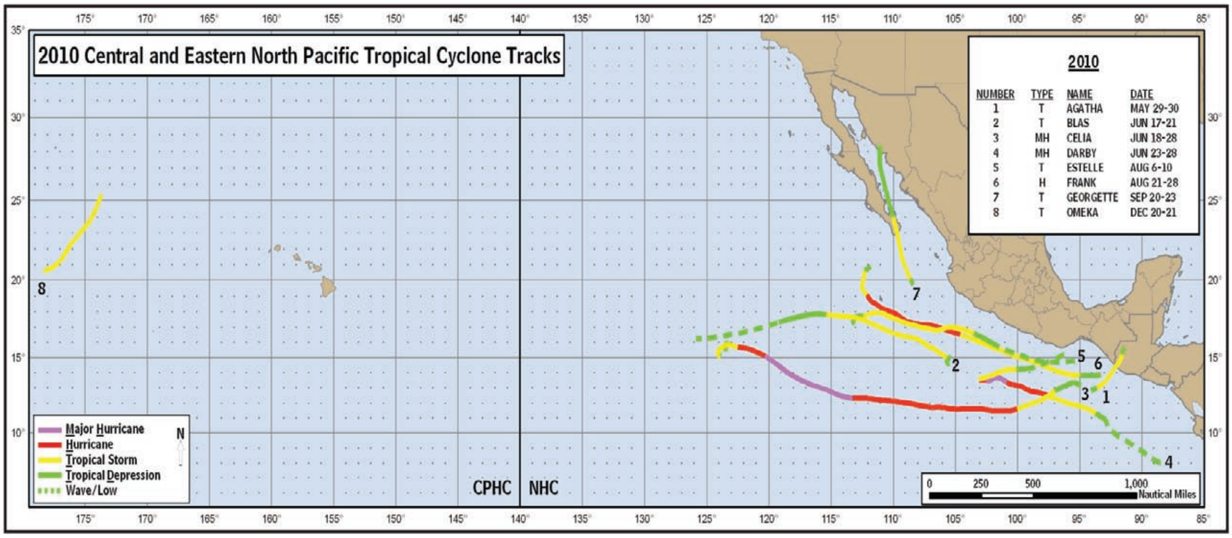

Fig. 4.19. Storm track map for the Eastern Pacific hurricane basins, including all tropical cyclones that occurred in the Eastern North Pacific and Central North Pacific basins [Source: NOAA's National Hurricane Center (NHC) and Central Pacific Hurricane Center (CPHC)]. Tracks are color coded by intensity (wave/low, tropical depression, tropical storm, hurricane, and major hurricane). Also shown is the delineation of the forecast area of responsibility at 140°W between NOAA's NHC and CPHC.

The 200-hPa velocity potential and divergent wind anomalies across the tropical Pacific Ocean during August–October were consistent with La Niña (Fig. 4.16b), as was the overall zonal wave-1 pattern of 200-hPa streamfunction anomalies in the subtropics of both hemispheres (Fig. 4.16a; Bell and Chelliah 2006). This pattern, which included anticyclonic streamfunction anomalies over the North Atlantic basin and Africa, reinforced that associated with the active Atlantic phase of the tropical multidecadal signal and resulted in the enhanced subtropical ridge extending across the entire MDR. Also within the western MDR, typical La Niña impacts during August–October included the anomalous upper-level easterly winds and decreased vertical wind shear noted previously. These conditions acted to extend westward the anomalously low shear associated with the tropical multidecadal signal.

3) Eastern North Pacific Basin—M. C. Kruk, P. A. Hennon, E. J. Gibney, J. Hobgood, and J. Weyman

(i) Seasonal activity

The Eastern North Pacific (ENP) basin is officially split into two separate regions for the issuance of warnings and advisories by NOAA's National Weather Service (NWS). NOAA's National Hurricane Center (NHC) in Miami, FL, is responsible for issuing warnings in the eastern part of the basin that extends from the Pacific Coast of North America to 140°W, while NOAA's Central Pacific Hurricane Center (CPHC) in Honolulu, HI, is responsible for issuing warnings in the Central North Pacific region between 140°W and the date line. In this section, analysis summarizing the tropical cyclone (TC) activity in both these warning areas is presented using combined statistics, along with information specifically addressing the observed activity and impacts in the central North Pacific (CNP) region.

The ENP hurricane season officially spans from 15 May to 30 November, although storms can develop outside of the official season, especially during El Niño-enhanced hurricane seasons. Hurricane and tropical storm activity in the eastern area of the basin typically peaks in September, while in the Central Pacific, TC activity normally reaches its seasonal peak in August (Blake et al. 2009). Figure 4.19 shows the tracks of all of observed TCs in the ENP and CNP in 2010. For the season as a whole, the number of named storms (NSs), hurricanes, and major hurricanes that developed was less than 50% of the long-term means. Primarily due to the development of La Niña conditions during the boreal summer and early autumn in the equatorial Pacific in 2010, the hurricane season was below average in the ENP basin, with eight NSs, three hurricanes, and two major hurricanes (Fig. 4.20a). These values are far below the 1980–2009 IBTrACS seasonal averages for the basin (21.5 NSs, 12.4 hurricanes, and 6.5 major hurricanes).

Along with the overall below-average activity in 2010 in terms of storm counts, the Accumulated

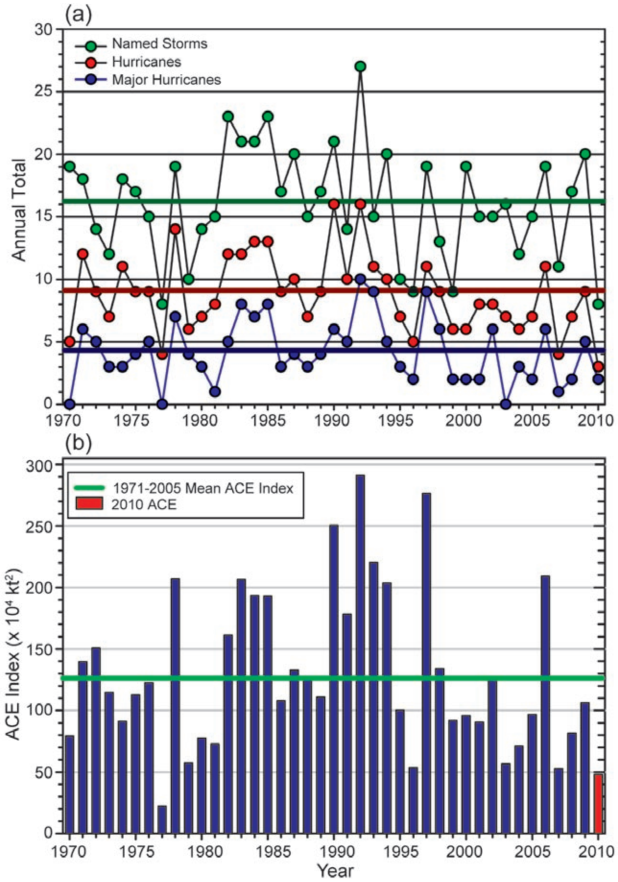

Fig. 4.20. Seasonal tropical cyclone statistics for the Eastern North Pacific (ENP) basin over the period 1970–2010: (a) number of named storms, hurricanes, and major hurricanes and (b) the Accumulated Cyclone Energy (ACE) Index with the seasonal total 2010 highlighted in red. All time series shown include the corresponding 1971–2005 base period means for each parameter.

Cyclone Energy (ACE) Index was also below normal for the basin with a seasonal total of 48.1 × 10^4 kt^2, which is well below the 1971–2005 mean (126.3 × 10^4 kt^2), and is the second lowest ACE season on record since 1975 (Fig. 4.20b).

Just one TC was observed in the CNP region in 2010 (TS Omeka, Fig. 4.19). Tropical Storm Omeka was the latest-forming central and eastern Pacific tropical storm since reliable records began in 1949. On 18 December 2010, the CPHC began monitoring a subtropical cyclone near the date line for possible tropical cyclogenesis. Over the following two days, the system tracked southwestward, entering the western Pacific basin, and began transitioning into a tropical cyclone. Shortly before crossing the date line on 20 December, the CPHC assessed the system to have become a tropical storm. The storm appeared to have reached its maximum intensity west of the date line. The storm was assigned the name Omeka several hours later as it moved into the Central Pacific basin. Shortly after crossing the date line into the central Pacific, wind shear increased, causing the system to weaken. By 21 December, the center of Omeka was devoid of convection and later transitioned into an extratropical cyclone.

Since 1995, the numbers of named storms in the ENP basin has been near average, fluctuating about the long-term mean (Fig. 4.20a). However, the numbers of hurricanes and major hurricanes have been generally below normal in most seasons, with above-normal activity having occurred in only three seasons. NOAA has identified 9 of the 15 seasons in the ENP as being below normal during 1995–2009, with only the El Niño–influenced seasons of 1997 and 2006 producing above-normal activity as measured by the ACE Index (NOAA 2009). In contrast, enhanced activity was observed during the preceding 1970–94 period, which had 6 of 25 (24%) below-normal seasons and 9 of 25 (36%) above-normal seasons, as measured by the ACE Index.

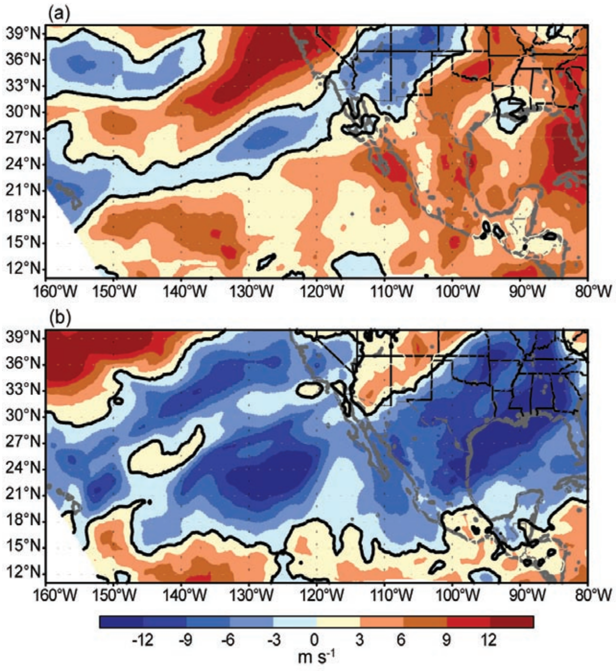

Fig. 4.21. The 200 hPa–850 hPa vertical wind shear anomalies (m s^{-1}) averaged over (a) June–August 2010 and (b) September–November 2010, with anomalies determined relative to the 1979–2004 base period mean. [Source: North American Regional Reanalysis (NARR) dataset, provided by the NOAA National Operational Model Archive and Distribution System.]

(ii) Environmental influences on the 2010 Season

The SSTs in the ENP exhibited a La Niña pattern that intensified as the hurricane season progressed. The cooler-than-normal SSTs extended over much of the ENP where TCs normally develop. The reduction of energy available in the upper ocean contributed to the decreased activity. There was a region of above-normal SSTs early in the hurricane season between latitudes 10°N–20°N and longitudes 120°W–132°W. However, fewer than 9% of ENP TCs normally form over this region and none formed there in 2010. Whitney and Hobgood (1997) suggested that changes of the SSTs in the ENP may be accompanied by a shift in the atmospheric flow pattern over the basin. This appears to have occurred in 2010.

At 850 hPa, the subtropical high was shifted approximately 10° of longitude west of its normal location during the ENP season. This also resulted in above-average vertical wind shear in the 200 hPa–850 hPa layer (Fig. 4.21a). In addition, a stronger-than-normal monsoonal trough extended west and south of Baja California at 850 hPa. The effect of that pattern was to produce anomalous westerly flow over the portion of the ENP where TCs typically form. By itself, the westerly flow might have been favorable for the development of TCs because it would have enhanced the production of low-level vorticity to the north of that flow. However, a stronger-than-normal subtropical ridge at 200 hPa produced faster-than-normal easterly flow over the ENP in the upper levels. The 200-hPa ridge was centered near its usual position in July, but was stronger than normal. By August, the 200-hPa ridge had shifted 15° of longitude east of its normal location. The result of the stronger ridge and eastward shift in its location was to increase the easterly flow over the ENP by 5 m s^{-1} – 10 m s^{-1} during August. However, from September through November, the 200 hPa–850 hPa vertical wind shear across the eastern Pacific basin was anomalously low, by as much as 12 m s^{-1} (Fig. 4.21b). The combination of highly variable wind shear pattern and below-normal SSTs was a potential cause for the quiet 2010 ENP hurricane season. The Quasi-Biennial Oscillation (QBO) phase would have favored more activity (Whitney and Hobgood 1997), but it does not appear to have had a significant impact over the ENP in 2010, consistent with Camargo and Sobel (2010). The fact that Hurricane Celia was able to intensify to a Category 5 level illustrates that, even during less-than-ideal conditions, if a tropical cyclone moves into a favorable environment for a couple of days, it can intensify into a major hurricane.

(iii) Tropical Cyclone Impacts

Just two tropical cyclones made landfall along the Pacific Coast of Mexico during the season (TS Agatha and TS Georgette). In comparison with climatology, the 2010 season is near the 1951–2000 average of 1.34 landfalling TCs (Jauregui 2003).

Along the Pacific Coast of Mexico, TS Agatha (29–30 May) made landfall near the Guatemala-Mexico border, causing widespread flooding. In Guatemala, over 360 mm of rain had fallen by evening on 29 May and resulted in the development of a large sinkhole. Preliminary damage reports suggested that Agatha was responsible for over 300 fatalities in Central America.

On 21 September, short-lived TS Georgette struck the Baja California Peninsula after spending less than a day over open waters. As the cyclone spent so little time over water, its intensity was weak and impacts were virtually negligible. An estimated 66 mm of rain fell in Guaymas and no damage was reported.

The strongest storm of the season in the ENP was Hurricane Celia, which attained Category 5 strength on 25 June with wind speeds of 140 kts (72 m s^{-1}). Two days later, on 27 June, the storm had weakened to tropical storm strength over the open waters of the eastern Pacific. The hurricane appeared impressively annular and had a path from near 98°W to 125°W between 10°N and 15°N. As the storm was so far out to sea, the only impacts were high seas and dangerous rip currents along western Mexico.

4) Western North Pacific basin—S. J. Camargo

The 2010 season featured a total of 19 storms (including five tropical depressions, TDs), forming in the western North Pacific (WNP) basin. Of these 19 active storms in the WNP, 14 reached NS intensity (one was unnamed: TS 2W), eight became typhoons (TYs), and one reached super-typhoon (STY) intensity (Megi). In Fig. 4.22a, the number of TSs, TYs, and STYs per year is shown for the period 1945–2010. The TC data presented here is from the Joint Typhoon Warning Center (JTWC) best-track dataset for 1945–2009 and from preliminary operational data for 2010, for the TCs forming in the WNP basin[6].

---

[6] It should be noted that there were differences between the 2010 warnings by JTWC and the Regional Specialized Meteorological Center at the JMA in Tokyo—the center responsible for naming the TCs. According to the Japan Meteorological Agency (JMA), 10 additional TDs occurred in 2010. Furthermore, TD 01C, which formed in the Central North Pacific, crossed into the western North Pacific as a tropical cyclone according to the CPHC, be-

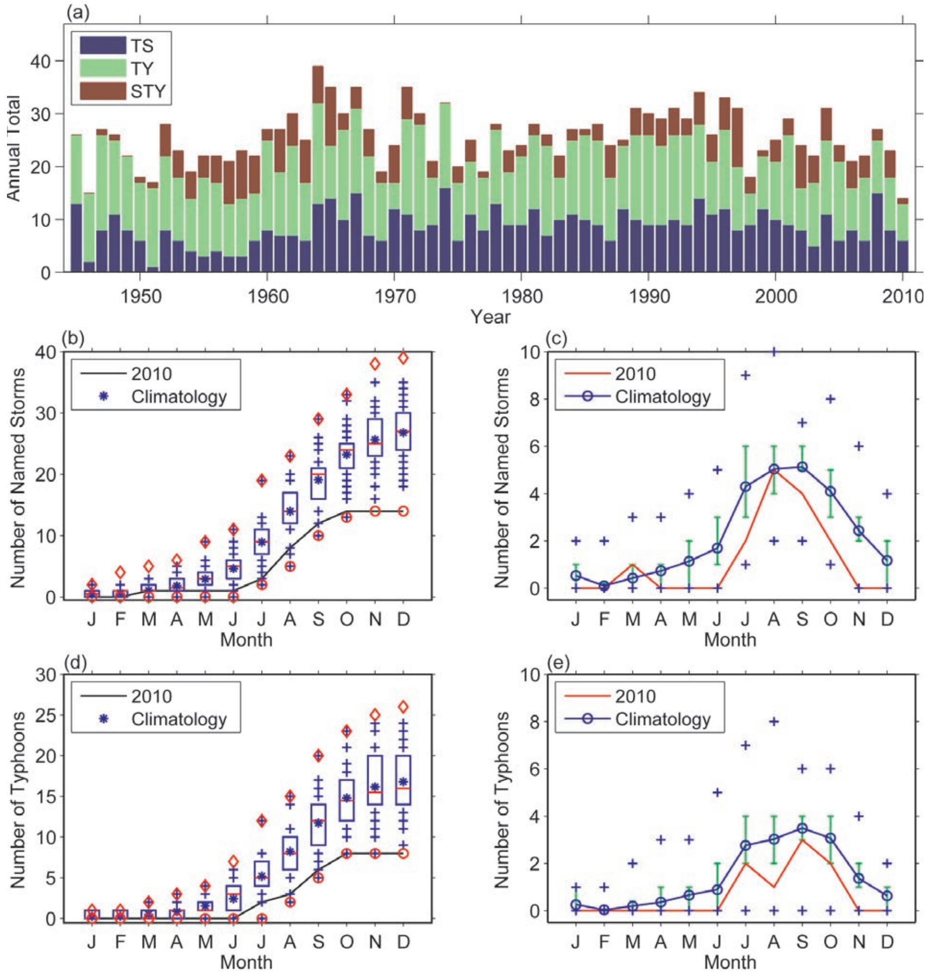

FIG. 4.22 (a) Number of tropical storms (TSs), typhoons (TYs), and super typhoons (STYs) per year in the Western North Pacific (WNP) for the period 1945–2010. (b) Cumulative number of tropical storms with TS intensity or higher (named storms) per month in the WNP: 2010 (black line), and climatology (1971–2000) shown as box plots [interquartile range: box, median: red line, mean: blue asterisk, values in the top or bottom quartile: blue crosses, high (low) records in the 1945–2009 period: red diamonds (circles)]. (c) Number of named storms per month in 2010 (red line), mean climatological number of named storms per month (blue line), the blue plus signs denote the maximum and minimum monthly historical values (1945–2010) and green error bars show the climatological interquartile range for each month. In the case of no error bars, the upper and/or lower percentiles coincide with the median. (d) Cumulative number of typhoons per month in the WNP: 2010 (black line), and climatology (1971–2000) shown as box plots. (e) Number of typhoons per month in 2010 (black line), mean climatological number of TYs per month (blue line), the blue "+" signs denote the maximum and minimum monthly historical values (1945–2010) and green error bars show the climatological interquartile range for each month. [Source: 1945–2009 Joint Typhoon Warning Center (JWTC) best-track dataset, 2010 JTWC preliminary operational track data.]

Climatology is defined using the period 1971–2000; and in addition, this season's activity is far below the 1980–2009 IBTrACS seasonal averages for the basin (26.3 NSs, 15.9 TYs, and 8.0 STYs).

The 2010 WNP TC season started in late January with TD 01W. The first named storm, TS Omais, formed in mid-March (see Fig. 4.22b,c). The WNP was then quiet until July, when TYs Conson and Chanthu occurred. The most active month in terms of number of TCs was August, when five NSs formed in the WNP, though only one reached TY intensity (Kompasu). In September, there were four NSs, three reaching TY intensity (Meranti, Fanapi, and Malakas). Although only two NSs—Megi and Chaba—occurred in October, they were both very intense typhoons, with TY Chaba reaching Category 4. Megi was the only super typhoon in 2010 and ranked among the top 10 strongest typhoons in the historical record for that region. The season finished with TDs 18W and 19W, which formed in November and December, respectively.

The total number of TCs (19), NSs (14), TYs (8), and STYs (1) were all equal or below the bottom fifth percentile of the climatological distributions (median: 30.5 TCs, 27 NSs, 16 TYs, 3 STYs; fifth percentile: 23 TCs, 19 NSs, 11 TYs, 1 STY). Only four previous seasons in the historical record had fewer or the same number of TCs as in 2010, namely 1946 (15 TCs), 1951 (17 TCs), 1950 (18 TCs), and 1954 (19 TCs).

---

fore crossing the date line again into the Central Pacific. A tropical storm (Domeng) was reported by the Philippine Atmospheric, Geophysical and Astronomical Services Administration in August, and not by JMA or JTWC.

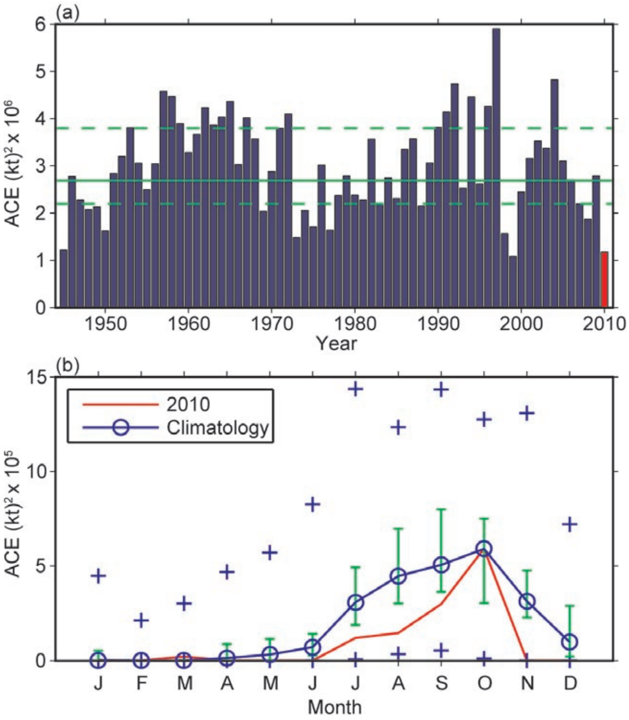

Fig. 4.23 (a) Accumulated Cyclone Energy (ACE) Index per year in the Western North Pacific (WNP) for 1945–2010. The solid green line indicates the median for the climatology years 1971–2000, and the dashed green lines show the climatological 25th and 75th percentiles. (b) ACE Index per month in 2010 (red line) and the median during 1971–2000 (blue line), where the green error bars indicate the 25th and 75th percentiles. In the case of no error bars, the upper and/or lower percentiles coincide with the median. The blue "+" signs denote the maximum and minimum values during the period 1945–2010. [Source: 1945–2009 Joint Typhoon Warning Center (JWTC) best-track dataset, 2010 JTWC preliminary operational track data.]

Note that all these seasons are in the pre-satellite era; therefore, weak storms could have been easily missed in those years. The 2010 season experienced the fewest number of TCs in the WNP in the satellite era. The season also had the lowest number of NSs and TYs in the historical record; the previous records were 15 NSs (in 1946) and nine TYs (in 1998). As the Eastern North Pacific hurricane season was very quiet as well in 2010, the entire North Pacific had a very low level of tropical cyclone activity in 2010. The cumulative distribution of NSs (Fig. 4.22b) and TYs (Fig. 4.22c) shows a very slow season start, with activity increasing in July and August, and flattening after October, never reaching the climatological cumulative values in the region. The only months in which the NSs reach the climatological medians are March and August. However, only one of the August NSs intensified to a TY, an uncommon occurrence in the region (August 1946: no TYs; August 1976, 1977, 2006, and 2008: one TY).

The accumulated cyclone energy (ACE) in the WNP (Fig. 4.23) reflects well the activity in NSs. The 2010 season ACE was the second lowest such value in the historical record. Only in 1999 did a lower value of ACE occur in the region. The monthly ACE values were in the bottom quartile of the climatological distribution in the peak months of the season (June–November), with the exception of October, when the ACE value reached the climatological median for that month. Super Typhoon Megi was responsible for this higher ACE value in October, corresponding to 71% of the ACE for that month and 36% of the ACE for the 2010 season. The ACE value of STY Megi was in the top one percentile of the historical and climatological distributions of ACE per storm.

There were only 74 days with TCs and 64 days with NSs in 2010 in the WNP, both record low values in the historical record (climatological medians: 161.5 and 144.25 days, respectively). From these active days, only 52.5 days had TYs, another record of lowest value in the historical record (climatological median 120.4 days). There were 8.25 days with intense TYs (Categories 3–5), the seventh lowest in the historical record (25th climatological percentile is 11 days). Climatologically, 74% (11%) of the TC days consist of days with (intense) TYs, very close to the rates in 2010—71% (11%). The median lifetime of NSs in 2010 was 5.5 days, below the climatological 25th percentile lifetime of 5.75 days. From the 14 NSs, 12 had a lifetime below the climatological median (eight days), and seven were in the bottom quartile of the climatological distribution. Only STY Megi had a lifetime (11.5 days) in the top quartile of the distribution (above 11.25 days).

The mean genesis location (17.1°N, 130.9°E) in 2010 was shifted northwest of the climatological mean genesis positions (12.9°N, 143.5°E). The mean track position (22.0°N, 125.0°E) was also shifted slightly northwestward of the climatological mean (19.0°N, 134.2°E). These shifts are consistent with typical La Niña events, which tend to have a northwestward genesis shift (Chan 1985; Chia and Ropelewski 2002). Many of the characteristics of the 2010 TY season are typical of La Niña events, such as: a northwestward track shift, few intense storms, low ACE values, and short-lived storms. The influence of ENSO events on the characteristics of the WNP tropical cyclone activity are well known (e.g., Wang and Chan 2002; Camargo and Sobel 2005; Camargo et al. 2007a,b).

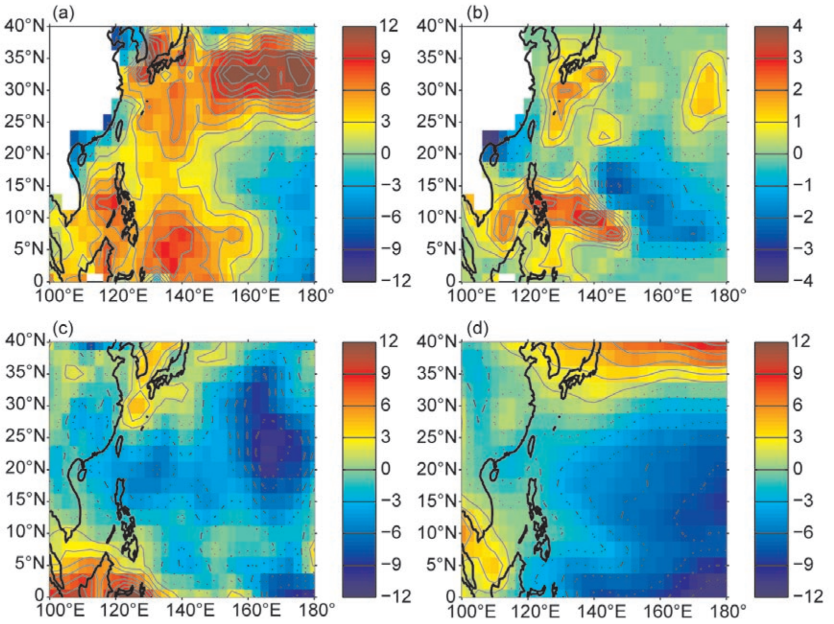

Fig. 4.24. (a) Potential intensity anomalies for July–October (JASO) 2010 from 1971–2000 climatology in m s^{-1}; (b) genesis potential index anomalies for JASO 2010; (c) 600-hPa relative humidity anomalies for JASO 2010 (in %); (d) 850-hPa zonal winds for JASO 2010. Contour interval in (a), (c,) and (d) is 1.5, in (b) contour interval is 1; positive contours are shown in solid lines, negative contours in dash dotted lines and the zero contour line in a dotted line. [Source: atmospheric variables: NCEP Reanalysis data (Kalnay et al. 1996); sea surface temperature (Smith and Reynolds 2005).]

La Niña conditions were present for a good portion of the TY season and were probably responsible for the low activity in the TY season of 2010. Based solely on ENSO SST indices, such as Niño-3.4 (Barnston et al. 1997), this La Niña event would be considered a moderate one. However, the event was quite strong when including the atmospheric component. The Southern Oscillation Index and the multivariate ENSO index (MEI; Wolter and Timlin 1993, 1998) both indicate the 2010 La Niña event as one of the strongest in the historical record. The MEI rank for this event during the TY season was either the strongest (August–September) or the second strongest (July–August and September–October periods); see http://www.esrl.noaa.gov/psd//people/klaus.wolter/MEI/rank.html.

Figure 4.24 shows the environmental conditions responsible for the low level of activity in 2010. The potential intensity (Emanuel 1988, 1995; Fig. 4.24a) shows a large region of negative anomalies near the date line. Similarly, the genesis potential index (GPI; Camargo et al. 2007a) shows negative anomalies in the eastern part of the basin (Fig. 4.24b). The strength and size of these negative anomalies are larger than during most La Niña years. The two years (since 1950) that have most similar patterns for the potential intensity and GPI are 1950 and 1999, which also had very low activity in the WNP. The negative anomalies of the midlevel relative humidity at 600 hPa (Fig. 4.24c) contributed to the negative anomalies in the GPI in the basin. In most La Niña events, there is an increase of GPI near the Asian continent, which is attributed mainly to an increase in relative humidity (Camargo et al. 2007a). In 2010, the region of increased relative humidity was shifted more northward (near Japan) than in other La Niña events. The decreased GPI near the date line in La Niña events is attributed mainly to the low-level vorticity, with some contribution from the vertical shear and midlevel relative humidity (Camargo et al. 2007a). This was also the case in 2010 (not shown). Very strong easterly anomalies in the region throughout the typhoon season led to a monsoon trough with an eastern extent restricted to a small region west of the Philippines (also typical of La Niña years), as shown in Fig. 4.24d, which further contributed to the low activity observed in 2010.

Eleven WNP TCs made landfall during 2010, which is below the 1951–2000 median of 15[7]. Two systems made landfall as a TD (median is three), five made landfall as a TS (median is six), and three struck as a TY (median is four). Megi made landfall as a Category 5 STY. Megi was one of the most intense landfalling tropical cyclones in the historical record, not only in the WNP, but globally.

As could be expected, the largest impacts in this TY season were due to STY Megi. The storm made landfall in the mountain range of Sierra Madre, Luzon Island, in the Philippines. According to a United Nations report (OCHA 2010), almost two million people were affected by the typhoon, mainly

---

[7] Here we consider only one landfall per TC. If a TC makes more than one landfall, the landfall event with the highest wind speed is considered.

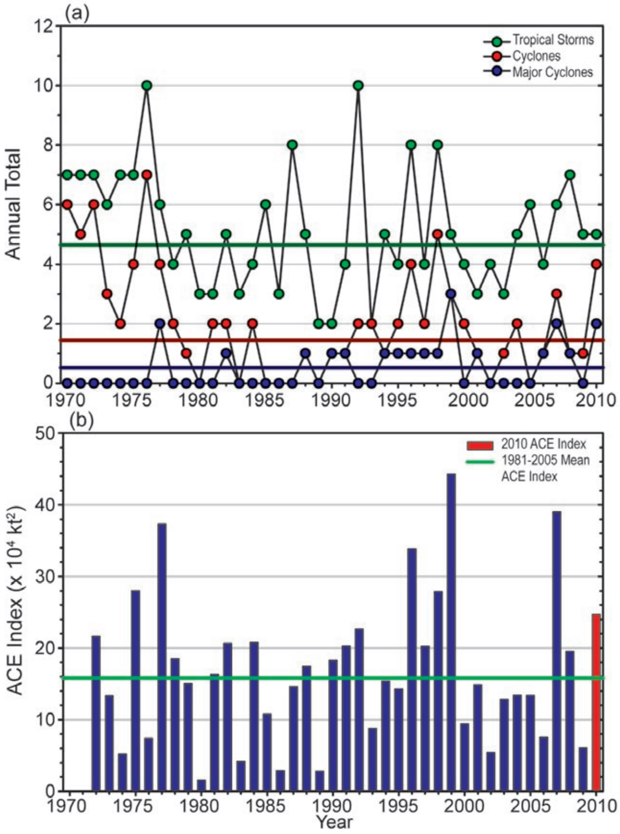

Fig. 4.25. Annual tropical cyclone statistics for the North Indian Ocean (NIO) over the period 1970–2010: (a) number of tropical storms, cyclones and major cyclones and (b) the estimated annual Accumulated Cyclone Energy (ACE) Index (in kt^2 x 10^4) for all tropical cyclones during which they were at least tropical storm strength or greater (Bell et al. 2000). The 1981–2005 base period means are included in both (a) and (b). Note that the ACE Index is estimated due to a lack of consistent six-hour sustained winds for every storm.

in Isabella province. There were 19 deaths associated with the storm. Approximately 30 200 houses were destroyed, and 116 000 were partially damaged. There was an estimated 80% loss of crops, such as rice and corn in the Province of Isabella, which is the second largest producer of rice in the Philippines.

Typhoon Mindulle also had a large impact. The storm brought heavy rainfall to Vietnam, leading to significant flooding and agricultural losses in that country, as well as the death of many fishermen.

5) INDIAN OCEAN BASINS

(i) North Indian Ocean—M. C. Kruk and K. L. Gleason

The North Indian Ocean (NIO) TC season typically extends from April to December, with two peaks in activity during May–June and November when the monsoon trough is positioned over tropical waters in the basin. Tropical cyclones in the NIO basin normally develop over the Arabian Sea and Bay of Bengal between latitudes 8°N and 15°N. These systems are usually short lived and relatively weak, and often quickly move into the Indian subcontinent. However, strong and "severe cyclonic storms" (Holland 1993) can develop with winds exceeding 130 kts (67 m s^{-1}; Neumann et al. 1993).

The 2010 TC season produced five named storms (NSs), four cyclones (CYC), and two major cyclones (MCYC; Fig. 4.25a). These values, except for NSs, are above the 1980–2009 IBTrACS seasonal averages of 6.3 NSs, 1.7 CYCs, and 0.8 MCYCs. The season produced an ACE Index value of 24.7 x 10^4 kt^2, which is above the 1981–2005 mean of 16 x 10^4 kt^2 (Fig. 4.25b). There is generally an enhancement in TC activity, especially in the Bay of Bengal, during La Niña (Singh et al. 2000), which the globe was transitioning to during the boreal summer 2010.

The first CYC of the season developed in the Bay of Bengal from 17 to 21 May and became CYC Laila with maximum sustained winds of 65 kts (33 m s^{-1}). Laila underwent rapid intensification before making landfall near Bapatla, Andhra Pradesh, on 20 May. Damage was extensive in Andhra Pradesh and more than a dozen persons were killed by the storm. Parts of the region experienced 24-hour rainfall totals between 320 mm and 510 mm.

The two MCYCs of the season occurred 31 May–6 June (Phet) and 21–22 October (Giri). Major Cyclone Phet developed in the Arabian Sea and eventually made landfall in Oman [125 kts (64 m s^{-1})] where first estimates of damages exceeded $780 million (U.S. dollars; http://in.reuters.com/article/2010/06/07/idINIndia-49106920100607). Phet was the second strongest storm on record to develop in the Arabian Sea (behind only MCYC Gonu in 2007). Major Cyclone Giri developed in the Bay of Bengal and made landfall near Kyaukpyu, Myanmar, with maximum sustained winds of 135 kts (69 m s^{-1}). The cyclone intensified into a Category 5 storm in just over a 24-hour period. Tens of thousands of citizens were displaced by the approximate 3.7-m storm surge and heavy rains that accompanied MCYC Giri. Over 150 people were believed to be killed by the storm.

The 2010 season ended with CYC Jal, which had maximum sustained winds of 70 kts (36 m s^{-1}). The track of CYC Jal was nearly identical to that of CYC Laila. Jal occurred 4–7 November and began as a weak disturbance in the South China Sea. The storm

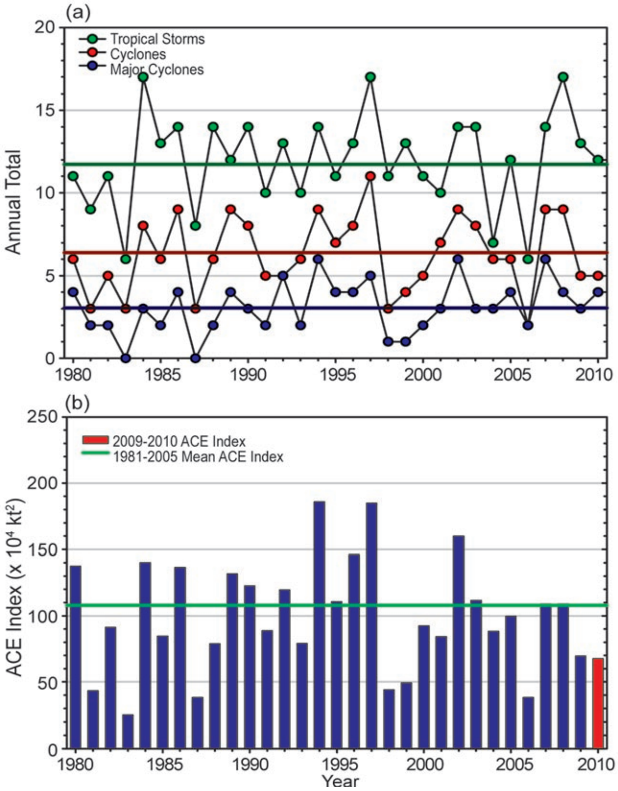

Fig. 4.26. Annual tropical cylone statistics for the Southern Indian Ocean (SIO) over the period of 1980–2010: (a) number of tropical storms, cyclones and major cyclones and (b) the estimated annual Accumulated Cyclone Energy (ACE) Index (in kt^2 x 10^4) for all tropical cyclones during which they were at least tropical storm strength or greater (Bell et al. 2000). The 1981–2005 base period means are included in both (a) and (b). Note that the ACE Index is estimated due to a lack of consistent six-hour sustained winds for every storm.

intensified to Category 1 strength before weakening as it headed toward the Indian coast. Jal produced widespread flooding and mudslides, and devastated the local rice crop. The storm was blamed for 54 fatalities in Andhra Pradesh.

(ii) South Indian Ocean—K. L. Gleason and M. C. Kruk

The South Indian Ocean (SIO) basin extends south of the Equator from 105°E to the African coastline[8], with most CYCs developing south of 10°S. The SIO TC season extends from July to June encompassing equal portions of two calendar years (i.e., the 2010 season is comprised of storms from July to December 2009 and January to June 2010). The peak activity typically occurs from December to April when the ITCZ is located in the Southern Hemisphere. Historically, the vast majority of landfalling CYCs in the SIO impact Madagascar, Mozambique, and the Mascarene Islands, including Mauritius and Réunion.

The historical SIO TC data is probably the least reliable of all the TC basins (Atkinson 1971; Neumann et al. 1993), primarily due to a lack of historical record keeping by individual countries and no centralized monitoring agency; however, the historical dataset for the region has been updated (Knapp et al. 2010). The historical data are noticeably deficient before reliable satellite data were operationally implemented in the region beginning about 1983.

The 2009/10 SIO season storm numbers were below average with 12 NSs, 5 CYCs, and 4 MCYCs (Fig. 4.26a). The 1980–2009 IBTrACS seasonal averages are 17.5 NSs, 8.9 CYCs, and 4.6 MCYCs. In addition, the 2009/10 ACE Index (~68 x 10^4 kt^2) was below the 1981–2005 average (Fig. 4.26b). With the exception of the 2001/02 season, each season since the mid-1990s has produced a near-average or below-average seasonal ACE in the SIO basin.

The strongest storm during the season was MCYC Edzani, which developed in the central Indian Ocean, north of the Cocos Islands during the first few days of January 2010. The disturbance initially showed two low-level circulation centers before they merged. As it became more organized, the system was upgraded to a tropical depression and continued to intensify over the next several days. Edzani became a strong Category 4 MCYC on 8 January with maximum sustained winds of 135 kts (69 m s^{-1}). At peak intensity, Edzani was located approximately 590 n mi east-southeast of Diego Garcia and continued on a west-southwestward track into cooler waters and an environment with stronger wind shear. By 14 January, Edzani had substantially weakened and was classified as extratropical by the Joint Typhoon Warning Center. Edzani remained over open ocean waters during its lifecycle and had little to no impact on land.

Only two TCs made landfall in the basin during the season. Tropical Storm Fami developed on 2 February in the Mozambique Channel and came ashore on the west side of Madagascar near Belo sur Mer with maximum sustained winds of 40 kts (21 m s^{-1}). While over land, Fami developed an eye-like feature in the mid-to-upper levels of the cyclone, which indicated it was maintaining strength. Friction from the land and wind shear caused Fami to dissipate prior to reemerging over open waters. Tropical Storm Hubert formed in the ocean waters east of Madagascar on 10 March

---

[8] In order to generate consistent basin statistics, the SIO basin boundary overlaps with the Australian Bureau of Meteorology's operational warning area from 90°E to 105°E.

and made landfall near Mahaela with sustained winds of 35 kts (18 m s^{-1}). Bringing heavy winds and rain to the already saturated soil in southeast and south-central Madagascar, TS Hubert began to dissipate and became a heavy rain event once on land. Most of the strongest winds and heaviest rains stayed south and east of the capital city of Antananarivo, although landslides and flooding stranded people in many towns and villages, disrupted communications and electricity, and caused at least 70 deaths.

6) SOUTHWEST PACIFIC BASIN—A. M. Lorrey, S. McGree, J. Renwick, and S. Hugony

During the 2009/10 TC season, New Zealand's National Institute of Water and Atmosphere (NIWA) forecast normal activity for most island nations and territories in the southwest Pacific region (between 135°E and 120°W). The overall TC activity was expected to be near normal, with 8–11 storms forecast for the 2009/10 season. Two or three storms were forecast to reach at least Category 3[9], and one storm was expected to reach at least Category 4, with mean wind speeds of at least 64 kts (33 m s^{-1}). Documentation of the TC activity during the season was collated from reports issued by the Regional Specialized Meteorological Center in Nadi, Fiji, the Australia Bureau of Meteorology, the Tropical Cyclone Warning Centre based at the New Zealand Meteorological Service in Wellington, and the Joint Typhoon Warning Center (JTWC).

In the Southwest Pacific sector, a total of ten TCs were documented for the season. The onset of the season did not occur until early December 2009. The storms that occurred during the first two months of the season (Mick, Neville, Olga, and Nisha) achieved only a Category 1 or 2 status. In contrast, the second half of the season from February to April saw the development of five systems that reached or exceeded Category 3 status (Oli, Pat, Rene, Tomas, and Ului). Three Category 4 storms had winds in excess of 86 kts (44 m s^{-1}; Oli, Rene, and Tomas), and one event had 10-minute sustained winds in excess of 108 kts (56 m s^{-1}; Ului). Tropical Cyclone Sarah, which formed on 26 February, 270 n mi northwest of Rarotonga in the Cook Islands, only attained Category 1 status.

The existence of El Niño saw the tropical and subtropical limbs of the South Pacific Convergence Zone (SPCZ) located to the northeast of their climatological positions during the season. This helped guide a number of tracks to the east of the date line, with ex-tropical transitions oriented to the southeast for some storms. The regional ENSO conditions and influence of the SPCZ's geometry were especially obvious for the second half of the TC season, which saw elevated TC activity in French Polynesia and the Southern Cook Islands (SCI). Of note, a traditional environmental knowledge climate indicator used in the SCI and elsewhere in the southwest Pacific (timing of mango flowering) was highlighted prior to the onset of the season by the director of the Cook Islands Meteorological Service. Based on the early flowering of the mangoes, it was suggested the TC season would see increased risk to the east of the date line. This piece of indigenous climate guidance compared favorably with the TC guidance issued by NIWA in October 2009, and the forecasted conditions came to fruition beginning in January 2010[10]. It should also be noted that the analog climate guidance[11] generated from looking at past seasonal activity was provided in the February 2010 update and suggested an increased risk in the Solomon Islands/north Coral Sea region. While this was apparently an odd component of the projection for an El Niño year, the new guidance was timely, and provided a three-week lead time prior to the onset of TC Ului (Category 5) that passed south of the Solomon Islands.

The onset of significant TC activity to the east of the date line was first observed for TC Oli, which impacted French Polynesia. This storm produced strong swells and made a direct impact on the island of Tubuai (Austral Islands). Oli crossed more than 2700 n mi from 1 to 6 February while in transit through the Southwest Pacific Ocean. It reached Category 2 status while passing by Mopelia Island, and the track then veered to the southwest of the Windward Islands before closing on Tahiti and Moorea late on 3 February. There were 39 kt (20 m s^{-1}) maximal 10-minute sustained winds, with gusts of 57 kts (29 m s^{-1}) recorded at Bora-Bora, and very high seas were noted with waves estimated at 6.1 m across the Society Island group.

---

[9] Storm categorizations in this basin are based on the Australian TC scale and not Saffir-Simpson. See http://www.bom.gov.au/weather/cyclone/faq/index.shtml for a definition of Australian TC categories.

[10] The scientific community is beginning to pay more attention to the value of traditional environmental knowledge and this information is included here in that light. See King et al. (2008) and Lefale (2010) as examples of the work being done in this area of research in the Pacific.

[11] See http://www.niwa.co.nz/our-science/pacific-rim/news/featured/tropical-cyclone-outlook-normal2/background-information-for-meteorological-services regarding the analog methodology employed here.

Several houses as well as some hotels were destroyed or partly damaged by strong winds and waves from TC Oli, but fortunately on Tahiti and Moorea there was only minimal damage, with some roofs torn off and coastal detritus washed up on the shore due to the significant wave activity. Oli intensified after passing Tahiti, reaching Category 4 status, and inflicted damage on Rurutu and Raivavae from wind and waves with estimated heights of 8 m. Only a few hours after the arrival of TC Oli on Tubuai, there was significant wave damage up to 100 m inland. The eye of TC Oli passed over Tubuai on 5 February, with a minimum sea level pressure of 955.8 hPa recorded and sustained winds of 55 kts (28 m s^{-1}), with gusts up to 92 kts (47 m s^{-1}). The northern and northeastern coasts of Tubuai were devastated, in contrast with southern, sheltered coastal areas.

The breadth of latitude covered by the Cook Islands meant that this island nation was battered by several tropical cyclones during the 2009/10 season. After feeling the effects of TC Oli, TC Pat (Category 3) directly impacted Aitutaki, Southern Cook Islands. Strong winds blowing consistently at 100 kts (51 m s^{-1}), with gusts up to 130 kts (67 m s^{-1}), for up to four hours overnight ripped off roofing, uprooted coconut palms and trees, damaged water tanks, and destroyed the local electricity distribution network by taking down power poles and lines. Many people took shelter on high ground in a local church, and the damage was significant enough for the Prime Minister to declare a state of disaster. It was suggested by eyewitnesses who are elders in the Aitutaki community that this was the worst storm to affect the island in living memory. These observations are very much in-line with emerging research related to traditional environmental knowledge that contributes to increased awareness of weather and climate risks in the region (King et al. 2008; Lefale 2010). For example, the ability and knowledge of the Samoans to forecast the onset of extreme weather and climate events, relying predominantly on local environmental changes, are vital tools that can be incorporated in the formulation of climate change adaptation strategies and contemporary weather forecasts (Lefale 2010).

Severe TC Rene (Category 4) affected American Samoa and Tonga in mid-February, with significant damage to roads and agricultural infrastructure from heavy rainfall in Samoa. Damage to buildings, electricity infrastructure, and roads were reported for Tonga, which experienced a direct impact from the storm eye. Subsequently, TC Sarah (Category 1) affected the Northern Cook Islands, but with no reports of major damage or fatalities. The brief respite from intense TC activity was curtailed with the joint onset of TCs Ului (Category 5) and Tomas (Category 4). The combination of these systems wreaked havoc across the central and northwest corners of the southwest Pacific during the second week in March. Ului caused significant flooding and damage in the Solomon Islands, while Tomas affected the island of Vanua Levu, Fiji, ripping off corrugated roofing iron and forcing thousands to take shelter in evacuation centers. "Overwhelming" damage was reported in the northern and eastern parts of the country by the Prime Minister of Fiji. Sea surges of up to 7 m were reported in the Lau Group in the eastern part of the country.

Overall, the TC activity in the region was in the normal range for the season, as forecast; however, the strength of many systems that developed during the latter part of the season, including three Category 4 storms and one Category 5 storm, were highlighted on the global stage (Terry and Etienne 2010) as the minimum estimated damage for the 2009/10 season was estimated at $163 million (U.S. dollars), and 14 fatalities were reported for the region as a result of seasonal TC activity.

7) Australian Region Basin—B. C. Trewin

(i) Seasonal Activity

The 2009/10 TC season was slightly below normal in the broader Australian basin (areas south of the Equator and between 90°E and 160°E[12], which includes Australian, Papua New Guinea, and Indonesian areas of responsibility). The season produced eight TCs, below the long-term average of 10. There were three TCs in the eastern sector[13] of the Australian region during 2009/10 (one of these entering from the Southwest Pacific region), four TCs in the western sector (one of which formed in the northern sector), and one in the northern sector. There were five landfalls during the season.

---

[12] The Australian Bureau of Meteorology's warning area overlaps both the southern Indian Ocean and Southwest Pacific.

[13] The western sector covers areas between 90°E and 125°E. The eastern sector covers areas east of the eastern Australian coast to 160°E, as well as the eastern half of the Gulf of Carpentaria. The northern sector covers areas from 125°E east to the western half of the Gulf of Carpentaria.

(ii) Landfalling and Other Significant Tropical Cyclones

The most intense TC of the season was Laurence, which affected Western Australia in mid-December. Laurence reached TC intensity on 14 December 2009 in the Joseph Bonaparte Gulf near 13°S, 128°E (approximately 135 n mi north of Wyndham, Western Australia). By the time it approached the north coast of Western Australia near Troughton Island, it had intensified to Category 3 intensity[14], then further intensified to Category 5 intensity as it moved southwest, parallel to the coast. Its initial intensity peak occurred on 16 December at 15.3°S, 124.2°E (offshore from Kuri Bay), with estimated maximum gusts of 155 kts (79 m s^{-1}), maximum sustained winds of 110 kts (56 m s^{-1}), and a minimum central pressure of 932 hPa. Laurence made landfall as a Category 3 system late on 16 December on a remote section of the coast northeast of Derby. After weakening to a tropical depression as it moved over land, it reintensified to a TC as it moved over water north of Broome on 19 December, and continued to intensify as it moved southwest, ultimately regaining Category 5 intensity on 21 December [maximum gusts 155 kts (79 m s^{-1}), maximum sustained winds 110 kts (56 m s^{-1}), minimum central pressure 929 hPa]. It made landfall shortly thereafter near Wallal, about 135 n mi east of Port Hedland. Both landfalls took place in sparsely populated areas and there was only limited wind damage, but heavy rain caused flooding and stock losses in the region east of Port Hedland. While weakening below TC intensity as it moved southeast, Laurence maintained its identity as a system well into the central continent, ultimately causing flooding as far east as northern New South Wales. Laurence was the first Category 5 landfall on the Australian mainland since George in March 2007; over the last 25 years, Category 5 landfalls have occurred once every three to four years on average.

Ului moved into the Australian region from the Southwest Pacific region on 15 March. Having reached Category 5 intensity [maximum gusts 155 kts (79 m s^{-1}), maximum sustained winds 115 kts (59 m s^{-1}), minimum central pressure 930 hPa] near 13°S, 161°E, just before entering the Australian region, it moved southwest across the Coral Sea while in a slowly weakening phase. It reintensified slightly before crossing the Queensland coast near Airlie Beach as a Category 3 system early on 21 March. Significant wind damage occurred between Airlie Beach and Mackay, with widespread crop and tree damage and power outages, and many boats in coastal harbors were damaged or destroyed by large seas and swell.

The other severe TC of the season was Magda, which made landfall as a Category 3 system near Kuri Bay (a very similar location to the first landfall of Laurence) on 22 January. The landfall region is very sparsely populated and only minor damage was reported. The other two landfalling systems of the season, both of which peaked at Category 2 and made landfall as Category 1 systems, were Olga, which made landfall on the Gulf of Carpentaria coast west of Karumba, Queensland, on 30 January (having earlier reached TC intensity in the Coral Sea and crossed the southern Cape York Peninsula as a tropical depression), and Paul, which made landfall on the Arnhem Land coast of the western Gulf of Carpentaria northwest of Groote Eylandt on 29 March. Both TCs brought heavy rain and subsequent flooding, particularly Paul, which produced 443 mm at Bulman, Northern Territory, on 31 March, the highest daily rainfall total in Australia in 2010.

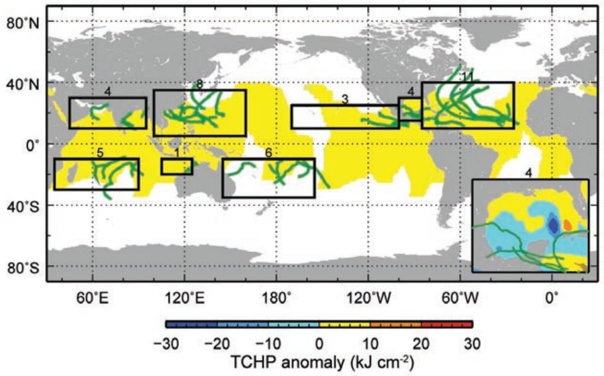

Fig. 4.27. Global anomalies of Tropical Cyclone Heat Potential (TCHP) corresponding to 2010 computed as described in the text. The boxes indicate the seven regions where tropical cyclones occur: from left to right, Southwest Indian, North Indian, West Pacific, Southeast Indian, South Pacific, East Pacific, and North Atlantic (shown as Gulf of Mexico and tropical Atlantic separately). The green lines indicate the trajectories of all tropical cyclones reaching at least Category 1 [one-minute average wind ≥ 64 kts (33 m s^{-1})] and above during November 2009–April 2010 in the Southern Hemisphere and June–November 2010 in the Northern Hemisphere. The numbers above each box correspond to the number of Category 1 and above cyclones that travel within each box. The Gulf of Mexico conditions during June–November 2010 are shown in detail in the insert shown in the lower right corner.

---

[14] Storm categorizations in this basin are based on the Australian TC scale and not Saffir-Simpson. See http://www.bom.gov.au/weather/cyclone/faq/index.shtml for a definition of Australian TC categories.

Three other TCs failed to make landfall: Neville (Category 1) in the Coral Sea in January, and Robyn and Sean (both Category 2) in the Indian Ocean in April. None had any impact on land areas.

e. *Tropical Cyclone Heat Potential*—G. J. Goni, J. A. Knaff, and I-I Lin

Variations in the Tropical Cyclone Heat Potential (TCHP) in each of the seven tropical cyclone basins are discussed in this section. The TCHP is defined as the ocean heat content contained between the sea surface and the depth of the 26°C isotherm. It has been shown that high TCHP values are more closely linked to intensity changes than SST (Shay et al. 2000; Goni and Trinanes 2003; Lin et al. 2008, 2009), provided that atmospheric conditions are also favorable.

Although SST data provide a measure of the surface ocean conditions, the data give no information about the subsurface (first tens of meters) ocean thermal structure. It is known that the ocean skin temperature erodes when the sea surface is affected by strong winds, creating a well-mixed layer that can reach depths of several tens of meters. As the TC progresses, it travels above waters with mixed layer temperatures similar to their skin temperatures. This provides the motivation to investigate and monitor the upper ocean thermal structure, which has become a key element in the study of tropical cyclone intensifications focused on predictions of sudden TC intensification. In addition, the inclusion of TCHP in statistical models has been shown to reduce intensity prediction errors for the most intense cyclones. Research has shown how the upper ocean thermal structure is a good indicator for predicting TC intensity (Mainelli et al. 2008).

Fields of TCHP show high spatial and temporal variability associated with oceanic mesoscale features that can be detected globally using satellite altimetry (Lin et al. 2008; Goni et al. 2009). It has been shown that areas with high values of TCHP can be an important factor for TC intensification (e.g., Shay et al. 2000; Mainelli et al. 2008). To examine the interannual variability of TCHP with respect to tropical cyclones, TCHP anomalies are computed during the months of TC activity in each hemisphere: June–November in the Northern Hemisphere and November–April in the Southern Hemisphere. Anomalies are defined as departures from the mean TCHP calculated during the same months for the period 1993–2010. These anomalies show large variability within and among the tropical cyclone basins (Fig. 4.27).

The west Pacific basin generally exhibits the anomalies related to ENSO events, with 2010 being characterized by the onset of La Niña conditions, which have been in place in the equatorial Pacific Ocean since approximately June 2010. Similar to the conditions during 2008 and 2009, the South Pacific basin showed mostly positive anomalies. The north Indian basin exhibited positive values in the Bay of Bengal and in the Arabian Sea. The Gulf of Mexico (Fig. 4.27 insert, lower right) showed mostly negative values except for a region of positive values in the northern region. Similar to 2009, the tropical Atlantic exhibited mostly positive values, which is also observed in sea height and SST fields (http://www.aoml.noaa.gov/phod/regsatprod/atln/index.php). The most evident changes in TCHP between 2010 and 2009 are the decrease in values in the Gulf of Mexico and the southwestern Pacific Ocean and the increase in values in the western Pacific Ocean, Arabian Sea, and Bay of Bengal (Fig. 4.28).

During 2010, a number of major TCs were positively identified to have gained strength when traveling into regions of high values of TCHP, three TCs exhibited a weak link, and three did not show any link between ocean heat content and intensification. Some examples of these intensification events are shown in Fig. 4.29. The results presented here correspond to four major TCs, where the location of their intensification coincided with an increase of the values of TCHP along their tracks. These TCs were Igor (tropical Atlantic), Celia (Eastern North Pacific, ENP), Megi (Western North Pacific, WNP), and Phet (Arabian Sea). The cooling associated with the wake of intense TCs, which reached

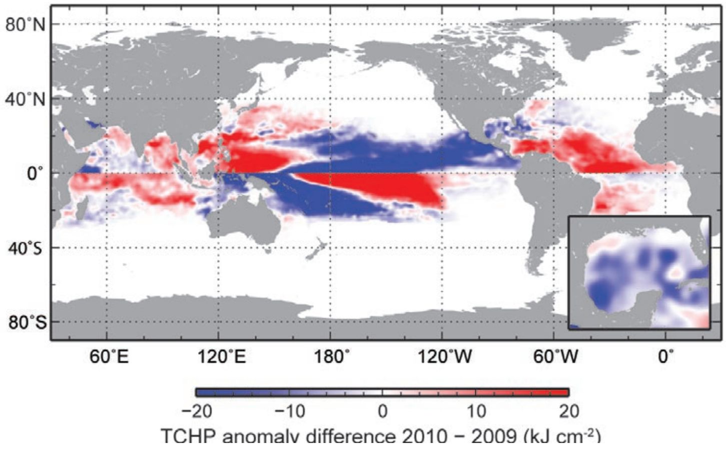

Fig. 4.28. Differences between the Tropical Cyclone Heat Potential (TCHP) fields in 2010 and 2009.

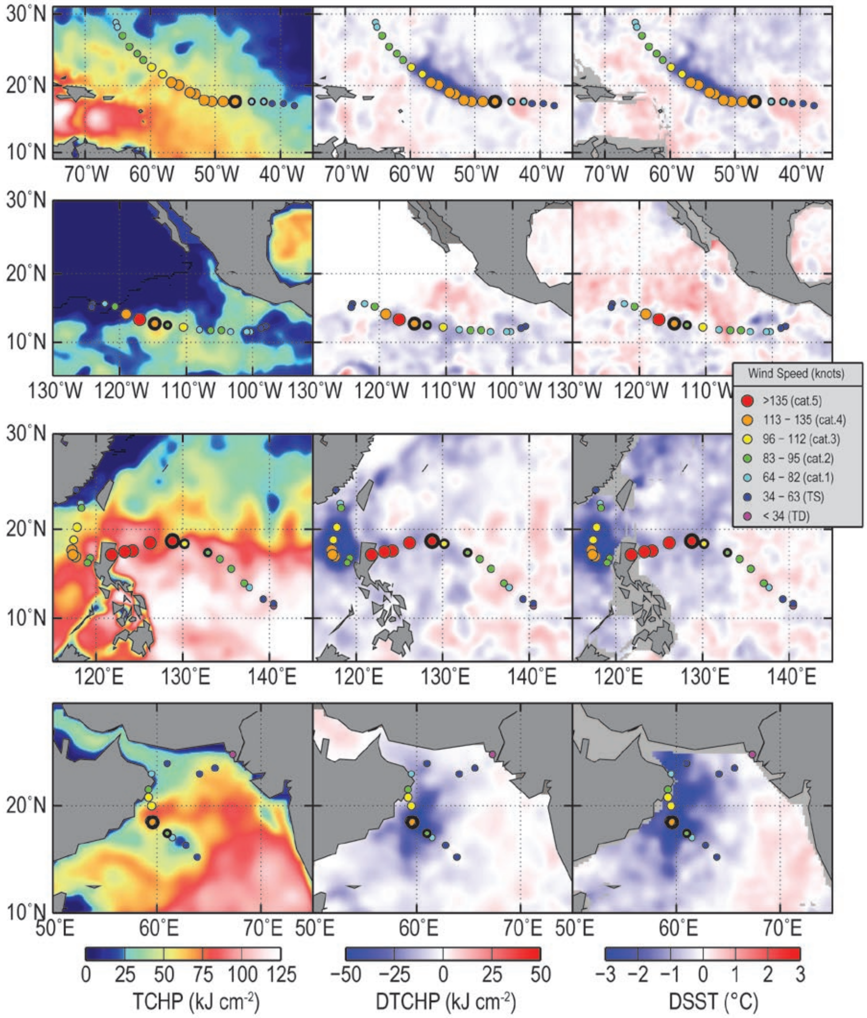

Fig. 4.29. (left) Tropical Cyclone Heat Potential (TCHP) and surface cooling given by the difference between post- and pre-storm values of (center) tropical cyclone heat potential and (right) sea surface temperature for (from top to bottom) Hurricane Igor, Hurricane Celia, Typhoon Megi, and Cyclone Phet.

values of up to 50 kJ cm^{-2} in TCHP and above 3°C in SST, is important since these factors influence the upper ocean thermal structure on regional scales within weeks to months after the passage of the storms (Emanuel 2001; Hart et al. 2007).

In the Atlantic, preliminary best track estimates show Igor intensifying from 65 kts (33 m s^{-1}) to 130 kts (67 m s^{-1}) in 24 hours while the TC slowed down and the environmental vertical wind shear conditions improved. Values of TCHP under the track of this TC during this time also increased to values greater than 70 kJ cm^{-2}, well above the 50 kJ cm^{-2} usually found in cases of Atlantic rapid intensification (Mainelli et al. 2008). The post-storm surface cooling associated with the wake of this hurricane reached very high values, of approximately 5°C and 50 kJ cm^{-2}.

In the ENP, both Major Hurricanes Celia and Darby occurred in late June and showed peak intensity nearly coincident with positive TCHP anomalies. Celia formed on 18 June, southeast of Acapulco, Mexico, and on 24 June, with appropriately favorable atmospheric conditions given by the weakening of the shear, this cyclone rapidly intensified and gained its peak strength with winds of 140 kts (72 m s^{-1}). This intensification occurred when Celia traveled over a warm eddy containing waters with increased TCHP values which were close to 65 kJ cm^{-2}. The cooling under the track of this TC was weaker than Igor in the Atlantic Ocean, with observed SST values near 3°C and TCHP of 30 kJ cm^{-2}. This weaker oceanic response may be a response to the generally stronger vertical stratification found in the eastern Pacific that makes the ocean more difficult to mix. Despite the higher anomaly values of TCHP in the WNP, the season was a record-low year of TC occurrence. Despite the small number of observed storms, the TCHP conditions in September and October 2010 were extraordinarily favorable in the WNP, especially to the west of 150°E and to the south of 20°N, with values ranging from 120 kJ cm^{-2} to 170 kJ cm^{-2}, which are values well above the TCHP values commonly observed for super typhoons in this region (Lin et al. 2008, 2009).

As compared to the conditions in 2009, 2010 TCHP values were significantly greater by approximately 20 kJ cm^{-2} to 50 kJ cm^{-2} (Fig. 4.28). These unusually high TCHP values provided very favorable ocean conditions for the intensification of Super Typhoon Megi, the most intense TC globally in 2010. Megi formed to the west of Guam on 12 October 2010, and strengthened to a Category 5 super typhoon by 17 October. According to the preliminary Joint Typhoon Warning

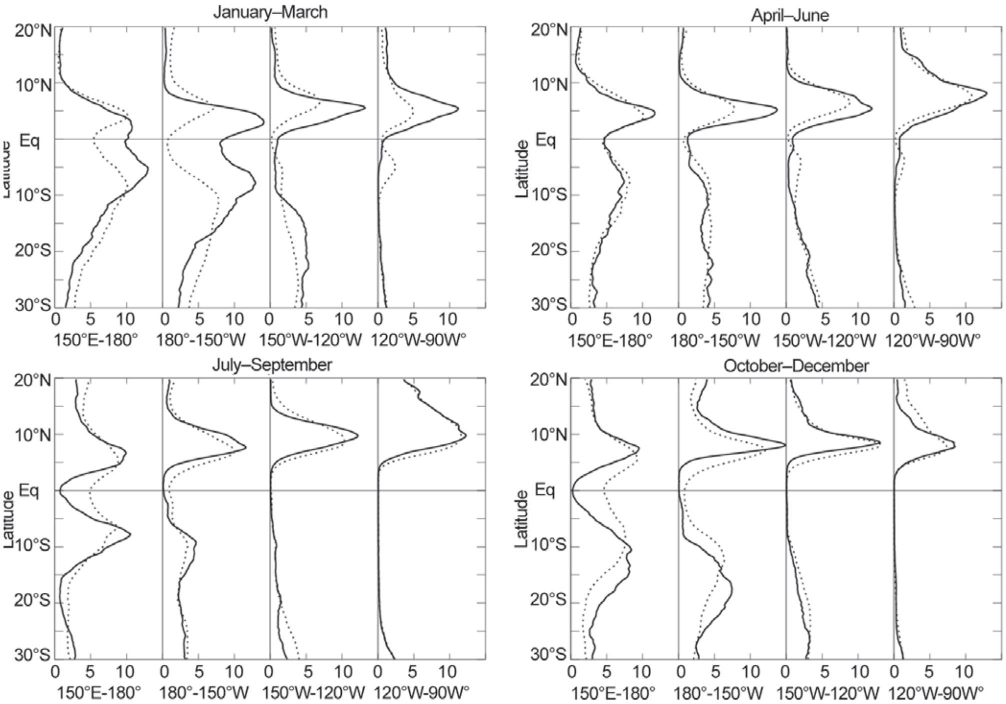

Fig. 4.30. Rainfall rate (mm day^{-1}) from TRMM 0.25° analysis for January–March, April–June, July–September, and October–December 2010. The separate panels for each three-month period show the 2010 rainfall cross-section between 20°N and 30°S (solid line) and the 1999–2008 climatology (dotted line), separately for four 30° sectors from 150°E–180° to 120°W–90°W.

Center (JTWC) report, Megi's intensity reached 160 kts (82 m s^{-1}), and an aircraft estimated its central pressure at 885 hPa, which is among the lowest TC pressures ever observed. Megi developed in this very favorable warm pool (Fig. 4.29) of extremely high TCHP values (typically ~100 kJ cm^{-2}–130 kJ cm^{-2}) throughout its genesis and intensification period. From 14 to 17 October, Megi intensified from a named storm to a Category 5 TC with maximum sustained winds of 160 kts (82 m s^{-1}). Megi subsequently made landfall in the Philippines.

Cyclone Phet was the most intense TC in the Arabian Sea in 2010 (Fig 4.29). The disturbance that eventually became Phet was identified early on 30 May and upgraded to a named storm on 31 May after a short genesis period. Early on 1 June, the moderate vertical wind shear relaxed and Phet intensified to a Category 1 cyclone with maximum sustained winds estimated at 65 kts (33 m s^{-1}) by JTWC. In the next 18 hours, it rapidly intensified from 65 kts (33 m s^{-1}) to 125 kts (64 m s^{-1}) to its peak at Category 4, an astonishing intensification rate well above the criteria for rapid intensification of 30 kts (15 m s^{-1}) in 24 hours (Kaplan and DeMaria 2003). The period of rapid intensification took place as Phet entered into a region of high TCHP of ~75 kJ cm^{-2}. After its departure from this high patch of TCHP, Phet weakened to approximately 105 kts (54 m s^{-1}) before making landfall in Oman, where it caused substantial damage estimated at ~$780 million (U.S. dollars) and accounted for 44 deaths. The storm later recurved over the northern Arabian Sea making a second landfall near the India-Pakistan border.

f. Intertropical Convergence Zones

1) Pacific—A. B. Mullan

This discussion for the Pacific sector covers the two prominent convergence zones: the Intertropical Convergence Zone (ITCZ) in the Northern Hemisphere, which lies approximately parallel to the Equator with a slight poleward tilt on its eastern end, and varying in position from around 5°N–7°N in February–May to 7°N–10°N in August–November; and the South Pacific Convergence Zone (SPCZ), which extends diagonally from around the Solomon Islands (10°S, 160°E) to near 30°S, 140°W, and is most active during November–April.

The behavior of the Pacific convergence zones in 2010 is readily characterized in two parts, with the first half of the year dominated by El Niño and the second half by La Niña. Thus, in the first half of 2010, both the ITCZ and SPCZ tended to be further equatorward than usual, with well-above-normal rainfall east of the date line near the Equator. In the second half of 2010, both the ITCZ and SPCZ tended to be poleward of their normal positions, with a much enhanced dry zone along the Equator. Figure 4.30 shows quarterly rainfall in the Pacific along transects from 20°N to 30°S, as derived from the 0.25°-resolution

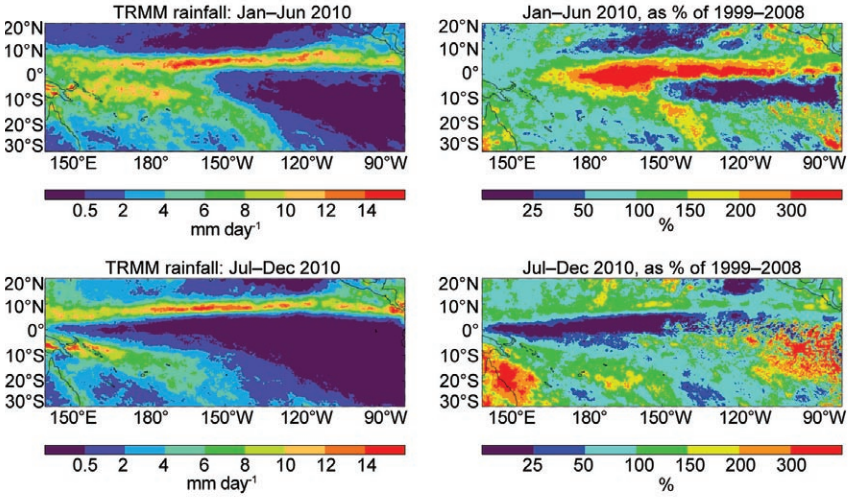

Fig. 4.31. Average rainfall rate (mm day^{-1}) from TRMM 0.25-degree analysis for January–June 2010 and July–December 2010, left-hand panels; and percentage anomaly from the 1999–2008 average, right-hand panels.

NASA TRMM rainfall data (3B-43 product; Huffman et al. 2007). The transects are broken up into four longitude sectors, depicting how the peak rainfall shifts poleward in each hemisphere as one progresses eastward across the Pacific. The 2010 positions of the convergence zones are compared with the 10-year climatology from 1999 to 2008.

The year began with a significant El Niño present in the Pacific. Although sea surface temperature anomalies decreased progressively from their peak in November–December 2009, temperatures remained at least 0.5°C above average through April 2010 and were sufficient to support enhanced deep tropical convection. Figure 4.30 shows substantially higher-than-normal rainfall in the first quarter of 2010 between 5°N–7°N and 10°S. Island groups within this band experienced wet conditions, with the month of February being particularly extreme; Christmas Island in eastern Kiribati (approximately 2°N, 157°W) recorded a new record rainfall for February with 818 mm, and Penrhyn in the Northern Cooks (10°S, 158°W) recorded a new February record of 1033 mm (ICU 2010).

Conversely, with the ITCZ contracting towards the Equator, islands north of about 7°N experienced dry conditions in the first half of the year. The Marshall Islands and Micronesia (around 7°N–10°N in the 150°E–180° sector, Fig. 4.30) were affected, as was Hawaii (near 20°N in the 180°–150°W sector); according to PEAC (2010), the Hawaiian wet season of October 2009 to April 2010 was the driest in the past 30 years. One convergence zone feature not present during 2010 was a double ITCZ, whereby a southern branch of the ITCZ appears in austral fall in the eastern tropical Pacific. Circulation and surface flux anomalies prevent this occurring in El Niño years (Masunaga and L'Ecuyer 2010), so it was not surprising to find the double ITCZ absent in 2010 (Fig. 4.31, top panels).

By July 2010, La Niña conditions were established across the Pacific and the climatic and circulation anomalies intensified further during the last quarter of the year. The peak rainfalls in the centers of the convergence zones were not markedly different from average, even on a monthly basis. However, both the ITCZ and SPCZ were shifted polewards and this had consequences for some island groups; the Fiji Islands (near the date line at 20°S) experienced

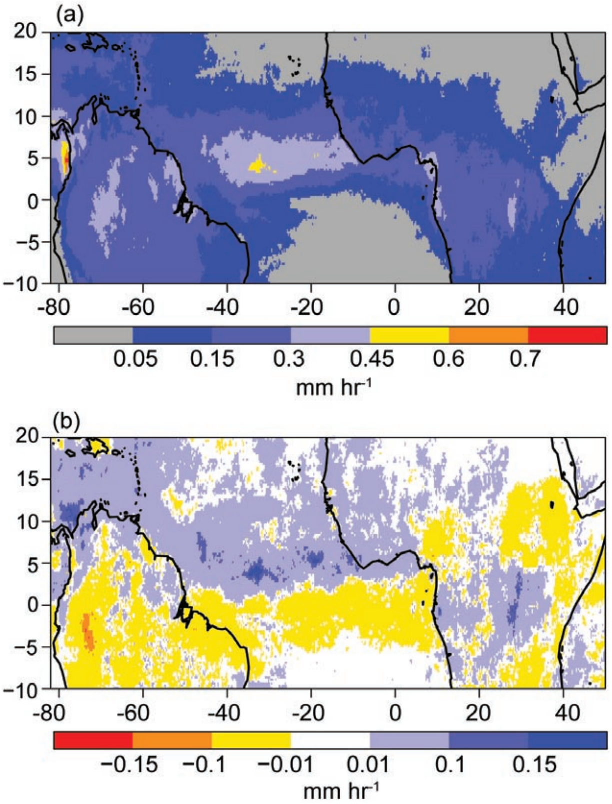

Fig. 4.32. TRMM (a) mean and (b) anomalous precipitation rate (mm hr^{-1}) for 2010. The anomaly was calculated based on the climatology for the period 1998–2009.

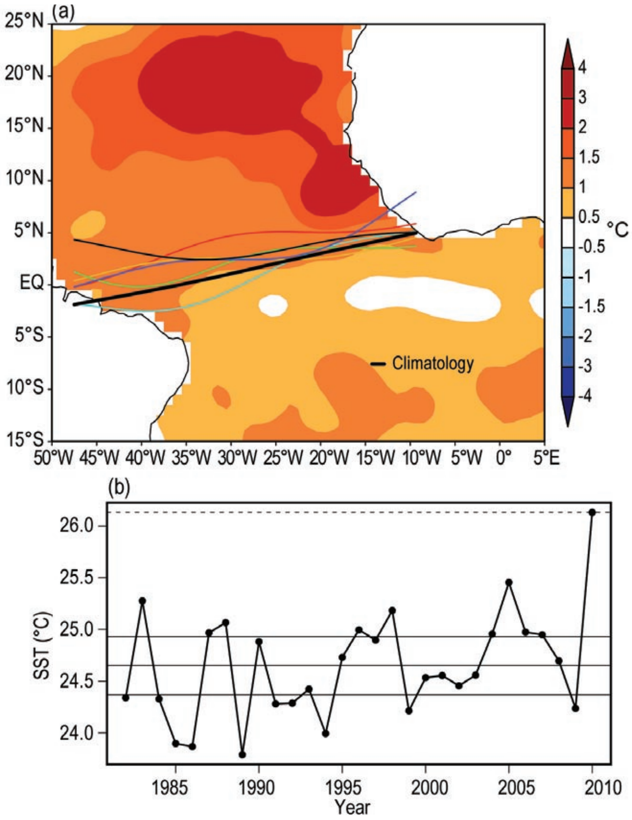

Fig. 4.33. (a) Atlantic Intertropical Convergence Zone (ITCZ) position inferred from outgoing longwave radiation during April 2010. The colored thin lines indicate the approximate position for the six pentads of April 2010. The black thick line indicates the Atlantic ITCZ climatological position. The sea surface temperature (SST) anomalies (Reynolds et al. 2002) for April 2010 based on the 1982–2009 climatology are shaded; and (b) April SST time series averaged over the tropical coast of northern Africa (20°E–50°E, 5°N–25°N) for the period 1982–2010. The solid horizontal central line indicates the long-term mean (climatology) of 24.6°C. The other two solid horizontal lines represent the upper and lower terciles of 24.9°C and 24.4°C, respectively. The dashed horizontal line puts the record value of 26.1°C measured in April 2010 in climate perspective.

wet conditions in the last quarter, as for the most part did New Caledonia on the eastern edge of the Coral Sea. More remarkable was the intensity of the dry zone along the Equator, which extended westwards of 150°E (Fig 4.31). The second panel in the October–December TRMM rainfall transects (Fig. 4.30) indicates almost no rainfall between about 5°N and 7°S east of the date line; in a major turnabout from February, Christmas Island (eastern Kiribati) received less than 10 mm in November, while in the same month Penrhyn (Northern Cooks) had only about 25% of its normal November rainfall.

2) Atlantic—A. B. Pezza and C. A. S. Coelho

(i) Description

The Atlantic ITCZ is a well organized convective band that oscillates approximately between 5°N–12°N during July–November and 5°N–5°S during January–May (Waliser and Gautier 1993; Nobre and Shukla 1996). Equatorial Kelvin waves can modulate the ITCZ interannual variability and ENSO is also known to influence the ITCZ on the seasonal time scale (Münnich and Neelin 2005). In 2010, the Atlantic ITCZ presented an anomalous displacement to the north of its normal position, indirectly contributing to a severe drought in the Amazon and northeastern Brazil (Fig. 4.32 and Fig. 4.33a). As a result, adverse impacts were felt on cargo and human transportation that rely on local rivers in the Amazon. Conversely, the ITCZ was also directly associated with above-average precipitation on the western tropical coast of Africa between 5°N and 20°N (Fig. 4.32b).

Although the year was highlighted by the onset of a moderate-to-strong La Niña beginning in July, with global climate anomalies typical of a positive Southern Oscillation Index (SOI) regime arising in many areas of the globe, it was the Atlantic SST gradient between the Northern and the Southern Hemispheres that played a fundamental role in explaining the anomalous behavior of the Atlantic ITCZ in 2010 (Fig. 4.33a). Since January, the Atlantic remained anomalously warm to the north of the Equator, reaching satellite-era record warming conditions of 26.1°C towards April (Fig. 4.33b). This record warming is

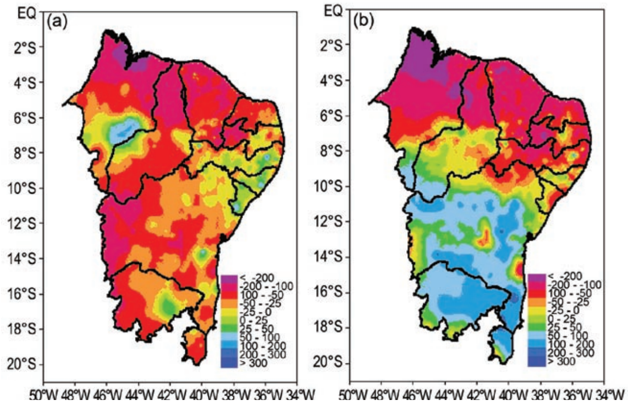

Fig. 4.34. Northeastern Brazil precipitation anomalies (mm) during (a) February and (b) March 2010 with respect to 1961–90 climatology based on high resolution station data. [Data source: several federal and regional networks based in Brazil (e.g., CMCD/INPE, INMET, SUDENE, ANEEL, FUNCEME/CE, LMRS/PB, EMPARN/RN, LAMEPE/ITEP/PE, CMRH/SE, SEAAB/PI, SRH/BA, CEMIG/SIMGE/MG, SEAG/ES)].

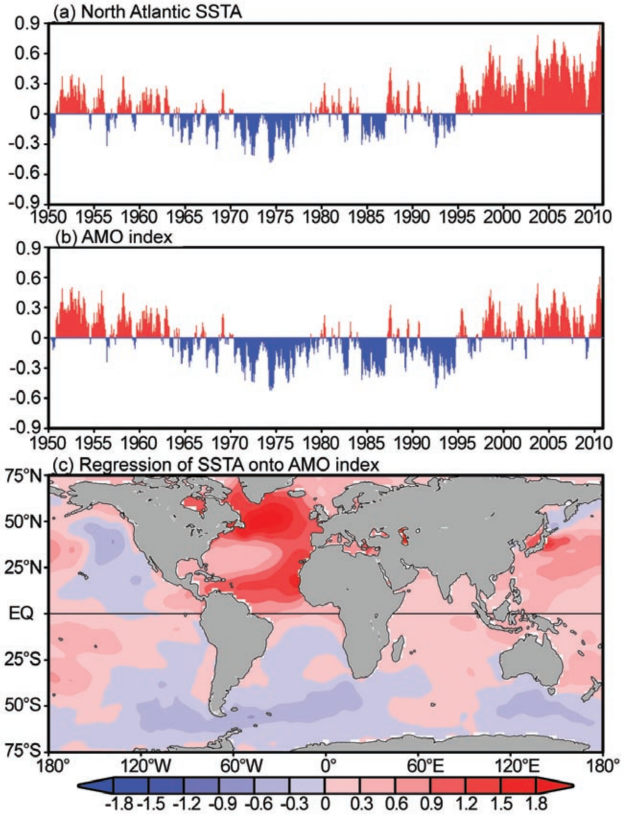

Fig. 4.35. The index of the Atlantic Multidecadal Oscillation (AMO) and its spatial pattern. Shown are: (a) the sea surface temperature (SST) anomalies (°C) in the North Atlantic for 0°–60°N and from the east coast of the Americas to 0° longitude; (b) the AMO index (°C) defined by the detrended (removing the linear trend) North Atlantic SST anomalies; and (c) regression (°C per °C) of global SST anomalies onto the AMO index of (b). The monthly SST anomalies are calculated as departures from the 1971–2000 climatology.

remarkable as it encompassed a very large area of the North Atlantic, and is more than 0.6°C above the second largest value of 25.5° C recorded in April 2005 in this region. The warming persisted throughout most of the year, losing intensity only in November, while La Niña conditions remained moderate-to-strong.

As a result, the ITCZ did not exert a significant contribution towards the rain in northeastern Brazil in 2010, with a large portion of the region experiencing much drier conditions than average, especially in February and March when the climatological influence of the ITCZ towards the Southern Hemisphere should have been important (Fig. 4.34).

g. Atlantic Multidecadal Oscillation—C. Wang

The Atlantic Multidecadal Oscillation (AMO) is an oscillatory mode defined by the detrended North Atlantic SST anomalies over the region of 0°–60°N and from the east coast of the Americas to 0° longitude (Figs. 4.35a,b; Delworth and Mann 2000; Enfield et al. 2001; Wang et al. 2008a; see also Sidebar 1.1). A driving mechanism for the AMO is the Atlantic meridional overturning circulation (Delworth and Mann 2000; Knight et al. 2005; Dijkstra et al. 2006; Zhang et al. 2007; see also section 3h for detailed information on the meridional overturning circulation). The AMO demonstrates an interannual variation via its connection to the tropical Atlantic Warm Pool (AWP; a large body of warm water comprising the Gulf of Mexico, Caribbean Sea, and the western tropical North Atlantic), and as such has exhibited a seasonal influence on the behavior of tropical cyclones (TCs) in the Atlantic and Eastern North Pacific (ENP) basins. The extended reconstructed SST (ERSST) data from 1950 to 2010 shows that the AMO was in the cold phase from the late 1960s to the early 1990s and in the warm phase before the late 1960s and again, after the early 1990s. The AMO is related to SST anomalies over the global oceans as shown in Fig. 4.35c.

The AMO variability is associated with changes of climate and extreme events, such as drought and flood in North America and Europe, and Atlantic hurricane activity (Enfield et al. 2001; McCabe et al. 2004; Goldenberg et al. 2001; Bell and Chelliah 2006; Wang et al. 2008a). Recent studies show that the importance of the AMO is due to its tropical component since the climate response to the North Atlantic SST anomalies is primarily forced at the low latitudes (Sutton and Hodson 2007; Wang et al. 2008b). Since the AWP is at the center of the main development region (MDR) for Atlantic tropical cyclones, the influence of the AMO on climate and Atlantic TC activity operates through the mechanism of the AWP-induced atmospheric changes by having an effect on vertical wind shear in the MDR. A large AWP reduces such shear, while a small AWP enhances it. A large AWP also weakens the southerly Great Plains low-level jet, thus reducing the northward moisture transport from the Gulf of Mexico to the eastern U.S. and decreasing the boreal summer rainfall over the central U.S., while a small AWP has the opposite effect (Wang et al. 2006; Wang et al. 2008b). It has also been shown that AWP variability can produce the observed out-of-phase relationship between TC activity in the tropical North Atlantic and ENP (Wang and Lee 2009).

The AMO in 2010 remained in its warm phase and showed extremely positive SST anomalies in the North Atlantic (Fig. 4.36a). The warm phase of the AMO was strongest in August (+0.90°C) and weakest

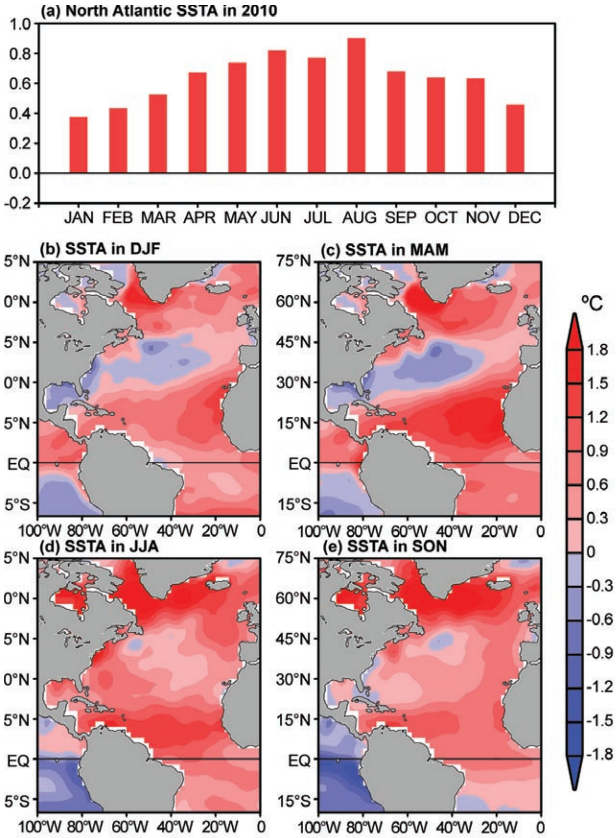

Fig. 4.36. The Atlantic Multidecadal Oscillation (AMO) in 2010. Shown are: (a) the monthly North Atlantic sea surface temperatures (SST) anomalies (°C) in 2010; (b) the DJF (December 2009–February 2010) SST anomalies (°C); (c) the MAM (March–May 2010) SST anomalies; (d) the JJA (June–August 2010) SST anomalies; and (e) the SON (September–November 2010) SST anomalies. The monthly SST anomalies are calculated as departures from the 1971–2000 climatology.

in January (+0.38°C). Spatially, the North Atlantic SST anomalies during the boreal winter and spring seasons showed a tripole pattern with the positive SST anomalies in the subpolar North Atlantic and the tropical North Atlantic and the negative SST anomalies in the subtropical North Atlantic (Figs. 4.36b,c). The SST anomaly pattern divided the AWP into two parts: a colder Gulf of Mexico and a warmer Caribbean Sea/western tropical North Atlantic. The opposite SST anomaly pattern was consistent with a previous study (Muñoz et al. 2010), which showed that the air-sea fluxes associated with ENSO events in the tropical Pacific and local processes were responsible for the SST anomaly distribution.

During the boreal summer and fall of 2010, the cold SST anomalies in the subtropical North Atlantic almost disappeared and the North Atlantic was consistently warm (Figs. 4.36d,e). During the 2010 Atlantic TC season, the AWP was also consistently large and the entire tropical North Atlantic was warm. A large AWP also tends to shrink the North Atlantic subtropical high eastward (C. Wang et al. 2007) and hurricanes are therefore steered away from the eastern coast of the United States. The extremely large AWP in 2010 was also associated with the out-of-phase relationship between TCs in the North Atlantic and the ENP as documented in sections 4d2 and 4d3.

h. Indian Ocean Dipole—J. J. Luo

Year-to-year climate variability in the tropical Indian Ocean (IO) is largely driven by local ocean-atmosphere interactions and ENSO. The Indian Ocean Dipole (IOD), as one major internal climate mode in the IO, may sometimes be originated from complex interactions between the IO and Pacific (J.-J. Luo et al. 2010). Owing to the warm mean state in the IO, the IOD often causes large climate anomalies in many countries surrounding the IO despite the fact that SST anomalies related to IOD are usually weak and more localized compared to the ENSO signal. During late boreal summer to fall in 2010, a negative IOD (nIOD) occurred, five years after the last nIOD event in 2005 (Luo et al. 2007). Compared to previous events, the 2010 nIOD was strong, with a peak warming of about 1°C above normal in the eastern IO (Fig. 4.37b) during 2010 fall season; this event may have contributed

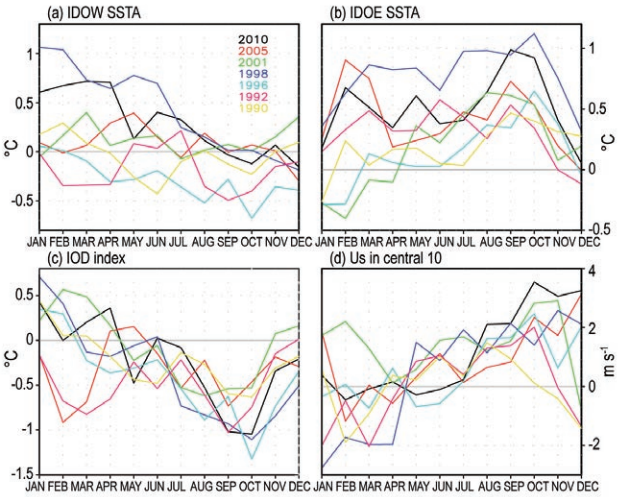

Fig. 4.37. Monthly anomalies of (a) sea surface temperatures (SST) in the western Indian Ocean (IODW, 50°E–70°E, 10°S–10°N); (b) SST in the eastern IO (IODE, 90°E–110°E, 10°S–0°); (c) the IOD index (measured by the SST difference between IODW and IODE) during the seven negative IOD events; and (d), as in (c), but for the surface zonal wind anomaly in the central equatorial IO (70°E–90°E, 5°S–5°N).

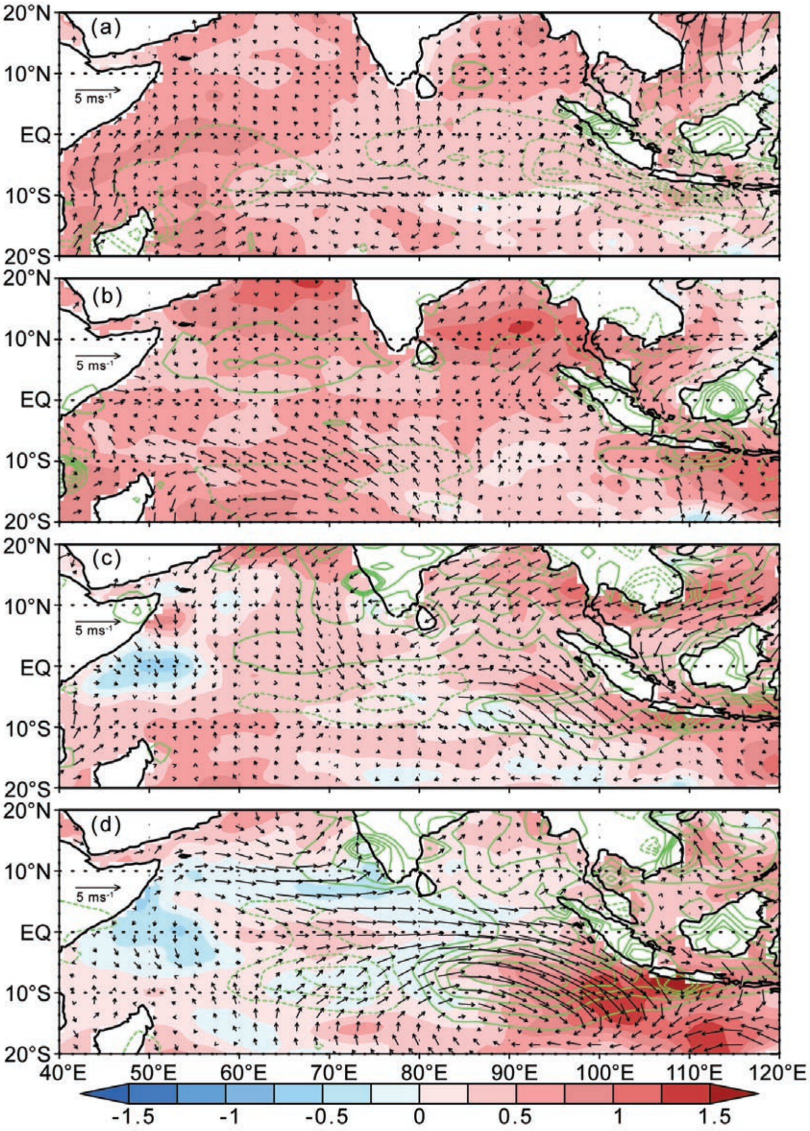

Fig.4.38. Sea surface temperature (°C, colored scale), precipitation (green contour: ±1, ±2, …,±5 mm day^{-1}), and surface wind anomalies during (a) December–February 2009/10; (b) March–May 2010; (c) June–August 2010; and (d) September–November 2010. Anomalies were calculated relative to the climatology over the period 1982–2009. These are based on the NCEP optimum interpolation SST (Reynolds and Chelton 2010), monthly GPCP precipitation analysis (http://precip.gsfc.nasa.gov/), and JRA-25 atmospheric reanalysis (Onogi et al. 2007).

to the floods in Indonesia and Australia.

Sea surface temperatures in major parts of the tropical IO during early 2010 were warmer than normal in association with influence of the strong El Niño, which peaked in December 2009 (Fig. 4.38a). This El Niño caused basin-wide drought in the IO; as a result, more surface solar radiation and less latent heat loss contributed to the IO basin-wide warming. Large warming appeared in the western IO mainly due to the surface heat flux forcing, whereas local subsurface temperature was below normal. The warming contrast between the western and eastern IO led to a weak positive IOD index during January–April 2010 (black line in Fig. 4.37c). In March–May 2010, the IO basin-wide warming persisted (Fig. 4.38b) despite the rapid weakening of the El Niño signal; this represents the well-known delayed impact of ENSO on the IO climate. Large warming appeared in the North IO and Indonesia-Australia area. The latter warming induced surface convergence and hence more rainfall along the south coast of Java. Correspondingly, a local northwesterly anomaly occurred along the west coast of Sumatra and persisted until July 2010 (Figs. 4.37d, and 4.38b,c). It is interesting to note that the IOD index in May 2010 reached about -0.5°C because of the sudden decrease (increase) of the western (eastern) IO SST anomalies (black lines in Figs. 4.37a–c). This monthly fluctuation, however, was not coupled with the surface wind anomaly in the central IO (Fig. 4.37d); it appears to have been induced by intraseasonal oscillations in the IO.

Massive westerly anomalies in the equatorial IO appeared in August 2010; this is related to the impact of a moderate-to-strong La Niña, which had developed quickly in mid-2010. The westerly anomalies in the central IO drove a downwelling oceanic Kelvin wave, which subsequently propagated eastward and deepened the thermocline along the west coast of Sumatra (Fig. 4.39a). As a result, the original warming near the Java coast intensified and expanded northward, and strong northwesterly anomalies occurred along the west coast of Sumatra during late summer to fall in 2010 (Figs. 4.38c,d). Meanwhile, SSTs in the western IO decreased due to both La Nina's influence and nIOD development. The warming (cooling) of SST in the east (west) and

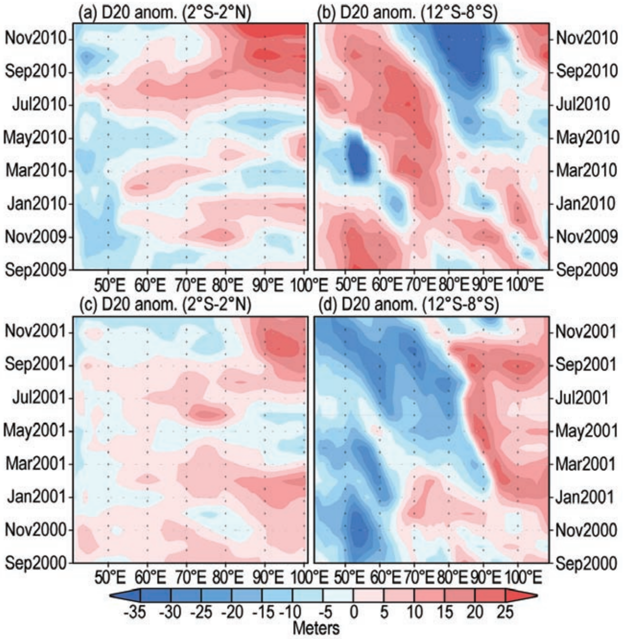

Fig. 4.39. 20°C isotherm depth (D20, meter) anomalies in (a) the equatorial Indian Ocean (2°S–2°N) and (b) off-equatorial South Indian Ocean (12°S–8°S) associated with the negative Indian Ocean Dipole (nIOD) development in 2010. (c) and (d) As in (a) and (b), respectively, but for the D20 anomalies related to the nIOD event in 2001. Data are derived from the NCEP ocean reanalysis (http://www.cpc.ncep.noaa.gov/products/GODAS/).

strengthening of the central IO westerly winds clearly represents the air-sea coupled process related to the nIOD growth. During November–December 2010, the nIOD signal weakened rapidly despite the strong westerly anomaly in the central IO (black lines in Fig. 4.37); this is due to the demise of warm SST anomalies in the eastern IO owing to the reversal of monsoonal winds. The stronger-than-normal winds and greater cloud coverage in the east weakened the SST warming in that region quickly.

The evolution of the nIOD in 2010 is similar to that of previous events (Fig. 4.37). Although significant variability among the seven nIOD events over the past two to three decades can be seen, the IOD index in most cases shows a positive value in early year, the onset in late spring to summer, the peak in fall, and the rapid demise in November–December (Fig. 4.37c). This is consistent with the strengthening of westerly winds in the central IO. While the western IO SST anomalies show a consistent decrease associated with the nIOD development, evolutions of SST anomalies in the eastern IO appear to be largely influenced by ENSO (Figs. 4.37a,b). In the four cases following El Niño events (1992, 1998, 2005, and 2010), warmer-than-normal SSTs in the eastern IO start to occur early in the year, persisting in spring and summer, and strengthening in fall. Contrasting this, in the three cases following La Niña events (1990, 1996, and 2001), SST anomalies early in the year were colder than normal or neutral. El Niño or La Niña events may also drive downwelling or upwelling oceanic Rossby waves propagating westward at about 10°S (Figs. 4.39b,d), which enhance or hamper the nIOD development in the following year. Therefore, it is possible that the nIOD event in 2010 may have been driven by both the previous El Niño and concurrent La Niña, but further research will be required to determine that more definitively.

SIDEBAR 4.1: EASTERN CANADA'S TROPICAL TAP—A RECORD YEAR FOR TROPICAL CYCLONE IMPACTS IN CANADA

—C. T. FOGARTY AND H. J. DIAMOND

The 2010 Atlantic Hurricane Season was an active one, with 19 named storms and 12 hurricanes—five of which reached major hurricane status. The large-scale pressure patterns over the western North Atlantic Ocean and eastern North America permitted many of this year's tropical storms and hurricanes to track northward toward eastern Canada, leaving the United States relatively unscathed. Two storms directly affected Canada in 2010. On 4 September, the very large Hurricane Earl made landfall in Nova Scotia, followed on 21 September by Hurricane Igor walloping Newfoundland. Canada was also impacted by indirect effects from Tropical Storm Nicole and Hurricane Tomas in the form of flooding rains courtesy of a high-amplitude flow pattern over eastern North America.

Hurricane Earl arrived in Nova Scotia as one of the most well-defined hurricanes that forecasters here have seen in many years (Fig. 4.40). Earl made landfall as a 65 kt ($33\ \mathrm{m\ s^{-1}}$) Category 1 hurricane, resulting in a drowning fatality. Winds uprooted many trees, generated widespread power outages, and caused exterior damage to buildings. Significant wave heights of 10 meters to 13 meters were recorded with peak waves up to 23 meters, and storm surge in Bedford Basin (at the head of Halifax Harbor) reached 1.2 meters; however, the coastal surge and wave impacts were minimal since the hurricane arrived at low tide.

Hurricane Igor was by far the most damaging tropical cyclone to strike Newfoundland in the modern era with total damage estimates near $185 million (Canadian dollars). The combination of the hurricane and a front to its north (Fig. 4.41) caused severe river flooding over the entire eastern portion of the island of Newfoundland. Many bridges were washed away, leaving giant chasms in most major roads, resulting in a fatality and causing major disruptions for several weeks after the event. High winds blew roofs off homes on the Avalon Peninsula and toppled many trees in the capital city of St. John's. The proposal by the Meteorological Service of Canada to have the name Igor retired from the list of hurricane names was approved in May 2011. This is only the second Canadian hurricane whose name was retired from the list. Juan was removed from the list after striking Nova Scotia as a Category 2 hurricane in 2003, inflicting an estimated $200 million (Canadian dollars) worth of damage.

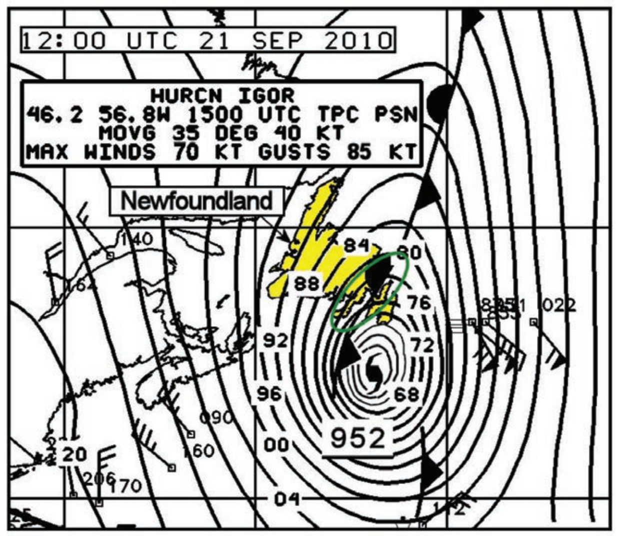

Fig. 4.41. Sea level pressure analysis of Hurricane Igor and large-scale pressure pattern with fronts at 12 UTC 21 September 2010. Image adopted from the NOAA Ocean Prediction Center. Area of extreme rainfall is shown by the green ellipse.

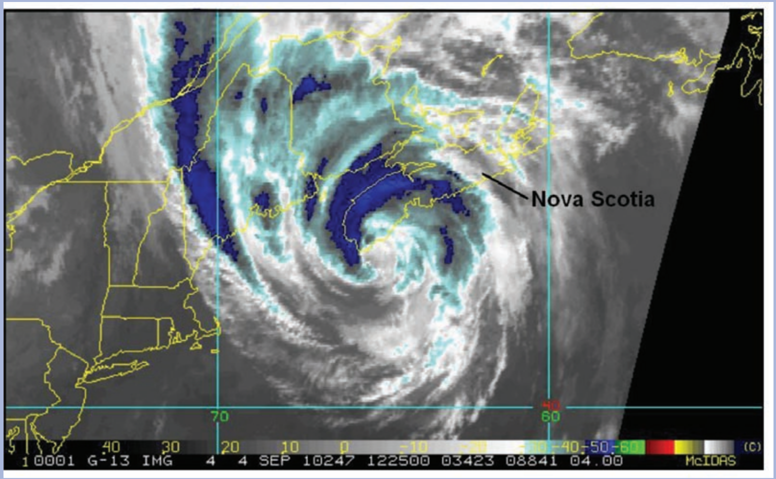

Fig. 4.40. Enhanced infrared satellite image of Hurricane Earl just before landfall in Nova Scotia at 1225 UTC 04 September 2010. Image courtesy of the NOAA/NESDIS tropical cyclone website at http://www.ssd.noaa.gov/PS/TROP/.

The moisture remnants of Tropical Storm Nicole (near Florida) swamped portions of southern Quebec, New Brunswick, and many U.S. states south of the Canadian border as a long front extended all the way from the province of Quebec to the remnant low associated with Nicole over the Bahamas. Two fatalities were reported in Canada from the heavy rainfall, which totaled almost 100 mm.

The tropical season's final assault on Canada was from the combined effects of

cont. SIDEBAR 4.1: EASTERN CANADA'S TROPICAL TAP—A RECORD YEAR FOR TROPICAL CYCLONE IMPACTS IN CANADA—C. T. FOGARTY AND H. J. DIAMOND

a dissipating Hurricane Tomas north of the Bahamas and a stationary belt of moisture streaming northward for several days (see Fig. 4.42). Similar to Nicole a little over a month earlier, a blocking pattern in the midlatitude flow was the culprit. A five-day deluge amounting to almost 300 mm caused major flooding over western Nova Scotia and southern New Brunswick. Some bridges were washed out and a number of homes were severely flooded. The example of Hurricane Tomas is very similar to a predecessor rain event as described by Galarneau et al. (2010).

The large-scale blocked weather pattern continued into December with four major marine storms pummeling eastern Canada in succession. Flood-weary New Brunswick was hit particularly hard with both ocean surge and freshwater flooding, marking the end of one of the stormiest spells of weather in recent memory for the region.

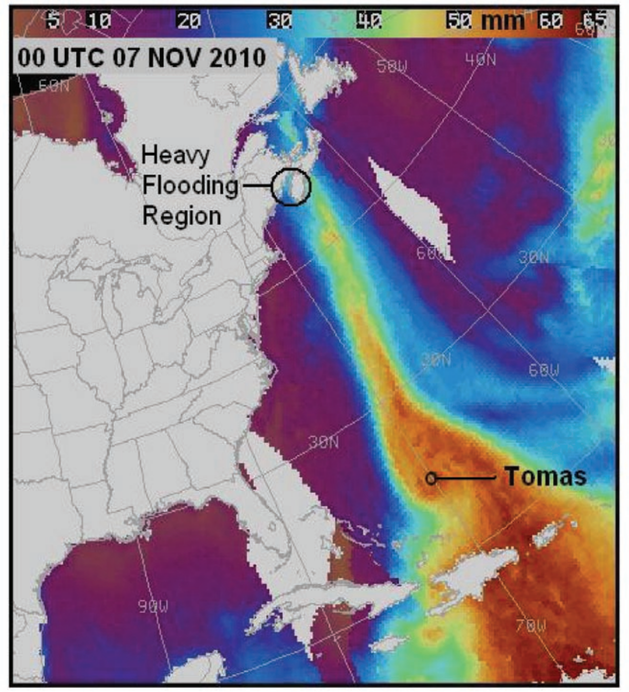

Fig. 4.42. Total column precipitable water at 00 UTC 07 November 2010 derived from the Special Sensor Microwave Imager (SSM/I) and Advanced Microwave Scanning Radiometer-Earth Observing System (AMSR-E) at the Cooperative Institute for Meteorological Satellite Studies (CIMSS).

5. THE ARCTIC—J. Richter-Menge and M. Jeffries, Eds.

a. Overview—J. Richter-Menge and M. Jeffries

This chapter describes observations of continuing change in the Arctic environmental system. It is organized into five broad sections: atmosphere, ocean, sea ice cover, land, and Greenland. The land section includes vegetation, permafrost, river discharge, terrestrial snow, and glaciers outside Greenland.

The year 2010 marks the end of the warmest decade on record in the Arctic since instrumental records began in 1900. The distribution of near-surface air temperature anomalies over the entire Arctic region continued to show a factor of two (or more) amplification relative to lower latitudes. Changes throughout the Arctic system exemplify this broad pattern of persistent warming and its integrated consequences. For instance:

- Events in Greenland in summer 2010 epitomize the high rate and magnitude of environmental change that is occurring in the Arctic. Unprecedented high surface and upper air temperature were the result of a persistent atmospheric circulation pattern that favored northward advection of warm air along the west side of Greenland in particular. The warm air from the south was responsible for the longest period and largest area of ice sheet melt since at least 1978, and the highest melt rate since at least 1958.
- West of Greenland, high summer air temperatures and a longer melt season also occurred in the Canadian Arctic, where the rate of mass loss from small glaciers and ice caps continued to increase. At the circum-Arctic scale, with the exception of Scandinavia, a combination of low winter (2009/10) snow accumulation and high spring air temperatures resulted in a record minimum spring snow cover duration.
- Eight of the ten smallest summer sea ice minima have occurred in the last decade, and the September 2010 Arctic sea ice extent was the third lowest of the past 30 years. After a record minimum summer sea ice cover in 2007, the upper Arctic Ocean remains relatively warm and fresh, a condition that is affecting marine biology and geochemistry.
- Observations of circumpolar changes to tundra vegetation indicate continued increases in greening associated with more abundant ice-free coastal waters and higher tundra land surface temperatures. Temperatures in coastal permafrost in northernmost Alaska continue to increase and there is evidence that the warming is propagating inland. Rising air and land temperatures continue to have hydrological consequences, with an earlier and more rapid rise in Eurasian river discharge in 2010.

b. Atmosphere—J. Overland, M. Wang, and J. Walsh

For the last decade, the average annual temperature over Arctic land has been the warmest in the record beginning in 1900 (Fig. 5.1). The annual mean air temperature for 2010 mirrored 2009, with slightly lower temperatures than in recent years. The distribution of 2010 annual average near-surface air temperature anomalies over the entire Arctic region continued to show a factor of two (or more) amplification relative to lower latitudes (Fig. 5.2a). This distribution was dominated by above-normal temperatures in northern Canada, the Baffin Bay region, including the west coast of Greenland, and the Pacific side of the central Arctic.

In general, all of the seasonal composites indicate widespread positive air temperature anomalies throughout most of the Northern Hemisphere relative to the baseline years of 1968–96 (Figs. 5.2b–e). Springtime above-normal temperature anomalies were observed from the Siberian Arctic coastal zone across to northern Baffin Bay and the west coast of Greenland and south into the northeastern U.S. (Fig. 5.2c). This continued the springtime pattern seen in the previous decade. These conditions set the stage for record-setting onset to spring snow melt across much

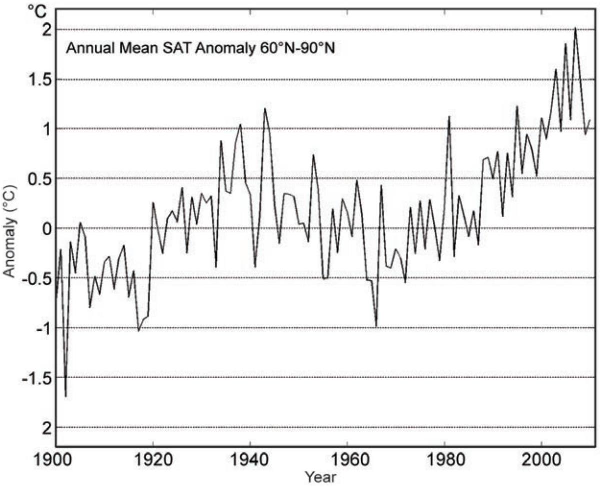

Fig. 5.1. Arctic-wide annual average surface air temperature (SAT, °C) anomalies relative to the 1961–90 mean, based only on land stations north of 60°N. Data are from the CRUTEM 3v dataset, http://www.cru.uea.ac.uk/cru/ data/temperature/.

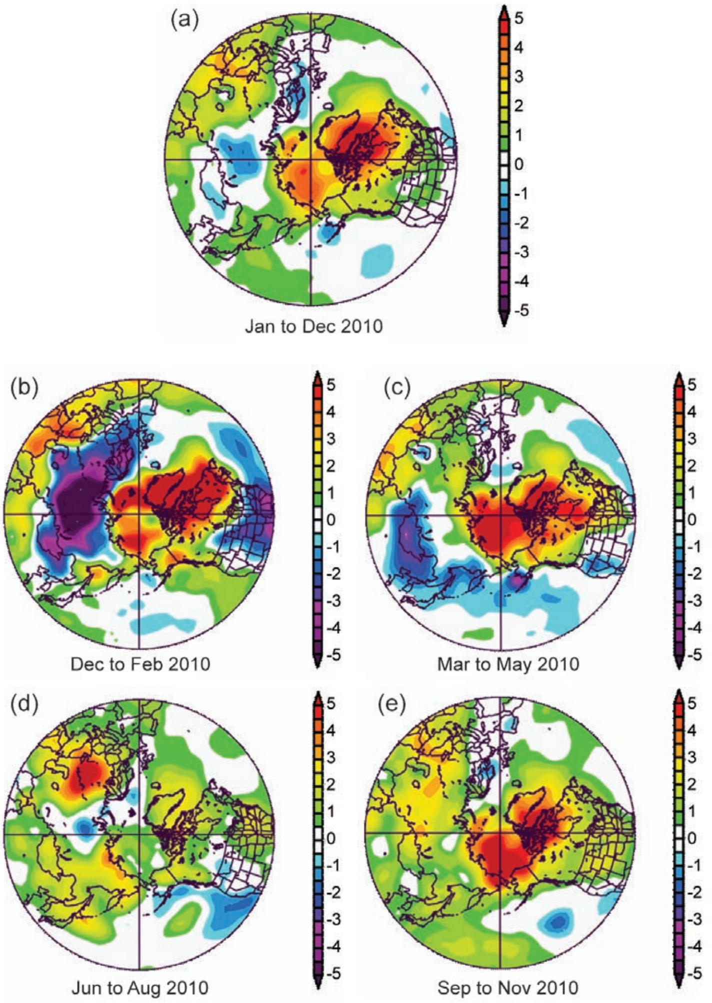

Fig. 5.2. Near-surface (1000 mb) air temperature (°C) anomalies, relative to the 1968–96 mean according to the NCEP/NCAR Reanalysis of the NOAA Earth Systems Research Laboratory (ESRL). (a) January–December 2010; (b) December 2009–February 2010; (c) March–May 2010; (d) June–August 2010; and (e) September–November 2010. These charts were generated online at www.cdc.noaa.gov.

of the Arctic region, contributing to a shorter-than-normal snow season (see section 5e4) and record-setting surface air temperatures along west Greenland (see section 5f). They also reflect the distribution of ice loss observed in arctic glaciers outside of Greenland (see section 5e5). Autumn shows a pattern of temperature anomalies (Fig. 5.2e) that relates to summer sea ice loss north of Alaska and eastern Siberia and from northeastern Canada and Baffin Bay (see section 5d1).

A strong meridional atmospheric circulation pattern in winter facilitated the advection of cold air from the Arctic southward into eastern midlatitude North America and Asia and northern Europe (Figs. 5.3a,b; Seager et al. 2010b). This has been called the Warm Arctic-Cold Continent climate pattern and is associated with a weak polar vortex. In winter, cold air is normally maintained in the Arctic by strong polar vortex winds consistent with a low geopotential height field and strong vorticity over the central Arctic. Two indicators of a weak polar vortex are a negative Arctic Oscillation index (AO) and a negative North Atlantic Oscillation (NAO) index (see Sidebar 1.1). December 2009 through February 2010 had the lowest NAO values in 145 years of historical record. Very negative AO values also occurred in the same period and in December 2010. Negative (cold) temperature anomalies during February and December 2010 over land in Siberia helped to offset its warm anomalies in spring and fall, thus giving lower annual mean values than in other recent years (Fig. 5.1).

Balancing the wintertime events that create a southerly flow of cold air towards the midlatitudes are regions of warm air moving northward during the same months. For example, warm anomalies are observed in December 2010 covering all of Greenland, northeastern Canada, and far eastern Siberia (Fig. 5.3b). The combination of overall warm anomalies in spring, summer, and fall combined with the warm Arctic-cold

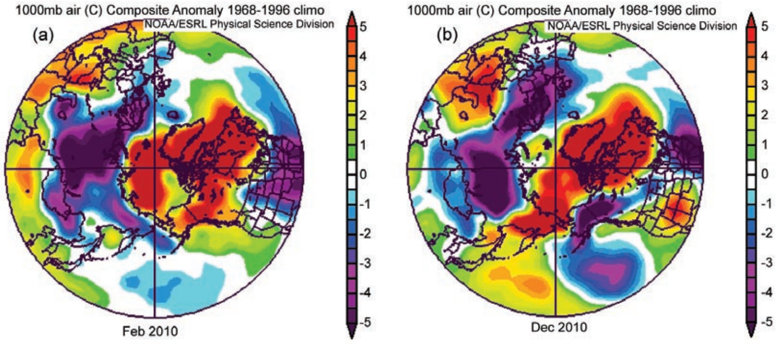

Fig. 5.3. The Warm Arctic-Cold Continent climate pattern for (a) February 2010 and (b) December 2010 illustrated by air temperature (°C) anomalies from the normal 1000 mb air temperature values observed during 1968–96. Data are from the NCEP/NCAR Reanalysis of NOAA ESRL. The charts were generated online at www.cdc.noaa.gov.

continent pattern in winter, gave a large positive temperature anomaly to west Greenland throughout the year. This included summer (June–August, Fig. 5.2d), with a pattern of warm anomalies over the Baffin Bay region and the east Siberian coastal region, similar to but weaker than spring and fall (Figs. 5.2c,e).

c. Ocean—A. Proshutinsky, M.-L. Timmermans, I. Ashik, A. Beszczynska-Moeller, E. Carmack, I. Frolov, M. Itoh, T. Kikuchi, R. Krishfield, F. McLaughlin, S. Nishino, B. Rabe, U. Schauer, K. Shimada, V. Sokolov, M. Steele, J. Toole, W. Williams, R. Woodgate, M. Yamamoto-Kawai, and S. Zimmermann

1) Wind-driven circulation

In 2010, the annual wind-driven ocean circulation regime was anticyclonic (clockwise) with a well-organized Beaufort Gyre and relatively weak transpolar drift system (Fig. 5.4). The current anticyclonic circulation regime has persisted since 1997, i.e., for 13 years, instead of the typical five to eight year pattern (Proshutinsky and Johnson 1997). It may be that after the anomalous 2007 conditions (a historical minimum of September sea ice extent and maximum upper-ocean warming and freshening) the Arctic climate system bifurcated towards a new state characterized by a more persistent anticyclonic regime and with relatively small changes from year to year.

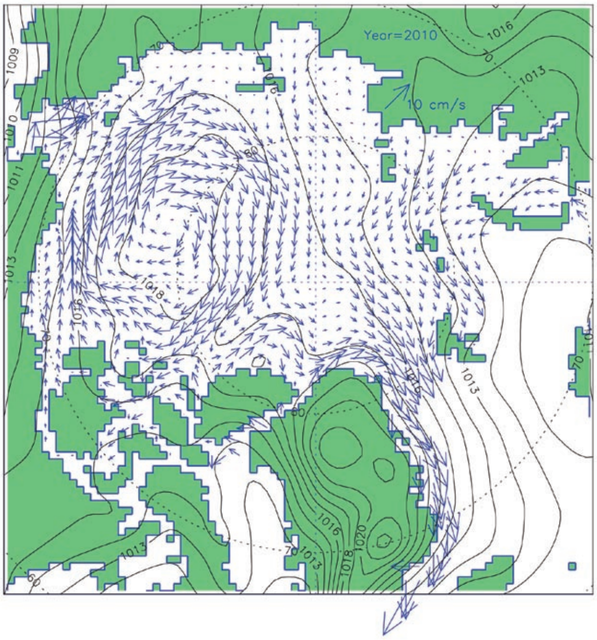

Fig. 5.4. Annual 2010 simulated wind-driven ice motion (arrows) and sea level atmospheric pressure (hPa, black lines). Results are from a 2-D coupled ice-ocean model (Proshutinsky and Johnson 1997, 2011) forced by wind stresses derived from 2010 NCEP/NCAR reanalysis six-hourly sea level pressure fields.

2) Ocean temperature and salinity

(i) Upper ocean

Upper-ocean temperature anomalies in summer 2010 (Fig. 5.5) were comparable to those in 2009 but remained lower than the record set in 2007 (Proshutinsky et al. 2010) Interannual variations in sea surface temperature (SST) anomalies reflect differences in the pace of sea ice retreat, as well as changing advection of warm ocean currents from the south (Steele et al. 2010). In recent years, solar radiation has penetrated more easily into the upper ocean under thinning and retreating ice cover to create high near-surface temperature maxima (Jackson et al. 2010; Yang 2009; Toole et al. 2010; McPhee et al. 2009).

Relative to the 1970s, surface waters in the Arctic Ocean in 2009–10 (Fig. 5.6) were generally saltier in the Eurasian Basin and fresher in the Canadian Basin, with the maximum freshwater anomaly centered in the Beaufort Gyre. The western Canada Basin surface waters were fresher in 2009 and 2010 than in 2007 and 2008, with saltier surface waters in the eastern Canada Basin. The region between Greenland and the North Pole was generally fresher in 2009–10 than in 2007–08, while the upper ocean was saltier in the western Makarov Basin in 2009 and 2010 (Timmermans et al. 2011).

(ii) Beaufort Gyre freshwater and heat content

The Beaufort Gyre (BG) is the largest reservoir of freshwater in the Arctic Ocean. In 2010, the magnitude of BG freshwater content was comparable to 2008 and 2009 conditions; however, the region of freshwater tended to spread out from the 2007–09 center (Fig. 5.7, right panels). During 2003–10, the BG accumulated more than 5000 km^3 of freshwater, a gain of approximately 25% (update to Proshutinsky et al. 2009) relative to climatology of the 1970s. The Beaufort Gyre heat content (Fig. 5.7, left panels) in 2010 increased relative to 2009 by approximately 5%.

Freshwater increases were not limited to the BG. Observations of the upper ocean freshwater content for the entire Arctic Ocean indicate that from 1992–99 to 2006–08 the freshwater content increased by 8400 ± 2000 km^3 (Rabe et al. 2011).

(iii) The Atlantic water layer

Warm water of North Atlantic origin, the Atlantic water layer (AWL), resides between approximately 200 meters and 900 meters and is characterized by temperatures greater than 0°C and salinities greater than 34.5. In 2009–10, AWL maximum temperature anomalies were generally highest on the Eurasian side

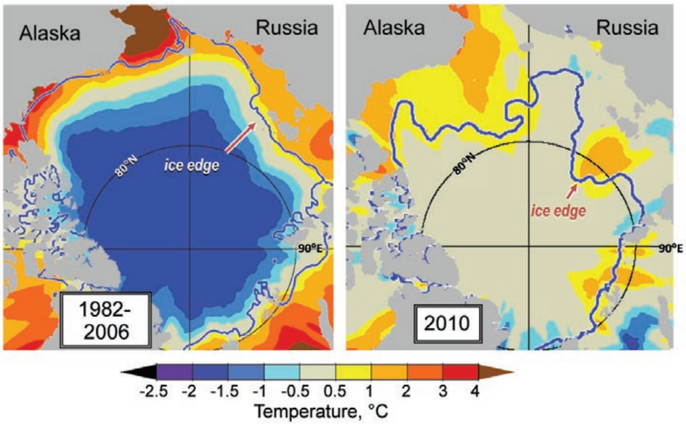

Fig. 5.5. Summer (June–September) SST anomalies in 2010 (right panel) relative to the summer mean during 1982–2006 (left panel). The anomalies are derived from satellite data according to Reynolds et al. (2002). The September mean ice edge (thick blue line) is also shown.

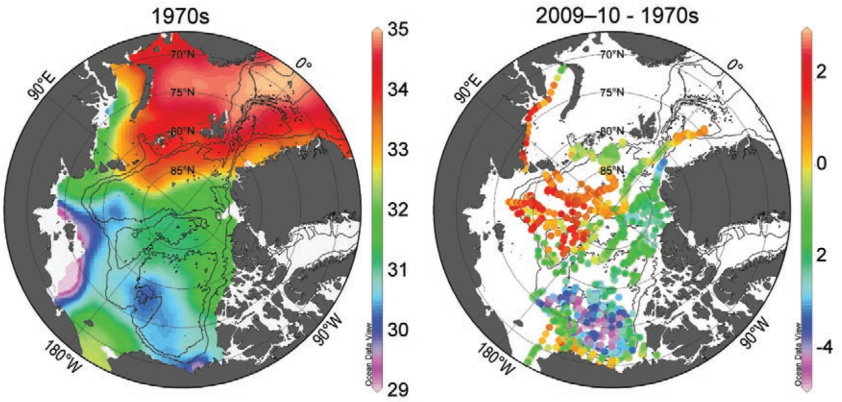

Fig. 5.6. Anomalies of salinity at 20 m depth in 2009–10 (right) relative to 1970s climatology (left). The 500 m and 2500 m isobaths have been plotted using the IBCAO grid.

of the Lomonosov Ridge, with maximum values about 1°C along the boundaries of the Eurasian Basin (Fig. 5.8). Warming was less pronounced in the Canada Basin than in the Eurasian Basin. There was little to no temperature anomaly (< 0.1°C) at the southeast boundary of the Canada Basin or in the basin boundary regions adjacent to Greenland and the Canadian Archipelago. Negative (cooling) temperature anomalies were detected in the vicinity of Nares Strait.

The characteristics of the AWL are regulated by the Atlantic water (AW) properties and transport at the inflow in Fram Strait. After reaching a maximum in 2006, AW temperature in Fram Strait decreased in 2007 and 2008. In 2009, AW temperature and salinity in northern Fram Strait increased, returning in summer 2010 to the long-term mean. The autumn and winter AW temperatures were slightly higher in 2009/10 than the previous year, while in summer 2010 the mean temperature remained close to that observed in summer 2009, with typical substantial seasonal variability.

(iv) The Pacific water layer

The Pacific water layer (PWL) is located in the Canada Basin at depths between approximately 50 meters and 150 meters (Steele et al. 2004) and originates from the Bering Strait inflow. The relatively warm and fresh PWL ($S < 33.5$) comprises about two-thirds of the Canadian Basin halocline by thickness and about half by freshwater content (e.g., Aagaard and Carmack 1989). In the period 2002–06 the PWL penetrated into the Beaufort Sea from the southern end of the Northwind Ridge, but in 2007–10 it took a different path, spreading northward along the Chukchi Plateau directly from the Herald Canyon (Fig. 5.9, lower panels). These changes in the physical environment cause changes in the biogeochemical environment (see section 5c3).

The characteristics of Pacific waters depend on water properties and transport, and atmospheric conditions in the Bering Strait. Preliminary data suggest that in 2008 and 2009 Pacific waters were slightly cooler than during 2002–07, but warmer than during 1999–2001. The 2009 volume transport (~0.9 Sv) was slightly higher than in 2008, but still less than the 2007 transport (> 1 Sv), which was the highest in the available record (spanning 1991–95 and 1998–2009). The 2009 heat flux was close to the long-term mean, while the freshwater flux in 2009 was somewhat higher than the mean (due in part to the higher-than-average transports), but still less than previous maxima in 2004 and 2007.

3) Biology and Geochemistry

As described above, the quantity of freshwater stored in the Beaufort Gyre increased substantially in 2007–10 due to both inputs of sea ice melt water (Yamamoto-Kawai et al. 2009) and strong Ekman pumping conditions (updates to Proshutinsky et al.

2009 and Yang 2009) that increased the depth of the upper halocline in the Canada Basin interior. These two effects combined to deepen the nitracline and the underlying associated chlorophyll maximum (McLaughlin and Carmack 2010). A consequence of the increased stratification is that overall nitrate fluxes are diminished, a condition which limits new production and favors smaller organisms at the base of the food web (Li et al. 2009). Another consequence of halocline deepening is that the nutricline and chlorophyll maxima are further removed from sunlight, and light limitation may play a greater role. The potential response of basin waters to climate forcing scenarios is thus distinct from scenarios on continental shelves which, in contrast, are expected to become more productive because of increased wind exposure and shelf-break upwelling (Yang 2009) that bring Pacific summer waters into the euphotic zone (Carmack and Chapman 2003). Preliminary analysis from 2010 shows a shallower chlorophyll maximum than in 2009, consistent with the slight relaxation of the Beaufort Gyre in 2009.

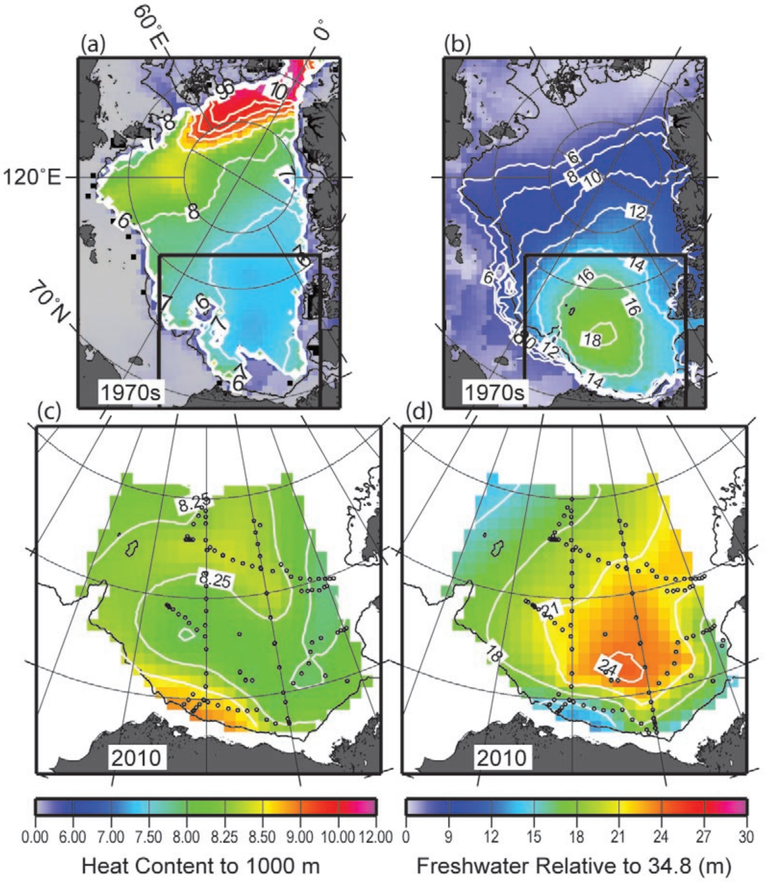

Fig. 5.7. Summer heat (× 10^{10} J m^{-2}) and freshwater content to the depth (m) of the 34.8 isohaline. The top row shows (a) heat content and (b) freshwater content in the Arctic Ocean based on 1970s climatology (Timokhov and Tanis 1997, 1998). The bottom panels show (c) heat content and (d) freshwater content in the Beaufort Gyre based on hydrographic surveys (black dots depict hydrographic station locations) in 2010. The Beaufort Gyre region is shown by black boxes in (a) and (b). Heat content is calculated relative to freezing temperature in the upper 1000 m of the water column.

Over the Chukchi Abyssal Plain, nutrient-rich water typically results in a strong chlorophyll maximum layer (~3 μg L^{-1}; Nishino et al. 2008). With sufficient nutrient availability, sea ice loss (and subsequent increased solar insolation) can enhance biological primary productivity in this region (Nishino et al. 2009). In 2010, however, increased surface freshening, vertical stratification, and nutricline deepening over the Chukchi Abyssal Plain resulted in a decrease of the chlorophyll maximum (< 0.5 μg L^{-1}).

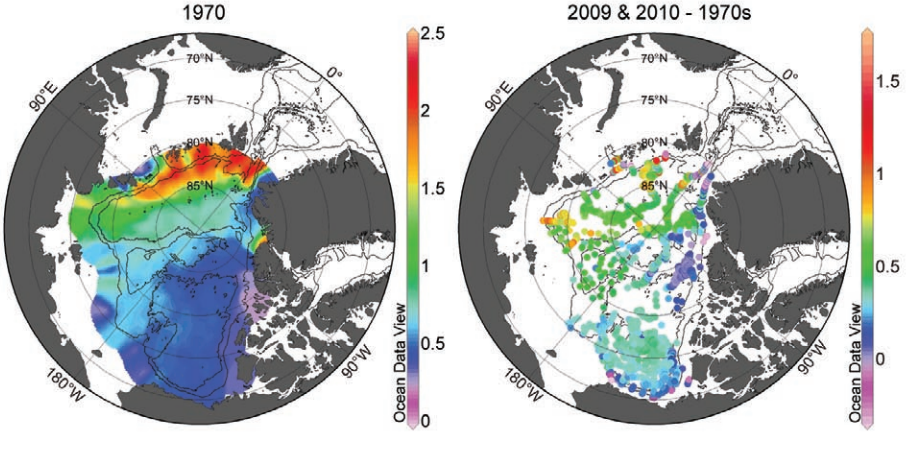

Fig. 5.8. Atlantic warm layer temperature maximum in °C. Left: 1970s climatology. Right: anomalies relative to 1970s climatology. The 500 m and 2500 m isobaths have been plotted using the IBCAO grid.

Undersaturation of the surface waters of the Canada Basin with respect to aragonite, a relatively soluble form of calcium

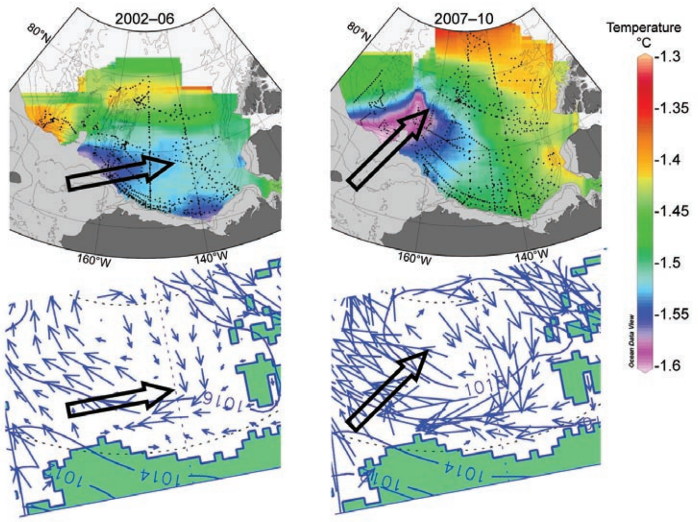

Fig. 5.9. Top panels: potential temperature (°C) in the Canada Basin at the S = 33.1 isohaline. Bottom panels: sea level atmospheric pressure (hPa) and simulated wind-driven component of ice drift. Left and right panels: 2002–06 and 2007–10, respectively. Large arrows show suggested spreading of Pacific winter waters.

carbonate found in plankton and invertebrates, was first observed in 2008 (Yamamoto-Kawai et al. 2009). The areal extent of the surface undersaturation increased in 2009 (results are not yet available for 2010). The reduction in the aragonite saturation state, Ω, is due to a number of factors. Yamamoto-Kawai et al. (2011) estimate that an increase in atmospheric carbon dioxide (CO_2) has lowered surface Ω by ~0.3 in the Canada Basin since the pre-industrial period. Recent melting of sea ice has further lowered mean Ω by 0.4, and of this, half was due to dilution of surface water and half was due to the change in air-sea disequilibrium state. Surface water warming has generally counteracted the mean decrease in Ω by 0.1.

The increased stratification and decrease in upper layer nutrient concentrations have also resulted in an increase in the number of picoplankton and a decrease in nanoplankton (Li et al. 2009). This trend of increasing summer picoplankton abundance in the upper water column of the Canada Basin was recorded in the previous five years. In 2009, there was evidence of a continued increase in picoplankton in late summer and early autumn, but only for the heterotrophic (bacterial) component. In contrast, an apparent departure from this trend for the picophytoplankton in 2009 indicates interannual variability and strong seasonality in the photosynthetic component, which leads to an aliased time series.

4) Sea level

Sea level is a natural integral indicator of climate variability. It reflects changes in practically all dynamic and thermodynamic processes of terrestrial, oceanic, atmospheric, and cryospheric origin. Sea level time series for the period of 1954–2010 are available for nine coastal stations in the Siberian seas (Arctic and Antarctic Research Institute data archives). In 2010, sea level along the Siberian coastline continued to decrease relative to 2008 and 2009 (see Fig. 5.10 in Proshutinsky et al. 2009). This caused a reduction, to 2.49 ±0.45 mm yr^{-1}, in the estimated rate of sea level rise for the nine stations since 1954 (after correction for glacial isostatic adjustment; Proshutinsky et al. 2004).

d. Sea Ice Cover—D. Perovich, W. Meier, J. Maslanik, C. Haas, and J. Richter-Menge

1) Sea ice extent

Sea ice extent is the primary variable for describing the state of the Arctic sea ice cover. Passive microwave satellites have routinely and accurately monitored ice extent since 1979. There are two periods that define the annual cycle and thus are of particular interest: March, at the end of winter, when the ice is at its maximum extent, and September, when it reaches its annual minimum. Ice extent in March 2010 and September 2010 are shown in Fig. 5.10.

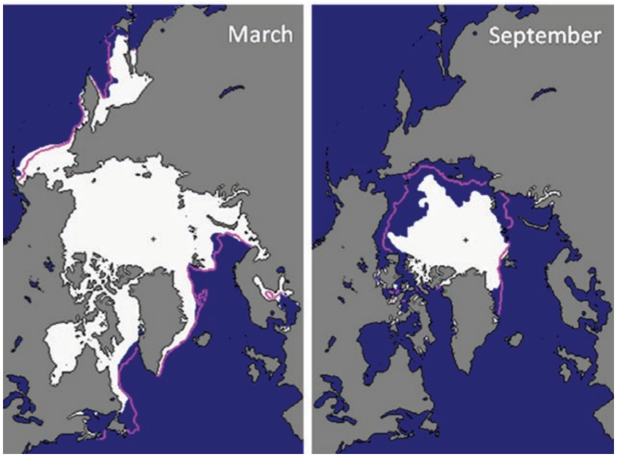

Fig. 5.10. Sea ice extent in March 2010 (left) and September 2010 (right) illustrates the winter maximum and summer minimum extents, respectively. The magenta line indicates the median maximum and median minimum ice extent each month for the period 1979–2000.

On 19 September 2010, ice extent reached its annual minimum, an area of 4.6 million km^2. This is the third-lowest minimum recorded since 1979, higher only than 2008 and the record minimum in 2007. Overall, the 2010 minimum was 31% (2.1 million km^2) lower than the 1979–2000 average. The last four summers have experienced the four lowest minima in the satellite record, and eight of the ten lowest minima have occurred during the last decade. Surface air temperatures through the 2010 summer were higher than normal throughout the Arctic, though less extreme than in 2007 (Stroeve et al. 2008). A strong atmospheric-driven wind surface circulation pattern during June 2010 pushed the ice away from the Alaskan and eastern Siberian coasts. However, the pattern did not persist through the summer as it did in 2007.

The March 2010 ice extent was 15.1 million km^2, about 4% less than the 1979–2000 average of 15.8 million km^2. Winter 2010 was characterized by a very strong atmospheric circulation pattern that led to higher-than-normal temperatures (see section 5b). Maximum ice extent occurred on 31 March. This was the latest date for maximum ice extent observed in the 30-year satellite record and was due primarily to late ice growth in the Bering and Barents Seas and the Sea of Okhotsk.

Time series of sea ice extent anomalies in March and September for the period 1979–2009 (Fig. 5.11) show a pronounced decline of -11.6% per decade, with large interannual variability in September summer minimum ice extent. The March winter maximum ice extent has also declined, but at a slower rate of -2.7% per decade.

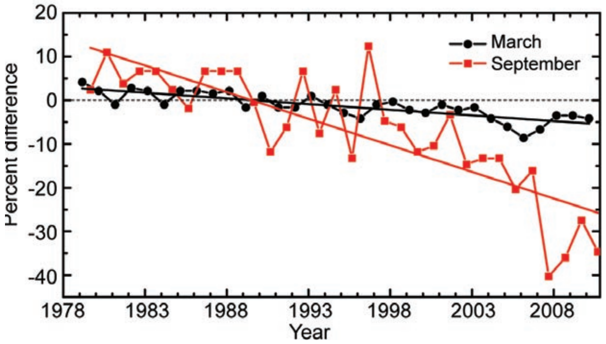

Fig. 5.11. Time series of ice extent anomalies in March (month of ice extent maximum) and September (month of ice extent minimum). The anomaly values are expressed as the percent difference between the annual value and the mean value for the period 1979–2000. The continuous straight black and red lines are regression lines that show long-term decline in the March ($R^2 = 0.66$) and September ($R^2 = 0.67$) ice extent, respectively. Based on data from National Snow and Ice Data Center, Arctic Sea Ice News and Analysis.

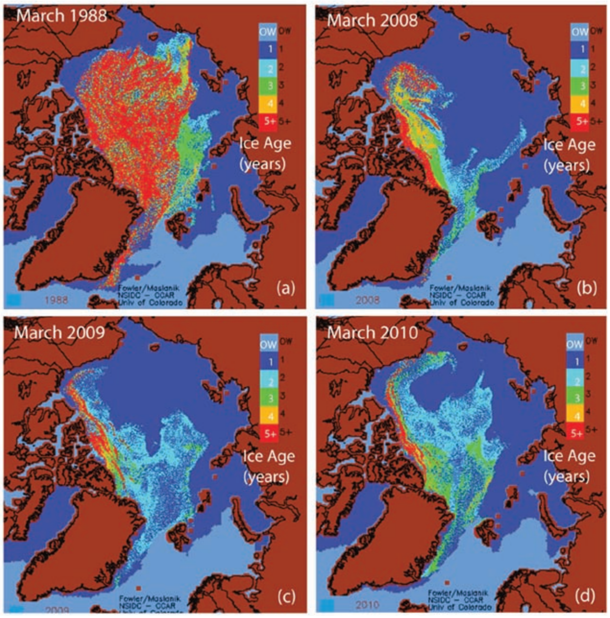

Fig. 5.12. Sea ice age in the first week of March, derived by tracking the drift of parcels of ice floes with satellite data, illustrates the substantial loss of old ice in the Arctic Basin in recent years compared to the late 1980s. (a) 1988, (b) 2008, (c) 2009, and (d) 2010. (Figure courtesy of National Snow and Ice Data Center, J. Maslanik and C. Fowler.)

2) Sea ice age

The age of the ice is another key descriptor of the state of the sea ice cover, since older ice tends to be thicker and more resilient than younger ice. Figure 5.12 shows that there has been a substantial loss of old, and thus thick ice in the Arctic Basin in recent years compared to the late 1980s (Kwok 2007; Nghiem et al. 2007; Maslanik et al. 2007). Following the record melt of summer 2007, there was a record-low amount of multiyear ice (ice that has survived at least one summer melt season) in March 2008. There was then a modest increase in multiyear ice in both 2009 and 2010. However, even with this recovery, 2010 had the third lowest March multiyear ice extent since 1980. Most of the two- to three-year old ice remained in the central Arctic during winter 2009/10. A lobe of older ice moved into the Beaufort and Chukchi Seas from the region of old thick ice north of the Canadian Archipelago. Despite being old and presumably relatively thick, Fig. 5.10 indicates this lobe of ice likely did not survive the 2010 summer melt period. Consistent with these observations, data from upward-looking sonars in the Beaufort Gyre (http://

www.whoi.edu/beaufort) show that the pack ice in the central Canada Basin is changing from a multiyear to a seasonal ice cover.

3) SEA ICE THICKNESS

Combined estimates of ice thickness from submarine and satellite-based instruments provide the longest record of sea ice thickness observation, beginning in 1980 (Kwok et al. 2009; Rothrock et al. 2008). These data indicate that over a region covering ~38% of the Arctic Ocean there is a long-term trend of sea ice thinning over the last three decades.

Haas et al. (2010) added to this record with results from a 2009 spring field campaign of airborne electromagnetic sounding surveys of sea ice thickness at multiple locations across the Arctic Basin. Consistent with the sea ice age results presented above, the thickest ice observed was along the coast of Ellesmere Island, Canada. Mean ice thicknesses were as high as 6 m, due to extensive ice deformation along the coast. The thinnest ice was found in the Chukchi and Beaufort Seas, with average thicknesses of 1.7 m to 1.9 m. Overall, the older ice was slightly thicker in 2009 relative to 2007. The 2009 modal thickness of undeformed first year ice was unchanged from 2007.

It is instructive to examine in detail the survey site in the Lincoln Sea north of Ellesmere Island (around 62.5°W and between 83°N and 84°N), which has been part of a sea ice mass balance observation program carried out in the same region since 2004 (Haas et al. 2010). The mean ice thickness in spring 2010 was 4.02 m (± 2.10 m standard deviation), with a modal thickness (representing multiyear ice) of 3.4 m. A comparison with thickness distributions from previous years shows that ice thicknesses were very large and relatively constant from 2004 to 2006. Then, more pronounced interannual variability was observed, with minimum thicknesses in 2008 (mean 4.37 ± 1.95 m, mode 3.2 m) and a temporal recovery in 2009. The more recent variability may be related to the reduced area and decreasing age of old ice north of Ellesmere Island (Fig. 5.12).

Other airborne electromagnetic surveys were performed in April in the Beaufort and Chukchi Seas and in April and August in Fram Strait by the Alfred Wegener Institute, Germany. While there was little change since 2007 in the Beaufort and Chukchi Seas, ice thicknesses in Fram Strait were as much as 0.5 m lower than in 2009 (S. Hendricks 2010, personal communication), which is most likely related to the strong interannual and spatial variability typical for Fram Strait.

e. *Land*

1) VEGETATION—D. A. Walker, U. S. Bhatt, T. V. Callaghan, J. C. Comiso, H. E. Epstein, B. C. Forbes, M. Gill, W. A. Gould, G. H. R. Henry, G. J. Jia, S. V. Kokelj, T. C. Lantz, S. F Oberbauer, J. E. Pinzon, M. K. Raynolds, G. R. Shaver, C. J. Tucker, C. E. Tweedie, and P. J. Webber

Circumpolar changes to tundra vegetation are monitored from space using the Normalized Difference Vegetation Index (NDVI), an index of vegetation greenness. In tundra regions, the annual maximum NDVI (MaxNDVI) is usually achieved in early August and is correlated with above-ground biomass, gross ecosystem production, CO_2 fluxes, and numerous other biophysical properties of tundra vegetation (Tucker et al. 1986; Stow et al. 2004). MaxNDVI is obtained each year from a 29-year record of NDVI derived from the AVHRR sensors on NOAA weather satellites (Bhatt et al. 2010).

MaxNDVI has increased during the period of satellite observations (1982–2010) in Eurasia and North America (Fig. 5.13a), supporting model predictions that primary production of Arctic tundra ecosystems will respond positively to increased summer warmth (Bhatt et al. 2008; Lawrence et al. 2008). Despite considerable spatial variation in the magnitude of change in each of the three variables examined, annual MaxNDVI patterns were also positively and significantly correlated with more abundant ice-free coastal waters (Fig. 5.13a) and higher tundra land temperatures (Fig. 5.13b) over most of the Arctic region (Bhatt et al. 2010). Trends in summer open water, summer land-surface temperatures, MaxNDVI, and time-integrated NDVI (TI-NDVI) in the adjacent land areas were calculated for the major sea basins in the Arctic. TI-NDVI is the sum of maximum NDVI occurring in bi-weekly intervals, and provides a perspective that includes the length of the growing season. For example, not only does Baffin Bay have a moderate MaxNDVI increase (13%) but it also has the largest TI-NDVI increase (38%). This indicates that major changes in greenness have occurred over the length of the growing season, likely due to extension of the snow-free and growing seasons (see sections 5e4 and 5f). Several new features are apparent that were not present in the *BAMS State of the Climate in 2009* (Walker et al. 2010). For example, the sea ice changes occurring in the eastern Kara Sea far exceed those elsewhere, but there has been no warming over adjacent lands or a major increase in MaxNDVI, as would have been expected. Instead, the adjacent land areas have cooled slightly and there is only a modest increase in NDVI.

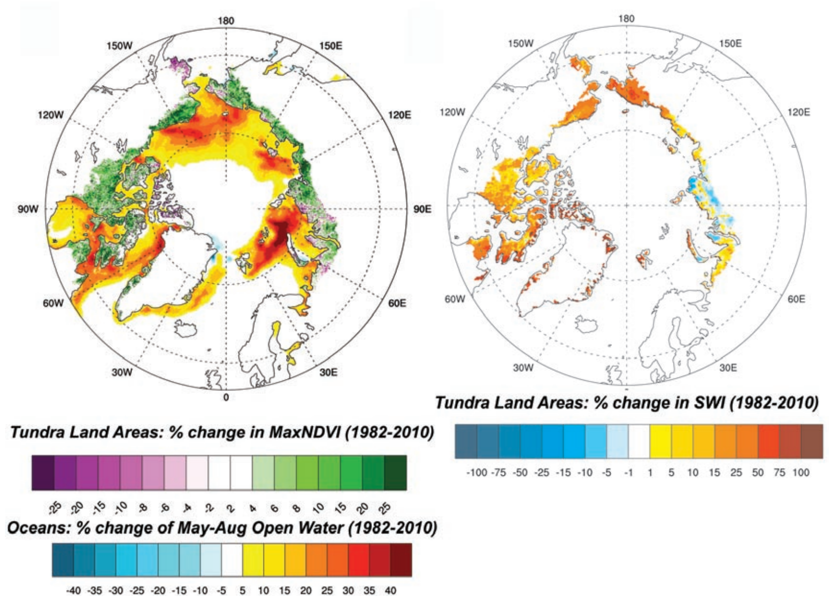

Fig. 5.13. Trends for (a) summer (May–August) open water and annual MaxNDVI, and (b) land-surface summer warmth index (annual sum of the monthly mean temperatures > 0°C) derived from AVHRR thermal channels 3 (3.5–3.9 μm), 4 (10.3–11.3 μm) and 5 (11.5–12.5 μm). Trends were calculated using a least squares fit (regression) at each pixel. The total trend magnitude (regression times 29 years) over the 1982–2010 period is expressed as a percent of the 1982 value.

Temporal changes in MaxNDVI for Arctic areas in Eurasia and North America show positive and nearly parallel increases amounting to a MaxNDVI increase of 0.02 NDVI units per decade (Fig. 5.14a). However, there is considerable variability in the rate of increase in different regions of the Arctic. For example, the MaxNDVI increase adjacent to the Beaufort Sea (+26%) is the most rapid in the Arctic and corresponds to large changes in open water (+31%) and summer land temperature (+17%). On the other hand, the MaxNDVI change in the western Kara Sea is among the smallest (+4.4%), corresponding to smaller changes in sea ice (+20%) and land temperatures (-6%; Fig. 5.14b).

In 2009 there was a circum-Arctic decrease in NDVI (Fig. 5.14a) that corresponded to elevated atmospheric aerosols over the Arctic in the same year (Stone et al. 2010). This coincided with generally lower temperatures across the Arctic in 2009 and 2010 (see section 5b). The elevated aerosols were attributed to an accumulation of pollutants in the upper troposphere from Eurasian industrial centers in combination with volcanic plumes from the eruption of Mount Redoubt in Alaska. The enhanced Arctic haze in 2009 was estimated to have reduced net shortwave irradiance by about 2 W m^{-2}–5 W m^{-2} (Stone et al. 2010).

Bi-weekly NDVI data reveal clear differences in phenological (green-up) patterns in North America and Eurasia (Fig. 5.15). Both regions show a ~0.06 unit MaxNDVI increase over the 29-year record. In Eurasia there is a somewhat more rapid green-up and peak NDVI was reached about 2 weeks earlier during 2000–09 than in the 1980s. In North America there is no significant shift in peak greenness. Neither continent shows a significant trend toward a longer growing season. However, whole-continent data appear to mask changes along latitudinal gradients and in different regions. For example, during 1982–2003, MaxNDVI along the Canadian Arctic climate gradient showed a ~1-week shift in the initiation of green-up and a somewhat delayed onset of senescence in the Low Arctic (Jia et al. 2009). The High Arctic did not show earlier initiation of greenness, but did show a ~1–2 week shift toward earlier MaxNDVI.

The increased Arctic greening observed in the satellite data is also observed in long-term in situ vegetation measurements. For example, the InternationTundra Experiment (ITEX), established in 1990, has made annual measurements of plant growth and

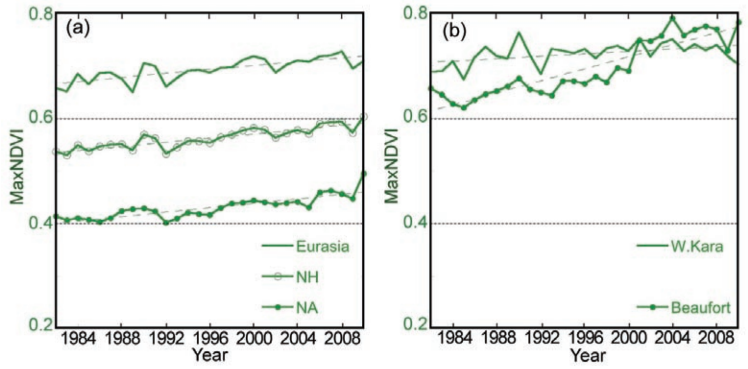

Fig. 5.14. Time series of MaxNDVI during 1982–2010 for coastal tundra in the (a) Northern Hemisphere as a whole, Eurasia, and North America, and (b) western Kara Sea and Beaufort Sea.

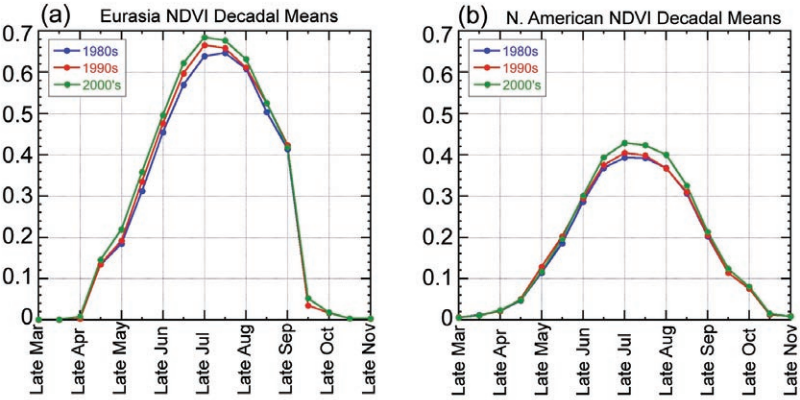

Fig. 5.15. Decadal changes in NDVI-derived phenology in (a) Eurasia and (b) North America.

phenology for up to 20 years using standardized protocols (Henry and Molau 1997). A recent synthesis of the long-term ITEX warming experiments has shown that effects on plant phenology differ by trait, community, and functional types (Elmendorf et al. 2010). Some of these results indicate there have been productivity increases consistent with warming (e.g., Hill and Henry 2011). In others, the links between local climate warming and vegetation change found in the NDVI data were not supported at the plot scale. There is a need for more careful evaluation of the causes of the observed changes, which may be driven by local long-term non-equilibrium factors other than climate warming, such as recovery from glaciation or changes in snow cover or precipitation (Troxler et al. 2010; Mercado-Díaz and Gould 2010).

The Back to the Future International Polar Year project, which revisited numerous Arctic research sites established between 15 and 60 years ago, is revealing decadal-scale changes. These include vegetation change and increases in plant cover at Barrow, Alaska, on Baffin Island, and at multiple sites throughout Beringia (Tweedie et al. 2010). Advanced phenological development and species shifts associated with drying occurred on Disko Island, Greenland. Warming of permafrost was documented in sub-Arctic Sweden, and dramatic changes in pond water column nutrients, macrophyte cover, and chironomid assemblages have been noted near Barrow. NDVI, gross ecosystem production, and methane efflux from wet vegetation types have increased at sites near Barrow, on Baffin Island and at the Stordalen mire in sub-Arctic Sweden. In most cases, air and ground warming appear to be the primary causes of change, but disturbances of various types are causing change at some sites (Johnson et al. 2010). Warming will cause changes in species distributions and biodiversity in the Arctic. Consequently, the Circumpolar Biodiversity Monitoring Program is launching an integrated biodiversity monitoring plan for Arctic land and freshwater ecosystems (McRae et al. 2010).

Other Arctic vegetation changes indirectly related to climate include those associated with landslides, thermokarst, and fires, which are increasing in frequency in several regions (e.g., Goosef et al. 2009; Lantz et al. 2010a,b; Mack et al. 2011 in revision; Rocha and Shaver 2011). Higher soil temperatures, thawing permafrost, more abundant water, and increased nutrients due to such disturbances result in pronounced greening often due to more abundant shrub growth. Increasing air and ground temperatures are predicted to increase shrub growth in much of the Arctic, with major consequences for ecosystems (Lantz et al. 2010b). Several studies have observed increased shrub growth due to artificial warming, although the increases are small and frequently not statistically significant (e.g., Bret-Harte et al. 2002). On the other hand, there is growing evidence for increased shrub abundance at climatically- and anthropogenically-disturbed sites (Lantz et al. 2010a,b; Walker et al. 2011). In the Russian Arctic, erect deciduous shrub growth closely tracks both the recent summer warming of ~2°C over more than half a century and a trend of increasing NDVI since 1981 (Forbes et al. 2010).

2) Permafrost—V. Romanovsky, N. Oberman, D. Drozdov, G. Malkova, A. Kholodov, and S. Marchenko

Observations show a general increase in permafrost temperatures during the last several decades in Alaska (Romanovsky et al. 2007; Osterkamp 2008; Smith et al. 2010), northwest Canada (Couture et al. 2003; Smith et al. 2010), Siberia (Oberman 2008; Drozdov et al. 2008; Romanovsky et al. 2010a) and Northern Europe (Harris and Haeberli 2003; Christiansen et al. 2010).

Most of the permafrost observatories in Alaska show a substantial warming during the 1980s and especially in the 1990s. The magnitude and nature of the warming varies between locations, but is typically from 0.5°C to 2°C at the depth of zero seasonal temperature variations (Osterkamp 2008). However, during the 2000s, permafrost temperature has been relatively stable on the North Slope of Alaska (Smith et al. 2010), and there was even a slight decrease (0.1°C–0.3°C) in the Alaskan interior during the last three years. The exception has been at Alaskan coastal sites, which have exhibited continuous warming during the last ten years. The warming trend at the Alaskan coastal sites has been particularly pronounced during the last four to five years (Fig. 5.16a). Data obtained in 2010 in Alaska suggest that the observed warming trend along the coast has begun to propagate south towards the northern foothills of the Brooks Range (approximately 200 km inland), where a noticeable warming in the upper 20 m of permafrost has become evident since 2008 (Fig. 5.16b).

A common feature at Alaskan, Canadian, and Russian sites is more significant warming in relatively cold permafrost than in warm permafrost in the same geographical area (Romanovsky et al. 2010b). Permafrost temperature has increased by 1°C to 2°C in northern Russia during the last 30 to 35 years. An especially noticeable temperature increase was observed during the last three years in the Russian Arctic, where the mean annual temperature at 15 m depth increased by > 0.35°C in the Tiksi area and by 0.3°C at 10 m depth in northern European Russia. However, relatively low air temperatures during summer 2009 and the following winter interrupted this warming trend at many locations in the Russian Arctic, especially in the western sector. Data on changes in the active layer thickness (ALT) in the arctic lowlands are less conclusive. In the Alaskan Arctic, ALT experiences a large interannual variability, with no discernible trends; this is likely due to the short length of historical data records and possible surface subsidence upon thawing of the upper, ice-rich permafrost (Streletskiy et al. 2008). At the same time, data from northern Quebec (Smith et al. 2010) and from the Nordic countries (Christiansen et al. 2010) show a distinct increasing trend in ALT during the last two decades.

The last 30 years of increasing permafrost temperatures have resulted in the thawing of permafrost in areas of discontinuous permafrost in Russia (Oberman 2008; Romanovsky et al. 2010a). This is evidenced by changes in the depth and number of taliks (a sub-surface layer of year-round unfrozen ground within permafrost), especially in sandy and sandy loam sediments compared to clay. A massive development of new closed taliks in some areas of the continuous permafrost zone, resulting from increased snow cover and warming permafrost, was responsible for the observed northward movement of the boundary between continuous and discontinuous permafrost by several tens of kilometers (Oberman and Shesler 2009; Romanovsky et al. 2010a).

3) River discharge—A. I. Shiklomanov and R. B. Lammers

River discharge from Eurasia to the Arctic Ocean during 1936–2009 increased at a mean rate of 2.7 ± 0.5 km^3 yr^{-1}. For the six largest Eurasian rivers (Severnaya Dvina, Pechora, Ob, Yenisey, Lena, and Kolyma), the most significant positive trend, 12 km^3 yr^{-1}, occurred during the last 23 years (1987–2009; Shiklomanov and Lammers 2009). Data available online from the U.S. Geological Survey (http://waterdata.usgs.gov/ak/nwis) and Environment Canada (http://www.wsc.ec.gc.ca/applications/H2O/index-eng.cfm) for 2009 showed 9% higher discharge

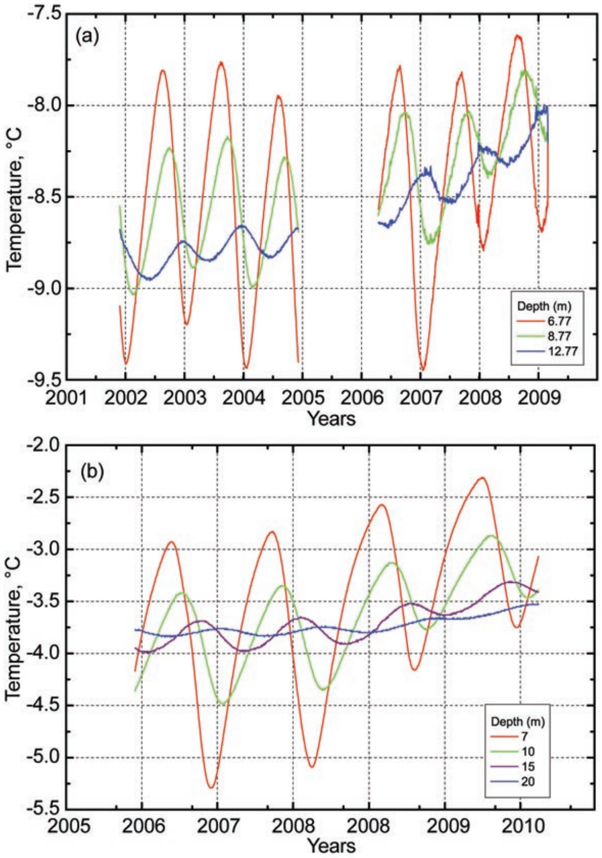

Fig. 5.16. Changes in permafrost temperature (a) between 2002 and 2009 at three different depths at the Barrow Permafrost Observatory on the northernmost coast of Alaska, and (b) between 2006 and 2010 at four different depths at the Imnaviat Creek Permafrost Observatory near the Toolik Lake research station, Alaska, approximately 200 km south of the Beaufort Sea coast. Note that the coastal permafrost (a) is colder than the inland permafrost (b). The gap in (a) between 15 May 2005 and 23 Sep 2006 is due to a datalogger malfunction.

over the 1969–2008 mean for the four largest North American rivers (Mackenzie, Yukon, Back, and Peel) flowing into the Arctic.

Officially-distributed river discharge data are usually processed and published after some delay (Shiklomanov et al. 2006). Through cooperation of the State Hydrological Institute and the Arctic and Antarctic Research Institute (AARI) in St. Petersburg, Russia, river discharge is estimated from the most important Russian monitoring sites in near real-time using provisional stage measurements, air temperature, and river ice data (http://neespi.sr.unh.edu/maps). Due to limited data availability, this technique cannot currently be applied to estimate near real-time river discharge for sites in North America.

Using this approach, the total annual discharge from the five largest Eurasian rivers (excluding the Kolyma) flowing into the Arctic Ocean in 2010 was estimated to be 1760 km^3, which is slightly higher than the long-term (1936–2009) mean of 1737 km^3. In 2010 the Yenisey discharge was 6% higher than the long-term mean and the discharge of both the Lena and Ob basins was close to the mean (Fig. 5.17, inset). During the same period, European Russia rivers (Sev. Dvina and Pechora) had 10% lower flow than the long-term mean. This was expected given the very dry and warm summer in 2010 across European Russia (see Sidebar 7.8).

An aggregated hydrograph for the five largest Eurasian rivers, based on provisional discharge estimates for 2010, is compared with discharge variability and the long-term mean hydrograph for 1994–2009, when the anthropogenic impact on discharge of these rivers was relatively stable and all variations can be attributed to the climate (Fig. 5.17). Aggregated 2010 Eurasian river discharge to the Arctic Ocean had an earlier spring snowmelt rise leading up to the peak flow and a more rapid recessional limb as the snowmelt pulse declined in the early summer. This is consistent with 2010 snow cover observations (see section 5e4) and expected changes in timing of river discharge due to increased warming in the region (Shiklomanov et al. 2007).

4) Terrestrial snow—C. Derksen and R. Brown

In 2010, a combination of low winter snow accumulation and above-normal spring temperatures created new record-low spring snow cover duration (SCD) over the Arctic since satellite observations began in 1966. Record persistence of the negative phase of the North Atlantic Oscillation (NAO) during the winter of 2009/10 (Cattiaux et al. 2010) favored cold, dry conditions and below-average snow accumulation over large areas of Eurasia and Alaska (Fig. 5.2b). In the spring, the advection of southerly air masses was responsible for high positive air temperature anomalies over much of Eurasia and the western North American Arctic (Fig. 5.2c), which contributed to early snow melt.

Annual SCD anomalies for the 2009/10 snow year (August–July) computed from the NOAA Interactive Multisensor Snow and Ice Mapping System (IMS) 24-km product (Helfrich et al. 2007) show below-average SCD over much of the Arctic land area (Fig. 5.18a). The exception was Scandinavia which, like much of the midlatitude regions, had SCD anomalies that were largely positive. The difference in the sign of the SCD anomalies for the Arctic (positive) versus the midlatitudes (negative) reflects the Warm Arctic-Cold Continent atmospheric circulation pattern described in section 5b. Snow cover duration was computed separately for the first (August–January) and second (February–July) halves of the 2009/10 snow year using the weekly NOAA Climate Data Record (CDR; maintained at Rutgers University) to provide information on changes in the start and end dates of snow cover. While the timing of the onset of snow

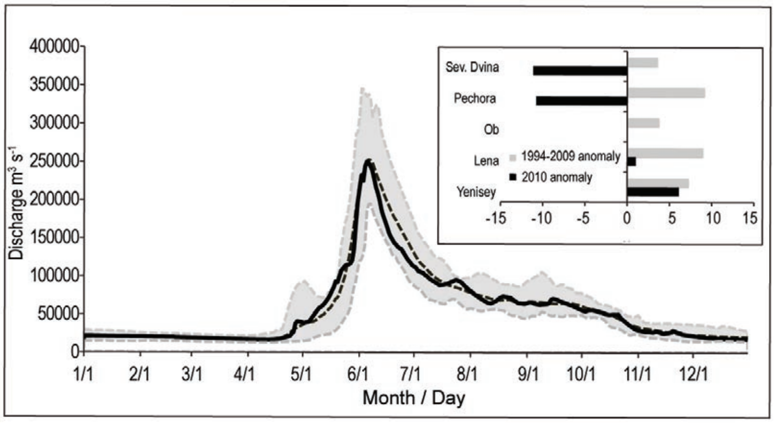

Fig. 5.17. Aggregate daily discharge hydrograph of the five largest rivers in the Eurasian Arctic in 2010 (solid black line) and long-term mean hydrograph (dashed black line) with discharge variation (gray area) during 1994–2009. Inset shows 2010 (black bars) and 1994–2009 (gray bars) anomalies relative to the long-term mean during 1936–2009 for these five rivers. Provisional estimates of annual discharge in 2010 for the five major Eurasian Arctic rivers are based on near real time data.

cover in fall continued to show little change over the satellite record (Fig. 5.18b), a new record-low spring SCD was observed over both the North American and Eurasian sectors of the Arctic during 2010 (Fig. 5.18c). This continued the trend to earlier spring snow melt over the Arctic, identified using multiple datasets (Brown et al. 2010) and reflected in the positive NDVI trends reported in section 5e1.

Northern Hemisphere spring snow cover extent (SCE), for months when snow cover is confined largely to the Arctic (Fig. 5.18d), continued to show decreasing trends that increase in magnitude over the April–June period in response to poleward amplification of SCE sensitivity to warming (Déry and Brown 2007).

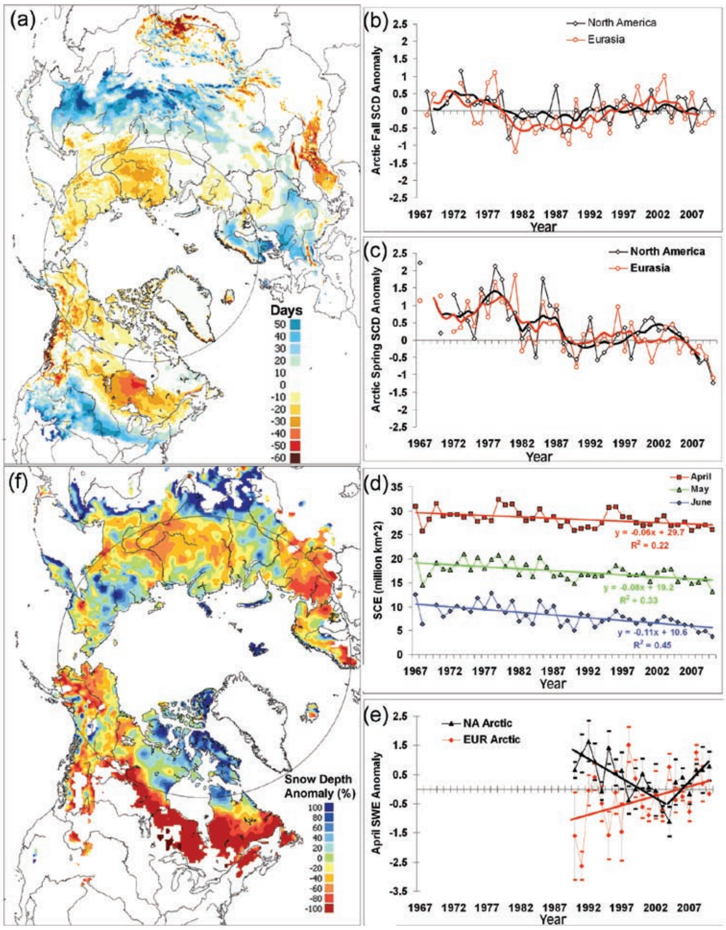

Fig. 5.18. (a) Annual snow cover duration (SCD) departures for the 2009/10 snow year (with respect to 1998–2010) from the NOAA IMS record. Arctic seasonal SCD standardized anomaly time series (with respect to 1988–2007) from the NOAA CDR record for (b) the first (fall) and (c) second (spring) halves of the snow season. Solid lines denote 5-yr moving average. (d) Monthly Northern Hemisphere snow extent from the NOAA CDR record for April, May, and June, 1967–2010. Solid lines denote linear trends (significant at 99%). (e) Multi-dataset time series of April snow water equivalent (SWE) standardized anomalies (± the standard error) relative to 1999–2009. (f) Mean monthly snow depth anomaly (% of 1999–2009 average) from the CMC snow depth analysis for April 2010.

Arctic snow water equivalent (SWE) time series were derived for 1990 through 2010 from two satellite passive microwave algorithms (Pulliainen 2006; Derksen et al. 2010), the Canadian Meteorological Centre (CMC) daily gridded global snow depth analysis (Brasnett 1999; Brown and Brasnett 2010), and ERA-interim atmospheric reanalysis (Simmons et al. 2007). In 2010, regionally-averaged April SWE anomalies (the month of maximum accumulation) were positive for North America, and near normal for Eurasia (Fig. 5.18e). Prior to 2004, SWE anomalies across the North American Arctic were out of phase with Eurasia, but both sectors are characterized by increasing SWE anomalies since then.

Mean monthly snow depth anomalies for April, derived from the CMC analysis, show unusually shallow snow over Alaska, sub-Arctic Canada, central Siberia, and western Russia, and deeper-than-normal snow over eastern Siberia and the eastern Canadian Arctic (Fig. 5.18f).

In summary, different regional responses to the strongly negative NAO during the snow accumulation season produced spatial variability in snow depth anomalies. A region-wide record early spring snow melt, however, resulted in a shorter-than-normal snow season across the pan-Arctic. Time series of snow parameters that extend over the past 40 years show general increases in SWE coupled with reduced spring SCD. These trends are consistent with earlier peak stream flow, a more rapid recessional limb, and higher peak runoff volumes noted in section 5e3.

5) Glaciers outside Greenland—M. Sharp and G. Wolken

Mountain glaciers and ice caps in the Arctic, with an area of > 400 000 km^2, are a significant contributor to global sea level change (Meier et al. 2007). They lose mass by surface melt and runoff and by iceberg calving. The net surface mass balance (B_n, the difference between annual snow accumulation and annual runoff) is widely used as a measure of glacier response to climate variability and change. In cold, dry regions like the Canadian High Arctic, interannual variability in B_n is largely coupled to variability in mean summer temperature, while in more maritime regions like Iceland and southern Alaska, it is also affected by variability in winter precipitation.

As measurements for the 2009/10 balance year are not yet available, measurements are summarized here for 2008/09. These are available for twenty glaciers: three in Alaska, four in Arctic Canada, nine in Iceland, and four in Svalbard. Nineteen of the glaciers had a negative annual balance and only one (Dyngjujökull in Iceland) had a positive balance. As predicted in last year's report (Sharp and Wolken 2010), measured mass balances were more negative than in 2007/08 in Svalbard, less negative in Iceland, and very negative in Alaska where, according to GRACE satellite gravimetry, the regional net balance for all Gulf of Alaska glaciers was -151 ± 17 Gt yr^{-1}, the most negative annual value in the GRACE record (A. Arendt and S. Luthcke 2011, personal communication). In Arctic Canada, surface mass balances of three of the four glaciers measured were among the six most negative balances in the 44- to 49-year record, extending the period of very negative balances that began in 1987.

The continued breakup of the floating ice shelves that fringe northern Ellesmere Island has been associated with recent warm summers. Large new fractures were detected in the Ward Hunt Ice Shelf on 7 and 14 August 2010, and further break up of the eastern part of the ice shelf was underway on 18 August. Some 65 km^2–70 km^2 of the ice shelf was lost by the end of August (Sharp and Wolken 2010).

Data from the NCEP/NCAR R1 Reanalysis illustrate meteorological conditions over the major glaciated regions of the Arctic in the 2009/10 mass balance year (Table 5.1). Winter (September 2009–May 2010) precipitation was near normal (relative to the 1948–2008 mean) over many of the major glaciated regions of the Arctic outside Greenland, significantly above normal in Arctic Canada and Novaya Zemlya, and below normal in southern Alaska, consistent with April terrestrial snow depth anomalies (see section 5e4). Summer (June–August 2010) temperatures at 700 hPa were anomalously positive over a region including Iceland, Greenland, the Canadian Arctic, and northern Alaska, but anomalously negative over the Eurasian Arctic, especially over Novaya Zemlya (Table 5.1; see also Fig. 5.2d). This pattern is mirrored in that of 700 hPa geopotential height anomalies, which were positive on the North American side of the Arctic and negative on the Eurasian side. Anomalous air flow associated with the positive geopotential height anomalies results in anomalous poleward-directed meridional winds over Davis Strait and Baffin Bay (see section 5b). These winds may be important in transporting heat to west Greenland and the Canadian Arctic from a region around southern Greenland, where summer sea surface temperature anomalies were +1°C to +2°C. The MODIS land surface temperature (LST) product provides a measure of the likelihood of summer melting on glaciers. In 2010, summer LST anomalies (relative to 2000–10) were positive in all glaciated regions of the Arctic, except Franz Josef Land, and very positive in the Canadian Arctic, where the average LST anomalies were +1.07°C (Table 5.1).

By comparing 2009/10 meteorological conditions with those in 2008/09, and considering 2008/09 glacier mass balances, we predict that mass balances in 2009/10 were probably more negative than in the previous year in Arctic Canada and Iceland, less negative than in 2008/09 in southern Alaska, Svalbard, and Novaya Zemlya, and similar to those of 2008/09 in Severnaya Zemlya and Franz Josef Land.

f. Greenland—J. E. Box, A. Ahlstrøm, J. Cappelen, X. Fettweis, D. Decker, T. Mote, D. van As, R. S. W. van de Wal, B. Vinther, and J. Wahr

1) Coastal Surface Air Temperatures

Record-setting high air temperatures were registered at all of the west Greenland long-term meteorological stations (Table 5.2). At Nuuk (Fig. 5.19), winter 2009/10 and spring and summer in 2010 were the warmest since 1873, when measurements began. At Prins Christian Sund, as at Nuuk, 2010 annual anomalies were three standard deviations above the 1971–2000 baseline. Warm anomalies were greatest at Aasiaat, where winter temperatures were 7°C above the 1971–2000 baseline, which is three standard deviations above the mean. Temperature anomalies extended west into Arctic Canada (see also section 5e5), but not into east and northeast Greenland.

These measurements are consistent with anecdotal data provided by a long-time resident of Greenland (2010, personal communication), who wrote on 4 February 2010: "we don't have snow, we don't have the cold" ... "This weather this year is really different, in 30 years that I live in Ilulissat, that is the first year in this conditions. We have lot of dog sledding tourists, but we cannot do the tour, too much ice on the hills and dangerous to drive by sled." ... "no snow at all".

Table 5.1: Summer (June –August) 2010 700 hPa air temperature, winter (September 2009–May 2010) precipitation, and summer MODIS Land Surface Temperature (LST) anomalies for major glaciated regions of the Arctic (excluding Greenland). For ranks, 1 = year with highest summer air or land surface temperature and winter precipitation, and n is the number of years in the record. Air temperature and precipitation anomalies are relative to 1948–2008 climatology from the NCEP/NCAR R1 Reanalysis. Mean summer LST values are calculated from eight day averages of daytime, clear sky values for a period centered on 15 July of each year. The length of the measurement period varies between regions and is equal to the mean (+4 standard deviations) annual melt duration in each region during the period 2000–09 derived using microwave backscatter measurements from the Seawinds scatterometer on QuikScat. LST is measured for blocks of 1-km by 1-km cells containing only glacier ice centered on high elevation regions of major ice caps in each region. Block size varies with the size of the ice cap, but is consistent between years. LST anomalies are relative to the mean LST for the period 2000–10.

Region	Sub-Region	Latitude (°N)	Longitude (°E)	2010 Jun–Aug 700hPa T Anomaly	2010 Rank	2009–10 Sep–May Ppt Anomaly	2009–10 Rank	2010 MODIS LST Anomaly	2010 Rank
				(°C)	(n=63)	(mm)	(n=62)	(°C)	(n-11)
Arctic Canda	N. Ellesmere Island	80.6–83.1	267.7–294.1	2.68	2	28.3	4	0.56	6
	Axel Heiberg Island	78.4–80.6	265.5–271.5	1.99	4	22.5	8	1.17	3
	Agassiz Ice Cap	79.2–81.1	278.9–290.4	2.03	4	55.8	9	1.34	2
	Prince of Wales Icefield	77.3–79.1	278–284.9	2.10	3	24.5	9	1.16	2
	Sydkap	76.5–77.1	270.7–275.8	2.11	1	57.3	8	1.28	2
	Manson Icefield	76.2–77.2	278.7–282.1	2.08	2	148.9	1	1.22	1
	Devon Ice Cap	74.5–75.8	273.4–280.3	1.96	2	19.9	16	1.02	1
	North Baffin	68–74	278–295	1.67	5	52.5	7	0.89	1
	South Baffin	65–68	290 – 300	1.65	5	-24.3	42	1.00	1
Eurasian Arctic	Severnaya Zemlya	76.25–81.25	88.75 – 111.25	-0.05	29	2.7	29	0.89	1
	Novaya Zemlya	68.75–78.75	48.75 – 71.25	-0.94-9	52	86.2	5	0.44	3
	Franz Josef Land	80–83	45 – 65	-0.01	32	-17	37	-0.06	7
	Svalbard	76.25–81.25	8.75 – 31.25	-0.30	44	16.9	23	0.49	2
	Iceland	63–66	338 – 346	1.62	2	-10	35	0.34	2
Alaska	SW Alaska	60–65	210 – 220	0.69	14	-29	36	0.38	3
	SE Alaska	55–60	220 – 230	0.57	17	-26	35	*0.53	2*

Later, the same source spoke of "10–12 days of" continuous "heat wave" like weather, in June, with "a lot of blue skies". Ilulissat is at 69.0°N on the west coast of Greenland, ~100 km northeast of Aasiaat, and ~560 km north of Nuuk (see Fig. 5.19).

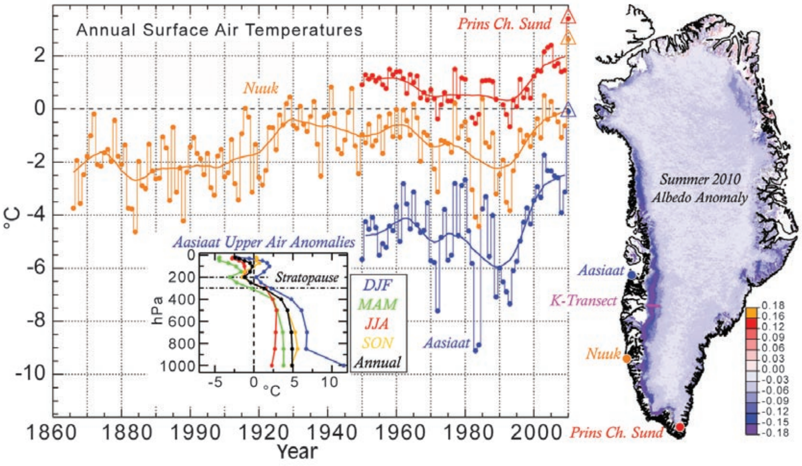

Fig. 5.19. Three Greenland meteorological station records illustrating the long-term time series of yearly-average temperatures. Triangles denote record-setting values, all in 2010. The inset shows upper air temperature anomalies in 2010 at Aasiaat relative to the 1971–2000 baseline. The map on the right shows summer (June–August) Greenland ice sheet surface albedo changes (from MODIS MOD10A1 data) and locations of meteorological stations and the K-Transect.

2) Upper Air Temperatures

Seasonally-averaged 2010 upper air temperature data, available from twice-daily radiosonde observations (Durre et al. 2006), indicate a pattern of record-setting warm anomalies below 300 hPa (e.g., Fig. 5.19, inset). This is consistent with a warming trend prevailing since reliable records began in 1964 and especially since the mid-1980s (Box and Cohen 2006). Upper air temperature anomalies in 2010 are consistent among all stations, but, as at the surface stations, they are most pronounced in central-west Greenland (Table 5.2) and closest to normal in east Greenland.

3) Atmospheric Circulation

The high, positive temperature anomalies over the inland ice sheet are largely explained by atmospheric circulation anomalies. NCEP/NCAR Reanalysis data

Table 5.2. 2009 Greenland station surface air temperature anomalies by season, relative to 1971–2000.

Station (Region), Latitude, Longitude, time range	Winter	Spring	Summer	Autumn	Annual
Thule AFB/Pituffik (NNW), 76.5° N. 68.8°W, 1961–2010	**4.1**	**2.6***	**1.3**	2.4	**2.1***
Upernavik (NW), 72.8°N, 56.2°W, 1873–2010	**6.1**	**4.0**	**1.4**	**2.8***	**3.7***
Aasiaat (W), 68.7°N, 52.8°W, 1951–2010	**7.1***	**5.2***	**1.5**	**2.5***	**4.1***
Nuuk (SW), 64.2°N, 43.2°W, 1873–2010	**5.4***	**3.6**	**2.1***	**3.3***	**3.8***
Prins Christian Sund (S), 60.0°N, 43.2°W, 1951–2010	**3.1***	1.5	**1.8***	**2.0***	**2.3***
Tasiilaq (SE), 65.6°N, 22.0°W, 1895–2010	**3.1**	0.8	**1.8**	**1.0**	**1.8**
Illoqqortoormiut (E), 70.4°N, 22.0°W, 1948–2010	0.3	-0.8	0.0	0.2	-0.1
Danmarkshavn (NE), 76.8°N, 18.8°W, 1949–2010	0.7	0.6	0.1	-0.4	0.0

*Bold values indicate anomalies that meet or exceed one standard deviation from the mean. Underlined values exceed two standard deviations from the mean. Italicized values exceed three standard deviations from the mean. Asterisks indicate record-setting anomalies. Winter values include December of the previous year.

for 2010 indicate abnormally large heat flux from the south over the southwestern part of the Greenland ice sheet. NCEP/NCAR Reanalysis geopotential height anomalies at 500 hPa in June, July, and August 2010 (referenced to the 1971–2000 baseline) were at least twice the 1971–2000 standard deviation (see also section 5b.).

4) Surface Melt extent and Duration and Albedo

The areal extent and duration of melting on the ice sheet, derived from daily passive microwave satellite remote sensing observations (Mote 2007), continued to increase in 2010. During April–September 2010 the melt area was ~8% more extensive than the previous record set in 2007 (Fig. 5.20). The 2010 melt extent through mid-September was 38% greater than the 1979–2007 average, and the June–August extent was 26% greater than the 1979–2007 average. Compared to summer 2007, when melt anomalies occurred in both the ablation and percolation zones (Tedesco et al. 2008), 2010 melt anomalies were concentrated in the lower elevation bare ice zone.

Abnormal melt duration was concentrated along the western margin of the ice sheet. This was consistent with the anomalous summer heat flux described above, preceded by abnormally high winter air temperatures that led to warm conditions prior to the onset of melt (Tedesco et al. 2011). The melt duration was as much as 50 days greater than average at elevations between 1200 and 2400 meters above sea level in west Greenland. In May, low elevation areas along the western ice margin melted for as much as 15 days longer than average.

The melt extent and duration observations are consistent with the observed coastal and upper air temperatures described above, and derived meteorological data. For example, NCEP/NCAR Reanalysis data suggest that May surface temperatures were up to 5°C above the 1971–2000 average. In June and August there were large positive degree day anomalies (up to 20 degree days) along the western and southern ice sheet. During August, temperatures were 3°C above average over most of the ice sheet, with the exception of the northeastern region. In August along the southwestern inland ice sheet, there has been an increase of 24 melting days during the past 30 years of passive microwave data coverage.

As melt extent and duration have increased during the last decade, MODIS10A1 data (Hall et al. 2006) indicate that the surface albedo of the ice sheet has also decreased, particularly along the western margin of the sheet (Fig. 5.19). The albedo decrease has been concentrated where bare ice has been exposed once the snow from the previous winter has melted away by mid-summer peak solar irradiance.

5) Surface Mass Balance along the K-Transect

The 150-km long K-Transect is located near Kangerlussuaq at 67°N between 340 m and 1500 m above sea level on the western flank of the ice sheet (van de Wal et al. 2005; Fig. 5.19). The surface mass balance between September 2009 and September 2010 was by far the lowest since 1990, when routine measurement began. Averaged over the length of the transect, the surface mass balance was 2.7 standard deviations below the 1990–2010 average. The altitude of the snow line, which describes the maximum areal extent of melting of the snow cover since the previous winter, was the highest on record, and a melt season that began very early (late April) continued until the beginning of September. Surface albedo values at the weather stations were below average and summer air temperatures were above average. In south Greenland, where the highest net ablation (~6 m of ice) of Greenland is found at low elevation, 2010 was unique in the observations since 1991, with about 9 m of ablation due to early melt and the lack of the commonly abundant winter precipitation, which usually takes one to two months to melt away.

The apparently strong link between negative surface mass balance and observed high air temperatures due to strong heat flux from the south and the record-high melt extent and duration, has been successfully simulated by the Modèl Atmosphérique Régional (MAR) regional climate data assimilation model. It simulated an ice sheet surface mass balance 90% less positive than normal, the lowest net mass accumulation rate since 1958 when

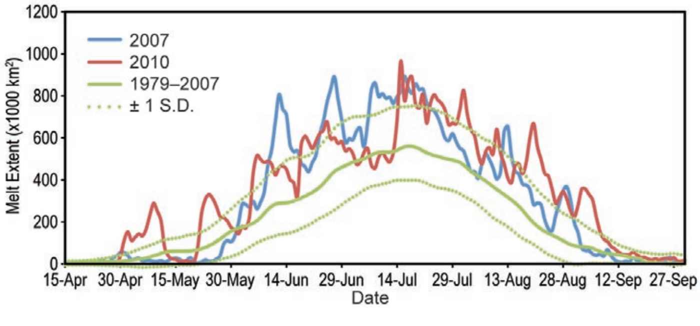

Fig. 5.20. Time series of Greenland melt extent derived from passive microwave remote sensing. The broken green lines are ±1 standard deviation (S.D) of the 1979–2007 average. After Mote (2007).

data to drive the model became available (Tedesco et al. 2011). This condition reflects a very heavy melt year combined with below-normal ice sheet snow accumulation.

6) Total Greenland Mass Loss from GRACE

GRACE satellite gravity solutions (Velicogna and Wahr 2006) are used to estimate monthly changes in the total mass of the Greenland ice sheet. For the hydrologic year 2009/10, i.e., from the end of the 2009 melt season, including October, through the end of October 2010, the ice sheet cumulative loss was -410 Gt, 177% (or two standard deviations) of the 2002–09 average annual loss rate of -231 Gt yr^{-1}. The 2010 mass loss is equivalent to a eustatic sea level rise contribution of 1.1 mm. This was the largest annual loss rate for Greenland in the GRACE record, 179 Gt more negative than the 2003–09 average. The 2009/10 hydrological year ended 206 Gt more negative than the recent (2002–09) hydrological year average. Using GRACE data, Rignot et al. (2011) found an acceleration of Greenland ice sheet mass budget deficit during 1979–2010, in close agreement with an independent mass balance model.

7) Marine-Terminating Glacier Area Changes

Marine-terminating glaciers are of particular interest because they represent the outlets through which inland ice can move most quickly and in the largest quantities out to sea. Iceberg calving from these glaciers represents an area reduction and mass loss from the ice sheet, which contributes to sea level rise.

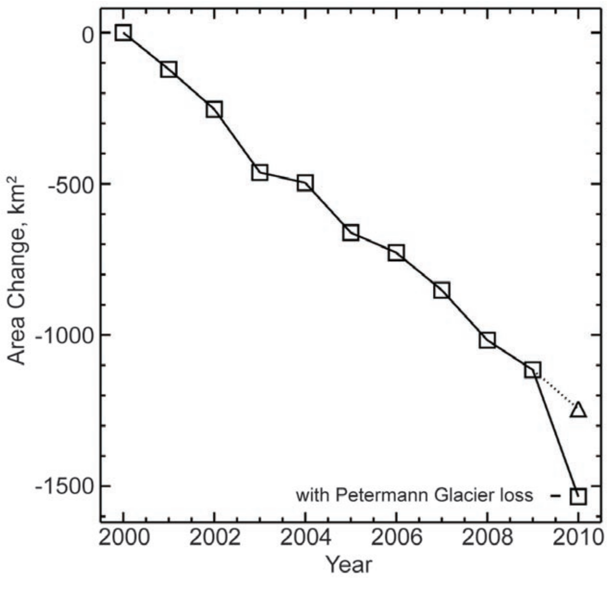

Fig. 5.21. Cumulative net annual area changes for the 35 widest marine-terminating glaciers of the Greenland ice sheet. Net area change in 2010 is shown with and without the Petermann Glacier loss. The trend without the Petermann Glacier loss in 2010 is illustrated by the triangle and dashed line.

Daily surveys using cloud-free MODIS visible imagery (Box and Decker 2011; http://bprc.osu.edu/MODIS/) indicate that, during 2010, marine-terminating glaciers collectively lost a net area of 419 km^2. This is more than three times the annual loss rate (121 km^2 yr^{-1}) of the previous eight years, 2002–09 (Fig. 5.21). The calving of 290 km^2 of ice from Petermann Glacier ice shelf in far northwest Greenland accounted for 70% of the loss (see http://bprc.osu.edu/MODIS/?p=69). Glacier ice area loss elsewhere in 2010 (i.e., excluding Petermann Glacier) remained near the average loss rate of 121 km^2 yr^{-1} observed since 2002. Glacier area change surveys (Howat and Eddy 2011) indicate that the ice area loss rate of the past decade is greater than loss rates since at least the 1980s.

A number of other large marine-terminating glaciers also lost a significant area of ice in 2010: Zachariae Isstrøm, northeast Greenland, 43 km^2; Humboldt Glacier, northwest Greenland, 20 km^2; Ikertivaq Glacier, Southeast Greenland, 15 km^2; and five glaciers that flow into Upernavik glacier bay in northwest Greenland, 14 km^2.

Since 2000, the net area change of the 39 widest marine-terminating glaciers is -1535 km^2 (17.5 times the size of the 87.5 km^2 Manhattan Island, New York) and the average effective glacier length change was -1.7 km. While the overall area change was negative, 7 of the 39 glaciers did advance in 2010 relative to 2009. The largest glacier area increases were at Ryder and Storstrømmen glaciers, 4.6 km^2 and 4.2 km^2, respectively.

6. ANTARCTICA

a. Overview—R. L. Fogt

The calendar year 2010 contained many record Antarctic climate anomalies. In particular, the austral winter was characterized by low pressure anomalies across the high southern latitudes and enhanced circumpolar zonal flow. This spatial pattern is consistent with a strong positive Southern Hemisphere Annular Mode (SAM) index. Although this pattern weakened in September, it strengthened again in October and remained positive throughout the rest of the year. A La Niña began in the tropical Pacific in July, which further amplified the low pressure anomalies particularly in the South Pacific/West Antarctic sector. The strength (in a statistical sense) and persistence of low pressure anomalies across much of Antarctica during austral winter and in the last part of 2010 gave rise to many record anomalies in sea ice extent, surface pressure, and temperature, while keeping continent-wide snow melt and precipitation values below climatological averages. Specific highlights in 2010 include:

- A record positive austral winter (June–August) averaged SAM index, and a record positive November SAM index. These records are based on the Marshall (2003) index, which now spans over 50 continuous years.
- Records of minimum pressure observed at many stations across Antarctica during the austral winter, and on the Antarctic Peninsula, above-average temperatures from May–December and record strong winds during June and October–November. In the northern Antarctic Peninsula, the below-average temperatures that began in April 2009 ended in March 2010 with the start of an above-average temperature period lasting throughout the rest of the year.
- Lower precipitation across Antarctica in general compared to 2009. The conditions were most different in coastal West Antarctica and the southern Antarctic Peninsula, where the simultaneous occurrence of La Niña-influenced conditions and enhanced cyclonic activity drastically altered the regional circulation.
- Surface snow melt in austral summer 2009/10 rebounded somewhat from its record low in austral summer 2008/09, but still remained well below the 30-year average based on satellite passive microwave records.
- Record high values of zonally-averaged sea ice extent from mid-June through late August and again from mid-November through early December. These records are based on over 30 years of data from satellite measurements of sea ice extent.
- A smaller than average, but unusually persistent, Antarctic ozone hole. The maximum area of the Antarctic hole peaked on 25 September 2010, but low ozone values persisted until mid-December 2010.

b. Circulation—A. J. Wovrosh, S. Barreira, and R. L. Fogt

The Antarctic large-scale circulation during 2010, based on NCEP/NCAR reanalysis data, is examined using a vertical cross-section of polar-cap averaged (60°S–90°S) geopotential height and temperature, and circumpolar (50°S–70°S) zonal wind anomalies within the troposphere and stratosphere (Fig. 6.1), as well as surface pressure and surface temperature anomalies (Fig. 6.2). Since the start of the modern satellite era, reanalysis data quality has improved drastically in southern high latitudes especially for circulation related fields (Bromwich and Fogt 2004; Bromwich et al. 2007), thus reanalysis data beginning in 1979 is used here. As in previous reports, the year was divided into periods where the circulation anomalies were fairly consistent (January–April, May–August, September–November, and December).

From Fig. 6.1, January–March were marked with above-average height/pressure anomalies over Antarctica, which were > 1 standard deviation from the 1979–2008 mean up to 30 hPa. At the surface, above-average pressures were observed across much of the continent but not the Peninsula (Fig. 6.2a). In terms of surface temperature, the Antarctic continent was warmer than average in the first part of the year (many places > 2 standard deviations from the 1979–2008 mean), while the northern Antarctic Peninsula was below average (Fig. 6.2b). In particular, the high temperature anomalies at South Pole in early 2010 make the previous long-term cooling trend there statistically insignificant. These circulation anomaly patterns are consistent with an El Niño influence on the Antarctic climate (i.e., Turner 2004), which lasted through the first part of 2010, and a negative Southern Hemisphere Annular Mode (SAM) index, which was the lowest in February (Fig. 6.1c, based on the Marshall (2003) index). The 2009–10 El Niño marked the highest sea surface temperature anomalies in the central equatorial Pacific in the last three decades (Lee and McPhaden 2010), and this event has been linked

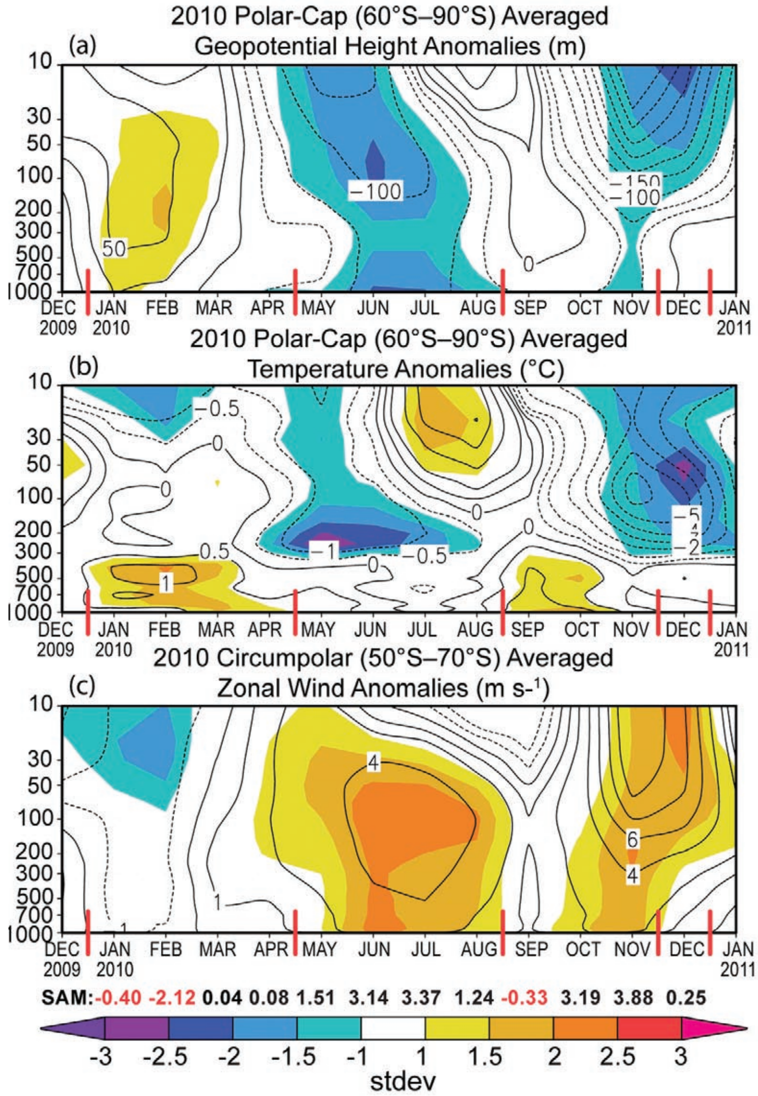

Fig. 6.1. Zonally-averaged climate parameter anomalies for the southern polar region in 2010 relative to the 1979–2008 period: (a) polar cap (60°S–90°S) averaged geopotential height anomalies (m); (b) polar cap averaged temperature anomalies (°C); (c) circumpolar (50°S–70°S) averaged zonal wind anomalies (m s^{-1}). The shading represents how many standard deviations the anomalies are from the 1979–2008 mean (color bar at bottom for scale). Red vertical bars indicate the four separate climate periods shown as spatial climate anomalies in Fig. 6.2. Primary contour interval is 50 m in (a), 1°C in (b), and 2 m s^{-1} in (c), with additional contours at ± 25 m, ± 0.5°C, and ± 1 m s^{-1} in (a), (b), and (c), respectively. Values for the SAM index are shown along the bottom in black and red. (Source: NCEP/NCAR reanalysis.)

to the high temperature anomalies in West Antarctica in 2010 (Fig. 6.2a; Lee et al. 2010). More generally, the warming in the central tropical Pacific has recently been linked to the overall warming trend in West Antarctica (Ding et al. 2011; Schneider et al. 2011).

A shift in the circulation pattern occurred in the austral winter, as negative geopotential height anomalies extended from the surface to 10 hPa over the polar cap (Fig. 6.1a). At the surface, this pattern of lower than average pressures is observed across nearly all of the high southern latitudes south of 60°S (especially off the coast of West Antarctica), while above-average pressure anomalies are observed throughout much of the southern midlatitudes (Fig. 6.2c). Such pressure decreases over Antarctica and increases in the midlatitudes strengthen the meridional pressure gradient, and therefore the circumpolar zonal flow was much stronger than average (> 2 standard deviations from the 1979–2008 mean) throughout the troposphere and into the lower stratosphere during austral winter in 2010 (Fig. 6.1c). These austral winter circulation anomalies are consistent with a strong positive SAM index (Fig. 6.1c). Indeed, the austral winter SAM index (an average value of 2.58 for June–August) was the highest value based on the 50+ year record of Marshall (2003). The temperature patterns in winter were less straightforward; there were negative polar-cap averaged temperature anomalies at 300 hPa < 2 standard deviations below the 1979–2008 mean throughout much of the winter, with higher-than-average temperatures above 100 hPa in late winter (July–August; Fig. 6.1b). Meanwhile, above-average temperatures were observed within the Weddell Sea region (Fig. 6.2d), which aided in generating negative winter sea ice anomalies in the northern Weddell Sea and Bellingshausen Seas (section 6f).

The low pressure and geopotential height anomalies across Antarctica weakened considerably in September (Fig. 6.1a), in turn weakening the meridional pressure gradient and thus the circumpolar zonal wind (Fig. 6.1c). From October to November, the pattern observed during the winter re-emerged, as polar-cap averaged geopotential heights were again negative, circumpolar zonal winds were again above average, and the Marshall (2003) SAM index reached another record in November. Of particular note are the spring surface temperature anomalies (Fig. 6.2f). The enhancement of above-average surface pressure in the midlatitudes east of

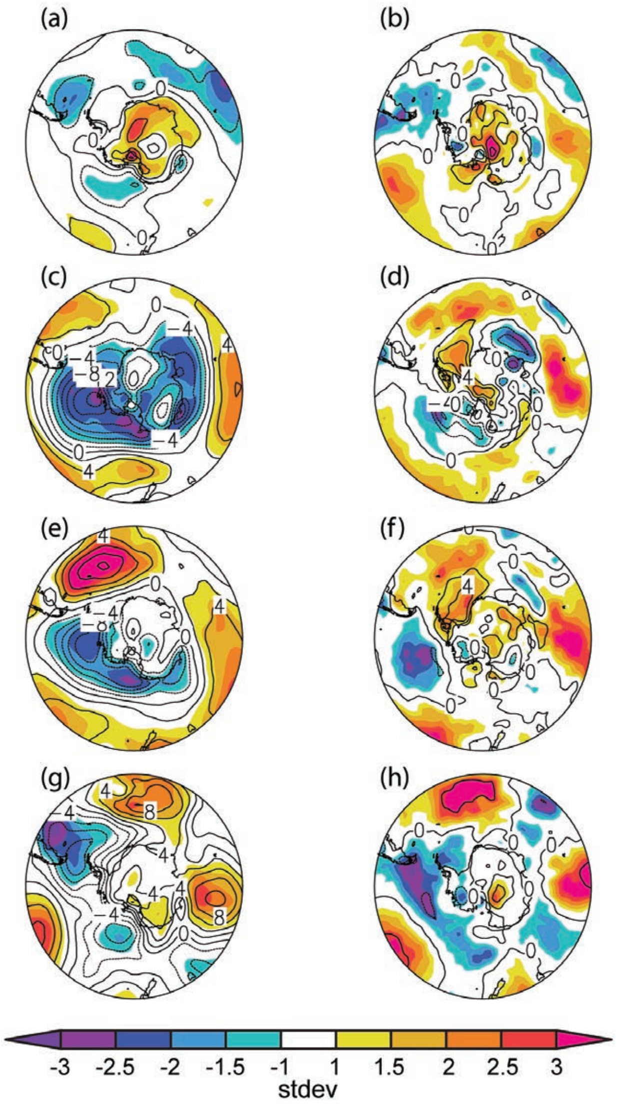

Fig. 6.2. (Left) Surface pressure anomaly and (right) surface temperature anomaly contours (in hPa and °C, respectively) relative to 1979–2008 climatology for (a,b) January–April 2010; (c,d) May–August 2010; (e,f) September–November 2010; (g,h) December 2010. The shaded regions correspond to the number of standard deviations the anomalies are from the 1979–2008 mean, as in Fig. 6.1. (Source: NCEP/NCAR reanalysis.)

South America (> 3.0 standard deviations) coupled with the low pressure west of the Antarctic Peninsula (Fig. 6.2e) generated northerly flow anomalies onto the Peninsula and Weddell Sea region, leading to the marked warming there in the austral spring (Fig. 6.2f; also reflected in polar-cap temperatures up to 500 hPa in Fig. 6.1b). The pattern of pressure anomalies in the Pacific and Atlantic sectors of Fig. 6.2e resemble a wave-train of pressure anomalies across the Pacific sector, a feature commonly observed during strong La Niña events (Turner 2004).

December was separated from the other months due to its unique circulation anomalies. Figure 6.1 shows below-average polar-cap temperatures and geopotential heights above 300 hPa and 50 hPa, respectively, and stronger-than-average circumpolar zonal winds > 1.5 standard deviations from the 1979–2008 mean above 300 hPa. At the surface, the wave-train of pressure anomalies is still observed (Fig. 6.2g), but its location in comparison to Fig. 6.2e acts to generate more southerly (cold) flow extending from the South Pacific across the Antarctic Peninsula, driving the very strong below average temperature anomalies there in December (Fig. 6.2h).

c. Surface Manned and Automatic Weather Station Observations—S. Colwell, L. M. Keller, and M. A. Lazzara

In general, both the automatic and manned stations (see Fig. 6.3a for locations) indicate well-below-normal (and often record-setting) pressures during the austral winter, similar to Fig. 6.2c. Stations in East Antarctica and over the Ross Ice Shelf recorded much lower temperatures throughout the year. Climate data from two representative manned stations (Rothera and Halley) and two automatic stations (Dome C II and Gill) are displayed in Figs. 6.3b–e.

Monthly mean temperatures on the northern Antarctic Peninsula were near average at the start of the year but in winter and spring were significantly above average (not shown). Farther south on the Peninsula, Rothera recorded its warmest October temperature ever (-1.9°C; Fig. 6.3b). The monthly mean pressure at Rothera was above average at the start of the year with February recording its highest ever value of 994 hPa. After this, the monthly mean pressures were well-below average with June recording a new minimum of 979.4 hPa. Overall, this meant that Rothera recorded its lowest annual mean pressure of 984 hPa (Fig. 6.3b). Record-high wind speeds were also observed across many sites on the Peninsula in October; Ferraz station reported a record wind gust of 49.4 m s^{-1} on 15 October.

In the Weddell Sea region, the monthly mean temperatures at Halley were above average for all months except July when it was 0.2°C below average (Fig. 6.3c), resulting in the annual mean temperature at Halley being the third highest on record. Monthly mean temperatures at Neumayer Station started off higher than average but temperatures of about 5°C below average were recorded in June and July. Around the coast of East Antarctica, the monthly mean temperatures at Mawson, Davis, and Casey tended to oscillate between higher and lower than average, with very low

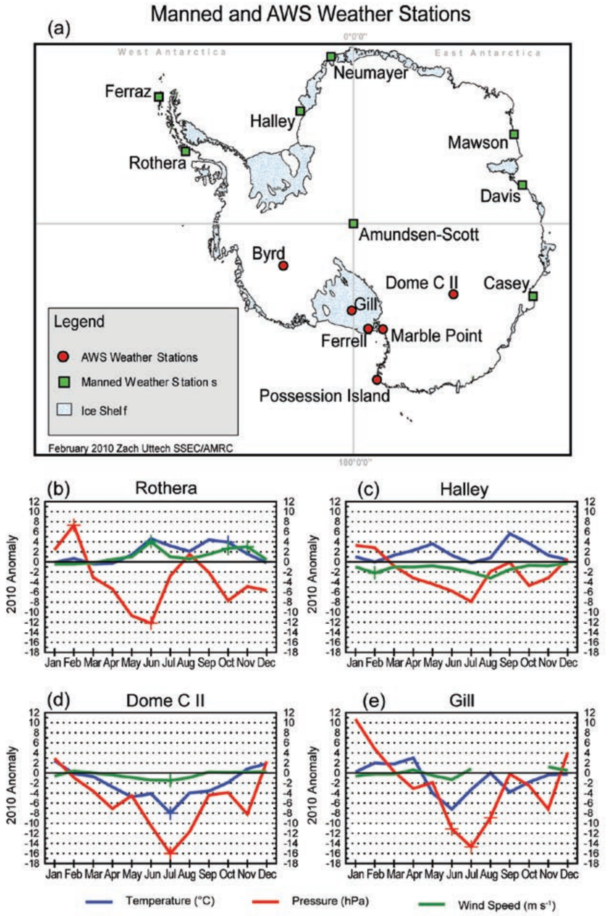

Fig. 6.3.(a) Locations of automatic and manned Antarctic weather stations described in Chapter 6. (b)–(e) 2010 Antarctic climate anomalies at four representative stations (two manned, two automatic). Monthly mean anomalies for temperature (°C), MSLP (hPa), and wind speed (m s^{-1}) are shown, with plus signs (+) denoting all-time record anomalies for a given month at each station. Climatological station data start in 1976 for Rothera, 1957 for Halley, 1980 for Dome C II, and 1985 for Gill. The base period for calculating the anomalies is 1979–2008 for manned stations, and the full record period for the automatic stations.

temperatures being recorded at Mawson and Davis in July and very high temperatures in September.

Monthly mean temperatures at Amundsen-Scott station at the South Pole varied over the year, sometimes significantly above average and sometimes below. In April, the temperature was 5.2°C below average at -62.6°C, which tied the lowest recorded April temperature back in 1998. In March, the values were 3.6°C above average, and 3.8°C above average in May.

Observations from automatic weather stations on the Polar Plateau, Ross Ice Shelf, and West Antarctica paint a very different picture for 2010 than was seen in 2009. Generally, above-average temperatures were found in the summer and fall, with below-average temperatures for the winter and spring. In addition, the stations reported lower pressures in the winter, with some low pressures breaking long-term records. On the Polar Plateau, Dome C II (Fig. 6.3d) had a record-low monthly mean temperature (8°C below the mean), a record-low monthly mean pressure, (16 hPa below the mean), and a record-low monthly mean wind speed (1.5 m s^{-1} below the mean) for July. In addition, the minimum temperature during the winter was below -73.3°C for April through September at Dome C II.

On the Ross Ice Shelf, Ferrell reported record-low pressures for July, August, and November (15 hPa, 9 hPa, and 7 hPa below the monthly mean, respectively), and Gill reported record-low pressures for June, July, and August (11 hPa, 15 hPa, and 9 hPa below the monthly mean, respectively; Fig. 6.3e). Closer to the Ross Sea, Marble Point also had a record-low pressure for July (14 hPa below the mean). In West Antarctica, record-low pressures for Byrd were below normal by 12 hPa for June and 17 hPa for July. Finally, at Possession Island near Cape Adare, record-low temperatures were 3°C below normal for both June and September and record low pressure was 11 hPa below the mean in July.

d. Net Precipitation—D. H. Bromwich and S.-H. Wang

Precipitation minus evaporation (P-E) closely approximates the surface mass balance over Antarctica, except for the steep coastal slopes (e.g., Bromwich et al. 2000; van den Broeke et al. 2006). Precipitation variability dominates P-E changes over the Antarctic continent. Precipitation and evaporation/sublimation fields from the Japanese Reanalysis (JRA; Onogi et al. 2007) were examined to assess Antarctic net precipitation behavior for 2010. The "evaporation" in JRA was calculated from the surface latent heat flux variable. In comparison to other long-term global reanalyses (e.g., NCEP1 and NCEP2), JRA has higher model resolution, both horizontally and vertically, greater observational usage, and a more advanced model configuration (Onogi et al. 2007). Nicolas and Bromwich (2011) show that the reliability of JRA P-E is highly ranked in relation to other contemporary global reanalyses.

Figure 6.4 shows the JRA annual anomalies of P-E and mean sea level pressure (MSLP) for 2010 (Figs. 6.4a,c) and 2009 (Figs. 6.4b,d). In general, the annual anomalies over the high interior of the continent are small (within ± 50 mm yr^{-1}), consistent with the low amount of snow accumulation in this region. Most coastal regions in 2010 display more negative P-E anomalies than during the previous year, with the exception of the Weddell Sea and Ellsworth Land (90°W). The most negative P-E anomalies can be observed to the west of the Antarctic Peninsula in 2009 (between 60°W and 150°W, centered in the Amundsen Sea, Fig. 6.4b), in contrast to both positive and negative anomalies in the same region in 2010 (Fig. 6.4a). Less precipitation (P-E) can also be found over Ross Sea and the northern edge of Queen Maud Land (between 0° and 60°E) during 2010 than during 2009. These annual P-E anomaly features are consistent with the mean atmospheric circulation implied by the MSLP anomalies (Figs. 6.4c,d). In 2009, a negative anomaly centered over the Drake Passage was observed; in 2010, a much deeper negative anomaly was observed in the Amundsen-Bellingshausen Seas (~105° W), mainly due to the negative anomalies in May–November (Figs. 6.2c,e). The latter produced stronger offshore flow and less precipitation along the coast from Pine Island Bay to the Ross Ice Shelf, and in combination with positive MSLP anomalies over the South Atlantic (Fig. 6.4c), brought more moisture to the Antarctic Peninsula and Weddell Sea region. Secondary negative MSLP anomalies observed along the East Antarctic coast in 2010 at 75°E and 120°E produced positive P-E anomaly features near Davis (80°E) and Dumont d'Urville (135°E) stations, respectively.

The austral fall (March–May) P-E anomalies (not shown) had the largest impact on 2010 annual anomalies, especially west of the Antarctic Peninsula, where they contributed more than 50% of the total annual P-E anomalies. The influence of La Niña on P-E is also noted, as the persistent low pressure in the Amundsen-Bellingshausen Seas since April (Figs. 6.2c,e,f) indicates greater-than-normal storm activity during most months of 2010, ultimately resulting in the large P-E anomaly just west of the Antarctic Peninsula (positive) and for Marie Byrd Land-Ross Ice Shelf (negative). Earlier studies suggest that such anomaly features are consistent with simultaneous strong La Niña (Bromwich et al. 2000, 2004) and positive SAM events (Fogt and Bromwich 2006; Fogt et al. 2011). Figure 6.4e shows the time series of average monthly total P-E over Marie Byrd Land (75°S–90°S, 120°W–180°) and monthly SOI and SAM indices (with 12-month running means). It is clear that SOI and SAM are in phase with each other but

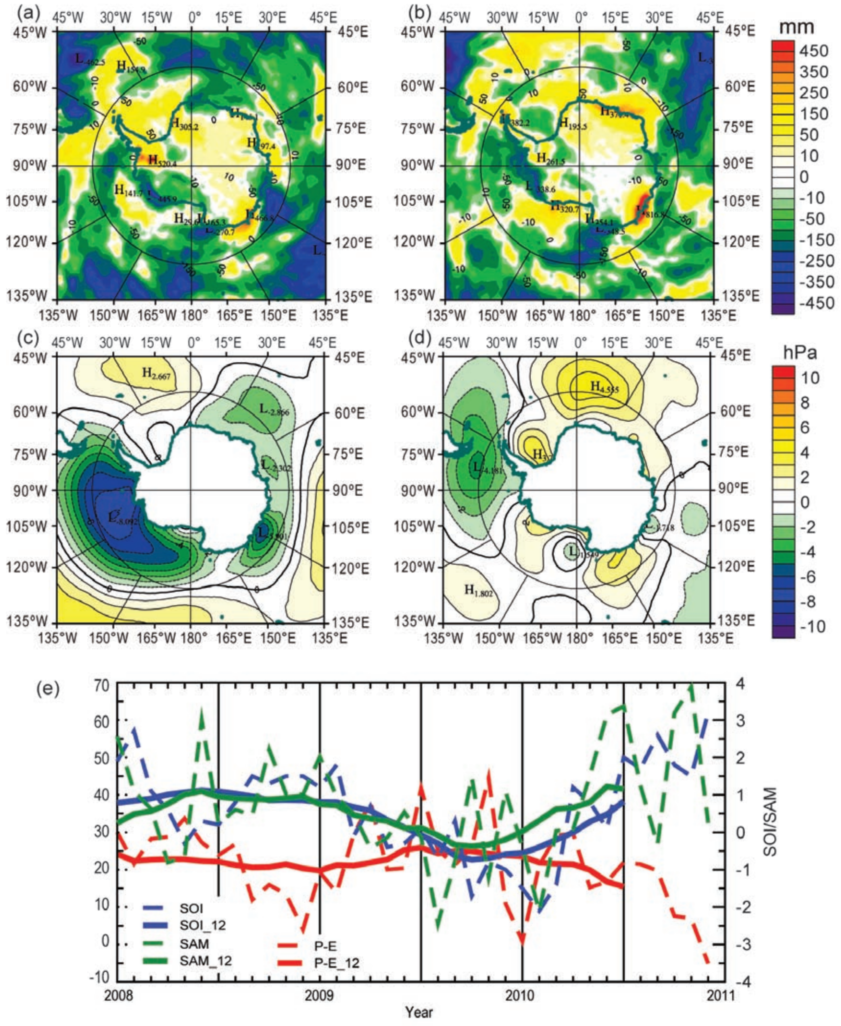

Fig. 6.4. (a–d) Annual precipitation minus evaporation (P-E) and annual mean sea level pressure (MSLP) anomalies: (a) 2010 P-E anomalies, departure from the 1979–2009 mean; (b) 2009 P-E anomalies, departure from the 1979–2008 mean; (c) 2010 annual MSLP anomalies; and (d) 2009 annual MSLP anomalies. (e) Monthly total P-E (mm; red) for the West Antarctic sector bounded by 75°S–90°S, 120°W–180°, along with the SOI (blue, from Climate Prediction Center) and SAM [green, from Marshall (2003)] indices since 2008. Centered annual running means are plotted as solid lines. (P-E data are from JRA-25 reanalysis.)

SIDEBAR 6.1: PINE ISLAND GLACIER, WEST ANTARCTICA—E. RIGNOT

Pine Island Glacier (75°S, 100°W; Fig. 6.5), in West Antarctica is a gigantic ice stream that discharges about 100 trillion tons of ice into the Amundsen Sea every year, one of the largest amounts in Antarctica (Rignot et al. 2008). This glacier was identified as a potential weak spot in Antarctica back in the 1970s because it is grounded well below sea level and is not buttressed by a large floating extension at sea (Hughes 1981). In the late 1990s, satellite data revealed for the first time this glacier was undergoing major changes; its line of grounding was retreating at a rate of 1 km yr^{-1} (Rignot 1998). Since then, additional data have shown that the glacier is accelerating and thinning (Wingham et al. 2009). During the last 18 years, the rate of glacier thinning has quadrupled, and its ice velocity has increased by more than 66%, rising more every year than the previous year (Rignot 2008). In late 2009, for the first time since 1992, the glacier speed stabilized and stopped its exponential increase (Joughin et al. 2010). The grounding line has now retreated by more than 20 km since 1992. The glacier has become afloat over a large sector that previously was only a few tens of meters above flotation. It is also now retreating into much deeper ice (getting deeper inland), a configuration that has been hypothesized to be unstable by glaciologists in the 1970s.

Recent data collected in situ by autosubmarine (Jenkins et al. 2010) and on airplanes using airborne gravity (Studinger et al. 2010) unveiled the presence of a major ridge beneath the floating ice shelf in front of the glacier that probably anchored the glacier back in the 1960s–1970s. Since 1996, this glacier has been coming in contact with warm waters by Antarctic standards, which regularly ablate large amounts of glacier ice from below every year (Jacobs et al. 1996). It is uncertain how much of the current retreat is driven by the detachment of the glacier from its former pinning point decades ago, and/or how much is caused by the advection of warmer water from the circumpolar current underneath the glacier in recent years.

However, the glacier is already a major participant in the overall mass budget of the Antarctic Ice Sheet—which is losing mass to the sea and raising sea level—and that it, along with its neighbors, if completely melted constitutes enough ice to raise global sea level by more than one meter. The glacier and its surrounding areas are now receiving international attention and are routinely monitored by satellites and surveyed by airborne platforms since the first field party in the 1980s. These data will bring new insights into the current and future evolutions of this region and, in particular, reexamine if models predicting that the glacier will soon resume its acceleration and triple its ice velocity are realistic or not (Thomas et al. 2004).

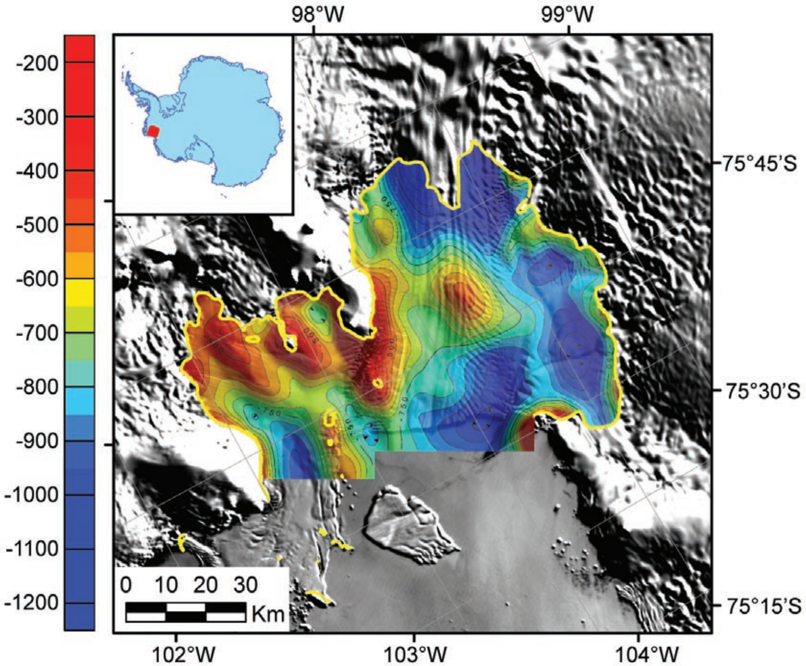

Fig. 6.5. Sea floor topography beneath the floating ice shelf in front of Pine Island Glacier, West Antarctica unveiled by the NASA-Icebridge mission in November 2009 using airborne gravity and showing a previously unknown sub-ice-shelf ridge at 76°S, 104°W that may have anchored the glacier five to six decades ago. Bed elevation color coded from blue (deep) to red (high) overlaid on a MODIS mosaic of Antarctica (Courtesy M. Studinger, NASA GSFC, 2010).

have opposite behavior to P-E in most months from 2008 onward. The correlation coefficients between monthly P-E and index values are highly significant: SOI -0.31 (-0.48 for annual running mean) and SAM -0.32 (-0.77 for annual running mean), respectively.

e. *2009/10 Seasonal Melt Extent and Duration*—L. Wang and H. Liu

Surface snow melt on the Antarctic ice sheet during the 2009/10 austral summer was estimated from the space-borne Special Sensor Microwave Imager (SSM/I) passive microwave observations at the 19 GHz horizontal-polarization channel. A wavelet-transform based edge detection method (Liu et al. 2005) is applied to track melt onset and end dates from time series of daily brightness temperatures for individual SSM/I pixels. The total annual melt duration is calculated by accumulating the number of melt days between each pair of onset and end edges. Figures 6.6a–c display the melt start day, melt end day, and melt duration, respectively.

Melt mainly occurred along the Antarctic coastline in austral summer 2009/10. The total area that experienced surface melt was 945 000 km^2, which is considerably larger than last year (681 900 km^2; L. Wang et al. 2010). However, this value is still below the 30-year average (1 290 700 km^2), below the 25-year median melt extent (1 277 500 km^2) reported in Liu et al. (2006), and below the 20-year average (1 280 000 km^2) reported in Torinesi et al. (2003). This year's melt index (calculated by accumulating the number of melting days over the entire Antarctic ice sheet; Liu et al. 2006) is 39 349 375 day km^2, which is almost double the amount of last year (20 533 000 day km^2; L. Wang et al. 2010). A larger melt index implies either an extended melt area or a longer melt season. The melt peak day was 9 January, with three other smaller peaks on 1 February, 13 February, and 6 March (Fig. 6.6d). The major melt season is from mid-December 2009 to mid-January 2010. Some short-period melt happened in late March. The off-season melt was mainly distributed on Wilkins Ice Shelf (Fig. 6.6b).

Most melt areas are located at latitudes equatorward of 75°S, including the ice shelves along the Antarctic Peninsula, Wilkins, Queen Maud Land, Amery, Shackleton, and Abbot (see Fig. 6.6 for locations). High-latitude melt is mainly found on Marie Byrd Land. There is still no surface melt or very small amount of melt detected on the Ronne-Filchner Ice Shelf, Ross Ice Shelf, Victoria Land, and Wilkes Land. Compared to the 2008/09 austral summer, extensive surface melt occurred on the coast of Queen Maud Land. The melt index for this sub-region is 11 908 125 day km^2. Comparing to the 25-year average melt index (7 471 500 day km^2; Liu et al. 2006) in Queen Maud Land, this year can be considered as an exceptionally high melting year for this area.

f. *Sea Ice Extent and Concentration*—R. A. Massom, P. Reid, S. Stammerjohn, S. Barreira, and T. Scambos

During 2010, zonally-averaged Antarctic sea ice extent was characterized by fluctuations that were closely associated with changes in large-scale atmospheric circulation patterns. Sea ice extent from January through late April was generally near to below average compared to the 1979–2008 mean (Fig. 6.7a), although major regional contrasts are apparent during this time. This pattern, and the underlying climate pattern in the far south, changed significantly for the period June–December. In general, a strong positive sea ice extent anomaly was observed during this time.

During the January–May period, there were strong positive anomalies in ice concentration and extent in the Weddell Sea, western Ross Sea, and western Pacific Ocean, balanced by strong negative anomalies in the Amundsen-Bellingshausen, outer Ross Sea, and Indian Ocean sectors (Fig. 6.7b). These patterns are indicative of large-scale wind patterns associated with atmospheric pressure fields (i.e., Fig. 6.2a) and are largely consistent with the regional 30-year trends in seasonality and extent (Comiso 2010; Stammerjohn et al. 2008). Early in the year, the negative anomaly in the Bellingshausen Sea coincided with a 30-year maximum in SST in that sector (Lee et al. 2010). An additional factor observed in the northwest Weddell Sea in the 2009/10 summer was the presence of ice blocks derived from the rapid retreat/disintegration of glaciers in the region, which impacted shipping operations by increasing local sea ice cover.

In May, the zonally-averaged sea ice extent anomaly changed to strongly positive, i.e., up to 2 standard deviations above the 1979–2008 mean (Fig. 6.7a). This major change coincided with Southern Hemisphere circulation anomalies that were consistent with transitions from a negative to positive polarity of the SAM index and El Niño to La Niña conditions in the tropical Pacific (i.e., section 6b; Fig. 6.2). Furthermore, Fig. 6.7a indicates that the zonally-averaged sea ice extent anomaly from mid-June through late August was the largest in the 30+ year record. Changes in two regions in particular were responsible for the major increase in overall ice extent at this time (May–June), namely: (1) a switch from negative to strongly positive ice-edge anomaly across eastern Ross to Amundsen

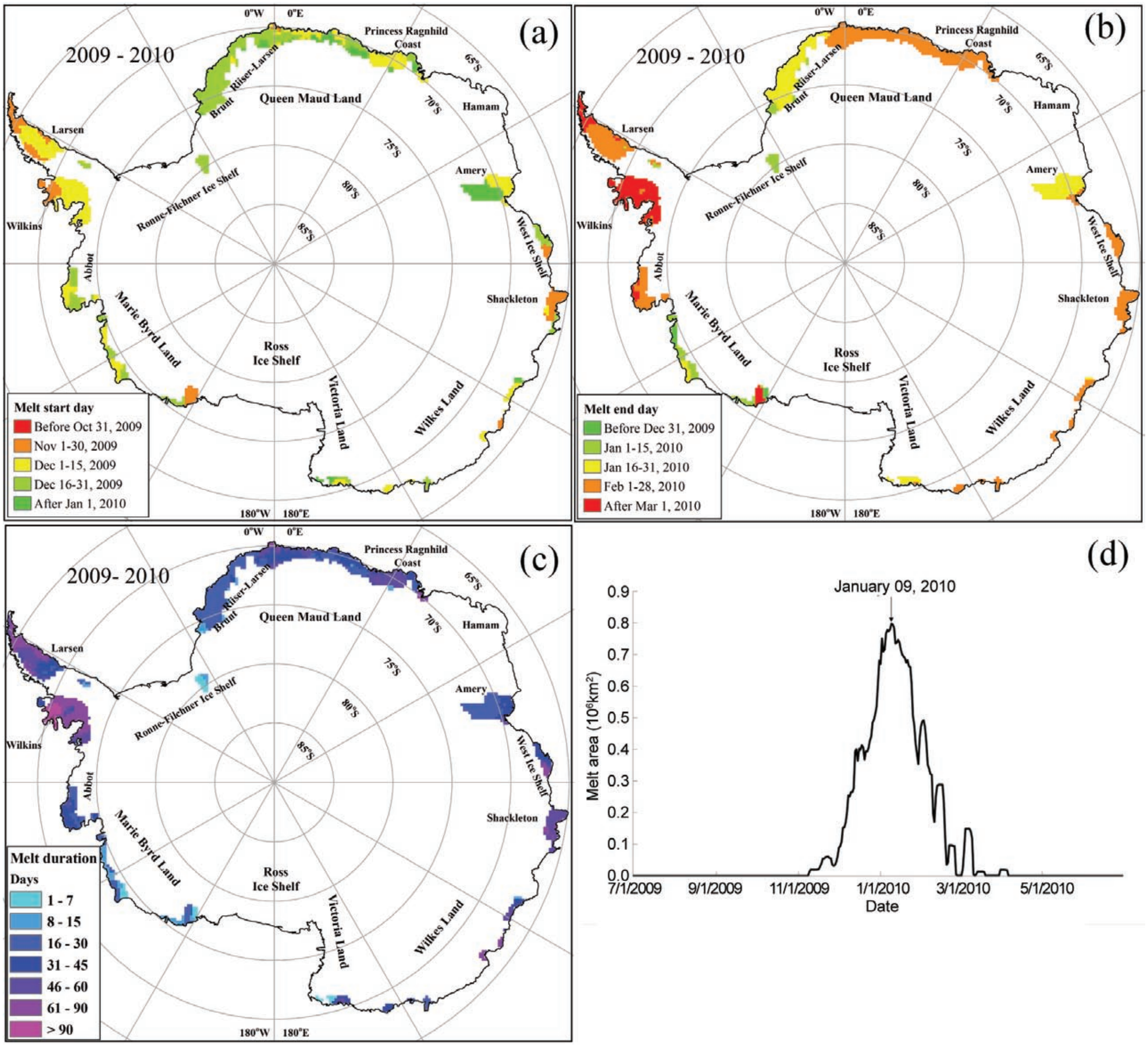

Fig. 6.6. Maps for (a) melt start day, (b) melt end day, and (c) melt duration of the Antarctic ice sheet during 2009/10 austral summer. Daily melt extent is shown in (d) with melt peak day indicated.

Seas sector and (2) the development of an extensive positive anomaly of similar magnitude off Enderby Land (Indian Ocean sector). These positive ice-edge anomalies are likely to be due to a combination of over extensive fronts, wind-driven ice advection and in situ thermodynamic growth, the latter associated with the development of cold pools of SST (particularly in the eastern Ross Sea from about June onwards). Elsewhere, sea ice extent was average to below average in May–June. The circumpolar pattern of extensive zones of strongly positive and more moderate negative ice-edge anomalies shown in Fig. 6.7c generally persisted from June through late December 2010 (with the positive regional ice-extent and concentration anomalies intensifying in late November through early December).

The pattern of regional sea ice anomalies in the Western Hemisphere described above and for the period from May–June onwards is consistent with the presence of a persistent negative mean sea level pressure (MSLP) anomaly in the Amundsen Sea region in May–November (Figs. 6.2c,e) and along the Antarctic Peninsula in December (Fig. 6.2g). Studies have demonstrated that negative MSLP anomalies in this region are commonly observed and displaced east of their mean location during La Niña events and during the positive polarity of the SAM index (Fogt and Bromwich 2006; Stammerjohn et al. 2008), although other local factors can also play a role. In general,

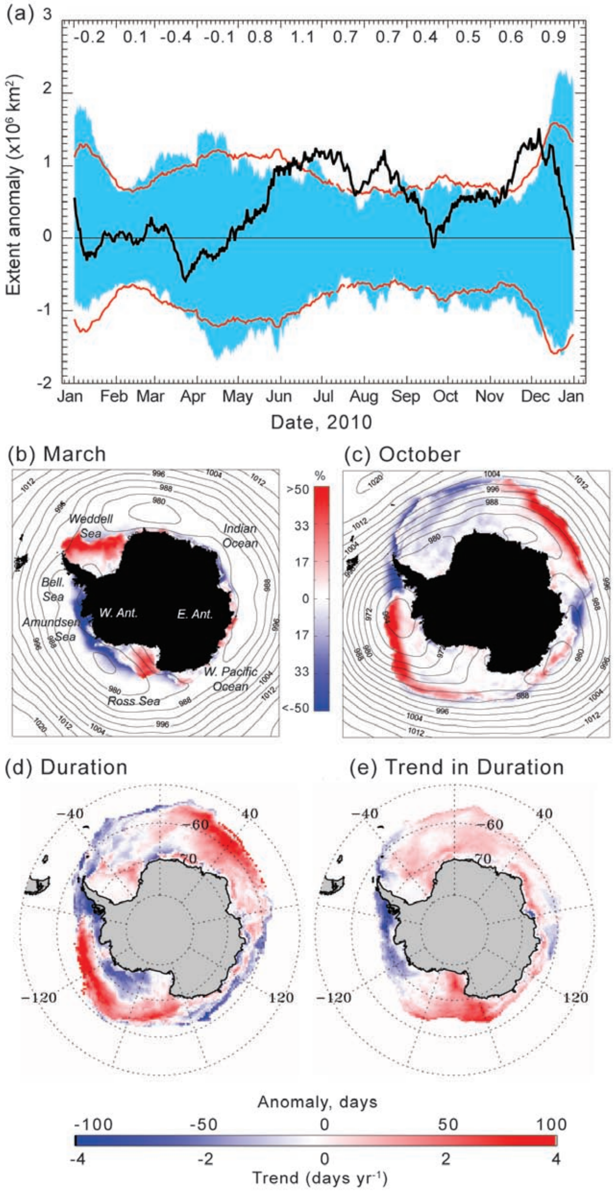

Fig. 6.7. (a) Plot of daily anomaly (black line) from the climatology (1979–2008) of daily Southern Hemisphere sea ice extent for 2010, based on satellite passive microwave ice concentration data from the GSFC Bootstrap Version 2 dataset (Comiso 1999, updated 2008). Blue banding represents the range of daily values for 1979–2008, while the red line represents ±2 standard deviations. At the top are monthly-mean extent anomalies ($x10^6$ km^2). (b–c) Sea ice concentration anomaly maps for March and October 2010 derived versus the monthly means for 1979–2007, with monthly-mean contours of MSLP [from the Australian Community Climate and Earth System Simulator (ACCESS)] provided by the Australian Bureau of Meteorology. (d) Sea ice duration anomaly for 2010/11, and (e) duration trend. For (d) and (e), see Stammerjohn et al. (2008) for a description of techniques (using daily satellite passive-microwave data). Both the climatology (for computing the anomaly) and trend are based on 1979/80–2007/08 data, for which GSFC Bootstrap Version 2.0 data were available (Comiso 1999, updated 2008), while the 2010/11 duration-year data are from the NASA Team Near-Real-Time Sea Ice (NRTSI) dataset (Maslanik and Stroeve, 1999). The 2010/11 duration anomaly is therefore the 2010/11 NRTSI data minus the 1979/80–2007/08 BS V2 Climatology. Discrepancies introduced by using these different data sources lead to an uncertainty (difference) level that is well below the magnitude of the large changes/anomalies.

the large zonally-averaged sea ice extent anomaly from June through December (with the exception of September; Fig. 6.7a) is consistent with the presence of negative temperature anomalies in the Pacific Ocean and the concurrent circumpolar pattern of increased westerly winds associated with a strong positive SAM index (Fig. 6.1c); the latter helps to drive the ice edge equatorward (via Ekman drift). Embedded within that zonally-forced atmospheric pattern are the more regional-scale anomalies (described above) associated with a predominantly wave-2 pattern for most of the latter half of the year.

An abrupt dip in zonally-averaged extent for a brief period in mid-September (Fig. 6.7a) was the result of increased cyclonic activity centered on 90°E which saw sea ice extent off the east coast of Antarctica (in the approximate sector 70°E–120°E) fall dramatically. At the same time, a major negative extent/concentration anomaly developed in the Bellingshausen Sea/West Antarctic Peninsula sector. Below-average sea ice extent and concentration persisted throughout the year in this sector, apart from a brief wintertime rebound to above-average in July–August. This pattern is again consistent with long-term trends in this region (Comiso 2010; Stammerjohn et al. 2008).

In terms of seasonality, the spatio-temporal pattern of Southern Hemisphere sea ice duration in 2010 was affected by a very late sea ice advance across the Bellingshausen-Amundsen Seas sector (not shown). Again, this appears to be consistent with the atmospheric circulation anomalies in May–July described above, and especially the low-pressure anomaly around 150°W–160°W (Fig. 6.2c). The annual retreat pattern (not shown) resembles the classic high-latitude response to La Niña (section 6b), with the low pressure anomaly moving towards, and in November–December straddling, the Antarctic Peninsula (Figs. 6.2c,e,g). East Antarctica has two distinct patterns in terms of duration anomaly, namely predominantly longer in the Indian Ocean

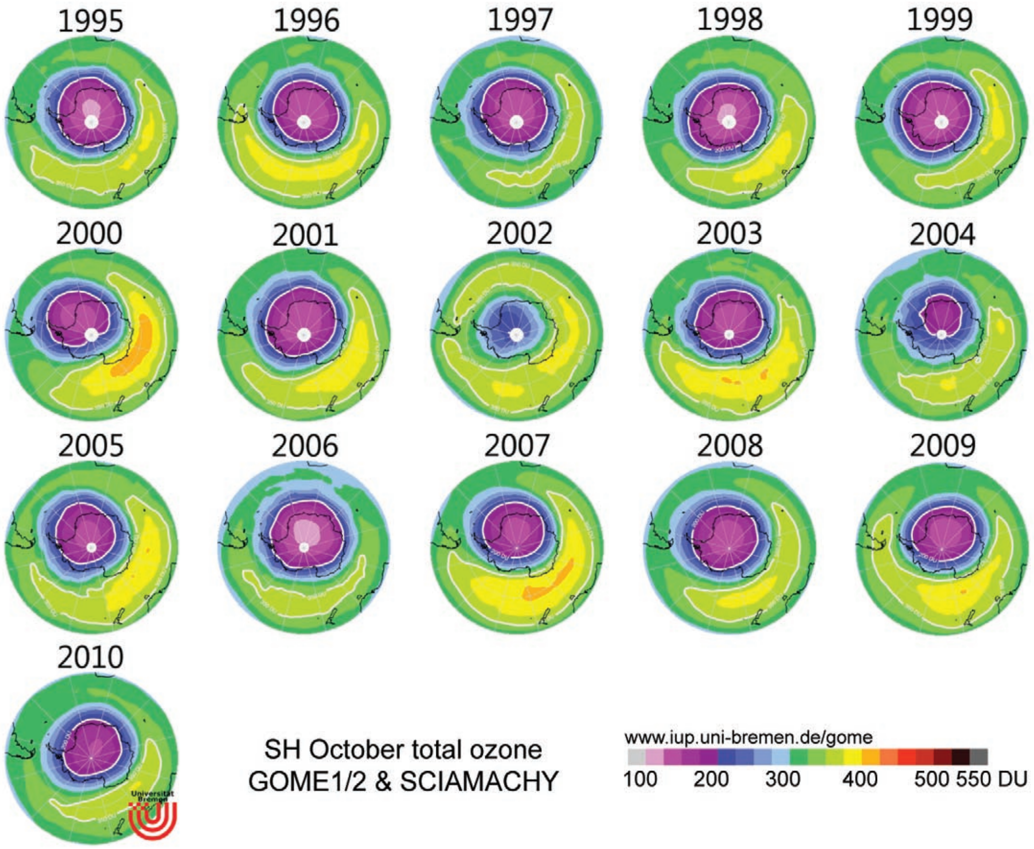

Fig. 6.8. October averages of total column ozone derived from the GOME 1 and 2, and SCIAMACHY instruments (courtesy of Prof. John Burrows, Univ. of Bremen).

(consistent with the long-term trend in Fig. 6.7e) but shorter over much of the West Pacific sector (where the long-term trend is generally positive).

g. Ozone Depletion—P. A. Newman, E. R. Nash, C. S. Long, M. C. Pitts, B. Johnson, M. L. Santee, and J. Burrows

The 2010 Antarctic ozone hole was in the low range of severity. Prior to 1980, severe ozone losses over Antarctica were not apparent. After 1990, every year has seen a severe loss. Compared to the 1990–2009 period, the 2010 ozone hole average area and the average minimum total ozone was in the lowest 20% of observed values. Figure 6.8 displays October averages of total ozone derived from the GOME/SCIAMACHY instruments from 1995 to 2010. Using Ozone Monitoring Instrument (OMI) total ozone observations, the area of the 2010 hole was approximately 19.0 million km^2, averaged over the period of most severe depletion from 7 September to 13 October. The peak area was observed on 25 September at 22.2 million km^2. This value is comparable to the smaller ozone hole of 2004 but larger than the record low area of 2002. The average depth of the ozone hole was 127 Dobson Units (DU), averaged over the period of lowest ozone from 21 September to 16 October (the lowest observed value was 118 DU on 1 October). In addition to the small area, the ozone hole began developing in mid-August rather than the early August period. Slightly different values for the area and depth of the ozone hole are found by the SCIAMACHY and NOAA SBUV/2 instruments, but the patterns are consistent between all of the satellite instruments.

Vertical profiles of ozone from the NOAA South Pole station (not shown) indicate that ozone dropped to a zero value by late September at altitudes of 16 km–17 km. These NOAA balloon-borne ozone instruments revealed that ozone values were near zero between 14 km and 20 km by 6 October 2010, and that these very low values persisted to mid-October. This vertical profile information forms a consistent picture with the observations from the total ozone instrumentation.

The ozone hole is caused by the conversion of chlorine molecules from the non-reactive forms into ozone reactive forms on the surfaces of polar stratospheric clouds or PSCs (i.e., $HCl+ClONO_2 \xrightarrow{PSC}$

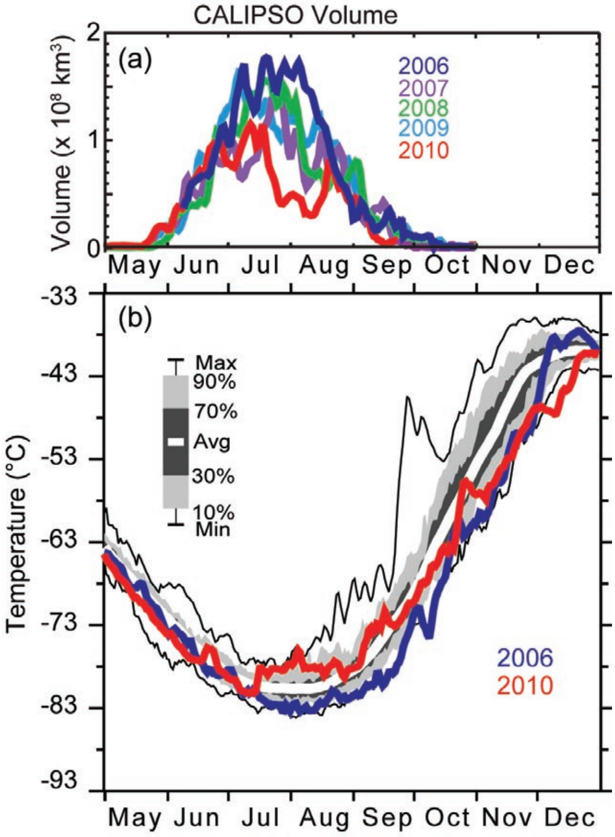

Fig. 6.9. (a) Daily time series of CALIPSO PSC volume for the Antarctic winter season (updated from Pitts et al. 2009). (b) Climatology of daily temperature averages for 50 hPa, 60°S–90°S as derived from 1979–2010 data. The red line shows 2010, while the blue line shows 2006. The thick white line shows the average for each day of this climatology. The gray shading shows the percentage range of those same values. The data are from NCEP CPC stratospheric analyses.

$\text{C1}_2 + \text{HNO}_3$). The molecular chlorine photolyzes as the sun rises in spring, and this chlorine (combined with bromine) directly causes catalytic ozone loss. CALIPSO satellite observations show that in late September 2010, PSC volume was the lowest observed over their 2006–10 Antarctic observations record (Fig. 6.9a), and was virtually zero by late September (update from Pitts et al. 2009). Ozone-depleting substances (ODSs) in the 2010 Antarctic ozone hole are estimated to have only decreased by about 5.3% (3.8 ppb) from the peak levels in the 2000–02 period (4.0 ppb). These ODSs have fallen 11% towards the 1980 level of 2.1 ppb.

The Microwave Limb Sounder (MLS) on the NASA Aura satellite measures the abundances of both non-reactive (HCl) and ozone-destroying (ClO) forms of chlorine and is thus able to track the activation and deactivation of chlorine as it is interconverted between them. Consistent with the unusually small volume of air exposed to PSCs (Fig. 6.9a), the enhancement of ClO (i.e., the magnitude of chlorine activation) was considerably weaker in 2010 than in other recent Antarctic winters. Not only were ClO abundances smaller, but also the enhancement did not extend as high in altitude as typical.

The temperature variability of the Antarctic stratosphere modulates the severity of the ozone hole from year to year. Lower-than-average Antarctic temperatures result in larger and deeper ozone holes, while higher temperatures lead to weaker ozone holes (Newman et al. 2004). Figure 6.9b shows the temperature time series (from NCEP) for 50 hPa averaged from 60°S–90°S. The 2010 July–September period was near or above average (see also Fig. 6.1b). The sharp increases of temperature in both mid-July and early September are accompanied by sharp decreases of PSC volume (Fig. 6.9a). Hence, the comparatively smaller 2010 ozone hole is primarily a result of the higher-than-average temperatures. This warming is a result of large wave events in mid-July and early September that sharply increased the temperature (Figs. 6.9 and 6.1b).

The 2010 ozone hole was unusually persistent. Low ozone values (< 220 DU) continued into mid-December 2010. Very weak wave forcing occurred during the late October to early December period. The depleted region of ozone remained centered on Antarctica until a large wave event in mid-December finally caused the ozone hole to disappear.

7. REGIONAL CLIMATES

a. Overview—L. A. Vincent and J. Renwick, Eds.

This chapter provides a regional perspective of the global climate in 2010, with a focus on unusual or extreme events. Analyses are provided for continents, broad geographic regions, and nations. Information for the year is placed into a historical context using anomalies (relative to 1961–90, unless otherwise noted), percentage anomalies, and rankings. Authors for most regions are local scientists and data is made available by their affiliated agency. While this chapter covers the climate of 2010, information from the previous year may be included in order to accurately cover relevant climate seasons (e.g., austral summer and boreal winter seasons typically include data from December 2009).

On average, temperatures were exceptionally warm in Canada and Greenland, western Russia, parts of the Middle East, much of south Asia, and over much of Africa. A few parts of the world were significantly colder than average, such as Western Europe and parts of North America during the winter months. Droughts affected large parts of South America, especially in Amazonia, Bolivia, Chile, and Argentina. Very wet conditions were recorded in Mexico, northern and western Africa, the Iberian Peninsula, Eastern Europe, Pakistan and the Himalayan region, and in central and eastern Australia.

b. North America

1) CANADA—R. Whitewood and D. Phillips

The year 2010 was the warmest year since nationwide records began in 1948. The temperature was above normal for most of the country and during all seasons. The country also experienced a slightly wetter than normal year in 2010.

(i) Temperature

The national average temperature for 2010 was 3.1°C above the 1961–90 normal, which was the warmest year since nationwide records began in 1948 (Fig. 7.1). The previous record year was 2006 (+2.5°C) and 1972 (-1.9°C) remains the coolest. The annual average temperature has been above normal since 1997. Much of Canada's above-normal temperatures during 2010 were experienced in the north, where temperatures were more than 3.5°C above normal (Fig. 7.2a). Most of Nunavut and northern Quebec were at least 4°C above normal and only a small area over southern Alberta and Saskatchewan was near normal. The national annual average temperature shows a linear increase of 1.8°C over the 63-year period (Fig. 7.1).

Seasonally, the Canadian winter 2009/10 was the warmest on record. The national average temperature was 3.9°C above normal. The mean temperature departure was above normal for most of the country, with some areas of the Arctic and northern Quebec more than 6°C above normal. A small area over the southern Prairies had a cooler-than-normal winter; in particular, in southern Saskatchewan, where temperatures were more than 1°C below normal.

Spring 2010 was also the warmest spring on record and had the greatest seasonal anomaly. The national average temperature for this period was 4.1°C above normal. The mean temperature departure was above normal across the country with no regions reporting below-normal temperatures; some areas of the Arctic and northern Ontario were more than 6°C above normal.

The national average temperature for summer 2010 was 1.3°C above normal, which makes this the third warmest summer on record. The mean temperature departure was above normal over most of the country, with some areas of Nunavut Territory, northern Quebec, and central Manitoba more than 2°C above normal. Only a small area over the southern Prairies was slightly cooler than normal.

Autumn 2010 was the second warmest autumn on record. The national average temperature was 2.4°C above normal. The mean temperature departure was above normal for most of the country, with most of Nunavut, northern Quebec and central Manitoba at least 4°C above normal. Southern British Columbia, Alberta, and Saskatchewan were near normal.

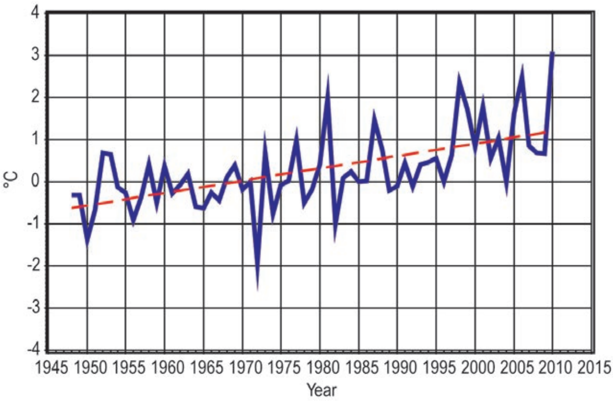

Fig. 7.1. Annual mean temperature anomalies for Canada (based on 1961–90) for the period 1948–2010. (Source: Environment Canada.)

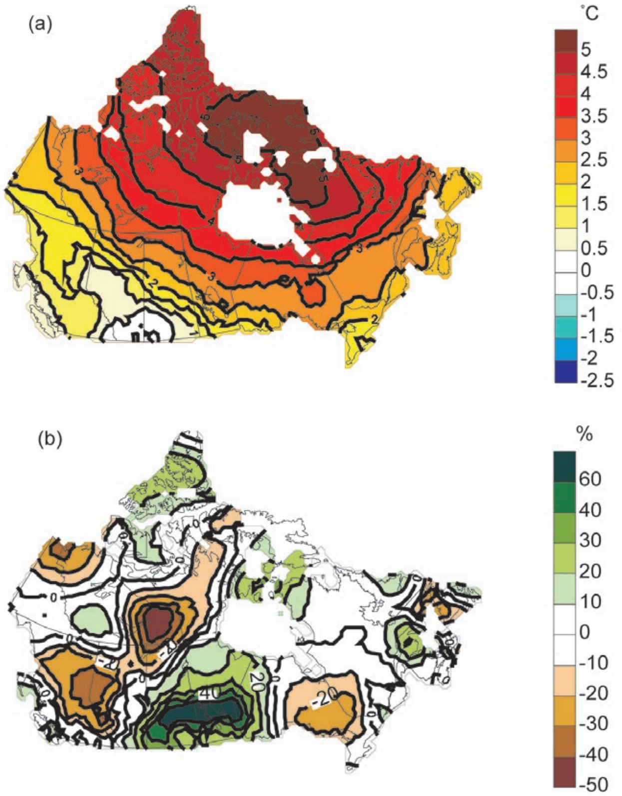

Fig. 7.2. (a) 2010 annual mean temperature anomalies (°C) for Canada (based on 1961–90 mean) and (b) 2010 annual precipitation anomalies (% of 1961–90 mean). (Source: Environment Canada.)

(ii) Precipitation

Overall, Canada experienced a slightly wetter-than-normal year in 2010 (2% above normal), which ranked as the 28th wettest in the 63-year period of record. Saskatchewan and Manitoba were more than 20% wetter than normal while central British Columbia, northern Alberta, Northwest Territories, and northern Ontario were at least 20% drier than normal (Fig. 7.2b). Since the 1970s, precipitation across Canada has tended to be higher than the 1961–90 average. The wettest year on record occurred in 2005 (15% above normal) and the driest year was 1956 (12% below normal).

Seasonally, winter set a record as the driest (22% below normal); the previous driest winter was observed in 1956/57 (20% below normal). The drier-than-normal conditions were widespread, with most areas of the country having at least 20% less precipitation than normal. Some areas, including parts of British Columbia, Alberta, Saskatchewan, and Ontario had 60% less precipitation than normal. Only two areas—central Nunavut and western Labrador—had more precipitation than normal.

Spring 2010 was 1% below normal (31st driest). The Canadian Prairies were wetter than normal, as well as areas of southern British Columbia, the Arctic islands, Newfoundland, and Labrador. Ontario through the Maritimes and areas of northern British Columbia, Yukon, southern Northwest Territories, and Nunavut were at least 20% drier than normal this spring.

Summer 2010 was 5% above normal (15th wettest). The Prairies, southern Ontario, northern Nunavut and western Northwest Territories all experienced at least 40% more precipitation than average. Almost all of British Columbia, along with southern Nunavut and Northwest Territories, experienced conditions that were at least 40% drier than normal.

Canada also experienced a wetter-than-normal autumn, at 5% above normal (22nd wettest). The Prairies, southern Quebec, the Maritimes, and areas of southern Nunavut and southern Yukon Territories all experienced at least 40% more precipitation than average this autumn. Northern Alberta, northern Yukon, northern and southern Northwest Territories, and northern Nunavut experienced conditions that were at least 40% drier than normal.

(iii) Notable events

In February, Canada was on the world stage hosting the XXI Olympic Winter Games in Vancouver-Whistler, British Columbia. The organizers could not anticipate that the Olympic city would experience its mildest winter ever and one that was practically snow-free. The winter started off well enough, with November setting a record of over five meters of snow in the alpine area of Whistler-Blackcomb and December colder than normal by about 1.5°C. However, the New Year brought a soaking Pineapple Express, making January in Vancouver feel more like April. The city did not receive any snow after 14 December, where it normally averages 35 cm. In the 50 days leading up to the opening ceremonies, Vancouver received no snow and 247.2 mm of rain. Up to 300 workers toiled around the clock at the snowboarding venue, moving 9000 cubic meters of snow from as far as 250 km away. By the beginning of the first full week of the Winter Olympics, the stubborn Pacific low moved south and was replaced by a blocking high pressure system with its bright, clear skies and mild, dry weather for seven straight days. In the final days, however, the blocking pattern broke and cloudy, showery weather took hold once again.

On 21 September, Hurricane Igor was still a hurricane as it tracked just offshore of Newfoundland but became a post-tropical storm as it came ashore. Hurricane-force winds ripped across eastern Newfoundland with a savagery that forced 22 flooded and wind-battered towns to declare states of emergency. Over 150 communities became isolated when swollen rivers washed away the only roads into town and all connecting bridges. A peak wind speed of 93 kts (48 m s^{-1}) was recorded at Cape Pine in southeastern Newfoundland and Labrador. In addition to taking out power for 70 000 hydro customers, water flowed everywhere, overwhelming culverts, filling basements, and eroding road beds. The Insurance Bureau of Canada reported that insurable claims related to Igor amounted to $65 million (Canadian dollars)—only a fraction of the total losses—yet was the biggest weather-related insurance claim in Newfoundland and Labrador in recent history.

The Prairies experienced a dramatic switch in weather during the growing season in 2010. At the beginning, Western ranchers said they had never seen such a dry spring. In Camrose, Alberta, a drought was declared before April and, across the Prairies, agricultural producers hoped and prayed for rain. With minimal snow cover and record-low precipitation between January and March, winter 2009/10 gave growers little optimism. However, spring brought above-normal temperatures and in April, it started to rain. Unfortunately, it did not stop, and by mid-May, farmers' drought worries were gone, replaced with worries of flooding, with some farmers unable to get on to their soaked fields. There was twice as much rain and snow as normal during April and May. As the rains persisted into June, farmers grew more concerned. Nearly a quarter of the Prairie grain crop had yet to be sown. With a scarcity of hot days and sunshine, water was not evaporating and crops were not maturing. Fortunately, growers finally got a break on the first day of the fall when warm, dry, and sunny conditions set in and prevailed through October. The perfect weather enabled farmers to make up for lost time. Almost every day over four weeks had maximum temperatures above normal and it was dry. Growers worked night and day and, incredibly, harvested a record 70% of the crop in three weeks. In the end, nearly 40 rural municipalities declared themselves agricultural disaster areas. Statistics Canada reported 15% less wheat harvested than in 2009.

2) United States—C. Fenimore, J. Crouch, and R. R. Heim Jr.

Based on preliminary data, the annual average temperature in 2010 for the contiguous United States was 12.1°C, which is 0.5°C above the long-term or 20th century average (LTA), the 23rd warmest year since records began in 1895 (Fig. 7.3). The Northeast had their third warmest year on record and it was the eighth warmest for the East North Central climate region (Great Lakes area). Only the Southeast experienced an average temperature that was below the LTA.

Above-average precipitation anomalies prevailed throughout much of the country in 2010, resulting in the 35th wettest year on record. Precipitation anomalies were especially high in the northern Great Plains and Upper Mississippi Valley, where the East North Central and the West North Central climate regions had their third and fifth wettest year on record, respectively. Only the South, Southeast, and portions of the Ohio River Valley had precipitation averages that were below normal for the year.

(i) Temperature

Anomalous warmth returned in 2010, after two years of experiencing near-normal temperatures in the contiguous United States. Since 1895, the contiguous U.S. has observed a temperature increase of about 0.07°C per decade. Extreme fluctuations in temperature during 2010 can be partially attributed to three large-scale atmospheric circulation patterns: the historically strong negative Arctic Oscillation (winter), the persistent Bermuda High (spring–summer), and La Niña (summer–fall). The 2010 temperature pattern on a statewide level consisted of warm anomalies throughout much of the country, especially in

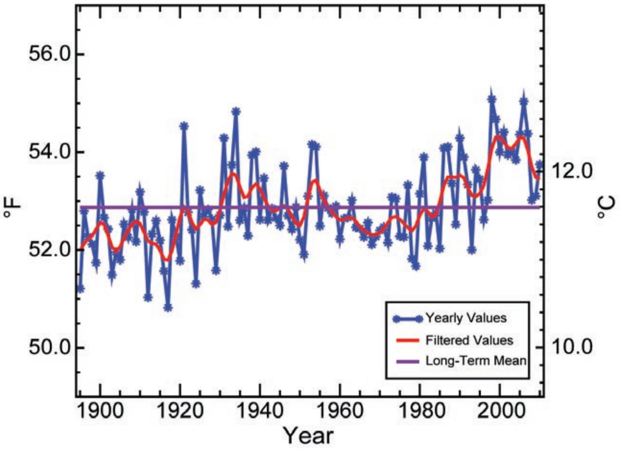

Fig. 7.3. Annual mean temperature for the contiguous United States for the period 1895–2010. The filter is a weighted average that is used to smooth the year-to-year changes in the data values which may help identify the presence/absence of trends throughout the data record. (Source: NOAA/NCDC.)

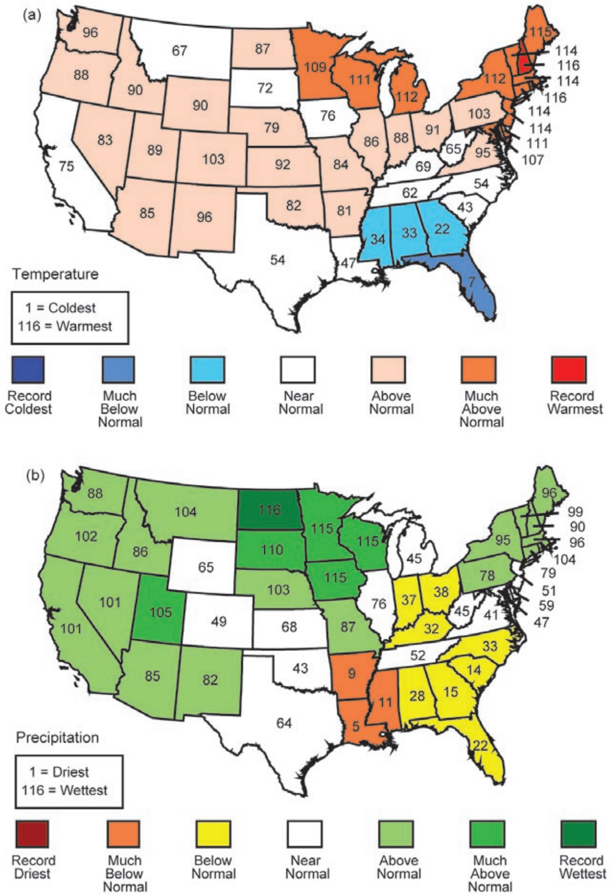

Fig. 7.4. Statewide ranks of annual 2010 (a) temperature and (b) precipitation. A rank of 116 represents the warmest/wettest year since 1895. Much-above-normal temperature/precipitation is defined as occurring in the top 10% of recorded years. Above-normal temperature/precipitation is defined as occurring in the warmest/wettest third of recorded years. Much-below-normal temperature/precipitation is likewise the bottom 10% of coolest/driest years since 1895, and below normal is defined as the coolest/driest third of the distribution. (Source: NOAA/NCDC.)

the Northeast where the warmest year on record for New Hampshire and Rhode Island (Fig. 7.4a) was attributed to the persistent warmth. Also among their top ten warmest were Michigan, Wisconsin, and Minnesota. The only four states that were cooler than normal were Florida, Georgia, Alabama, and Mississippi.

Cool anomalies were present across much of the contiguous U.S. during the winter (December 2009–February 2010) season. Consistent with what is typically seen during negative Arctic Oscillation events, the coldest temperature anomalies for the period occurred in the Southeast and Southern Plains, where the majority of states experienced an average temperature that was among their coldest 10% on record. In the extreme Northeast, a blocking pattern that typically occurs during negative Arctic Oscillation events contributed to Maine's third warmest winter, nearly 3.3°C above the LTA. Nationally, the average winter temperature was 1.0°C below the LTA, resulting in the 15th coolest on record and coolest winter period since 1964.

Extreme warmth continued in much of the Northeast during the spring, contributing to the region's warmest March–May on record. The regional temperature average was more than 3.0°C above the LTA. Eight northeastern states experienced their warmest spring on record, as did Michigan. Cool anomalies were present in several western states and in Florida. Nationally, it was the 19th warmest spring on record.

Warmer-than-average conditions prevailed throughout much of the contiguous U.S. during the summer. Induced by a combination of a persistently strong Bermuda High that extended abnormally westward and a strengthening La Niña episode, the Southeast had its warmest summer on record. Demonstrative of this irregularity, there were several other climate regions that were abnormally warm: Central (3rd warmest), Northeast (4th warmest), and the South (7th warmest). It was the warmest summer in 116-years of record keeping for every state in the Southeast climate region. A total of 12 states were record warm, while only two (Montana and Oregon) experienced an average temperature that was below the LTA. Overall, it was the fourth warmest summer on record for the contiguous U.S., with an average temperature of 1.0°C above the LTA.

Abnormal warmth continued into the fall season. While spatial temperature averages were variable across climate divisions, nearly every state averaged a temperature that was above the LTA. Rhode Island (6th warmest), Delaware (7th), and New Jersey (11th) each experienced the warmest anomalies, while Florida, Georgia, Michigan, Montana, and Washington were the only states with average temperatures near the LTA.

The average annual temperature for Alaska in 2010 was 0.4°C above the 1971–2000 average. Following a year with below-average temperatures, these above-normal temperatures were a continuation of the upward trend of the last 20 years. Temperatures during winter 2009/10 were 1.7°C above average. Seasonal anomalies in Alaska coincided with the contiguous U.S. during the remainder of the year as spring temperatures were 0.4°C above average, summer was 0.2°C above average, and fall was 1.7°C above average.

(ii) Precipitation and snowpack

Average precipitation for the contiguous United States in 2010 was 26 mm above the long-term average of 740 mm. Precipitation across the U.S. during the year was characterized by persistent wetness in the Upper Midwest, resulting in record to near-record averages for the area (Fig. 7.4b). While not as extreme as the aforementioned area, much of the western United States also experienced above-normal precipitation. Elsewhere, precipitation averages in the South and Southeast were below the LTA. Examining precipitation anomalies at the statewide level, it was the wettest year on record for North Dakota and second wettest for Iowa, Minnesota, and Wisconsin. Persistent dryness in the South contributed to the fifth driest year on record for Louisiana and ninth driest for Arkansas. Seasonally, it was the third wettest winter period for the Southeast and the 11th wettest for the Southwest.

It was the 15th wettest winter (December 2009–February 2010) for the U.S. in the 1895–2010 period of record. As a result of the ongoing El Niño episode, a persistent Pacific jet stream extended over the southern half of the contiguous United States. The episode contributed to the third wettest winter in the Southeast. It was the fifth wettest winter for Georgia, North Carolina, and South Dakota and the sixth wettest such period for Alabama, New Jersey, New Mexico, South Carolina, and Virginia.

Spring precipitation varied in 2010, resulting in a national average that was near normal. Based on climate division averages, record dryness occurred in the Upper Peninsula of Michigan and northern Louisiana. At the statewide level, Louisiana had its fifth driest spring on record.

Summer precipitation, when averaged across the contiguous United States, was the ninth wettest on record. The active pattern across the northern tier states peaked in June, resulting in the wettest June on record for the Great Lakes area. Both Michigan and Iowa had their wettest June on record, while Illinois, Indiana, and Wisconsin each had their second wettest. The relentless pattern subsided only slightly in July, when the region experienced its third wettest such period. For the entire summer period, Wisconsin was record wet, and it was second wettest for Iowa, third wettest for Michigan and Nebraska, while Indiana, Minnesota, and South Dakota each had their sixth wettest such period.

Several states experienced a precipitation average that was either in the top or bottom 10% on record during the fall season. Florida had its second driest fall on record while the precipitous pattern continued for the Great Lakes region where Minnesota had its third wettest such period. Elsewhere, Maine and Nevada experienced their fifth and seventh wettest fall on record, respectively.

During winter 2009/10, snowpack levels varied across the mountainous western United States. Mountain snowpack was below normal for the Cascade Mountains and the northern and central Rockies. Some regions of the Oregon Cascades, western Wyoming, the Bitterroot Range, and the Columbian Plateau had snow packs that were less than 50% of normal. While almost all of Alaska had snow packs below normal, the central regions of the state had snow packs less than half their normal levels. Conversely, the Sierra Nevada range of California and the southern Rockies had snow packs that were above normal by the end of the winter season. Additionally, the mountains of Arizona and New Mexico also had snow packs that were more than 180% of normal.

The 2009/10 winter brought unusually snowy conditions to the eastern two-thirds of the United States. An active storm track across the Northern Plains as well as the Southeast and along the Eastern Seaboard brought several large record-breaking snow storms. During December 2009, the U.S. experienced its largest snow cover extent on record. It was the sixth largest January snow cover extent and the third largest February extent. Several locations broke seasonal snowfall records, including Washington, D.C. (186 cm), Baltimore (204 cm), and Philadelphia (200 cm). It was also the snowiest February on record for New York City (94 cm) and Pittsburgh (130 cm).

(iii) Drought and wildfires

The drought epicenters during 2010 were the western Great Lakes, much of the Southeast, the Ohio Valley, the mid-Atlantic states, Hawaii, and parts of the West. The year started out with drought in the West, small parts of the Southern Plains, and the Great Lakes. During the spring, drought developed in parts of the South and intensified in the western Great Lakes. Drought conditions contracted in the West and western Great Lakes, but intensified in the Southeast and mid-Atlantic states during the summer. By October, moderate to extreme drought had developed in the South and spread into the Ohio Valley. Drought relief occurred in the Ohio Valley with heavy rains at the end of November. About 75% of Hawaii suffered through a prolonged dry spell for most of the year, but heavy rains brought limited relief in December. In spite of the rains, this year's drought ranked as the worst drought episode of the decade for Hawaii. In the contiguous U.S., low stream, reservoir, and stock pond levels, and depleted soil moisture combined with hot temperatures and high evaporation to ravage agricultural lands as the growing season progressed: in the Mid-Atlantic states by mid-summer, and the South and Ohio Valley by early to mid-fall. Dryness was especially severe in the Lower Mississippi Valley, with parts of Arkansas, Louisiana, and Mississippi having the driest year on record.

The United States had a below-average wildfire season for 2010. Wet conditions across the western regions of the country helped to limit the number of large fires and total acreage burned. During 2010, 71 839 fires burned nearly 1.4 million hectares. This marked the least acreage burned annually nationwide since 1998. Despite the below-average season, the Long Butte Fire in Idaho burned approximately 133 000 hectares during August, about nine percent of all acres burned in the United States during the year. The Fourmile Canyon fire near Boulder, Colorado in September only burned 2500 hectares, but containment costs and damages totaled more than $225 million (U.S. dollars)—the costliest fire in Colorado's history.

(iv) Tornadoes

Across the United States, 2010 was an above-average year for tornadoes. As of March 2011, confirmed tornado reports and estimates for 2010 indicated that there were 1280 tornadoes from January to December, which is above the 10-year (2000–09) average and the seventh highest annual count since 1990. The number

SIDEBAR 7.1: AN ASSESSMENT OF 2010 NORTH AMERICAN TEMPERATURES—M. HOERLING, D. EASTERLING, J. PERLWITZ, J. EISCHEID, P. PEGION, AND D. MURRAY

A Persistent Pattern of 2010 North American Temperature Anomalies

Surface air temperatures were very warm across Canada during all seasons of 2010, while the contiguous United States experienced much-below normal temperatures over the South and East in the first and latter portions of 2010. These cold conditions ended record high temperatures in those same U.S. regions during the warm half of the year (Fig. 7.5, left panels).

January–March 2010 conditions included greater than +3°C departures over all Canadian provinces from the Pacific to the Atlantic coast; statistics compiled by Environment Canada indicated that winter 2010 was the warmest in Canada since records began in 1948. In sharp contrast, up to -3°C departures

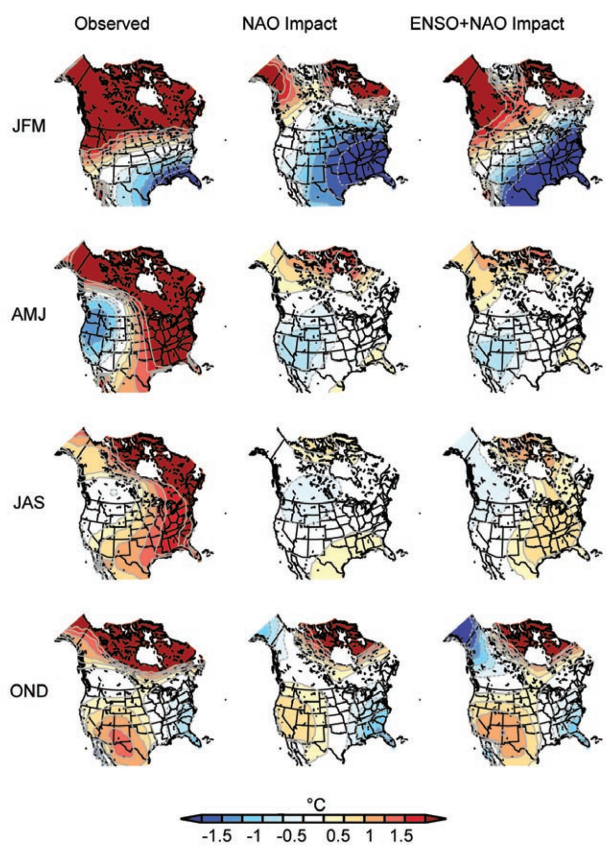

Fig. 7.5. (Left panels) North American surface air temperature departures (°C) during 2010 for winter (JFM), spring (AMJ), summer (JAS), and fall (OND) based on NASA gridded departures (based on 1961–90); (middle panels) surface temperature signal (°C) attributable to the state of the 2010 North Atlantic Oscillation (NAO); (right panels) surface temperature signal (°C) attributable to the combined effects of the state of NAO and ENSO. The NAO signal is calculated by regressing the monthly surface temperatures upon the Climate Prediction Center's NAO index time series for 1950–2009, and the 2010 anomalies are derived by multiplying the regression pattern by the observed 2010 standardized NAO index for each season. The ENSO signal is calculated by regressing the monthly surface temperatures upon a Nino-3.4 SST index time series for 1950–2009 and then scaling by the observed 2010 index values of Nino-3.4 SSTs. The combined 2010 anomalies are derived by adding the separate NAO and ENSO signals. All data used in regression were detrended. (Source: NOAA/ESRL-PSD1/GISS.)

of strong-to-violent tornadoes (rated EF3–EF5) reported in 2010 was 43, which was also above average, although no tornadoes were rated EF5. There were 45 tornado fatalities reported during 2010, associated with 21 tornadoes. The most deadly tornado of the year occurred in the state of Mississippi on 24 April, when a long-track EF4 killed 10 people in three counties. The tornado was on the ground for 240 km, the fourth longest tornado track for Mississippi on record.

Texas led the national tornado count with 107 individual tornadoes during 2010. Also remarkable were the 105 confirmed tornadoes that occurred in Minnesota, ranking the state as having the second most tornadoes in the United States during the year. The 105 tornadoes broke the state's previous annual record of 74, which occurred in 2001. Forty-eight of the Minnesota tornadoes occurred on 17 June alone, as part of the largest tornado outbreak during 2010 for the entire country. During this large severe weather episode, there were 74 confirmed tornado reports across the Upper Midwest and Northern Plains, including four EF-4 tornadoes. This high count marked the busiest tornado day for the U.S. since 23 May 2008 and one of the largest tornado outbreaks to occur across the region in the past decade.

3) México—V. Davydova-Belitskaya and F. J. Romero-Cruz

The year 2010 was a unique year for México. According to the National Meteorological Service, nationally-averaged annual mean temperature was about 21.0°C, only 0.3 °C above the normal temperature of 20.7°C (Fig. 7.7a). However, for precipitation,

occurred over the U.S. Gulf Coast region. Following seasons showed a reversal in U.S. temperature conditions even while Canada remained consistently warm; April–September 2010 was very warm across the eastern U.S. and cold across the West. As a further testament to intense seasonal temperature variability over the U.S., fall 2010 saw a sharp turn to cold conditions in the East and the Gulf Coast region.

A Persistent Phase of the North Atlantic Oscillation during 2010

A notable extreme climate event during 2010 was the intense negative phase of the North Atlantic Oscillation (NAO), with the annual mean value of the Jones NAO index ranking as the most negative in historical record, which began in 1823. This negative phase is indicative of high latitude blocking, which was a prevailing feature during all seasons. The middle panels of Fig. 7.5 show the seasonal surface temperature signals attributable to the seasonal NAO index of 2010 based on regression analysis. The best agreement between observations and the NAO signal occurs over eastern North America. In particular, the Canadian warmth juxtaposed with the southeast U.S. cold during winter and fall seasons can be largely reconciled with a meridional dipole pattern of NAO-related temperature anomalies, features linked with persistent atmospheric blocking that extended from eastern Canada across Greenland.

A Sharp Reversal in the ENSO During 2010

Strong El Niño conditions prevailed over the tropical Pacific from January to March 2010, which swiftly transitioned to moderate La Niña conditions by early summer and continuing into fall. In light of ENSO's known impact on North American climate conditions, it is reasonable to inquire whether the strong seasonality in contiguous U.S. temperatures may have been linked to this abrupt swing of the ENSO cycle. We calculated the ENSO impact on 2010 North American temperatures using a regression analysis and combined that signal with the NAO signal of 2010, the result of which is shown in the right panels of Fig. 7.5. For North America as a whole, the spatial correlation of the observed anomalies and this combined signal is 0.7, 0.7, 0.8, and 0.8 for the winter, spring, summer, and fall 2010 seasons, respectively. What emerges clearly from this diagnosis is the dominant effect of the persistent NAO in generating cold eastern U.S. conditions in early and late 2010, with some indication that the reversal to warm summer conditions in the eastern U.S. was partly due to the region's sensitivity to La Niña conditions, which had emerged with considerable vigor by July 2010.

By no means are all the seasonal features of 2010 North American temperatures interpretable as a signal of NAO variability. In particular, the spatial scale and intensity of the observed Canadian warmth was considerably greater than one would have expected from NAO and ENSO relationships. An important research task is to ascertain the effect of other modes of variability and boundary forcings on North American conditions of 2010, including the state of global sea surface temperatures, sea ice, and anthropogenic greenhouse gas forcing.

SIDEBAR 7.2: BILLION DOLLAR U.S. WEATHER DISASTERS: 2001–10

—A. SMITH

The U.S. sustained 47 weather-related disasters over the 2001–10 period in which overall damages/costs reached or exceeded $1 billion (U.S. dollars; Fig. 7.6). The total normalized losses (i.e., insured and uninsured loss) for the 47 events exceed $350 billion. The following is a comparison of the disaster loss record for U.S. severe thunderstorms, winter storms, hurricanes, wildfires, flooding, and drought in 2010 against the full 2001–10 period.

Severe thunderstorm losses totaled $10.8 billion in 2010 alone—the highest annual value in the 2001–10 period. During the period, the U.S. annual loss average was $7.1 billion. Since 1980, there has been a pronounced trend in the amount of thunderstorm losses in the contiguous United States. Studies by reinsurer Munich Re have shown a quadrupling of U.S. losses associated with tornado, and hail and high wind damages occurred since 1980 (Hedde 2010). A number of research papers demonstrate that much of this increase is driven by socioeconomic factors such as increases in wealth and population (Changnon 2001; Diaz and Murnane 2008).

Winter storm losses in 2010 were the fifth highest ($1.2 billion), behind 2003, 2007, 2005 and 2004. The average loss for the 2001–10 period was $1.3 billion.

There were no U.S. land falling hurricanes in 2010; therefore, the $185 million worth of losses was well below the 2001–10 loss average of $25.7 billion. The 2001–10 period was punctuated by 2004 and 2005 hurricane seasons, where numerous hurricanes formed and made landfalls over many parts of the South and Southeast region and caused extensive damage.

The 2010 wildfire season was below normal for the number of wildfires reported (71 839) nationally, which was slightly below the 10-year average (78 352). However, the number of hectares burned in 2010 (1 385 169) was well below the 10-year average (2 820 186 hectares). The middle years of the decade represented the highest number of hectares burned—2006, 2007, 2005, and 2004. However, the location of wildfires near the urban-wildland interface is the driving issue on losses and increased firefighting costs. Namely, 2000, 2002, 2003, and 2008 were years in which firefighting costs and fire damages together annually exceeded $2 billion—well above the 2001–10 annual cost/loss average ($750 million).

An estimated $3.2 billion in flood losses occurred in 2010, which was above the 2001–10 annual average of $2.4 billion. These estimates do not include storm surge or inland flooding associated with hurricanes. In late March 2010, the Northeast experienced a severe flooding event. Heavy rainfall over portions of the region caused extensive flooding across the states of Rhode Island, Connecticut, Massachusetts, New Jersey, New York, and Pennsylvania. The event caused the worst flooding in Rhode Island's history and resulted in over $1.5 billion in damages/costs. The mid-South flooding event of 30 April–2 May was also significant, as flooding in the Nashville, Tennessee area alone contributed more than $1 billion in damages. Western and middle Tennessee were the hardest hit, with local rainfall amounts of 460 mm–510 mm to the south and west of greater Nashville. Total losses exceeded $2.3 billion in damages/costs.

While the U.S. drought economic loss numbers are still being finalized, it appears that 2010 was near the 2001–10 average of $1.4 billion. For 2001–10, the most severe drought loss events occurred in 2002, 2006, and 2008, where insured crop losses averaged more than $2 billion. The total cost (e.g., uninsured crop loss and interrupted municipal water services) of drought events may be considerably higher, but difficult to quantify accurately.

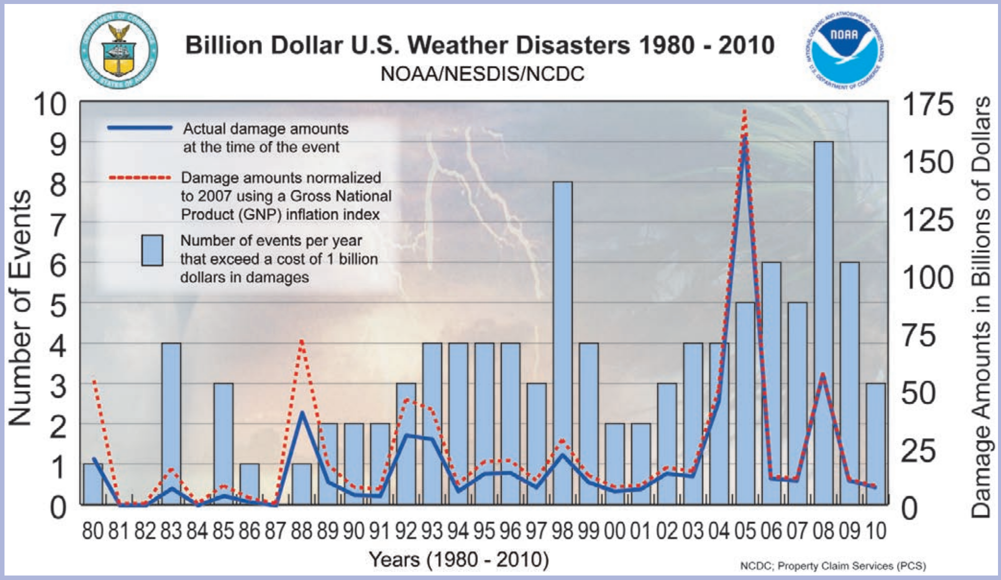

FIG. 7.6. Billion Dollar U.S. Weather Disasters 1980–2010. (Source: NOAA/NCDC.)

2010 ranked as the second wettest year since records began in 1941 (Fig. 7.7b). Total amount was about 935.5 mm compared with the normal value of 777.9 mm (1941–2010 average). New monthly records were also reported during the year; 2010 had the wettest February and July, and driest October and December on record.

(i) Temperature

The annual mean temperature anomaly ranged from -0.3 to +0.3°C across the country and was considered near normal. The highest positive anomalies in monthly mean temperatures (1.0°C–3.0°C) were recorded in May, June, and August in almost all of the country and in January and December in the northern and northeastern regions. In February and March, there were strong negative anomalies (2.0°C–5.0°C below normal) due to humidity from the Pacific, which brought cloudy skies and heavy and unusual rain. October, November, and December also recorded temperatures below normal as a result of large and dry high pressure air masses in most of the country.

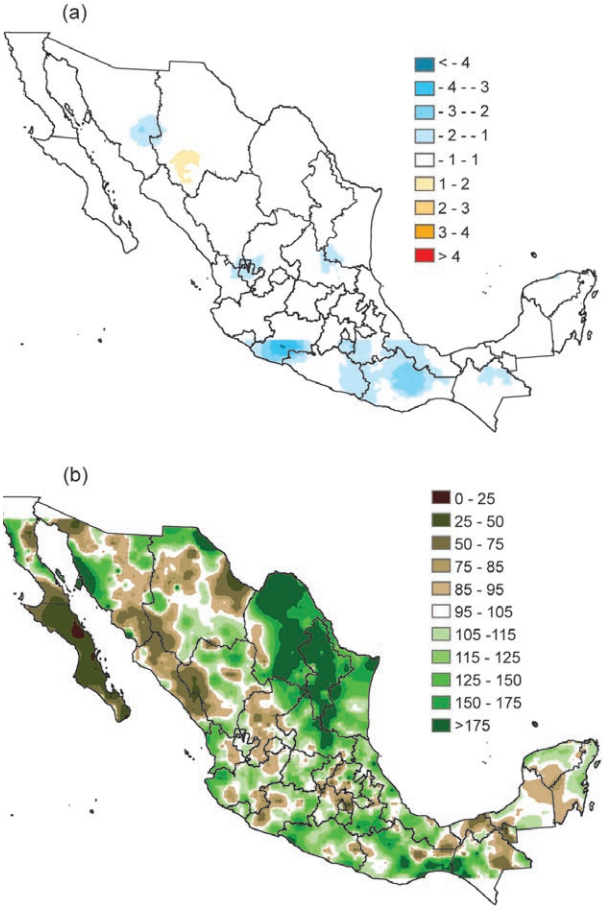

Fig. 7.7. (a) 2010 annual mean temperature anomalies (°C) for México (based on 1980–2004 mean) and (b) 2010 annual precipitation anomalies (% of 1941–2010 mean). (Source: National Meteorological Service of México.)

(ii) Precipitation

During the first months of 2010, El Niño conditions in the Pacific affected precipitation patterns in northern, northeastern, western, and central regions of México, where heavy winter rains were registered. The accumulated amount during January and February at a national level ranked these months as the third wettest and wettest months, respectively, since records began in 1941.

By July 2010, the transition to La Niña was officially taking place; this climatic event typically strengthens precipitation in the western, central, and southern regions of México. The fast intensification of this event resulted in intense precipitation during July and September in most of country; July registered an estimated 244.2 mm (average is about 140 mm) and was the wettest July on record.

However, autumn was extremely dry. October 2010 was the driest such period on record. The accumulated precipitation estimated at a national level was about 6.7 mm (average is 27.5 mm).

(iii) Notable events

Heavy rains, present since the beginning of the year, generated several floods and landslides in many states. The first occurred in February and affected states in the western, central, and southern regions of México. Intense rain up to 200 mm–250 mm was registered from 1 to 5 February in Michoacán and Estado de México. In spite of the damages, dam volumes in the region recovered from a large period of drought conditions, especially those dams that form the Cutzamala system. These had a deficit up to 80% due to the hydrological drought present in the area since the summer of 2009.

In México City and surrounding areas, the accumulated rainfall for the first five days of February was about 57.2 mm (average for that period is about 8.2 mm). As a consequence, some highly populated areas were affected, especially those considered poor zones.

Hurricane Alex created serious damage in México in 2010. The storm impacted Campeche, Tamaulipas, and Nuevo León; thousands of people were affected and millions of pesos were lost in damages. From 30 June to 2 July, the estimated amount of rain was up to 700 mm and caused severe floods as well as some dam overflows in the region. The maximum 24-hour accumulated rainfall was registered in the Pedro Méndez dam in Tamaulipas (399.7 mm) and in the La Boca dam in Nuevo León (389.9 mm).

During the second half of August, there were several tropical depressions, which brought intense rain along the southern Pacific coast. Maximum 24-hour precipitation of 360 mm was registered in the mountains of Oaxaca (Cerro de Oro), which caused a landslide and some lives were lost.

Although August 2010 was classified by the National Meteorological Service as the eighth wettest August in 70 years of record keeping, precipitation registered in Chiapas, Oaxaca, Tabasco, and Veracruz caused several damages to the infrastructure and populations of these states.

In September, the government of Veracruz reported damages due to the floods in the region of the Papaloapan river basin; the floods were caused by the continuous precipitation registered from August through the first half of September. During this period, Hurricane Karl affected 114 counties in the state of Veracruz due to strong winds and heavy rain (up to 350 mm in 24 hours in some regions). Two weeks after Karl, the southern region of Veracruz had another impact, this time from the remnants of Tropical Storm Matthew (24–28 September). The station in Coatzacoalcos registered 411.9 mm in 24 hours on 27 September.

c. Central America and the Caribbean

1) Central America—J. A. Amador, E. J. Alfaro, H. G. Hidalgo, and B. Calderón

For this region, eleven stations were analyzed from the following six countries: Belize, Guatemala, Honduras, Nicaragua, Costa Rica, and Panama.

(i) Temperature

On the Caribbean side, the year 2010 was warmer than average since it showed a clear pattern of small positive departures with respect to both the 1971–2000 climatology and the last decade (Fig. 7.8). This result appears to be consistent with the persistence of positive sea surface temperature (SST) anomalies in the tropical North Atlantic throughout the year. In contrast, 2010 behaved differently on the Pacific side, where most stations presented a shift to the left in the 2010 distribution, possibly associated with the influence of La Niña conditions in that region. Most stations on the Caribbean side also showed a warmer 2000–09 decade than their corresponding climatology. Two stations on the Pacific side, in southwestern Central America [Tocumen (Tm6) and David (Tm7)], shared the same characteristics as those on the Caribbean side. The other stations indicated a complex behavior with a shift to the left in the 2000–09 distribution (a cooling effect) in Liberia (Tm8) and practically no significant temperature departures at the other two stations [Cholutera (Tm9) and San Jose Tm10)].

Since many stations have a large amount of missing data in their daily minimum (T_{min}) and maximum temperatures (T_{max}), these two variables were analyzed regionally by taking an average of the five stations on the Pacific side and the five stations on the Caribbean side. On the Pacific side, T_{min} for 2010 indicated small positive departures from the climatology while T_{max} for 2010 indicated small negative departures. On the Caribbean side, T_{min} and T_{max} were slightly warmer than the last decade average but substantially warmer than their climatology.

(ii) Precipitation

The start date (SD) and end date (ED) of the rainy season were calculated at all selected rain-gauge stations. The SDs observed during 2010 were considered near normal when compared with to those of the 1971–2000 climatology and 2000–09 decade (Fig. 7.8). The 2010 EDs were early at each station except Tocumen (P6) when compared to the climatology; however, compared to the 2000–09 average, almost all stations had a late ED, except David (P7).

All stations located on the Caribbean side showed that the accumulated precipitation for 2010 was below the 1971–2000 average, except for Tocumen (P6). On the Pacific side, accumulated values for 2010 were greater for Tocumen (P6), David (P7), and San Jose (P10) when compared to 1971–2000 and less for Liberia (P8) and Choluteca (P9).

(iii) Tropical cyclone activity

The year 2010 was very active for tropical storms in the Caribbean basin. By July 2010, La Niña had developed and winds associated with the Caribbean low-level jet were much weaker than normal, an attribute of ENSO cold events in the region and a condition favorable for tropical cyclone development, in addition to the persistent warm SST anomalies observed in the Caribbean and the tropical North Atlantic. There were 13 named storms in the Caribbean (19 in the Atlantic), with seven hurricanes (12 in the Atlantic), and three major hurricanes (five in the Atlantic). Typical observed values, given by the median, in the Caribbean during the last four decades are four named storms, two hurricanes, and one major hurricane. Additionally, some tropical cyclones landed or reached positions close to the Caribbean Central American coast: Alex (25 June–2 July), Karl (14–18 September), Matthew (23–26 September), Paula (11–15 October), and Richard (21–26 October). Important impacts were reported associated with Tropicasl Cyclone Nicole (28–30 September) and Hurricane Tomas (29 October–7 November). In contrast, tropical cyclones in the Pacific affected the Central American isthmus less; the first cyclone of the 2010 season, Agatha (29–30 May), made landfall near San Marcos, Guatemala, causing considerable damage and impacting the region, mainly in the northern countries of Central America.

2) THE CARIBBEAN — I. G. García, R. P. Suárez, B. L. Pedroso, V. C. Cancino, D. B. Rouco, A. L. Lee, V. G. Velazco, T. S. Stephenson, M. A. Taylor, J. M. Spence, and S. Rossi

Countries considered in this region include: Cuba, Jamaica, Puerto Rico, and the U.S. Virgin Islands.

(i) Temperature

For Cuba, 2010 was characterized by warm temperatures, with an annual mean anomaly 0.15°C above normal (1971–2000). The summer temperature neared the 1998 record (1997 and 1998 were the warmest years on record). June was particularly warm, with average temperature more than 1.0°C above normal (Fig. 7.9a). In contrast, the winter months registered below-normal temperatures. December 2010 was the coldest December in 60 years,

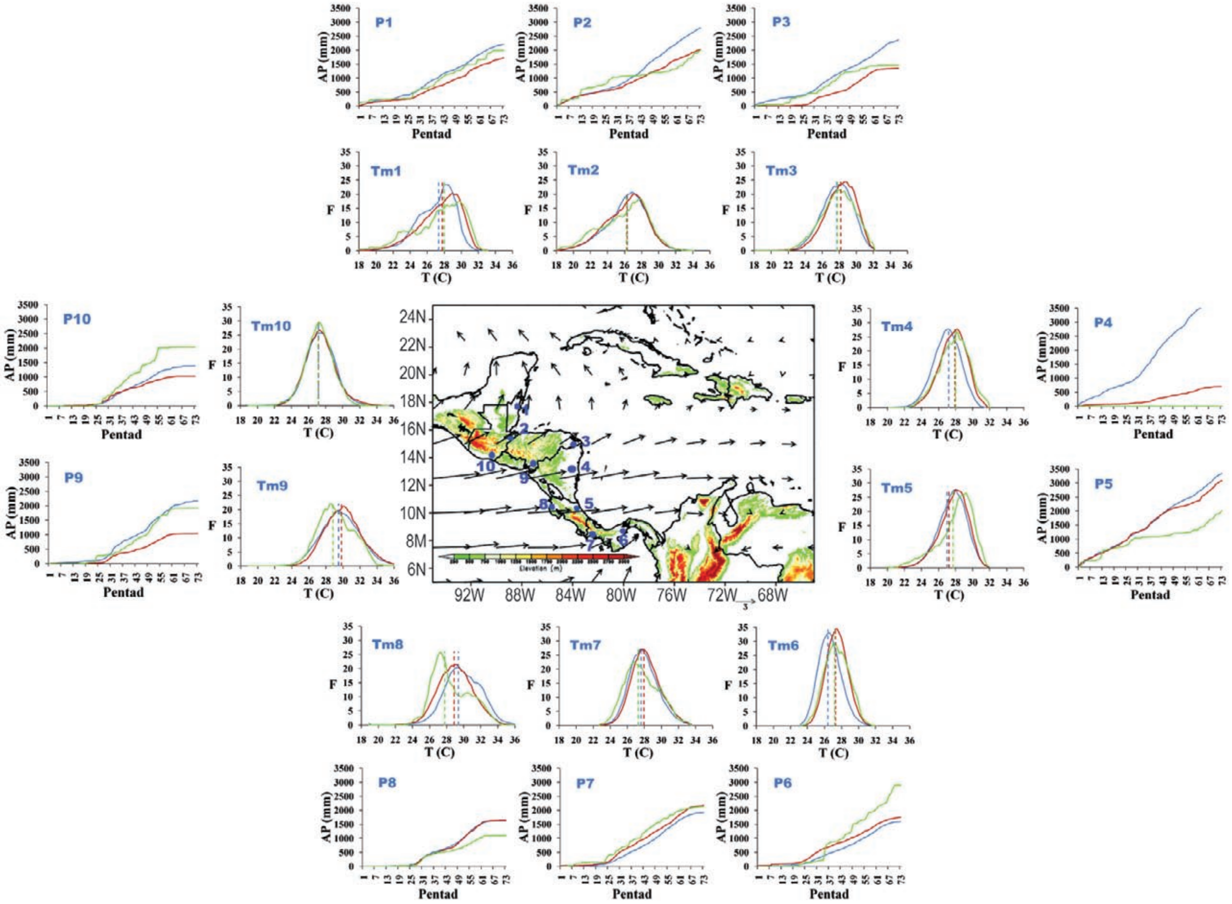

FIG. 7.8. Location of the 10 stations in Central America: (1) Phillip Goldson Int. Airport, Belize; (2) Puerto Barrios, Guatemala; (3) Puerto Lempira, Honduras; (4) Puerto Cabezas-Bluefields, Nicaragua; (5) Puerto Limon, Costa Rica; (6) Tocumen Int. Airport, Panama; (7) David, Panama; (8) Liberia, Costa Rica; (9) Choluteca, Honduras; and (10) San Jose, Guatemala. Wind anomalies at 925 hPa based on 1958–99 for July. Mean surface temperature frequency (TmN) and accumulated pentad precipitation (PN) are shown for each station N. Blue represents the 1971–2000 average (climatology), red the 2000–09 decade, and green 2010. Note that station 4 does not show 2010 precipitation due to a large number of missing data. (Source: NOAA/NCDC.)

SIDEBAR 7.3: SOCIOECONOMIC IMPACTS ASSOCIATED WITH METEOROLOGICAL SYSTEMS AND TROPICAL CYCLONES IN CENTRAL AMERICA IN 2010—J. A. AMADOR

Busy cyclone activities over the Caribbean basin and heavy rainfall heavily impacted Central America in 2010. From 23 to 28 May, a low pressure system affected most of the countries, inflicting damages due to floods in infrastructure, bridges, electrical and water services, and roads. Tropical Cyclone Agatha (29–30 May) struck northern Central America with very heavy rains, resulting in landslides and floods and damages of several millions of dollars (U.S.) in this region. The eruption of the Pacaya Volcano near Guatemala City was an additional factor to heavy rains that accounted for the large number of deaths in Guatemala.

On 20 June, a low pressure system developed about 300 km southwest of Guanacaste Province in Costa Rica, moved northwest and gained hurricane strength (Darby) west of 96°W during 23–25 June, and reached major hurricane status during 25–26 June; however, no major losses were reported due to this system in the region.

Alex (25 June–2 July) formed off of the Caribbean coast of Honduras and acquired tropical storm status on 26 June. As a consequence of rains and floods, six people died in Nicaragua, five in El Salvador, and two in Guatemala. Although Honduras suffered from heavy rains and floods, no human casualties were reported.

From 28 to 30 September, Tropical Storm Nicole affected Costa Rica, Nicaragua, El Salvador, and Guatemala. Main damages were in electrical and road infrastructure, housing, and agriculture. Costa Rica and El Salvador reported $13 million (U.S. dollars) and $2 million (U.S. dollars) in losses, respectively.

From 29 October to 7 November, Hurricane Tomas moved slowly over the Caribbean and hit Panama and Costa Rica with heavy and long-lasting rains, leaving these two countries with several human casualties and damages in several important social sectors. On 29 October, a landslide caused by very intense rains near Pico Blanco in Escazu, Costa Rica, left 28 people dead. Nearly 1000 houses were destroyed and economic losses of more that $330 million (U.S. dollars) were reported due to Tomas.

Although some figures are uncertain, Central America was severely impacted by frequent rainfall events and hurricane activity that, in total, left at least 300 people dead and caused more than $2 billion (U.S. dollars) in losses in 2010.

with a monthly anomaly of almost -3.5°C. In December 2010, many Cuban stations broke their all time minimum temperature record.

For Jamaica, some coastal stations recorded above-normal temperatures that corresponded with warmer-than-normal sea surface temperatures around the island for most of the year.

For Puerto Rico, temperatures ranged from 8.3°C on 6 February in Adjuntas to 36.7°C on 25 July in Ponce. By the end of the year, 2010 tied for the eighth warmest year since 1899 across the San Juan metro area, with an average temperature of 27.3°C (the 1971–2000 average is 26.6°C). The year 2010 joins 2007 and 2009 as three of the 10 warmest years since 1899 in the San Juan metro area (Fig. 7.10a).

Across the U.S. Virgin Islands, temperatures ranged from 13.3°C at Beth Upper New Works on Saint Croix, recorded on both 22 and 25 November, to 34.4°C at the Cyril E. King Airport on Saint Thomas, recorded on both 16 June and 24 August. Annual temperatures across the U.S. Virgin Islands were 0.2°C below their 1971–2000 average.

(ii) Precipitation

For Cuba, the annual average rainfall for 2010 was near normal. During the rainy season (May–October), the western half of the country was dry with 11% below-

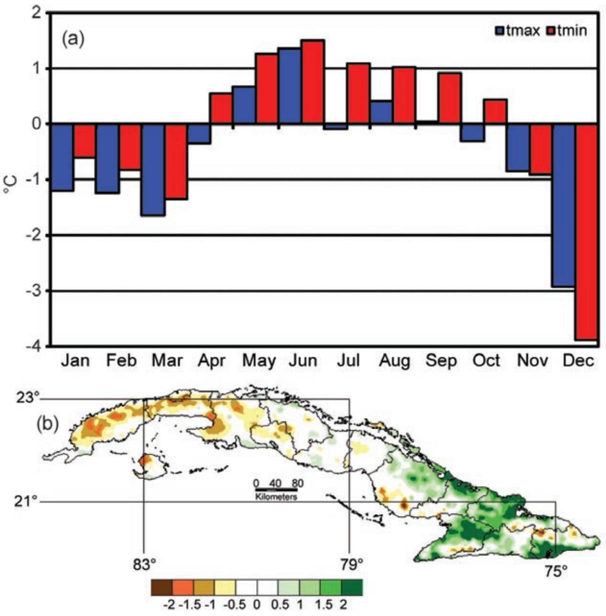

FIG. 7.9. (a) 2010 monthly mean maximum (tmax) and minimum (tmin) temperature anomalies for Cuba; (b) May to October precipitation anomalies represented as Standardized Precipitation Index (unitless; based on 1971–2000 base period). (Source: Institute of Meteorology of Cuba.)

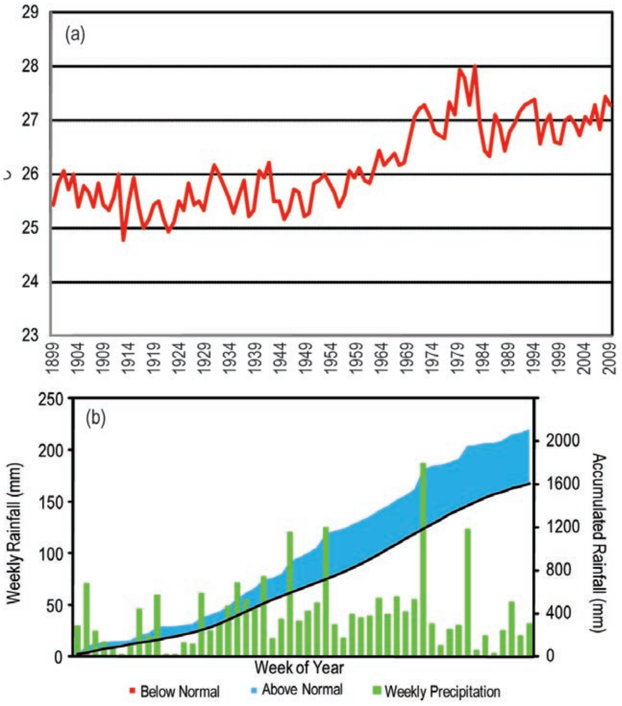

Fig. 7.10. (a) Annual mean temperature recorded in San Juan's metro area, Puerto Rico; (b) weekly mean rainfall for Puerto Rico, based on over 50 cooperative weather stations, with accumulated rainfall displayed on the right-hand axis of the chart. Year-to-date surpluses are displayed in blue shading. (Source: NOAA/NWS.)

normal rainfall while the eastern half was wet with rainfall 23% above normal (Fig. 7.9b). During the dry season, the pattern was reversed; the western half of the country was wet (22% above normal) while the eastern half was dry (23% below normal).

For Jamaica, the annual average rainfall for 2010 was above normal in spite of the fact that during the first three months of the year, the island experienced below-normal rainfall. The early rainfall deficit caused significant water shortages as it continued a drying pattern that began in the latter half of 2009 and was associated with persistent El Niño conditions. For April–October, above-normal and near-normal monthly rainfall totals were observed (Fig. 7.11). The transition to wetter conditions was due to a decline in the El Niño state and the onset of La Niña conditions in the Pacific and the associated reduction in tropical Atlantic vertical wind shear. Particularly significant was the 560 mm of rainfall recorded for September which represented the second highest rainfall experienced during this month since records commenced in 1881. All parishes were above normal. The rainfall was primarily due to a broad area of low pressure associated with Tropical Storm Nicole, which was preceded by Tropical Storm Karl in the same month.

For Puerto Rico, due to El Niño conditions and a strong subtropical jet across the Atlantic Basin during the winter months, several cold fronts helped enhance precipitation across both Puerto Rico and the U.S. Virgin Islands during the typical dry season. In addition, with an early start to the tropical season, highlighted by a strong tropical wave that brought record rainfall the weekend of 20 June, numerous rainfall records were broken across the region in 2010. Across San Juan's metro area, a total of 2273 mm of rain was recorded at the Luis Muñoz Marin International Airport during the year, which broke the previous record of 2224 mm recorded in 1931 This total was nearly 1000 mm above the normal annual rainfall of 1289 mm.

Across the U.S. Virgin Islands, a total of 1559 mm of precipitation fell at the Cyril E. King Airport on Saint Thomas during 2010 and a total of 1267 mm of precipitation fell at the Christiansted Airport on Saint Croix. These totals represented the second and seventh wettest years at each site since record keeping began in 1953 and 1951, respectively.

(iii) Notable events

May and June 2010 were very warm in Cuba; the percentage of warm nights (night when the minimum temperature is above the 90th percentile) was the highest since 1961. However, December 2010 was very cold and the percentage of cold nights (night when the minimum temperature is below the 10th percentile) was a new record for December.

For Jamaica, the broad area of low pressure associated with Tropical Storm Nicole impacted 133 communities—107 by flooding, 16 by landslides,

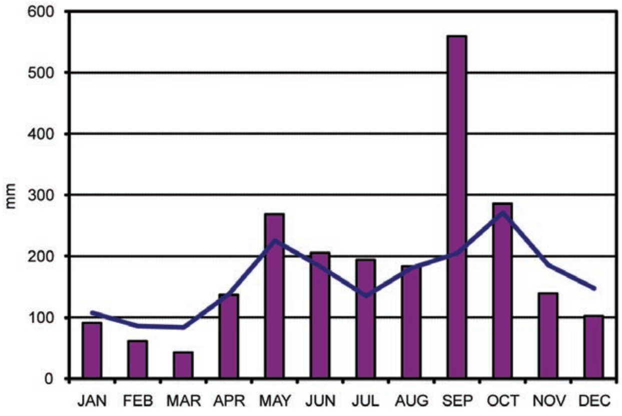

Fig. 7.11. Monthly Jamaican rainfall for 2010 (purple bars) and long-term average 1951–80 (blue line). (Source: Meteorological Service of Jamaica.)

one by storm surge, three by unusual storms, and six by wind damage. There were six confirmed deaths. The estimated cost of damages was $10.6 billion (U.S dollars). The agricultural sector was one of the most harshly affected; over $500 million (U.S. dollars) worth of crops were lost during the event.

The typical dry season across the northeastern Caribbean was nonexistent in 2010, with the remnants of several cold fronts bringing persistent periods of wet weather across both Puerto Rico and the U.S. Virgin Islands during the typical dry months of January –April (Fig. 7.10b). This unusually wet start to the year was followed by four significant tropical systems that affected the region. While both Puerto Rico and the U.S. Virgin Islands were spared any direct hits from tropical systems during the 2010 Atlantic hurricane season, three organized tropical systems (Bonnie, Otto, and Tomas) all brought widespread flooding rainfall across the local islands over the course of the season. The fifth wettest day on record at the Cyril E. King Airport on Saint Thomas (168 mm) was recorded on 5 October with the passage of Hurricane Otto and an impressive 547 mm was recorded at Red Hook Bay on Saint Thomas over a period of four days, also with the passage of Hurricane Otto. Across Puerto Rico, an impressive 397 mm of precipitation was recorded along the Rio Portugues in southern Puerto Rico over the same four-day period due to the storm.

d. South America

The 2010 annual mean temperature was near normal to above normal in northern South America and the tropical Andes, and near normal to below normal in Amazonia and most of southern South America (Fig. 7.12a). The annual total precipitation was generally below normal, with significant negative anomalies in Bolivia, Chile, and Argentina; however, significant positive anomalies occurred in Colombia and Venezuela (Fig. 7.12b).

1) NORTHERN SOUTH AMERICA AND THE TROPICAL ANDES—R. Martínez, C. Euscátegui, E. Jaimes, G. León, and A. Quintero

(i) Temperature

The year 2010 was characterized by the occurrence of both ENSO phases: the end of El Niño near the beginning of 2010 and the development of La Niña in mid-2010. The ENSO influence was evident on the temperature of Venezuela, Colombia, and Ecuador but was relatively weak in Peru and Bolivia. Temperature anomalies from +1°C to +1.5°C were observed in Venezuela, Colombia, and Ecuador during the first half of the year. From June to December, temperature was near normal in Venezuela and Colombia, but below normal in most of Ecuador and Peru.

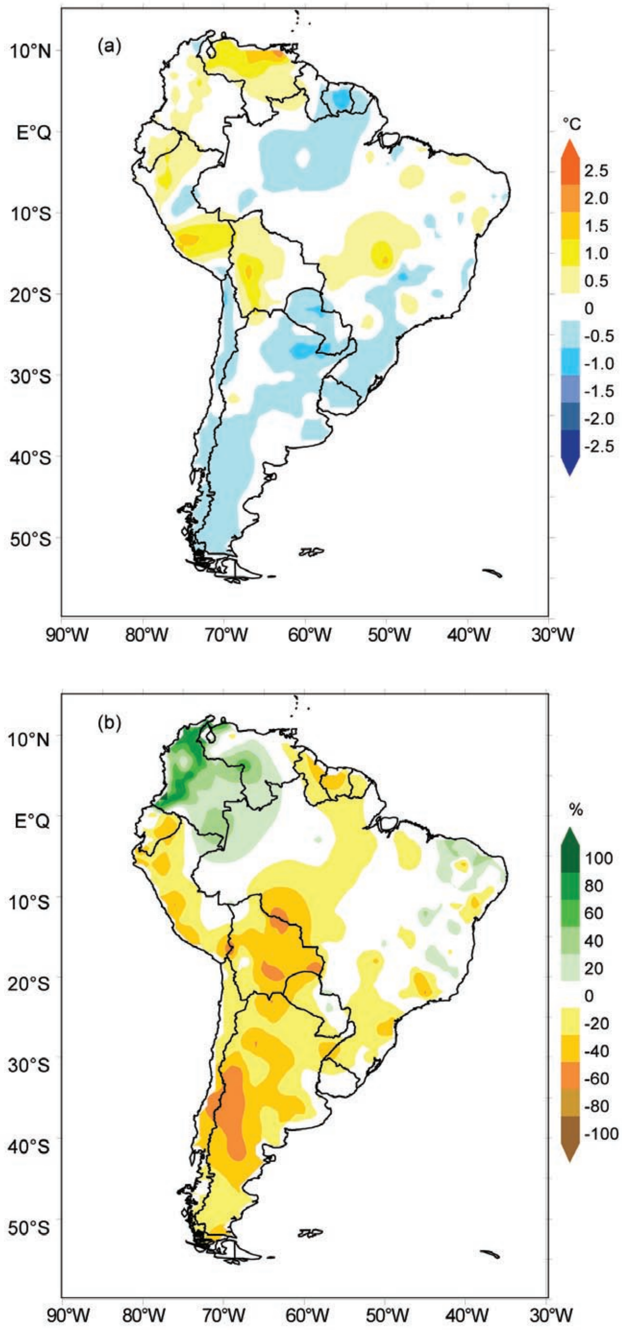

FIG. 7.12. (a) 2010 annual mean temperature anomalies (°C) for South America (based on 1971–2000 mean) and (b) 2010 annual precipitation anomalies (% relative to 1971–2000 mean). (Sources: National Meteorological Services of Argentina, Brazil, Bolivia, Chile, Colombia, Ecuador, Paraguay, Perú, Surinam, Uruguay, and Venezuela. The data was compiled and processed by International Research Center on El Niño, 2010.)

(ii) Precipitation

In Venezuela, a large precipitation deficit was observed across the country in January–March, which severely affected hydropower generation and agriculture. From April to June, precipitation was near normal and positive anomalies were registered at some locations. In July–September, precipitation anomalies became positive in most of the country. During the last trimester, especially in November, precipitation records were observed at several locations; the highest anomalies were observed in Falcon (over the past 88 years), Maracay (71 years), Barcelona (53 years), and Caracas (45 years). Thousands of people were affected by floods and millions of economic losses were reported.

In Colombia, precipitation deficits of 40%–70% were observed in the Andean and Pacific regions from January to May. In January, the deficit was near 100% at some locations. Dry conditions, along with high temperatures, led to larger-than-usual forest fires. From June to August, precipitation anomalies gradually became positive, generating flash floods and landslides in the central Andean zone and eastern Llanos. The last four months of the year were characterized by significant wet conditions associated with La Niña. In November, positive anomalies from 100% to 300% were registered in most of the country. Although December is usually the month of transition from wet to dry conditions, positive anomalies from 40% to 70% were observed across northern and central Colombia. Floods and landslides generated serious damages and affected more than two million people; 300 000 houses were destroyed, and thousands of kilometers of roads were affected. The year 2010 became the rainiest year in Colombia since the beginning of the instrumental record.

In Ecuador, the El Niño event produced an opposite effect on the precipitation, similar to past El Niño events observed after 1998. From January to April, precipitation anomalies were below normal to near normal. In May, significant positive anomalies from 50% to 70% were observed on the north coast. From June to October, negative precipitation anomalies prevailed along with precipitation deficit from 40% to 70% over the Andean region. From November to December, positive anomalies were observed across the country. Precipitation records have indicated some evidence of the weak influence of ENSO events over Ecuadorian climate, which has been consistent in the last decade.

In Peru, the influence of El Niño was also very weak. From January to March, precipitation was below normal mainly in the northeast of the country and southern highlands with deficits from 60% to 100%. However, during this period, extreme events occurred in Lima, Cuzco, and the northern coast. During April–June, dry conditions prevailed with the exception of northern Peru and southern highlands, where deficits turned to precipitation of 40% to 60% above normal. From July to September, precipitation decreased and deficits up to 100% were observed. During the last four months, precipitation deficits prevailed across most of the country, except for specific locations on the north coast and Cuzco, where positive anomalies up to 60% were observed.

In Bolivia, precipitation patterns changed from month to month from January–March. While February was characterized by positive anomalies in central and south of the country, a deficit up to 50% was observed mainly in the northeast in March. From April to June, precipitation deficits peaked in April in most of the country with anomalies from 50% to 100%. This condition gradually changed to near-normal precipitation in June. From July to September, near-normal precipitation was observed. The last trimester of the year was characterized by below-normal precipitation, although positive anomalies up to 50% were observed in northwestern Bolivia in October.

(iii) Notable events

In Venezuela, several tornadoes were observed in the municipalities of Buchivacoa and Dabajuro (24 April), Cumana (6 June), El Palotal (22 September), and Palmarito (16 October). These events affected hundreds of houses and more than 256 families.

In Peru, strong precipitation and hail storms in January generated an increase in the stream flow of the Vilnacota River which reached up to 600 m^3 s^{-1} (214% of normal). This flooding interrupted the railway and isolated the Machu Picchu area. Thousands of tourists were evacuated and the area was declared in a state of emergency for 60 days. Seven people died and millions of dollars in economic losses were reported. In April, severe storms affected the Huanuco region, resulting in floods and landslides; 23 people died, and 47 disappeared. In July, extreme low temperatures were observed in central and southern highlands; record anomalies were observed in Junín (-5.7°C), Puno (-7.5°C), and Chuapalca (-8.3°C).

2) Tropical South America East of the Andes—J. A. Marengo, L. M. Alves, J. Ronchail, and J. Baez

The year 2010 began with an El Niño event well established in the Pacific Ocean. A rapid transition took place and La Niña was present by July. The La Niña event in 2010 one of the strongest on record. The El Niño-to-La Niña transition was similar to the event occurring in 1998, another very warm year, although El Niño was weaker and La Niña stronger in 2010. The annual mean temperature and total precipitation were mainly near normal across the region (Figs. 7.12a; 7.12b).

(i) Temperature

From January to February, the maximum temperature in most of eastern South America was 3°C–4°C above normal. At the beginning of February, a heat wave affected the Brazilian city of Santos in the coastal region of the state of São Paulo, with the temperature reaching up to 40°C and very low relative humidity; 32 elderly people died due to heat exposure. The city of Rio de Janeiro registered peak temperatures of 45°C–48°C and in Porto Alegre in southern Brazil, temperatures were above 40°C. Similar values of 40°C–44°C were also recorded over the Chaco region of Argentina and Paraguay.

From March to April, while the tropical North Atlantic was about 2°C–3°C above normal, maximum air temperature in northern Amazonia and northeastern Brazil was 2°C–4°C above normal. In the city of São Paulo, as well as in the interior of the state, the temperature reached above 34°C in March, breaking the record previously set in 1943.

From May to August, various cold spell episodes occurred in the southern part of South America, reaching the tropical regions of Brazil and Bolivia. The strongest episode was accompanied by heavy snowfall lasting nearly a week (11–18 July). Unusually low temperatures were observed: 4°C in the Bolivian Amazon lowland at Santa Cruz de la Sierra; -3°C in Pratts Gill, west of the Paraguay Chaco; -8°C in the state of Santa Catarina in southern Brazil; and -14°C in the vineyard Bolivian city of Tarija. The lowest temperatures, < -20°C, were recorded in the Peruvian and Bolivian Altiplano, where the density of poor farmers is large. Many people, especially young children and elderly, died from hypothermia, pneumonia, and other respiratory diseases. A state of emergency was declared in the Andean regions of Peru and in the Amazon basin where night temperatures as low as 10°C were recorded along the Madre de Dios and Ucayali rivers when they usually exceed 20°C.

From September to December, temperatures 1°C above normal were observed in regions of eastern South America and temperatures 2°C above normal were observed in northeastern and southern Brazil in November and December. This warming in west central Brazil, northwest of Paraguay and Bolivia, was accompanied by rainfall deficits, which increased the number of fires in these regions.

(ii) Precipitation

From January to February, heavy rainfall and floods affected Bolivia and western Amazonia. In the Urubamba valley, mudslides destroyed train tracks and bridges and more than 4000 tourists were trapped in Aguas Calientes, at the foot of the Machu Picchu, Peru. In large areas of the Brazilian states of São Paulo, Rio de Janeiro, and Mato Grosso, rainfall was 100 mm–200 mm above normal in January and February. As a consequence, São Paulo and Rio de Janeiro were affected by floods, leaving thousands of people homeless. In Mato Grosso, more than 20 000 people were isolated due to floods in February, and the Cuiaba River in the Pantanal region experienced the largest flood in the last 15 years. A similar situation occurred in northern Paraguay, south of the Pantanal basin, where, over the Vallemí, 200 mm of rainfall was observed in an eight-hour period, affecting 300 families. Most of the rainfall anomalies in January and February were due to the presence of an upper level cyclonic vortex over northeastern Brazil, which, together with the El Niño phenomenon, also inhibited rainfall over the Northeast Brazil region until April.

Drought conditions were detected in eastern and northern Amazonia, with between 100 mm and 200 mm below-normal precipitation in January 2010, and by February and March, the deficit extended all the way to central Amazonia. More than 200 mm below-normal precipitation was found over the mouth of

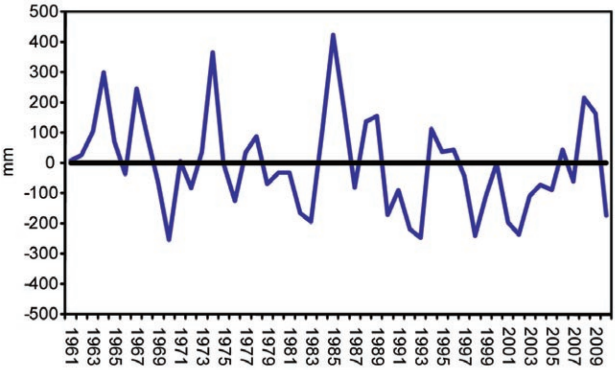

Fig. 7.13. Annual precipitation anomalies (mm) for the semiarid regions of northeastern Brazil (10°S–5°S, 45°W–38°W) during the peak of the rainy season Feb–May (based on the 1961–2010 long-term average of 541 mm). (Source: National Institute for Space Research, Brazil.)

the Amazon River and in northeastern Brazil. From March to May, the rainy season in northeastern Brazil was relatively weak and rainfall was 100 mm–150 mm below normal, becoming the fourth driest season in the last 40 years (Fig. 7.13).

From July to September, the unusually dry period in northwestern Brazil, along with rainfall 100 mm below normal, resulted in reduced stream flow in many parts of the Amazon catchments; the Rio Negro, a major Amazon tributary, fell to its lowest level on record—13.63 m—in Manaus in October. See Sidebar 7.4 for more details on the Amazonian drought.

SIDEBAR 7.4: THE DROUGHT OF AMAZONIA IN 2010—J. A. MARENGO AND L. M. ALVES

After the drought of 2005, drought struck the Amazon region again in 2010. Drier-than-normal conditions were observed in northwestern, central, and eastern Amazonia during austral summer and the rest of Amazonia until the end of the year. Below-normal rainfall and warm temperatures affected the water level of the Rio Negro River, which reached its lowest level since record keeping began 107 years ago. The drier conditions also favored the forest fires in southern Amazonia; the number of fires reported by September was about 200% higher compared to 2009.

The drought started during El Niño and became more intense during La Niña. Some previous droughts in Amazonia were associated with El Niño; however, in 1964, 2005, and part of 2010, the droughts were also associated with warmer-than-average sea surface temperatures in the tropical Atlantic Ocean north of the Equator. From March to April 2010, the sea surface temperature in this region was about 2°C–3°C above normal while it was only 1°C–2°C above normal during the same season in 2005. The droughts of 2005 and 2010 were similar in terms of meteorological severity; however, the hydrological impacts of the drought in 2010 were more extensive with respect to water levels. In addition, the seasonal rainfall anomalies indicate drier-than-expected conditions almost the entire year (Fig. 7.14).

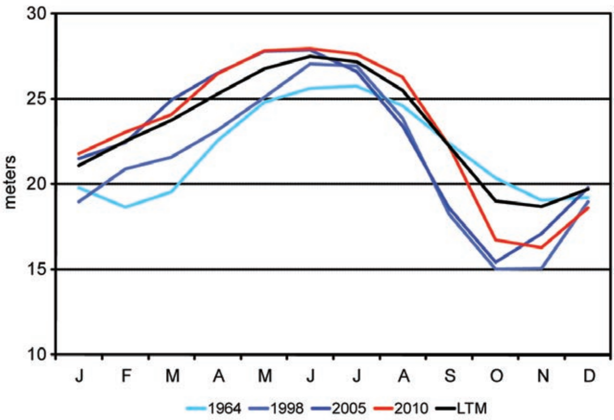

Fig. 7.15. Monthly levels of the Rio Negro in Manaus, Brazil, for some extreme dry years (1964, 1998, 2005, and 2010) as compared to the 1903–86 long-term average. (Source: CPRM-Manaus, Brazil.)

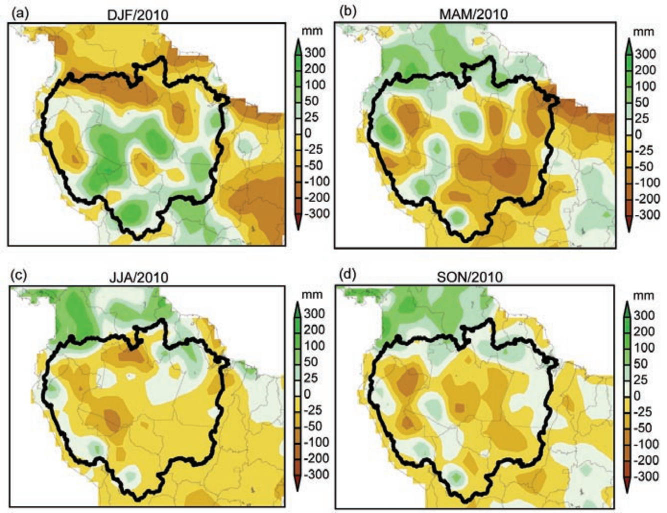

Fig. 7.14. Seasonal rainfall anomalies (mm) in tropical South America for (a) Dec 2009–Feb 2010; (b) Mar–May 2010; (c) Jun–Aug 2010; and (d) Sep–Nov 2010 (based on 1951–2000). (Source: GPCC.)

The levels of the Rio Negro River, which flows near Manaus in the northern part of the basin, were lower than the levels of the previous drought in 2005 at the beginning of the year; the water levels recovered by May–September, then dropped again to a record low in October–November (Fig. 7.15). On 24 October, the Rio Negro River reached its all time low of 13.63 m at the Manaus site, edging 1963 when water levels reached 13.64 m, according the Geological Survey of Brazil. For the Rio Madeira River, located in the southern part of the Amazon basin, the levels during 2010 were closer to previous records during the drought of 2005.

Transportation, fishing activity, and water supply in the region were affected due to the anomalously low river levels. Local newspapers in Manaus reported that fishing production dropped due to the drought.

The Amazon is periodically subject to floods and droughts, but the recent droughts of 2005 and 2010 and floods of 2009 draw attention to the vulnerability today's climate extremes impose on human populations and the ecosystems upon which they depend.

From October to December, drier-than-normal conditions continued across the region. In the Chaco sector of Paraguay, especially in the central and western parts, rainfall deficits were severe, particularly when only one day of rain was recorded in central of Paraguay.

3) Southern South America—M. Bidegain, M. Skansi, O. Penalba, and J. Quintana

(i) Temperature

Near-normal to slightly-below-normal temperatures were observed over most of southern South America during 2010, with anomalies ranging between -0.5°C and +0.0°C (Fig. 7.12a). During austral summer (January–February 2010), positive anomalies were observed in northern Argentina, Uruguay, and central Chile. This behavior was accompanied by positive minimum temperature anomalies and heavy rainfall during El Niño. Furthermore, northern Argentina was affected by a warm air mass, bringing the highest minimum temperature on record since 1961. However, in February, Patagonia, Rio Gallegos, and San Julián in southern Argentina, and Coyahique and Balmaceda in Chile recorded very low temperatures, leading to the coldest February in the past 50 years.

The Southern Hemisphere autumn (March–May) showed positive temperature anomalies over Uruguay and central Chile and negative anomalies over northern Argentina and Paraguay.

During austral winter (June–August), negative temperature anomalies were observed over the entire region, and July and August were the coldest months with anomalies of -0.5°C to -2.0°C. Below-average temperatures were widespread across southern South America in July. In Chile, negative anomalies of -2.0°C were registered for both minimum and maximum temperatures. According to the Argentinean Meteorological Service, temperature anomalies of 2°C–3°C below average were observed across Argentina in July. A cold snap during the middle of the month brought temperatures 12°C below average for several days. This cold wave affected Paraguay, Uruguay, Bolivia, Chile, Brazil, and Peru. Minimum temperatures, as low as -24°C, were reported in the Andes Mountains. Several deaths were reported in Argentina, Uruguay, Paraguay, and Bolivia as direct or indirect consequences of these low temperatures. This invasion of cold air covered half of the region with snow, from Cuyo region (northwestern Argentina) to the south of Buenos Aires, where snow is rare.

During the austral spring (September–November), negative mean temperature anomalies remained in northern Argentina while positive anomalies were observed over central Chile and the Patagonia region of southern Argentina.

(ii) Precipitation

Annual total precipitation was generally below normal across the region (Fig.7.12b). During January and February (austral summer), positive precipitation anomalies in southeastern South America were driven by the El Niño event; the regions most affected by the rains were eastern Argentina, Uruguay, and southern Brazil.

During the first week of February, extreme rainfall took place in the center of the Uruguay, Entre Ríos (eastern Argentina), and northeast of the province of Buenos Aires. Flooding affected the Negro river basin in Uruguay and the maximum accumulated seven-day total was recorded in Algorta (Department of Paysandú) with 467 mm. February was quite rainy for Uruguay, not only for record rainfall amount but also with respect to the number of rainy days, which ranged between 13 and 15 days in many places (average is 6 to 9 days).

During the second half of 2010, negative sea surface temperature anomalies generated negative rainfall anomalies in southern South America, mainly during October–December. Central and southern Chile were dominated by rainfall deficits of 30%–50%. Eastern Argentina, Uruguay, and southern Brazil experienced below-normal rainfall during these months, which caused damage to agriculture and cattle farming. These conditions exacerbated the water shortage for summer crops (soybean, maize, and rice) and pastures.

Intense rainfalls were also observed in Uruguay in September, causing serious floods that displaced about a thousand people in various areas of the country, led to 16 road closures, and caused at least two deaths. The regions of Agosto and Santa Lucia were the most affected.

(iii) Notable events

An intense cold front, moving through Bariloche city (Argentinean side of Andes Mountain) and its surroundings, brought a drop in minimum temperature to 4°C along with rain, freezing rain, and snow on mountains peaks above 1500 meters. This unusual event occurred from January to February and last occurred three years ago.

On 6 January, in the Tucumán province of northern Argentina, 75 km hr^{-1} winds and heavy rain were observed, causing rivers to overflow and stranding the affected population. In Cordoba, rainfall totals of 175 mm within a few hours led to severe flooding that destroyed bridges.

In February, heavy rains were recorded in the province of Entre Ríos in eastern Argentina, the northeastern region of Buenos Aires province, and Uruguay. Monthly totals exceeded 600 mm locally, leading to anomalies greater than 400 mm. All-time monthly records were broken in several locations. Monthly totals of 469.1 mm in the Entre Rios city of Concordia and 420.3 mm in the city of Buenos Aires were the highest February rainfall amounts for those cities since records began in 1903 and 1861, respectively (Table 7.1).

On 18 April, a heavy hail storm hit the northeastern region Buenos Aires province, causing considerable damage in some areas(with hail 5 cm in diameter).

On 10 July, the Aysen region (46°S) of Chile was affected by extreme snowfall associated with a cold front. Accumulation of more than 1 m of snow caused severe damage to agriculture and livestock. Prior to 2010, this weather phenomenon—called "white earthquake"—last occurred in 1995.

Table 7.1. Record February 2010 precipitation for select locations in Uruguay and Argentina.

Location	Precipitation February 2010 (mm)	Previous record (mm) and year of occurrence	Reference period
Young (URU)	631.0	528.2 (1984)	1931–2009
Durazno (URU)	543.0	467.0 (1977)	1931–2009
Melo (URU)	531.5	461.3 (1990)	1931–2009
Tacuarembo (URU)	502.3	350.1 (2003)	1931–2009
Concordia (ARG)	469.1	404.4 (1984)	1903–2009
Buenos Aires (ARG)	420.3	403.3 (2003)	1861–2009
Punta Indio (ARG)	349.0	310.9 (1958)	1925–2009

SIDEBAR 7.5: SAND PRECIPITATION REACHES RIO DE LA PLATA IN JULY 2010—M. BIDEGAIN AND M. SKANSI

On 18 July, strong winds whipped thick clouds of dust across the Bolivian highlands. Much of the pale dust originated from small salt pans (dry lake beds) south and southwest of Salar de Uyuni. In La Quiaca, a town 3462 m above sea level, the wind reached 95 km hr^{-1} for many hours and, combined with the sand, reduced visibility to less than 100 meters. A high-resolution satellite image on 19 July (Fig.7.16) shows the sand (brown color) on the edge of the cloud layer. The strong winds associated with the movement of a cold front carried the dust from Bolivia to Buenos Aires, Argentina, and southern Uruguay. Mixed with clouds, sand precipitated along with the rain in these regions because of the low pressure system instability in central and northern Argentina, Uruguay, and southern Brazil.

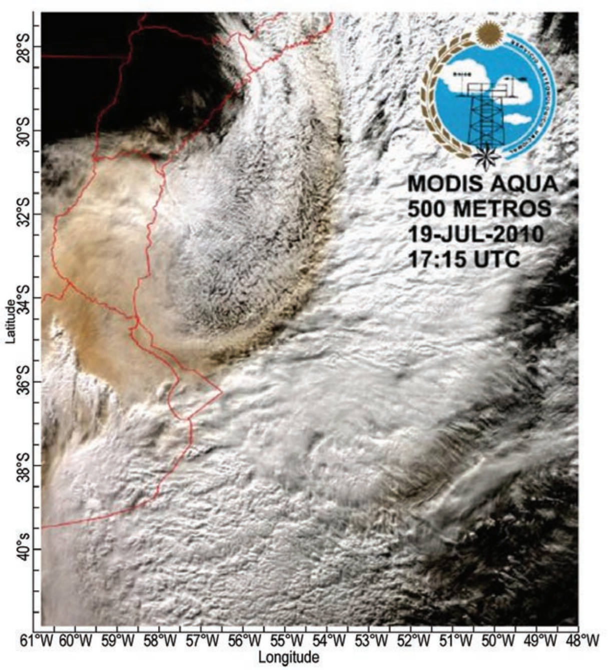

Fig. 7.16. Aqua MODIS satellite imagery of dust over Rio de la Plata on 19 Jul 2010. (Source: Servicio Meteorológico Nacional-Argentina).

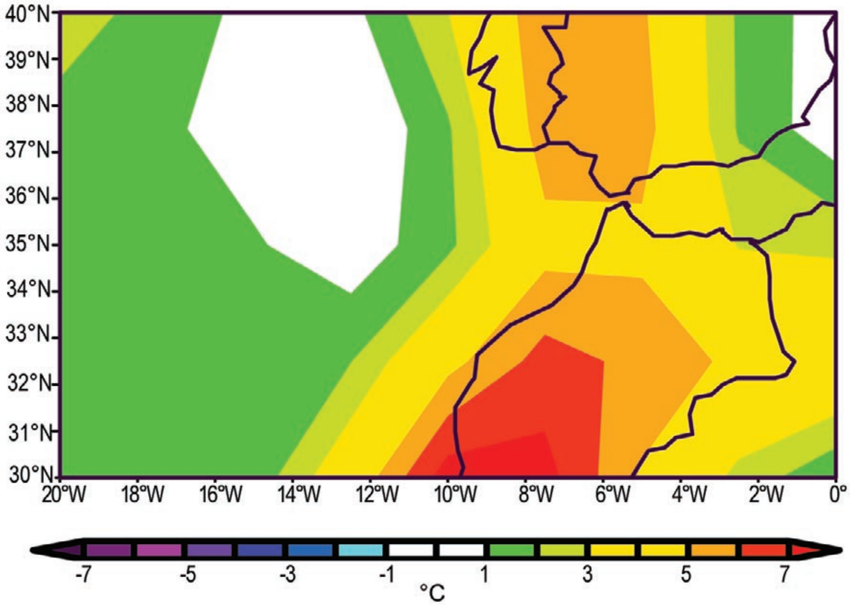

Fig. 7.17. Daily maximum temperature anomalies (°C) on 29 Aug 2010 for Morocco (based on 1971–2000). (Source: NOAA/ESRL.)

e. *Africa*

1) Northern Africa—K. Kabidi, A. Sayouri, S. M. Attaher, and M. A. Medany

Countries considered in this region include Morocco, Algeria, Tunisia, and Egypt.

(i) Temperature

The year 2010 was an exceptionally warm year in northern Africa. Annual temperature was 1.0°C–3.0°C above normal in most regions (based on 1971–2000 base period). The warmth was influenced by extreme temperatures, which were reported mainly during the summer. The annual mean temperature anomaly was between +0.1°C and +2.5°C in Morocco. Winter was relatively warm, with monthly minimum temperature anomalies exceeding +3.5°C in the northern Atlantic region. During summer, exceptional heat waves were frequent and strong monthly anomalies were recorded, for example, +3.5°C in August in the northern Atlantic city of Larache. During July and August, the daily maximum temperature reached 46°C in some parts of Algeria and 45°C in many parts of Morocco. The daily temperature was more than 5°C above normal on 29 August for most of Morocco (Fig. 7.17). Some locations set their record-high daily temperatures in 2010: 42°C in Ouarzazate (24 July); 45.8°C in Rabat (26 August); and 45.4°C in Taza (27 August).

In Egypt, the 2010 annual mean temperature was remarkably warm, with an anomaly of +2.9°C (Fig. 7.18). The annual mean maximum and minimum temperature anomalies were +1.4°C and +4.8°C, respectively. All weather stations around Egypt indicated above-average annual minimum temperature anomalies, varying from +0.6°C to +10.1°C. Stations located on the northern coast experienced annual mean temperature anomalies ranging from +0.2°C to +1.3°C, whereas anomalies varied from +1.0°C to +6.9°C in Middle and Upper Egypt. While northern Egypt experienced an annual maximum temperature of about 2°C below average, the rest of the country was 1.1°C–7.5°C above average.

(ii) Precipitation

Very wet conditions were recorded during 2010 in North Africa; winter and autumn were characterized by episodes of intense rainfall and floods. Heavy rainfall exceeded the monthly average by more than 500% for most locations over the region. Storms occurring from 27 to 30 November caused heavy rains exceeding 150 mm in six hours in the Moroccan cities of Chefchaouen (175 mm) and Casablanca (172.8 mm),

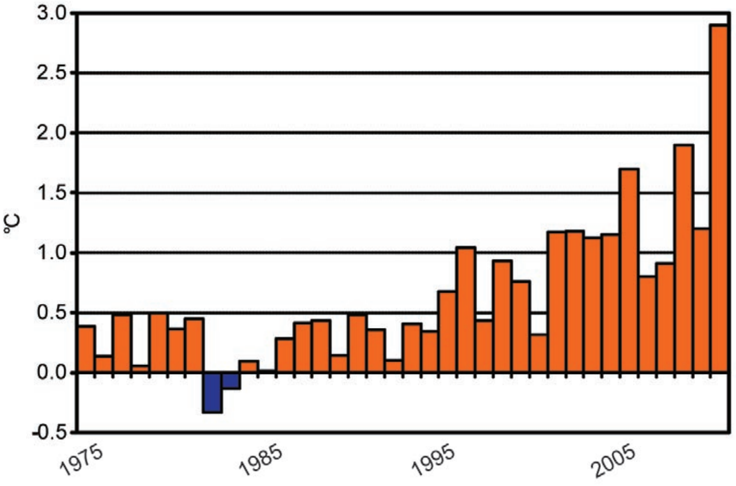

Fig. 7.18. Annual mean temperature anomalies for the period 1975–2010 (based on 1961–90 mean) for Egypt. (Source: Egyptian Meteorological Authority.)

resulting in floods in many parts of the northwest region. From September to December, the rainfall amount was more than 2.5 times higher than average at many locations (e.g., 804 mm in Chefchaouen, 761 mm in Ifrane, 508 mm in Larache, 438 mm in Casablanca, and 422 mm in Rabat).

(iii) Notable events

October and November were marked by significant heavy rainfall, leading to several floods in Morocco, Algeria, and Tunisia. These events caused major infrastructure damage and deaths.

Many 24-hour rainfall records were broken during the year: 92 mm in Nador (25 January); 75.3 mm in Taroudante (16 February); 66.9 mm in Tanger Port (15 September); 98.9 mm in Tetouan (29 November); 175 mm in Chefchaouen (29 November); and 86.9 mm in Taza (29 November).

According to the High Commission of Waters and Forests of Morocco, almost 500 hectares were destroyed by several forest fires in the extreme north during July and August; the Chefchaouen region was the most affected, especially during the heat wave when daily temperature exceeded 47°C.

2) Western Africa—L. N. Njau and W. M. Thiaw

Western Africa extends from the Guinea coast to Chad and the Central African Republic.

(i) Temperature

The year 2010 was exceptionally warm in Western Africa. The monthly temperature remained above average for every month and across the region. In January, the temperature was 1.5°C above normal and the greatest anomalies (3.5°C above the reference period 1971–2000) were observed in Mauritania, central Niger, and northern Sudan. The positive

SIDEBAR 7.6: ADVERSE WEATHER IN EGYPT—S. M. ATTAHER, M. A. MEDANY

At the beginning of 2010, from 15 to 20 January, Egypt was hit by heavy rains exceeding 80 mm day^{-1}, leading to the worst flash floods since 1994. The floods affected the Sinai Peninsula, Red Sea coast, and Aswan Governorate in Upper Egypt (Fig. 7.19), causing 15 deaths, 780 destroyed homes, and 3500 evacuations. Material losses were estimated at $25.3 million (U.S. dollars).

near the end of 2010, from 12 to 15 December, adverse weather conditions, including snow, rain storms, and strong winds swept across Egypt, causing fatalities, extensive material damage, and disruption to ports and airports. The storm, which caused temperatures to plunge to below freezing in some places and wind speeds to reach 60 km hr^{-1}, ended weeks of unseasonably warm and dry dust storms. Eighteen people were killed and 59 injured in traffic accidents associated with the bad weather, and a factory building collapsed in Alexandria. The storm closed several ports and airports and disrupted traffic in the Suez Canal.

Climate disaster risk management in Egypt is currently facing several challenges. Accurate and detailed information regarding the impact of extreme climate events is very limited. Further, effective forecasting tools and early warning systems for these events are not yet available to national meteorological and research authorities. There is an urgent need to study the impact of extreme events on different sectors and activities, establish accurate and detailed statistics and records, and develop forecasting tools and early warning systems to reduce harmful impacts.

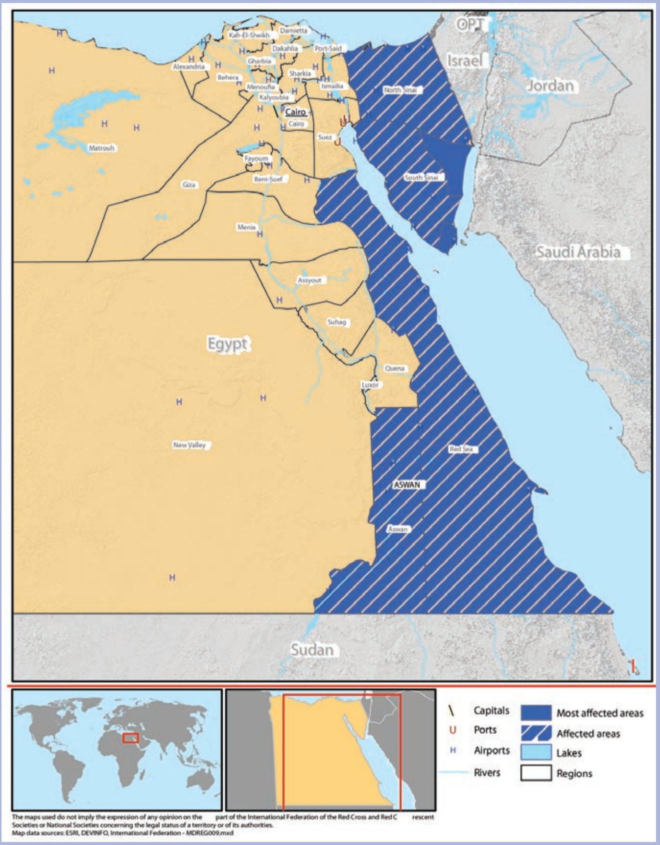

Fig. 7.19. Areas affected by flash floods in Egypt in the middle of January 2010. Source: Flash Floods DREF operation no. MDREG009 Final Report, International Federation of Red Cross and Red Crescent Societies (IFRC).

anomalies increased in February, with temperatures 3.5°C above average in northern Sudan, Chad, Niger, central Mali, and southeast Mauritania. In March, the temperature declined but was still 1.5°C above normal. The anomalies remained at +1.5°C in April, with the highest departures from normal (> 3.0°C) over Mali and northeastern Mauritania. In May, temperature was also generally 1.5°C above average, with the highest anomalies (> 2.5°C) over northern Nigeria and southern Niger. The temperature declined tremendously by midyear, becoming near normal in June, July, August, and September. However, very warm temperatures returned in October, with temperature anomalies of +2.5°C to +3.0°C over northern Niger. In November, positive temperature anomalies (> 2.5°C) were observed over the eastern part of the Sahel. In December, very warm temperatures continued, with anomalies of +3.0°C covering Mauritania and northern Senegal. Many people died from heat stress in this region in 2010.

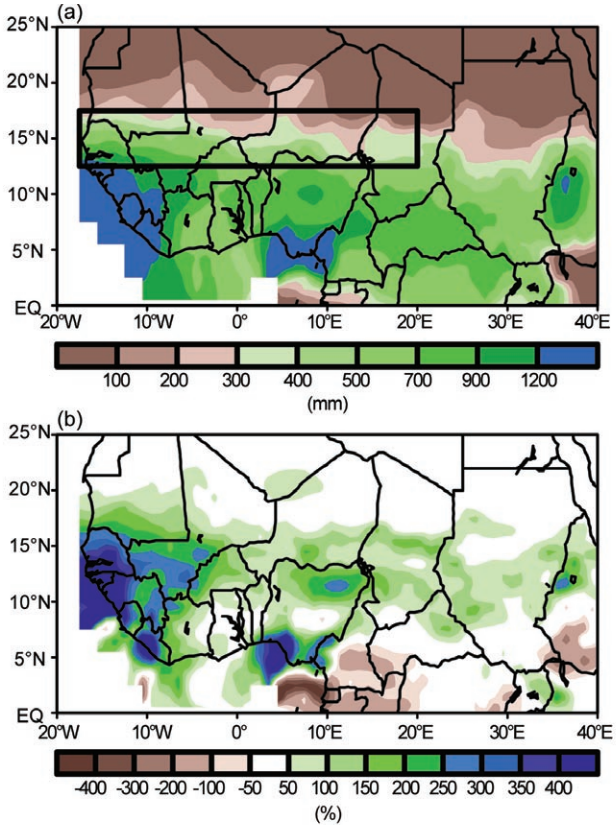

Fig. 7.20. June–September 2010 (a) rainfall (mm) for Western Africa and (b) anomalies (% of 1971–2000 base period). The boxed region indicates the approximate boundaries of the Sahel region. (Source: NOAA/NCEP.)

(ii) Precipitation

The year 2010 was characterized by very wet conditions in Western Africa. Rainfall totals from June to September ranged between less than 100 mm in the northern part of the Sahel to over 1200 mm in the western Guinean coast, southern Nigeria, and northwest Cameroon (Fig. 7.20a). The rainy season was above average across the Sahel and portions of the Gulf of Guinea. In the Sahel, it was the wettest season since 1958. Specifically, rainfall surpluses ranged between 50 mm and 100 mm across the Sahel in June and moisture was sustained throughout the season, exceeding 150 mm above average in portions of the western Sahel in September. South of the Sahel, rainfall surpluses exceeded 200 mm over southern Mauritania, and ranged between 250 mm and 350 mm over northern Senegal and parts of Mali. Rainfall surpluses exceeded 400 mm from southern Senegal to western Guinea and along the Nigerian southwestern coast (Fig. 7.20b). The rainfall extremes that soaked the Sahel, especially in the west, resulted in flooding, loss of life and property, and damages to infrastructure in many places, including Senegal, Guinea, and Mali.

3) Eastern Africa —C. Oludhe, L. Ogallo, P. Ambenje, Z. Athery, and W. Gitau

The Great Horn of Africa (GHA) region is divided into three main sectors. The northern sector of the GHA covers Sudan, Ethiopia, Eritrea, Djibouti, and northern Somalia; the equatorial sector covers Uganda, Kenya, Burundi, Rwanda, southern Somalia, and northern Tanzania; and the southern sector covers central and southern Tanzania. December–February marks the main rainfall season over much of the southern sector, while March–May marks the main rainfall season (known as the long rainfall season) over the equatorial sector. A secondary rainfall season (known as the short rainfall season) over the equatorial sector is usually observed from late September to early December. The northern sector mainly receives rainfall from June to early September.

(i) Temperature

Warmer-than-average minimum and maximum temperature anomalies were observed over most parts of the GHA throughout 2010. February was exceptionally warm, with minimum temperature anomalies greater than +2°C recorded over much of Sudan, central and western Ethiopia, Kenya, Rwanda, northern Burundi, and southern Uganda (Fig. 7.21).

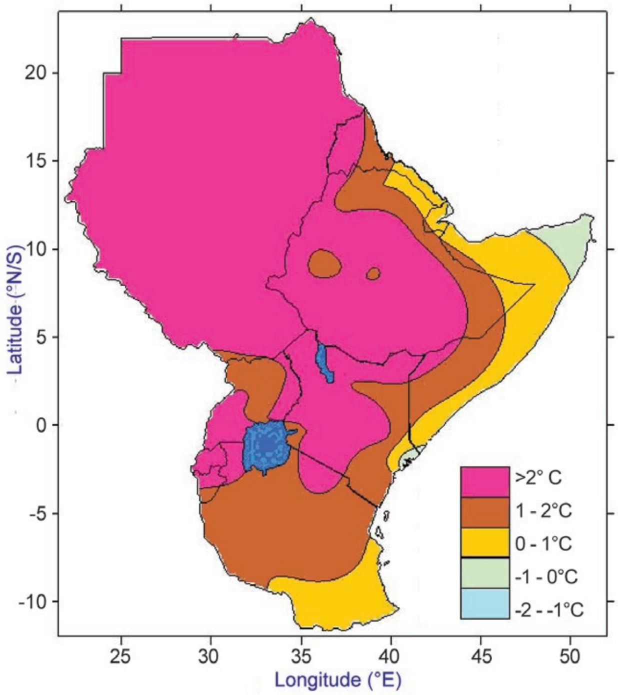

Fig. 7.21. February 2010 minimum temperature anomalies for the Great Horn of Africa (based on 1961–90 base period). (Source: ICPAC.)

(ii) Precipitation

From December 2009 to February 2010, much of Somalia, Ethiopia, Kenya, northern Uganda, and southern Sudan received more than 175% of their long-term average (1961–90). Southern and western parts of Kenya, southern Uganda, Tanzania, Rwanda, and localized parts in Sudan, Djibouti, and Ethiopia received between 125% and 175% of their long-term average. However, it was drier than normal in the southern regions where less than 25% of average was observed in southern Tanzania, southern Eritrea, and parts of Ethiopia and Sudan.

Over the equatorial sector, most of the region received near-average rainfall from March to May, with anomalies between 75% and 175% of their long-term average (Fig. 7.22a). The western parts of the southern sector and northeastern parts of northern sector of the GHA received less than 75% of their long-term average.

June–August marks the main rainfall season over the northern sector and the coldest period over the equatorial sector. The western parts of the equatorial sector received substantive rainfall over this period. The northern and southeastern parts of the northern sector, southwestern and southern parts of equatorial sector as well as most of the southern sector received less than 75% of their long-term average. Much of the central and southern parts of the northern sector, and northwestern, central, and eastern parts of the equatorial sector received between 75% and 125% of their long-term average. Localized areas over northeastern Sudan, western Uganda, and central and eastern Kenya received more than 125% of their long-term average for the three-month period.

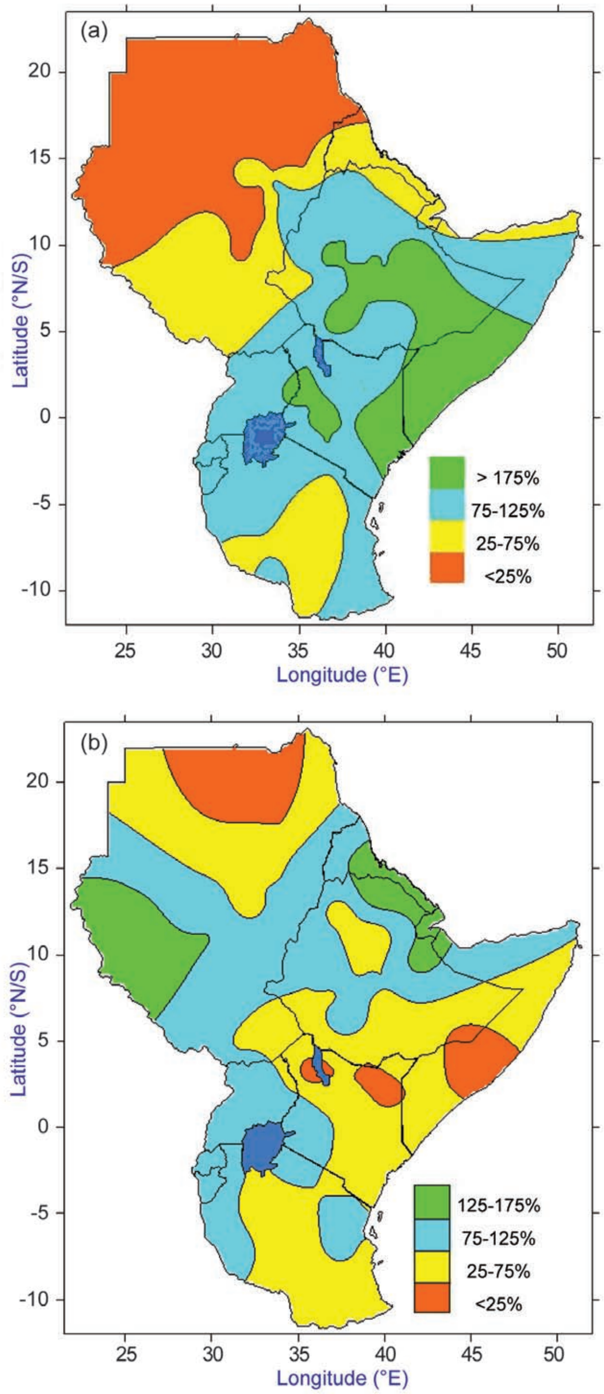

Fig. 7.22. (a) March–May 2010 and (b) September–December 2010 rainfall anomalies (% of 1961–90 base period) for the Great Horn of Africa. (Source: ICPAC.)

The second rainfall season for the equatorial sector is from September to December. Much of the eastern parts of the equatorial and southern sectors as well as the northern parts of the northern sector received less than 75% of their long-term average (Fig. 7.22b). The western parts of the equatorial and southern sector as well as central parts of the northern sector received between 75% and 125% of their long-term average rainfall for the period.

(iii) Notable events

The eastern equatorial sector recorded deficient rainfall, especially during the second rainfall season (September–December). Both direct and indirect impacts from the below-average rainfall resulted in cumulative climate stress on climate-dependent sectors. Such impacts observed in 2010 included loss of livestock due to inadequate pastures, food insecurity from crop failure, rationing of hydropower and limited water for domestic and industrial uses from scarcity of the water resources, water contamination, and poor health from malnutrition.

4) SOUTHERN AFRICA—A. Kruger, C. McBride, and W. M. Thiaw

This region includes the countries south of 15°S, with a focus on South Africa.

(i) Temperature

The year 2010 was a warm year for Southern Africa, where the annual mean temperature was above average. For South Africa, annual mean temperature anomalies, based on preliminary data from 27 climate stations, were about 0.8°C above the reference period (1961–90); this makes 2010 the second warmest year for the region since 1961 (Fig. 7.23).

(ii) Precipitation

In South Africa, January–March was characterized by above-normal rainfall over the central and western interior, but drier than normal elsewhere. During April–June, the northern interior received above-normal rainfall, while it was drier in the western interior. For July–September, very dry conditions were experienced over most of the country, including regions in the southwest where the bulk of its annual rainfall is received during this time of the year. October–December shows normal to above-normal rainfall over most of the country. In December, some summer rainfall regions received rainfall well above average, with flooding in many areas. The annual rainfall anomalies indicate that regions primarily in the coastal provinces were dry in 2010 (Fig. 7.24).

For Southern Africa, rainfall totals from November 2009 to April 2010 ranged between less than 100 mm along West Coast South Africa and coastal Namibia to over 1200 mm along the border between northern Zambia and the Democratic Republic of Congo, and along northern and east coast Madagascar (Fig. 7.25a). Southern Africa austral summer features two basic climate zones. The southwestern sector is much drier on average than the remainder of region. The area of maximum precipitation in the northern part of the region registered rainfall amounts between 700 mm and 1200 mm. To the south, rainfall in the crop areas of eastern Botswana, Zimbabwe, central Mozambique, and northeastern South Africa received 300 mm–800 mm, while the climatologically dry zone recorded less than 100 mm–300 mm. Overall,

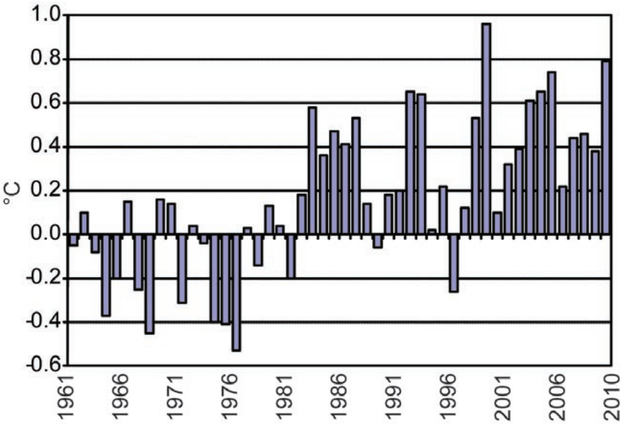

FIG. 7.23. Annual mean temperature anomalies in South Africa (average of 27 stations) for the period 1961–2010 (based on 1961–90 base period). (Source: South African Weather Service.)

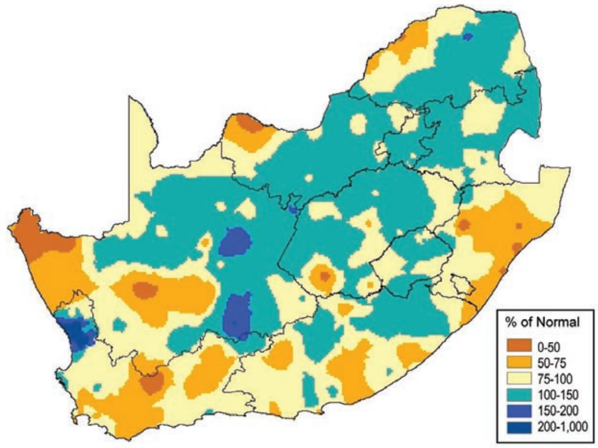

FIG. 7.24. 2010 rainfall anomalies (% of 1961–90 base period) for South Africa. (Source: South African Weather Service.)

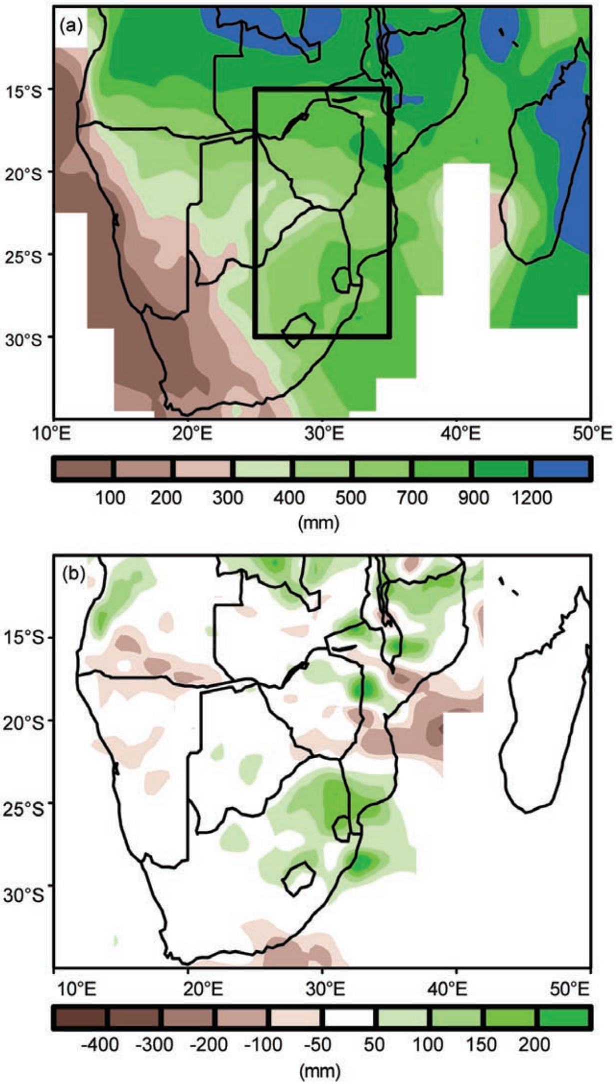

Fig. 7.25. November 2009–April 2010 (a) rainfall (mm) for Southern Africa and (b) rainfall anomalies (% of 1971–2000 base period). (Source: NOAA/NCEP.)

the rainfall season did not exhibit significant departures from climatology during the 2009/10 season (Fig. 7.25b). Rainfall was near average across most areas in the central sector of Southern Africa. Areas of enhanced rainfall included the Maize Triangle of northeastern South Africa and the northern areas of Mozambique, Zambia, and western Angola. Rainfall was below average over central Mozambique, southern Zimbabwe, and along the border between Angola and Namibia.

(iii) Notable events

In South Africa, heavy rains fell over Gauteng, Limpopo, and North West during January. A number of people drowned and many people had to be rescued from low-lying areas. Houses and informal settlements suffered damages, with many families temporarily housed in community halls. The Vaal Dam was over 100% full for the first time in 13 years and the sluice gates had to be opened, causing flooding downstream of the dam. Bloemhof Dam and the Wolwespruit Nature Reserve in North West were closed due to flooding of the Vaal River. Towards the end of January, heavy rain caused damage in the eastern province of KwaZulu-Natal.

Snow was reported on the mountains of Western and Eastern Cape on 14 and 15 June, resulting in several road closures. Snow also fell as far as Murraysburg in the Karoo for the first time in 18 years. During this period, about 600 of 700 penguin chicks died on Bird Island, which is part of the Addo Elephant Park near Port Elizabeth in the Eastern Cape.

KwaZulu-Natal experienced very hot conditions on 14 September, which negatively affected many people, especially the elderly and children. Some stations, especially along the coastal regions, reported maximum temperatures above 38°C, some of which were new record maximum temperatures.

Severe hailstorms damaged houses and cars and killed livestock in Limpopo on 24 October. The most affected areas were Tzaneen, Tubatse (Burgersfort), and Polokwane. A severe hail and rainstorm also hit Levubu district, resulting in the loss of as much as 30% of banana crop. According to reports, it was the worst hailstorm in 15 years and some of the hailstones were the size of golf balls.

Veld fires ignited by lighting and fanned by strong winds burned at least 88 000 hectares of grazing pastures in Limpopo at the beginning of October. The fires destroyed an area covering about 170 km^2 in the Waterberg area. More than 250 people, including teams from the Working on Fire Programme, the police, emergency services, farmers, and farm workers, tried to get the fires under control. Lighting also ignited nine veld fires in the Soutpan, Free State, on 7 October. At least three people died and seven were seriously injured.

A tornado with large hailstones caused extensive damage in the towns of Dewetsdorp and Winburg in Free State on 27 December. On a farm in Kleinfontein near Dewetsdorp, parts of a large storeroom were destroyed while a caravan was picked up and dropped down about 60 meters away. Roofs were damaged and windows were broken. Electricity and telephone poles were also blown over. In and near Winburg, hail caused damage to buildings and cars.

In Broederstroom, North West province, on 16 December, more than 100 mm of rain fell within 30 minutes. At least four families living along the Crocodile River were cut off from the outside world after the river burst its banks. Three houses were flooded. Heavy rain also fell in Pretoria, causing damage to infrastructure. The worst affected areas were in Centurion and north of Pretoria where a bridge on the Klipgat Road near Mabopane was destroyed. The flooding also affected parts of the Centurion Lake Hotel, damaging several cars. A low water bridge at the Apies River in Capital Park was closed after flood waters caused some structural damage to the bridge. In Mabopane, a man was rescued after he was trapped in raging water for nearly five hours when he tried to cross a small spruit (stream that flows only during the wet season) near Morula Sun.

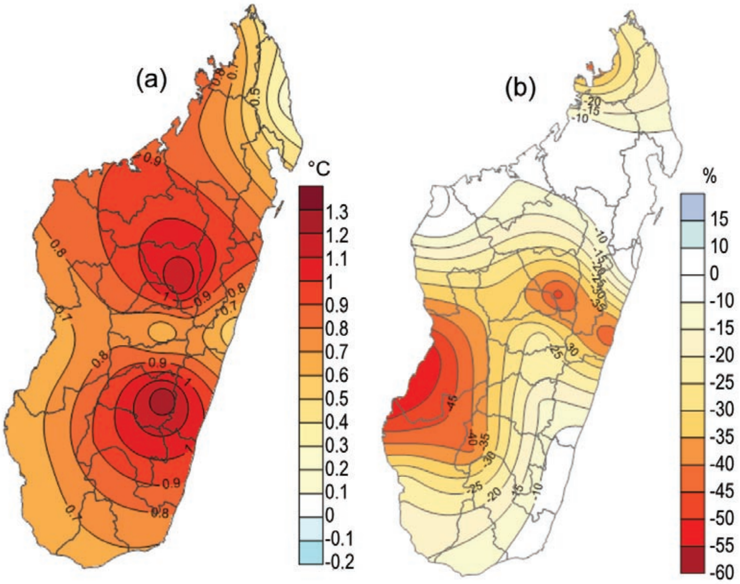

Fig. 7.26. 2010 (a) annual mean temperature anomalies (based on 1971–2000 base period) and (b) annual precipitation anomalies (% of 1971–2000 base period) in Madagascar. (Source: Service Météorologique de Madagascar).

5) Western Indian Ocean Countries—R. Faniriantsoa, S. Andrianiafinirina, G. Jumaux, D. Schueller, P. Booneeady, and V. Amelie

This region is made of many islands grouped into five countries, namely Madagascar, Reunion (France), Mauritius, Comoros, and Seychelles.

(i) Temperature

For Madagascar, the annual mean temperature was 0.4°C–1.3°C above the 1971–2000 average across the country (Fig. 7.26a). The highest annual temperature anomalies were observed at Fianarantsoa (+1.3°C) and Ivato (+1.2°C). February, April, May, June, and October were generally well above average across the entire country. The highest monthly anomaly was observed in Ranohira (+2.1°C) in April and in Mrorondava (+2.0°C) and Nosy-Be (+2.2°C) in June. Some negative anomalies were found in Taolagnaro in January (-0.6°C), Morondava in September (-0.5°C), and Sambava in November (-0.6°C).

For Reunion, 2010 was the warmest year on record since 1971 (Fig. 7.27), with an annual mean temperature anomaly of +1.05°C (+0.87°C and +1.23°C for annual minimum and maximum temperature, respectively). The year 2009 is the second warmest year on record, and 9 of the 10 warmest years occurred during the 2001–10 decade. The year 2010 had the warmest May, June, and October recorded since 1971. On Tromelin Island, 2010 was the warmest year on record, with an annual temperature anomaly of +0.96°C. At Mayotte (Pamandzi Airport), 2010 was slightly warmer than 1998, with an annual temperature anomaly of +1.06°C.

The year 2010 was also the warmest year on record in Mauritius during the decade 2001–10. The annual mean temperature was above the 1971–2000 average by around 1.2°C for Mauritius, 1.1°C for Rodrigues, 1.0°C for St. Brandon, and 0.7°C for Agalega.

For Seychelles, the annual mean temperature for 2010 was 0.6°C above average. Except for November, with a departure of -0.2°C from average, all months recorded monthly mean temperatures above average (Fig. 7.28). Seychelles also observed an annual warm anomaly of +0.5°C and +0.7°C in maximum and minimum temperatures, respectively.

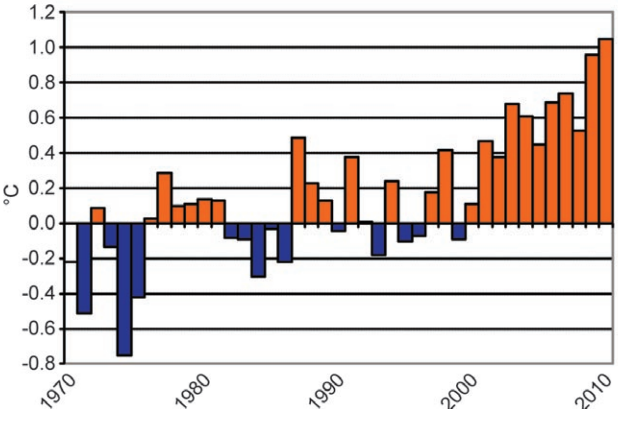

Fig. 7.27. Annual mean temperature anomalies for Reunion (average of 10 stations), for the period 1970–2010. (Source: Météo-France.)

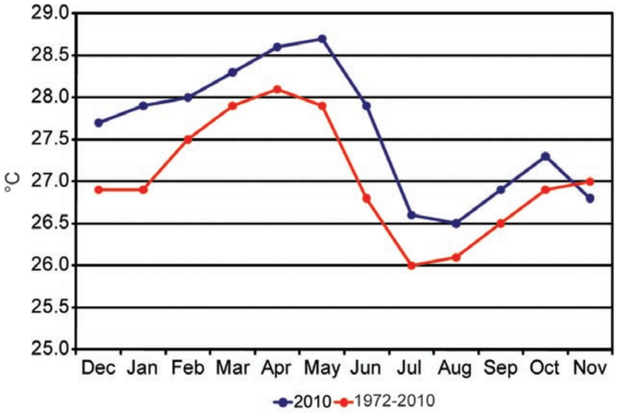

Fig. 7.28. December 2009–November 2010 monthly mean temperatures and 1972–2010 monthly averages for Seychelles International Airport. (Source: Seychelles Meteorological Services.)

(ii) Precipitation

Annual accumulated precipitation was generally below average across Madagascar (Fig. 7.26b) with a few exceptions; Antsohihy, Taolagnaro, Besalampy, Toamasina, Sainte Marie, and Farafangana were all near average. Monthly rainfall was generally below average during the rainy season. March and May were the exceptions, with monthly rainfall above average for a few stations; in March, total rainfall was 836.6 mm for Farafangana (150% of normal), 363 mm for Fianarantsoa (170%), and 490.4 mm for Taolagnaro (217%); and in May, total rainfall was 35.7 mm for Morombe (208%) and 86.6 mm for Toliara (587%). These strong anomalies were due to the passage of Tropical Cyclones Hubert (9–11 March) and Joel (25–29 May).

For Reunion, the average precipitation anomaly was -6% (17th driest year since 1971), with values ranging from -30% to +30% from the west to high elevations of the southeast. October–December was the second driest such period on record, behind 1992. Annual negative precipitation anomalies were also registered in Tromelin (-12%) and Pamandzi Airport (-15%).

In Mauritius, total rainfall recorded in 2010 was slightly below average in Plaisance and Vacoas while it was near normal at Rodrigues, St. Brandon, and Agalega. December 2010 rainfall was the lowest ever recorded in the main island—15 mm—amounting to 8% of the 1971–2000 long-term average.

(iii) Notable events

In Seychelles, the rainy season started late and November 2010 had the lowest recorded November rainfall, at 85% below average. Rainfall deficit continued in December, a month which normally receives enough rain to fill the country's main dam. But at the end of the month, the dam was only 50% of full capacity, forcing the government to impose strict restriction on water supply; many households and business establishments received only a few hours of this essential commodity per day.

f. Europe—F. Maier, A. Obregon, P. Bissolli, J. J. Kennedy, D. E. Parker, R. M. Trigo, D. Barriopedro, C. M. Gouveia, S. Sensoy, and C. Achberger

1) Overview—F. Maier, A. Obregon, P. Bissolli, R. M. Trigo, J. J. Kennedy, and D. E. Parker

Europe was on average warmer than normal in 2010, but cooler than in recent years (Fig. 7.29), and some parts were even colder than normal (Fig. 7.30). The mean land surface air temperature for the European region (35°–75°N, 10°W–30°E) from the CRUTEM3 dataset (Brohan et al. 2006) was 0.24 ± 0.13°C above the 1961–90 normal. According to interpolated CLIMAT and ship observations, only

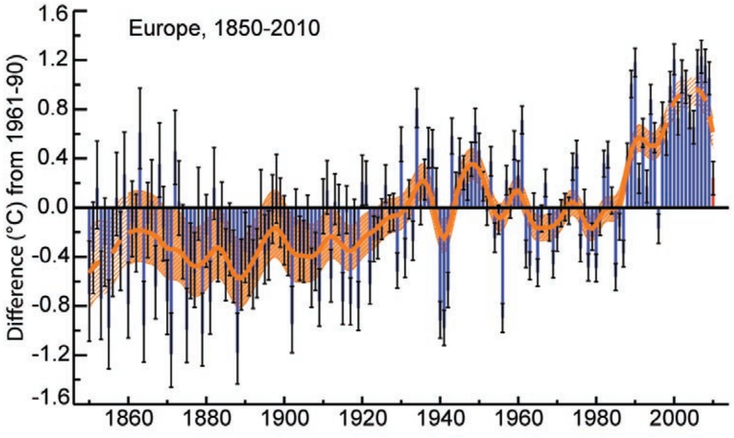

Fig. 7.29. Annual average land surface air temperature anomaly for Europe (35°N–75°N, 10°W–30°E). The blue bars show the annual average values and the black error bars indicate the 95% confidence range of the uncertainties. The red bar is the annual value for 2010. The smooth orange line shows the annual values after smoothing with a 21-point binomial filter. The dashed portion of the line indicates where the smoothed curve is affected by the choice of endpoint padding and is liable to change in future. The hatched orange area indicates the 95% confidence range on the smoothed values. Data are from the CRUTEM3 dataset (Brohan et al. 2006.)

a few areas were significantly warmer than average (Fig. 7.30). Temperatures were especially high across Greenland with a maximum positive anomaly[1] of more than +4°C, and in parts of Eastern Europe and the Middle East with +3°C. In contrast, much of Northern, Western, and Central Europe had below-average temperatures in 2010. It was the coldest year since 1996 in several countries in Western and Northern Europe, mainly due to well-below-normal temperatures during winter 2009/10, autumn, and December 2010. Western and Central Europe experienced their most severe winter season (DJF 2009/10)[2] for at least 14 years (Fig. 7.31, DJF). In contrast, Greenland, Svalbard, and large parts of southeastern Europe and the Middle East had much warmer-than-usual winter temperatures, with anomalies surpassing +4°C.

The mean European spring (MAM, 2010) temperatures were above normal across the region, with some local exceptions in Central and Northern Europe (Fig. 7.31, MAM).

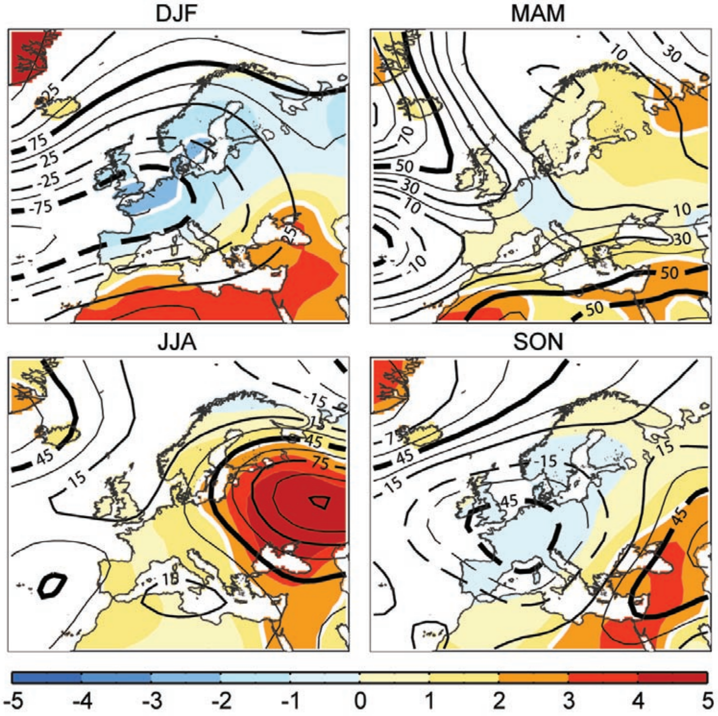

Fig. 7.31. Seasonal anomalies (relative to 1961–90 base period) of 500-hPa geopotential height (contour, gpm) and 850-hPa temperature (shading, °C) using data from the NCEP/NCAR reanalysis (Kalnay et al. 1996). Winter (DJF), spring, (MAM), summer (JJA), and autumn (SON). Black (white) thick lines highlight those geopotential height (temperature) contours with all the encircled grid points having absolute anomalies outside the ± 1 standard deviation range of the base period.

During summer (JJA, 2010), a persistent omega block over European Russia caused an exceptionally extensive heat wave that affected Eastern Europe. The blocking lasted for more than one month and new records of daily maximum temperature and minimum monthly precipitation were set in many locations in Eastern Europe and Finland. Only a few northernmost European areas had below-average temperatures in summer (Fig. 7.31, JJA).

In autumn (SON, 2010), Greenland, the Middle East, and southeastern parts of Europe had local all-time records of positive seasonal temperature, with anomalies up to +3°C (Fig. 7.31, SON). September and October were colder than normal in most of continental Europe. The situation changed during November when temperatures became very mild for this time of year in Central and Eastern Europe. In the United Kingdom, Ireland, and Spain, the conditions

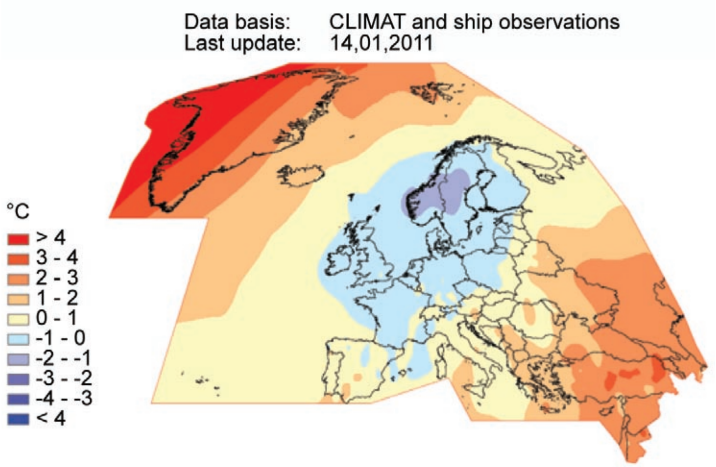

Fig. 7.30. Annual mean temperature anomalies for 2010 in Europe and over the North Atlantic (°C, 1961–90 base period) based on CLIMAT and ship observations. (Source: Deutscher Wetterdienst.)

---

[1] The standard reference period used in this section for European averages is 1961–90 for temperature and precipitation, unless otherwise specified.

[2] All seasons mentioned in this section refer to the Northern Hemisphere (months given in brackets).

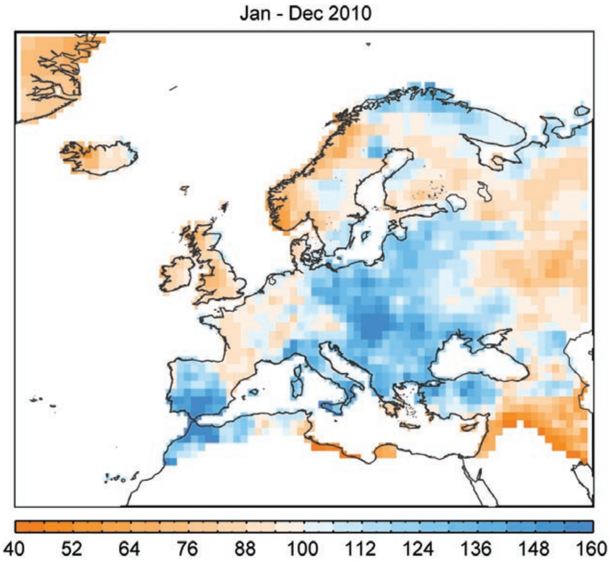

Fig. 7.32. European precipitation totals (% of 1961–90 normal) for 2010. [Source: Global Precipitation Climatology Centre (GPCC), Schneider et al. 2008.]

were reversed, with mild temperatures in September and lower-than-average temperatures towards the end of autumn.

The first three weeks of December brought severe winter weather to most of Europe, many parts being gripped by frigid Arctic air. Several minimum temperature records were broken. In contrast, the eastern Mediterranean countries experienced positive temperature anomalies.

Precipitation totals in 2010 were generally above average across much of the region, except northern and western parts of Europe, western Russia, and the Middle East (Fig. 7.32). Particularly, the Iberian Peninsula and most of the Mediterranean basin were characterized by significantly higher-than-usual annual averages (Fig. 7.32).

Northern, Western, and Central Europe experienced abundant snowfall in winter 2009/10, but mostly below-normal precipitation totals (Fig. 7.33, DJF). However, the rest of continental Europe showed mostly above-average seasonal precipitation. Spring precipitation anomalies were heterogeneous (Fig. 7.33, MAM). In May, heavy rainfall led to major flooding in eastern Central Europe. Very dry conditions were observed in the UK, France, and southern Scandinavia as well as in the Middle East.

September and November precipitation totals were higher than normal across Central and Western Europe (Fig. 7.33, SON). However, October had mostly negative anomalies in these areas. The Nordic countries experienced drier-than-usual conditions during autumn, with some parts down to 40% of normal.

December precipitation was generally higher than normal in Western, Central, and Eastern Europe and in most of Iberia, exceeding 300% of the long-term average in parts of southern Spain, but very low in Northern and northwestern Europe.

The European climate in 2010 was dominated by strong negative readings of the North Atlantic Oscillation (NAO) and the Arctic Oscillation (AO), enabling the frequent advection of Arctic air masses to the south while the Arctic regions were more influenced by warmer air masses (Cattiaux et al. 2010). The negative NAO was particularly relevant during the wet winter (DJFM) months, when it caused an attenuation of the westerlies from the North Atlantic, resulting in severe winter cold surges across Central Europe (yet milder than comparable spells in past decades because of the long-term warming trend, Cattiaux et al. 2010). However, the negative NAO-like phases dominated the entire year, giving moist conditions over the Mediterranean countries (Vicente-Serrano et al. 2011).

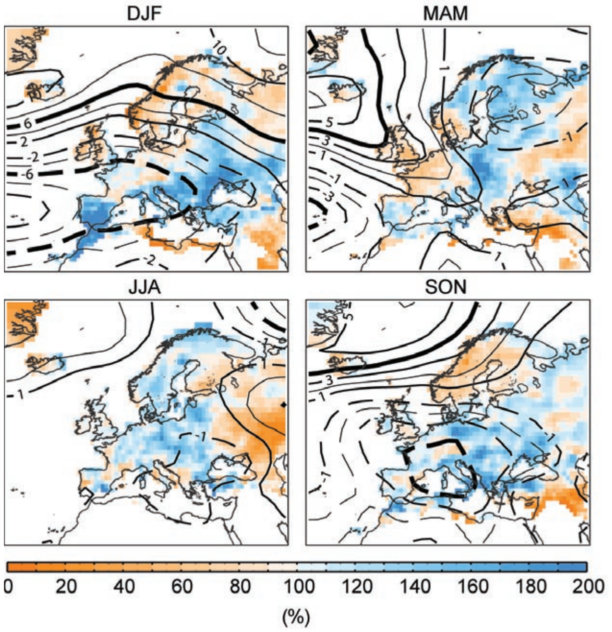

Fig. 7.33. Seasonal anomalies of sea level pressure (hPa, relative to 1961–90 base period) from NCAR/NCEP reanalyses (contours). Colored shading represents the percentage of accumulated seasonal precipitation compared with the 1961–90 climatology from the seasonal GPCC precipitation dataset (only values above 15 mm per season are represented). Thick black lines highlight those sea level pressure anomalies which are more than one standard deviation from the mean.

2) Central and Western Europe—F. Maier, A. Obregón, P. Bissolli, J. J. Kennedy, and D. E. Parker

Ireland, United Kingdom, the Netherlands, Belgium, Luxembourg, France, Germany, Switzerland, Austria, Poland, Czech Republic, Slovakia, and Hungary.

(i) Temperature

Most of Western and Central Europe had a cold year (Fig. 7.30). The UK averaged about 0.4°C below normal. Ireland experienced its coldest year since 1986. In France, 2010 tied with 1996 as the coldest year since 1987. In Germany, the 2010 mean temperature was below average for the first time after 13 consecutive warmer-than-normal years.

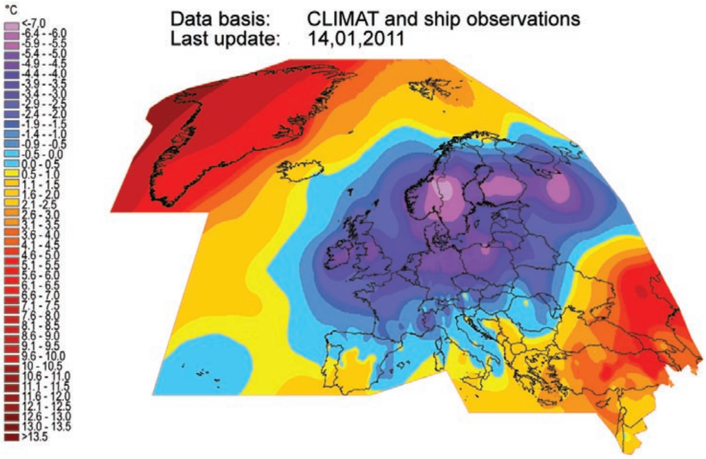

Fig. 7.35. December 2010 mean temperature anomalies in Europe. (°C, 1961–90 base period) (Source: Deutscher Wetterdienst.)

Winter was colder than normal over most of Western and Central Europe (Fig. 7.31, DJF). Many countries had their coldest winter for many years (see Sidebar 7.7).

In spring, a warm April contrasted with a mostly cool May, particularly in Central Europe. However, April 2010 was not as warm as the outstanding April months in 2007 and 2009, at least in France and Germany. The Netherlands experienced the coolest May since 1991.

Warmer-than-average summer temperatures were recorded throughout Western and Central Europe (Fig. 7.31, JJA). The UK monthly mean temperature anomaly decreased from +1.5°C in June to 0.0°C in August, the coldest August since 1993. July was particularly warm in Central Europe, at least +3°C warmer than normal in Germany, Poland, the Czech Republic, and Slovakia (Fig. 7.34).

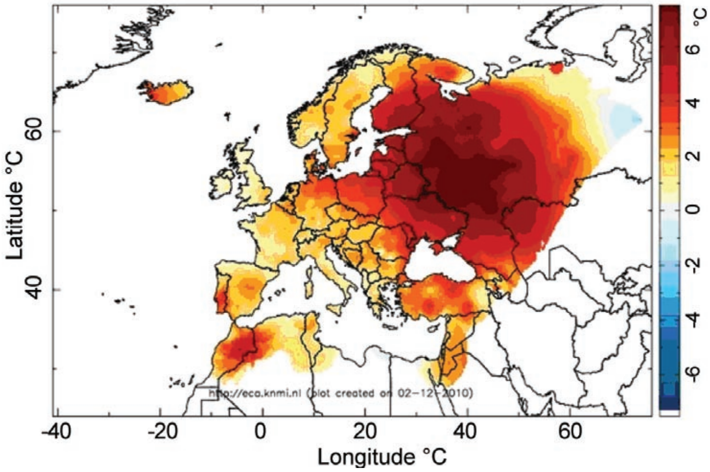

Fig. 7.34. European temperature anomalies (°C relative to 1961–90 base period) during July and the first two weeks of August. (Source: ECA&D.)

Most of Central Europe saw negative anomalies in September and October, from slightly below 0°C to below -2°C. November, conversely, was warmer than usual in Central Europe but had negative anomalies in Western Europe. The UK experienced a November temperature anomaly of -1.3°C, making it the coldest November since 1993. The last week of November was particularly cold everywhere in Western and Central Europe. In Switzerland, several locations set new records of minimum temperatures (e.g., La Brévine on 30 November with -31.4°C). In contrast, November was more than +3°C warmer than average in Hungary, and more than 4°C above normal in parts of Bosnia and Herzegovina.

December was extremely cold in Western and Central Europe (Fig. 7.35). The monthly temperatures were between -3°C and -5°C below normal in Germany and France, making it the coldest December for more than 40 years. In the UK, it was the coldest December for more than 100 years and the second coldest in the 352-year Central England Temperature series.

(ii) Precipitation

Western Europe experienced generally negative precipitation anomalies whereas Central Europe had near- or above-normal precipitation amounts (Fig. 7.32). Only 85% of the 1961–90 average fell in the UK in 2010. On the other hand, almost all parts of eastern Central Europe received more than 125% of normal rainfall.

Winter precipitation was much-below normal in most of Western and Central Europe, except southeastern parts (Fig. 7.33, DJF). In Ireland, Dublin Airport had its driest winter since 1963/64. January was particularly dry (80% of normal or less) over large areas of Western and parts of Central Europe. Nevertheless, winter 2009/10 was one of the snowiest in Western Europe (see Sidebar 7.7 for further details).

Spring precipitation totals were below average in Western Europe but above average in most of Central Europe, particularly in the east (Fig. 7.33, MAM). April was very dry over much of the region except the southeast. Germany reported its third driest April since 1901, but an unusually wet May. Over large areas from eastern Austria to Hungary, May 2010 was among the wettest ever registered. The UK experienced its driest spring season since 1984 as April and May were particularly dry with about 50% of the 1961–90 normal in England and Wales.

Summer rainfall was close to average in Western Europe, though with high temporal variability. June was very dry in Ireland, the UK, and most of Central Europe, whereas most of France, Slovakia, and Hungary were very wet. In July, large amounts of rain hit Ireland and most of the UK, but large parts of the French coasts were significantly dry. August was extremely wet all over Central Europe, whereas another dry spell prevailed over Ireland, western parts of the UK, and southwestern France. August was the wettest or second wettest in many parts of Central Europe for more than a century (e.g., the Netherlands, Germany, Slovakia), with around two to three times the monthly normal.

September and November precipitation totals were mostly above normal across Central Europe, exceeding the 90th percentile in Poland and eastern Germany in both months. These wet spells were interrupted by a mostly dry October, with some local exceptions. Poland, which had several flooding events in May, August, and September, experienced an extremely dry October, with less than 20% of the monthly normal rainfall in places. In the last week of November, widespread snowfall occurred over Western and Central Europe.

(iii) Notable events

On 27–28 February, the violent Atlantic cyclone Xynthia (969 hPa) tore along coastal Western Europe. It was the worst storm in the region since 1999, killing 62 people, mostly in France where sea walls broke in L'Agillon-sur-Mer, Vendée because of exceptional flooding. One million people were left without power across Portugal, Spain, France, Belgium, Netherlands, Germany, and southeast England after wind speeds reached nearly 160 km hr^{-1}.

On 9 August, violent floods hit eastern Central Europe, killing 11 people and damaging hundreds of houses. The Neisse River on the Polish-German border rose to 4.5 m above normal and more than 1400 residents had to leave their homes.

Severe winter weather affected Western and Central Europe during the first three weeks of December 2010 due to advection of cold arctic air (Fig. 7.35) associated with a strongly negative Arctic Oscillation. Most of the United Kingdom had snow during at least half of the month (Fig. 7.36). Airports were forced to close in Switzerland, Germany, France, Belgium, and the Netherlands. The Italian Isle of Capri experienced its first snow in 25 years on 3 December. On 28 December, the lowest temperature ever recorded in Northern Ireland was measured with -18°C at Castlederg.

3) The Nordic and Baltic Countries—F. Maier, A. Obregón, P. Bissolli, and C. Achberger

Iceland, Norway, Denmark, Sweden, Finland, Estonia, Latvia, and Lithuania.

(i) Temperature

The year 2010 was the coldest year since 1996 in most parts of Northern Europe, mainly due to well-

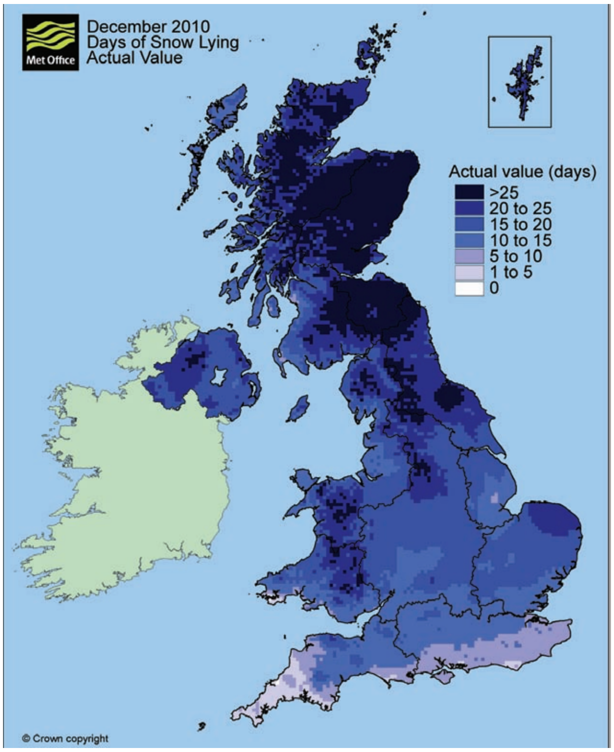

Fig. 7.36. Number of days of snow lying in December 2010 for the UK. (Source: UK Met Office.)

below-average temperatures during winter 2009/10 and December 2010. Norway reported an anomaly of -1.0°C, the 10th lowest value since 1900. In stark contrast, Iceland and Greenland experienced positive anomalies exceeding up to +4.0°C (Fig. 7.30).

All regions of Northern Europe had negative anomalies in winter, except Greenland and Svalbard, which had temperature anomalies exceeding +4°C (Fig. 7.31, DJF). The Norwegian winter was the 11th coldest on record, -2.5°C below average.

Spring temperatures were above normal across Northern Europe (Fig. 7.31, MAM). Only a few regions in Norway were colder due to a cold March and May in some areas. April, however, was mild in Northern Europe as a whole, except Iceland. Highest positive anomalies in April were reported in western Greenland (> +4°C). In northern parts of Sweden, unusually high temperatures, combined with heavy rain, caused locally severe mudslides in late spring.

Except areas in the far north, all regions experienced positive summer anomalies with maxima over Greenland and the Baltic countries exceeding +2°C (Fig. 7.31, JJA). While June was colder than normal across Fennoscandia, both July and August were warmer than normal. July was around +3°C above normal in Denmark, Sweden, and Finland. During July, the 500-hPa circulation featured a strong and persistent ridge over Fennoscandia, leading to exceptionally warm and dry conditions. A couple of stations in southern Sweden reported new all-time high temperatures since measurements began in the mid-19th century. Finland reported an extremely warm July in the country, breaking many local records. For example, a new all-time temperature record of 37.2°C was set on 29 July at Joensuu Airport, Liperi, beating the former record set in Turku in 1914 by +1.3°C. Also, Latvia and Lithuania reported the hottest July since the beginning of meteorological observations with country average temperatures of 21.5°C (+4.8°C anomaly) and 22.2°C (+5.4°C), respectively.

Only Iceland, Svalbard, and Greenland experienced positive anomalies in autumn, while several regions of Northern Europe were colder than average (Fig. 7.31, SON). Denmark had its coldest autumn since 1998 when mean temperatures around 8°C prevailed. Norway's average autumn temperature was 1.1°C below normal, which was also the most extreme negative seasonal anomaly in Northern Europe. Lithuania was unusually warm during November with daily maxima up to 15°C in many places, exceeding all previous records for November.

The winter season 2010/11 of Northern Europe started with enormous negative anomalies, except for Iceland and the Arctic. With nationwide average temperatures of -6.6°C for December, Latvia experienced its fourth coldest month in the last 67 years. Norwegian average temperatures for December were the fourth coldest ever recorded (4.7°C below normal).

(ii) Precipitation

Total annual precipitation was generally normal or slightly below normal over the Nordic countries and the Baltic region. Iceland had the lowest number of days with snow cover since 1921.

The lack of normal westerly flow during winter 2009/10 resulted mostly in dry conditions in Northern Europe (Fig. 7.33, DJF), with western Norway having its driest winter on record (28% of normal). Norway as a whole had around half of its normal seasonal precipitation totals and its second driest winter on record, surpassed only by winter 1899/1900. January was generally dry over almost all of northern continental Europe, with precipitation totals as low as 40% of normal in some regions.

Spring precipitation was mostly above normal in Northern Europe (Fig. 7.33, MAM), locally up to twice the normal in northern Norway. Only Svalbard, parts of Greenland and Iceland, southern parts of Norway and Sweden, and most of Denmark saw a dry spring; in southern Norway totals were less than 50% of normal.

Summer precipitation totals were between 125% and 150% of normal in large parts of the Nordic and Baltic countries with a few exceptions, namely Greenland, Svalbard, Iceland, and southern Finland (Fig. 7.33, JJA). Summer 2010 was the third wettest in Latvia since meteorological measurements began.

Autumn precipitation in Denmark and the Baltic countries was slightly above average. In contrast, most of Fennoscandia and Iceland experienced a rainfall deficit down to 40% of normal (Fig. 7.33, SON). A snow depth of 85 cm occurred locally in southern Sweden in November, which was a new record.

(iii) Notable Events

During April and May, upper level winds advected ash over the UK and continental Europe due to the Eyjafjallajokull volcanic eruption in Iceland. Although the eruption seldom rose above the tropopause, it caused the largest disruption of air traffic since World War II (Petersen 2010). As a consequence of the eruption, the glacier surrounding of the volcanic crater melted and caused flash floods that destroyed the infrastructure of the region. Almost 800 people had to leave their homes, but no fatalities were reported.

In northwest Greenland, a huge chunk of ice broke off the Petermann Glacier into the Nares Strait on 5 August. The ice floe was 251 km^2 in size, meaning a quarter of the floating ice shelf of the Petermann Glacier. It was the largest breakup in the Arctic since 1962 (see also section 5f7).

4) Iberia—R. M., Trigo, D. Barriopedro, C. M. Gouveia, F. Maier, A. Obregón, and P. Bissolli

Portugal and Spain.

(i) Temperature

Annual mean temperatures in Iberia were above the 1961–90 average throughout most of the region, though anomalies were mostly below +1°C (Fig. 7.30), and in Portugal only +0.24°C. Nevertheless, 2010 was the second coolest year since 1997 in Spain. Winter 2009/10 was slightly cooler than normal on most of the Iberian Peninsula, although not as cold as the rest of most of Western and Northern Europe (Fig. 7.31, DJF). The average temperature over Spain was 0.3°C below its normal value. The coldest month in Spain was February, with a mean temperature anomaly of -0.6°C.

Spring temperatures were slightly warmer than normal in most of the Iberian Peninsula (Fig. 7.31, MAM), +0.6°C averaged over Spain. However, spring 2010 was the second coolest since 1996. It was the coldest March in Portugal in the last 24 years. In contrast, April and May were warmer than normal, particularly in western and southern Iberia.

Although June temperature was near normal or slightly above normal, with a Spanish mean of +0.4°C above the 1971–2000 average, it was the coolest June since 1997. In contrast, July and August were exceptionally warm particularly over Portugal and eastern Spain. For July and August, the mean temperature anomaly averaged over Spain was +2.1°C and +1.3°C, respectively. The most significant hot spell occurred from 25 to 27 August. During this event, the 2010 highest maximum temperature of 43.0°C was recorded on the eastern coast of Spain. At many meteorological stations in eastern Spain (e.g., Murcia, Valencia), maximum August temperatures exceeded the historical records for this month. Similarly, maximum temperatures observed for Portugal in July (August) were the highest (second highest) since 1931. Generally, the temperatures during the rest of the year oscillated around their normal values on the Iberian Peninsula, with monthly mean anomalies mostly within ±1°C (Fig. 7.31).

(ii) Precipitation

Annual precipitation was above the 1961–90 average in most parts of the Iberian Peninsula, most notably in southern Spain, where the annual precipitation rate exceeded the average by more than 50% (Fig. 7.32). Portugal as a whole had its rainiest year of the last decade (2001–10), with total precipitation of 1063 mm, which is 120% of normal.

Winter 2009/10 precipitation over the Iberian Peninsula doubled its normal value (Fig 7.33, DJF). Because of the persistence of Atlantic air masses bringing abundant precipitation to the southwestern part of the Peninsula, the winter in Spain became the third wettest since 1947. Winter precipitation totals in large areas of southern Iberia and Madeira Island were the most extreme on record. According to Vicente-Serrano et al. (2011), more than 70% of 45 Iberian stations recorded monthly values higher than the 70th percentile (some higher than the 98th percentile) of the corresponding distribution in the winter months (DJF 2009/10); during March that threshold was surpassed by "only" 44% of stations. Lisbon received 958.6 mm of precipitation from December 2009 to March 2010, an all-time record since the beginning of regular measurements in 1865. The Iberian Peninsula experienced near-normal precipitation in spring with a slight north-to-south gradient (Fig 7.33, MAM). Local areas in Northern Iberia received less than 80% of the climatological average whereas the southern parts received up to 125%.

After a relatively wet June, July and August were mostly drier than normal. In particular, July was anomalously dry, with the highest negative anomalies of all months in 2010. Average July precipitation over Spain was around 50% of average, which is generally very low in summer months (less than 20 mm month^{-1} over most of southern Iberia).

Considering the Iberian Peninsula as a whole, average autumn precipitation was near normal (Fig. 7.33, SON). The season was wet in northern Spain whereas the Spanish Mediterranean regions were drier than normal.

December 2010 precipitation on the Iberian Peninsula was among the highest in Europe, consistent with the tendency for above-normal precipitation in this region during negative NAO periods, such as in December 2010. The average cumulative rainfall for December over the Spanish territory was 160% of normal. Only small parts of northeastern Spain registered below-average precipitation values.

(iii) Notable Events

On 20 February 2010, the island of Madeira was hit by torrential rainfall, with several stations above the capital city of Funchal registering more than 350 mm in 24 hours. The extreme event triggered catastrophic flash floods in three streams that crossed Funchal, leading to 45 deaths. Above-average winter precipitation in the previous months led to a saturation of moisture in soil, favoring increased surface runoff and these flash floods. This event was the deadliest hydrometeorological catastrophe in the Portuguese territory in the last four decades and economic damages were estimated at $ 1.9 billion (U.S. dollars).

Following the unusual rainy winter (DJF) season of 2009/10, large areas of the south and southwest of Iberia were affected by floods, particularly along the Guadalquivir River, with important socioeconomic impacts on agriculture, road and rail traffic, buildings, and infrastructure. Floods were directly responsible for nine fatalities and for displacing about 1000 people (Vicente-Serrano et al. 2011).

Torrential precipitation occurred in some locations of Andalucía on 16 August, in the middle of the dry season, causing three deaths and damage to infrastructure, mainly houses and transport networks (road and rail). Daily rainfall amounts of over 200 mm were measured in some places such as in Aguilar de la Frontera, Córdoba, where this amount accumulated in just a few hours.

5) MEDITERRANEAN, ITALIAN AND BALKAN PENINSULAS

—F. Maier, A. Obregón, P. Bissolli, J. J. Kennedy, D.E. Parker, and S. Sensoy

Italy, Malta, Slovenia, Croatia, Serbia, Montenegro, Bosnia and Herzegovina, Albania, Macedonia, Greece, Bulgaria, and Turkey. Detailed summaries for Turkey, Iran, and Iraq may be found in section 7g4.

(i) Temperature

Mean annual temperatures in southeastern Europe were above the 1961–90 average, with annual temperature anomalies increasing from +0.2°C in northern Italy to more than +3.0°C in Turkey, which experienced its warmest year on record since 1940 (Fig. 7.30).

Winter 2009/10 temperature anomalies were high in the eastern parts of the region, exceeding +4°C in Turkey (Fig. 7.31, DJF). In Greece, New Year's Day was recorded as the warmest January day in 50 years. In Italy, a cold outbreak of Arctic air during the "giorni della merla" ("days of the blackbird", 29–31 January) brought widespread snowfall over northern Italy and were the coldest days of the year.

Anomalous warmth was widespread in the Mediterranean region in spring and particularly in summer with seasonal anomalies up to +2°C. Cold air outbreaks occurred only occasionally (e.g., in northern and central Italy associated with a strong cutoff low at the end of June). The highest monthly anomalies were recorded in August, when Macedonia and Greece reported their highest temperatures of the year.

Autumn was also warm in southeastern Europe (up to +3.0°C warmer than normal in the east), while Italy had near-normal temperatures (Fig. 7.31, SON). September and October were cold in Italy and most of the Balkan Peninsula (e.g., -3.5°C October anomalies in Serbia), followed by a very mild November (anomalies > +4°C) in large parts of southeastern Europe.

December showed strong contrasts within the Mediterranean region. Below-average temperatures were recorded in Italy, Slovenia, and Croatia, with anomalies locally below -2°C, while positive anomalies were observed in Greece, Macedonia, and Turkey up to over +4°C.

(ii) Precipitation

The year 2010 brought well-above-average precipitation over most of the Balkan Peninsula and over some parts of the Mediterranean region. Precipitation totals exceeded 125% of normal in some areas.

Above-average precipitation occurred in almost all parts of the southern region in winter 2009/10 (Fig. 7.33, DJF). Much of the precipitation fell as snow. Heavy rainfall affected southeastern Europe, particularly in February. The highest daily precipitation total in Serbia of 39.1 mm was measured on 25 February in Belgrade, exceeding the previous local February maximum recorded (3 February 1962) by 4.3 mm.

Spring was wetter than normal over the Italian and northern Balkan Peninsulas. Other parts of the region experienced drier-than-average conditions (Fig. 7.33, MAM). In March, there were still snowfalls in northern Italy, on the Ionian coasts, and in northern and central Greece, but heavy rain in Sicily. There were heavy thunderstorms in many parts of the region during April and May. The precipitation record for May was broken in Kikinda, Serbia, with a total of 202.6 mm.

In summer, Southern Europe was mostly very wet in June, but became very dry in August, except in its northern parts. Italy was hit by thunderstorms in August, particularly over its central and northern areas.

Wetter-than-average conditions prevailed during autumn in Southern and southeastern Europe (Fig. 7.33, SON). In Slovenia, estimated average rainfall total across the country during a 48-hr period in mid-September amounted to 170 mm–180 mm, making it the most severe precipitation event in the last 60 years (and exceeding the 100-year average return interval value) at several Slovenian stations. In October, Serbia monthly precipitation totals reached 300% of normal. A Mediterranean mesocyclone, originating from a cutoff low, affected the western Mediterranean basin during the second week of October. In contrast, eastern parts of the Mediterranean region experienced far-below-average precipitation in November.

December precipitation was generally above normal in northern Italy, most of Turkey, and the northern Balkan Peninsula, and well below average (less than 60%) in parts of central and southern Italy and Greece. Extremely heavy precipitation occurred in eastern and southern Bosnia and Herzegovina on 2 December.

(iii) Notable Events

On 12 February, Rome and the coasts of the central Tyrrhenian Sea were covered with snow, an unusual occurrence.

During the third week in June, heavy rains in Bosnia led to more than 30 landslides and caused river floods, forcing thousands of homes to be evacuated. Many Bosnians feared that land mines that had been planted during the Bosnian War in the 1990s were shifted by the floods.

In northwest Bosnia and Herzegovina (Bosanska Krupa) on 4 August, severe thunderstorms occurred, with very strong winds and hail up to the size of tennis balls. There were huge losses of infrastructure and agricultural production.

On 13-14 October, 123 mm of rainfall was recorded during a 24-hour period in Bursa, Turkey. This amount of rain in 24 hours is estimated to have an average return interval of 200 years.

6) EASTERN EUROPE—F. Maier, A. Obregón, P. Bissolli, and J. J. Kennedy

European Russia, Belarus, Ukraine, Moldova, and Romania.

(i) Temperature

Eastern Europe was warmer than average during 2010 (Fig. 7.30). Anomalies were highest in the east and south and lowest in the west and north, ranging from +2.0°C to +0.2°C.

The winter season was colder than average in northern European Russia, but warmer in the other parts of Eastern Europe (Fig. 7.31, DJF). During a cold spell on 24–28 January, new records for lowest daily minimum and maximum temperatures were set in places in Romania.

The spring season brought positive anomalies over Eastern Europe (Fig. 7.31, MAM). Southern European Russia was especially warm in March, the other areas particularly in April and May. During May, the 500-hPa circulation featured a trough over Central Europe and a ridge over northwestern Russia whose impacts were the well-above-average temperatures in western Russia, with some areas recording anomalies exceeding +4.0°C.

The predominant event in summer was the exceptional heat wave in Eastern Europe, particularly European Russia, extending from early July to the middle of August (see Sidebar 7.7 for details).

In autumn, Eastern Europe experienced anomalous warmth on average, despite a cold October across almost the whole region. November, however, was much warmer than average except in northern European Russia, due to a broad ridge in the 500-hPa circulation over south-central Russia. This resulted in monthly mean temperatures of more than 4°C above normal over large parts of Eastern Europe.

December temperatures were significantly below average over most of Eastern Europe (except southern European Russia and eastern Ukraine). In northern European Russia, anomalies were below -5.0°C.

(ii) Precipitation

Precipitation totals in 2010 were generally close to normal in Eastern Europe (Fig. 7.32). Only Romania, Moldova, and small parts of Belarus and the Ukraine experienced precipitation totals above 125% of normal. Some central areas of European Russia had totals down to 50% of normal.

Winter precipitation was above normal in southwestern Eastern Europe and below normal in the northeast (Fig. 7.33, DJF). In January and February, precipitation was above average throughout Romania and Moldova.

In spring, the north and south of the region received above-average precipitation whereas the central parts were drier than normal (Fig. 7.33, MAM). In Romania, March was the third consecutive month with above-normal precipitation, particularly in the south. During May, wetter-than-normal conditions occurred over western parts of Eastern Europe, with some regions recording totals above the 90th percentile whereas eastern European Russia remained very dry.

Precipitation amounts in summer were below normal in most of Eastern Europe with a few exceptions in westernmost parts (Fig. 7.33, JJA). During June, the 500-hPa circulation featured a north-south dipole pattern of geopotential height anomalies with above-normal heights extending from Northern Europe to Mongolia and below-normal heights over central Siberia. This situation reflected a strong positive phase (+2.1) of the Polar/Eurasia teleconnection pattern (see http://gcmd.nasa.gov/records/GCMD_NOAA_NWS_CPC_POLAREUR.html for an explanation of this pattern). It was associated with exceptionally warm and dry conditions between the Black Sea and Caspian Sea where precipitation was below the 10th percentile. The mean precipitation signals during July indicated excess precipitation in Romania but below average totals (mainly below the 10th percentile) in European Russia, caused by a strong and persistent ridge over that area. August precipitation in Romania was above normal in the mountainous and western regions while precipitation amounts were low in the southeast, and even more so in the eastern Ukraine and southern European Russia.

Autumn precipitation totals were near normal or above average in Eastern Europe (Fig. 7.33, SON). November brought high monthly precipitation amounts to the region, within the upper tercile, except in the south.

Precipitation anomalies formed a tripole in December with a negative anomaly center north of 60°N and another over southern European Russia. Above-average totals, exceeding 250% of normal, were recorded in central areas.

(iii) Notable events

A week of heavy rains and subsequent floods between 20 and 30 June caused 24 deaths in northeastern Romania. The maximum 24-hour precipitation amount was 163.3 mm at Padureni. Nearly 10 000 houses were flooded and several roads and bridges suffered severe damage.

Maximum temperature records across European Russia affected animals in November. During the first half of November, temperatures in European Russia were around 10°C above average. The extreme temperatures meant that badgers and hedgehogs could not go into hibernation and some species of hares and red squirrel did not receive their warmer winter coats. This can negatively affect the animals when regular temperatures return.

7) MIDDLE EAST—F. Maier, A. Obregón, P. Bissolli, and J. J. Kennedy

Israel, Cyprus, Jordan, Lebanon, Syria, western Kazakhstan, Armenia, Georgia, and Azerbaijan

(i) Temperature

Widespread anomalous warmth affected much of the Middle East in 2010 (Fig. 7.30). The average land surface air temperature anomaly ranged between +2°C and +4°C. It was the warmest year recorded in Israel since at least the middle of the 20th century.

In winter 2009/10, anomalies exceeded +2°C across almost the entire Middle East and +4°C locally. Western Kazakhstan was only slightly warmer than normal.

Warmer-than-average conditions also prevailed throughout the region in spring, mostly above +2°C. March was exceptionally warm in the Middle East, whereas during April and part of May, temperatures were colder than normal in western Kazakhstan and the southern Caucasus, up to 2°C below the monthly average.

Summer had high positive anomalies across the Middle East. Extreme weather conditions were recorded in Azerbaijan where national average anomalies surpassed +6°C. A heat wave during July in Armenia set an all-time record of 10 consecutive days with temperatures above 38°C. August was unusually warm for the Middle East, with positive anomalies exceeding +4.0°C in several areas. While the monthly normal temperatures in Cyprus were average in June and July, a monthly record was reached for August, +3.0°C above normal. On 1 August, the temperature in Athalassa was 45.6°C, the highest temperature ever recorded in Cyprus and 8.4°C above normal for August. Israel reported several heat waves, particularly in August, with record-breaking daily maximum temperatures above 45°C in some locations.

Temperatures during the remainder of the year were above average in all months, locally exceeding +4°C. Only western Kazakhstan had near-normal temperatures in October.

(ii) Precipitation

Annual precipitation was mostly below normal in the Middle East, only locally rising above average (Fig. 7.32).

Precipitation totals for winter were generally close to average for the Middle East, with a few positive deviations in western Kazakhstan, Armenia, and Cyprus, and negative anomalies in the south (e.g., Syria).

The spring was drier than average over the southeastern Middle East while the Caucasian areas and west Kazakhstan were wetter than average. In March, rainfall amounts in northern Israel were only 5 mm–15 mm (10% of normal); only two other years had comparably low rainfall in March in the last 70 years (1962 and 2004). April brought wet conditions to the south Caucasus, and many parts of Armenia received above-normal amounts of precipitation in May, up to nearly 250% of normal.

During summer, the southeastern Mediterranean region experienced near-normal precipitation amounts while Cyprus and the Caucasian countries had negative anomalies down to 30% of normal. In June, most of the southern Middle East experienced above-average precipitation totals, whereas the south Caucasus and west Kazakhstan were dry. Armenia had lower-than-normal June values down to 14% of normal. In contrast, Azerbaijan had intensive rainfalls at the beginning of June, causing severe countrywide flooding. July was especially dry in most of the Middle East except Armenia, Azerbaijan, and some local mountain sites in other parts. August

SIDEBAR 7.7: SEVERE WINTER 2009/10 IN CENTRAL AND WESTERN EUROPE—F. MAIER, A. OBREGÓN, P. BISSOLLI, C. ACHBERGER, J. J. KENNEDY, AND D. E. PARKER

The climate patterns over Central and Northern Europe in winter 2009/10 were characterized by a strong negative North Atlantic Oscillation (NAO) and frequent attenuation of westerly air flow, resulting in severe cold spells across the region. The winter-average NAO index was the lowest since records began in 1821 (Fig. 7.37).

Snowstorms and negative temperature anomalies were the consequence (Fig. 7.31, DJF). Both Scotland and Ireland had their coldest winter since 1962/63; Ireland was 2°C below average. Many other countries in Western and Central Europe had their coldest winter since 1978/79 (UK was 1.6°C below average), 1986/87 (Germany, Switzerland), or 1995/96 (the Netherlands were 0.5°C below average). In January, the monthly temperatures were 1.5°C below normal in Austria and 2.2°C below normal in the Czech Republic. In February the Swiss meteorological office reported the coldest winter temperatures for its summit stations for up to 40 years.

The number of days with snowfall of 1 cm or more was higher than normal across the region. Northern Germany reported 20–40 more snow days and the Netherlands had an average of 42 days with snow (29 more than the long-term average), the highest value since 1979.

In the Baltic Sea, formation of sea ice started late after a relatively warm autumn with above-normal sea surface temperatures. Towards the end of 2009, very cold weather conditions over Scandinavia ensured a rapid development of the ice cover in the northern part of the Gulf of Bothnia, the Gulf of Finland, and Riga. Ice formation continued in all parts of the Baltic Sea until the middle of February and reached the maximum ice extent on 17 February (244 000 km^2), almost two weeks earlier than normal. Although the Baltic Sea ice season of 2009/10 is classified as a normal one, its impact on the maritime transport was considerable, with numerous traffic restrictions.

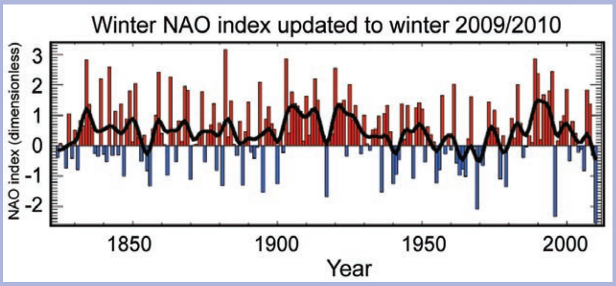

Fig. 7.37. Time series of winter North Atlantic Oscillation (NAO) Index (after Jones et al. 1997, December–March average). (Image from http://www.cru.uea.ac.uk/~timo/datapages/naoi.htm, updated 28 Jan 2011.)

One of the cold spells in January forced Frankfurt's airport to close over the weekend on 8 January. More than 90% of flights had to be cancelled. The anomalous cold also resulted in a blackout in the area around Leszno, Poland, where snow accumulated to a depth of 1.5 m. About 200 000 houses were left without power.

The UK Met Office reported January snowfalls to be the most significant and widespread across the UK since the mid-1980s. Thousands of schools were closed; there was severe disruption to transport networks, interruptions to water and electricity supplies to thousands of homes and businesses, and a number of fatal accidents related to the freezing weather conditions. In contrast to the cold and snowy conditions across Central and Western Europe, it was warmer and drier than usual in Greenland. This exceptional pattern reflected an extremely strong negative Arctic Oscillation (AO), the lowest December–February average since at least 1900 (compare Fig. 7.37 for the North Atlantic Oscillation). The persistent strong ridge of high pressure over Greenland enabled the advection of cold Arctic air far into Central Europe.

precipitation was mostly below normal in the Middle East and in the Caucasian countries.

The monthly Armenian precipitation totals continued to be low during September, but in October, Armenia had monthly rainfall amounts of 80 mm–120 mm (220%–250% of normal). Neighboring Caucasian countries had similar positive precipitation anomalies. November was again very dry for the whole Middle East. Middle Eastern countries close to the Mediterranean received less than 40% of the normal precipitation in November. In most parts of Israel, there was virtually no rain, making it one of the three driest November months in the last 70 years (only 1946 and 1966 were similarly dry).

(iii) Notable events

Heavy rainfall over Israel and Jordan on 17–21 January resulted in the worst flooding in over 10 years. The floods claimed the lives of 15 people and approximately 700 houses were engulfed. Precipitation totals of 70 mm were reported countrywide, a substantial fraction of normal monthly rainfall for most locations falling in only five days. For example, Jerusalem receives about 130 mm for the month of January on average.

On 12 March, heavy rainfall combined with melting snow resulted in severe floods in southern Kazakhstan. Over 40 people lost their lives and thousands of people were affected. This year's springtime floods were amplified by intense snowfall in the winter, followed by a rapid thaw.

On 2 December, a forest fire broke out close to Haifa, Israel. Dry conditions and strong winds helped it become the biggest wildfire in Israeli history. Over 41 people died in a bus that was caught in the flames. An estimated 17,000 people were forced to leave their homes, and almost 5000 hectares of land were burned.

On 11–12 December, an extratropical cyclone brought heavy rainfall and strong winds to the eastern Mediterranean and the Middle East. Five people lost their lives and shipping was disrupted in the Suez Canal. Along the coast of Lebanon, waves up to 10 m were observed. In Jordan, highways were closed because winds reached speeds above 90 km hr^{-1}.

g. Asia

1) Russia—O. N. Bulygina, N. N. Korshunova, and V. N. Razuvaev

(i) Temperature

By and large, the year 2010 was warm in Russia. The annual temperature anomaly averaged over the Russian territory was +0.7°C (Fig.7.38). Temperature anomalies averaged over the Russian territory were positive for all seasons, except for winter (December 2009–February 2010, DJF), with the summer (June–August, JJA) temperature anomaly being the highest. Winter 2009/10 in Russia as a whole was one of the ten

SIDEBAR 7.8: SUMMER HEAT WAVES IN EASTERN EUROPE AND WESTERN RUSSIA—F. MAIER, A. OBREGÓN, P. BISSOLLI, C. ACHBERGER, J. J. KENNEDY, D. E. PARKER, O.BULYGINA, AND N. KORSHUNOVA

Western Russia was affected during summer 2010 by extreme heat waves and very dry conditions, resulting in droughts, wildfires, and poor air quality. Temperature records with anomalies 4°C–8°C above normal were measured widely across the region (Fig. 7.34). The June–August temperature was 4.1°C above normal in central and southern European Russia. It was the hottest Russian summer in 130 years of record, on an areal average.

The heat wave started in early July, with increasing temperature maxima during that month. On 29 July, Moscow recorded its all-time highest temperature of 38.2°C, followed by further 32 consecutive days with temperatures exceeding 30°C. According to the governmental agency for the environment, the smog levels were five to eight times higher than normal. About 14 000 people lost their lives, half of them around Moscow alone. Over 20% of Russian crops growing on 8.9 million hectares of farmland were destroyed. There were more than 600 wildfires and 948 forest fires in 18 counties at the beginning of August, with thousands of people made homeless. Economic losses amounted to $15 billion (U.S. dollars). Adjacent countries such as Belarus, Ukraine, and Finland also recorded exceptional maximum temperatures. A record high number of extreme warm nights was reported in southeastern Europe.

According to NOAA's monthly *State of the Climate* report (http://www.ncdc.noaa.gov/sotc/2010/7), prior to 2010, the highest temperature recorded in Moscow was 36.8°C set 90 years ago. Russia is climatologically disposed toward blocking events during summer (Tyrlis and Hoskins 2007), and many of its prior July heat waves also were associated with such blocking patterns. Consistent with this, a composite analysis of the average temperature anomalies and 500-hPa heights associated with the ten largest prior heat waves in this region since 1880 shows patterns similar to 2010 (Barriopedro et al. 2011; Dole et al. 2011).

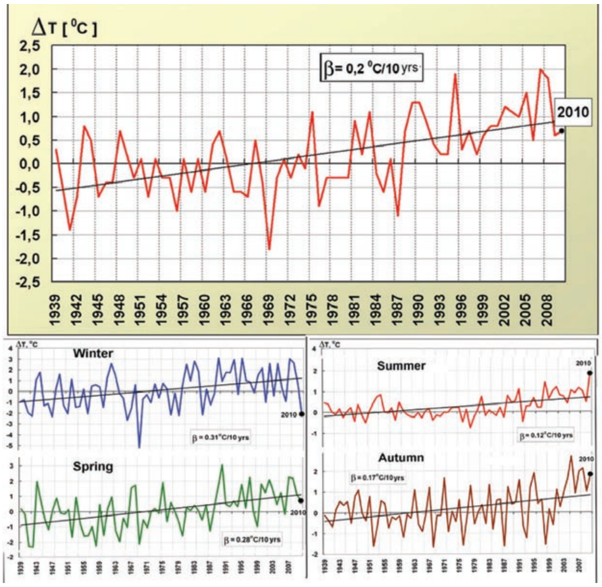

FIG. 7.38. Anomalies of average annual and seasonal air temperatures averaged over the Russian territory for the period 1939–2010 (1961–90 base period).

coldest winters in the instrumental record, associated with the extreme negative phase of the Arctic Oscillation (see Sidebar 7.7).

January 2010 was characterized by severe frosts over the large area covering southern Siberia and European Russia. Average monthly temperatures in the Novosibirsk and Kemerovo Regions and the Altai Territory, which were at the center of the cold island, were 9°C–10°C below normal. In Evenkia, on the first days of January, temperatures were even lower, -55°C. In central European Russia, average monthly temperature anomalies were 8°C to -8.5°C. Record temperature minima were recorded in Tambov, Ulyanovsk, and Penza, as well as some other cities. Such abnormally cold weather in central European Russia is related to a cold wedge of the Siberian anticyclone that propagated far westward. An important feature of January 2010 was a complete absence of thaws in Russia, which has been not recorded for several decades.

In February, Western Siberia experienced much-below-normal temperatures. The center of the cold island was above the Yamalo-Nenets Autonomous District, where average monthly temperature anomalies were -9°C to -11°C. On the coldest days, average daily temperature was 20°C–22°C below normal. Record-breaking temperature minima were recorded in both early and late February. Northern and northeastern European Russia experienced colder-than-usual weather. Severe frosts (-38°C to -46°C) were observed in the second part of the month (17–28 February). On 19 February, in the extreme northeastern regions of European Russia, the air temperature dropped to a record -52°C, which is the lowest February minimum temperature for the period of record. Meteorological station Hoseda-Hard registered the second lowest minimum temperature ever recorded in Europe, -57.0°C (Fig. 7.39). The lowest minimum temperature was registered at station Ust-Shugur, Komi Republic, in December 1978, -58.1°C. In early February, the first thaw set in central Russia and in the middle of the month, warm air from Africa reached Sochi, which led to a new record maximum winter temperature over the area of Russia, +23.8°C.

Spring 2010 over the Russian territory was generally warmer than the long-term average. March was warm over most of Western Siberia. Most of the Far East region experienced cold weather, particularly in Kamchatka and the southern Far East, where average monthly temperatures were 2°C–3°C below normal.

Over most of Russia, April was warm, especially in northeastern European Russia, where average monthly temperatures were 4°C–5°C above normal. In early April, record-breaking maximum temperatures were registered in northwestern European Russia (St. Petersburg, Pskov, Arkhangelsk, Kotlas, and Syktyvkar), and in the Urals region (Orenburg, Perm, Ufa, and Magnitogorsk). In the third ten-day period of April, record-breaking warm weather settled in southern Western Siberia. Although rivers were still icebound and snow was on the ground in places, temperatures rose as high as +25°C, the highest since 1972. Record-breaking cold weather was observed during the first week of the month in Kolyma and eastern Yakutia. In Oimyakon, which is known as "cold pole", a new daily minimum temperature was set.

May 2010 was warmer than the long-term average. As early as the beginning of the month, record-breaking temperatures were registered in northern European Russia, Upper and Mid-Volga, the Urals region, and central Russia, where average daily air temperatures were 7°C–11°C above normal. Unusually warm weather propagated from central European Russia outside the Arctic Circle. By the end of the first ten-day period, average daily temperature anomalies were larger than +10°C. On 11 May, record-breaking maximum temperatures were recorded in many northern cities (Naryan-Mar, Pechora, and Syktyvkar). Weather in northern European Russia was warmer than in the south. On 18 May, air temperature in Murmansk reached 26.4°C, nearly 5°C higher than the previous record set in 1984.

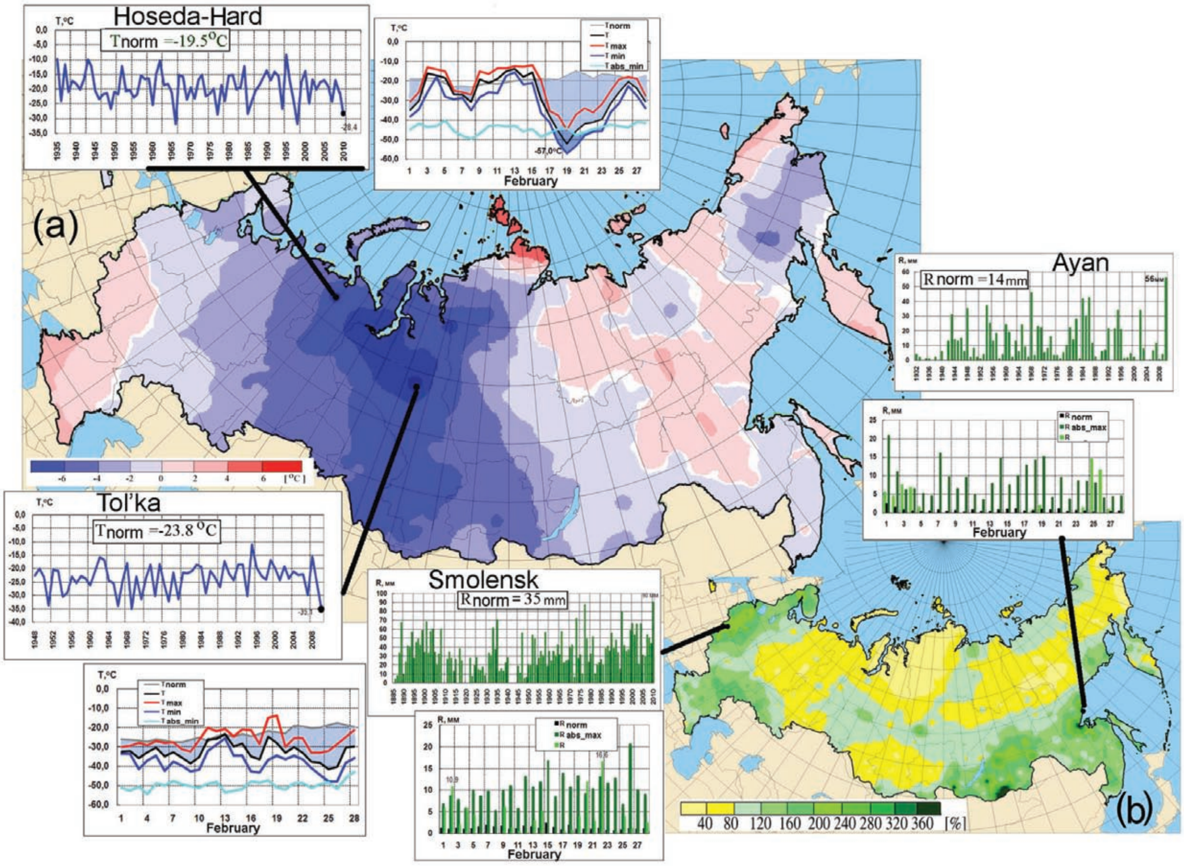

Fig. 7.39. Weather conditions for Russia in February 2010, showing (a) air temperature anomalies. Insets show the series of average monthly air temperatures and average daily temperatures during February at meteorological stations Hoseda-Hard and Tol'ka and (b) percentage of monthly precipitation totals. Insets show monthly precipitation total series and daily precipitation during February at meteorological stations Smolensk and Ayan.

Summer in Russia was the warmest such period on record, with a temperature anomaly of +1.8°C (Fig. 7.38). It was particularly warm in central and southern European Russia, where the seasonal temperature anomaly was +4.1°C.

In June, positive temperature anomalies prevailed over the Russian territory. In European Russia, a heat island formed over the Volga region and the Southern Urals, where average daily air temperatures were 7°C–11°C above normal; maximum daily temperatures reached 33°C–38°C. On 25 June, a maximum temperature record was also set in Moscow, 32.8°C. In southern Siberia, strong heat with maximum temperatures of 33°C–43°C persisted throughout the third ten-day period of the month. In Chita and most other cities of the region, record daily maximum temperatures were observed. June temperature records were also broken in many southern regions of the Far East. On 9 June, the temperature in Vladivostok reached 29.9°C, which is more than 3°C above the record previously set in 1969. Such weather is atypical for early summer in the Maritime Territory, where the weather is usually dull, moist, and cool, due to monsoon effects.

July 2010 became the hottest July on record in Russia, despite the fact that over much of the country (Urals and Western Siberia) it was substantially colder than normal. For an extended period, most regions in European Russia experienced extreme heat due to a stationary anticyclone that brought hot air from Central Asia. Nearly every day brought new temperature records. Abnormally hot weather settled in northern and eastern Yakutia on 1–5 July, with average daily temperatures 8°C–12°C above normal. On 4 July, a new daily record maximum temperature of 30.6°C was established in Oimyakon. A record maximum temperature of 32°C was set on 19 July in the north of Kamchatka. Western Siberia was the only Russian region where average monthly July temperature was below normal. In Surgut, a new record minimum temperature of 3.5°C was established on 20 July.

During the first half of August, most of European Russia experienced abnormally hot weather. However, the heat island that formed above central European Russia in July moved slightly southward. In the third ten-day period of August, high temperatures declined in central and eastern European Russia and the first frosts were recorded in the Urals, Upper Volga, and Northwestern regions (see Sidebar 7.8 for further details about this heat wave).

In September, maximum average monthly temperature anomalies were recorded in Chukotka (4°C–5°C). Average monthly temperatures over European Russia were above long-term averages. In the third ten-day period, the Urals region was in the warm rear part of the anticyclone that moved to Kazakhstan. Therefore, sunny and dry weather prevailed. Temperatures reached 25°C–28°C, which was 7°C–10°C above normal, resulting in new maximum temperature records.

October in the Urals region, Western Siberia, Chukotka, and Kamchatka was very warm. In the Altai Territory, maximum temperatures reached 13°C–15°C. October was colder than the long-term average over most of European Russia (except for northern and northeastern European Russia). In early October, an extensive cold anticyclone led to new daily minimum temperature records in Tver, Tula, Saratov, and other cities. In most of the Upper Volga regions, snow cover formed ten or more days earlier than their respective long-term averages.

November was abnormally warm over most of the Russian area. The first half of the month was particularly warm over most of European Russia and southern Western Siberia. In many cities (Smolensk, Tver, Vladimir, Kostroma, Nizhni Novgorod, Izhevsk, Cheboksary, Bryansk, Kursk, and Lipetsk), new temperature records were set. Warm and moist Atlantic air masses moving to Siberia over European Russia brought warm rainy weather to southern Western Siberia. On the last days of the month, cold Arctic air masses over European Russia transported warm air southward and genuine winter came to the central regions. In late November, winter weather also settled in northern Western Siberia. The Taimyr Peninsula and Evenkia experienced hard frosts in the third ten-day period of the month (-40°C to -47°C).

A large cold island formed over the Russian territory in December. The island had two centers, one of which was located above northwestern European Russia and the other above central Eastern Siberia. Average monthly air temperature anomalies were -6°C to -7°C and -8°C to -10°C, respectively. December was warm in southern European Russia, with average monthly temperature anomalies greater than +7°C to +8°C in individual regions. On the Black Sea coast, daily temperatures rose as high as 25°C. In the North Ossetia valleys, tree buttons swelled and roses bloomed and in some villages, strawberries bloomed. On 26 December, the temperature in Stavropol reached 17.1°C, breaking the record previously set in 1954 by 6°C. A more extensive warm island formed over the northeastern Far East. Average monthly temperature anomalies were more than +10°C. At meteorological station Omolon, the average monthly temperature was -23.1°C, compared with the normal value -35.8°C.

(ii) Precipitation

Precipitation over Russia was generally near normal (80%–120%) for 2010 as a whole. Above-normal precipitation was recorded in northwestern European Russia and in some areas of southern Siberia (120%–140%). Precipitation deficit was recorded in central European Russia (< 80%).

In February, a precipitation deficit was recorded in northeastern European Russia and northern Western Siberia due to prevailing anticyclones. Western and southern European Russia received considerably more precipitation, more than twice the monthly average in some places. Smolensk (Fig. 7.39b) received 90 mm of precipitation, compared with the normal value of 35 mm—the highest February precipitation on record since 1885. The southern Far East also received much-above-normal precipitation. At some stations, record-breaking monthly precipitation totals were observed.

In March, much-above-normal precipitation (more than two to three times the respective monthly averages) was recorded in Northern Caucasia and in southern Western Siberia. In May, much-below-normal precipitation was recorded in eastern European Russia and in the northeastern Far East.

Central and southern European Russia experienced a substantial rainfall deficit in June. During the last ten-day period of June, the Central and Volga Federal areas, as well as Lower Volga received no or a few millimeters of rainfall. In July, a precipitation deficit was registered in European Russia (4%–40% of monthly normal). In August, precipitation deficit was registered over the area from the Upper Volga region to the southern regions in European Russia. During this month, drought spread farther south: Rostov Region, Krasnodar and Stavropol Territories, and republics of Northern Caucasia. The southern part of Western Siberia received below-normal precipitation.

In September, much-above-normal precipitation (more than three to four times the monthly averages) was recorded in the east of Russia (Kamchatka, Chukotka, and eastern Yakutia). In October, southern European Russia received above-average precipitation, especially the Astrakhan Region and the Republic of Kalmykia, where the monthly precipitation totals were three to five times higher than normal.

In December, much-above-normal precipitation was recorded in some regions of the Far East. Monthly rainfall was four to five times higher than normal in many locations. Petropavlovsk-Kamchatsky was inundated with heavy rains throughout the first half of the month (high temperatures turned snow into rain). On 9 and 11 December, daily precipitation records were set and the monthly precipitation total, 446.3 mm, was the highest on record for December at the station. Heavy snowfalls in the southern Far East were the highest amounts recorded in the past 60 years. At many stations, monthly precipitation was four to five times higher than normal.

(iii) Notable events

Due to heavy snowfalls, avalanche-hazardous conditions and human-induced avalanching were recorded in the mountains of Northern Caucasia in February.

In March, in the third ten-day period, spring floods were recorded on the rivers in southern European Russia. Due to significant snow accumulation during the winter, despite preventive measures taken, a very complex hydrological situation existed on the rivers of the Voronezh, Volgograd, and Rostov regions (e.g., Don, Medveditsa, Khoper, Ilovlya, and Chir). In places, water levels rose to six to seven meters, which resulted in the inundation of many houses and evacuation of residents.

Due to large snow accumulation, torrential spring floods were recorded in May in Western Siberia. Particularly complex hydrological situations existed on the Ob, Chaya, Chulym, Peschanaya, and Tom rivers. Break-up of the Tom River in the vicinity of Tomsk was accompanied by ice clogging with an abrupt water level rise.

In the first ten-day period of May, abnormally hot weather settled central European Russia; maximum daily temperatures reached 28°C–31°C. As a result, the area experienced hot winds and extreme fire hazards. Forest fires were registered in the Lipetsk and Tambov regions.

In June, hot weather, combined with significant rainfall deficits and strong hot winds, contributed to severe soil moisture deficits and drought conditions. Abnormally hot and dry weather gave rise to extreme fire hazards in central European Russia. In the last ten-day period it was very hot in the Altai Territory, where temperatures reached 36°C in places. Hot winds and soil drought were observed in the northern Altai Territory and steppe areas of the Kemerovo Region. Hot and dry weather contributed to forest fires.

In July, a combination of abnormally hot weather and substantial rainfall deficit (4%–40% of monthly normal) observed in many regions resulted in damage, crop destruction, and forest fires over vast areas.

In August, extreme fire hazards persisted and forests and peat bogs were still on fire. During the first days of August, dense smog wrapped Moscow, Ryazan, and other cities. A fire that engulfed the roads and led to zero visibility brought traffic along highway Moscow-Chelyabinsk to a standstill and disturbed railroad movement.

Heavy rains (47 mm–93 mm) that occurred on 15–16 October in the Apsheron and Tuapse Regions of the Krasnodar Territory caused an abrupt water level rise on local rivers (3.40 m–9.16 m). Fifteen people were killed.

Freezing rain was observed in central regions of European Russia on 25–26 December. Operations at large Moscow airports were brought to a standstill

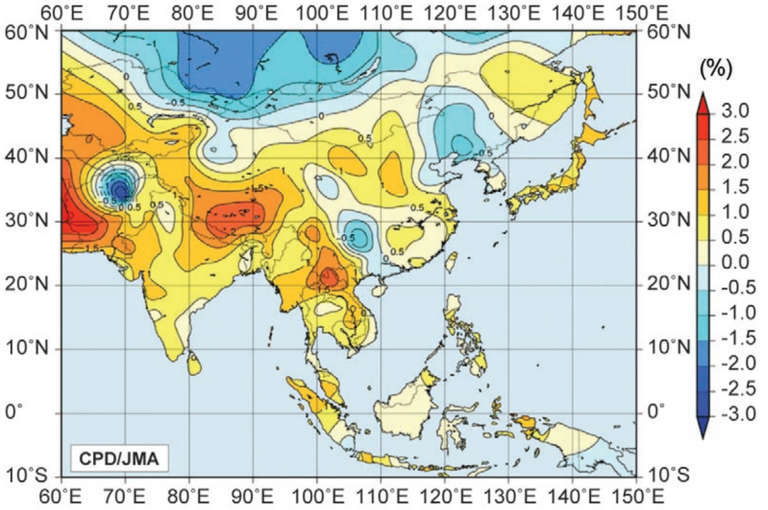

Fig. 7.40. Annual mean temperature anomalies (°C; 1971–2000 base period) over East Asia in 2010. (Source: Japan Meteorological Agency.)

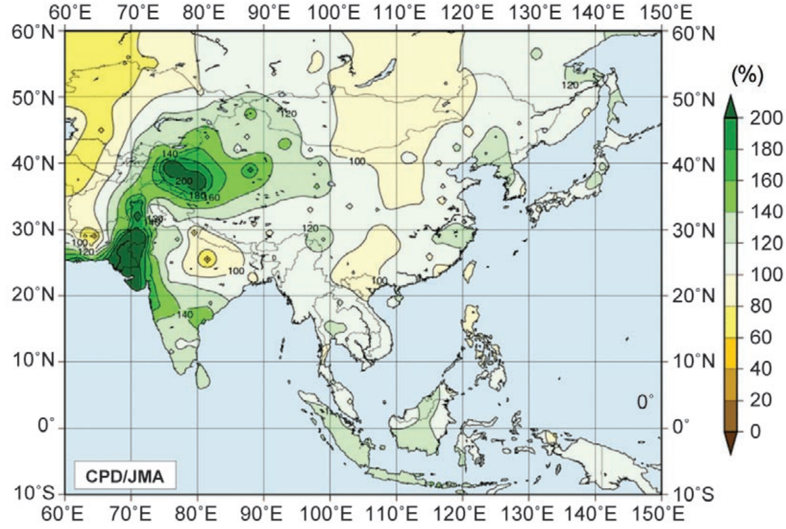

Fig. 7.41. Annual precipitation ratio as percentage of normal (1971–2000 base period) over East Asia in 2010. (Source: Japan Meteorological Agency.)

owing to ice glaze and hundreds of settlements in the Smolensk, Moscow, and Nizhniy Novgorod Regions lost their electricity supply.

2) East Asia—P. Zhang, Y. Liu, and H. Ishihara

Countries considered in this section include: China, Korea, Japan, and Mongolia.

(i) Overview

Annual mean temperatures across East Asia showed a nonuniform pattern in 2010 (Fig. 7.40), with negative anomalies over southern and northern China and the Korean Peninsula, and positive anomalies over Japan, central China, and parts of Mongolia. Annual total precipitation was near normal in most regions (Fig 7.41).

(ii) Temperature

The average temperature over China for 2010 was 9.5°C, 0.7°C above the 1971–2000 average, ranking as the 10th warmest year since 1961 and the 14th consecutive above-average year since 1997. Annual mean temperatures for 2010 were above normal over most of China except central and southern Northeast China, some part of eastern North China, and northern Xinjiang, and 1°C–2°C above normal in Northwest and Southwest China. Seasonal mean temperatures were higher than normal in all seasons of 2010, except for spring. The seasonal surface temperature anomalies over China were 0.7°C, -0.1°C, 1.1°C, and 1.0°C for winter, spring, summer, and fall respectively. The spring temperatures in China were below normal for the first time since 1997. However, the summer was the warmest since 1961. In 2010, the annual mean number of hot days (daily maximum temperature ≥ 35°C) all over China was 11.1 days, 4.1 days more than normal and ranked the highest frequency since 1961.

The average surface temperature over Japan (averaged over 17 observatories confirmed as being relatively unaffected by urbanization) in 2010 was 0.86°C above the 1971–2000 average, making 2010 the fourth warmest year since 1898. Area-averaged annual mean temperature anomalies were +1.0°C in northern Japan, +1.0°C in eastern Japan, +0.8°C in western Japan, and +0.4°C in Okinawa/Amami. In 2010, Japan experienced the hottest summer in more than 100 years. The three-month mean temperature for June–August in Japan was the highest in the historical record held by Japan Meteorological Agency that dates back to 1898, 1.64°C above the 1971–2000 average. In particular, August was so warm that monthly mean temperature records for August were broken at 77 out of 144 observatory stations in Japan.

(iii) Precipitation

The mean annual precipitation averaged across China was 681.0 mm, 11.1% above normal, which ranked the second highest since 1961 (highest was 14% above normal in 1998). Moreover, the precipitation in each season was above normal, especially in spring, which ranked the second highest since 1961. The annual number of rainstorm days were 21.5% more than normal and ranked the third highest since 1961. The rainstorms occurred mainly in southern Northeast China, middle and lower reaches of Huanghe River and Yangtze River Basin, and South China.

In 2010, there were frequent extreme weather and climate events caused by extreme precipitation. As a result of receiving 30% to 80% less-than-normal precipitation from September 2009 to March 2010, Southwest China experienced a rare severe autumn-winter-spring drought. During January–March, the most serious snowstorm struck northern Xinjiang, with 36 days and 94.8 mm of average precipitation, breaking the previous historical record. From May to July, heavy rainstorms struck southern China 14 times, bringing 800 mm–1200 mm accumulated precipitation in some areas from south of the Yangtze River to southern China. From mid-July to early-September, severe rainstorms and induced flooding also struck northern and western China 10 times. From 1 to 19 October, seldom-consecutive heavy rainstorms appeared in Hainan where the regionally-averaged precipitation was 1060 mm, ranking highest since 1951. Serious geological hazards such as mountain torrents and mud-rock flow occurred in Zhouqu of Gansu province and other isolated places.

In Japan, due to cold spells, many parts on the Sea of Japan side of the country were hit by heavy snow during the first half of January and the first ten days of February. In early February, Niigata, on the Sea of Japan side in eastern Japan, received up to 81 cm of snow, the deepest since a fall of 87 cm during the 1983/84 winter. Since cyclones and fronts frequently passed near the mainland of Japan, seasonal precipitation amounts were significantly above normal in northern, eastern, and western Japan in spring. Seasonal precipitation was significantly above normal on the Sea of Japan side in northern Japan due to the influences of fronts in summer. Seasonal precipitation amounts were significantly above normal in Okinawa/Amami in autumn.

The South China Sea summer monsoon (SCSSM) broke out in the fifth pentad of May (near normal) and withdrew in the fifth pentad of October (five pentads later than normal). The intensity of the SCSSM was -3.9, which was the weakest year since 1951. The SCSSM was much weaker than normal as a whole except for two periods: one from the fifth pentad of May to the first pentad of June and one during the first two pentads of September. After the full onset of the SCSSM, the front of the East Asian subtropical summer monsoon (EASSM) maintained over the region from South China to the south of the Yangtze River from the fifth pentad of May to June. In the first pentad of July, the front of the EASSM advanced to a region from the middle and lower reaches of the Yangtze River to the Yangtze-Huaihe River basins. With the northward movement of the monsoon surges and the subtropical high over the western North Pacific, the major rain belt in eastern China correspondingly moved northward. In June, the rain belt was mainly located in the south of the Yangtze River. From the first to third pentad of July, the major rain belt advanced to the middle and lower reaches of the Yangtze River. From the fourth to fifth pentad of July, the rain belt continued to move northward, with a large area of rainfall in the Yangtze-Huaihe and Yellow-Huaihe river basins. In fifth pentad of August, the front of the EASSM advance to North China and then North China entered the rainy season. In the second pentad of September, with the ridge of the subtropical high retreating southward, the rain belt in eastern China shifted from southern Northeast China and North China to southern North China and the Huanghe-Huaihe River basins. During late September, the warm and wet air swiftly retreated southward to regions south of 25°N. Due to the active tropical storm systems during this period, the warm and wet air remained there about one month, which resulted in persistent precipitation over South China and the South China Sea. In the fifth pentad of October, with the cold and dry air from North China intruding to the coastal areas and the northern South China Sea, thermodynamic properties of the air mass over the South China Sea changed. The front of summer monsoon then began to withdraw from the South China Sea and the SCSSM ended.

(iv) Notable events

There were 14 named tropical cyclones formed over the western North Pacific and the South China Sea in 2010, significantly less than the 1971–2000 average frequency of 26.7 and the lowest number since 1951. Super Typhoon Megi developed intensively with a central surface pressure less than 900 hPa. After hitting the Philippines, the storm turned northward in the South China Sea, causing damage to southern China and Taiwan. From November to December, for the first time since 1951, no named tropical cyclones formed in this region (see section 4d4 for further details on the 2010 western North Pacific hurricane season).

In early May, the strongest wind and hail storms of the past 20 years occurred in Chongqing China, with local maximum wind speed more than 108 km hr^{-1}, and causing heavy casualties.

In spring 2010, China was affected by 16 dust and sand storms, which was below the normal frequency for 1971–2000 but more than the 2000–09 decadal average of 12.7. The average number of dust days in northern China was 2.5 (3.1 days less than the 1971–2000 average). During 19–22 March, a strong dust storm affected 21 provinces in China, which was the widest influence in 2010.

Meanwhile, Kosa (yellow sand/aeolian dust) events were observed at 58 of 61 stations in Japan on 21 March 2010, marking the highest number on record. Also significant in 2010 were new records set in May, November, and December in terms of the number of days when any meteorological station in Japan observed Kosa. There were 41 days in which any meteorological station in Japan observed Kosa in 2010, nearly double the normal number (20.1 days). A cumulative total of 526 observations of Kosa were made in 2010, more than triple the average of 153.9.

3) South Asia—M. Rajeevan, A. K. Srivastava, Z. Lareef, and J. Revadekar

(i) Temperatures

South Asia continued to experience unusually warm temperatures in 2010. The summer months of March, April, and May were characterized by abnormally high temperatures over northern/northwestern parts of India and Pakistan with many days of extreme heat wave conditions.

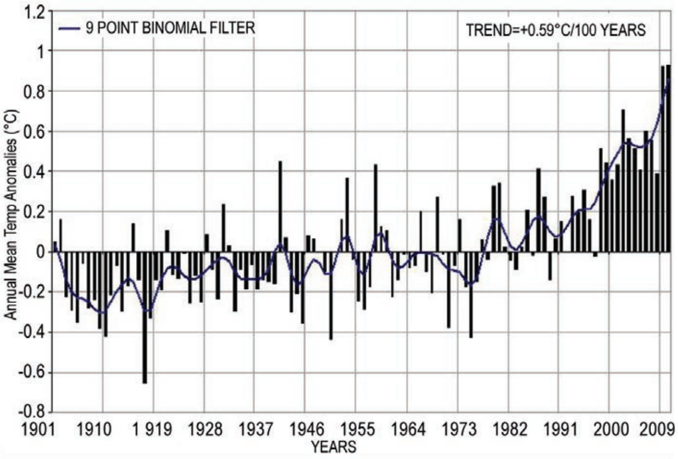

Fig. 7.42. Annual mean temperature anomalies (with respect to 1961–90 normal) averaged over India for the period 1901–2010. The smoothed time series (9-point binomial filter) is shown as a continuous line.

The annual mean temperature for India was 0.93°C above the 1961–90 average, making 2010 the warmest year on record since nationwide records commenced in 1901 (Fig. 7.42). This superseded the previous five warmest years, which have all occurred since the turn of the century: 2009 (+0.92°C), 2002 (+0.71°C), 2006 (+0.60°C), 2003 (+0.56°C), and 2007 (+0.55°C). Mean monthly temperature anomalies over the country as a whole were the highest for March (+2.27°C), April (+2.02°C), and November (+1.17°C), and the second highest for May (+1.17°C), since records began in 1901. The recent decade (2001–10) was the warmest decade on record over India with a decadal mean temperature anomaly of +0.60°C.

(ii) Precipitation

The summer monsoon season (June–September) contributes 60%–90% of the annual rainfall over major portions of South Asia. During the 2010 monsoon season, while India, Pakistan, and Sri Lanka experienced above-normal rainfall activity, Bangladesh experienced its driest monsoon since 1994.

For India, the long-term average (LTA) value of the summer monsoon rainfall, calculated using all data from 1941 to 1990, is 890 mm. For 2010, the summer monsoon seasonal rainfall over India was 102% of its LTA. During the season, the monsoon trough (an east-west elongated area of low pressure) was mostly located south of its normal position and monsoon low pressure systems moved south of their normal tracks. This resulted in an uneven spatial distribution with above-normal rainfall over peninsular and northwest India and deficient rainfall over central and northeastern parts of India (Fig. 7.43). Consistent with the recent decreasing trend of the frequency of monsoon depressions over the Indian Ocean, none of the 14 low pressure systems formed over the Bay of Bengal intensified into a monsoon depression.

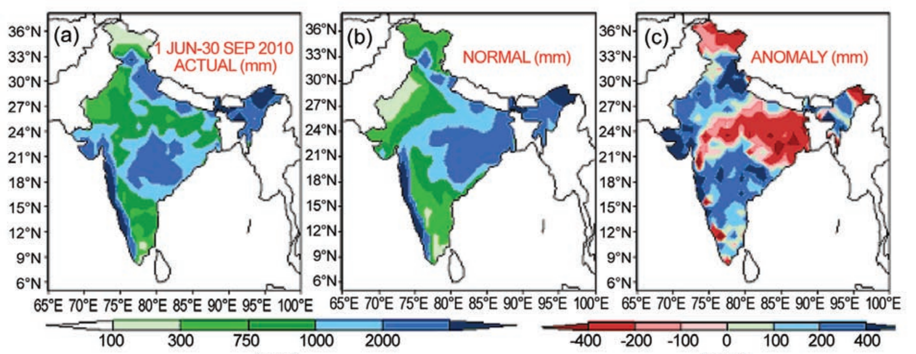

Fig. 7.43. Spatial distribution of 2010 monsoon seasonal (June–September) rainfall (mm) over India.

The monsoon advanced into southern parts of India on 31 May, close to its normal schedule. However, formation of Tropical Cyclone Phet over the Arabian Sea disrupted the northward progress of the monsoon and caused a prolonged hiatus of about two weeks. The slow progress in the monsoon advancement resulted in a rainfall deficiency of 16% for June over the country. However, the rainfall activity in July, August, and September months was normal with monthly rainfall of 103%, 105%, and 110% of LTA respectively. During the season, of the 36 meteorological subdivisions, 14 received excess rainfall, 17 received normal rainfall, and the remaining five subdivisions received deficient rainfall.

Pakistan, which is at the western edge of the pluvial region of the South Asian monsoon, experienced the worst flooding in its history as a result of exceptionally heavy monsoon rains (Fig. 7.41). The flooding was caused by a major rain spell from 28 to 29 July, when the rainfall totals exceeded 120 mm over a large area of northern Pakistan. There were additional heavy rains further south from 2 to 8 August (Webster et al. 2011). During the following days, flooding extended through the entire Indus Valley, leaving behind a wake of devastation and destruction. The death toll was close to 2000 and over 20 million people were affected. The agricultural losses were estimated at more than $500 million (U.S. dollars). Over the northwest and central parts of the country, the seasonal rainfall was more than 75% above normal. The total monsoon seasonal rainfall in 2010 was the fourth highest on record and the highest since 1994. These heavy rainfall events over Pakistan could be attributed to an interaction of extended monsoon flow and an upper level trough in the westerly jet stream. The persistent trough in the jet stream associated with the upper-layer blocking pattern over West Asia caused strong upper-layer divergent flow and ascent of warm and moist surface air. Near the surface, the monsoon easterly winds extended unusually far along the Himalayan foothills into northern Pakistan.

Since the monsoon trough was mostly located south of its normal position, the rainfall activity was subdued over Bangladesh. The monsoon season typically brings the country more than 75% of its annual rainfall. In 2010, Bangladesh experienced one of the driest monsoon seasons since 1994, with the seasonal rainfall about 19% less than the 30-year long term average rainfall.

The northeast monsoon (NEM) contributes 30%–50% of the annual rainfall over southern peninsular India and Sri Lanka as a whole. Over south peninsular India, active monsoon conditions continued unabated during the NEM season also. Above-normal rainfall activity over the region was associated with the presence of an active Intertropical Convergence Zone (ITCZ) across the region and formation of five low pressure systems (two severe cyclonic storms, two depressions, and one low pressure area) over the warm waters of the south Bay of Bengal. The 2010 NEM seasonal rainfall over south peninsular India was significantly above normal (155% of LTA), which is the second highest since 1901, behind 2005.

Rainfall over Sri Lanka was up to 30% below normal during January–March, was wetter than normal from July to September and, after a dry October, was much wetter than normal during November and December. The rainfall anomalies during January–March were typical of anomalies during an El Niño episode that prevailed until April 2010 and the wet anomaly from June to September was typical of that during the La Niña event that commenced in July. However, the enhanced rainfall (more than 50% above normal) during the main planting season from October to December was anomalous but not unprecedented. During La Niña episodes, there is usually below-normal rainfall (Zubair and Ropelewski 2006) but in the 43 La Niña events from 1869 to 1998, wet conditions were reported on six occasions. The cumulative impact of wet conditions since April led to many landslides and floods that intensified to the end of the year.

(iii) Notable Events

Severe cold wave conditions with temperatures 5°C–10°C below normal prevailed over northern parts of India in January and during the first fortnight of February, claiming more than 600 lives. On 18 April, Delhi, the capital city of India, recorded its highest April temperature (43°C) in nearly 60 years. In May, severe heat wave conditions with daytime temperatures 4°C–5°C above normal prevailed over northern and central parts of India claiming more than 300 lives. In Pakistan, record daytime temperatures were reported for several days during the last week of May; the heat wave conditions claimed at least 18 lives. A maximum temperature of 53.7°C was recorded at Mohenjo-daro on 26 May. This was the warmest temperature ever recorded in Pakistan and possibly the fourth warmest temperature ever recorded anywhere in the world.

On 13 April, a severe convective storm with strong winds of more than 26 m s^{-1} caused widespread damages in West Bengal and Bihar, claiming more than 120 lives, and leaving nearly one million people homeless. The severe cyclonic storm Laila that formed over the southeast Bay of Bengal, crossed the Andhra coast on 20 May, causing widespread damage and claiming the lives of more than 50 people. An unusually heavy rainfall event in the early hours of 6 August in Leh (Jammu and Kashmir) claimed more than 150 lives and more than 500 people were reported missing. Rainfall records for India during 2010 are listed in Table 7.2.

Table 7.2. Record rainfall over India during the 2010 monsoon season

S. NO.	Station	24-hr Rainfall (mm)	Date	Previous record (mm)	Date of record	Year of Record
June						
1	N. Lakhimpur	207.8	16	183.0	22	1990
2	Osmanabad	111.2	23	68.2	3	2000
3	Cial Cochi	160.6	13	93.9	6	2004
July						
1	Phoolbagh	146.2	21	123.6	11	2003
2	Damoh	253.6	26	225.1	18	1973
3	Okha	330.5	27	283.3	10	1973
4	Nandyal	143.2	11	116.0	16	1989
5	Dharmapuri	117.0	9	91.6	12	1989
August						
1	Okha	226.5	3	119.8	11	1981
2	Bhira	380.0	30	350.0	23	1997
3	Osmanabad	149.8	22	85.0	21	2009
4	Arogyavaram	111.0	21	90.0	9	1970
September						
1	Ranchi AP	205.8	12	168.4	28	1963
2	Pant Nagar	117.2	7	105.0	10	1967
3	Bharatpur	107.0	4	91.8	17	1990
4	Dhar	170.8	8	151.0	21	1973
5	Narsapur	115.7	13	88.9	24	1997
6	Mangalore AP	150.2	24	125.5	6	1902
7	Panambur	125.2	24	113.6	26	1998
8	Belgaum (AP)	150.0	24	100.4	20	1981
9	Cochi AP	183.5	24	128.0	28	2009
10	Cial Cochi	108.0	24	77.4	18	2009

4) SOUTHWEST ASIA

(i) Iraq—M. Rogers

(A) TEMPERATURE

Temperatures in Iraq during 2010 were 2°C–4°C above normal. Many locations had above-average temperatures every month, with temperatures reaching at least 50°C in many central and southern areas during the summer. Figure 7.44 shows the seasonal temperature anomalies for three locations.

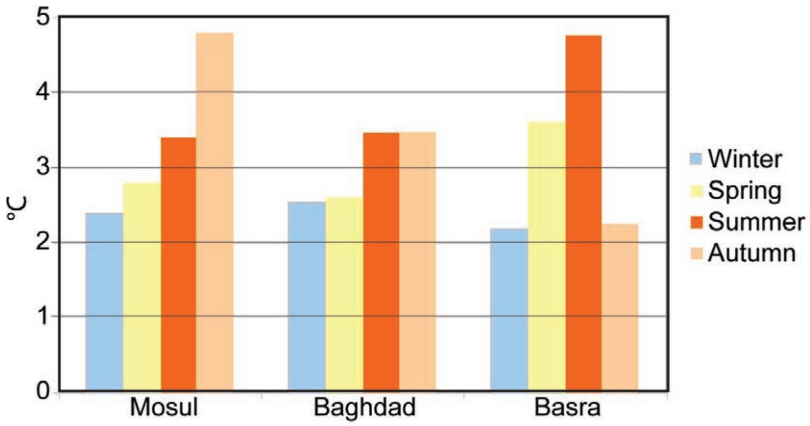

Fig. 7.44. 2010 seasonal temperature anomalies (°C) for three Iraqi cities compared with 1961–90 normal.

Winter temperatures, as with the rest of the year, were significantly above average, with most locations having no frost at all. The airbase at Tallil in the south did have a couple of nights where the temperature fell below freezing during the late winter but overall the season was still above normal. Spring followed in a similar pattern with some locations having record daytime temperatures. Summer and autumn continued to be well above average across most areas although temperatures were closer to normal during November in the south.

(B) Precipitation

Rainfall over Iraq was well below average across all areas for the third consecutive year. The winter period, December 2009–February 2010, was the wettest part of the year. December 2009 was wetter than normal at Mosul but elsewhere, and for the rest of the season, it was significantly drier than average. Below-average rainfall continued for the rest of the year, with the dry summer conditions continuing well into the autumn. Mosul received above-average rainfall during December as the 2010/11 winter began unsettled in the north while drier-than-normal conditions continued across central and southern areas.

(C) Notable Events

The major event of 2010 was the continued drought, especially during the autumn. For the third consecutive year, below-average rainfall had a major effect on the country's agriculture. The drought led to falling river levels in the Tigris and Euphrates. Further, dust storms occurred more frequently during the year and fog occurred less.

(ii) Iran—M. Khoshkam and F. Rahimzadeh

(A) Temperature

Warmer-than-average conditions occurred during winter 2009/10 (Table 7.3). The highest values occurred in parts of northwest including West Azerbaijan, East Azerbaijan, and Kordestan provinces, with anomalies of +5°C with respect to the long-term mean. The highest anomalies occurred in Ghorveh, Kordestan, with +7°C anomalies. During spring, the country experienced temperatures mostly 0°C–2°C above the long-term mean; however, in some small parts of central Iran, temperature anomalies were +2°C to +3°C. And in some isolated areas, mean temperatures were up to 0.8°C below average. In the summer, a vast area, including some parts of northeast and central Iran, reported mean temperatures that were 0°C–1.7°C below average. The rest of the country experienced temperatures 1°C–2°C above

Table 7.3. Seasonal amount of precipitation and temperature over Iran 2010.

Parameter	Season		Winter	Spring	Summer	Autumn
Precipitation	**Average (mm)**		**75.4**	**62.9**	**6.63**	**19.3**
	Respect to (%)	Long term	31%	30%	34%	72%
		previous year	23%	20%	47%	78%
	Range from–to (mm)		0.5–450.5	0–310	0–324	0–586
Temperature	Respect to long term (°C)		0.5 to 7	-0.8 to 3	-1.7 to 4	-0.5 to 6.5
	Range from-to (°C)		-1.7–23	8–33	15–41	5–30

*red: above long term, blue: below long term, dashed: mixed below and above long term the long term average, although anomalies of up to +4°C were experienced at two stations. In autumn, warmer-than-average temperatures persisted across the country, while cooler-than-average conditions were limited to a small part in the southeast. The highest positive anomalies were in the northwest and in some parts of the Caspian Sea area, where temperatures were around 2.5°C above the long-term average. Khore-Birjand station in eastern Iran recorded a +6°C anomaly, while Zahedan in the southeast recorded an anomaly of 0.5°C.

Comparing patterns of average seasonal temperatures, anomalies over the country tended to be uniform (except in spring), with the northwest exhibiting larger positive anomalies than other areas. This part of the country is a mountainous area with low average temperatures. Such a pattern has been projected by climate models, as discussed in a joint project by the Atmospheric Science and Meteorological Research Center in Tehran (http://www.asmerc.ac.ir/) and the Climatological Research Institute in Mashhad (http://www.irimo.ir/english/index.asp). In summer, the central part the country was warmer than other regions, where temperatures were mostly below normal.

(B) Precipitation

Iran experienced drier-than-normal conditions for winter, summer, and autumn in 2010 (Table 7.3). Spring, summer, and autumn also received less rainfall in 2010 than in 2009. During winter, areas with average or above-average rainfall (up to 170% of normal) were confined to parts of the northeast, northwest, southeast, and small parts of the Zagross mountains, while the rest of the country received precipitation amounts no more than 90% of normal. However, total winter rainfall in Golpaygan and through western parts of the country was up to 400% of normal. Similar to 2009, the largest total winter rainfall of 450 mm was observed in Koohrang, located in the Zagross mountain area. Through the middle and east of the country, and in localized regions in Hormozgan province (across the Persian Gulf), rainfall was less than 25 mm. In spring, the amount of precipitation was 30%–60% of normal in some parts of the north and southeast, but up to 170% of normal in the west and northwest. Chahbahar station recorded 300% of normal precipitation. In total, spring 2010 was the only season this year in which average precipitation was above the long-term normal. During summer, most parts of the country received below-normal precipitation, although the northwest and some isolated areas elsewhere received above-normal precipitation. While the highest recorded summer precipitation was 323.7 mm in Bandar-Anzali, some widespread areas in different parts of the country (especially west and central areas) received no measured rainfall at all. During autumn, all parts of the country received less than 90% of their normal rainfall.

(C) Notable events

The potential for air pollution increased due to the extent of cold high pressure systems and stable air masses during October and November for many consecutive days, especially in metropolitan and industrial cities including the capital city of Tehran.

Significant dust storms during winter, spring, and summer spread over large parts of south and southwest Iran. Low-pressure systems with very low humidity accompanied by troughs over Iraq and Saudi Arabia and associated with increased wind speeds were the main cause of the dust storms. Eastern and southeastern Iran experienced dust as usual in spring and summer. However, the source of those typical events is completely different to that associated with the dust in the south and southwest.

In 2010, methane gas production from dried leaves, accompanied by low pressure systems over the north of the country, induced a number of forest fires in the Golestan, Mazandaran, and Gilan Provinces.

(iii) Turkey—S. Sensoy and M. Demircan

(A) Temperature

The annual average temperature for Turkey (based on data from 130 stations) in 2010 was 15.54°C. The 2010 mean temperature was 1.95°C above the 1971–2000 average of 13.59°C. Generally, the whole country had temperatures above the mean, with highest anomalies occurring in eastern regions (Fig. 7.45). Positive temperature anomalies have been observed every year since 1994, apart from 1997. Monthly average temperatures during 2010 were above the 1971–2000 average during most months but were near normal in April and October. A negative correlation (-0.30) was found between the North Atlantic Oscillation (NAO) index and Turkey's winter temperature (Sensoy et al. 2010). The NAO was negative during all months of 2010.

(B) Precipitation

Rainfall in Turkey is affected by topography. For example, Rize (located in the eastern Black Sea region) receives an average of 2200 mm precipitation annually

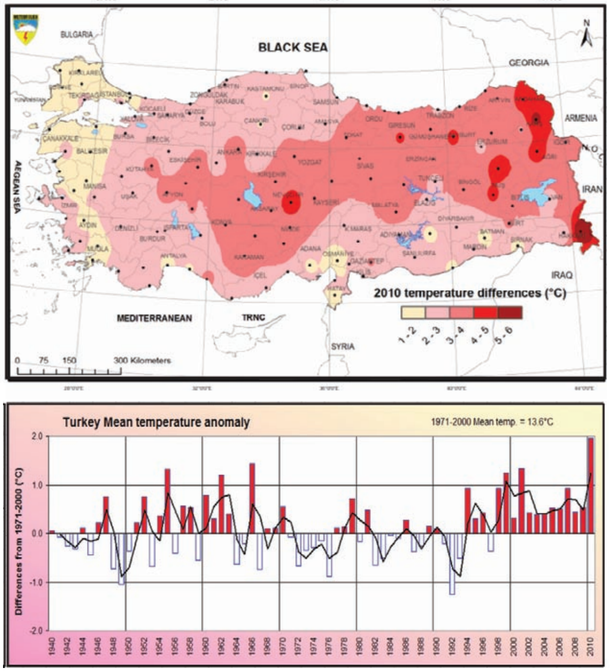

Fig. 7.45. Temperature anomalies for 2010 in Turkey (°C). The top panel shows the spatial distribution of anomalies for 2010 while the bottom panel shows a time series of national average anomalies since 1940.

while Konya (located in central Anatolia) receives an average of only 320 mm (Sensoy 2004).

Average annual total precipitation for Turkey as a whole is about 635 mm. In 2010, the annual rainfall was 729 mm (Fig. 7.46). Generally, western and northeastern parts of the country had precipitation above the mean total, except Southern Anatolia region where slightly-below-normal rainfalls were observed. Large positive anomalies occurred in Bursa, Balikesir, Edremit, and Yalova, with some rainfall events leading to hazardous floods in these cities. Bursa had its wettest year on record [1328 mm, 96% above normal (WMO 2010)].

Monthly precipitation totals were much above normal in January, February, June, October, and December, and below normal in March, April, May, August, and November. A negative relationship was found between Turkey's precipitation and the NAO index (0.50), which is particularly strong in winter and was negative throughout 2010. The NAO affects Turkey's climate more strongly than ENSO (Sensoy et al. 2010).

(C) Notable events

The highest number of extreme events in Turkey since 1940 was reported in 2010 (555 events). There is an increasing trend of 25 events decade^{-1}. The most frequent and hazardous extreme events are storms, floods, drought, and hail. During 2010, nearly half of the extreme event total was made up of storms (46%). Floods were the next most frequent extreme event in 2010 (29%), followed by hail (14%). Although rare, landslides, lightning, tornadoes, and avalanches are other disastrous extreme events that occur in Turkey.

On 13–14 October, 122.8 mm of rainfall was recorded in 24 hours in Bursa. For this amount of rain in 24 hours, the average return interval was estimated to be 200 years (WMO 2010). Similar heavy rainfall occurred again on 27 October. Both events resulted in many floods and landslides. There was one death, and several primary and secondary schools were suspended for two days.

In Rize, extreme rainfall was associated with floods and landslides on 26 August 2010. According to the disaster report, 13 people died, one person was missing, 168 houses were destroyed, and 1729 hectares of fields, roads, and water pipes were damaged. Total economic lost was estimated as 30 million Turkish Lira ($20 million U.S. dollars).

h. Oceania

1) Southwest Pacific—A. Peltier and L. Tahani

Countries considered in this section include: American Samoa, Cook Islands, Fiji, French Poly-

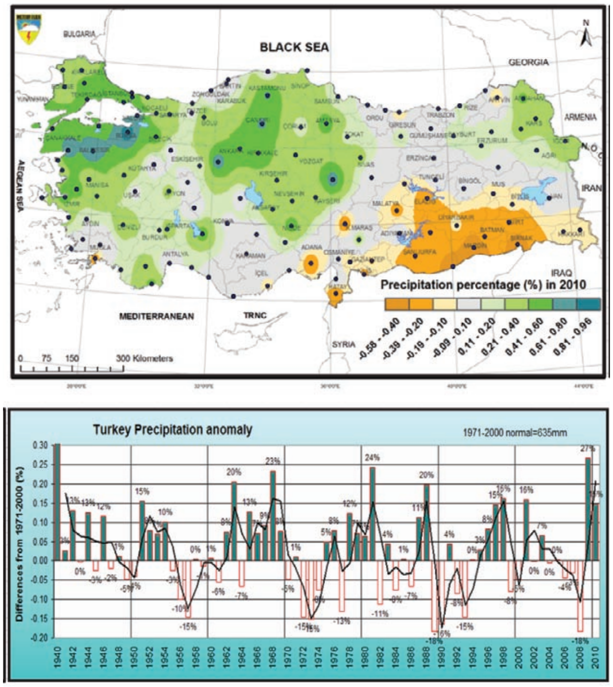

Fig. 7.46. Annual total precipitation anomaly for 2010 across Turkey, expressed as a percent departure from the 1971–2000 normal. The top panel shows the spatial distribution of anomalies for 2010 while the bottom panel shows a time series of national average anomalies since 1940.

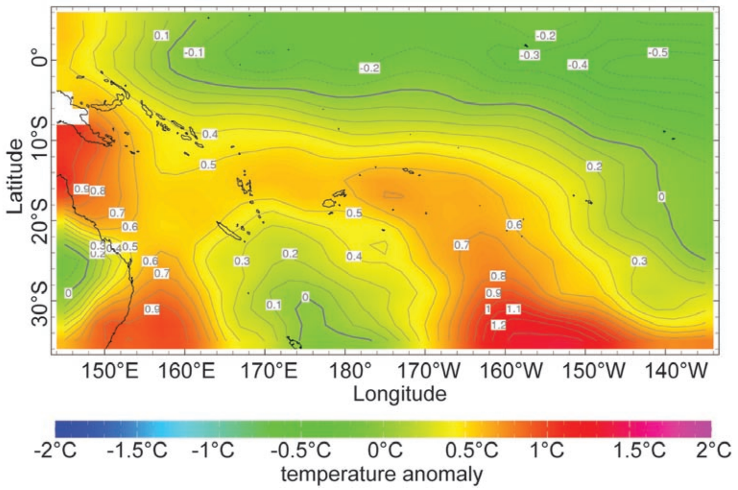

Fig. 7.47. Annual surface air temperature anomalies (°C) for 2010 (1971–2000 base period) over the southwest Pacific from NOAA NCEP.

nesia, Kiribati, Nauru, New Caledonia, Niue, Papua New Guinea, Samoa, Solomon Islands, Tokelau, Tonga, Tuvalu, and Vanuatu. Unless otherwise noted, temperature and precipitation anomalies are relative to a 1971–2000 base period. The year in the Southwest Pacific was strongly influenced by the transition from a moderate El Niño over the southern summer to a strong La Niña in the second half of the year (see section 4bf).

(i) Temperature

Above-average surface air temperatures, with anomalies mostly exceeding +1°C, were recorded at numerous stations in the equatorial Pacific as well in Wallis and Futuna, Samoa, and most of the French Polynesia during austral summer as a result of El Niño. In contrast, an extended area of cooler air (less than 0.5°C below average) encompassed the Solomon Islands, New Caledonia, southern islands of Vanuatu, Fiji, Tonga, Niue, Southern Cook Island, and Austral Islands. With the development of La Niña conditions around July, the temperature pattern reversed with well-below average temperatures restricted to the equatorial Pacific and relatively high air temperatures over most of the southwestern Pacific. On average, surface temperatures were above normal in 2010, since La Niña prevailed most of the year (Fig. 7.47).

(ii) Precipitation

Rainfall patterns over the southwestern (SW) Pacific are heavily influenced by ENSO fluctuations. As 2010 was dominated by two opposite phases of similar intensity, the overall rainfall anomaly was rather weak in most of the SW Pacific (Fig. 7.48). Exceptions were Marquesas, which had drier-than-average conditions (less than 60% of normal rainfall, compared to the 1979–95 base period), and Eastern Kiribati, where heavy rainfalls during the first two months contributed to a slight annual surplus (120% of normal). For most Pacific islands, the rainfall pattern observed in 2010 was fairly typical of El Niño conditions early in the year and representative of La Niña conditions during the second half.

During the first three months of 2010, the Intertropical Convergence Zone (ITCZ) was displaced towards the Equator (section 4f). Convection was then enhanced from west of Nauru across Western Kiribati to Eastern Kiribati, and suppressed over Papua New Guinea. On a smaller scale, the Madden Julian Oscillation (MJO) also contributed to intense precipitation along the Equator with the enhanced phase located across the western and central Pacific from late January to early February. Also consistent with El Niño, the South Pacific Convergence Zone (SPCZ) was shifted eastward during January–March, hence above-average precipitation occurred over the eastern edge of the Solomon archipelago, Tuvalu, Tokelau,

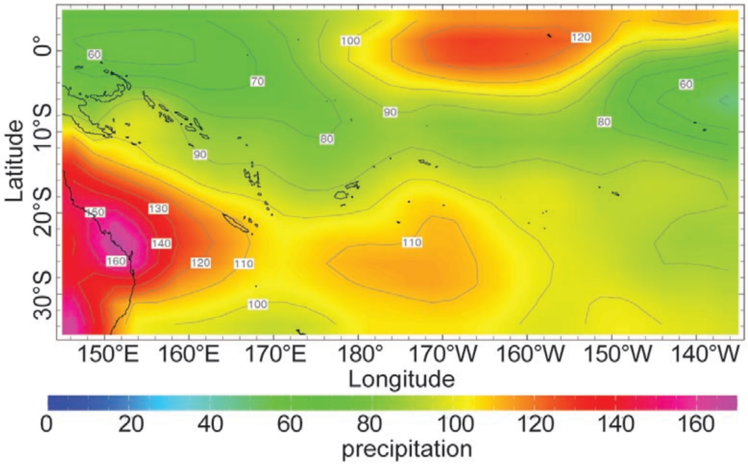

Fig. 7.48. Percentage of average annual rainfall for 2010 (1979–95 base period) over the southwest Pacific from NOAA NCEP CPC CAMS_OPI v0208.

Samoa, Northern Cook islands, and parts of French Polynesia (Society Islands, Tuamotu archipelago, and Gambier islands). Meanwhile, rather dry conditions persisted across New Caledonia, Vanuatu, Fiji, Tonga, Wallis and Futuna, Niue, and Southern Cook Island. These islands did not receive the water supply usually expected during austral summer.

Soon after the decay of El Niño during austral autumn, convection remained suppressed in the equatorial Pacific. As expected during La Niña conditions, mainly below-average rainfall was recorded each month from June to December 2010 in Nauru, Tuvalu, Tokelau, Kiribati, and Marquesas Islands. Heavy precipitation was confined to the very western edge of the equatorial Pacific. Parts of Papua New Guinea and Solomon Islands were affected by a rather contracted SPCZ during austral winter.

In the islands farther south, La Niña effects became apparent during the last quarter of 2010. As the SPCZ was displaced southwest of its normal position, above-average rainfall was recorded in New Caledonia, Vanuatu, Fiji, Tonga, Niue and the Southern Cook Islands, and Austral Islands, whereas precipitation was less abundant over the rest of French Polynesia and the Northern Cook Islands. Over Wallis and Futuna, as well as Samoa, precipitation amounts were near normal during late 2010.

(iii) Notable events

Fourteen synoptic-scale low pressure systems formed in the Southwest Pacific in 2010, seven of them intensifying into tropical cyclones within the SW Pacific basin. Tropical cyclone (TC) activity was prominent during the first quarter of 2010; a single storm developed during the end of year. Because of the El Niño conditions, cyclonic activity was shifted easterly towards the center of the Pacific during the 2009/10 season. Also typical of El Niño, the mean genesis location was displaced towards the Equator.

Tropical Cyclone Oli originated near the Tuvalu archipelago and started its 5000 km-long journey through the southwest Pacific on 29 January. As it moved southeastward, the tropical depression intensified progressively and reached Category 4 status as it passed 300 km west of Society Islands on 3 February. There, hundreds of families coped with damages caused by wind and wind-waves of up to seven meters. The storm's trajectory then turned south toward the Austral Islands. The eye of Oli passed over Tubuai on 5 February, with a minimum sea level pressure of 955.8 hPa and sustained winds of 55 kts (28 m s^{-1}) with gusts up to 92 kts (47 m s^{-1}). Along the northern and northeastern coasts 145 homes were completely shattered by winds and flooding sea water. Oli became the second most intense tropical cyclone recorded in French Polynesia. (The most violent was Orama in 1983 with a minimal pressure recorded at 870 hPa.)

Cyclone Tomas formed in the vicinity of Tokelau on 7 March, moved west, then south and threatened at first Wallis and Futuna archipelago. On 17 March it passed within 100 km of Futuna while a Category 2–3. No casualties were reported but severe damage to coastal areas, crops (80% destroyed), and infrastructure occurred on Futuna. Most traditional "fales" were damaged or destroyed because of wind action and storm surge. Unfortunately, the semi-automatic weather station ran out of battery power early on the 17th and therefore no maximum wind speed were recorded at Futuna's synoptic station. Maximum wind speed was nonetheless estimated at 92 kts (47 m s^{-1}), probably the highest value since 1979. With estimated winds near the center gusting up to 135 kts (69 m s^{-1}), Tomas reached its peak intensity near Vanua Levu (Fiji) while it moved southward. Five thousand people were evacuated in the island's Northern division. Many coastal villagers in this area had their food crops ruined for months because of salt intrusion into the soil (see section 4d6 for more information on the southwest Pacific hurricane season).

2) NORTHWEST PACIFIC, MICRONESIA—C. Guard and M. A. Lander

(i) Overview

This assessment covers the area from the International Date Line west to 130°E, between the Equator and 20°N. It includes the U.S.-affiliated islands of Micronesia, but excludes specific discussions concerning the western islands of Kiribati and the Republic of Nauru. In this Pacific region, the regional climate is strongly influenced by the phase and phase changes of ENSO (section 4b).

Temperature, rainfall, sea level, tropical cyclone distribution, and most other climate variables roughly corresponded to the behavior that would be expected in a year that began as El Niño and then transitioned rather rapidly to a La Niña event. Such years tend to be warm and dry across Micronesia. During the first half of 2010, Micronesia experienced enhanced easterly trade winds, strong subsidence, and dry weather, typical of a post-El Niño year. The mid-year transition to La Niña conditions further enhanced the trade winds, shifting monsoon trough activity and tropical cyclone (TC) development far to the north and west of normal. As a result, Micronesia experienced one of its least active TC seasons on record. Tropical cyclone activity across the whole North Pacific basin was far below normal (50%) and set new historical record lows (see section 4d4).

(ii) Temperature

Average monthly maximum temperatures (maxT) and minimum temperatures (minT) across most of Micronesia have been rising for several decades at a rate that exceeds the reported rise of global average temperature of +0.74°C in the last century. The temperature time series at Guam's Andersen Air Force Base (AAFB) is typical (Fig. 7.49).

The anomalies of maxT and minT across Micronesia during the first and second half of 2010 (Table 7.4) were mostly above normal. However, the minT at two stations, Yap and Pohnpei, has shown a long-term decrease. In keeping with this trend, the minT at Pohnpei was below normal in both halves of 2010, but the minT at Yap during the first and second half of 2010 was +2.08°C and +2.07°C above normal, respectively. While minTs from January through June were expected to be cooler than normal, they were in fact, considerably warmer than normal at several locations, possibly as a result of the higher than normal sea surface temperatures (SSTs) across much of the region.

Table 7.4. Maximum and minimum temperature anomalies and rainfall anomalies for selected Micronesian locations for January through June 2010 (Jan–Jun) and for July through December 2010 (Jul–Dec). Maximum and minimum temperature anomalies are in degrees Celsius per month (°C mo^{-1}) for the indicated periods and rainfall anomalies are in millimeters (mm) for the indicated periods. "N" is the normal rainfall taken from the NCDC 1971–2000 base period. Locations (latitude and longitude) are approximate. NA indicates that the temperature normals are not available from NCDC. Kapinga stands for Kapingamarangi Atoll in Pohnpei State, Federated States of Micronesia (FSM).

Location	**Max Temp Min Temp**		**Rainfall**							
	Jan–Jun	Jul-Dec	Jan–Jun			Jul–Dec			Jan-Dec	
	°C mo^{-1}	°C mo^{-1}	N mm	2010 mm	%	N mm	2010 mm	%	2010 mm	%
Saipan 15°N,146°E	NA	NA	414.8	342.4	82.5	1293.1	1036.8	80.2	1379.2	80.8
Guam 13°N,145°E	+0.29 +0.52	-0.07 +0.28	612.1	466.9	76.3	1555.5	1484.1	95.4	1951.0	90.0
Yap 9°N,138°E	-+0.75 +2.08	+1.12 +2.07	1168.9	804.9	68.9	1818.6	1957.8	107.7	2762.8	92.5
Palau 7°N,134°E	+0.04 -0.22	-0.07 +0.39	1724.7	1030.7	59.8	2043.9	1676.9	82.0	2707.6	71.8
Chuuk 7°N,152°E	+0.63 +1.33	-0.31 +1.23	1538.0	1553.0	101.0	1864.9	2093.2	112.2	3646.2	107.2
Pohnpei 7°N,158°E	+0.35 -0.82	+0.10 -0.10	2277.6	2122.9	91.6	2411.5	2068.8	85.1	4191.8	88.3
Kapinga 1°N,155°E	NA NA	NA NA	1670.8	1956.1	117.1	1123.7	312.9	27.8	2269.0	81.2
Kosrae 5°N,163°E	+0.57 +1.66	-0.47 +0.56	2387.3	20.93.2	79.5	2128.8	1845.8	78.2	3939.0	78.9
Majuro 7°N,171°E	+0.57 +1.91	-0.18 +1.08	1455.4	1517.1	104.2	1888.7	2337.3	123.8	3854.5	115.3
Kwajalein 9°N,168°E	+0.43 +0.80	0.00 +0.14	959.6	660.2	68.8	1590.5	1557.3	97.9	2217.4	87.0

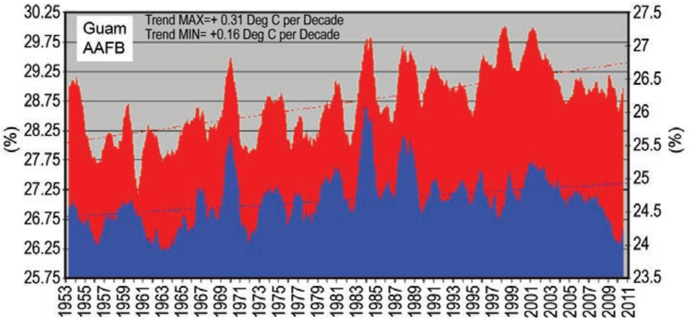

Fig. 7.49. Time series of MaxT (red) and MinT (blue) at Andersen Air Force Base, Guam. Values are 12-month moving average of the monthly averages. General features of this time series are: a substantial warming trend, a peak of MaxT and MinT in the late 1990s, and recent cooling during the 2000s.

Sea surface temperatures around Chuuk and Yap were 1°C–2°C warmer than normal, and this may have influenced their rather large respective average minT anomalies of +1.66°C and +2.08°C. Farther east, Pohnpei experienced January–June maxT anomalies of +0.35°C and minT anomalies of -0.82°C. Still farther east, anomalies at Kosrae were larger (maxT +0.57°C for January–June), as a result of clearer weather and higher SSTs. At the eastern end of the region, Majuro had warmer-than-normal January–June average maxT anomalies of +0.57°C and minT anomalies of +1.91°C. Farther north at Kwajalein, average maxT (+0.43°C) and minT (+0.80°C) anomalies for the first six-month period were both warmer than normal, but not as warm as at Majuro.

Temperatures for July–December were closer to normal than those during the first half of the year at most locations. As in the first half of the year, Yap showed the greatest anomalies with a maxT of +1.12°C and a minT of +2.07°C. MaxT and minT anomalies were small for the last six months of the year at Pohnpei, Kwajalein, and Guam. MaxT and minT anomalies at Chuuk (-0.31°C and +1.23°C), Kosrae (-0.47°C and +0.56°C), and Majuro (-0.18°C and +1.08°C) were larger than normal, especially the minT values.

(iii) Precipitation

Precipitation was typical for a year that begins with El Niño conditions and ends with La Niña conditions. In the first half of the year, the western half of the basin and islands north of 8°N were drier than normal, while most of the islands east of 150°E were either drier than normal or near normal. Palau's rainfall for the first six months was only 59.8% of normal, while Yap was 68.9%, and the rainfall amounts at Guam and Saipan in the Mariana Islands were 76.3% and 82.5% of normal, respectively. Conditions at Kwajalein and Kosrae were also dry with 68.8% and 79.5% of normal rainfall, respectively. Several islands (Chuuk, Pohnpei, and Majuro) experienced near normal rainfall.

During the last half of the year, most locations saw a 20%–30% increase in rainfall over the first half of the year as El Niño gave way to La Niña. From west to east across Micronesia, Palau rainfall increased to 82.0% above normal (a 22.2% increase from the January–June average); Yap rainfall increased to 107.7% (+38.8%); Chuuk increased to 112.2% (+11.2%); Majuro to 123.8% (+19.6%); Kwajalien to 97.9% (+29.1%); and Guam to 95.4% (+19.1%). Rainfall at Pohnpei and Kosrae were less than expected, partly as a result of the unusually far westward and northward extent of the equatorial wedge of cold SSTs and its effect on the trade wind trough.

A major exception to the Micronesian rainfall pattern was at the near-equatorial location of Kapingamarangi Atoll (1°N, 155°E) in Pohnpei State of the Federated States of Micronesia, where it was wetter than normal (117%) during the first half of the year in response to the El Niño-induced equatorial warm SSTs. Once the La Niña pattern set in, warm equatorial SSTs were replaced by a cool tongue of SSTs, and conditions at Kapingamarangi became very dry (27.8% of normal) through the end of 2010 and into 2011. The Weather Forecast Office in Guam issued weekly Drought Information Statements for the Atoll from August 2010 well into 2011.

For the most part throughout Micronesia, rainfall for the first and second halves of 2010 was between 75% and 125% of average. Of the major islands, annual rainfall amounts ranged from a high of 4191.8 mm at Pohnpei (88.3% of normal) to a low of 1379.2 mm at Saipan in the U.S. Commonwealth of the Northern Mariana Islands (80.8% of normal). Palau at the western edge of the area was also dry with 2707.6 mm (71.8% of normal), while Majuro at the eastern edge of the area was wet with 3854.5 mm (115.3% of normal). The six-month and annual rainfall values for selected locations are summarized in Table 7.4. Figure 7.50 shows the annual rainfall amount and percent of normal for the major Micronesian islands.

(iv) Notable events

Tropical cyclone activity in 2010 was at record low levels in the western North Pacific (see section 4d4) and it was virtually non-existent across Micronesia. Only two tropical cyclones developed in Micronesia, and both were in the northwest part of the region.

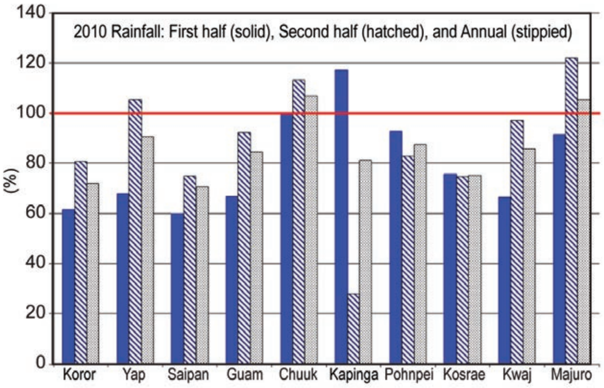

Fig. 7.50. Annual rainfall as a percentage of normal (NCDC 1971–2000 base period) for selected locations on various Micronesian islands for 2010. Kapinga stands for Kapingamarangi Atoll in Pohnpei State, Federated States of Micronesia (FSM).

Neither intensified significantly until after moving west of 130°E longitude and neither tropical cyclone affected populated locations of Micronesia.

The high sea levels that prevailed in 2007 to early 2009 began to fall by mid-2009 as El Niño conditions reduced the easterly wind stress that caused water to mound up in the west of the basin. The development of oceanic Kelvin waves also caused much of the heat content in the upper 300 meters of the ocean to be transported eastward toward Central and South America, reducing ocean volume in the equatorial western Pacific and causing sea levels to fall. This fall in sea level reduced the incidence of destructive coastal inundation events in the Micronesian islands during the latter half of 2009 and early 2010. After La Niña became re-established, the strengthening trade winds increased the easterly wind stress, and once again, water began to mound up in the west of the basin. This caused warm water to mix downward, increasing the oceanic volume and causing sea levels to further rise by the last three months of the year.

After the El Niño peaked in late 2009, sea levels in Micronesia reached their lowest levels around February 2010. The lowest anomalies (compared to the 1975–95 average) occurred in the west at Palau (-16 cm) and Yap (-12 cm) and diminished eastward at Chuuk and Pohnpei to around 0 cm. At some locations, sea level anomalies remained positive, such as at Marshall Island locations where the lowest anomalies were +5 cm, and at Guam (+6 cm). The sea level in Micronesia increased from boreal spring and grew most rapidly towards the end of the year, reaching their highest values in November and December. Average anomalies ranged from +18 cm to +20 cm at Palau, Yap, Chuuk and Guam to +23 cm at Pohnpei. Positive sea level anomalies occurred despite the reduced ocean volume (and reduced sea level) resulting from the cooler-than-normal equatorial SSTs.

3) Australia— C. Ganter and S. Tobin

(i) Overview

Australia experienced its second wettest year on record in 2010. As is typical during strong La Niña events, 2010 brought with it significant flooding, especially in the eastern states. The year was the wettest on record for Queensland and the Murray-Darling Basin, third-wettest for the Northern Territory, New South Wales, and South Australia, and fifth-wettest for Victoria. In stark contrast, southwest Western Australia had its driest year, austral winter (June–August), and growing season (April–October) on record, while Tasmania received near-average rainfall. Unless otherwise noted, anomalies in this section are relative to a 1961–90 base period.

(ii) Temperature

Despite widespread rainfall and increased cloudiness, the national mean temperature for 2010 remained above average (22.0°C, +0.19°C above average). Although this was Australia's coolest year since 2001, the last decade (2001–10) was the warmest 10-year period on record (0.52°C above average). In 2010, overnight minimum temperatures (Fig. 7.51) were the eighth highest on record (0.59°C above average). Mean maximum temperatures (Fig. 7.52) were 0.21°C below average.

Annual maximum temperature anomalies exceeded +0.5°C across most of Western Australia, the far north, and Tasmania. Cool anomalies below -0.5°C were recorded across much of inland New South Wales, Queensland, South Australia, and the Northern Territory. The warmest anomalies were in the west of Western Australia (+1.5°C) and the coolest in the southeastern Northern Territory (2.5°C).

Annual minimum temperatures were above average through most of Australia, especially along the northern coasts, in part due to record high sea surface temperatures. Minimum temperature anomalies exceeded +2.0°C in parts of the Northern Territory and inland of Cairns in Queensland. Below-average minima occurred in southwest Western Australia, around Port Augusta in South Australia, and through areas of interior Australia. The largest negative anomalies (-0.5°C) were in western Queensland.

The largest positive maximum temperature anomalies occurred in February; +5.0°C in areas of the Pilbara and Gascoyne in Western Australia. April

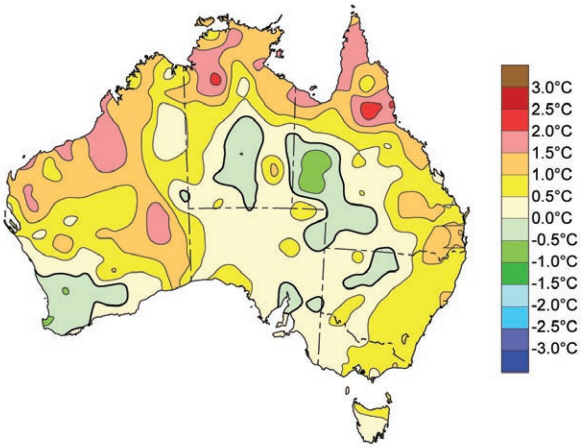

Fig. 7.51. Australian mean annual minimum temperature anomalies (base period of 1961–90) for 2010.

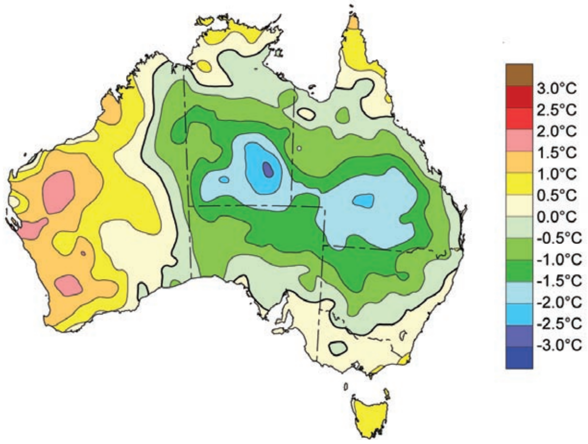

Fig. 7.52. Australian mean annual maximum temperature anomalies (base period of 1961–90) for 2010.

temperatures were above normal, particularly in the west. The Australia-wide, area-averaged April anomaly (+1.68°C) was the second highest on record.

The tropics were particularly warm for July–September, with widespread areas of record high means and minima. The largest positive anomalies were recorded for July, with minima 4°C–6°C higher than usual across large parts of northern Australia. Below-average maxima covered most of the remainder of Australia in September, and most of Australia, except the far west, in October; anomalies of -4.0°C in central Australia were associated with record high rainfall in the region.

Below-average temperatures were most widely recorded in November; maxima were more than 5°C below average across a large area of inland Queensland, while minima were more than 3°C below average in a large area of central Australia.

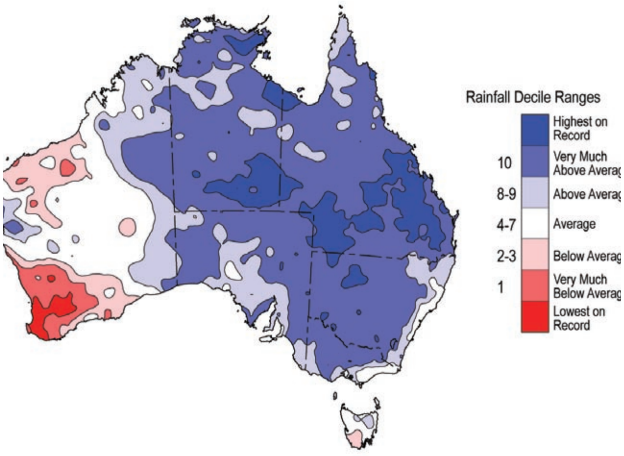

Fig. 7.53. Australian annual rainfall deciles (since 1900) for 2010.

(iii) Precipitation

Australia's mean annual rainfall for 2010 was 701 mm, 51% above average (465 mm) and second highest since records began in 1900. Above-average rainfall was recorded in all months except June. Rainfall was significantly above average in all states except Tasmania and Western Australia (Fig. 7.53). Record totals fell across southern Queensland, parts of central Australia and the far north, New South Wales, Victoria, and South Australia. Southwest Western Australia had its driest year on record—395 mm, well below the previous low of 439 mm set in 1940.

For parts of the southeast, particularly Victoria and South Australia, 2010 was the first year of above-average rainfall since 1996. Similarly, 2010 marked a reversal of dry conditions which had dominated since 2001 across Queensland and New South Wales, including much of the nation's food basket in the Murray-Darling Basin. Areas along the eastern coast of New South Wales and south of the Great Dividing Range in Victoria, where relationships between La Niña and rainfall are weaker, received near-average rainfall.

January–March rainfall was generally above average, especially in northern Queensland and the Northern Territory during January, and across the central interior and east during February and March. However, it was dry in the west of Western Australia, where Perth Airport experienced a record 122 consecutive rainless days between 20 November 2009 and 22 March 2010.

April and May saw above-average rain in much of Australia (except for the east coast and west of Western Australia), including record falls around the Gulf of Carpentaria and central South Australia in April, and in the northwest in May. June rainfall Australia-wide was the fourth-lowest on record, and was the only month in which the tropics saw consistently dry conditions typical of the season.

Record-breaking rain fell in the interior and northwest in July; in northern, central, and eastern Australia in August; throughout northern and central Australia and western New South Wales in October; and was exceptionally widespread in September. November and December saw very-much-above-average rainfall in Queensland, New South Wales, Victoria, and eastern South Australia. Record-breaking December rain fell in southeast Queensland and in a large area of Western Australia around Carnarvon. Averaged over Australia, austral spring (September–November), the July–December period, and December were the wettest on record.

(iv) Notable events

The most notable aspect of Australia's climate during 2010 was the numerous flooding events resulting from the La Niña event (see Sidebar 7.9).

Early in the year, there were two occurrences of severe thunderstorms producing damaging large hailstones. The first, which occurred in Melbourne on 6 March, produced heavy rain, strong wind gusts, and hailstones over 5 cm in diameter across a large area of Melbourne's suburbs, including a 10-cm hailstone, a record for the Melbourne region. There was also widespread severe thunderstorm activity from 5 to 7 March across central and north central Victoria, stretching into southern New South Wales. The second notable occurrence of severe thunderstorms occurred on 22 March in Perth, producing heavy rain, severe winds, and large hail, including a 6-cm hailstone in the northwest suburbs, a record for Perth. Both storms caused insured losses exceeding $1 billion (U.S. dollars).

The northern tropics of Australia experienced very warm temperatures, particularly minima, through winter, with coastal areas and islands strongly influenced by abnormally high sea surface temperatures. On 26 July, Cape Don in the Northern Territory set an Australian record high minimum for July with 26.9°C. Darwin (26.6°C) also broke the previous record. Timber Creek and Bradshaw (both 37.5°C on 30 July) set a new July maximum record for the Northern Territory, just 0.1°C short of the Australian record. Richmond recorded a maximum of 36.1°C on the same day, a Queensland record. In August, Horn Island and Coconut Island in the Torres Strait broke the previous Queensland record high minimum temperature for the month, 25.4°C, on no fewer than 24 separate occasions between them, with 26.8°C at Horn Island, on 19 August, the new record.

While northern Australia was very warm during the 2010 austral winter (JJA), southern Western Australia had persistently low minimum temperatures during late June and early July, associated with unusually dry conditions. Norseman Aerodrome (on the western Nullarbor) recorded a minimum of 6.0°C on 27 June, equaling the Western Australian June record.

Four tropical cyclones made landfall in Australia in 2010, Olga, Paul, Tasha, and Ului. Wind damage was generally minor but all contributed to flooding.

Significant statistics

- Mean annual maximum temperature anomaly: –0.21°C
- Mean annual minimum temperature anomaly: +0.59°C
- Mean annual rainfall anomaly: +51% (second highest of 111-year record)
- Highest annual mean temperature: 29.6°C, Wyndham (Western Australia)
- Lowest annual mean temperature: 4.3°C, Thredbo (New South Wales)
- Highest annual total rainfall: 12 438 mm, Bellenden Ker Top Station (Queensland) – second highest on record (record 12 461 mm, set in 2000 at the same station)
- Highest temperature: 49.2°C, Onslow (Western Australia), 1 January
- Lowest temperature: –19.6°C, Charlotte Pass (New South Wales), 20 July – second lowest on record (record –23.0°C, set on 29 June 1994 at the same station)
- Highest one-day rainfall: 443 mm, Bulman (Northern Territory), 31 March
- Highest wind speed (measured): 202 km hr^{-1}, Hamilton Island (Queensland), 21 March

4) New Zealand—G. M. Griffiths

(i) Overview

Annual mean sea level pressures were above average in the New Zealand region in 2010. The increased prevalence of anticyclones near New Zealand produced a relatively settled and mild climate for the year overall, with average or above-average annual temperatures in all regions, and normal or above-normal annual sunshine hours in most regions. There were relatively few rainfall extremes. The Southern Annular Mode (SAM), which affects the westerly

SIDEBAR 7.9: AUSTRALIA, A LAND OF (DROUGHT AND) FLOODING RAINS—C. GANTER AND S. TOBIN

Note: Many Australians, and visitors to Australia, will be familiar with Dorothea Mackellar's iconic poem "My Country". First published in 1908, the poem describes the breaking of a drought, highlighting the contrast and extremes found within the Australian landscape and climate. The well-known second stanza, from which the title of this box is derived, is given below-

I love a sunburnt country,
A land of sweeping plains,
Of ragged mountain ranges,
Of droughts and flooding rains.
I love her far horizons, I love her jewel-sea,
Her beauty and her terror -
The wide brown land for me!

Australia experienced flooding across many regions during 2010. Much of the flooding occurred in the second half of the year, during the strong La Niña event in the Pacific. In addition, record high tropical sea surface temperatures near Australia for 2010, partly associated with La Niña, fed extra moisture into the region. The flooding events listed here are the most significant for 2010, but by no means represent an exhaustive list.

The first major flooding for the year occurred in late February and early March. A monsoon low passed over the Northern Territory and into southern Queensland, continuing through northern New South Wales. This system produced heavy rainfall in its path, resulting in widespread, and in places record-breaking, flooding. Major flooding occurred in most of the catchments in southern inland Queensland, and some of these areas had their highest river peak on record. The rainfall on 2 March 2010 was Queensland's wettest day on record (area-average of 32 mm) and daily falls exceeded 100 mm over 1.9% of the country (a record), indicating the wide extent of the heavy rains. This event also brought significant flooding downstream in northwest New South Wales, with some areas remaining affected by flood waters well into April.

The second major flooding event occurred during September in northern Victoria. A complex low pressure system moved over Victoria on 3–4 September, producing widespread heavy rainfall along and north of the Divide. Some locations in northern Victoria had new record flood peaks as a result of this event. There were further floods on various rivers in northern Victoria and southern New South Wales over the following weeks. Although these were generally less significant, an event in mid-October caused substantial damage in parts of the Riverina region of New South Wales.

The Gascoyne region, located along the central coast of Western Australia, stretching inland, experienced one of the most extreme rainfall events in 2010. A monsoon low passed over the region during mid-December, producing heavy falls and flooding. Carnarvon Airport recorded 207.8 mm on 17 December, almost tripling its annual rainfall total to date in one day and far surpassing its previous daily record of 102.6 mm on 13 July 1998. Historically, rainfall events during December in this region are rare. Besides a single daily total of 77 mm during 1995, prior to this event Carnarvon Airport hadn't recorded a December total above 6 mm in its 66 years of record.

The final major flooding event of 2010 continued through the last weeks of the year, and was the result of four rain events affecting eastern Australia between late November through to the end of December (flooding continued into early 2011). These rain events were mostly the result of persistent inland troughs over eastern Australia; however one was the result of a combination of moist easterly flow over Queensland, with further moisture brought in by the circulation associated with Tropical Cyclone Tasha. The most severe flooding occurred in Queensland and far northern and central western New South Wales during the last week of December, with downstream impacts continuing into January 2011. These events resulted in the wettest December on record for Queensland and eastern Australia as a whole (includes Queensland, New South Wales, Victoria and Tasmania). See Fig. 7.54 for Australian December rainfall deciles[3] .

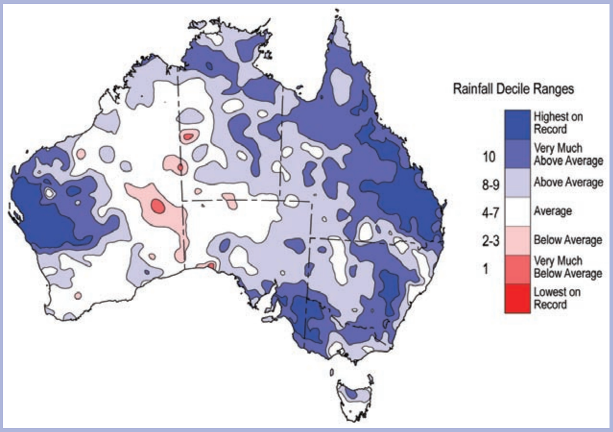

Fig. 7.54. Australian rainfall deciles for December 2010.

---

[3] Australian rainfall deciles based on a 111-year climatology of gridded fields from 1910 to 2010. Decile range 1 means the lowest 10% of records, decile range 2 the next lowest 10% of records,..., decile 10 the highest 10% of records.

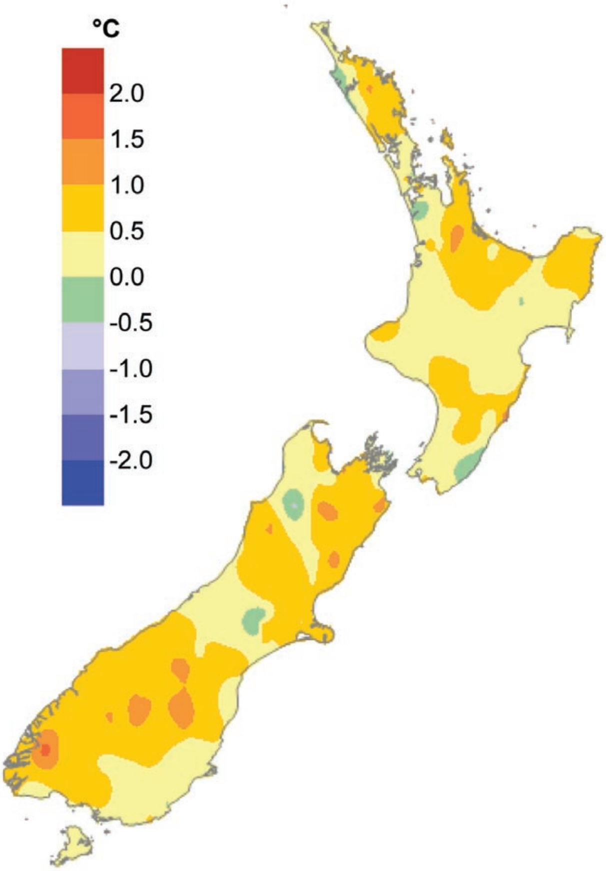

Fig. 7.55. New Zealand annual mean temperature anomaly (°C) for 2010 relative to 1971–2000 average.

wind strength and location over and to the south of New Zealand, was strongly positive overall in 2010, and contributed to the prevalence of anticyclones experienced over the country. In the following discussion, the base period is 1971–2000 for all variables. The New Zealand national temperature is based upon a seven-station record found at http://www.niwa.co.nz/our-science/climate/news/all/nz-temp-record/seven-station-series-temperature-data.

(ii) Temperature

Mean annual temperatures (Fig. 7.55) were above average (between 0.5°C and 1.2°C above the long-term average) in the northeast of the North Island and for much of the South Island (Nelson, Marlborough, parts of Canterbury, Fiordland, parts of Westland, the southern Lakes District, and central Otago). Mean annual temperatures were near average elsewhere (within 0.5°C of the long-term average). The national average temperature for 2010 based on a seven-station series was 13.1°C, 0.5°C above the 1971–2000 annual average. The year 2010 was the fifth warmest year since 1900, based on this seven-station series.

Of the 12 months of 2010, seven (February, April, May, August, September, November, and December) were warmer than normal, one (October) was cooler than normal, and four (January, March, June, and July) were near normal. The largest positive anomalies were in the northeast of the North Island (Northland, Auckland, and Bay of Plenty), in the northeast of the South Island (Marlborough and north Canterbury), and in Fiordland and central Otago.

(iii) Precipitation

Annual rainfall totals for 2010 were in the near-normal range (80%–119% of normal) across most of New Zealand. The exceptions were eastern parts of the North Island (specifically Coromandel, parts of the Bay of Plenty, Gisborne, Hawke's Bay, and Wairarapa), Blenheim, parts of North Canterbury, and southwest Fiordland, which experienced above normal annual rainfall (with totals greater than or equal to 120% of normal). In contrast, areas of Northland, Auckland and Waikato, Otago, the Lakes District, and parts of the West Coast and Buller recorded below normal annual rainfall totals (between 50% and 79% of normal).

Dry conditions predominated in many areas during February–April, July, and in October–November. The year began and ended with very large soil moisture deficits and drought conditions in several North Island regions, and in parts of the east of the South Island. January, May, August, and September saw predominantly wet conditions in many regions. There was also significant rainfall in the last week of December, affecting mostly western regions and the Nelson/Marlborough area (northern South Island). The highest recorded rainfall for the year was at Cropp River in the Southern Alps (12 374 mm), while the lowest recorded rainfall total was 345 mm at Alexandra in Central Otago.

(iv) Notable Events

Notable climate features of 2010 (in various parts of the country) included two droughts, several heat waves, and four significant rainfall events. Drought was declared in January in Northland, and in Auckland, Waikato, Bay of Plenty, South Taranaki, South Canterbury, and Otago during April. The drought broke in May, only to be declared again in December in Northland, Waikato, and the Ruapehu District.

Heat waves affected the West Coast at the end of January, Central Otago on 8–9 March, and numerous locations on 28–30 November, 12–15 December, 22 December, and 27 December. Many all-time station maximum temperature records were set during these events.

Exceptionally heavy rain occurred on 31 January in the northeast North Island. Widespread heavy rain and flooding occurred in the southwest South Island from 25–27 April, resulting in flood-threshold levels of Lake Wakatipu; and a sustained period of heavy rain during 24–30 May in the eastern South Island caused numerous floods, slips, road and property damage. On 28 December, heavy rain, flooding, and high winds caused havoc for many areas of the country.

An extremely significant snowfall event occurred during 15–23 September, with heavy snowfalls, high winds, and extremely cold conditions observed in the southwest of the South Island. On 18 September, conditions were particularly extreme, causing the roof of Stadium Southland in Invercargill to collapse due to snow. Other parts of Southland were also affected, meaning milk was unable to be collected because of dangerous roads, and thousands of lambs were lost across the region.

Significant statistics

- The highest annual mean temperature for 2010 was 16.5°C, recorded at Whangaparaoa (Auckland).
- The lowest annual mean temperature (not including remote alpine sites) for 2010 was 8.0°C, recorded at Chateau Ruapehu (central North Island).
- Of the regularly reporting gauges, Cropp River in the Hokitika River catchment (West Coast) recorded the highest annual rainfall total of 2010, with 12 374 mm.
- The driest of the regularly reporting locations was Alexandra (Central Otago), which recorded 345 mm of rainfall in 2010.
- Milford Sound experienced the highest 1-day rainfall in 2010 (314 mm), recorded on 25 April.
- The highest recorded air temperature in 2010 was 35.6°C, observed at Cheviot on 22 February.
- The lowest recorded air temperature for 2010 was -12.6 °C, recorded at Lake Tekapo on 10 August.
- The highest recorded wind gust for 2010 was 217 km hr^{-1} at Baring Head, Wellington, on 12 March (a new all-time record there).

8. SEASONAL SUMMARIES—M. Halpert

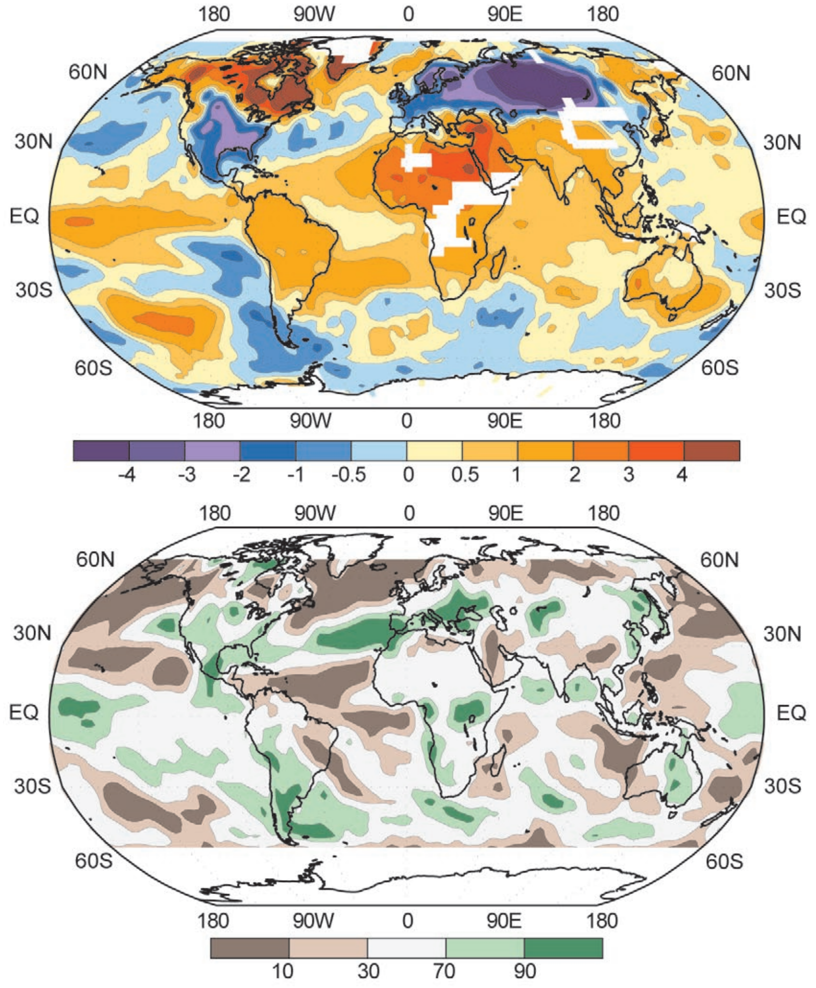

Fig. 8.1. Dec 2009–Feb 2010 (top) surface temperature anomalies (°C) and (bottom) precipitation percentiles based on a gamma distribution fit to the 1979–2000 base period. Temperature anomalies (1971–2000 base period) are based on station data over land and sea surface temperature data over water. Precipitation data were obtained from the CAMS-OPI data set that is a combination of rain gauge observations and satellite-derived estimates (Janowiak and Xie 1999). Analysis was omitted in data-sparse regions (white areas).

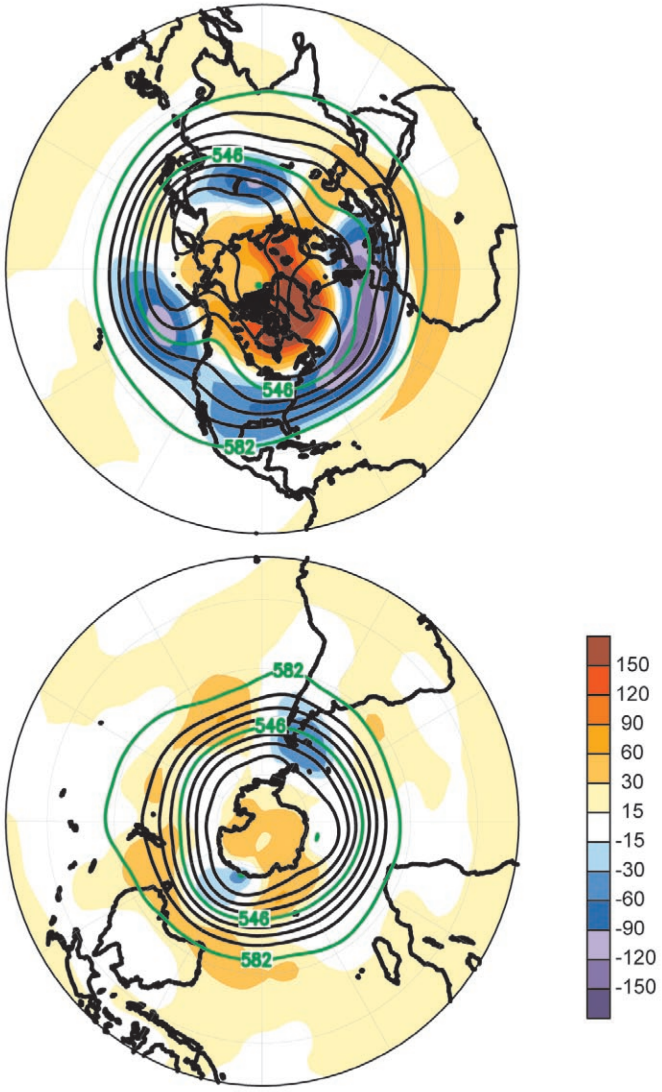

Fig. 8.2. Dec 2009–Feb 2010 (top) Northern Hemisphere and (bottom) Southern Hemisphere 500hPa geopotential heights (9-dam contour interval) and anomalies (shading) determined from the 1979–2000 base period means. Data is from the CDAS/Reanalysis Project (Kalnay et al. 1996).

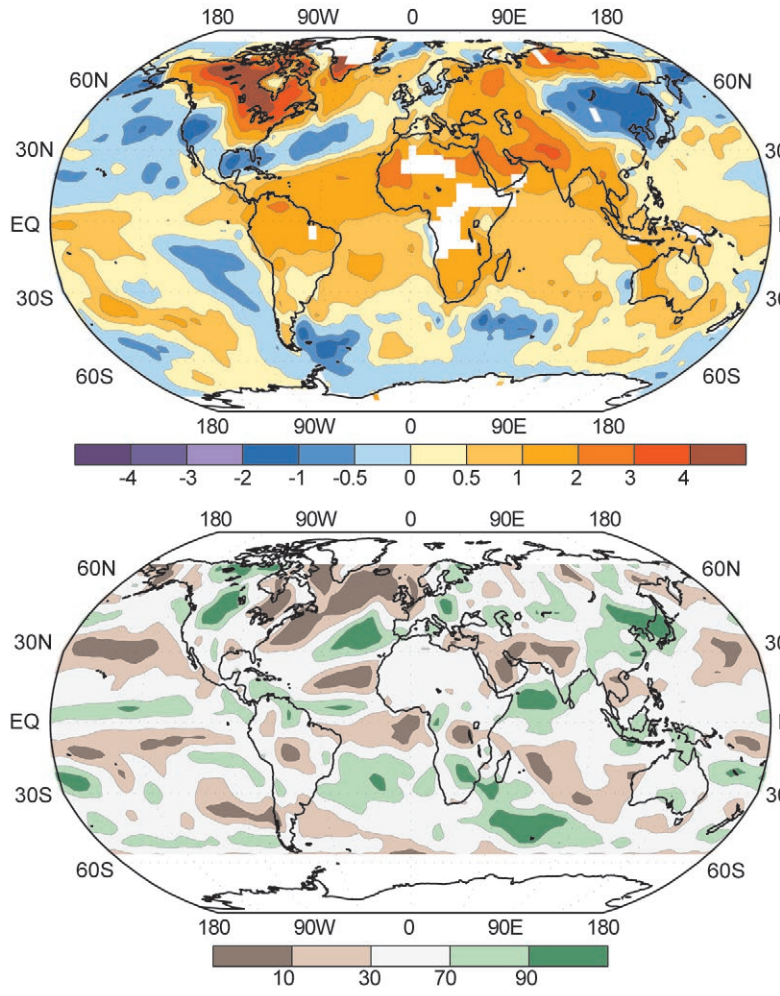

Fig. 8.3. Mar–May 2010 (top) surface temperature anomalies (°C) and (bottom) precipitation percentiles based on a gamma distribution fit to the 1979–2000 base period. Temperature anomalies (1971–2000 base period) are based on station data over land and sea surface temperature data over water. Precipitation data were obtained from the CAMS-OPI data set that is a combination of rain gauge observations and satellite-derived estimates (Janowiak and Xie 1999). Analysis was omitted in data-sparse regions (white areas).

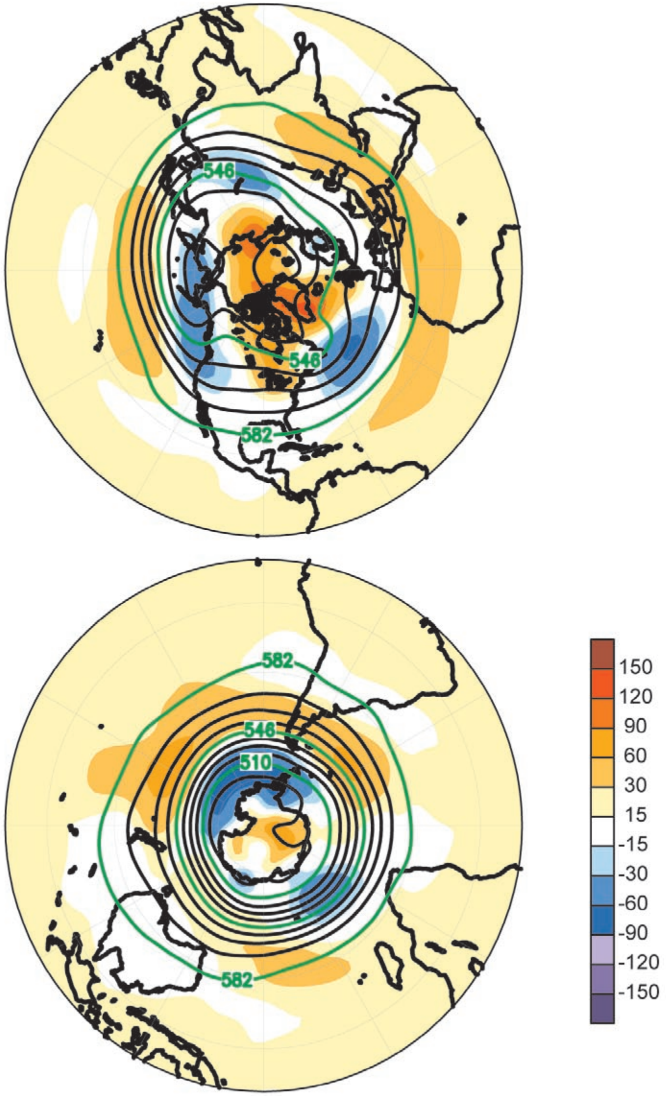

Fig. 8.4. Mar–May 2010 (top) Northern Hemisphere and (bottom) Southern Hemisphere 500hPa geopotential heights (9-dam contour interval) and anomalies (shading) determined from the 1979–2000 base period means. Data is from the CDAS/Reanalysis Project (Kalnay et al. 1996).

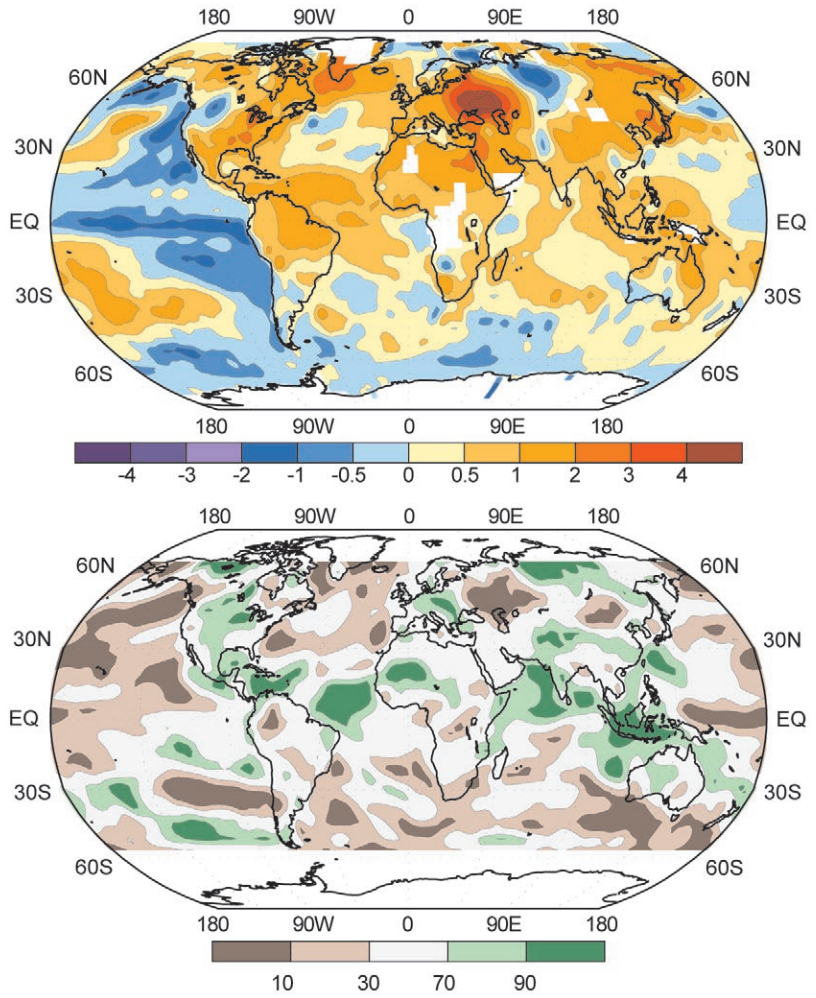

Fig. 8.5. Jun–Aug 2010 (top) surface temperature anomalies (°C) and (bottom) precipitation percentiles based on a gamma distribution fit to the 1979–2000 base period. Temperature anomalies (1971–2000 base period) are based on station data over land and sea surface temperature data over water. Precipitation data were obtained from the CAMS-OPI data set that is a combination of rain gauge observations and satellite-derived estimates (Janowiak and Xie 1999). Analysis was omitted in data-sparse regions (white areas).

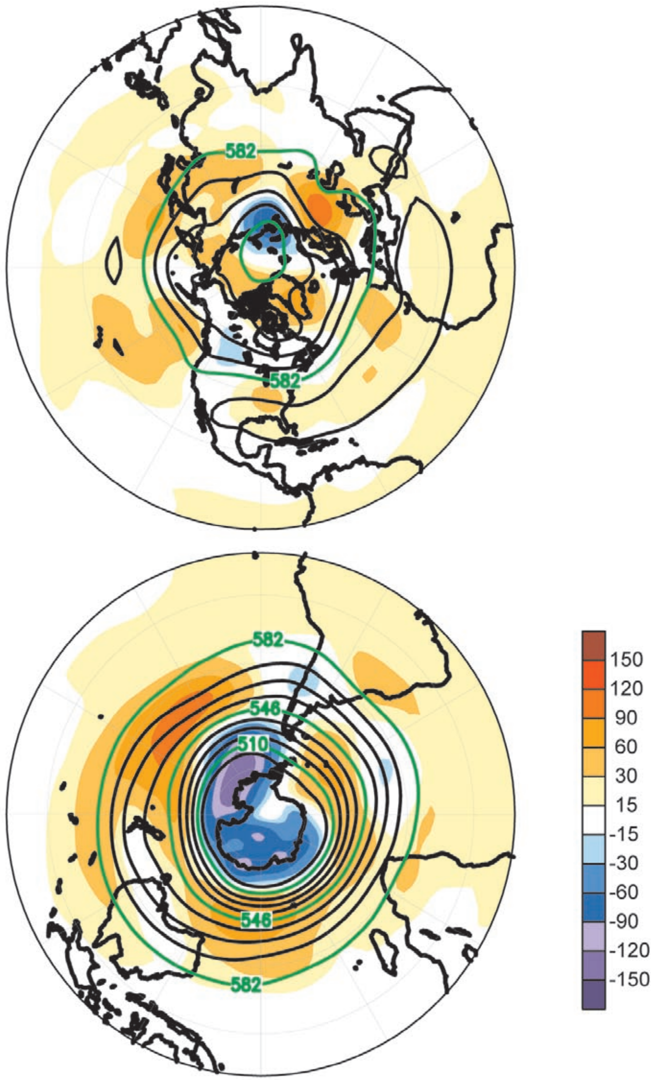

Fig. 8.6. Jun–Aug 2010 (top) Northern Hemisphere and (bottom) Southern Hemisphere 500hPa geopotential heights (9-dam contour interval) and anomalies (shading) determined from the 1979–2000 base period means. Data is from the CDAS/Reanalysis Project (Kalnay et al. 1996).

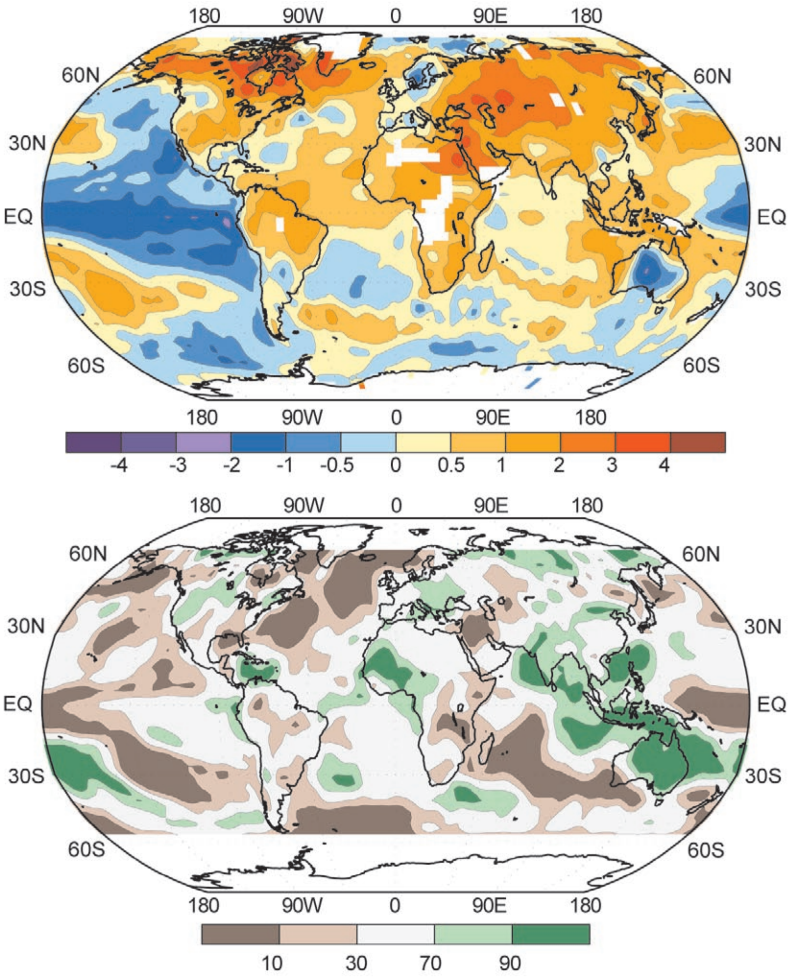

Fig. 8.7. Sep–Nov 2010 (top) surface temperature anomalies (°C) and (bottom) precipitation percentiles based on a gamma distribution fit to the 1979–2000 base period. Temperature anomalies (1971–2000 base period) are based on station data over land and sea surface temperature data over water. Precipitation data were obtained from the CAMS-OPI data set that is a combination of rain gauge observations and satellite-derived estimates (Janowiak and Xie 1999). Analysis was omitted in data-sparse regions (white areas).

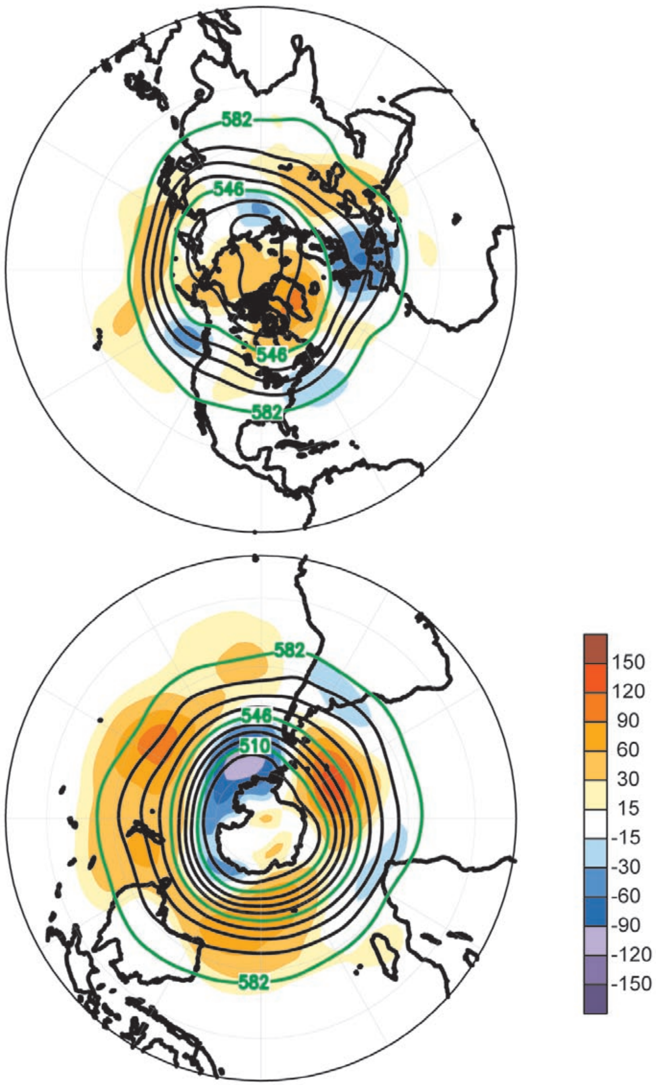

Fig. 8.8. Sep–Nov 2010 (top) Northern Hemisphere and (bottom) Southern Hemisphere 500hPa geopotential heights (9-dam contour interval) and anomalies (shading) determined from the 1979–2000 base period means. Data is from the CDAS/Reanalysis Project (Kalnay et al. 1996).